Sixteen Research Reports

BY THE NIELS BOHR FELLOWS OF THE
ROYAL DANISH ACADEMY OF SCIENCES AND LETTERS
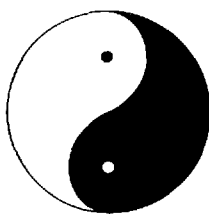
Part One: *Ten Papers in the Exact Sciences and Geology*

When appointed Knight Grand Cross of the Order of Dannebrog,
Niels Bohr chose for his coat-of-arms the Taoistic Yin-Yang symbol of
Complementarity and Harmony and the words
Contraria sunt complementa.

All contributions to this volume
were submitted to the editor before February 1st, 1985.

Contents of Part One

Contents of Part Two

Foreword

On the occasion of the centenary of the birth of Niels Bohr, the Royal Danish Academy of Sciences and Letters herewith publishes 16 treatises, where the »Niels Bohr Stipendiater« of the Academy give accounts of the main themes and progress of their work. The papers are presented in two separate volumes, of which Part One concerns the exact sciences and geology, while Part Two comprises the biological sciences.

This introduction to the two volumes is intended to describe both the background for the creation of the Niels Bohr Fellowships and the manner in which the Academy has supported the work of the Niels Bohr Fellows.

The general background is connected with the economic recession in Denmark during the last decade. As a consequence of the recession, Danish universities were subjected to annual reductions in their budgets, which has led to an increasingly difficult situation for basic research. Numerous temporary or part-time positions have been abolished as have new positions. Vacancies due to retirement have not been filled, and it became hard to obtain support for new equipment. The outstanding feature of the mounting crisis has been the lack of renewal in the scientific community, within both the natural sciences and the humanities. Many of the young, talented researchers have had to give up their scientific career, or to leave Denmark, because no university positions were available.

In 1981 early preparations for the Niels Bohr Centenary were started at the Niels Bohr Institute. It seemed natural to hope for some economic support from wide circles within Danish society. The industrial leader Dr. Haldor Topsøe was one of the first prospective donors to be contacted by Aage Winther from the Institute. Dr. Haldor Topsøe asked which problem at the Niels Bohr Institute was the most urgent one. When it was realized that the need was primarily the recruitment of young, talented physicists, the idea of research fellowships came into focus. Since the problem was a general one, not limited merely to physics, and since it would be in the spirit of Niels Bohr's conception of the Unity of Knowledge to regard all sciences as one common venture, it became clear that the fellows, Niels Bohr Fellows, ought to belong to all fields of basic science. Moreover, because of the urgency of the problem,

it was deemed necessary to establish the fellowships as soon as possible. Finally, the funds collected from private sources and the resulting fellowships could hardly be given directly to the government and channelled through the ministries to universities and research institutes. Being an independent institution, the Royal Danish Academy of Sciences and Letters became a natural choice for the guardian of the fellowships. In this way one also hoped to encourage the Danish government to reconsider seriously the problem of recruitment and renewal in the sciences.

In the winter 1981/82 the Niels Bohr Stipend Committee was set up, comprising three prominent citizens, Mr. NIELS ARNTH-JENSEN, Director of F. L. Smidth & Co., Ltd., Dr. ERIK HOFFMEYER, Director of the Danish National Bank, and Dr. HALDOR TOPSØE, Director of Haldor Topsøe, Ltd., as well as two scientists of renown, BENGT STRÖMGREN and H. H. USSING. Aage Winther acts as Secretary to the Committee, while Christian Crone and Ben Mottelson were advisors during its initial work.

The five Committee Members made contact with a number of companies, banks, and private foundations, and within a few months a total sum of some 12 mill. D.kr. was raised by a concerted effort. This remarkable result was due to the immediate and positive response from the following donors:

THE AUGUSTINUS FOUNDATION
BIKUBENFONDEN
DANFOSS, LTD.
DEN DANSKE BANK
THE DANISH SUGAR CORPORATION
THE EGMONT H. PETERSEN FOUNDATION
THE F. L. SMIDTH & CO. DONATION FOUNDATION
HAFNIA HAAND I HAAND
HALDOR TOPSØE, LTD.
THE KNUD HØJGAARD FOUNDATION
COPENHAGEN HANDELSBANK
THE NOVO FOUNDATION
PRIVATBANKEN
THE ROCKWOOL FOUNDATION
FOUNDATION OF SCANDINAVIAN TOBACCO COMP.
SPAREKASSEN SDS
THE THOMAS B. THRIGE FOUNDATION
THE TJÆREBORG FOUNDATION
THE TUBORG FOUNDATION

It was assumed that fellowships should be for a period of about three years. Therefore, the amount of 12 mill. D.kr., paid by the donors in three yearly instalments, would suffice for the payment, including overheads, of more than a dozen fellows. However, the number of fellows could not be immediately fixed, due to uncertainty with regard to inflation and salary changes.

The Niels Bohr Stipend Committee asked the Academy to take over the responsibility for the funds as well as for the selection and care of the Niels Bohr Fellows, stipulated to all be within the natural sciences. The Academy accepted this responsibility at its meeting on April 15, 1982, where a Steering Committee was elected. The Committee has the following members:

> Erik Dal, editor
> Jes Forchhammer, secretary
> Jens Lindhard, chairman
> Ove Sten-Knudsen
> Henning Sørensen
> Aage Winther.

Mr. Hans Kloch, Head of Department, The Danish National Bank, acts as associated member of the Steering Committee and accountant of the funds. His assistance, foresight, and the apparently effortless way in which he has taken care of the funds, are highly appreciated by all.

The fellowships were proclaimed open for applications within the natural sciences, by younger scientists who, although suitably qualified, had not yet acquired a permanent position at a university or research institute. In response, and to our surprise, as many as 130 applications for fellowships were received. It turned out that most of the applicants were well qualified for the fellowships. This large number of candidates clearly showed the need for further openings for promising scientists.

The Academy had already selected a group of members who were to evaluate the applicants: Svend Olav Andersen, Hans Jørgen Hansen, Kjeld Marcker, C. Overgaard Nielsen, Morten Simonsen, Ove Sten-Knudsen, Diter von Wettstein, Thor A. Bak, Ove Nathan, Gert Kjærgård Petersen, Henning Sørensen, and Poul Erik Nissen.

In consequence of the careful and rapid work of the evaluation group, the Steering Committee could finally propose 16 candidates for Niels Bohr Fellowships. This number of fellows is somewhat larger than originally expected, the reason for the increase being that, in Denmark, the rate of inflation was gradually becoming less serious. The Niels Bohr Fellows are:

Lars Døvling Andersen
Torben Dabelsteen
Thomas Døssing
Else Marie Friis
Jørgen Frøkjær-Jensen
Preben Bach Holm
Claus Schelde Jacobsen
Hans Plesner Jakobsen
Jens Kirkeskov Knude
Jens Konnerup-Madsen
Birger Lindberg Møller
Peter Eigil Nielsen
Hans Uffe Petersen
Jon Steen Petersen
Irene Shim
Hans Lomholt Skriver.

The candidates commenced their fellowship at the earliest opportunity, most of them in the beginning of 1983. Since that time, the Niels Bohr Fellows and the Steering Committee have met regularly in the Academy and in various research institutes, at which meetings the fellows have given accounts of their work in colloquia, and practical problems have been discussed. In particular, subject to approval by the Steering Committee, each fellow has at his disposal an overhead of some 25.000 D.kr. per year, for purchase of scientific equipment, for travels, for guests, etc. Several of the Niels Bohr Fellows have used a considerable part of their fellowship abroad, mainly at research institutions in the US.

Since the Steering Committee has to take care of the fellows in many ways, economic as well as scientific, there has been a close contact with all fellows. Here, Jes Forchhammer, as secretary of the Steering Committee, and Erik Dal, as editor, have been responsible for a sustained and impressive effort.

During the last year, a number of fellows have acquired tenure positions. Although they no longer receive a salary from the Academy, they still continue as Niels Bohr Fellows in all other respects. Partly because of the consequent savings of salaries, the remaining fellowships can be prolonged somewhat beyond the stipulated three years.

All who have taken part in it, have felt the success of the small scientific community formed by the Niels Bohr Fellows. The external mark of the efforts of this community is to be found in the present two volumes, published on the centenary of the birth of Niels Bohr, and

containing accounts of their scientific work by all of the fellows. The publication of the two volumes is one proper way of expressing our gratitude, primarily to all donors and to the Niels Bohr Stipend Committee, but also to all others who have contributed to the success of the Niels Bohr Fellowships. At the same time it is hoped that the two volumes show that scientific work and collaboration in the spirit of Niels Bohr still continues.

JENS LINDHARD.
President of the Academy.

The Authors

Hans Plesner Jakobsen
was born in 1949 and studied at the University of Aarhus, obtaining the degree of cand.scient. in mathematics in 1974. In 1976 he acquired the Ph.D. from Massachusetts Institute of Technology, Cambridge, Mass., on a thesis with the title: *Conformal Harmonic Analysis and Intertwining Differential Operators.* His Ph.D. advisor was I. E. Segal. He was then employed 1976-79 as an Assistant Professor at Brandeis University, Waltham, Mass., and returned to Denmark 1979, where, during the period 1979-1982, he held various Danish University fellowships. In 1983 he became a Niels Bohr Fellow, but already in 1984 he obtained an associate professorship at the Mathematical Institute at the University of Copenhagen.

Through his thesis Plesner Jakobsen has initiated an investigation of the unitarizability of highest weight modules, of covariant differential operators, and of applications of these concepts into mathematical physics. Major results include a full description of the set of unitary holomorphic (positive energy) representations on hermitian symmetric spaces as well as a description of all homomorphisms between generalized Verma modules originating or terminating in scalar modules.

Specific results about wave and Dirac operators in relation to the conformal group have been obtained in joint work with M. Vergne. Further results for this group as well as applications towards modular forms have been reached in collaboration with M. Harris. In recent work with K. Kac, results concerning the unitarizability of modules over Kac-Moody algebras have also been established.

He has given invited talks at international meetings and is a referee for scientific journals and for the National Science Foundation (USA).

Lars Døvling Andersen
was born in 1950 and studied at the University of Aarhus, obtaining his degree of cand. scient. in 1975. He pursued his studies in England at the University of Reading and got his Ph.D. in 1979; his thesis was entitled *Latin Squares and Their Generalizations;* later, he spent a period at the Department of Mathematics at the University of Toronto.

In periods, Andersen has been teaching at Aarhus University and the Technical University of Denmark (Danmarks tekniske Højskole, DTH); as a Niels Bohr Fellow he was in 1984 affiliated to Aalborg University Centre, where he has now been appointed Assistant Professor as from February, 1986.

Andersen's main mathematical interests are graph theory and combinatorics, and he has been particularly interested in various ways of colouring the edges of a graph and in completing and embedding partial latin squares and partial Steiner triple systems, as well as in the interrelation between these topics. His thesis contains contributions to all of these areas. Earlier papers on edge-colourings of graphs include new bounds on the chromatic index and on the cover-index of a graph.

More recently, in collaboration with A. J. W. Hilton and C. A. Rodger, he has solved the embedding problem for partial latin squares with prescribed diagonal, and with A. J. W. Hilton he has proved a strengthening of the famous Evans conjecture characterizing all non-completable partial latin squares of side n with at most n cells occupied (this result is improved further in the present volume). With E. Mendelsohn, Andersen has given a construction for latin squares of side n without proper subsquares for all n not of the form $2^a 3^b$.

He has been active as lecturer and organizer of international meetings within his field of research.

Jens Kirkeskov Knude

was born in 1946 and studied at the University of Copenhagen, where he obtained his cand. scient. degree in 1975. After his degree he continued as a stipendiate at the University Observatory until 1981. In 1980 he obtained the Dr. of Science degree from the University of Copenhagen on a thesis with the title *Properties of the Local Interstellar Medium as Deducted from uvbyβ Photometry of A and F Stars in 84 Small Volumes*. After a short employment at the University of Aarhus he became a Research Fellow of the Danish Space Board until 1983, when he obtained a Niels Bohr Fellowship. In 1985 he became Assistant Professor at the University of Copenhagen.

Jens Knude's field of research is observational astronomy and he has spent long periods at the astronomical observatories at la Silla in Chile, Kitt Peak in Arizona, Mitzpeh Ramon in Israel, la Palma on the Canary Islands, and most lately as a Niels Bohr Fellow at San Pedro Martir in Mexico. Through these observations he has obtained data for the study of the existence, distribution, and physical properties of local interstellar

material. Among the objectives are the search for dust features with linear dimensions smaller than 1 pc and particularly the dust distribution in the obvious windows to the universe, the galactic poles.

The dust structures are discovered by means of coherent color excesses resulting from observations of stars in fine networks. Any clear understanding of the spatial distribution of the local matter has not been obtained so far. On the contrary new data, for about 9000 lines of sight, indicate that the local material is dispersed in a more complex manner than anticipated.

Thomas Døssing

was born in 1947, and studied at the University of Copenhagen, where he obtained the cand. scient. degree in 1974. From 1975 he held a candidate stipendium at the Niels Bohr Institute until he (1977-78) obtained a Max-Planck-Institute stipendium to work at the Max-Planck-Institut für Kernphysik in Heidelberg. After his lic.scient. (Ph.D.) thesis from 1978, which dealt with angular distributions and correlations in statistical nuclear gamma-decay, he was employed as a Nordita fellow 1979-82 and as a Staff Scientist at Lawrence Berkeley Laboratory, University of California 1982-83. He became a Niels Bohr Fellow from September 1983, but stayed at Lawrence Berkeley Laboratory until August 1984.

The main theme of Døssing's scientific work has been the study of rapidly rotating nuclei, and especially nuclear states for which the angular momentum is aligned with the symmetry axis of the density distribution. The cascades of particles emitted from rotating nuclei was the subject of his thesis from 1978 and this subject was followed up in 1981 by a general formulation of angular correlations in direct nuclear reactions.

One of the ways in which nuclei attain a high angular momentum is through strongly damped nuclear reactions. In 1978 Døssing showed in collaboration with Carlos Dasso and Hans Christian Pauli that the Hartree-Fock approximation to this problem was inadequate to describe the observed spread in mass distribution in such reactions. In a fruitful collaboration with Jørgen Randrup in Berkeley he very successfully used a nucleon transfer transport theory to account for the dynamical evolution of the angular momentum in damped nuclear reactions which has lead to new insight in the relaxation phenomena in these reactions.

During the ten years from 1975-1985 he has been invited speaker at more than ten international conferences and summer schools, and has published seven scientific papers during his time as a Niels Bohr Fellow.

Irene Shim

was born in 1945 and studied at the University of Copenhagen and later at the Technical University of Denmark (Danmarks tekniske Højskole, DTH), obtaining the degree lic.techn. (Ph.D.) in 1977. The title of her dissertation was *The Electronic Interaction between Two Nickel Atoms and the Underlying Theory*, and her superviser was Professor Jens Peder Dahl. Her work has mainly been concentrated on employing the most sophisticated quantum chemistry methods presently available to elucidate the electronic structure and the nature of bonding in coordinatively unsaturated molecules containing transition metal. The work performed on the transition metal dimers has revealed unusual chemical bonds that cannot be described appropriately in the molecular orbital picture. The bonding in such molecules is mostly due to a delocalized molecular orbital formed by the outermost s orbitals. The d orbitals split in energy due to the lowering of symmetry. The split d orbitals give rise to a large number of low-lying electronic states. Recently, the basic results obtained by Irene Shim have been confirmed by experimental work of other scientists.

After she had obtained the degree Dr. Shim worked for two years as a post-doctoral fellow on a grant from the Danish National Science Council.

After a short employment at the Royal Danish School of Pharmacy she went to Texas A & M University as a post-doctoral research associate, and from 1983 she has been visiting Associate Professor at the university. In september 1983 she was given a Niels Bohr Fellowship and she has since been working at Chemical Laboratory B, Technical University of Denmark, and at Texas A & M University.

During her recent work she has utilized the results obtained earlier for the transition metal dimers to gain deeper understanding of the nature of magnetism. In addition the calculational work performed on the coordinatively unsaturated transition metal carbides and nitrides provide basic results that are important for the understanding of catalysis. Thus, the investigations performed have led to detailed descriptions of chemical bonds that are formed or broken in the course of catalytic processes.

Dr. Shim has presented her results at numerous international meetings in the field of theoretical chemistry.

Hans Lomholt Skriver

was born in 1944, studied af the Technical University of Denmark (Danmarks tekniske Højskole, DTH) and obtained the degree of cand. polyt. in physics in 1970. In 1973 he acquired the lic.techn. (Ph.D.) at the DTH

based on the thesis *The Electronic Structure of the Ordered Brass Alloys β'-CuZn and β'-AgZn as Determined by the APW Method,* and in 1985 he defended a doctoral thesis *One-electron Theory of Metals* to the University of Copenhagen. He has been employed at Physics Laboratory I, DTH, from 1970-1964. In 1974-75 he worked at Division of Physics, National Research Council of Canada, Ottawa. He was guest scientist at Kamerlingh Onnes Laboratory, Leiden, Holland during the years 1975-1976. Since then he has worked at the Physics Department, Risø National Laborarory, Roskilde – interrupted by longer visits to the Max-Planck-Institut für Festkörperforschung. During a period his work was supported by NORDITA, and since 1983 he has been a Niels Bohr Fellow.

Skriver's theoretical work on solid state physics has always been centred on the application of one-electron theory to metals and alloys based on coded computations. In this study he has made much progress during the past fifteen years, and his work is highly appreciated internationally.

His collaboration with the experimentalist J.-P. Jan led to successful calculations of band structures and interpretations of dHvA measurements for many metals and ordered alloys.

Since his return to Risø he has worked in close collaboration with O. K. Andersen, at the DTH., now in Stuttgart, as well as with B. Johansson, Aarhus and Uppsala. He has studied the properties of the actinides in great detail, as well as the rare earths. He has calculated the structural energy differences for about forty metals and has been able to determine theoretically which crystal structure a given metal will take on at normal conditions.

In recent years he has given some twenty invited talks at international conferences.

Claus Schelde Jacobsen
was born in 1949, and studied at the Technical University of Denmark (Danmarks Tekniske Højskole, DTH), obtaining the degree of cand. polyt. in electrical engineering in 1973. Since that time he has been employed as assistant at Physics Laboratory III, DTH. until he became a Niels Bohr Fellow in 1983. He worked at the Department of Physics, University of Pennsylvania, on leave of absence from DTH during the years 1973-1974. In 1976 he acquired the degree of Ph.D. (lic.techn.); his thesis was *Infrared Properties of the Organic Conductor TTF-TCNQ.*

Jacobsen has made many valuable contributions to the pioneering

work on the development of new synthetic metals and superconductors commenced during his stay in Pennsylvania. In order to study the basic electronic structure of organic solids he has in particular applied infrared and optical spectroscopy, and investigated transport properties. This work was performed with support from the Danish Natural Science Research Council and the NATO Research Grants Programme.

He has given elementary courses in atomic and nuclear physics and statistical mechanics, and has taken part in organisation of scientific collaboration within solid state physics. He was awarded Fabrikant Gorm-Petersens Mindelegat in 1981 and the ESSO-Prize in 1985.

Hans Uffe Petersen

was born in 1948. He obtained his degree of cand.polyt. in chemical engineering at the Technical University of Denmark (Danmarks tekniske Højskole, DTH) in 1972. He then moved to the Institut de Biologie Physico-Chimique, Paris, 1973-1978, where he worked in the Department of Biochemistry under the supervision of Dr. Marianne Grunberg-Manago. He became doctor of natural sciences (Docteur ès-Sciences d'État) from the University of Paris in 1980.

He returned to Denmark in 1979 to work as a research biochemist in the Institute of Chemistry, Department of Biostructural Chemistry, University of Aarhus, headed by professor Brian F. C. Clark. His scientific work has concentrated on the molecular mechanism of protein biosynthesis and especially the function of tRNA and translation factors in the initiating steps. In prokaryotic, but not in eukaryotic cell cytoplasma, the initiator methionyl-tRNA is formylated. He has proposed a specific role for this modification in the translation of polycistronic messenger RNAs. This is part of the work for which he received the French degree of Doctor of Sciences at the University of Paris in 1980. The title of the thesis is *Contribution à l'etude du rôle du met-tRNA$_f^{Met}$ initiateur et sa formylation dans l'initiation de la traduction chez E. coli*. Most recently Petersen has studied the structural regions within the initiator tRNA which are involved in interactions with proteins during the initiation of translation. The results reveal specificities in the interactions of fMet-tRNA$_f^{Met}$ as compared to elongator tRNAs and also suggest which parts of the initiator tRNA molecule are binding to the proteins in each of the reactions prior to the formation of the first peptide bond.

Hans Uffe Petersen has been working as visiting scientist in many different laboratories, some of which are: Max-Planck-Institut für Molekulare Genetik, Berlin (prof. Olaf Pongs), 1975, Institut Laue-Langevin,

Grenoble (prof. Bernard Jacrot), 1976 and 1980, Institut de Biologie Moleculaire et Cellulaire, Strasbourg (prof. Jean Pierre Ebel), 1980, Department of Biological Chemistry, Medical School, University of California, Davis (prof. John W. B. Hershey), 1981, and 1982, Department of Biochemistry, Institut de Biologie Physico-Chimique, Paris (dr. Marianne Grunberg-Manago), 1984-85. He has organized several international meetings.

Jon Steen Petersen
was born in 1947. He obtained his cand.scient. degree in 1973 at the University of Aarhus.

He worked 1973-78 in the Geology Department of the University of Aarhus as a university stipendiate and assistant teacher, 1978-1981 he was a Research Council stipendiate, 1981-1983 Assistant Professor at the University of Oslo, and since 1983 he has been a Niels Bohr Fellow.

1975-1976 was spent at Université de Paris VII, Institut de Physique de Globe, and at Centre d'Etudes Atomique, Lab. P. Sue, Saclay, 1976-77 at the Mineralogical Museums, the University of Oslo, and 1984-85 at the NASA-Johnson Space Center, Solar System Exploration Division & Experimental Planetology Branch, Houston, Texas. He has worked for Norsk Hydro A/S and B. P. Minerals Exp. in mineral exploration in Norway (phosphates, nepheline, molybdenum, gold) and for Dansk Geoteknik with engineering geological problems involved in dam construction at Jos, Nigeria.

Jon Steen Petersen's research work has covered various aspects of the petrology of igneous and metamorphic rocks. The main themes have been: structural geology and metamorphic petrology of high-grade gneiss complexes; rift zone magmatism and tectonics; geochemistry and petrology of magmatic differentiation processes; and crystalization kinetics and experimental petrology. Most of the field studies have been carried out in the Precambrian basement of Southern Norway and in the igneous rocks of the Permian Oslo Province. His research has provided new information on the *mise en place* of the plutonic rocks of the Oslo Province which has been of fundamental importance for all subsequent studies in this Province. He has for instance demonstrated that the large masses of larvikite are composite multiphase intrusions. The petrogenetic studies in zoned plutonic rock complexes, especially in the Oslo Province, by means of whole-rock, major and trace element geochemistry as well as mineralogical studies by NAA and microprobe analysis of individual minerals have resulted in a better understanding of the chem-

ical segregation during crystalization. These results suggest that element distribution is governed by dynamic magma processes rather than by equilibrium phase-relations, and have promoted the experimental studies of such processes in relevant synthetic and natural systems. The concept of macrosegregation is a result of these studies and has initiated experimental studies that emphasize its potential to important petrogenetic problems.

Petersen has participated in many international conferences, in part as invited speaker, in the Nordic countries and other European countries, and USA.

Jens Konnerup-Madsen

was born in 1948. He obtained his cand. scient. degree in geology at the University of Aarhus in 1976 and his lic.scient. (Ph.D.) at the University of Copenhagen in 1980.

1973-74 was spent at Université de Nancy I, France, supported by a grant from the French government. During this period Madsen was introduced to the study of fluid inclusions in minerals by Drs. Bernard Poty and Jacques Touret.

1977-1983 he was a Research Council stipendiate at the Institute of Petrology, University of Copenhagen. 1977-80 he studied fluid inclusions in certain minerals from the Gardar Province in Greenland, a subject which was treated in his lic.scient. thesis, entitled *Fluid Inclusions in Minerals from Igneous Rocks Belonging to the Precambrian Continental Gardar Rift Province, South Greenland: the Alkaline Ilimaussaq Intrusion and the Alkali Acidic Igneous Complexes*. This line of studies was 1981-83 expanded to cover volatile components of deep crustal and upper mantle origin as revealed by fluid inclusions and stable isotopes, and since 1984 as a Niels Bohr Fellow especially the hydrocarbons in the Earth's crust and upper mantle as revealed by fluid inclusions in minerals. In shorter periods he has studied the fluid phase involved in the formations of porphyry Mo-deposits and he has supervised a study of fluid inclusions in sediments in an attempt to use such inclusions in the evaluation of source rocks for oil and natural gas.

The main part of Madsen's research work has been focused on volatiles in deep crustal and upper mantle rocks, as inferred from studies of fluid inclusions trapped during growth of the minerals, and starting with work on deep-seated granitic intrusions and high-grade metamorphic rocks from South Norway. Subsequent work has dealt with igneous rocks from South Greenland and nodules of upper mantle materials in

order to elucidate the role of CO_2 and CH_4, and other hydrocarbons, in lower crustal and upper mantle magmatic processes, the carbon-bearing gases being of non-biogenic origin.

One of the results of these studies is, that although hydrocarbons are often observed also in mantle derived rocks, the hydrocarbons are generally though not always of a relatively late origin and owe their existence to reactions between CO_2 and H_2O, both of which species appear to be the dominant gases in the upper mantle. Hence the studies do not support the idea of any major degassing of the methane from deep levels.

Jens Konnerup-Madsen has been responsible for graduate and post-graduate teaching in petrology, fluid inclusion analyses, etc. at the Institute of Petrology. – He has participated in a number of international conferences, in part as invited speaker.

Hans Plesner Jakobsen

Subspace Structures of Holomorphic Representations

ABSTRACT. *A set of basic covariant differential operators between holomorphic (»positive energy«) representations on hermitian symmetric spaces is described. The set is in a bijective correspondence with a collection of particularly fundamental homomorphisms between highest weight modules. A method, by which one may approach the general situation from this, is presented. A symmetry principles is also introduced.*

Secondly, two different natural ways of producing irreducible mixtures of unitarizable highest weight modules are exemplified. One is by means of restriction to a maximal parabolic subgroup, the other is through the imbedding of one hermitian symmetric space into another.

Mathematics Institute, Universitetsparken 5,
DK-2100 Copenhagen Ø, Denmark

Introduction

In the perhaps vain hope that the following may be read, at least in part, by somebody from outside the mathematical community, we begin by making a few general remarks about mathematics, and after that, about the area of mathematics to which the following belongs. Only then, and with somewhat less pathos, do we become specific and turn to the content of the present paper.

Let us then assert, with a slight reformulation of a definition in the fascinating book »The Mathematical Experience« by Davis and Hersh ([D&H]) that mathematics is the science of spaces and numbers. In rather simple terms, and in analogy with everyday life, one defines objects, and lays down rules according to which one may manipulate with, or operate upon, these. (Or, the analogy is to a property of an object which was defined in analogy with everyday life. Etc.). Through logical deduction one then tries to reveal deep and non-obvious properties of these creations. One develops tools for the investigation, one invents (or, as many are inclined to say, discovers) new models, and one classifies, calculates

on, solves problems on, dissects, welds together, and even sometimes performs experiments on, these structures. Led by an intuition founded on logic, and in the firm belief that abstraction goes in the direction of simplicity, clarity, and verity, theories of great intricacy and beauty are created. Included among the objects of mathematical interest have always been those which at a given time have been considered to correspond to »reality«, but mathematics is much richer. At the same time it should be mentioned that to many mathematicians, their objects are real and have as much right to be called such, as more down to earth fundamentals.

The area of mathematics to which the following belongs is the representation theory of semi-simple Lie groups.

A typical way in which a Lie group emerges is if one has a set M carrying, or equipped with, a certain structure (e.g. a differential equation on $\mathbb{R}^n$). The group of maps of M onto M that preserve this structure is then often a Lie group. Closely related to this is the occurrence of symmetry groups in physics. The Poincaré group is, for instance, the group of causality (and scale) preserving transformations of Minkowski space. Another interesting example is the conformal group SU(2,2). In fact, the investigations of Segal into the notions of time and causality that led him to propose the conformal group as a possible fundamental symmetry group ([S], see also [S,J,Ø,P,&S] and references cited therein) was what motivated us to persue the kind of representation theory presented below.

Specifically, we are concerned with representations living in spaces of vector valued holomorphic functions on a hermitian symmetric space $\mathscr{D}$ of the non-compact type. The property of holomorphy is closely related to the physical concept of positivity of the energy. For simplicity assume that $\mathscr{D}$ is a tube domain; $\mathscr{D} = \mathbb{R}^n + iC^+$, where C^+ is an open proper convex cone in $\mathbb{R}^n$. Then $\mathbb{R}^n$ is the Shilov boundary of $\mathscr{D}$ and in the regular (generic) case the spaces of holomorphic functions that carry the unitary representations of the group G of holomorphic transformations of $\mathscr{D}$, are Fourier-Laplace transforms of spaces of functions living on C^+.

The current article deals with the subspace structure of such representations, also outside the realm of unitarity. Chapter 1 is mainly concerned with invariant subspaces defined by covariant differential operators. Let us take time here to stress that even though the formulation is infinitesimal, one can always quite easily integrate to an appropriate covering group of G.

We describe in Section 1.2 what we call the basic covariant differential operators on $\mathscr{D}$, namely those which originate or terminate in scalar modules. In Section 1.3 we indicate how one can approach the general situation by means of these results, and finally Section 1.4 is concerned with the conformal group, where the analysis can be brought to a full conclusion. At the same time a principle, which we believe will be fundamental for the further investigations, is introduced.

Chapter 2 deals with irreducible mixtures of unitarizable modules. Through some simple examples, two different situations are presented where one, in a natural way, encounters such a phenomenon. The first circumstance is with representations which, when restricted to a maximal parabolic subgroup, decompose into a finite sum of irreducibles, and the other occurs when a hermitian symmetric space is embedded compatibly into a bigger one. It is remarkable how rich the structures are that result from such simple phenomena.

1. Covariant differential operators

1.1. Fundamentals

Let $\mathfrak{g}$ denote the Lie algebra of the group of holomorphic transformations of an irreducible hermitian symmetric space $\mathscr{D}$. It is well-known that $\mathfrak{g}$ is a simple Lie algebra over $\mathbb{R}$ and that there are compact Cartan subalgebras. Specifically, let $\mathfrak{g} = \mathfrak{k} + \mathfrak{p}$ be a Cartan decomposition of $\mathfrak{g}$. Then $\mathfrak{k}$ has a one-dimensional center η. Let h_0 denote one of the two elements of η whose eigenvalues on $\mathfrak{p}^{\mathbb{C}}$ are $\pm\,i$, and let $\mathfrak{p}^+$ and $\mathfrak{p}^-$ denote the $+i$ and $-i$ eigenspace, respectively, for this fixed element. Let $\mathfrak{k}_1 = [\mathfrak{k},\mathfrak{k}]$ denote the semi-simple part of $\mathfrak{k}$ and let $\mathfrak{h}$ be a maximal abelian subalgebra of $\mathfrak{k}$. Then $\mathfrak{k} = \mathfrak{k}_1 \oplus \mathbb{R} \cdot h_0$, $\mathfrak{h} = (\mathfrak{h}\cap\mathfrak{k}_1) \oplus \mathbb{R} \cdot h_0$, $(\mathfrak{h}\cap\mathfrak{k}_1)^{\mathbb{C}}$ is a Cartan subalgebra of $\mathfrak{k}_1^{\mathbb{C}}$, and $\mathfrak{h}^{\mathbb{C}}$ is a Cartan subalgebra of $\mathfrak{g}^{\mathbb{C}}$.

The sets of compact and non-compact roots of $\mathfrak{g}^{\mathbb{C}}$ relative to $\mathfrak{h}^{\mathbb{C}}$ are denoted Δ_c and Δ_n, respectively; $\Delta = \Delta_c \cup \Delta_n$. We choose an ordering of Δ such that $\mathfrak{p}^+$ corresponds to Δ_n^+. Throughout β denotes the unique simple root in Δ_n^+ and ϱ denotes one half of the sum of the positive roots. For $\gamma \in \Delta$ let H_γ denote the unique element of $i\mathfrak{h} \cap [(\mathfrak{g}^{\mathbb{C}})^\gamma, (\mathfrak{g}^{\mathbb{C}})^{-\gamma}]$ for which $\gamma(H_\gamma) = 2$. Finally, following [R&V] we let γ_r denote the highest root. Then $\gamma_r \in \Delta_n^+$ and $H_{\gamma_r} \notin [\mathfrak{h}\cap\mathfrak{k}_1]^{\mathbb{C}}$.

If Λ_0 is a dominant integral weight of $\mathfrak{k}_1$ and if $\lambda \in \mathbb{R}$ we denote by $\Lambda = (\Lambda_0,\lambda)$ the linear functional on $\mathfrak{h}^{\mathbb{C}}$ given by

$$\Lambda\big|_{(\mathfrak{h}\cap\mathfrak{k}_1)^{\mathbb{C}}} = \Lambda_0, \quad \Lambda(H_{\gamma_r}) = \lambda. \tag{1.1.1}$$

Such a Λ determines an irreducible finite-dimensional $\mathscr{U}(\mathfrak{k}^{\mathbb{C}})$-module which we, for convenience, denote by V_τ. Here $\tau = \tau_\Lambda$ denotes the representation corresponding to Λ of the connected simply connected Lie group $\widetilde{K}$ with Lie algebra $\mathfrak{k}$. Further, let

$$M(V_\tau) = \mathscr{U}(\mathfrak{g}^{\mathbb{C}}) \underset{\mathscr{U}(\mathfrak{k}^{\mathbb{C}} \oplus \mathfrak{p}^+)}{\otimes} V_\tau \qquad (1.1.2)$$

denote the generalized Verma module of highest weight Λ, and let M_Λ denote the Verma module of which $M(V_\tau)$ is a quotient.

In what follows, we choose to represent our Hermitian symmetric space $\mathscr{D}$ as a bounded domain in $\mathfrak{p}^-$. Consider an (irreducible) finite-dimensional $\mathscr{U}(\mathfrak{k}^{\mathbb{C}})$-module V_τ. Through the process of holomorphic induction, the space $\mathscr{P}(V_\tau)$ of V_τ-valued polynomials on $\mathfrak{p}^-$ becomes a $\mathscr{U}(\mathfrak{g}^{\mathbb{C}})$-module consisting of $\mathfrak{k}$- (or $\widetilde{K}$-) finite vectors. We maintain the notation $\mathscr{P}(V_\tau)$ for this module and let dU_τ denote the corresponding representation of $\mathfrak{g}^{\mathbb{C}}$. Explicitly, let

$$(\delta(z_0)f)\,(z) = \frac{d}{dt}\,\Big|_{t=0} f(z+tz_0)$$

for $z_0, z \in \mathfrak{p}^-$, and $f \in C^\infty(\mathfrak{p}^-)$. Then, for $p \in \mathscr{P}(V_\tau)$ we have ([J&V; II]):

$$(dU_\tau(x)f)\,(z) = -\,(\delta(x)f)\,(z) \qquad\qquad \text{for } x \in \mathfrak{p}^-, \ (1.1.3)$$
$$(dU_\tau(x)f)\,(z) = d\tau(x)f(z) - (\delta([x,z])f)\,(z) \qquad \text{for } x \in \mathfrak{k}^{\mathbb{C}}, \text{ and}$$
$$(dU_\tau(x)f)\,(z) = d\tau([x,z])f(z) - \tfrac{1}{2}(\delta([[x,z],z])f)\,(z) \text{ for } x \in \mathfrak{p}^+.$$

It follows from these formulas (especially the first) that the space

$$W(\tau) = \mathrm{Span}\{dU_\tau\,(u) \cdot v \mid v \in V_\tau, \ u \in \mathscr{U}(\mathfrak{g}^{\mathbb{C}})\} \qquad (1.1.4)$$

is contained in any invariant subspace. In particular, $W(\tau)$ is irreducible.

Let V_τ and V_{τ_1} be finite-dimensional (irreducible) $\mathscr{U}(\mathfrak{k}^{\mathbb{C}})$-modules, and let D be a constant coefficient holomorphic differential operator on $\mathfrak{p}^-$ with values in $\mathrm{Hom}(V_\tau, V_{\tau_1})$.

Definition 1.1.5. $D: \mathscr{P}(V_\tau) \to \mathscr{P}V_{\tau_1})$ *is covariant iff*
$$\forall x \in \mathfrak{g}^{\mathbb{C}}: DdU_\tau(x) = dU_{\tau_1}\,(x)D.$$

Along with $\mathscr{P}(V_\tau)$ we consider the space $\mathscr{E}(V_{\tau'})$ of holomorphic constant coefficient differential operators on $\mathfrak{p}^-$ with values in the contragredient module, $V_\tau' = V_{\tau'}$, to V_τ. For $p \in \mathscr{P}(V_\tau)$ and $q \in \mathscr{E}(V_{\tau'})$ let

$$(q,p) = (q(\frac{\partial}{\partial z}),p(\cdot))\,(0). \qquad (1.1.6)$$

This bilinear pairing clearly places $\mathscr{P}(V_\tau)$ and $\mathscr{E}(V_{\tau'})$ in duality and as a result, $\mathscr{E}(V_{\tau'})$ becomes a $\mathscr{U}(\mathfrak{g}^\mathbb{C})$-module. The following result is straight-forward. See [H&J].

Proposition 1.1.7. *As $\mathscr{U}(\mathfrak{g}^\mathbb{C})$-modules,*
$$\mathscr{P}(V_\tau)' = \mathscr{E}(V_{\tau'}) = M(V_{\tau'}).$$

The following is proved in [JV].

Proposition 1.1.8. *A homomorphism* $\varphi\colon M(V_{\tau_1'}) \to M(V_{\tau'})$ *gives rise, by duality, to a covariant differential operator* $D_\varphi\colon \mathscr{P}(V_\tau) \to \mathscr{P}(V_{\tau_1})$, *and conversely.*

Through the results of Bernstein, Gelfand, and Gelfand [B,G,&G] this proposition yields a condition (»condition (A)«) which must be satisfied in order that there may be a covariant differential operator. This observation was crucial in the determination of the full set of unitarizable highest weight modules [JIV] (see also [JII] and [JIII]):

For Λ_0 fixed it is known through the results of Harish-Chandra [H-C] that the modules $W(\tau) = W(\tau)\,(\lambda)$ are unitarizable for λ sufficiently negative. Due to the polynomial behavior, as a function of λ, of the restriction of the hermitian form to finite-dimensional subspaces of $\mathscr{P}(V_\tau)$ (where V_τ, as a vector space, is independent of λ), it follows that the first $\lambda = \lambda_1$ where the hermitian form becomes degenerate (»the first possible place of non-unitarity« – though of course a place at which there is unitarity) is a place where $W(\tau)\,(\lambda_1) \neq M(V_\tau)$. It follows that the annihilator $W^0\,(\tau)$ of $W(\tau)$ is non-trivial. Hence, there is a covariant differential operator or, equivalently, »condition (A)« must be satisfied. The point λ_1 is then easily determined through a diagrammatic presentation of Δ_n^+; described in [JIV]. Furthermore, by looking at the first $\lambda = \lambda_0$ where there is a first order covariant differential operator (»the last possible place of unitarity«; [JIII]) and by paying attention to the exact forms of the homomorphisms at λ_0 and λ_1, one may in fact determine the full set of points above λ_1 at which there is unitarity. In particular, λ_0 is a such. The complete proof also relies on the results in [K&V], [R&V], and [W]. (A different proof has been given in [E, H, & W]).

Let I be an invariant subspace; $W(\tau) \subset I \subset M(\tau)$, and assume that all inclusions are proper. The annihilator I^0 is then non-trivial, and it makes sense to talk about the lowest order elements in I^0. These elements must be annihilated by $\mathfrak{p}^+$ and it follows that there is at least one homomor-

phism into $\mathscr{P}(V_\tau)'$ whose image is contained in I^0. In case I^0 is a union of such images of homomorphisms, the description by covariant differential operator is then complete. Furthermore, the $\mathfrak{k}$-types of I can be determined as those that are dual to »the $\mathfrak{k}$-types not contained in I^0«, and the $\mathfrak{k}$-types of I^0 can be computed essentially just from the knowledge of the $\mathfrak{k}$-types of modules of the form $\mathscr{P}(V_{\widetilde{\tau}})$. One must examine, though, exactly how the images overlap.

However, it may happen that I^0 is not completely covered by the images of homomorphisms. An example of this phenomenon is given in [B&C], and there an example of a reducible socle is also furnished. Some other peculiarities are exemplified in [JV]. All the same, it is clear that it is of importance to know as much about covariant differential operators as possible.

1.2. Basic covariant differential operators

By a scalar module we mean a module $M(V_\tau)$ for which dim $V_\tau = 1$ or, equivalently; $\tau = \tau(0,\lambda)$. In this section we quote the results of [JV] concerning the set of homomorphisms originating from, or terminating in, scalar modules.

Let $\gamma_1 = \beta$, $\gamma_2,\ldots,\gamma_r$ be a maximal set of orthogonal roots in Δ_n^+, constructed so that γ_i is the element in $\Delta_n^+ \cap \{\gamma_1,\ldots,\gamma_{i-1}\}^\perp$ with the smallest height; $i = 2,\ldots,r$. Let $\delta_i = \gamma_1 + \ldots + \gamma_i$; $i = 1,\ldots,r$.

Proposition 1.2.1. ([Smd]). *The set of highest weights of the irreducible submodules of the* $\mathfrak{k}^{\mathbb{C}}$-*module* $\mathscr{U}(\mathfrak{p}^-)$ *are*

$$\{-i_1\delta_1-\cdots-i_r\delta_r \mid (i_1,\ldots,i_r) \in (\mathbb{Z}_+)^r\}.$$

There are no multiplicities.

Let p denote the dimension of an »off-diagonal« root space in $\mathfrak{g}$ for a maximal abelian subalgebra $\mathfrak{a}$ of $\mathfrak{p}$ (cf. [R&V; (2.2.2)]), and let $\lambda_s = -(s-1) \cdot p/2$; $s=1,\ldots,r$.

Proposition 1.2.2.
a) If there is a non-trivial homomorphism
$$M\big(V_{(0,\lambda)-\Sigma_{s=1}^r i_s\delta_s}\big) \to M(V_{(0,\lambda)})$$
then at most one i_s is different from 0.
b) There is a non-zero homomorphism
$$M(V_{(0,\lambda)-n\delta_s}) \to M(V_{(0,\lambda)})$$
exactly when $\lambda = \lambda_s + (n-1)$ where λ_s is given as above and $n \in \mathbb{N}$.

Let ω_1 be the Weyl group element that satisfies

$$\omega_1(\beta) = \gamma_r \; ; \; \omega_1 (\Delta_c^+) = \Delta_c^-. \tag{1.2.3}$$

Let

$$\hat{\gamma}_i = \omega_1(\gamma_i) \; ; \qquad i=1,...,r. \tag{1.2.4}$$

Proposition 1.2.5. *There exists a non-zero homomorphism* $M(V_{(0,\lambda)}) \rightarrow$ $M(V_\tau)$ *exactly when* $\tau \equiv (0,\lambda) + n\omega_1(\delta_i)$ *for some* $n \in \mathbb{N}$, $i \in \{1,...r\}$ *and* $\lambda = \lambda_i - n - \varrho(\hat{\gamma}_i)$. *The homomorphism is unique.*

1.3. The general case on $\mathscr{D}$; an approach

Whereas the Jantzen-Zuckerman translation functor itself, when applied to the results of the previous chapter, does not quite yield the detailed information that we are seeking about general $M(V_\tau)$'s, it is still natural to apply the idea of tensoring with finite-dimensional representations along the lines of ([V; Lemma 4.5.9]) to the present situation. As we shall see, it is in fact possible, by applying such ideas to the dual modules, to obtain a tool which, in particular for some of the classical groups, is remarkably powerful.

Let $\tau = \tau_{(\Lambda_0,\lambda)}$ be fixed, let λ_3 be determined by $(\Lambda_0{}',\lambda_3) (H_\beta) = 0$, and choose $\lambda_4 \geq \lambda_3$ such that $\lambda_4 - \lambda_3$ is an integer. Then $(\Lambda_0{}',\lambda_4)$ is the highest weight of an irreducible finite-dimensional representation $F(\Lambda_0{}',\lambda_4)$ of $\mathfrak{g}^{\mathbb{C}}$. Observe the following simple facts:

Lemma 1.3.1. *a) For the dual module $F'(\lambda_0{}',\lambda_4)$ we have*

$$F'(\Lambda_0{}',\lambda_4) \simeq W(\tau_1), \tag{1.3.2}$$

where $\tau_1 = \tau_{(\Lambda_0,\lambda_3-\lambda_4)}$ and $W(\tau_1)$ is given by (1.1.4).
b) The $\widetilde{K}$-type $\tau_2 = \tau_{\Lambda_2}$ which is annihilated by $\mathfrak{p}^+$ in $W(\tau_1)$ satisfies

$$\Lambda_2 = (\widetilde{\Lambda_0}{}',\lambda_4) = -\omega(\Lambda_0{}',\lambda_4) \tag{1.3.3}$$

where ω is the Weyl group element which maps the negative Weyl chamber onto the positive, and $\widetilde{\Lambda_0}$ is a dominant integral weight of $\mathfrak{k}_1$.
c) τ' is of highest weight $(\Lambda_0{}',\lambda')$ with

$$\lambda' = -(\Lambda_0,\lambda)(H_\beta). \tag{1.3.4}$$

Proof. a) It is obvious that $F(\Lambda_0{}',\lambda_4)$ is the irreducible quotient of $M(V_{(\Lambda_0{}',\lambda_4)})$ and hence it follows by Proposition 1.1.7 and (1.1.4) that (1.3.2) holds with a τ_1 of the form $\tau_1 = \tau_{(\Lambda_0,\widetilde{\lambda})}$ for some $\widetilde{\lambda}$. Let ω_1 be the

Weyl group element that satisfies (1.2.3). Then clearly $(\Lambda_0, \widetilde{\lambda}) = -\omega_1(\Lambda_0', \lambda_4)$. Hence $\widetilde{\lambda} = (\Lambda_0, \widetilde{\lambda}) (H_{\gamma_r}) = -(\Lambda_0', \lambda_4) (H_\beta) = -(\lambda_4 - \lambda_3)$.
b) It is obvious that $\Lambda_2 = -\omega(\Lambda_0', \lambda_4)$, and this equals $(\Lambda_0^{\widetilde{}'}, \overset{\vee}{\lambda})$ for some $\overset{\vee}{\lambda}$. What needs to be proved is that $\overset{\vee}{\lambda} = \lambda_4$. This, however, follows by observing that $\omega(\gamma_r) = -\gamma_r$ since γ_r is the highest root.
c) This follows as in a). Q.E.D.

As $\mathcal{U}(\mathfrak{k}_1{}^{\mathbb{C}})$-modules, $V_{(\Lambda_0, \lambda)} = V_{(\Lambda_0, 0)}$. Hence, by Lemma 1.3.1, the elements of $W(\tau_1)$ may be considered as taking values in $V_{\tau'}$. We denote the duality by $(.,.)$ and observe that we thereby may associate, to any $p \in \mathcal{P}(V_{\tau'})$ and $q \in W(\tau_1)$, a $\mathbb{C}$-valued polynomial

$$(p,q) (z) = (p(z), q(z)) \text{ (pointwise)} \qquad (1.3.5)$$

Proposition 1.3.6. *Let* $p \in \mathcal{P}(V_{\tau'})$, $q \in W(\tau_1)$, *and let* $x \in \mathfrak{g}^{\mathbb{C}}$.
Then

$$(dU_{\tau'}(x)p, q) + (p, dU_{\tau_1}(x)q) = dU_{(0, -\lambda - \lambda_4 + \lambda_3)} (x)(p,q).$$

Proof. Let h_0 denote the element of the center of $\mathfrak{k}$ as in section 1.1. Since ω_1 preserves the set of positive non-compact roots, $\omega_1(h_0) = h_0$. Equation (1.3.7) now follows from (1.1.3) together with the observation that $d\tau'(h_0)$ on $V_{\tau'}$ is given by $-\sqrt{-1}\,\omega_1\,(\Lambda_0, \lambda) (h_0) = -\sqrt{-1}(\Lambda_0, \lambda)(h_0)$, whereas $d\tau_1 (h_0)$ on V_{τ_1} is given by $\sqrt{-1}\,(\Lambda_0, \lambda_3 - \lambda_4) (h_0)$. Q.E.D.

Let V_{τ_2} denote the $\widetilde{K}$-type in $W(\tau_1)$ which is annihilated by $\mathfrak{p}^+$.

Corollary 1.3.8. *Let* $p \in W(\tau')$ *and let* $q \in V_{\tau_2}$. *Then*

$$(p,q) = \sum_{i=1}^{n} d\, U_{(0, -\lambda - \lambda_4 + \lambda_3)}(u_i)\, (v_i, q_i)$$

for some elements $u_1, \ldots, u_n \in \mathcal{U}(\mathfrak{p}^+)$, $v_1, \ldots, v_n \in v_{\tau'}$, *and* $q_1, \ldots, q_n \in V_{\tau_2}$.

Proof. By (1.1.4), it suffices to take p of the form $dU_{\tau'}(u) \cdot v$ for $u \in \mathcal{U}(\mathfrak{g}^{\mathbb{C}})$ and $v \in V_{\tau'}$. Since $\mathcal{U}(\mathfrak{g}^{\mathbb{C}}) = \mathcal{U}(\mathfrak{p}^+)\mathcal{U}(\mathfrak{p}^-)\mathcal{U}(\mathfrak{k}^{\mathbb{C}})$ by Poincaré-Birkhoff-Witt, we may assume that $u \in \mathcal{U}(\mathfrak{p}^+)$. Thus, the statement follows directly from Proposition 1.3.6. Q.E.D.

To apply this, observe that by Proposition 1.2.2 and Proposition 1.1.7 there are certain values of λ_0 at which there is a finite number of invariant subspaces $I_{\lambda_0}^i$; $i = 1, \ldots$, of $\mathcal{P}(V_{(0, \lambda_0)})$. These are given as the kernels of covariant differential operators. Moreover, since there are no multiplicities at this level, for each $I_{\lambda_0}^i$ there is an n and a δ_{i_0} such that, in the

terminology of Proposition 1.2.1, the $\mathfrak{k}$-types of $I^i_{\lambda_0}$ exactly are those whose contragredient representation does not contain $-n\delta_{i_0}$. That is, if the contragredient $\mathfrak{k}$-type is of the form $(0, -\lambda_0) - \Sigma^r_{i=1} n_i\delta_i$, then $\Sigma^r_{i=i_0} n_i <$ n. Equivalently, the $\mathfrak{k}$-types are exactly those which are not in the ideal generated by the polynomials in the $\mathfrak{k}$-type generated by $p^n_{-\delta_s}$. (By choosing the γ_i's of Proposition 1.2.1 differently we could of course avoid having to go to the dual picture.)

It follows by Proposition 1.3.6 that for each $I^i_{\lambda_0}$,

$$\{p \in \mathscr{P}(V_{\tau'}) \mid \forall q \in W(\tau_1): (p,q) \in I^i_{\lambda_0}\} \qquad (1.3.9)$$

is an invariant subspace $(\lambda_0 = -\lambda - \lambda_4 + \lambda_3)$. Further, if the space

$$\mathscr{S}_{\lambda_0} = \mathrm{Span}\{ (v,q(z)) \mid v \in V_{\tau'}, \ q \in V_{\tau_2}\} \qquad (1.3.10)$$

(still, $\lambda_0 = -\lambda - \lambda_4 + \lambda_3$) is contained in $I^i_{\lambda_0}$ for some i, then by Corollary 1.3.8.

$$\{(p(z),q(z)) \mid p \in W(\tau') , \ q \in V_{\tau_2}\} \qquad (1.3.11)$$

is also contained in $I^i_{\lambda_0}$. Since $I^i_{\lambda_0}$ as a set of $\mathfrak{k}$-types is equal to those that do not occur in a certain ideal, it is clear that $W(\tau')$ *cannot equal the full set* $\mathscr{P}(V_{\tau'})$ since we can choose $p_0 \in \mathscr{P}(V_{\tau'})$ with coordinate functions in the mentioned ideal, and then $(p_0(z),q(z)) \notin I^i_{\lambda_0}$.

We shall give an example of how to use the last observation. First observe that by Lemma 1.3.1, for $k \in \widetilde{K}$,

$$\begin{aligned}(U_{(0,-\lambda-\lambda_4+\lambda_3)} (k) (v,q(\cdot))) (z) \\ = (\tau'(k)v,\tau_1(k)q(k^{-1}z)) = (\tau'(k)v,(\tau_2(k)q) (z)),\end{aligned} \qquad (1.3.12)$$

i.e. the $\widetilde{K}$-types of $\mathscr{S}_{\lambda_0}$ are contained in $\tau' \otimes \tau_2$.

We now specialize to $Sp(n, \mathbb{R})$. Assertions about V_{τ_2} analogous to the one below can also be made for $SU(p,q)$ and for »most« of the finite-dimensional representations of $SO\star(2n)$. Also observe that the following remark in fact itself deals with a significant subset of the modules that are the target of this chapter:

Let $\mathfrak{g} = sp(n, \mathbb{R})$. Based on the imbedding of $Sp(n, \mathbb{R})$ into $SU(n,n)$ we choose the following conventional realization of $\mathfrak{g}$ according to which

$$\mathfrak{k} = \left\{\left(\begin{smallmatrix} ih & 0 \\ 0 & -i^t h \end{smallmatrix}\right) \mid h = h^\star \in M(n, \mathbb{C})\right\},$$

$$\mathfrak{p}^- = \left\{\left(\begin{smallmatrix} 0 & 0 \\ z & 0 \end{smallmatrix}\right) \mid z = {}^t z \in M(n, \mathbb{C})\right\}, \text{ and}$$

$$\mathfrak{p}^+ = \left\{\left(\begin{smallmatrix} 0 & w \\ 0 & 0 \end{smallmatrix}\right) \mid w = {}^t w \in M(n, \mathbb{C})\right\}.$$

Let τ_1 and τ_2 be as in Lemma 1.3.1.

Lemma 1.3.13. *For* $v \in V_{\tau_1}$ *the prescription*

$$\varphi_v \colon z \rightarrow \tau_1(z^{-1})v$$

defines a V_{τ_1}*-valued polynomial which belongs to* V_{τ_2}*.*

Proof. Observe that in the present situation, $\tau_1' = \tau_2$. Since τ_2 corresponds to the highest weight of a finite dimensional $\mathscr{U}(\mathfrak{g}^{\mathbb{C}})$-module, it is clear that it is polynomial. For $u \in U(n)$ we have

$$\tau_1(u)\tau_1(({}^t uzu)^{-1})v = \tau_1(z^{-1})\tau_1({}^t u^{-1})v,$$

hence it is clear that φ_v transforms according to τ_2. Finally observe that for $x = \begin{pmatrix} 0 & x \\ 0 & 0 \end{pmatrix} \in \mathfrak{p}^+$,

$$[x,z] = \begin{pmatrix} xz & 0 \\ 0 & zx \end{pmatrix}, \text{ and } [[x,z],z] = \begin{bmatrix} 0 & 0 \\ -2zxz & 0 \end{bmatrix}.$$

Hence, by (1.1.3)

$$(dU_{\tau_1}(x)\varphi_v)(z) = d\tau_1(xz)\tau_1(z^{-1})v - \tfrac{1}{2}\,d\tau_1(2xz)\tau_1(z^{-1})v = 0. \text{ Q.E.D.}$$

Let $e_1,\dots,e_n$ denote the standard orthonormal basis of $\mathbb{R}^n$.
Then

$$\begin{aligned}
\Delta_c^+ &= \{e_i - e_j \mid 1 \le i < j \le n\}, \text{ and} \\
\Delta_n^+ &= \{e_i + e_j \mid 1 \le i \le j \le n\}.
\end{aligned}$$

$\Lambda = (\lambda_1, \lambda_2, \dots, \lambda_n)$ is $\mathfrak{k}_1$-dominant and integral if and only if $\lambda_1 \ge \dots \ge \lambda_n$ and $\lambda_i - \lambda_j \in \mathbb{Z}$. $\varrho = (n, n-1, \dots, 1)$, and $\lambda = \lambda_1$.

Example. Consider $Sp(4, \mathbb{R})$ and let $\Lambda = (\lambda, \lambda, \lambda-1, \lambda-2)$. We put $\lambda_3 = \lambda_4$ and observe that

$$\tau_1 = (0, 0, -1, -2), \text{ and } \tau_2 = (2, 1, 0, 0).$$

Tensor products are computed by means of the Littlewood-Richardson rule (see e.g. [Jms]) which also gives the full solution to $\tau_a \otimes (?) = \tau_b$. To begin with, then, we observe that according to (1.3.12) and Proposition 1.2.1, the possible $\mathfrak{k}$-types of $\mathscr{I}_{-\lambda}$ are $(-\lambda, -\lambda, -\lambda, -\lambda) \otimes (4,2,0,0)$ and $(-\lambda, -\lambda, -\lambda, -\lambda) \otimes (3,3,0,0)$. Since, if e denotes the highest weight vector

for τ_2, $(e,\tau_1(z^{-1})e) = (e,\tau_2(z)e)$ is a highest weight vector as a $\mathbb{C}$-valued polynomial, it follows that the first of these does occur. Further, it is easy to see that the corresponding set of polynomials does not exhaust $\mathscr{S}_{-\lambda}$. Hence both of these types occur.

Now, the smallest λ at which a sequence of elements from Δ_n^+ can satisfy condition (A) for any pair $(\cdot,\Lambda+\varrho)$ is evidently $\lambda = -3$, corresponding to $\{e_3+e_4\}$. However, this does not correspond to a highest weight of $\mathfrak{p}^- \otimes V_\tau$ (cf. the proof of Proposition 7.3 in [JIII]). It is also straightforward to see that at $\lambda = -5/2$ there can be no sequence satisfying condition (A) for a pair $(\Lambda_1+\varrho,\Lambda+\varrho)$ with Λ_1 $\mathfrak{k}_1$-dominant. We will in this example study the values $\lambda = -2,-3/2,-1,-1/2$, and 0. Note that the value of p in Proposition 2.2 is 1 for $sp(n,\mathbb{R})$.

$\lambda = -2$: Consider the imbedding of $sp(4,\mathbb{R})$ into $sp(5,\mathbb{R})$ for which, if $e_1,...,e_5$ is a basis of $\mathbb{R}^5$ as above, the space $\mathfrak{p}^+$ for $sp(4,\mathbb{R})$ is contained in the $\mathfrak{p}^+$ for $sp(5,\mathbb{R})$, and corresponds to the roots e_i+e_j with $2 \le i,j$. Let $\widetilde{\Lambda} = (\lambda,\lambda,\lambda,\lambda-1,\lambda-2)$ $(\lambda = -2)$ and proceed with $sp(5,\mathbb{R})$: It follows from Proposition 1.2.2 and the remarks following (1.3.11) that $W(\tau')$ cannot equal the full set $\mathscr{P}(V_{\tau'})$. The invariant subspace $I^i_{\lambda_0}$ to be used for this argument is, as a space of polynomials, a complement to the ideal generated by the polynomial representation contragredient to $(-2,-2,-2,-2,-2)$. $((-2,-2,-2,-2,-2)$ is, in the language of Proposition 1.2.1, equal to $-\delta_5$ and corresponds to the one-dimensional representation space $\mathbb{C} \cdot \det z$. $-\delta_4 = (0,-2,-2,-2,-2)$ corresponds to 4×4 minors of z, etc.) We have that $(2,1,0,0,0) \otimes (2,2,2,1,0)$ contains $(2,2,2,2,2)$ and it is, anyway, straightforward to see that the only possible choice of a sequence of elements of Δ_n^+ satisfying condition (A) for a pair $(\Lambda_1+\varrho,\widetilde{\Lambda}+\varrho)$ has $\Lambda_1 = (-2,-2,-2,-2,-2) \otimes (0,-1,-2,-2,-2)$. Finally, since the highest weight vector in $\mathfrak{p}^- \otimes \mathfrak{p}^- \otimes V_\tau$ corresponding to this Λ_1 actually only lives on the $sp(4,\mathbb{R})$ above, it follows that we do have a non-zero homomorphism

$$M(V_{(-3,-4,-4,-4)}) \to M(V_\tau),$$

and there can only be one such since Λ_1 has multiplicity one in $\mathscr{U}(\mathfrak{p}^-) \otimes V_\tau$.

$\lambda = -3/2$: This may be treated analogously by using the ideal generated by the polynomial representation contragredient to $(0,-2,-2,-2,-2)$ $(4\times4$ minors). But there is no need to pass to $sp(5,\mathbb{R})$; $(-2,-2,-2,-2)$ for $sp(4,\mathbb{R})$ can also be used (then it is just the determinant). However, this is also a point at which a first order differential operator exists by

Proposition 1.6 in [JV]. Specifically, $\lambda = e_2 + e_3$. Moreover, it is easy to see that the corresponding homomorphism is the only possible.

$\lambda = -1$: It follows from Proposition 1.5 in [JV] (or [B,G,&G]), by trial and error, that there can be no homomorphisms for this value.

$\lambda = -\frac{1}{2}$: By looking at the ideal generated by the polynomials in the $\mathfrak{k}$-type whose contragredient is $(-4,-4,-4,-4)$ $(= -2\delta_4)$ it follows that $W(\tau') \neq \mathscr{P}(V_{\tau'})$. Moreover, one can see that the $\mathfrak{k}$-type $\Lambda_1 = (\frac{1}{2},\frac{1}{2},\frac{1}{2},\frac{1}{2})$ $\otimes$ $(4,4,3,2)$ does not belong to $W(\tau')$ and one can find a sequence of elements of Δ_n^+ satisfying condition (A) for the pair $(\Lambda_1'+\varrho, \Lambda+\varrho)$. However, there are other sequences also satisfying this condition but corresponding to lower order differential operators. In fact, there is a first order differential operator corresponding to $\lambda = e_1+e_3$. This phenomenon seems to be quite typical: When the method fails to give more information than $W(\tau') \neq \mathscr{P}(V_{\tau'})$ (which just implies the existence of *some* covariant differential operator) one can usually quite easily establish the existence of the lowest order operator and, more generally, obtain a sequence of differential operators of lowest possible degree. The present situation furnishes an example of this: There is a system of non-zero homomorphisms

$$M(V_{(-\frac{1}{2}-3,-\frac{1}{2}-4,-\frac{1}{2}-4,-\frac{1}{2}-4)}) \xrightarrow{\varphi_1} M(V_{(-\frac{1}{2}-2,-\frac{1}{2}-3,-\frac{1}{2}-4,-\frac{1}{2}-4)}) \xrightarrow{\varphi_2}$$

$$M(V_{(-\frac{1}{2}-1,-\frac{1}{2}-3,-\frac{1}{2}-3,-\frac{1}{2}-4)}) \xrightarrow{\varphi_3} M(V_{(-\frac{1}{2}-1,-\frac{1}{2}-1,-\frac{1}{2}-1,-\frac{1}{2}-4)}) \xrightarrow{\varphi_4}$$

$$M(V_{(-\frac{1}{2},-\frac{1}{2}-1,-\frac{1}{2}-1,-\frac{1}{2}-3)}) \xrightarrow{\varphi_5} M(V_{(-\frac{1}{2},-\frac{1}{2},-\frac{1}{2}-1,-\frac{1}{2}-2)}).$$

Of these, all but φ_3 correspond to first order. The existence of φ_3 follows along the lines of the cases $\lambda = -\frac{3}{2}$ and $\lambda = -2$. Finally, by looking at the images of the various homomorphisms and observing that everywhere there is multiplicity one, it is easy to conclude that $\varphi_5 \circ \varphi_4$, $\varphi_5 \circ \varphi_4 \circ \varphi_3$, $\varphi_5 \circ \varphi_4 \circ \varphi_3 \circ \varphi_2$, and $\varphi_5 \circ \varphi_4 \circ \varphi_3 \circ \varphi_2 \circ \varphi_1$ all are non-zero and that they, along with φ_5, constitute the full set of homomorphisms into $M(V_\tau)$.

$\lambda = 0$: There is a sequence of non-zero homomorphisms

$$M(V_{(-3,-4,-5,-5)}) \xrightarrow{\varphi_1} M(V_{(-1,-2,-3,-5)}) \xrightarrow{\varphi_2}$$
$$M(V_{(0,-2,-3,-4)}) \xrightarrow{\varphi_3} M(V_{(0,0,-1,-2)}).$$

The existence of φ_1 and φ_3 follows as above, and φ_2 corresponds to a first order operator. It might seem that there could be two distinct homomorphisms at the level of φ_1, but it follows easily from Proposition

1.5 in [JV] that $M(V_{(-3,-4,-5,-5)})$ is irreducible, and the existence of two distinct homomorphisms would contradict this. By looking at multiplicities it follows that $\varphi_3 \circ \varphi_2$ is non-zero and, moreover, is the unique such. However, $\varphi_3 \circ \varphi_2 \circ \varphi_1$ is zero. To wit, $V_{(-3,-4,-5,-5)}$ does not occur in $\mathcal{U}(\mathfrak{p}^-) \otimes V_{(0,0,-1,-2)}$, and thus there can be no non-zero homomorphism at this level.

1.4. Conformal covariance

Given a generalized highest weight module $M(V_\tau)$, Bernstein, Gelfand, and Gelfand [B,G,&G] gives the highest weights of the $\mathfrak{k}$-types that may possibly be annihilated by $\mathfrak{p}^+$ and thus define homomorphisms into $M(V_\tau)$. As described in the previous section, the results of [JV] are quite useful in the description of the set of homomorphisms; indeed, in many cases it yields directly the full set. However, there are some complicated situations, e.g. those in which one (or several) of the »BGG $\mathfrak{k}$-types« occurs with multiplicity greater than one. We believe that there is a principle which can handle those situations, and whose applicability goes even further. It should be noted that there are no examples of multiplicity greater than one in the sets of homomorphisms as above. The principle in its mildest formulation states (tube domain case) that only for very special Λ_0's can it happen that a $\mathfrak{k}$-type $p \in M(V_\tau)$ of the form $p = u \cdot q$ with $q \in M(V_\tau)$ and $u \in \mathcal{U}(\mathfrak{p}^-)^{\mathfrak{k}_1}$ is annihilated by $\mathfrak{p}^+$. Actually, this principle was the main motivation behind the results in [JV].

We will now furnish an example based on the Lie algebra su(2,2) of the conformal group. Here the formulation is quite precise and may in fact be proved to be sufficient to determine the full set of conformally covariant differential operators. Let

$$\square = \frac{\partial^2}{\partial t^2} - \frac{\partial^2}{\partial x^2} - \frac{\partial^2}{\partial y^2} - \frac{\partial^2}{\partial z^2} \ .$$

Consider those covariants that operate on spin $(\frac{n}{2}, \pm)$:

Proposition 1.4.1. *The only covariant differential operators that contain $\square$ (to some power) as a factor are those that intertwine spin $(\frac{n}{2}, \pm)$ with spin $(\frac{n}{2}, \pm)$;* n=0,1,2,... .

The proof of this proposition will appear elsewhere. The situations corresponding to n=0 and n=1 are described in [J&V;I].

Let e_1, e_2, and e_3 denote the standard orthonormal basis of $\mathbb{R}^3$. Then

$$\Delta_c^+ = \{(e_2-e_3),(e_2+e_3)\} \text{ , and}$$
$$\Delta_n^+ = \{\beta = (e_1-e_2),\ \alpha_1 = (e_1-e_3),\ \alpha_2 = (e_1+e_3),\ \gamma_r = (e_1+e_2)\}$$

(su(2,2) is of type A_3) . $\Lambda = (\lambda_1,\lambda_2,\lambda_3)$ is $\mathfrak{k}_1$-dominant and integral if and only if $\lambda_2 \pm \lambda_3 \in \{0,1,...\}$, and $\varrho = (2,1,0)$. For $\alpha \in \Delta$ we denote the reflexion corresponding to α by S_α. We label, for convenience, the homomorphisms by a sequence of reflexions involved in the corresponding »condition (A)«.

Example. $\Lambda = (\lambda,1,1)$ $(\lambda \in \mathbb{R})$.

At $\lambda = -3$, S_{γ_r} satisfies »condition (A)« but $S_{\gamma_r}(\Lambda+\varrho)-\varrho$ does not correspond to an element of $\mathfrak{p}^- \otimes V_\tau$.

At $\lambda = -2$, S_{γ_r} and $S_{\gamma_r}S_{\alpha_2}$ are ruled out for the same reason, but S_{α_2} defines a first order covariant differential operator.

At $\lambda = -1$, the situation is similar to $\lambda = -2$; the only difference is that S_{α_2} here gives an operator of order 2.

At $\lambda = 0$, $S_{\alpha_1}S_{\alpha_2}$ corresponds to the situation in Proposition 1.4.1 and is, moreover, the only sequence which corresponds to an element of the module.

At $\lambda \in \mathbb{N}$, S_β, $S_{\alpha_1}S_{\alpha_2}$, and $S_{\alpha_1}S_{\alpha_2}S_\beta$ correspond to elements of the module, However, due to the principle, only S_β and $S_{\alpha_1}S_{\alpha_2}$ survive.

2. Irreducible mixtures of unitarizable modules

Consider the following very general situation: One is given two groups, G_1 and G_2, a family $(\Pi_\alpha,V_\alpha)_{\alpha\in A}$ of representations Π_α of G_1 on spaces V_α, and a representation π_m of G_2 on $V = \underset{\alpha\in A}{} V_\alpha$. Let us insist that A contains more than one element and assume that it makes sense to inquire about irreducibility or indecomposability. One may then talk about V having one of these properties with respect to either G_2 or $G_1 \times G_2$, and one may say that G_2 makes V into an irreducible or indecomposable module of G_1-representations, respectively. Naturally, additional assumptions about the representations may be inserted, e.g. unitarity.

Let us from now on restrict ourselves to the case in which G_1 is isomorphic to a subgroup $\widetilde{G}_1$ of G_2 and assume that the representations of G_1 are irreducible. Those representations of Chapter 1 that have invariant subspaces defined by covariant differential operators, furnish

examples for which $\widetilde{G}_1 = G_2$ and A is finite. In these cases, the represen-
tation of G_2 is never unitary. On the other hand one may take a unitary
irreducible representation of G_2 and restrict it to G_1, but this, especially
when G_1 is non-compact, tends to give sets A which are uncountable.

Below we present, through some simple examples, two different cir-
cumstances under which one in a natural way gets irreducible mixtures
of unitary representations, and where A is countable. In both examples
$\widetilde{G}_1$ may be taken to be equal to G_2 and in the first example, A is in fact
finite.

2.1. *Representations which do not remain irreducible when restricted to the extended Poincaré group.*

The general situation is the following: G_2 is (a covering group of) a
group of holomorphic transformations of an irreducible hermitian sym-
metric space $\mathscr{D}$ of the non-compact type. Assume for simplicity that $\mathscr{D}$
is of tube type; $\mathscr{D} = \mathbb{R}^n + iV$ for an open convex cone $V \in \mathbb{R}^n$. Let P
be the maximal parabolic subgroup of G_2 which contains the translations
$L_{x_0}(x+iv) = x + x_0 + iv$ of $\mathscr{D}$ for all $x_0 \in \mathbb{R}^n$. Consider an irreducible
unitary representation π_m of G_2 on a space of vector valued holomorphic
functions on $\mathscr{D}$. Then $\pi_m|_P = \bigoplus_{i=1}^{N} \pi_{i,m,P}$ for some $N \in \mathbb{N}$, with $\pi_{i,m,P}$ ir-
reducible and unitary for all $i=1,\ldots,N$. In some special cases, $N=1$, and
for some of the most singular of these, the representation remains ir-
reducible when restricted to a normal subgroup P_0 of P for which P/P_0 is
isomorphic to the one-dimensional center of the reductive (linear) part of
P. (Cf. below.)

The decomposition of the restriction of π_m to P is handled by im-
bedding π_m into a degenerate principal series representation, and this is
accomplished by taking boundary values on the Shilov boundary of
$\mathscr{D}$, $\lim_{v\to 0} f(x+iv)$ (which exists at least on a dense set of functions). See
[JV;I] for an example. Furthermore, each representation $\pi_{i,m,P}$ is recog-
nized as the restriction of an irreducible unitary holomorphic representa-
tion of G_2 to P. We denote the last group by G_1 since is should really be
thought of as distinct (in fact, $G_1 \cap G_2 = P$); and thus get the promised
phenomenon. One interesting question to which we do not know the
answer is: How big is the group generated by G_1 and G_2; does it have a
geometric interpretation?

Let us now be specific: In the following formulas, the letters
a,b,c,d,x,y,z, and w denote 2×2 complex matrices. Moreover, in the
following definitions, 0 is the trivial 2×2 matrix, and 1 is the identity.

$$G_2 = SU(2,2) = \{g = \begin{pmatrix} a & b \\ c & d \end{pmatrix} \mid \det g = 1 \text{ and } g^\star \begin{pmatrix} 0 & 1 \\ -1 & 0 \end{pmatrix} g = \begin{pmatrix} 0 & 1 \\ -1 & 0 \end{pmatrix} \}.$$

$$P = \{g = \begin{pmatrix} a & ax \\ 0 & a^{\star-1} \end{pmatrix} \mid \det a \in \mathbb{R} \setminus \{0\}, \text{ and } x = x^\star \}.$$

$$\mathscr{D} = \{z \mid (z\text{-}z^\star)/2i \text{ is strictly positive definete}\} \qquad (2.1.1)$$
$$= \mathbb{R}^4 + iC^+,$$

where $C^+ = \{y \mid y=y^\star, \text{ tr } y > 0, \text{ and } \det y > 0\}$.

P is isomorphic to a 2-fold covering of the extended Poincaré group. The title of this section is motivated by [M&T], this investigation being complementary to that.

On the space of holomorphic functions on $\mathscr{D}$ with values in $\mathbb{C}^2 \times \mathbb{C}^2$ we consider the one-parameter family of representations U_j of G_2 given by

$$(U_j(g)f)(z) = \det(cz+d)^{-j}(cz+d)^{-1} \otimes (zc^\star+d^\star)f(g^{-1}z) \qquad (2.1.2)$$

for $g^{-1} = \begin{pmatrix} a & b \\ c & d \end{pmatrix} \in SU(2,2)$, $g^{-1}z = (az+b)(cz+d)^{-1}$, and $j \in \mathbb{Z}$. It follows from [JI, p. 324] that there exists a $K > 0$, independent of j, such that the reproducing kernel $K_j(z,w)$, which is given by

$$K_j(z,w) = \det(z-w^\star)/2i)^{-j}((z-w^\star)/i)^{-1} \otimes ((z-w^\star)/i), \quad (2.1.3)$$

may be written, for $j \geq 3$, as

$$K_j(z,w) = K \cdot \int_{C^+} e^{itr(zw)} F_j(y)dy \qquad (2.1.4)$$

with $F_j(y) = \det y^{j-3}[y \otimes \tilde{y} + (j-2)^{-1} \det y \cdot T]$; $\tilde{y}$ being the matrix for which $y \cdot \tilde{y} = \det y$ and T being the matrix which, in a basis f_1, f_2, f_3, f_4 of $\mathbb{C}^4 = \mathbb{C}^2$
$\otimes \mathbb{C}^2$ satisfying that f_1, f_2, f_3 corresponds to the symmetric subspace and f_4 to the antisymmetric, is the diagonal matrix $T = d(1,1,1,-1)$. T then satisfies that $T(a \otimes b) = (b \otimes a)T$ for all a and b. For details about reproducing kernels we refer to [J&V;I]. It is the positive – definiteness of F_j for $j \geq 3$ (for $j = 3$ only semi-definiteness) that implies the unitarity of the representations U_j for $j \geq 3$. Let us from now on assume that $j \geq 4$. The Hilbert space then consists of functions of the form

$$F_f(z) = \int_{C^+} e^{itrzy} f(y)dy \qquad (2.1.5)$$

and the inner product is given by

$$<F_{f_1}, F_{f_2}> = \int_{C^+} <F_j^{-1}(y)f_1(y), f_2(y)> dy. \qquad (2.1.6)$$

The subgroup of $SU(2,2)$ whose elements are of the form

$g = \left(\begin{smallmatrix} a & 0 \\ 0 & a^{\star-1} \end{smallmatrix}\right)$ (the linear part of P) acts as

$$(U_j(g)F_f)\,(z) = \int_{C^+} e^{itrzy}\,(a^{\star-1}\otimes a)\det a^{4-j}\,f(a^{\star}ya)dy. \qquad (2.1.7)$$

To make the decomposition under P straightforward, we would like the action on functions on C^+ to be $\det a^{2-j}\,(a\otimes a)f(a^{\star}ya)$, which is unitary in the inner product

$$<f_1,f_2> = \int_{C^+} <G_j(y)f_1(y),f_2(y)> dy, \qquad (2.1.8)$$

with $G_j(y) = (y\otimes y)\,(\det y)^{-j}$. Thus, we seek an intertwining operator of the form: multiplication by a matrix $M_j(y)$ which satisfies that $M_j(a^{\star}ya) = (a\otimes a)^{-1}M_j(y)\,(a^{\star-1}\otimes a)$ for all a and all $y \in C^+$. This property is satisfied by any $M_\beta\,(y) = (1+\beta T)\,(\tilde{y}\otimes 1)$, and it is sufficient to consider this family. To wit, the additional requirement of unitarity; that $M_\beta(y) \cdot G_j(y) \cdot M_\beta(y) = c\cdot F_j^{-1}(y)$ for some $c > 0$, is satisfied provided that $\beta^2+\beta(j-2)+1 = 0$ and $(\beta^2+1)\,(j-2)+\beta > 0$, and this has a solution when $j \geq 4$.

We observe that the representations of G_1 which we obtain are

$$(U_{1,j}(g)f)\,(z) = \det(cz+d)^{-j-2}(zc^{\star}+d^{\star})\otimes_s(zc^{\star}+d^{\star})f(g^{-1}z) \qquad (2.1.9)$$

and

$$(U_{2,j}(g)f)\,(z) = \det(cz+d)^{-j-1}f(g^{-1}z), \qquad (2.1.10)$$

for $g^{-1} = \left(\begin{smallmatrix} a & b \\ c & d \end{smallmatrix}\right)$, and functions with values in $\mathbb{C}^2 \otimes_s \mathbb{C}^2$ and $\mathbb{C}^2 \otimes_a \mathbb{C}^2$, respectively.

Transformed back to the space of $\mathbb{C}^2 \otimes \mathbb{C}^2$-valued holomorphic functions on $\mathscr{D}$ the intertwining operator is

$$(1+\beta T)\,(c({}^tD) \otimes 1), \qquad (2.1.11)$$

$c({}^tD)$ being »one-half« of the Dirac operator as in [J I]. Since any function $f: \mathscr{D} \to \mathbb{C}^4$ can be written as a sum of functions of the form $f_i \otimes v_i$, with $f_i: \mathscr{D} \to \mathbb{C}^2$ and $v_i \in \mathbb{C}^2$ ($i \leq 2$), we may apply the covariance property of $c({}^tD)$ ([JI]):

Let dV_0 denote the representation of $su(2,2)$ corresponding to the action $(g\cdot f)\,(z) = f(g^{-1}z)$, let dU_j be the representation corresponding to U_j, and consider e.g. $\tilde{x} = \left(\begin{smallmatrix} 0 & -x \\ x & 0 \end{smallmatrix}\right)$ in $su(2,2)$ ($x = x^{\star}$). Then

$$dU_j(\tilde{x}) = j\,tr\,xz + xz\otimes 1 - 1\otimes zx + dV_0(\tilde{x}) \qquad (2.1.12)$$

and

$$(c({}^tD) \otimes 1)\ (dU_j(\widetilde{x})) = \qquad\qquad\qquad\qquad (2.1.13)$$
$$(c({}^tD) \otimes 1)\ (\text{tr } xz + xz \otimes 1 + dV_0\ (\widetilde{x}) + (j-1)\text{ tr } xz - 1 \otimes zx) =$$
$$((j+2)\text{ tr } xz - zx \otimes 1 - 1 \otimes zx + dV_0\ (\widetilde{x}))\ (c({}^tD) \otimes 1) +$$
$$(c({}^tD) \otimes 1)\ [\ (j-1)\text{ tr } xz - 1 \otimes zx]\ ,$$

where the last term means $c({}^tD) \otimes 1$ acting on [...]. We recognize here $((j+2)\text{ tr } xz - zx \otimes 1 - 1 \otimes zx + dV_0\ (\widetilde{x}))$ as the infinitesimal action corresponding to the representation $(U(g)f)(z) = \det(cz+d)^{-j-2}(zc^\star + d^\star) \otimes (zc^\star + d^\star)f(g^{-1}z)$. To make the computation complete we should of course introduce the inverse to $c({}^tD) \otimes 1$, and this can only be done by returning by the Fourier–Laplace transform to the space of functions on C^+ on which this makes sense. Let us also remark that instead of using a decomposition based on $a \otimes a$ we might as well have used one based on $a^{\star -1} \otimes a^{\star -1}$. Then we would have obtained representations involving $(cz+d)^{-1} \otimes (cz+d)^{-1}$.

We conclude this section by a brief description of the situation when $j = 3$. Let V_4 denote the representation on $\mathbb{C}$-valued functions given by

$$(V_4(g)f)\ (z) = (cz+d)^{-4}f(g^{-1}z). \qquad\qquad (2.1.14)$$

Then there exists a first order constant coefficient differential operator D such that for all $g \in SU(2,2)$:

$$V_4(g)D = DU_3(g). \qquad\qquad\qquad (2.1.15)$$

U_3 is unitary and irreducible on the kernel of D (inside the space of holomorphic functions) and so is the restriction to P. V_4 is unitary and irreducible on $SU(2,2)$ as well as on P.

We finally mention that there is a non–linear equation left invariant by U_3. Unlike a similar construction for spin $\frac{1}{2}$ given by B. Ørsted and the author, independently, this equation may be taken to be holomorphic:

Let $<.,.>$ be a complex bilinear form on $\mathbb{C}^2 \otimes \mathbb{C}^2$. Consider the 2×2 complex matrix $m = \left(\begin{smallmatrix} 0 & 1 \\ -1 & 0 \end{smallmatrix}\right)$. Then for all 2×2 complex matrices a, $mam^{-1} = {}^t\widetilde{a}$. For any $c \in \mathbb{C}$ the equation

$$Df = c((m \otimes m)f, f)^{2/3} \qquad\qquad\qquad (2.1.16)$$

is then invariant, as is straightforward to see $(\det(cz+d) = \det(zc^\star + d^\star))$.

2.2. *Mixings resulting from compatible imbeddings.*

Let $\mathscr{D}$ be a bounded homogeneous domain in $\mathbb{C}^n$ containing the origin 0, let G be a group of holomorphic transformations of G, K the subgroup of G that fixes 0, and assume that $\mathscr{D}$ is homogeneous with respect to G ($\mathscr{D} \approx G/K$). We will say that we have a compatible imbedding of a hermitian symmetric space $\mathscr{D}_1$, (of the non-compact type) into $\mathscr{D}$ if there is a complex submanifold $\mathscr{D}_{1,s}$ of $\mathscr{D}$ containing (for convenience) 0 such that $\mathscr{D}_1$ and $\mathscr{D}_{1,s}$ are bi-holomorphically equivalent and such that $\mathscr{D}_{1,s}$ is homogeneous with respect to the subgroup G_1 of G that leaves $\mathscr{D}_{1,s}$ invariant. We let $K_1 = K \cap G_1$.

Let τ be a unitary representation of K on a finite dimensional vector space V_τ and assume that the representation U_τ of G, obtained from τ through holomorphic induction, is unitary in a Hilbert space H_τ of V_τ-valued holomorphic functions on $\mathscr{D}$. As described in [J&V;II], the decomposition of the restriction of U_τ to G_1 can be obtained from the filtration of H_τ defined by the order of vanishing on $\mathscr{D}_{1,s}$. As a result one gets

$$H_\tau = \bigoplus_{i=1}^{\infty} H_{\tau_i}$$

and

$$U_\tau = \bigoplus_{i=1}^{\infty} U_{\tau_i}$$

where the U_{τ_i}'s are unitary representations of G_1 obtained through holomorphic induction of finite-dimensional unitary representations τ_i of K_1. There may be multiplicities (always finite) and the sum is always at most countable. Evidently, the elements of G outside of G_1 will mix up, through the representation U_τ, the spaces H_{τ_i}. Thus, it is natural to look for another copy of G_1 inside G. This copy does not necessarily have to be of the same nature, i.e. the direct inclusion of SO(4,2) into SU(4,2) does not correspond to a compatible imbedding, but for now we will assume that it is. Even then, the two copies do not have to be conjugate inside G. For instance, if $\mathscr{D} = \mathscr{D}_3 \times \mathscr{D}_3$ then there are at least three interesting and isomorphic submanifolds, namely $\mathscr{D}_3 \times \{0\}$, $\{0\} \times \mathscr{D}_3$, and the diagonal in $\mathscr{D}$, and the corresponding groups are not conjugate. We shall not discuss questions concerning irreducibility here since it is quite clear how such questions should be approached. Rather, we conclude this general discussion with the remark that a K_1-type in a fixed H_{τ_i}, under the action of K, will only travel into a finite number of other H_{τ_i}'s. This is clear from the decomposition.

Let us give a simple example: Let $\{e_1, e_2, e_3, e_4, e_5\}$ be a standard basis of $\mathbb{C}^5$ and let SU(2,3) be the group of linear transformations of $\mathbb{C}^5$ that leaves invariant the sesquilinear form which, in the given basis, is defined by the diagonal matrix $d(1,1,-1,-1,-1)$. We have that $K = \{ (u,v) \in U(2)\mathrm{x}U(3) \mid \det u \cdot \det v = 1\}$. As G_1 we take SU(2,2). Copy no. 1 is taken to be the subgroup defined by (e_1, e_2, e_3, e_4) and copy no. 2 to be the one defined by (e_1, e_2, e_4, e_5), though for some purposes it might be more natural to take a more twisted version as copy no. 2. We shall here be content to give the decomposition of some representations of SU(2,3) under copy no. 1. We let z denote a complex matrix with 2 rows and 3 columns; the space $\mathscr{D}$ corresponding to SU(2,3) may be taken to be a bounded subset containing the origin, of the vector space of all such matrices.

Our first example is with $\tau(u,v) = \det u^{-n}$. The corresponding representation is denoted by U_n. Restricted to K it has the form

$$(U_n(u,v)f)\, (z) = \det u^{-n} f(u^{-1}zv). \tag{2.2.1}$$

For $n \in \mathbb{N}$, U_n is unitary. The decomposition is obtained by expanding functions in the variables corresponding to the 3rd column. The set of τ_i's is then equal to $\{\det u^{-n} \underset{s}{\otimes} u \mid j=0,1,2,\ldots\}$. This is the case even for $n = 1$, where the representation space is annihilated by a second order differential operator. The reason is that this operator does not contain a summand which is purely a differential operator in the variables corresponding to the 3rd column.

Our second, and final, example is with $\tau = u(\det u)^{-n}$; the corresponding representation U_τ is denoted by V_n. Restricted to K, V_n has the form

$$(V_n(u,v)f)\, (z) = u \det u^{-n} f(u^{-1}zv), \tag{2.2.2}$$

where now f takes values in $\mathbb{C}^2$. For $n \geq 2$, V_n is unitary. For $n > 2$ the set of τ_i's is $\{\det u^{-n} \underset{s}{\otimes} u \mid j = 1,2,\ldots\} \cup \{\det u^{-n+1} \underset{s}{\otimes} u \mid j=0,1,2,\ldots\}$, but for $n = 2$, where the representation space is annihilated by a first order (matrix valued) differential operator, we only get $\{\det u^{-n} \underset{s}{\otimes} u \mid j=1,2,\ldots\}$.

References

B, G, & G:··I. N. Bernstein, I. M. Gelfand, and S. I. Gelfand, Differential operators on the base affine space and a study of g-modules, in »Lie Groups and Their Representations« (I. M. Gelfand, Ed.), Adam Hilger; London, 1975.

B&C: B. D. Boe and D. H. Collingwood, A comparison theory for the structure of induced representations, Preprint, 1983.

D&H: P. J. Davis and R. Hersh: *The Mathematical Experience,* Birkhäuser; Boston, 1980.

E,H,&W: T. Enright, R. Howe, and N. Wallach, A classification of unitary highest weight modules, in *Representation Theory of Reductive Groups* (P. C. Trombi, Ed.), Birkhäuser; Boston-Basel-Stuttgart, 1983.

H-C: Harish-Chandra, Representations of semi-simple Lie groups V&VI, Amer. J. Math. **78** (1956), 1-41 and 564-628.

H&J: M. Harris and H. P. Jakobsen, Covariant differential operators, in *Group Theoretical Methods in Physics* (M. Serdaroglu and E. Ínönü, Eds.), Lecture Notes in Physics **180,** Springer; Berlin-Heidelberg-New York-Tokyo, 1983.

J&V;I: H. P. Jakobsen and M. Vergne, Wave and Dirac operators, and representations of the conformal group, J. Funct. Anal. **24** (1977), 52-106.

J&V;II: H. P. Jakobsen and M. Vergne, Restrictions and expansions of holomorphic representations, J. Funct. Anal. **34** (1979), 29-53.

JI: H. P. Jakobsen, Intertwining differential operators for $Mp(n, \mathbb{R})$ and $SU(n,n)$, Trans. Amer. Math. Soc. **246** (1978), 311-337.

JII: H. P. Jakobsen, On singular holomorphic representations, Invent. Math. **62** (1980), 67-78.

JIII: H. P. Jakobsen, The last possible place of unitarity for certain highest weight modules, Math. Ann. **256** (1981), 439-447.

JIV: H. P. Jakobsen, Hermitian symmetric spaces and their unitary highest weight modules, J. Funct. Anal. **52** (1983), 385-412.

JV: H. P. Jakobsen, Basic covariant differential operators on hermitian symmetric spaces, preprint 1984. To appear in Ann. Scient. Éc. Norm. Sup.

Jms: G. D. James, *The Representations Theory of the Symmetric Groups,* Lecture Notes in Math. **682,** Springer; Berlin-Heidelberg-New York, 1978.

K&V: M. Kashiwara and M. Vergne, On the Segal-Shale-Weil representation and harmonic polynomials, Invent. Math. **44** (1978), 1-47.

M&T: G. Mack and I. Todorov, Irreducibility of the ladder representation of $U(2,2)$ when restricted to the Poincaré subgroup, J. Math. Phys. **10** (1969), 2078-2085.

R&V: H. Rossi and M. Vergne, Analytic continuation of the holomorphic discrete series of a semi-simple Lie group, Acta Math. **136** (1976), 1-59.

Smd: W. Schmid, Die Randwerte holomorpher Funktionen auf hermitesch symmetrischen Räumen, Invent Math. **9** (1969), 61-80.

S: I. E. Segal, *Mathematical Cosmology and Extragalactic Astronomy,* Academic Press; New York, 1976.

S,J,Ø,P,&S: I. E. Segal,   H. P. Jakobsen,   B. Ørsted,   S. M. Paneitz,   and   B. Speh,

Covariant chronogeometry and extreme distances: Elementary particles, Proc. Natl. Acad. Sci. USA **78** (1981), 5261–5265.

V: D. Vogan, *Representations of Real Reductive Lie Groups,* Birkhäuser; Boston–Basel–Stuttgart, 1981.

W: N. Wallach, Analytic continuation of the discrete series II, Trans. Amer. Math. Soc. **251** (1979), 19–37.

Lars Døvling Andersen

Completing Partial Latin Squares

ABSTRACT. *The paper gives a survey of completion results for symmetric and unsymmetric partial latin squares. Several embedding results are mentioned, but the emphasis is on proper completion where, given a partial latin square of side n, one looks for a completion to a latin square of the same side.*

For latin squares with no symmetry required we prove a strengthening of the known results concerning the Evans conjecture, which was proved to be true in 1981.

We then state some new results about the corresponding problem for symmetric latin squares and describe their proofs briefly; complete proofs will be given elsewhere.

Institute of Electronic Systems, Aalborg University Centre,
Strandvejen 19, DK-9000 Aalborg, Denmark

1. Introduction

The subject of this paper belongs to the branch of mathematics called *combinatorics*. This area is concerned with arranging, counting, and choosing from a number of objects. Very often only a finite number of objects are considered at a time, and the discrete nature of the subject gives it a striking feature not so common in other parts of mathematics: frequently a deep mathematical problem can be explained in very simple terms, easy to understand for anybody who cares to listen.

Probably the most famous problem sharing this particular beauty of combinatorics is the so-called *four colour problem:* Is it true that any map in the plane or on a sphere can be coloured so that any pair of countries with a common boundary always get different colours, using altogether at most four colours? (It must be required that each country consists of just one connected region). The four colour problem was unsolved for more than a century, though many skilled mathematicians have worked very hard on it (and so have many amateur mathematicians!) It has now been established that four colours do suffice to colour any map; a proof was announced in 1976 and published in 1977 (Appel & Haken 1976 and 1977, Appel, Haken & Koch 1977). But the proof depends heavily on the

use of a computer, and so the 'simple' four colour problem still puzzles the minds of combinatorialists hoping to find a more direct proof.

This article is about a concept in combinatorics called *latin squares* (completely unrelated to the four colour problem), a topic which in the course of time also has contained some simply stated problems that turned out to be extremely difficult. Consider the following example.

Let n be a positive integer. Given an n×n array (chessboard) in which n-1 of the cells (squares) are filled with one of the integers 1,...,n, so that no integer occurs twice in any row or column, is it always possible to fill all the remaining cells to obtain an n×n array in which *each* of the numbers 1,...,n occurs *exactly once* in each row and column?

This question was first posed by T. Evans (Evans 1960), and the assumption of an affirmative answer became known as *the Evans Conjecture*. Despite the fact that the problem received much attention, and many partial solutions were published, no complete solution was given until 1981, when B. Smetaniuk proved that the Evans Conjecture is true, and so the answer to the above question is indeed yes (Smetaniuk 1981).

The present paper is closely related to the Evans Conjecture, but before continuing the discussion we have better put the topic in its proper context of latin squares.

A *partial latin square* of side n on the symbols $s_1,...,s_n$ is an n×n matrix of cells in which each cell either is empty or contains one of the symbols $s_1,...,s_n$, and, furthermore, no symbol occurs twice in any row or twice in any column. It is a *latin square* if there are no empty cells. Thus in a latin square each symbol must occur exactly once in each row and column. We shall almost always assume that the set of symbols is {1,...,n}. Figure 1 shows two latin squares and two further partial latin squares, all of side 6.

With the above definitions, the Evans Conjecture can be formulated like this: Any partial latin square of side n with at most n-1 non-empty cells

Figure 1

1	3	4	6	2	5
3	6	5	1	4	2
4	5	1	2	3	6
6	1	2	3	5	4
2	4	3	5	6	1
5	2	6	4	1	3

a

1	2	4	5	6	3
5	4	6	3	2	1
2	1	5	6	3	4
6	3	2	4	1	5
4	6	3	1	5	2
3	5	1	2	4	6

b

1	2	4			
5	4	6			
2	1	5			
			4		
				5	
					6

c

1	2	3	4		
				5	
				6	

d

can be completed to a latin square of side n. The same conjecture has been stated on at least two other occasions (Klarner 1970; Dénes 1974).

After B. Smetaniuk's proof, an independent proof was published by A. J. W. Hilton and the present author proving, however, a stronger result (Andersen & Hilton 1983). T. Evans arrived at his conjecture partly because he could find no counterexamples, and partly because it is easy to find examples of a partial latin square of side n with n non-empty cells which *cannot* be completed to a latin square of side n (Figure 1d is such an example). The paper by Andersen and Hilton actually contained a *complete characterization* of those partial latin squares of side n with n non-empty cells that cannot be completed to a latin square of side n.

In Section 5 of this paper we extend the characterization to include all those partial latin squares of side n with *n+1* nonempty cells which cannot be completed to a latin square of side n.

It may be asked where the importance of determining such a further class of non-completable partial latin squares lies. The author believes that throughout mathematics determining extreme cases is very valuable and so, in particular, there is a large difference between knowing that squares with n non-empty cells can be completed *except* in a well-defined, non-empty class of situations and just knowing that squares with n-1 non-empty cells can be completed. Furthermore, by characterizing exceptions 'one step beyond' the extreme cases, a good deal more insight in the structure of the problem is gained (accordingly, we believe that the exceptions presented in Section 5 give a good idea about how non-completable squares can be obtained if yet more non-empty cells are introduced). In the present case it is also useful for the proof of one of the main results of Section 6.

Another possible question could be whether a 'nice' characterization of non-completable squares with *any* number of non-empty cells is obtainable. The answer is almost certainly no, as the problem of completing partial latin squares is known to be *NP-complete* and so belongs to a class of problems that are not expected to have 'easy solutions'. We discuss this in more detail in the next section.

While on the subject of questions, a simple, but natural one is: What is the purpose of latin squares in general and of completing partial latin squares in particular? It is beyond the scope of this paper to discuss applications of latin squares at any great length, but we can single out the subject of *design of experiments* as probably the main field concerned with practical applications of latin squares. They are used in some situations where one wants to gather data for statistical analysis, and the purpose of

the latin squares is to eliminate the effect of certain systematic differences from the data. We mention briefly two examples of slightly differing nature:

1. Sheer planning purposes:
   Suppose that we want to test the effect of n different diets on the milk yield of cattle. We select n cows and n time periods and use a latin square of side n with a row for each cow and a column for each time period. Then, if, say, the cell common to the row of cow 1 and the column of period 2 contains the symbol 3 it means that cow 1 is given diet 3 in period 2, etc. With proper handling of the data, this would eliminate differences between cows and time periods, as each diet is tested on each cow and in each time period.
2. As a 'physical' latin square:
   If n varieties of a crop are to be tested on a rectangular field, it will often be advantageous to superimpose an n×n latin square on the field, thus dividing it into n^2 smaller rectangular plots all having the same size, and growing crop 1 in the n plots corresponding to the occurrences of 1 in the latin square, etc. There is a good chance that this will eliminate yield differences due to fertility differences of the plots.

In both of the above examples, further properties of the latin squares (such as *row completeness*) would be desirable, so the description here is much simplified. We must omit further discussion and refer the reader to some of the many books on the subject (Dénes & Keedwell 1974; Fisher 1935; Cochran & Cox 1950; Cox 1958; The Open University 1981). It is not hard to imagine situations like the examples above, where it would be convenient to have certain entries of the latin squares fixed *a priori;* this is where completion of partial latin squares comes in.

An even simpler example of this is obtained when considering the completion of a partial latin square as a *time-tabling* problem in the following way. We have two sets S_1 and S_2, each consisting of n persons, and we must schedule one meeting between each person from S_1 and each person from S_2, all meetings taking place within n time periods. The set S_2 could consist of participants of a course and S_1 be the teachers of the course with the meetings corresponding to examinations. Such a schedule is readily provided by a latin square of side n with the rows corresponding to S_1, the columns to S_2 and the entries 1,...,n to the time

periods. If some of the meetings have to take place at prescribed times, we have our completion problem. It may be argued that in a situation such as the above, it is unlikely that the number of teachers is equal to the number of participants; it follows, however, from one of the simplest completion results of Section 3 that our results will cover the case of $|S_1| \neq |S_2|$ also (for any set A, $|A|$ denotes the number of elements of A).

If we have just one set S of persons and we want to schedule one meeting between each pair of persons we can use a *symmetric latin square*. We have defined latin squares as matrices, and so it is customary to enumerate the rows from the top and the columns from the left, so that cell (i,j) is the cell common to the ith row from the top and the jth column from the left. We say that a partial latin square of side n is *symmetric* if, whenever one of the cells (i,j) and (j,i) is non-empty then so is the other, and they have the same entry ($1 \leq i < j \leq n$). Figure 1a shows a symmetric latin square. The *diagonal* is the set of cells $\{(i,i) | 1 \leq i \leq n\}$. In a symmetric latin square of odd side each symbol occurs exactly once on the diagonal, and in a symmetric latin square of even side each symbol occurs an even number of times on the diagonal.

We can use a symmetric latin square for scheduling meetings between each pair from a group of n persons (for example as required for a round-robin tournament) by letting persons i and j meet in time period k, where k is the entry of cells (i,j) and (j,i). This will require n time periods although each person has just n-1 meetings; in each time period occurring on the diagonal one or more persons have no meetings, person i having time period k off where k is the entry of cell (i,i). When scheduling pairwise meetings for an odd number of persons, clearly one person *has* to be unpaired in each period, and so n time periods are indeed needed altogether. If n is even, however, the symmetric latin square again brings n time periods into the schedule, where only n-1 are needed, as we shall see. One way of getting round this is to require that all cells on the diagonal of the symmetric latin square contain the entry n; then no meeting will be scheduled for period n, so only n-1 periods are used. But perhaps a more natural way of looking at round-robin tournaments with an even number of participants is from the point of view of *complete graphs*.

A graph G = (V,E) consists of a set V called *vertices* and a set E of *edges*, which are pairs of distinct vertices. An edge e = $\{V_1, V_2\}$ is said to *join* vertices V_1 and V_2, and to be *incident* with V_1 and V_2, and we write e = $V_1 V_2$. We also say that V_1 and V_2 are *neighbours*. A *complete* graph is a
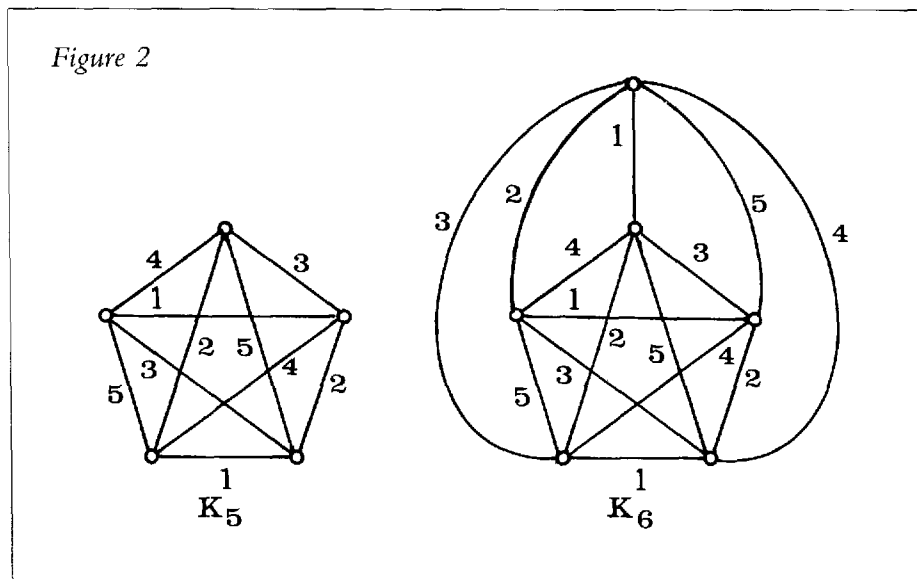
Figure 2

graph in which each pair of vertices are joined by an edge, and the complete graph with n vertices is denoted by K_n. Figure 2 shows drawings of K_5 and K_6. The numbers on the edges are explained below.

An *edge-colouring* of a graph G with k colours is an assignment of one of k colours to each edge of G such that edges incident with the same vertex always have different colours. We shall always use the set of 'colours' $\{1,...,k\}$. Each of the graphs K_5 and K_6 of Figure 2 has been given an edge-colouring with 5 colours. The *chromatic index* q(G) of G is the least k for which G has an edge-colouring with k colours. A famous theorem states that if d(G) is the *maximum degree* of G (the largest number of edges incident with any one vertex), then q(G) is either d(G) or d(G)+1 (Vizing 1964). It is wellknown that

$$q(K_n) = \begin{cases} n-1 & \text{if n is even,} \\ n & \text{if n is odd.} \end{cases}$$

Thus the edge-colourings given to K_5 and K_6 in Figure 2 are minimal, i.e. with as few colours as possible.

If the vertices of a graph G correspond to persons, then clearly an edge-colouring of G provides a schedule for meetings between all pairs joined by an edge: each meeting between a pair takes place in the time period designated by the colour of the edge joining the pair. If only q(G)

colours are used for the edge-colouring, then as few time periods as possible are used.

The round-robin tournament problem then corresponds to constructing an edge-colouring of K_n with $q(K_n)$ colours, possibly with the colour of some edges prescribed. We consider this problem, as well as that of completing partial symmetric latin squares, in Section 6, where we present two new results and some corollaries that we have recently obtained with A. J. W. Hilton and E. Mendelsohn, respectively. We only sketch the proofs; they are too complicated to be included here and will appear elsewhere.

Given an edge-colouring of K_n with $q(K_n)$ colours it is easy to construct a symmetric latin square of side n. Let the vertices be $V_1,\ldots,V_n$ and place the colour of the edge V_iV_j in cells (i,j) and (j,i), $1 \leq i < j \leq n$. If n is odd, place the colour not occurring at the vertex V_i in cell (i,i) and if n is even, place the colour n in all cells (i,i), $1 \leq i \leq n$. This is easily seen to be a symmetric latin square of side n. Actually, if n is even we can obtain a symmetric latin square of side n-1 also by deleting the last row and column and placing the entry of cell (n,i) in cell (i,i) instead, $1 \leq i \leq n-1$.

We close this introductory section by noting that also the problem of completing partial latin squares with no symmetry required has a graph analogue. A graph G = (V,E) is called *bipartite* if V can be partitioned into two disjoint sets L and R such that each edge joins a vertex of L to a vertex of R. If *each* vertex from L is joined to *each* vertex from R then G is a *complete bipartite* graph, and it is denoted by $K_{m,n}$ where m = |L| and n = |R|. For any bipartite graph G, q(G) = d(G) (König 1936). A latin square of side n is equivalent to an edge-colouring of $K_{n,n}$ with n colours simply by considering cell (i,j) to be an edge joining vertices ℓ_i and r_j where L = $\{\ell_1,\ldots,\ell_n\}$ and R = $\{r_1,\ldots,r_n\}$, and $1 \leq i \leq n, 1 \leq j \leq n$. So completing a partial latin square of side n to a latin square of side n is equivalent to finding an edge-colouring of $K_{n,n}$ with n colours, with the colour of some edges being prescribed.

The author is aware that this introduction has been much more diffuse (and longer!) than is usual for a mathematical research paper, even for a survey paper. This is due to the context in which this paper appears, a context enhancing the possibility that non-mathematicians may stumble upon the paper. It has been the purpose of the introduction to give such non-professionals an opportunity of getting an impression of the subject and of getting some idea of the contents of the paper. We shall *not* keep up this style in the remainder of the paper. We intend to survey part of the enormous amount of material on completions of partial latin squares,

with emphasis on the results already mentioned in this introduction, and from now on we shall use standard terminology without defining all the concepts used. Quite often the definitions can be found in the references that we give.

2. The complexity of completing partial Latin Squares

For the theory of NP-completeness we refer the reader to one of the excellent books on the subject (Garey & Johnson 1979). Here we remark that the class of decision problems which can be solved by polynomial time algorithms is called P, and that $P \subseteq NP$, where NP is a class of problems containing several apparently very difficult problems unlikely to be solvable in polynomial time (here, a polynomial time algorithm is considered 'good', problems which cannot be solved in polynomial time are considered 'hard', and a 'problem' should not be confused with an 'instance' of a problem). It is not known whether $P = NP$, but it is considered extremely improbable.

A subclass of NP consists of the *NP-complete* problems. Any NP-complete problem has the property that if it can be solved in polynomial time then $P = NP$. So no NP-complete problem is expected to be solvable by a polynomial time algorithm.

C. J. Colbourn has been interested in the complexity of completing partial latin squares. He first proved that completing partial *symmetric* latin squares is NP-complete (and used this to prove that embedding partial Steiner triple systems is NP-complete as well) (Colbourn 1983). Shortly afterwards, Colbourn proved that also completing partial latin squares is NP-complete (Colbourn 1984). We sketch his proof for partial latin squares and use that result to present a new, simpler proof for the symmetric case.

The investigation of the complexity of completing partial latin squares makes use of another link between latin squares and graph theory, different from the connection described in Section 1.

A graph $G = (V,E)$ is called *tripartite* if V can be partitioned into three mutually disjoint sets V_1, V_2 and V_3 such that the end-vertices of each edge of E are in distinct sets. If each pair of vertices from distinct sets are joined by an edge, G is said to be a *complete tripartite* graph, and it is denoted by $K_{\ell,m,n}$ where $\ell = |V_1|$, $m = |V_2|$ and $n = |V_3|$. It is easy to see that a latin square of side n is equivalent to a decomposition of $K_{n,n,n}$ into mutually edge-disjoint K_3's; just let V_1, V_2 and V_3 be the set of rows,

columns and symbols respectively, and identify an occurrence of the symbol k in cell (i,j) with the K_3 with vertices corresponding to row i, column j and symbol k. This idea is exploited in the following.

It is known that the problem of determining whether a graph can be decomposed into mutually edge-disjoint K_3's is NP-complete (Holyer 1981a). Modifying the proof of this, Colbourn obtained:

Theorem 2.1. Deciding whether a tripartite graph can be decomposed into mutually edge-disjoint K_3's is NP-complete.

A tripartite graph is *uniform* if each vertex has the same number of neighbours in each of the vertex classes not containing it. If a tripartite graph is not uniform, then it is obvious that it cannot be decomposed into mutually edge-disjoint K_3's. So we have

Corollary 2.2. Deciding whether a uniform tripartite graph can be decomposed into mutually edge-disjoint K_3's is NP-complete.

Now let G = (V,E) be a tripartite graph with vertex classes $\{r_1,...,r_x\}$, $\{c_1,...,c_y\}$ and $\{s_1,...,s_z\}$. A *latin framework* LF(G;s) for G, s $\geq$ max $\{x,y,z\}$, is a partial latin square of side s on symbols 1,...,s with the following properties:

(i)   Cell (i,j) of LF(G;s) is empty if and only if $r_ic_j \in$ E.
(ii)   If $r_is_k \in$ E then k does not occur in row i of LF(G;s).
(iii) If $c_js_k \in$ E then k does not occur in column j of LF(G;s).

Colbourn proved that G always has a latin framework with s = $2|V|$:

Theorem 2.3. Given a uniform tripartite graph G with n vertices, a latin framework LF(G;2n) can be produced in polynomial time.

With this, it is an easy matter to prove the main result of this section.

Theorem 2.4. Deciding whether a partial latin square of side n can be completed to a latin square of side n is NP-complete.

Proof. The problem is clearly in NP. To prove that it is NP-complete, by Corollary 2.2 it suffices to reduce the problem of decomposing a uniform tripartite graph into mutually edge-disjoint K_3's to the problem of completing a partial latin square, the reduction taking place in polynomial time. But this can be done by Theorem 2.3 and the observation that

Figure 3

S(P):

S_n	P
P^T	S_n

G can be decomposed into mutually edge-disjoint K_3's if and only if LF(G;2n) can be completed to a latin square of side 2n. We leave this argument to the reader (note that (i) and the uniformity of G imply that the converse of (ii) also holds: if k does not occur in row i, then $r_i s_k \in E$).

From Theorem 2.4 we get a new proof of the next theorem.

Theorem 2.5. Deciding whether a partial symmetric latin square of side n can be completed to a symmetric latin square of side n is NP-complete.

 Proof. Obviously the problem belongs to NP. For any n, let S_n be any symmetric latin square of side n on symbols n+1,...,2n. If P is any partial latin square of side n on symbols 1,...,n, let S(P) be the partial symmetric latin square of side 2n on symbols 1,...,2n indicated in Figure 3.

 Clearly S(P) can be constructed in polynomial time, and clearly S(P) can be completed to a symmetric latin square of side 2n if and only if P can be completed to a latin square of side n. Thus we have obtained a polynomial time reduction from completion with no symmetry to completion with symmetry, and Theorem 2.5 follows from Theorem 2.4.

It follows from the proof of Theorem 2.5 that completing partial symmetric latin squares is NP-complete even when restricted to the class of squares which are as in Figure 3, a class which at first sight might look rather limited.

 Colbourn's original proof of Theorem 2.5 made use of the following result, which we include for completeness (Holyer 1981b):

Theorem 2.6. It is NP-complete to determine the chromatic index of a graph G. In fact, it is NP-complete even to determine the chromatic index of a graph which is regular of degree 3.

The moral of this section is that it is probably a desperate undertaking to try giving a simple characterization of those partial latin squares of side n that can be completed to a latin square of side n. So it seems reasonable that most of the research in the area has concentrated on determining families of partial latin squares that *can* be completed. The next sections contain many examples of such families. Let us make it clear, however, that when we prove, or state without proof, that a partial latin square of a certain type can be completed, we do not present an algorithm for actually doing so. As a general rule, our existence proofs are not very constructive.

3. Embedding results

We have seen that not all partial latin squares can be completed, in the sense that not all partial latin squares of side n can be completed to a latin square of side n. A natural question to ask then is whether a partial latin square of side n can always be completed to a latin square of side t for some t > n? In the same paper as where the Evans Conjecture was posed, Evans proved that the answer is affirmative, and that any t≥2n will do (and for each n≥4 he gave examples where no t<2n-1 works) (Evans 1960).

When we have a completion as above, we say that the partial latin square P can be *embedded* in the larger latin square S. Usually we think of P as being situated in the top left hand corner of S, as in Figure 4.

There are two ways of looking at the situation of Figure 4. One is as described above, a straightforward embedding of a partial latin square P of side n in a latin square S of side t. The other sees it as a completion of a partial latin square of side t, where all non-empty cells just happen to

Figure 4
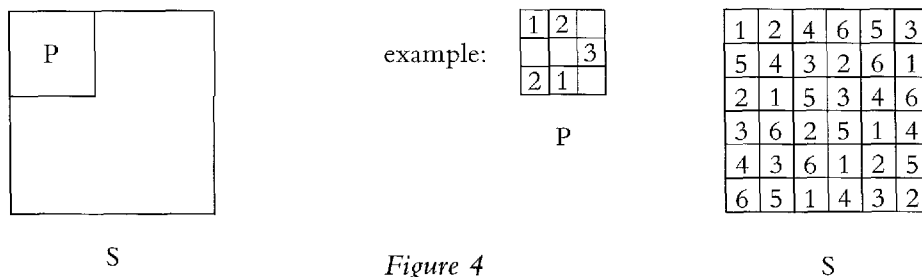
occur inside an n×n subarray. The former seems the more appropriate, but allows only n distinct symbols to occur in P, whereas the latter would allow all t symbols to do so. We compromise and choose embedding terminology, but allow t symbols to occur in P. Hence we shall speak of a partial latin square *of side n on t symbols*.

As mentioned in the introduction, our main interest will be some completion theorems in the vein of the Evans Conjecture, and our survey of embedding results will be brief. The reader will be able to find more on this topic in the recent survey paper by C. C. Lindner (Lindner 1984).

Before we begin listing results, we need one more definition. Following Lindner, an *r×s latin rectangle on symbols 1,...,n* is an r×s array in which *each* cell contains an element of $\{1,...,n\}$, such that each symbol occurs at most once in each row and column. Note that this also applies to the case r=s, so that an r×r latin rectangle has no empty cells, and yet it need not be a latin square!

If R is a latin rectangle on symbols 1,...,n we let R(i) denote the number of occurrences of the symbol i in R, $1 \leq i \leq n$. We first prove a lemma which contains a necessary condition for embedding that appears in a variety of situations.

Lemma 3.1. Let R be an r×s latin rectangle which is embedded in a latin square S of side n on symbols 1,...,n, and let D be as in Figure 5. Then R(i) = r+s−n+D(i) for all i, $1 \leq i \leq n$.

Proof. Follows from the facts that for all i, R(i)+B(i)=s and B(i)+D(i) = n−r.

If an n×n array S is partitioned as in Figure 5, and if R is r×s, then the *diagonal outside R* is the set of cells (r+1,s+1), (r+2,s+2),...,(r+n−s,n) if r≤s, and the set of cells (r+1,s+1),(r+2,s+2),...,(n,s+n−r) if r≥s. They all lie in D.

The strongest embedding result we have when no symmetry is required is the following (Andersen & Hilton 1983). It is concerned with embedding of a latin rectangle with the additional requirement that the diagonal outside R is prescribed (each symbol i must occur f(i) times on it). The Figures 1c and 1b give an example of such an embedding. However, if r = s then for Theorem 3.2 to work at least one cell on the diagonal must be left unprescribed (Andersen, Häggkvist, Hilton & Poucher 1980).

Figure 5

S:

R	A
B	D

Theorem 3.2. Let R be an $r \times s$ latin rectangle on symbols $1, \ldots, n$, and for each i, $1 \leqslant i \leqslant n$, let $f(i)$ be a non-negative integer such that $\sum_{i=1}^{n} f(i) \leqslant \min\{n-r, n-s\}$ with strict inequality if $r=s$. Then R can be embedded in a latin square of side n with symbol i occurring at least $f(i)$ times on the diagonal outside R for all i, $1 \leqslant i \leqslant n$, if and only if

$$R(i) \geqslant r+s-n+f(i) \text{ for all } i, 1 \leqslant i \leqslant n.$$

From Theorem 3.2 it is easy to deduce some wellknown results.

Corollary 3.3. (Ryser 1951). An $r \times s$ latin rectangle R on symbols $1, \ldots, n$ can be embedded in a latin square of side n if and only if

$$R(i) \geqslant r+s-n \text{ for all } i, 1 \leqslant i \leqslant n.$$

Proof. Put all $f(i)$ equal to zero in Theorem 3.2.

Corollary 3.4. (Evans 1960). A partial latin square of side n on t symbols can be embedded in a latin square of side t for all $t \geqslant 2n$.

Proof. All empty cells of the partial latin square can be filled with one of the t symbols, as at most $2(n-1)$ symbols can be forbidden for a given cell. Now apply Corollary 3.3, where the condition is satisfied because $R(i) \geqslant 0 \geqslant 2n-t$.

The condition $t \geqslant 2n$ is best possible, as we remarked earlier.

Corollary 3.5. (Hall 1945). An $r \times n$ latin rectangle on n symbols can always be completed to a latin square of side n.

A time-table for all meetings between pairs of persons, one belonging to a set of r persons and the other to a set of $n > r$ persons disjoint from the first set, in as few time periods as possible, corresponds to an $r \times n$ latin rectangle on n symbols (and to an edge-colouring of $K_{r,n}$ with n colours). Corollary 3.5 shows that trying to complete such a time-table

with some preassigned entries is equivalent to trying to complete to a latin square of side n.

Theorem 3.2 does not hold with r=s and $\sum_{i=1}^{n} f(i) = n-r$, i.e. with completely prescribed diagonal. This is unfortunate, because a frequent requirement on a latin square is that it is *idempotent,* meaning that cell (i,i) contains the symbol i for all i. No necessary and sufficient condition for a latin rectangle to be embeddable in an idempotent latin square is known, which is valid in all cases. Problems concerning this have been extensively studied (Lindner 1971; Hilton 1973; Andersen 1982; Hilton & Rodger 1982; Rodger 1983; Andersen, Hilton & Rodger 1983; Bryant 1984). We state only two results, the first very important theorem due to C. A. Rodger giving a necessary and sufficient condition for the case r=s and n $\geq$ 2r+1 (and r$\geq$ 10).

Theorem 3.6. (Rodger 1984). Let R be an r×r latin rectangle on symbols 1,...,n where r $\geq$ 10 and n $\geq$ 2r+1. For each i, 1$\leq$i$\leq$n, let f(i) be a nonnegative integer such that $\sum_{i=1}^{n} f(i)=n-r$. Then R can be embedded in a latin square of side n with each symbol i occurring f(i) times on the diagonal outside R for all i, 1$\leq$i$\leq$n, if and only if (i)-(iii) are satisfied.

(i)   R(i) $\geq$ 2r−n+f(i) for all i, 1$\leq$i$\leq$n.
(ii)   For all i, 1$\leq$i$\leq$n: if R(i)=r then f(i)$\neq$n−r−1.
(iii) If R is a latin square and n=2r+1 then $\sum_{R(i)>0} f(i) \neq 1$.

For n $\geq$ 10, the next theorem is a corollary of Theorem 3.6.

Theorem 3.7. (Andersen, Hilton & Rodger 1982). A partial idempotent latin square of side n can be embedded in an idempotent latin square of side t for all t $\geq$ 2n+1.

When Theorem 3.7 first appeared it settled a long standing conjecture in the affirmative. The inequality t $\geq$ 2n+1 is the best possible.

Turning now to embedding theorems for partial symmetric latin squares we first present a new result due to A. J. W. Hilton and the author. It is used in the proof of one of the main results of Section 6; in this paper we state both theorems without proofs. Because of the close connection between symmetric latin squares and edge-colourings of complete graphs, it is useful to consider embedding of a symmetric latin rectangle R in a symmetric latin square S where *both* entries of S on the diagonal outside R *and* entries of S corresponding to independent edges
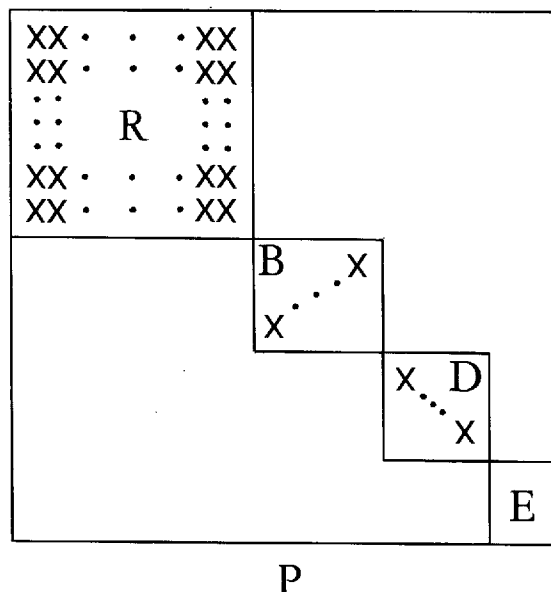
Figure 6

outside the complete subgraph determined by R are prescribed. This can be pictured as in Figure 6.

Theorem 3.8. Let P be a partial symmetric latin square of side n on symbols $1,\ldots,n$, and let P be of the form of Figure 6 with the non-empty cells being exactly all cells of R, the back diagonal of B and the diagonal of D. Here R is an $r \times r$ symmetric latin rectangle and B has even side. Some of R, B, D, and E may have side zero, but if B has positive side, then so has E. For all i, $1 \le i \le n$, let f(i) be the number of times the symbol i occurs in B $\cup$ D.

Then P can be completed to a symmetric latin square of side n if and only if (i) and (ii) hold.

(i) $R(i) \ge 2r - n + f(i)$ for all i, $1 \le i \le n$.

(ii) $R(i) + f(i) \equiv n$ (mod 2) for at least $r + d$ different $i \in \{1,\ldots,n\}$, where d is the side of D.

If n is odd, condition (ii) reduces to requiring that all symbols on the diagonal of P are distinct.

Theorem 3.8 extends a known result with B and E not appearing (Hoffman 1983; Andersen 1982). This in turn generalized a wellknown theorem due to A. B. Cruse.

Corollary 3.9. (Cruse 1974). Let R be an r×r symmetric latin rectangle on 1,...,n. Then R can be embedded in a symmetric latin square of side n if and only if

R(i) ⩾ 2r−n for all i, 1⩽i⩽n, and
R(i) ≡ n (mod 2) for at least r different i ∈ {1,...,n}.

   Proof. Put f(i) = 0 for all i, 1⩽i⩽n, in Theorem 3.8.

Cruse also obtained the following results. They are easy consequences of Corollary 3.9. All inequalities are best possible.

Corollary 3.10. A partial symmetric latin square of side n on t symbols can be embedded in a symmetric latin square of side t for all even t ⩾ 2n.

Corollary 3.11. A partial symmetric latin square of side n on t symbols, in which each symbol occurs at most once on the diagonal, can be embedded in a symmetric latin square of side t for all t ⩾ 2n.

Corollary 3.12. A partial symmetric idempotent latin square of side n on t symbols can be embedded in a symmetric idempotent latin square for all odd t ⩾ 2n+1.

4. Outline of the proofs of the next sections, and some lemmas

In the next section we shall characterize all partial latin squares of side n with at most n+1 non-empty cells that cannot be completed to a latin square. In Section 6 we do the same for partial symmetric latin squares. We only give a complete proof in the non-symmetric case, but the course of proof is fairly similar for both results. We now give a very broad outline of these proofs, and the remainder of this section will be devoted to some rather technical lemmas to be used.

   Both proofs are by induction on n, and the general induction step is as follows. We take the partial square P which is to be completed, delete the entry of one or two cells to obtain a partial latin square P' of smaller side, satisfying our conditions. Then we complete P' by the induction hypothesis. We now partition the completion as in Figure 5 or Figure 6 so that all non-empty cells of P are in R, on the diagonal outside R or, in the

symmetric case, on the back diagonal of B of Figure 6. We then introduce the missing symbol or symbols in R in such a way so as to be able to apply Theorem 3.2 or Theorem 3.8 to embed R in a latin square of side n, which will then be a completion of P.

This is a very brief description of the proofs, leaving out a large number of details and of cases not fitting into the general pattern, but hopefully it gives the reader some motivation to try understanding the lemmas of this section.

The first lemma (Andersen and Hilton 1983) will be used in obtaining bounds on the latin rectangle R. A cell of a partial latin square (or of any array) is called *diagonal* if it is the sole non-empty cell in its row and its column. In Figure 6, all cells of B $\cup$ D are diagonal.

Lemma 4.1. Let R be an r$\times$s array containing exactly q non-empty cells of which none are diagonal, and having no empty row or column. Then

$$r+s \leq \lfloor \frac{3q}{2} \rfloor.$$

Proof. Let r_2 be the number of rows with at least 2 non-empty cells. Then $2r_2 + (r-r_2) \leq q$, implying $r \leq q - r_2$. Each column of R containing no cell from these r_2 rows must contain at least 2 of the remaining $r -r_2$ cells, and so $s \leq \frac{1}{2}(r-r_2) + q - (r-r_2) = q - \frac{1}{2}(r-r_2)$, implying $2s + r \leq 2q + r_2$. Therefore $2(r+s) \leq q - r_2 + 2q + r_2 = 3q$, as required.

If the non-empty cells are symmetrically placed, and if d of them occur on the diagonal of R, Lemma 4.1 can be strengthened to $2r \leq \lfloor \frac{3q-d}{2} \rfloor$.

The next lemmas will be applied in finding the cells of R whose entries should be changed into a new symbol used in the completion of P, but not in that of P'. In the non-symmetric case, all cells changed in this way must have distinct symbols, and they must not be preassigned in P'. A *partial transversal* of a latin rectangle is a set of cells in distinct rows, in distinct columns, and containing distinct symbols. The *length* of a partial transversal is the number of cells.

Lemma 4.2. Let R be an x$\times$y latin rectangle and assume that R contains p forbidden cells with at least one in each column, and that

$$(p+1-x)(p-y) \geq p > 0$$

Let s be one of the symbols of R.

Then R has a partial transversal of length $t \geqslant x+y-p$ avoiding all forbidden cells and all cells containing the symbol s.

Proof. Let R be on the symbols $1, \ldots, n$. From the assumptions $p \geqslant y$, so the inequality gives $p > y$ and $p \geqslant x$. Now $p = x$ would imply $p-y \geqslant p$ which is impossible. So we have $x < p$ and $y < p$. Let t be the length of a maximum partial transversal avoiding the forbidden cells and the symbol s. The result is true if $t \geqslant x - 1$ or $t \geqslant y - 1$, so we now assume that $t \leqslant x - 2$ and $t \leqslant y - 2$. Then $t \leqslant p - 3$.

We consider a partial transversal of length t with the required properties. We can assume that it consists of cells $(1,1), \ldots, (t,t)$ with entry i in cell (i,i), $1 \leqslant i \leqslant t$ (so that $s > t$). By the maximality, no symbol from $\{t+1, \ldots, n\} \setminus \{s\}$ can occur in rows $t + 1, \ldots, x$ of columns $t+1, \ldots, y$ except in forbidden cells.

Let

$A_0 = \varnothing$

$A_j = \{ i \in \{1, \ldots, x\} \,|\, \text{cell } (i, t+j) \text{ is not forbidden and its entry} \in (A_{j-1} \cup \{t+1, \ldots, n\}) \setminus \{s\}\}$, $1 \leqslant j \leqslant y-t$.

Define an oriented graph $\vec{G}$ on vertices

$$\bigcup_{j=1}^{y-t} (A_j \times \{t+j\})$$

(corresponding to some cells in the last y-t columns) and edges

$\{((a,t+j), (b,t+k)) \,|\, j < k \text{ and cell } (b,t+k) \text{ contains the symbol } a\}$.

We claim:

(*) For all j, $1 \leqslant j \leqslant y - t$: $\{t+1, \ldots, x\} \cap A_j = \varnothing$.

Proof of (*): Suppose that (*) fails. Then $\vec{G}$ contains a vertex $(a_j, t+j)$ with $a_j \in \{t+1, \ldots, x\}$ and $1 \leqslant j \leqslant y - t$. It follows from the definitions that $\vec{G}$ contains a directed path ending in $(a_j, t+j)$ and starting in a vertex $(a_k, t+k)$ with $k < j$, where cell $(a_k, t+k)$ has an entry from $\{t+1, \ldots, n\} \setminus \{s\}$.

Let $(g_0, t+i_0), (g_1, t+i_1), \ldots, (g_\ell, t+i_\ell)$ be a shortest directed path of $\vec{G}$ with the property that the entry of cell $(g_0, t+i_0)$ is in $\{t+1, \ldots, n\} \setminus \{s\}$ and $g_\ell \in \{t+1, \ldots, x\}$. So $g_k \leqslant t$ for $0 \leqslant k \leqslant \ell - 1$.

Then the cells

$(g_k, t+i_k)$, $0 \leqslant k \leqslant \ell$, and

(j , j) , $1 \leqslant j \leqslant t$, $j \neq g_k$ for $0 \leqslant k \leqslant \ell-1$,

form a partial transversal of length $t+1$, contradicting the maximality of t. We prove that these $t+1$ cells do indeed form a partial transversal satisfying the requirements:

(i) By definition, the cells are in R, they are not forbidden and their entries are different from s.

(ii) The cells are in distinct rows, because otherwise we would have $g_h = g_k$ for some $h < k$, where $k \neq \ell$ as $g_h \leq t < g_\ell$, and then the entry of cell $(g_{k+1}, t+i_{k+1})$ would be $g_k = g_h$, so that $(g_0, t+i_0)$, ..., $(g_h, t+i_h)$, $(g_{k+1}, t+i_{k+1})$, ..., $(g_\ell, t+i_\ell)$ would be a shorter path.

(iii) The cells are obviously in distinct columns.

(iv) The entries are distinct, namely $\{1, ..., t\}$ and the entry of $(g_0, t+i_0)$. This completes the proof of $(\star)$.

Let p_j be the number of forbidden cells and δ_j the number of occurrences of the symbol s in the column j, for $1 \leq j \leq y$. Then $p_j \geq 1$ by assumption, and $\delta_j \in \{0,1\}$.

From the definition of A_j and from $(\star)$ we get

$$|A_j| \geq x - (t-|A_{j-1}| + \delta_{t+j}+p_{t+j})$$

giving

$$|A_{y-t}| \geq (y-t)(x-t) - \sum_{j=1}^{y-t}\delta_{t+j} - \sum_{j=1}^{y-t}p_{t-j}.$$

By $(\star)$, $|A_{y-t}| \leq t$, and as $\sum_{j=1}^{y-t}p_{t+j} = p - \sum_{j=1}^{t}p_j \leq p - t$

and $\sum_{j=1}^{y-t} \delta_{t+j} \leq y-t$ we get

$$t \geq (y-t) (x-t) - (y-t) - (p-t)$$

and, introducing the condition of the lemma,

$$0 \leq p - (y-t) (x-t-1)$$
$$\leq (p+1-x) (p-y) - (y-t) (x-t-1)$$
$$= (t-x-y+p+1) (p-t).$$

If we have strict inequality somewhere in these calculations, we get $t-x-y+p+1 > 0$ (as $p-t \geq 3$) implying $t \geq x+y-p$ as required. So assume that $t = x+y-p-1$ and that we have equality; in particular $p_j = 1$ for $1 \leq j \leq t$, $(y-t) (x-t-1) = p$ and $|A_{y-t}| = t$, from which we deduce that column y has no forbidden cell and no cell containing s among the first t cells. By the maximality of t, this must be true with any ordering of the last y-t columns, so in fact it holds for each of columns $t+1, ..., y$. We now prove

(⋆⋆) Each entry in any of the first t cells of any of the last y-t columns
       belongs to $\{1, ..., t\}$.

Proof of (⋆⋆):

As $p > y$ we may assume that $p_k \geq 2$ for some k, $t + 1 \leq k \leq y$. If some
cell (i,k), $1 \leq i \leq t$, contains a symbol $u > t$, we can replace (i,i) of our
partial transversal with (i,k), and we no longer have $p_j = 1$ for all col-
umns j containing a cell from the transversal. Assume next that some cell
(i,ℓ) contains a symbol $u > t$, where $1 \leq i \leq t$ and $t + 1 \leq \ell \leq y, \ell \neq k$.
Some cell of column k contains the symbol i, say cell (j,k). Then $1 \leq j \leq
t$, $j \neq i$, and replacing cells (i,i) and (j,j) by (i,ℓ) and (j,k) we obtain the
same contradiction as before. This proves (⋆⋆).

It follows from (⋆⋆) that the cells common to the last $x - t$ rows and
the last $y - t$ columns contain symbols greater than t. Any such cell can
be added to the partial transversal unless it is forbidden or contains s. So
we get

$$(x-t)\,(y-t) \leq (p-t) + (y-t)$$

contradicting $(y-t)\,(x-t-1) = p$, and so Lemma 4.2 has been proved.

Lemma 4.2 strengthens a result due to A. J. W. Hilton and the author
(Andersen & Hilton 1983). The similar lemma for the symmetric case is
most easily stated in graph terminology. A *path system* of a graph is a
subgraph consisting of disjoint paths. As we only aim at sketching the
proof in the symmetric case we state the lemma in a form less complicat-
ed than what is needed in the proof.

Lemma 4.3. Let $4 \leq r \leq \frac{3n-6}{4}$ and let K_r have an edge-colouring with
any number of colours. Let F be a set of at most $\frac{n+1}{2}$ forbidden edges
of K_r such that each vertex is incident with an edge of F. Let M be a set of
at most 2 mandatory edges of K_r, disjoint from F and not containing 2
edges of the same colour.

Then K_r contains a path system containing all edges from M and no
edge from F, with all edges having distinct colours, and with at least 2r-n
edges.

The proofs of Lemmas 4.2 and 4.3 have been inspired by work on the
existence of long partial transversals in latin squares (Drake 1977; Brou-
wer, de Vries & Wieringa 1978; Woolbright 1978). It can be proved that

an edge-coloured K_n has a path system with all edges having distinct colours with at least $n - \sqrt{2n}$ edges (Andersen 1985).

5. Completion of partial Latin Squares

This section is primarily devoted to characterizing those partial latin squares of side n with at most n+1 non-empty cells which cannot be completed to a latin square of side n, thus extending the knowledge gained from previous proofs of the Evans Conjecture.

A forerunner for the complete proofs was a paper by R. Häggkvist, where he proved that the conjecture is true for n > 1111 (Häggkvist 1978); we shall use one of Häggkvist's lemmas in our proof. The proof of B. Smetaniuk was based on a remarkable completion theorem, which we state below (although we shall not apply the result here).

Theorem 5.1. (Smetaniuk 1981). Let A be any latin square of side n on symbols 1,...,n, and let P(A) be the partial latin square of side n+1 on symbols 1,...,n+1 in which, for all i,j, $1 \leqslant i \leqslant n+1$, $1 \leqslant j \leqslant n+1$, cell (i,j) contains the entry of cell (i,j) of A if (i,j) is above the back diagonal of P(A) (so that $1 \leqslant j < n+2-i$), cell (i,j) contains the symbol n+1 if (i,j) is on the back diagonal of P(A) (j=n+2−i), and otherwise cell (i,j) is empty.

Then P(A) can be completed to a latin square of side n+1.

Smetaniuk actually gave a specific algorithm for completing P(A), and he showed that if $A \neq B$, then the completions of P(A) and P(B) obtained in this way are also different. It follows that the number of latin squares of side n is a strictly increasing function of n (Smetaniuk 1982).

The proof of the Evans Conjecture by A. J. W. Hilton and the author also proved that a partial latin square of side n with exactly n non-empty cells can be completed unless it is of the form of one of the partial squares of Figure 7, $1 \leqslant y \leqslant n-1$, (i.e., by permuting the rows, permuting the columns and renaming the symbols it can be transformed into one of these squares). This was actually conjectured to be true by D. Klarner in 1970 in a conversation with Hilton. In 1983 R. M. Damerell showed that it can be proved using Theorem 5.1 (Damerell 1983).

The theorem that we shall prove in this section states that if a partial latin square of side n with n+1 non-empty cells cannot be completed then it is of the form of one of the squares of Figure 8, or n=4 and it is as in Figure 9, or it contains one of the squares of Figure 7.
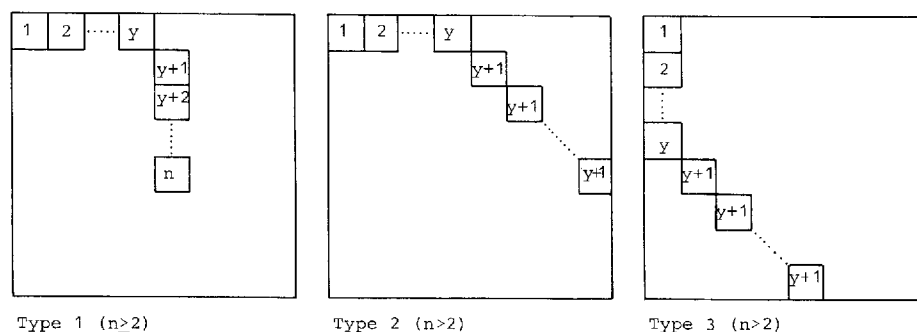
Type 1 (n≥2)   Type 2 (n≥2)   Type 3 (n≥2)

Fig. 7

We call a partial latin square of side n with at most n+1 non-empty cells *bad* if it has n or n+1 non-empty cells of which n cells form a square of the type of one of the squares of Figure 7, $1 \leq y \leq n-1$, or it has n+1 non-empty cells forming a square of the type of one of the squares of Figure 8 or Figure 9; otherwise we call it *good*. If a good partial latin square of side n≥2 has less than n+1 non-empty cells, we can fill further cells so as to obtain a good square with exactly n+1 non-empty cells.

It is easy to see that a bad partial latin square of side n cannot be completed to a latin square of side n; we leave this little exercise to the reader.

In section 2, it was explained how a latin square of side n corresponds to a decomposition of $K_{n,n,n}$ into mutually edge-disjoint K_3's. It follows from this that there is symmetry among rows, columns and symbols. For example, if S is a latin square of side n and S' is obtained from S by placing the symbol j in cell (i,k) whenever S contains the symbol k in cell (i,j), $1 \leq i \leq n$, $1 \leq j \leq n$, $1 \leq k \leq n$, then S' is also a latin square of side n. We say that S' is obtained from S by *interchanging columns and symbols*. Similarly, other permutations of (rows, columns, symbols) give rise to latin squares. We call these *conjugates* of S. Conjugates of partial latin squares are defined in the same way.

Clearly, a partial latin square of side n can be completed to a latin square of side n if and only if any one of its conjugates can.

In Figures 7 and 8, partial latin squares in the same row are conjugates of each other. All conjugates of the square of Figure 9 are of the same form.

The proof in this section is very similar to that of A. J. W. Hilton and the author for the case of n non-empty cells. Some proofs are almost identical, others are a bit more complicated in this paper.

We first verify the result in a particular case where the general proof does not work.

Fig. 9

Fig. 8

Type 4 ($n \geq 3$) Type 5 ($n \geq 3$) Type 6 ($n \geq 3$)

Type 7 ($n \geq 4$) Type 8 ($n \geq 4$) Type 9 ($n \geq 4$)

Type 10 ($n \geq 5$) Type 11 ($n \geq 5$) Type 12 ($n \geq 5$)

Figure 10

Lemma 5.2. If P is a good partial latin square of side n with n+1 non-empty cells such that each row and each column contains a non-empty cell, and each of symbols 1,...,n occurs in P, then P can be completed to a latin square of side n.

Proof. If we pick n non-empty cells of P belonging to distinct rows, then at most 2 of them can belong to the same column. It follows that P contains at least n−1 non-empty cells belonging to distinct rows and distinct columns. We can distinguish between two cases, according to

whether n such cells exist or not. Considering the different positions for the unique symbol occurring twice, we see that P must be of the form of one of the partial latin squares of Figure 10.

We prove cases 1a, 1b and 2a simultaneously. First for $n \geqslant 11$. By Theorem 3.7 there is an idempotent latin square S_5 of side 5 with diagonal 1,2,3,4,5, and by the same theorem there is an idempotent latin square of side n on symbols 1,2,...,n with S_5 in the top left hand corner. If we replace this S_5 by the latin square of side 5 in Figure 11, we still have a latin square, and it clearly is a completion of the squares of cases 1a, 1b, and 2a. For $5 \leqslant n \leqslant 10$ completions of all 3 cases are shown in Figure 11. For n=4 case 1a gives a bad square, and cases 1b and 2a are easily completed. For n=3 all three cases give bad squares (and for n=2 only case 1a applies and is trivial).

Case 1c also follows from the above constructions (for all $n \geqslant 5$, the symbol 2 not on the diagonal can be found in the row of the diagonal 4, in column 5 or 6). For n=4, case 1c gives a bad square.

Case 1d is obvious, it follows from the existence of idempotent latin squares of side n for all $n \geqslant 3$.

Case 2b yet again follows from Figure 11 and the construction related to it (for $6 \leqslant n \leqslant 10$, one of symbols 5 and 6 is repeated rather than the symbol 4). For n=4, case 2b gives a bad square.

Case 2c only applies for $n \geqslant 5$, and here we copy the argument for the first three cases, but with the latin squares of Figure 12.

```
1 2 5 3 4        1 2 6 5 4 3        1 2 5 7 4 3 6
5 1 4 2 3        3 1 5 6 2 4        3 1 6 5 7 4 2
2 4 3 5 1        2 4 3 1 6 5        2 4 3 1 6 7 5
3 5 1 4 2        5 6 1 4 3 2        5 6 7 4 3 2 1
4 3 2 1 5        6 3 4 2 5 1        6 7 4 2 5 1 3
                 4 5 2 3 1 6        7 5 2 3 1 6 4
                                    4 3 1 6 2 5 7
```

Figure 11

```
1 2 5 7 8 9 6 4 0 3        1 2 5 7 8 9 6 4 3        1 2 5 7 8 3 6 4
3 1 6 8 7 4 9 0 2 5        3 1 6 8 7 4 9 5 2        3 1 6 8 7 4 2 5
2 4 3 1 6 0 5 9 7 8        2 4 3 1 6 8 5 9 7        2 4 3 1 6 8 5 7
9 6 0 4 3 2 8 1 5 7        9 6 7 4 3 2 8 1 5        5 6 7 4 3 2 8 1
8 7 9 0 5 1 3 6 4 2        8 7 9 2 5 1 3 6 4        8 7 4 2 5 1 3 6
7 5 8 3 9 6 0 2 1 4        7 5 8 3 9 6 4 2 1        7 5 8 3 1 6 4 2
4 0 2 6 1 5 7 3 8 9        4 9 2 6 1 5 7 3 8        4 8 1 6 2 5 7 3
6 9 4 5 0 7 2 8 3 1        5 3 4 9 2 7 1 8 6        6 3 2 5 4 7 1 8
0 8 7 2 4 3 1 5 9 6        6 8 1 5 4 3 2 7 9
5 3 1 9 2 8 4 7 6 0
```

```
5 3 4 1 2
1 2 5 4 3
4 5 3 2 1
3 1 2 5 4
2 4 1 3 5
```

```
2 6 4 3 1 5
1 2 5 6 4 3
5 1 3 2 6 4
3 4 6 5 2 1
6 3 1 4 5 2
4 5 2 1 3 6
```

```
2 6 4 3 7 5 1
1 2 7 6 4 3 5
5 1 3 2 6 7 4
7 4 6 5 2 1 3
3 7 2 1 5 4 6
4 3 5 7 1 6 2
6 5 1 4 3 2 7
```

```
2 6 4 9 0 5 8 1 3 7
1 2 7 6 9 0 5 3 4 8
5 1 3 2 8 7 0 9 6 4
7 8 6 5 2 9 3 4 0 1
3 9 8 1 5 4 6 0 7 2
4 5 0 8 3 6 1 7 2 9
9 0 1 4 6 2 7 5 8 3
6 4 2 0 7 3 9 8 1 5
0 3 5 7 1 8 4 2 9 6
8 7 9 3 4 1 2 6 5 0
```

```
2 6 4 9 7 5 8 1 3
1 2 7 6 9 8 5 3 4
5 1 3 2 8 7 4 9 6
7 8 6 5 2 9 3 4 1
3 9 8 1 5 4 6 2 7
4 5 9 8 3 6 1 7 2
9 3 1 4 6 2 7 5 8
6 7 2 3 4 1 9 8 5
8 4 5 7 1 3 2 6 9
```

```
2 6 4 3 7 5 8 1
1 2 7 6 4 8 5 3
5 1 3 2 8 7 4 6
7 8 6 5 2 1 3 4
3 7 8 1 5 4 6 2
4 5 2 8 3 6 1 7
8 3 1 4 6 2 7 5
6 4 5 7 1 3 2 8
```

Figure 12

This completes the proof of Lemma 5.2.

Lemma 5.4 below is a strengthening of a very useful result due to C. C. Lindner, which was used also by Smetaniuk and by Damerell (Lindner 1970). We first state another lemma; a *1-factor* of a graph G is the edge-set of a subgraph F with the same vertex set as G and with each vertex having degree 1 (sometimes the term 1-factor is used for the subgraph itself and not just the edge-set).

Lemma 5.3. (Häggkvist 1978). Let G be a regular bipartite graph of degree m with 2n vertices. Let B_1 be a set of b_1 independent edges, and let B_2 be a set of b_2 edges disjoint from B_1. If $m-b_1 \geq \frac{1}{2}(n-1)$ and $b_1+b_2 \leq m-1$, then G contains a 1-factor F such that $B_1 \subseteq F$ and $F \cap B_2 = \emptyset$.

Lemma 5.4. Let P be a good partial latin square of side n with exactly $n+1$ non-empty cells. Let the number of non-empty cells in row i be r_i, $1 \leq i \leq n$, and assume that $r_1 \geq r_2 \geq ... \geq r_n = 0$. Then the first $\lfloor \frac{1}{2}(n+1) \rfloor$ rows of P can be completed.

Proof. The particular case where $n=4$, $r_1=r_2=2$ and $r_3=1$ turns out to be an exception in several arguments. Rather than go through all the details every time the exception is encountered, we ask the reader to verify the lemma in this case. So we shall assume that if $n=4$ then $r_1 \neq 2$.

With P we associate a bipartite graph $K_{n,n}$ with vertex classes C and S corresponding to columns and symbols respectively. For $1 \leq i \leq n$, let B_i be the set of r_i independent edges of $K_{n,n}$ corresponding to the non-empty cells of row i, i.e. the edge joining column j and symbol k is in B_i if and only if k is in cell (i,j) of P ($1 \leq j \leq n$, $1 \leq k \leq n$). Extending B_i to a 1-factor corresponds to assigning a symbol to each cell of row i.

We first prove that we can complete the first row of P. Let $G = K_{n-r_1, n-r_1}$ be obtained from $K_{n,n}$ by deleting all end-vertices of edges of B_1. We must find a 1-factor of G, disjoint from the set $B = (B_2 \cup B_3 \cup ... \cup B_n) \cap E(G)$ of at most $n+1-r_1$ edges. By a wellknown theorem (Hall 1935), it suffices to show that in G-B any k vertices from C have at least k neighbours in S altogether, $1 \leq k \leq n-r_1$. This is true for $k = n - r_1$ because otherwise B would contain $n - r_1$ edges of G incident with the same vertex of S, and so P would be a bad square, containing a Type 2 square. If it fails for $k = n - r_1 - 1$, then B must contain all edges between 2 vertices of S and the k vertices of C, and so $2(n - r_1 - 1) \leq n + 1 - r_1$ implying $n - r_1 \leq 3$; if $n - r_1 = 3$ it implies that P is of Type 4, 7 or 10, and if $n - r_1 = 2$ it implies that P contains a Type 1 square with $y = n - 2$, both cases contradicting that P is good. Hall's condition cannot fail for a k with $3 \leq k \leq n - r_1 - 2$, because then B would contain at least $k(n - r_1 - k + 1) > n - r_1 + 1$ edges. If it fails for $k = 2$ we would get $n - r_1 \leq 3$ as above, and so $k = n - r_1$ or $k = n - r_1 - 1$, both cases covered above. Finally, if it fails for $k = 1$ then P contains a Type 1 square, which is a contradiction. Thus we have proved that the first row can be completed.

Now suppose that we have a sequence of graphs $G_0, G_1, ..., G_p$, where $G_0 = K_{n,n}$ and, for $1 \leq r \leq p$, $G_r = G_{r-1} - F_r$, where F_r is a 1-factor of G_{r-1} containing B_r and disjoint from $B_{r+1}, ..., B_n$. This corresponds to p rows having been completed. The sequence exists for $p = 1$. We assume that $p < \lfloor \frac{1}{2}(n+1) \rfloor$ and want to extend the sequence by finding a 1-factor F_{p+1} of G_p containing B_{p+1} and disjoint from $B_{p+2}, ..., B_n$. In most cases, this can be done by applying Lemma 5.3; some cases are done separately.

Let $G = G_p$, $b_1 = r_{p+1}$, $b_2 = \sum\limits_{i=p+2}^{n} r_i$ and $m = n - p$. We examine the two inequalities of Lemma 5.3 one by one.

We must have $r_1 \geq 2$ and so

$$b_1 + b_2 = \sum_{i=p+1}^{n} r_i = n + 1 - \sum_{i=1}^{p} r_i \leq n + 1 - (p+1) = n - p = m$$

so $b_1 + b_2 \leq m - 1$ if we have strict inequality. If $p \geq 2$ then there is strict inequality, because $r_1 + r_2 \geq 4$ as $r_n = 0$. If $r_1 \geq 3$ the strict inequality is also satisfied, so we now consider the case $p = 1$, $r_1 = 2$ separately. Then $r_2 = 2$,

and, by assumption, $n \ne 4$. We use the same method as we did when completing the first row. Let G' be obtained from G by deleting the end-vertices of the edges of B_2, and all edges of $B = (B_3 \cup \ldots \cup B_n)$. Then G' is $K_{n-2,n-2}$ with a set of at most $n-2$ independent edges (from F_1) and a set of at most $n-3$ further edges deleted. We use Hall's condition to find a 1-factor of G', considering k vertices of C, $1 \le k \le n-2$. If it fails for $k = n-2$, then all edges incident with some vertex of S have been deleted, corresponding to having a partial latin square as in Figure 13. But then the symbol 3 in the first row is not preassigned, because if it were, P would contain a Type 2 square with $y=2$. It follows that we can change the first row so as to place 3 elsewhere, as P is not of Type 6, 9 or 12. If the Hall condition fails for $k = n-3$ then at least $2(n-3)$ edges incident with 2 particular vertices have been deleted, and as at most 2 of these can be in the set of independent edges we get $2(n-3) \le 2 + (n-3)$ implying $n-2 \le 3$. It follows that we have one of the situations of Figure 14. Then we can change the first row so as to have the condition satisfied for $k=2$, as P is not of Type 4 or 7 (and it will still be satisfied for $k=3=n-2$, as Figure 13 does not apply). If $3 \le k \le n-4$ the Hall condition cannot fail, because then $n \ge 7$ and at least $k(n-1-k) - \min\{k, n-1-k\}$ edges not among the independent edges have been deleted, which implies $n \le 6$. If the condition fails for $k=2$ we can deduce $n \le 5$ and so $k=n-3$. If it fails for $k=1$ then $n \ge 5$ as the case $n=3$ and $k=n-2$ is covered above, and we have the situation of Figure 15. Unless the symbol 3 is prescribed in its cell, or both symbols 1 and 2 are prescribed somewhere in row 1, we can interchange occurrences of 3 and either 1 or 2 to avoid the situation; but in these cases P is bad (Type 1 with $y=2$, Type 5, 8 or 11).

So henceforth, when trying to find the 1-factor F_{p+1}, we can assume that the inequality $b_1 + b_2 \le m-1$ holds.

We now consider the other inequality of Lemma 5.3, which in our case is $r_{p+1} \le \frac{1}{2}(n+1) - p$. As $p < \lfloor \frac{1}{2}(n+1) \rfloor$ this is true if $r_{p+1} = 1$. So assume that $r_{p+1} \ge 2$. If $r_p \ge r_{p+1} + 1$ then $r_1 \ge 3$ and we get, for $p \ge 2$,

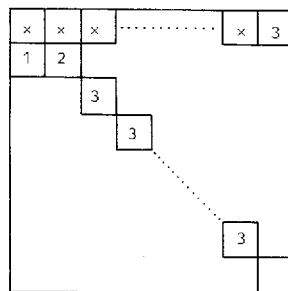*Fig. 13*

Fig. 14

Fig. 15

$$r_{p+1}=r_2\leqslant\tfrac{1}{2}(r_1+r_2-1)\leqslant\tfrac{1}{2}(n-\sum_{i=3}^{n}r_i)\leqslant\tfrac{n}{2}=\tfrac{1}{2}(n+1)-p+\tfrac{1}{2}$$

and for $p=1$:

$$r_{p+1}=r_2\leqslant\tfrac{1}{2}(r_1+r_2-1)\leqslant\tfrac{1}{2}(n-\sum_{i=3}^{n}r_i)\leqslant\tfrac{n}{2}n=\tfrac{1}{2}(n+1)-p+\tfrac{1}{2}$$

so the inequality is true unless $r_3=r_4=\ldots=r_n=0$ and n is even, $r_1=\tfrac{n}{2}+1$ and $r_2=\tfrac{n}{2}$. But in that case we can find a 1-factor directly: delete all end-vertices of edges of B_2 from G_1; we must find a 1-factor in the remaining graph, which is just $K_{\frac{n}{2},\frac{n}{2}}$ with some or all edges of a 1-factor deleted, and this can be done by Hall's condition, because if $k\geqslant 2$ then all vertices in the other class is joined to one of the k vertices, and a single vertex ($k=1$) has a neighbour, because $\tfrac{n}{2}>1$.

So we now assume that $r_p=r_{p+1}$. If $\sum_{i=p+2}^{n}r_i\geqslant 2$ then

$$r_{p+1}=\tfrac{1}{2}(r_p+r_{p+1})\leqslant\tfrac{1}{2}(n+1-\sum_{i=1}^{p-1}r_i-\sum_{i=p+2}^{n}r_i)\leqslant\tfrac{1}{2}(n+1-2(p-1)-2)$$

and the inequality is satisfied. Now assume that $\sum_{i=p+2}^{n}r_i=1$. Then the inequality is true if $\sum_{i=1}^{p-1}r_i>2(p-1)$, and if this is not the case, then *either* $p=1$ and so $r_p=r_{p+1}=\tfrac{n}{2}$, *or* $r_1=r_2=\ldots=r_{p+1}=2$ implying $p=\tfrac{n}{2}-1$. In both cases n is even and, by assumption, $n\geqslant 6$. In the former case the usual method works without problems; we now consider the latter case. In G_p, each vertex has degree $\tfrac{n}{2}+1$. Let G' be obtained from G by deleting the end-vertices of the two edges of B_{p+1} and, if neither of its end-vertices have been deleted, the single edge e of B_{p+2}. Then each vertex has degree at least $\tfrac{n}{2}-1$ in G' except possibly the end-vertices of e which may have degree $\tfrac{n}{2}-2$. Hence Hall's condition is certainly satisfied for $k\leqslant\tfrac{n}{2}-2$ and also for $k=\tfrac{n}{2}-1$ because $\tfrac{n}{2}-1>1$ so there is a vertex not incident with e in any set of k vertices. If $k\geqslant\tfrac{n}{2}$ then any vertex in the other class will be joined to at least one of the k vertices (except possibly an end-vertex of e), and the condition holds.

The only case left to consider in trying to establish the inequality $r_{p+1} \leqslant \frac{1}{2}(n+1) - p$ is when $r_{p+2} = r_{p+3} = \ldots = r_n = 0$. From before we have that $r_p = r_{p+1} \geqslant 2$. We show that the inequality can fail in four ways. (i) If $p=1$ then n is odd and $r_1 = r_2 = \frac{1}{2}(n+1), r_3 = r_4 = \ldots = r_n = 0$. If $p \geqslant 2$ the inequality is true for $r_1 \geqslant 4$, as

$$r_{p+1} = \tfrac{1}{2}(r_p + r_{p+1}) = \tfrac{1}{2}(n+1 - \sum_{i=1}^{p-1} r_i) \leqslant \tfrac{1}{2}(n+1-r_1-2(p-2)) \leqslant \tfrac{1}{2}(n+1)-p,$$

so we can assume that $r_1 \leqslant 3$. If $r_1 = r_2 = 3$ then it is satisfied for $p \geqslant 3$; but we get the exception (ii) $p=2$, $n=8$, $r_1 = r_2 = r_3 = 3$, $r_4 = r_5 = \ldots = r_8 = 0$. Finally, we have exceptions (iii) $r_1 = 3$, $r_2 = r_3 = \ldots = r_{p+1} = 2$, $r_{p+2} = r_{p+3} = \ldots = r_n = 0$, $p = \frac{n}{2} - 1$, n even and $n \geqslant 6$, and (iv) $r_1 = r_2 = \ldots = r_{p+1} = 2$, $r_{p+2} = r_{p+3} = \ldots = r_n = 0$, $p = \frac{1}{2}(n-1)$, n odd and $n \geqslant 5$. In each exceptional case we apply Hall's condition on the usual subgraph of $K_{n-r_{p+1}, n-r_{p+1}}$ to try to find a 1-factor.

In case (i) we have $K_{\frac{1}{2}(n-1), \frac{1}{2}(n-1)}$ with some independent edges deleted. Hall's condition cannot fail unless $\frac{1}{2}(n-1) = 1$, so that $n=3$, and if it does then P is easily seen to be bad. In case (ii), we have a subgraph of $K_{5,5}$ in which each vertex has degree at least 3, and Hall's condition is easily seen to be satisfied. Case (iii) gives us a subgraph of $K_{n-2,n-2}$ in which each vertex has degree at least $n-2-(\frac{n}{2}-1) = \frac{n}{2}-1$; but then Hall's condition is obviously true for $k \leqslant \frac{n}{2}-1$, and for $k \geqslant \frac{n}{2}$ it is true because any vertex in the other class must be joined to one of the k vertices.

Finally, in case (iv) we are looking at a subgraph of $K_{n-2,n-2}$ in which each vertex has degree at least $n-2-\frac{1}{2}(n-1) = \frac{1}{2}(n-1)-1$. So Hall's condition is true for $k \leqslant \frac{1}{2}(n-1)-1$. It is also true for $k \geqslant \frac{1}{2}(n-1)+1$, because in that case each vertex in the other class is joined to one of the k vertices. However, the condition may fail for $k = \frac{1}{2}(n-1)$. If it does, we can describe the graph G_p (in which every vertex has degree $\frac{1}{2}(n+1)$) very accurately: Let the edges of B_{p+1} have end-vertices c_1 and c_2 in C, s_1 and s_2 in S. Then $C = \{c_1, c_2\} \cup A \cup B$ and $S = \{s_1, s_2\} \cup T \cup U$, where $|A| = |U| = \frac{1}{2}(n-1)$, $|B| = |T| = \frac{1}{2}(n-1)-1$, every vertex of A is joined to every vertex of $T \cup \{s_1, s_2\}$, every vertex of U is joined to every vertex of $B \cup \{c_1, c_2\}$ and apart from these edges, G_p contains $c_1 s_1, c_2 s_2$ and $\frac{1}{2}(n-1)-1$ independent edges each joining a vertex from B to a vertex from T. Figure 16 illustrates the graph G_p and the corresponding partial latin square.

It follows from the structure of the graph that the p rows completed so far actually have p of the columns forming a latin square. The remaining columns form a latin square with one row missing. We can then simply find a row which contains a non-preassigned entry from each latin
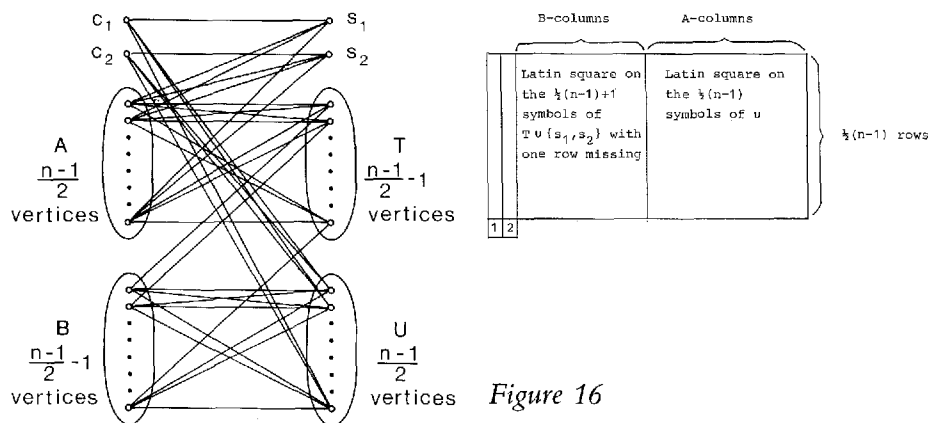
c_1 s_1
c_2 s_2

A $\frac{n-1}{2}$ vertices

T $\frac{n-1}{2}-1$ vertices

B $\frac{n-1}{2}-1$ vertices

U $\frac{n-1}{2}$ vertices

B-columns   A-columns

Latin square on the $\frac{1}{2}(n-1)+1$ symbols of $T \cup \{s_1, s_2\}$ with one row missing	Latin square on the $\frac{1}{2}(n-1)$ symbols of u	$\frac{1}{2}(n-1)$ rows

1 2

Figure 16

square and interchange the two entries. Then we no longer have the situation of Figure 16, and hence we can complete the $(p+1)$st row. If no row contains two such non-preassigned entries, then $\frac{1}{2}(n-1)=2$ implying $n=5$, and all cells in the 2×2 latin square are preassigned; but then P is of type 4, which is a contradiction.

We have now shown how to complete row $p+1$ in all cases not satisfying the conditions of Lemma 5.3. If those conditions are satisfied, the lemma provides us with the required 1-factor, thus enabling us to fill row $p+1$. This completes the proof of Lemma 5.4.

Corollary 5.5. If P is a good partial latin square of side n with $n+1$ non-empty cells, and if P has an empty row and all non-empty cells outside a given column lie in $\lfloor \frac{1}{2}(n+1) \rfloor$ rows, then P can be completed to a latin square of side n.

Proof. By Lemma 5.4, the rows containing the non-empty cells outside the given column can be completed, and by Corollary 3.5 the partial latin square containing these rows can be completed; but then it is just a matter of permuting the remaining rows to get the column right.

Corollary 5.6. A good partial latin square of side n with $n+1$ non-empty cells, all lying in $\lfloor \frac{1}{2}(n+3) \rfloor$ rows, can be completed to a latin square of side n.

Lemma 5.7. Let P be a good partial latin square of side n with $n+1$ non-empty cells all lying in the top left $r\times s$ subarray R or on the diagonal

outside R, and assume that $s \leqslant \lfloor \frac{1}{2}(n+1) \rfloor$, and that P has an empty column.

Then P can be completed to a latin square of side n.

Proof. Figure 5 shows the partition of P. We can assume that R has no empty columns. By Lemma 5.4 with rows replaced by columns, the first s columns can be completed. By the same argument as in the proof of Lemma 3.1 this implies that $R(i) \geqslant r+s-n+f(i)$ for all i, $1 \leqslant i \leqslant n$, where P is supposed to be on symbols $1,2,\ldots,n$ and $f(i)$ is the number of times that symbol i occurs on the diagonal outside R, $1 \leqslant i \leqslant n$. But then R can be completed by Theorem 3.2.

Lemma 5.8. Let P be a good partial latin square of side n with $n+1$ non-empty cells. If each row contains a non-empty cell, then P can be completed to a latin square of side n.

Proof. By Lemma 5.2, it suffices to consider the case where either P has an empty column, or some symbol does not occur in P. We can interchange columns and symbols if necessary, so assume that P has an empty column. Let t be the number of non-empty columns of P, and let v be the number of columns with exactly one non-empty cell. By Corollary 5.6, we can complete P if $t \leqslant \lfloor \frac{1}{2}(n+3) \rfloor$, so we suppose that $t \geqslant \lfloor \frac{1}{2}(n+3) \rfloor +1$. Then

$$t-v=(2(t-v)+v)-t \leqslant n+1-t \leqslant n-\lfloor \tfrac{1}{2}(n+3) \rfloor = \lfloor \tfrac{1}{2}(n-2) \rfloor.$$

All the non-empty cells outside the t-v columns are in distinct columns, and they are also in distinct rows except that one row may contain two of them. So all non-empty cells outside s columns are diagonal, where

$$s \leqslant t-v+2 \leqslant \lfloor \tfrac{1}{2}(n-2) \rfloor +2 = \lfloor \tfrac{1}{2}(n+2) \rfloor.$$

So $s \leqslant \lfloor \frac{1}{2}(n+1) \rfloor$ unless n is even and we have equality everywhere. But in that particular case $t = \lfloor \frac{1}{2}(n+3) \rfloor +1 = \frac{1}{2}(n+4)$ and $2(t-v)+v=n+1$, implying $v=2t-n-1=3$, and two of the three non-empty cells outside the t-v columns are in the same row; therefore all non-empty cells not in this row are in $\frac{1}{2}(n+4)-2=\frac{n}{2}$ columns, and so P can be completed by Corollary 5.5.

Hence we can assume that $s \leqslant \lfloor \frac{1}{2}(n+1) \rfloor$. And then P can be completed by Lemma 5.7, and Lemma 5.8 has been proved.

Lemma 5.8 implies that P can be completed if any of its conjugates satisfy the condition. So if P is good and all rows are used, all columns are used, or all symbols are used, then P can be completed.

Corollary 5.9. If P is a good partial latin square of side n⩽5 with n+1 non-empty cells, then P can be completed.

  Proof. For n⩽5, $\lfloor \frac{1}{2}(n+3) \rfloor \geqslant n-1$.

We need just one more lemma, before we can prove our main result.

Lemma 5.10. Let P be a partial latin square of side n with q non-empty cells, and with the property that neither P nor any of its conjugates have any diagonal non-empty cells. Let r and s be the number of non-empty rows and columns respectively, and let t be the number of distinct symbols occurring in P. Then

$$\min\{r+s, s+t, t+r\} \leqslant \frac{4q}{3}.$$

  Proof. Let R and S be the set of cells in rows with at least two non-empty cells and the set of cells in columns with at least two non-empty cells respectively, and let T be the set of cells containing symbols occurring at least twice in P.

  Put $x = |(R \cap T) \setminus S|$, $y = |R \cap S) \setminus T|$, $z = |(T \cap S) \setminus R|$ and $w = |R \cap S \cap T|$.

  Then $q = x+y+z+w$, $|R| = x+y+w$ and so
  $r \leqslant z + \frac{1}{2}|R| \leqslant \frac{1}{2}(q+z)$
  Similarly, $s \leqslant \frac{1}{2}(q+x)$ and $t \leqslant \frac{1}{2}(q+y)$. So we have
  $(r+s) + (s+t) + (t+r) = 2r+2s+2t \leqslant 3q+x+y+z \leqslant 4q$

as required.

We can now state and prove our main theorem.

Theorem 5.11. For any n⩾1, a good partial latin square of side n with at most n+1 non-empty cells can be completed to a latin square of side n.

  Proof. We proceed by induction on n, along the lines explained at the beginning of Section 4. We can assume that exactly n+1 cells are non-empty (n=1 is trivial!). By Corollary 5.9, the theorem is true for n⩽5.

  Let P be a good partial latin square of side n⩾6 with n+1 non-empty cells and assume that the theorem holds for partial latin squares of smaller side. Let P be on symbols 1,...,n. We must show that P can be completed to a latin square of side n.

Case 1. P, or a conjugate of P, contains a diagonal non-empty cell. We assume that P is chosen among its conjugates so as to have as many diagonal preassignments as possible. Let R be an $r \times s$ subarray, containing all non-diagonal non-empty cells of P, chosen as small as possible (and placed in the top left hand corner). We can assume that $r \geq s$, and that all non-empty cells of P occur in R or on the diagonal outside R. By Lemma 5.8, we can assume that the last row and column are empty, and that the symbol n does not occur in P. We also assume that $s > \lfloor \frac{1}{2}(n+1) \rfloor$, by Lemma 5.7.

For all i, $1 \leq i \leq n$, let f(i) be the number of times the symbol i occurs on the diagonal outside R. Let ℓ be a symbol with $f(\ell) \geq 1$. Let P' be obtained from P by deleting the last row and column, and a diagonal preassignment of the symbol ℓ. Then P' is a partial latin square of side n-1 on symbols 1,2,...,n-1 with n non-empty cells. As $n \geq 6$, $\lfloor \frac{1}{2}(n+1) \rfloor \geq 3$, and if P' is bad then Corollary 5.5 applies to P or one of its conjugates. So we assume that P' is good, and, by the induction hypothesis, we can complete P' to a latin square L' of side $n-1$. By Lemma 3.1 we have, in L':

$R(i) \geq r+s-n+1+f(i)$ for all $i \neq \ell$, $1 \leq i \leq n-1$.

For the symbol ℓ we have $R(\ell) \geq r+s-n+1+f(\ell)-1 = r+s-n+f(\ell)$.

We now disregard what is outside R, except the diagonal preassignments of P. We want to apply Theorem 3.2 to embed a modified version R_m of R in a latin square L which is a completion of P. To do that we must have

$R_m(i) \geq r+s-n+f(i)$ for all i, $1 \leq i \leq n$.

This holds for the symbol ℓ with $R_m(\ell) = R(\ell)$. It will hold for any symbol $i \neq \ell$, with $1 \leq i \leq n-1$, if $R_m(i) \geq R(i)-1$. We must make the symbol n not occurring in R occur $r+s-n$ times in R_m.

Suppose that we can find a partial transversal of length $r+s-n$ in R, avoiding all preassigned cells and the symbol ℓ. Then we can place the symbol n in all cells of the partial transversal to obtain R_m. It will then satisfy the inequality for all i, and we can complete by Theorem 3.2.

To find the required partial transversal we apply Lemma 4.2 with the non-empty cells of P in R as forbidden cells and ℓ as the forbidden symbol. There are at most n non-empty cells of P in R; by adding cells arbitrarily we can assume that we have exactly n forbidden cells (there are enough cells to add). Lemma 4.2 then gives the partial transversal we need, if $(n+1-r)(n-s) \geq n$. By Lemma 4.1, $r+s \leq \lfloor \frac{3n}{2} \rfloor$ and so, if $n-r \geq 3$ then $s \leq \frac{1}{2}(r+s) \leq \frac{3n}{4}$, implying

$(n+1-r) (n-s) \geq 4 \cdot \frac{n}{4} \geq n$,

and if $r=n-2$ then $s \leq \lfloor \frac{3n}{2} \rfloor - (n-2) = \lfloor \frac{n}{2} \rfloor + 2$, giving

$(n+1-r) (n-s) \geq 3(\lfloor \frac{n+1}{2} \rfloor - 2) \geq n$

for $n \geq 11$. Close inspection shows that the condition is satisfied except in the following three cases: (i) $n=10$, $r=8$, $s=7$. (ii) $n=8$, $r=s=6$. (iii) $n=7$, $r=s=5$. In all cases, $r+s > \frac{3(n-1)}{2}$, so P can contain only one diagonal preassignment. It follows that in case (iii) P contains a row with at least 2 non-empty cells such that all other non-empty cells are in at most $\lfloor \frac{1}{2}(n+1) \rfloor = 4$ columns, and so P can be completed by Corollary 5.5. Consider cases (i) and (ii). Here $r+s = \frac{3n}{2}$, and it follows from the proof of Lemma 4.1 that each non-empty cell of P is either alone in its row or alone in its column. But as all conjugates of P have at most one diagonal preassignment, at most one of the non-empty cells alone in their rows can have an entry which occurs just once in P, and similarly for the cells alone in their columns. So at most $2 + \frac{1}{2}(n+1-2)$ distinct symbols occur in P. This is $\frac{1}{2}(n+3)$, so P can be completed by Corollary 5.6.

Case 2. Neither P nor any of its conjugates contains a diagonal non-empty cell. We suppose that P is chosen among its conjugates so as to have $r \geq s$ and $r+s \leq \frac{4(n+1)}{3}$ (Lemma 5.10), where all non-empty cells are inside the $r \times s$ subarray R having no empty rows or columns. By Corollary 5.6, we can assume $s \geq \lfloor \frac{1}{2}(n+3) \rfloor + 1$. By the same corollary, we can assume that there is a symbol which is preassigned exactly once in P; by symmetry let it be the symbol 1 in cell $(1,1)$. Let P' be obtained from P by deleting the last row and column and removing the symbol 1 from cell $(1,1)$. Then P' is partial latin square of side $n-1$ on symbols $2,\ldots,n$ with n non-empty cells. As in Case 1, we see that we can assume that P' is good. By the induction hypothesis, we can complete P' to a latin square L' of side $n-1$, and we have, in L',

$R(i) \geq r+s-n+1$ for all i, $2 \leq i \leq n$,

and we need to modify R to R_m with

$R_m(i) \geq r+s-n$ for all i, $1 \leq i \leq n$.

Having obtained R_m, we can complete by Theorem 3.2. So what we have to do is make the symbol 1 occur $r+s-n$ times, and we can delete any other symbol once.

Let k be the symbol placed in cell $(1,1)$ of L'. We replace this occur-

rence of k by the symbol 1. Then we cannot delete any further occurrences of k, and we need $r+s-n-1$ additional occurrences of 1.

We look for a partial transversal of length $r+s-n-1$ in the $(r-1)\times(s-1)$ latin rectangle R' obtained from R by deleting the first row and column. We let the preassigned cells of R' be forbidden cells, and in each column of R' with no preassigned cell we choose an arbitrary cell as a forbidden cell (then the cell of that column which is in R but not in R' must be preassigned in P). Of the $n+1$ non-empty cells of P, at least 2 do not correspond to forbidden cells in R', namely cell (1,1) and some other cell in the first column of R, because if (1,1) were the sole prescribed cell in its column, a conjugate of P would have a diagonal cell (as the symbol 1 was not prescribed anywhere else). So at most $n-1$ cells are forbidden in R'. We may add cells so as to have exactly $n-1$. By Lemma 4.2, we can find the required partial transversal of length $r+s-n-1=(r-1)+(s-1)-(n-1)$ in R', avoiding all forbidden cells and the symbol k, if

$$((n-1)+1-(r-1))\,((n-1)-(s-1))\geqslant n-1$$

which is

$$(n+1-r)\,(n-s)\geqslant n-1.$$

If $n-r\geqslant 3$ then $s\leqslant\frac12(r+s)\leqslant\frac{2(n+1)}{3}$ and so $(n+1-r)\,(n-s)\geqslant\frac{4(n-2)}{3}\geqslant n-1$ as $n\geqslant 6$.

If $n-r\leqslant 2$ then $s\leqslant\lfloor\frac{4(n+1)}{3}\rfloor-(n-2)=\lfloor\frac{n+10}{3}\rfloor\leqslant\lfloor\frac12(n+3)\rfloor$ unless $n=8$ or $n=6$. In the latter case we must have $r=5$ but then we get $s\leqslant 4=\lfloor\frac12(n+3)\rfloor$. In the former case we get $r=s=6$, and each of the 7 symbols occurs at least 5 times in R (before k is replaced by 1); it follows that exactly one symbol occurs 6 times, say the symbol b. Then b occurs at least 4 times in the 5×5 subsquare (with at most 6 prescribed cells) that we consider for our transversal, and at most 2 of the occurrences can be in prescribed cells (this follows from the proof of Lemma 5.10). Thus we can let b occur twice in our 'transversal' (if $b=k$, b occurs 5 times in the 5×5 subsquare, and we can let the transversal include k). Then it is easy to see that we can find the required 'transversal'.

So in all cases, we can add $r+s-n-1$ occurrences of the symbol 1 and then embed R_m to obtain a completion of P.

This finishes the proof of Theorem 5.11.

We finally mention some recent results and conjectures on completing partial latin squares with no symmetry required, all of which are contained in work at least partly due to R. Häggkvist.

Theorem 5.12. (Chetwynd & Häggkvist 1984). There is a constant $c > 10^{-5}$ such that every partial latin square of even side $n > 10^7$ in which every row, column and symbol is used at most cn times can be completed to a latin square of side n.

For large n, this improves a previous result stating that completion is possible if $n \equiv 0$ modulo 16 and each row, column and symbol is used at most $2^{-7} \sqrt{n}$ times (Daykin & Häggkvist 1984). Theorem 5.12 is probably far from best possible:

Conjecture A. (Daykin & Häggkvist 1984). A partial latin square of side n in which every row, column and symbol is used at most $\frac{n}{4}$ times can be completed to a latin square of side n.

A related problem is expressed in the following conjecture.

Conjecture B. (Häggkvist 1984a). Let P be a partial latin square of side n in which all non-empty cells lie in an $r \times s$ subarray, and assume that each row is used at most $n-r$ times and that each column is used at most $n-s$ times. Then P can be completed to a latin square of side n.

Häggkvist also proved

Theorem 5.13. (Häggkvist 1984b). If P is a partial latin square of side n in which the non-empty cells are precisely all cells in the first q rows and all cells in the first q columns, and in which the cells common to the first q rows and the first q columns form a latin square of side q, then P can be completed to a latin square of side n.

Theorem 5.12 gives a partial solution to a problem of L. Fuchs, which can be formulated:

Let $n = n_1 + n_2 + \ldots + n_k$ be a partition of n. When does there exist a latin square of side n with latin subsquares of sides $n_1, n_2, \ldots, n_k$ on mutually disjoint sets of rows, mutually disjoint sets of columns and mutually disjoint sets of symbols? By Theorem 5.12, such a latin square exists if $n_i \leq cn$ for all i, $1 \leq i \leq k$, and n is large enough. We refer to the literature for further results on Fuchs' problem (Dénes & Pásztor 1963; Dénes & Keedwell 1974; Heinrich 1984).

6. Completion of partial symmetric Latin Squares

The purpose of this section is mainly to state two results on completion of partial symmetric latin squares which are analogous to the Evans Conjecture. Both results are very recent.

The diagonal of a partial symmetric latin square of side n is called *admissible* if the number of symbols occurring with parity different from n does not exceed the number of empty cells. If n is odd, the diagonal is admissible if and only if all its entries are distinct. If the diagonal is not admissible, then the square cannot be completed to a symmetric latin square of side n. The parity condition of Theorem 3.8 and Corollary 3.9 simply ensures that the diagonal is admissible.

Figure 17 shows some partial symmetric latin squares with admissible diagonal, which cannot be completed to symmetric latin squares of the same side.

Theorem 6.1. (Andersen & Hilton 1985). Let n ⩾ 3, and let P be a partial symmetric latin square of side n with admissible diagonal.

If P has less than n non-empty cells, then P can be completed to a symmetric latin square of side n.

If P has exactly n non-empty cells then P can be completed if and only if P is not of the form of any of the squares E1, O1, or O2.

If P has exactly n + 1 non-empty cells then P can be completed if and only if P is neither of the form of any of the squares E1, O1 or O2 with a further cell filled nor of the form of any of E2, E3, O3, 5A or 5B.

The proof of Theorem 6.1 is very long. The general idea is very similar to that of the proof of the main theorem of the last section and so is by induction on n, but there are more complications. In particular, the case where all or all but one of the rows are used is very elaborate. When that is done, it is possible to delete a symmetric pair of entries from the square of side n to be completed so as to obtain a partial symmetric latin square of side n − 2 (with the same parity as n). We complete by the induction hypothesis and focus on the latin rectangle R of Figure 6. By Lemma 4.1, we know something about the side of R. We add occurrences of two new symbols by applying Lemma 4.3, and we embed by Theorem 3.8 to obtain the required completion.

Theorem 6.1 can be used to give results on completions of edge-colourings of K_n with the colours of some edges prescribed. Below we state two such results, one for even n and one for odd n. The odd case is
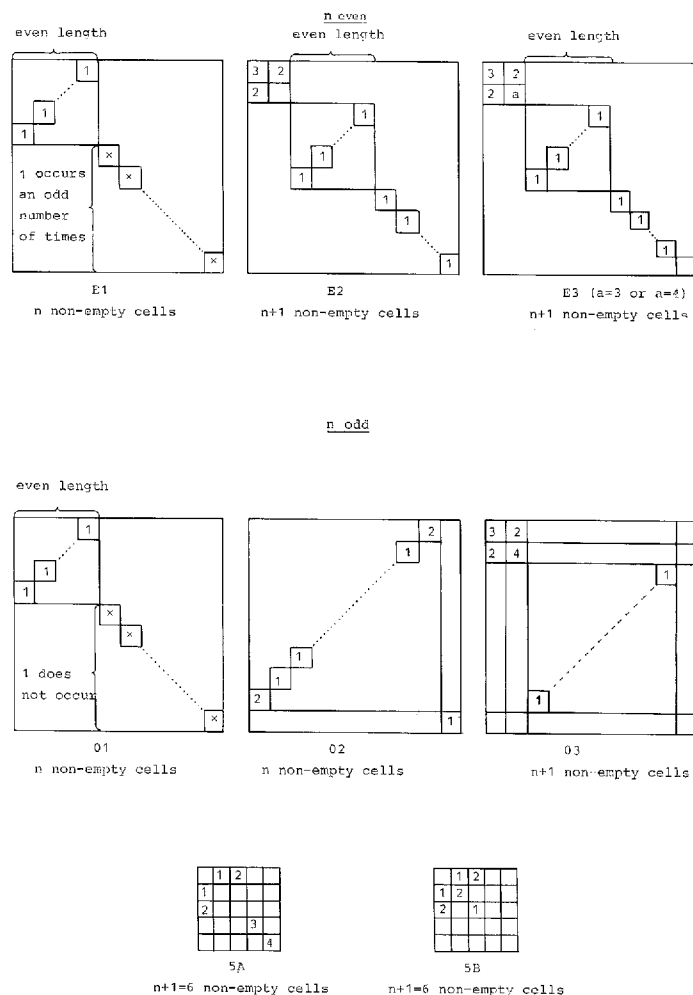
Fig. 17

an easy consequence of the even case, and the even case follows from Theorem 6.1 for odd n alone. The two results are not the strongest possible corollaries of Theorem 6.1 in this direction.

Corollary 6.2. Let C be a set of edges of K_{2m}, $m \geq 3$, and assume that the subgraph spanned by the edges of C has an edge-colouring. Then:

a) If $|C| \leq m-1$, then the edge-colouring can be extended to an edge-colouring of K_{2m} with $2m-1$ colours.

b) If $|C| = m$ then the edge-colouring can be extended to an edge-colouring of K_{2m} with $2m-1$ colours if and only if the edge-coloured subgraph is not of Type 1 of Figure 18.

c) If $|C| = m+1$ then the edge-colouring can be extended to an edge-

Figure 18

colouring of K_{2m} with $2m-1$ colours if and only if the edge-coloured subgraph is neither of Type 1 with an edge added nor of Type 2, 3, 6i or 6ii of Figure 18.

Corollary 6.3. Let C be a set of edges of K_{2m-1}, $m \geq 3$, and assume that the subgraph spanned by the edges of C has an edge-colouring. Then:

a) If $|C| \leq m$ then the edge-colouring can be extended to an edge-colouring of K_{2m-1} with $2m-1$ colours.

b) If $|C| = m+1$ then the edge-colouring can be extended to an edge-colouring of K_{2m-1} with $2m-1$ colours if and only if the edge-coloured subgraph is not of Type 4 or 5 of Figure 19.

The next result that we state is more related to Corollaries 6.2 and 6.3 than to Theorem 6.1, as it is concerned with edge-colourings of complete graphs, where each colour is prescribed *at most once*. The theorem was obtained by E. Mendelsohn and the author, and a formulation compatible with the statements above is the following.

Theorem 6.4. (Andersen & Mendelsohn 1985). Let D be a set of edges of K_n with at most $q(K_n)-1$ edges. Then K_n has an edge-colouring with $q(K_n)$ colours so that all edges of D have distinct colours, except if n is even and D is the edge-set of the graph H_{2m} of Figure 20, or if n=6 and D is the edge-set of $H_5^!$ or $H_6^!$, or if n = 5 and D is the edge-set of $H_5^!$.

Theorem 6.4 for odd n follows from the result for even n. We also state a reformulation of the even case which stresses that it is a result about 1-factorizations of the complete graph. A *1-factorization* of a graph G = (V,E) is a decomposition of E into mutually disjoint 1-factors. Especially 1-factorizations of the complete graph K_{2m} of even order have been studied extensively (Mendelsohn & Rosa 1984).

Corollary 6.5. Let D be a set of edges of K_{2m}, and let $|D| \leq 2m-2$. Then K_{2m} has a 1-factorization with all edges of D in distinct 1-factors if and only if D is not the edge-set of the graph H_{2m}, or, if m = 3, of $H_5^!$ or $H_6^!$.

If most edges of D are concentrated in a 'small' subgraph K_r of K_{2m}, corresponding to R of Figure 6 not being too large, then Corollary 6.5 is proved in the same way as Theorem 6.1.

If not, the proof is completely different (although both cases are treated within the same induction proof); if R is large, the proof relies on a lemma saying that then the vertices of K_{2m} can be split into two sets of m vertices each, so that exactly m or m+1 edges of D join a vertex from one class to a vertex of the other. Then Theorem 5.11 is used on the $K_{m,m}$ formed in this way.
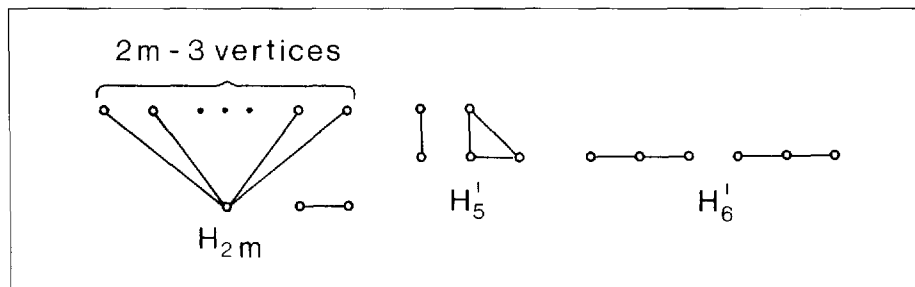
Figure 19
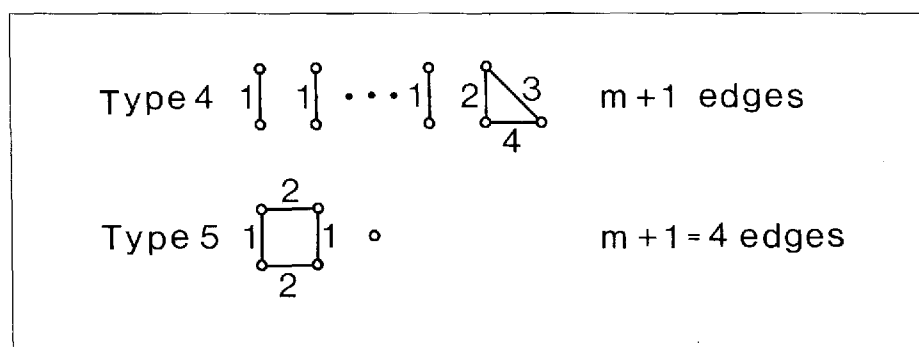
Figure 20

Conjecture C. Let $m \geqslant 5$, and let D be a set of edges of K_{2m} with $|D| \leqslant 2m-1$. Then K_{2m} has a 1-factorization with all edges of D in distinct 1-factors, if and only if

(i) D does not contain the edge-set of H_{2m}, and

(ii) K_{2m} does not have two distinct vertices U and V for which $UV \notin D$ but each edge of D is incident with either U or V, $|D| = 2m-1$.

For $m \leqslant 4$, there are several exceptions to Conjecture C.

The work on Theorem 6.4 was to a large extent initiated by a paper by A. Hartman on partial triple systems and edge-colourings (Hartman 1984). It has some consequences for completions of partial symmetric latin squares, supplementing Theorem 6.1.

If we define an *appearance* of a symbol in a partial symmetric latin square as either an occurrence in a diagonal cell or two occurrences in a symmetric pair of cells, then n non-empty cells may correspond to as little as $\frac{n}{2}$ appearances. In the case where no symbol *appears* more than once, we can strengthen Theorem 6.1 by applying Corollary 6.5.

Corollary 6.6. Let P be a partial symmetric latin square of odd side $2m-1$ in which one symbol does not appear and each of the remaining $2m-2$ symbols has at most one appearance. Then P can be completed to a symmetric latin square of side $2m-1$ if and only if P is not of the form of any of the squares of Figure 21.

Corollary 6.7. Let P be a partial symmetric latin square of even side 2m in which one symbol does not appear and each of the remaining $2m-1$ symbols has at most one appearance, one of them not appearing outside
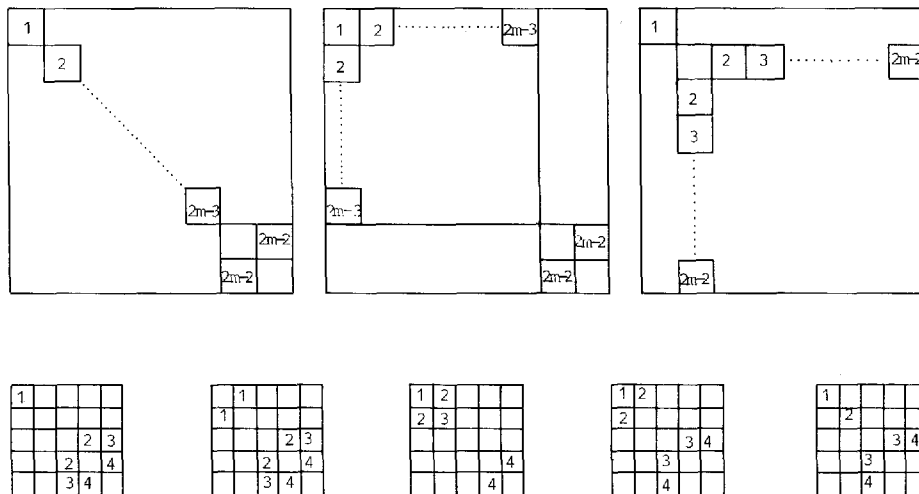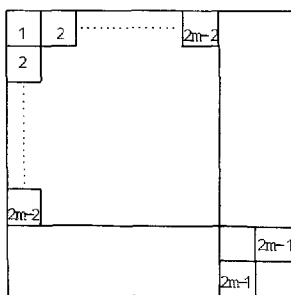
Figure 21

Figure 22

the diagonal. Then P can be completed to a symmetric latin square of side $2m$ if and only if P is not of the form of the square in Figure 22, and at most m symbols occur on the diagonal.

7. Final remarks

Many topics and results that would fit in well with the title of this paper have not been included. And we do not even claim to have covered the most *important* subjects. The choice of material has been as much affected by the author's personal preferences as by any assignment of different levels of importance to the topics. It has also been a wish to make the contents coherent rather than desultory.

For example, we have not mentioned the word *quasigroup* at all, and yet it a concept almost identical to that of a latin square.

A quasigroup $(Q, \star)$ is a set Q with an operation $, \star$, such that for all a and b in Q, each of the equations $a \star x = b$ and $x \star a = b$ is uniquely solvable in x. A latin square is the same as a multiplication table for a quasigroup. We have imposed very little extra structure on our latin squares in this paper, basically only symmetry $(x \star y = y \star x)$ and idempotency $(x \star x = x)$. If the quasigroup is required to satisfy other simple identities, further interesting completion problems arise (one of the more famous problems among these is that of completing partial Steiner triple systems). We refer the reader to the literature (Lindner 1984).

The book which is the standard reference on latin squares is that by J. Dénes and A. D. Keedwell. It emphasizes the quasigroup point of view and contains many references (Dénes & Keedwell 1974). At the time of writing, Dénes and Keedwell are editing a new, comprehensive volume on latin squares (two of the references that we have given are to manuscripts written for this volume) (Dénes and Keedwell 1986?).

The present paper is meant to have two purposes: Partly to survey the area of completing partial latin squares, and partly to announce some new results in that area, carrying out the details of proof for one of these. We hope that the reader has realized that such completion problems, even though they are often very easy to formulate, can be quite intricate. So it appears to be a fitting end to this paper to ask: Just *how* intricate is the problem of completing partial latin squares?

We can define the intricacy of completing partial latin squares as the least integer k satisfying the following:

For any integer n, any partial latin square of side n can be partitioned into k partial latin squares of side n each of which can be completed to a latin square of side n.

Partitioning a partial latin square P into $P_1, ..., P_k$ means filling some cells of the P_t's such that if cell (i,j) of P is non-empty, then its entry occurs in cell (i,j) of one of the P_t's, and all non-empty cells of the P_t's are obtained in this way.

D. E. Daykin and R. Häggkvist posed the problem of showing that the intricacy of completing partial latin squares is 2. The concept of intricacy was later generalized to a large class of combinatorial construction problems (Daykin and Häggkvist 1981; Daykin and Häggkvist 1984; W. E. Opencomb 1984).

It follows from Corollary 3.3 (Corollary 3.4 is enough if n is even) that there exists a finite k satisfying the condition of the definition of

intricacy, because k=4 will do. So the question is whether the intricacy is 2, 3 or 4.

Conjecture D. The intricacy of completing partial latin squares is 2.

References

L. D. Andersen, *Embedding latin squares with prescribed diagonal,* Ann. Discrete Math. *15* (1982), 9-26.

L. D. Andersen, *Hamilton circuits with many colours in edge-coloured complete graphs,* preprint, Aalborg University Centre (1985).

L. D. Andersen & A. J. W. Hilton, *Thank Evans!,* Proc. London Math. Soc. (3) 47 (1983), 507-522.

L. D. Andersen & A. J. W. Hilton, *Analogues of the Evans conjecture for symmetric latin squares and complete graphs,* preprint, Aalborg University Centre (1985).

L. D. Andersen, A. J. W. Hilton & C. A. Rodger, *A solution to the embedding problem for partial idempotent latin squares,* J. London Math. Soc. (2) *26* (1982), 21-27.

L. D. Andersen, A. J. W. Hilton & C. A. Rodger, *Small embeddings of incomplete idempotent latin squares,* Ann. Discrete Math. *17* (1983), 19-31.

L. D. Andersen, R. Häggkvist, A. J. W. Hilton & W. B. Poucher, *Embedding incomplete latin squares whose diagonal is almost completely prescribed,* Europ. J. Combinatorics *1* (1980), 5-7.

L. D. Andersen & E. Mendelsohn, *1-factorizations of K_{2m} with given edges in distinct 1-factors,* preprint, Aalborg University Centre (1985).

K. I. Appel & W. Haken, *Every planar map is four colorable,* Bulletin of the American Mathematical Society *82* (1976), 711-712.

K. I. Appel & W. Haken, *Every planar map is four colorable. Part I: Discharging,* Illinois Journal of Mathematics *21* (1977), 429-490.

K. I. Appel, W. Haken & J. Koch, *Every planar map is four colorable. Part II: Reducibility,* Illinois Journal of Mathematics *21* (1977), 491-567.

A. E. Brouwer, A. J. de Vries & R. M. A. Wieringa, *A lower bound for the length of partial transversals in a latin square,* Nieuw Arch. Wisk. (3), *XXVI* (1978), 330-332.

V. W. Bryant, *Extending latin rectangles with restraints,* Europ. J. Combinatorics 5 (1984), 17-21.

A. Chetwynd & R. Häggkvist, *Completing partial $n \times n$ latin squares where each row, column and symbol is used at most cn times,* preprint, University of Stockholm (1984).

W. G. Cochran & G. M. Cox, *Experimental designs.* John Wiley, New York (1950). (Second edition 1957).

C. J. Colbourn, *Embedding partial Steiner triple systems is NP-complete,* J. Combin. Theory (A) *35* (1983), 100–105.

C. J. Colbourn, *The complexity of completing partial latin squares,* Discrete Appl. Math. *8* (1984), 25–30.

D. R. Cox, *Planning of Experiments.* John Wiley, New York (1958).

A. B. Cruse, *On embedding incomplete symmetric latin squares,* J. Combin. Theory (A) *16* (1974), 18–22.

R. M. Damerell, *On Smetaniuk's construction for latin squares and the Andersen-Hilton theorem,* Proc. London Math. Soc. (3) *47* (1983), 523–526.

D. E. Daykin & R. Häggkvist, *Problem 6347,* Amer. Math. Monthly *88* (1981), 446.

D. E. Daykin & R. Häggkvist, *Completion of sparse partial latin squares,* in Graph Theory and Combinatorics (B. Bollobás, ed.), Proceedings of the Cambridge Combinatorial Conference in Honour of Paul Erdös, Academic Press, London (1984), 127–132.

J. Dénes, in a lecture at the University of Surrey. Quoted in Dénes & Keedwell (1974), p. 115.

J. Dénes & A. D. Keedwell, *Latin Squares and their Applications.* Akadémiai Kiadó, Budapest, and English Universities Press, London (1974).

J. Dénes & A. D. Keedwell (eds.), *Latin squares,* symposium, in preparation (1986?).

J. Dénes & E. K. Pásztor, *Some problems on quasigroups,* Magyar Tud. Akad. Mat. Fiz. Oszt. Közl *13* (1963), 109–118. (In Hungarian).

D. A. Drake, *Maximal sets of latin squares and partial transversals,* J. Stat. Planning and Inference *1* (1977), 143–149.

T. Evans, *Embedding incomplete latin squares,* Amer. Math. Monthly *67* (1960), 958–961.

R. A. Fisher, *The Design of Experiments.* Oliver and Boyd, Edinburgh (1935). (Eighth edition 1966).

M. R. Garey & D. S. Johnson, *Computers and Intractability. A guide to the theory of NP-completeness.* W. H. Freeman, San Francisco (1979).

M. Hall, *An existence theorem for latin squares,* Bull. Amer. Math. Soc. *51* (1945), 387–388.

P. Hall, *On representatives of subsets,* J. London Math. Soc. *10* (1935), 26–30.

A. Hartman, *Partial triple systems and edge colourings,* Preprint, IBM Israel Scientific Center (1984).

K. Heinrich, *Latin Squares with and without subsquares of prescribed type,* manuscript (1984), to appear in Dénes & Keedwell (1986?).

A. J. W. Hilton, *Embedding an incomplete diagonal latin square in a complete diagonal latin square,* J. Combin. Theory (A) *15* (1973), 121–128.

A. J. W. Hilton & C. A. Rodger, *Latin squares with prescribed diagonals,* Canad. J. Math. *XXXIV* (1982), 1251–1254.

D. G. Hoffman, *Completing incomplete commutative latin squares with prescribed diagonals,* Europ. J. Combinatorics *4* (1983), 33–35.

I. Holyer, *The NP-completeness of some edge-partition problems,* SIAM J. Computing *10* (1981a), 713–717.

I. Holyer, *The NP-completeness of edge-colouring,* SIAM J. Computing *10* (1981b), 718–720.

R. Häggkvist, *A solution to the Evans Conjecture for latin squares of large size,* in Com-

binatorics (A. Hajnal & V. T. Sós, eds.), Colloquia Mathematica Societatis János Bolyai, 18, North Holland, Amsterdam (1978), 495-514.

R. Häggkvist, *Restricted edge-colourings of bipartite graphs*, preprint, University of Stockholm (1984a).

R. Häggkvist, *A family of completable partial latin squares*, preprint, University of Stockholm (1984b).

D. A. Klarner, *Problem*, in Combinatorial Theory and its Applications III (Erdös, Renyi & Sós, eds.), Colloquia Mathematica Societatis Janós Bolyai, 4, Budapest (1970), 1167. (Distributed by North-Holland, Amsterdam-London).

D. König, *Theorie der Endlichen und Unendlichen Graphen*, Akademische Verlagsgesellschaft, Leipzig (1936). (Reprinted by Chelsea Publ. Co., New York 1950. In German.)

C. C. Lindner, *On completing latin rectangles*, Canad. Math. Bull. *13* (1970), 65-68.

C. C. Lindner, *Embedding partial idempotent latin squares*, J. Combin. Theory (A) *10* (1971), 240-245.

C. C. Lindner, *Embedding theorems for partial latin squares*, manuscript (1984), to appear in Dénes & Keedwell (1986?).

E. Mendelsohn & A. Rosa, *One-factorizations of the complete graph – a survey*, to appear in J. Graph Theory.

W. E. Opencomb, *On the intricacy of combinatorial construction problems*, Discrete Math. *50* (1984), 71-97.

The Open University, *Design of Experiments*. Graphs, Networks and Design Interfaculty Course Unit 6, The Open University Press, Milton Keynes (1981).

C. A. Rodger, *Embedding incomplete idempotent latin squares*, in Combinatorial Mathematics X (L.R.A. Casse, ed.), Proceedings of the conference held in Adelaide, Australia, August 23-27 1982, Lecture notes in Mathematics 1036, Springer, Berlin (1983), 355-366.

C. A. Rodger, *Embedding an incomplete latin square in a latin square with a prescribed diagonal*, Discrete Math. *51* (1984), 73-89.

H. J. Ryser, *A combinatorial theorem with an application to latin rectangles*, Proc. Amer. Math. Soc. *2* (1951), 550-552.

B. Smetaniuk, *A new construction on latin squares – I: A proof of the Evans Conjecture*, Ars Combinatoria *XI* (1981), 155-172.

B. Smetaniuk, *A new construction for latin squares – II: The number of latin squares is strictly increasing*, Ars Combinatoria *XIV* (1982), 131-145.

V. G. Vizing, *On an estimate of the chromatic class of a p-graph*, Diskret. Analiz *3* (1964), 25-30. (In Russian).

D. E. Woolbright, *An $n \times n$ latin square has a transversal with at least $n - \sqrt{n}$ distinct symbols*, J. Combin. Theory (A) *24* (1978), 235-237.

Jens Knude

The Reddening
at the North Galactic Pole

ABSTRACT. *Results from a recently completed photometric survey are presented. A complete sample of A5-G0 stars brighter than $V \sim 11.2$ mag and at latitudes above $b = + 70°$ has been observed in the uvbyβ system.*

With an average of 4 stars deg^{-2} these data allow detailed studies of the local interstellar dust distribution at high latitudes.

The data obtained agree consistently with a previous uvbyβ investigation of polar A and F stars, Hill, Barnes and Hilditch. The mean E(b-y) difference, HBH-K, is only -0.005 ± 0.018 mag for 650 stars in common.

Substantial fractions of the north pole region are found to have color excesses larger than E(b-y) = 0.050 mag. The most reddened areas seem to be organized in longish features a few degrees wide and ten or more degrees long. The dust strings are parallel to the direction l: 37-217. Dust filaments are most frequent in the section $37 \lesssim l \lesssim 217$ but prominent structures also exist in the region 217 $\lesssim l \lesssim 37$.

An irregular distribution of absorbing matter will influence counts of galaxies and clusters of galaxies and thus the angular distribution of these objects. As a first approximation to the effects caused by the presence of high latitude dust, the dust distributions angular autocorrelation function is computed for separations between adjacent lines of sight in the range from 10' to 3 deg.

The dust is found to be uncorrelated in this sense. The autocorrelation function equals zero for the whole range of separations. Quite a surprising result because the autocorrelation of the gas column density distribution is a very clean exponential for $b > 40$ deg.

Assuming a constant ratio between gas and dust, which may not be a proper assumption, the clumping of the dust is studied in the context of a two component emission model for the diffuse soft X-ray background. The two component model is particularly interesting for high latitudes, where the proposed remote contribution originates in the halo. The effective absorption cross sections obtained from the best fits to the observed background in the B and C bands, Burrows et al., show a perfect agreement to the cross sections computed from the dust observations but deviates a factor two from those computed from the radio observations of the same regions. The radio and dust results lead to disagreeing conclusions on the existence of a hot halo. The dust distribution reconciles the soft background observations and the existence of a hot galactic halo.

Copenhagen University Observatory,
Øster Voldgade 3, DK-1350 Copenhagen K.

Introduction

Most fields of astronomy study physical processes where the radiation is influenced by the presence of solid material – dust. A particularly interesting part of the sky is the Galactic Poles, being the windows for extra galactic research, and because here the short lines of sight facilitate the study of individual interstellar structures.

The density structure of the interstellar matter with varying distance from the Galactic plane is important for understanding how it evolved and how it is energized. It is consequently a very serious problem that no consensus on the mere existence of high latitude dust has been reached. This disagreement implies several problems. As the distribution of dust is known only very fragmentary models are often adopted to correct for the reddening assumed to be present. This is the case in some extragalactic studies, where two models have been suggested. The most obvious model is a coherent plane parallel layer which results in a cosecant dependence of the estimated dust column on latitude; de Vaucouleur and Buta (1983) have reviewed the evidence for the plane layer concept. The sun may also be located in a sort of cavity in a plane layer of dust with a finite extent from the plane, Sandage (1973). The latter suggestion is a very attractive one because several bubble-like structures have recently been observed in the Galaxy. If such structures are frequent it is not unresonable that the sun could be inside one. If so should be the case many problems will find easier solutions because reddening corrections would only be required for low latitude objects beyond a few hundred parsecs and many calibrations would be facilitated and more accurate. A testing ground for the two concepts is the North Galactic Pole, NGP, where they disagree on the amount of matter present. The first model predicts substantial amounts of reddening, $E(B-V) \sim 0.05$ mag, whereas the second model estimates that no solid dust is present above latitude 50°.

In the search for high latitude dust some sort of a continuous background source is required. Variations in such a background could be interpreted as caused by absorbing matter. If faint galaxies have a homogeneous distribution the variation of their surface density with latitude may indicate whether matter is present or not. With a local cavity in a finite dust layer the surface density will level off at a certain latitude whereas the surface density will increase all the way to the pole in the first model. Counts of galaxies/clusters of galaxies are not able to set the zero point of the extinction but variations in the counts may

indicate the existence of matter at the poles. However, the counts are based on the assumption that the large scale distribution of luminous matter in the universe is homogeneous and isotropic – the fair sample hypothesis. There is also a disagreement on whether the counts of galaxies are too noisy, Burstein and Heiles (1978), to discriminate between a steadily increasing or a constant surface density above latitude 50°. The noise may depend on the reseau size used for the counts but may also contain some information on a variable absorption.

The problems mentioned lead naturally to ask how an irregular distribution of absorbing dust may influence the intrinsic distribution of galaxies. A recent study, using the Hat Creek 21 cm intensity, Seldner and Uson (1983), as an indicator for the dust, implies that if the dust is distributed analogous with the gas it may modify the intrinsic galaxy distribution significantly. The gas column densities have a correlated distribution and their autocorrelation obeys an exponential law. A correlated dust distribution may change the amplitude of the intrinsic power law distribution of galaxies and also reproduce the observed change of slope in the power law at separations ~3°. A mapping of the high latitude dust will naturally bear on this important problem.

The structure of the Galactic halo is most important in several respects. Here is only considered some aspects of the interstellar medium at the halo. Studies of ultraviolet absorption lines in LMC OB supergiants have revealed that the Galaxy has a hot ~10^5 K, high latitude plasma, Savage and de Boer (1981). Speculations on how interstellar clouds with high z-distances maintain pressure equilibrium suggest that a low density gas with even higher temperatures may confine such clouds, Spitzer (1956). The halo could contain substantial amounts of a 10^6 K gas which might be an important source of diffuse soft X-rays. With a soft X-ray halo and intervening neutral gas, intensity variations due to simple photoelectric absorption are to be expected in the background observations. On small angular scales the observations of the diffuse background are extremely smooth only showing variations on the 10% level. A global fit of soft X-ray count rates does however anticorrelate with the distribution of neutral hydrogen, McCammon et al. (1983). There is no straight forward explanation on this complex picture. Several models of the solar X-ray surroundings suggest that the dominating part of the X-ray emission originates within the nearest few 10^{19}cm^{-2} of neutral hydrogen gas, Fried et al. (1980). In these models the background is virtually unabsorbed. Smooth intensity variations as observed are however also compatible with an extremely clumped spatial

distribution of an absorbing gas. It is possible to fit a two component emission model to the data: a local unabsorbed source and a remote absorbed. But an extreme clumping of the matter is required in order to reduce the efficiency of the absorption. In the modelling the effective absorption cross sections were taken as free parameters and the best fit values were found to be a factor of two lower than the computed atomic cross sections, McCammon et al. (1983). Continuum absorption of stellar light do not give any direct information on the gas clumping, only on the distribution of the solid component of the interstellar medium. Optical observations have however two advantages compared to most radio observations: an upper limit to the length of the dust column is given by the stellar distance and the optical beam is infinitely narrow without any side lobes. In principle the three dimensional distribution of the dust may result from the optical observations. If there is a constant – or known – ratio of gas to dust, the dust results may be applied to the gas distribution. But except, perhaps, for the cold gas, one still have to assume a constant ratio.

The influence of the diffusely dispersed dust on radiation has so far mostly been studied by its dimming and polarising effects on starlight. With the advent of the IRAS satellite more stringent investigations may be performed of the physical properties of the diffuse dust concentrations, because grain temperatures and compositions now may be brought into the discussion on an empiric basis. A promising field of research will be a combination of the dust observations as in the present study and the IRAS maps at 100μ. As the following discussion shows there is no unique spatial relationship between the amount of gas and dust but since significant patches of the NGP are much reddened one might expect fairly strong 100μ emission even though only minor amounts of neutral hydrogen is reported. The 100μ maps will probably have a streaked appearence as that displayed by the color excess distribution.

An observing programme

One of the exciting issues raised in interstellar studies is the structure of the interstellar medium (ISM) at the Galactic poles. Regarding the solid component of the interstellar matter (ism), it has long been questioned whether the optical data actually were related to the effects of intervening dust on radiation. Several photometric programmes have however indicated that matter is present but unfortunately about as many that it is

not. Some of the color excess catalogues were planned in a systematic way but often this has not been the case and the lines of sight were selected on a rather casual basis. It was therefore considered to be of some value to have a survey based on all stars of a given spectral range down to a rather faint limiting magnitude. The data forming the basis for the present study approximate the fulfilment of these requirements. Color excesses, E(b-y), for about 5000 lines of sight with b > 70° were obtained.

E(b-y) measures the integrated dust column out to the star used as a background source. The whole idea to study the ism this way is based on a complete knowledge of the background sources' intrinsic continuum spectrum. Interstellar grains have a scattering cross section showing a λ^{-1} wavelength dependence in the optical, and is thus scattering the blue light more efficiently than the red. The continuum absorption results in apparent stellar colors redder than their intrinsic colors.

Accurate photometry is a must in interstellar studies. The gas density in the ISM is expected to be rather low: 10^{-2}-10^{+2} atoms cm^{-3} is the range anticipated in the diffuse medium. As the part of the interstellar space studied is within a few hundred pc, the expected gas columns are ranging from 6 10^{18} to 10^{21} atoms cm^{-2}. If the ism has a constant gas/dust ratio 7.5 10^{21} atoms mag^{-1}, Knude (1978), these columns translate to color excesses in the range from 0.001 to 0.13 mag. If columns with the smallest value are frequent the demands to the photometric accuracy are extreme. For fainter objects they can not be met presently. The best obtainable color excesses have a mean error $\sigma(E(b-y)) \lesssim 0.01$ mag. It has been proposed that the ism in the solar neighbourhood might be concentrated in small, still diffuse, clouds; if so, detailed observations are required for the detection of these features. If the ism on the other hand has a continuous distribution information on the dust distribution is obtainable from observations along a limited number of lines of sight. A principal objective of interstellar studies must be to find the characteristic linear scales of the mass concentrations. As a consequence observations must be performed in fine networks to ascertain a high detection probability even of the smaller features. Data samples representative of the ism consequently involve observations of several thousand stars.

The photometric system used by the author is the uvbyβ system by Strömgren (1966) and Crawford and Mander (1966). For interstellar purposes this system is presently calibrated for not too evolved population I stars of spectral type late A and for the whole F star range, Crawford (1975, 1978, 1979).

Fig. 1. Surface density of lines of sight where the color excess E(b-y) was measured. The smooth distribution is a contributory cause to assure an equal probability to observe identical dust features all over the polar cap, b > 70°.
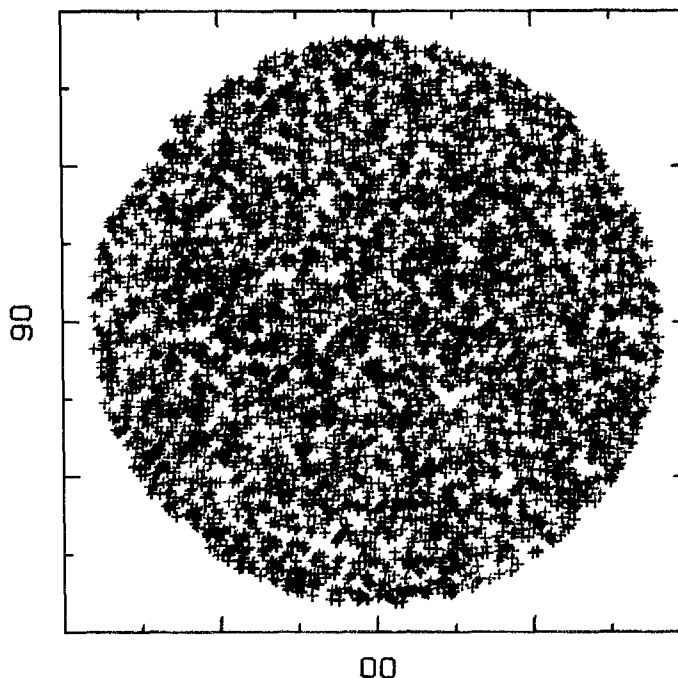
For statistical computations an ideal network should have equal – and adjustable – spacings. The stellar distribution does of course not meet this demand, but as seen on Figure 1 the present sample has a fairly homogeneous distribution across the polar area.

When photometric surveys are planned the main obstacle is the scarcity of spectral cataloques from which candidate stars in the proper spectral range may be drawn. Candidate catalogues must further be complete in some respect either to a given limiting magnitude or to a limited distance range for subsequent evaluation of the completeness of the results obtained.

Spectral surveys of large areas are not abundant in the literature. It was therefore most fortunate that we learned that a rather deep, V ~ 11-11.5 mag, survey of the NGP was nearing completion, when the NGP programme was considered. The survey has been done by T. Oja, Uppsala, and was kindly put at the disposal of Professor B. Strömgren in the form of a handwritten catalogue containing 5458 entries.

Three problems remained before a photometric mapping of the dust distribution at the NGP could be attempted: accurate coordinates of the candidate stars which were identified either by a DM number or by

indicating the number of the nearest DM star, a suitable, efficient photo-
meter and finally sufficient blocks of observing time on moderate sized
telescope(s).

Coordinates were procured in collaboration with M. Winther, Insti-
tute of Astronomy, Aarhus University by using the Carte du Ciel Cata-
logues. The photometer, which was to become the prototype of a new
generation six channel combination of the formerly used 4 and 2 channel
uvby and Hβ photometers, was designed and built in the Brorfelde
workshops of the Copenhagen University Observatory on a grant from
the Carlsberg Foundation to B. Strömgren and P. E. Nissen. Generous
amounts of observing time was granted on La Silla, Kitt Peak, Roque de
los Muchachos and San Pedro Martir.

Finally the author had the pleasure of spending more than 180 observ-
ing nights on this particular programme between March 1, 1982 and
May 15, 1984.

Heavy reddening at latitudes above +70°

As emphasized by Burstein and Heiles (1978), in the paper where the
HI/GC method for reddening estimates is evaluated, only photometry of
high latitude distant objects with well known intrinsic color may settle
the dispute on the distribution and amplitude of the galactic pole redden-
ing. The HI/GC method was calibrated on RR Lyrae stars and individual
stars in globular clusters. Anyway the HI/GC reddening estimates are
claimed to have an accuracy 0.010 mag in E(B-V) or 0.007 mag in
E(b-y), comparable to the best obtainable intermediate band photo-
metry, calibrated on local unreddened population I stars, with known
metalictiy and evolutionary stage.

During the last few years new conclusions on the NGP reddening
have been published. Hill, Hilditch and Barnes (1983) have presented a
segmented reddening map of the NGP above b = 75°. Half of this
region, l: 270-0-90, was found to have an average reddening E(b-y) =
0.008 mag, furthermore a small dust feature with E(b-y) = 0.024 mag
was identified and found to coincide with a confined 21 cm feature on the
maps by Heiles (1975). The stellar sample observed by HHB was drawn
from the literature Hill, Barnes and Hilditch (1982). A list of common
stars with DM numbers has been prepared and 650 stars from this sam-
ple have E(b-y) observations both by HHB and the present author. The

Fig. 2. Local heavily obscured regions in the polar direction. Lines of sight with color excesses measured to be above E(b-y) = 0.050 mag. The stellar background sources have photometric distances smaller than 100 pc. The dust seems to be confined to a filamentous structure. See also Fig. 3-8.
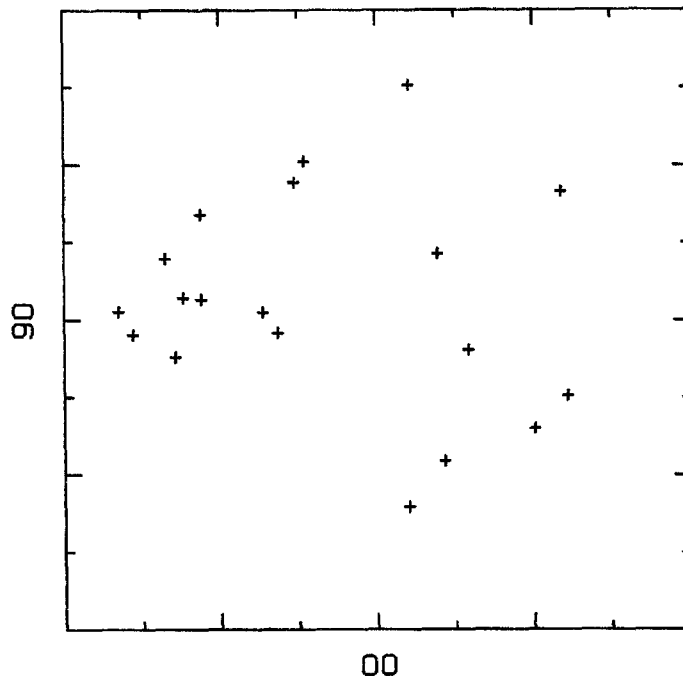
comparison of the photometry will be presented elsewhere. The mean difference of the color excesses $\langle E(b-y)_{HHB} - E(b-y)_K \rangle = -0.005$ mag with a standard deviation in the distribution of the residuals of only 0.018 mag. The common sample is made up mainly of F stars, for which Crawford (1975) quotes a standard deviation 0.012 mag of the color residuals for the basic calibrators assumed unreddened.

The programme has 75 stars in common with the Perry and Johnston (1982) reddening survey of the northern part of the volume within 300 pc. $\langle E(b-y)_{PJ} - E(b-y)_K \rangle = -0.014 \pm 0.014$. Perry and Johnston's sample is primarily A stars and their reddenings were reduced by Perry and Johnston by 0.009 mag in order to have identical mean reddenings for the F and for the A stars. If this reduction is not performed the mean difference will change to about -0.007 mag. There are hardly any significant zero point differences in the three samples. One might add – as was to be expected. Without the zero point amendment of the PJ sample the mean difference of the HHB and PJ sample becomes $\langle E(b-y)_{HHB} - E(b-y)_{PJ} \rangle = -0.003 \pm 0.015$ mag for 41 stars. Without the A star correction the reddening of the 90 Perry and Johnston stars above $b = 70°$ is 0.007 mag, or $E(B-V) = 0.010$ mag. If it is permissible to use Burstein

and Heiles calibration formula in the reverse sense and further ignore the variable gas/dust ratio controlled by the galaxy counts, their equation four in the 1978 paper estimates an average HI column 2.9 10^{20} cm^{-2} from E(B-V) = 0.010, which is much larger than observed. Whether the amendment of Perry and Johnston's A star reddenings is a requisite or not is not evident.

From the NGP programme uvbyβ data for about 4800 stars are available for immediate computation of color excesses. Figure 1 shows the resulting distribution of lines of sight. The coverage is seen to be fairly homogeneous across the entire cap. Thus there is an identical probability to detect the effects of 'large scale' extinction features over the whole region. With four stars per square degree the average separation between adjacent lines of sight is 30' so quite small features may also be studied using this sample. A detailed discussion of absorbing material at the NGP is not attempted here, but some new discoveries are presented mostly as a picture gallery. As one of the most disputed questions has been the existence of substantial amounts of nearby absorbing material in the pole directions, Perry, Johnston and Crawford (1982), Figure 2 shows what may be termed as obscured local polar regions. Nearby is
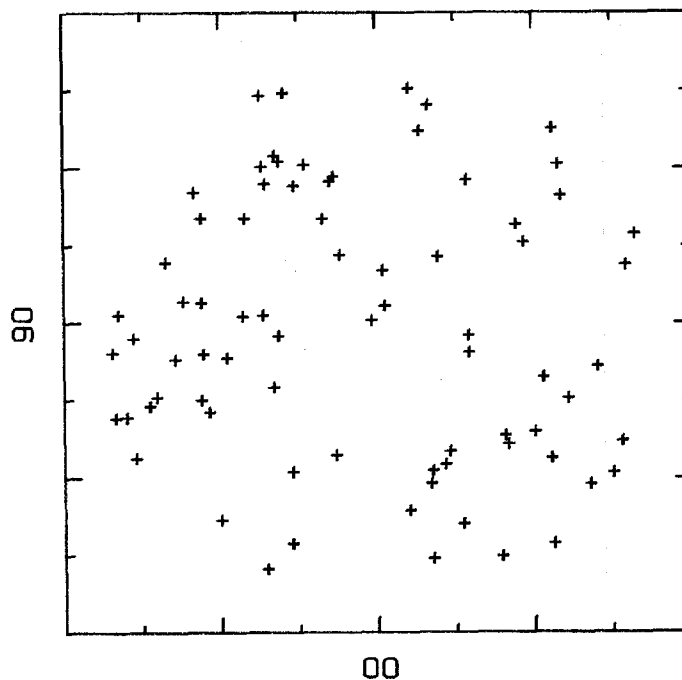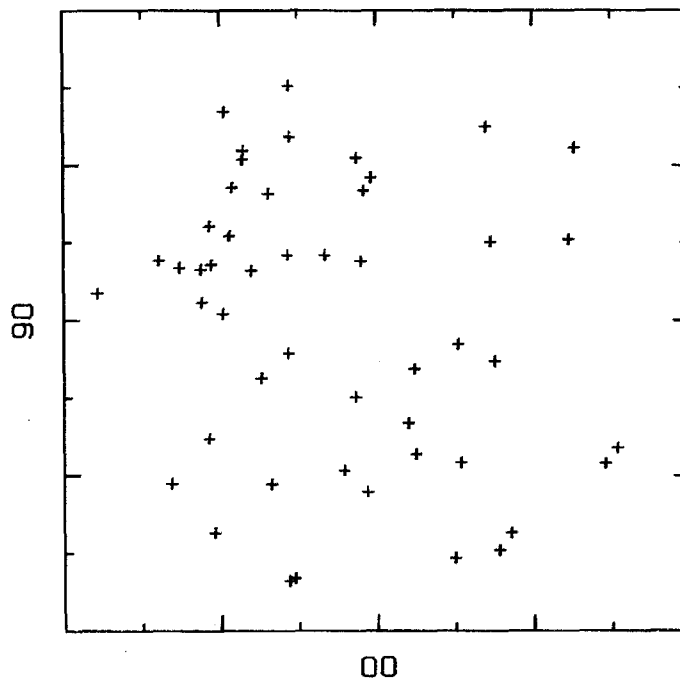

Fig. 3. Caption as to Fig. 2 except that this diagram has a lower reddening limit E(b-y) = 0.030 mag. The distance range is 0-100 pc.

Fig. 4 Caption as to Figure 2 but for the distance range from 100 to 150 pc.

defined as within 100 pc, substantial reddening as a color excess beyond 0.050 mag. With almost any photometric accuray 0.050 mag is more than three sigmas above zero reddening. Most of the cap is free from such large local reddening. But even with these few points a clustering of the reddened directions is noticed. The high local excesses tend to concentrate in the quadrants l: 270°-360° and l: 90°-180°. Most local reddening is found at l~90° and b in the range from 70° to 80°. The distribution on Figure 2 may just indicate what is to become apparent for the more distant intervals, that the most reddened parts of the NGP is confined to filaments which stretch across the pole region. The dust filaments may be made up by smaller discrete features. In the galactic plane individual 'coherent' clouds with reddenings as small as 0.015 mag were found, Knude (1979). For comparison Figure 3 is a polar diagram of all directions with E(b-y) > 0.030 mag for the same distance interval as Figure 2. Note that all excesses > 0.050 are located in well confined 0.030 mag features. Two stars with E(b-y) > 0.030 mag and within 100 pc are located inside the 0.024 mag feature noted by Hill, Barnes and Hilditch (1983). The remaining dust structures on Figure 2 and 3 have not been seen previously. The appeerence of the dust distribution is filamentous. The orientation of the threads on Figure 3 is not unambiguous. There are
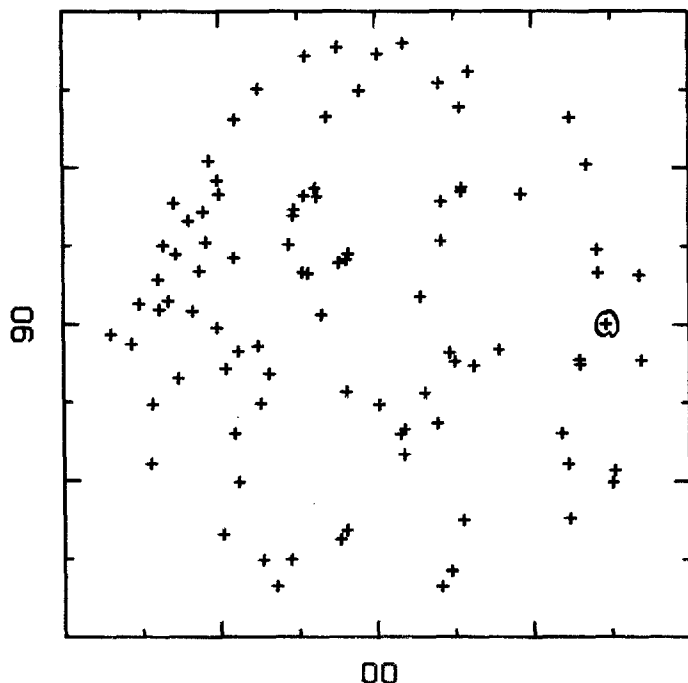
Fig. 5. Caption as to Figure 2 but for the distance range from 150 to 200 pc. The line of sight crossing Burstein and Heiles (1982) intensity maximum above latitude +70° is marked. Note the thready character of the distribution.

two clear, dust free lanes parallel to l: 55-235 but only in the l: 235-360-55 part of the cap. In the range l: 55-235 the preferred direction of the filaments is almost perpendicular to the direction 55-235. Figure 4 to 7 is a sequence of 50 pc wide distance segments – note *not* z-distances.

On Figure 4 is seen a clustering tendency in the distribution of excesses above 0.050 mag as on Figure 3 for the smaller excesses, but with a higher concentration of large excesses in the 90-180 quadrant. In the three remaining quadrants the distribution is filamentous. The distance range 150-200 pc is shown on Figure 5. Again a very prominent structure is seen near the rim for l: 90-120 and b: 70-73. It is difficult to tell whether the distribution is best conceived as a coherent entity or as a sequence of nearly parallel filaments stretching from the rim of the area towards the pole. As an example of the strong variations found the longitude 143 is considered. First there is some dust along the rim then a 5° wide void followed by a very sharp reddening ridge, then another void and again a sharp ridge and finally a clear region up to the pole. The reddening distribution for the stars in this distance interval is demonstrably thready. Figure 6, 200-250 pc, corroborates the thready tendency, but here the dust is concentrated almost exclusively in the longitude range from 37 to 217 degrees and confined to two dust bands parallel to

Fig. 6. Caption as to Figure 2. Distance range from 200 to 250 pc. The dust is almost exclusively found in the longitude range l: 45°-225°.
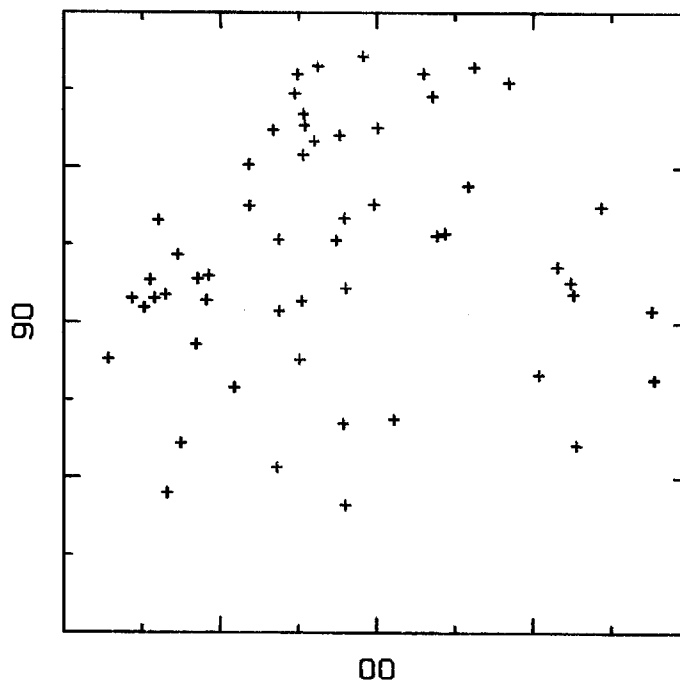
the 37-217 diagonal. Figure 7 is a very clean specimen of the filamentous general distribution. One has to conclude that the most reddened parts of the NGP are confined to filaments organized in a parallel pattern.

Finally Figure 8 displays the projected distribution of all lines of sight measured to have a color excess larger than $E(b-y) = 0.050$ mag. The projection is characterized by a broad, ~5° wide band almost without any heavy obscuration stretching across the entire cap including the pole itself. The distribution of the heavy reddening outside the clear path is indeed patchy but as suggested by the reddening distribution in the sequence of distance bins the reddening seems mostly to be found in string-like structures. The general direction of the system of strings is more or less lined up with the clear path l: 37-217. The strings may be made up by smaller structures some of which are oriented perpendicular to the general string direction. This 'clear' picture of the reddening distribution will be smoothed when the lesser reddenings are taken into account.

It is a surprise that the only feature in common to the HHB map is the curved feature delineated on Figure 8. Burstein and Heiles (1982), Figure 7(a), also show this feature in atomic hydrogen. Except for a few addi-
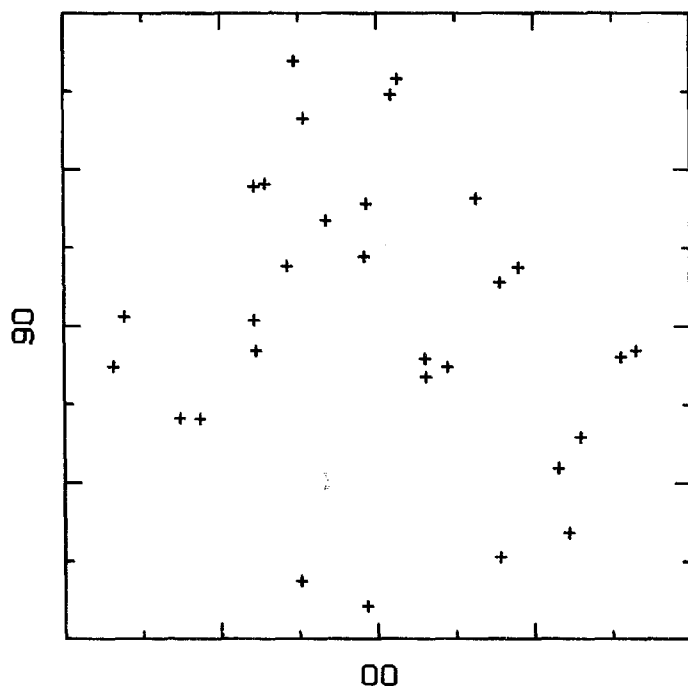
Fig. 7. Color excesses larger than E(b-y) = 0.050 mag for stars in the distance range from 250 to 300 pc. Note the very narrow dust filaments.

tional very small structures it is the only conspicuous HI entity above 70°. The maximum reddening estimate by the HI/GC method is at (l,b) = (270,74) and equals E(b-y) = 0.030 mag. A single line of sight with excess above 0.050 crosses this region. The distance to the dust is probably in the range from 150 to 200 pc. A most striking conclusion that follows from a comparison of Figure 8 to Figure 7 (a) of Burstein and Heiles (1982) is that there are indications of a large scale *anticorrelation* between the dust and the atomic gas distribution. Most of the heavily reddened regions are located in the section l: 30-210, which is the part of the polar cap where the lowest HI contours are located. An immediate qualitative result is to expect large variations in the ratio N(HI)/E(b-y) in this part of the sky. It is tentatively suggested that there may be extended regions at the NGP where dust exists without atomic gas.

Fig. 8. Projected dust distribution for stars with E(b-y) > 0.050 mag. The only NGP dust feature reported previously is delineated. Burstein and Heiles intensity maximum is also indicated. The reddening distribution is characterized by a patch free from heavy obscuration stretching across the pole in the direction l: 37-217. There may be a tendency that the dust bands are oriented in the same direction. A qualitative comparison to 21 cm intensity maps indicates that the most reddened part of the NGP coincides with the smallest 21 cm intensities.
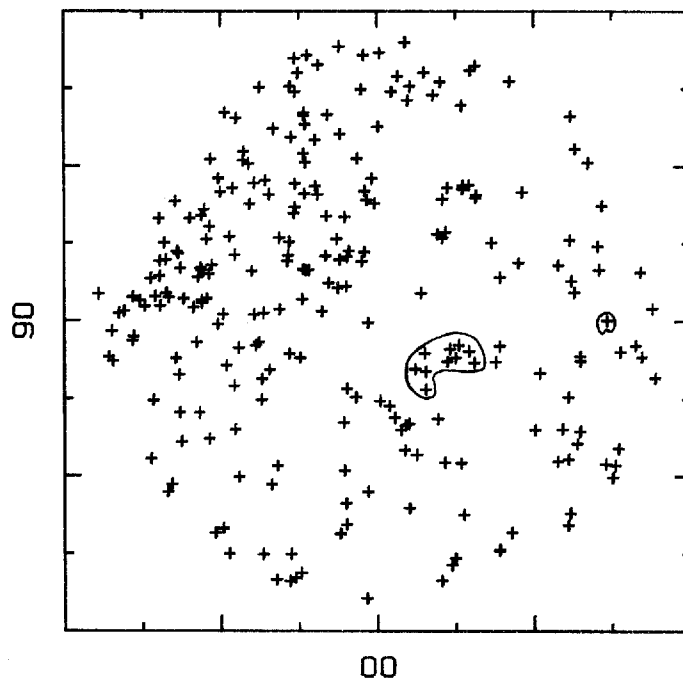
The autocorrelation function of high latitude dust

We have seen that the counts of galaxies have been used as an indicator of the variation of extinction with latitude at high latitudes and in the HI/GC method galaxy counts were further used as an estimator of changes in the ratio between gas and dust. Conversely the observed dust distribution will find applications in the study of the intrinsic galaxy clustering. Davis, Groth and Peebles (1977) conclude that the two-point correlation function is not seriously effected by variable extinction whereas Seldner and Uson (1983) try to explain the observed galaxy autocorrelation by a combination of an intrinsic unbroken power law and clumped galactic obscuration represented by the HI column density distribution.

The angular autocorrelation function has been computed for several cataloques of galaxy counts and is found to obey a combination of two power laws·where the change of power occurs at an angular separation at about 3°. It is an important problem whether the amplitude and the power is a consequence of local galactic obscuration or they represent properties of the intrinsic galaxy distribution. The intrinsic galaxy distribution is assumed to be a power law. The galactic extinction may be important because the probability, dp, to observe a galaxy with apparent magnitude, m, in the range m, m+dm, within a solid angle $d\Omega$ in a direction (l,b) depends on the absorption in this direction:

$$dp(m,l,b) = d\Omega dm \int_0^\infty r^2 dr\ \Phi(m - 5 \log r - 5 - A(l,b))$$

Φ is the galaxy luminosity function, A(l,b) the absorption out of the Galaxy in the direction (l,b). Catalogues of deep galaxy counts are often presented as a listing of a surface density of galaxies as a function of position. What is counted is mostly the number of galaxies brighter than certain limiting magnitudes within a given solid angle. Obscuration has several effects on galaxy counts, either it dims a galaxy so much that it falls below the detector threshold or also the appearance of the galaxy is modified so it can not be discriminated from a stellar object. Only the first effect is considered here: a galaxy with a certain luminosity is only counted if its distance and the obscuration place it above the catalogues' limiting magnitude, m_o

$$dp = d\Omega_1 \int_0^\infty O(A,l,b)dA \int_{-\infty}^{m_o-A} dm \int_0^\infty r^2\ dr\ \Phi(m - 5 \log r - 5)$$

where O(A)dA is the probability to encounter an obscuration in the range A,A+dA in the direction (l,b). O(A) is not known as a function of galactic coordinates. The probability to have a simultaneous sighting of two galaxies brighter than m_o in two directions separated by an angle Θ_{12} is similarly

$$dp = d\Omega_1 d\Omega_2 \int_0^\infty \int_0^\infty O_{12}(A_1,A_2,\Theta_{12})$$

$$\int_{-\infty}^{m_o-A_1} dm_1 \int_{-\infty}^{m_o-A_2} dm_2 \int_{-\infty}^\infty \int_0^\infty r_1^2 dr_1 r_2^2 dr_2$$

$$(\Phi(m_1 - 5 \log r_1 - 5) \cdot \Phi\ (m_2 - \log r_2 - 5) + \text{cross term})$$

$O_{12}(A_1, A_2, \Theta_{12})$ is the joint probability to observe the absorptions A_1 and A_2 along two lines of sight separated by Θ_{12}. The frequency function $O_{12}(A_1, A_2. \Theta_{12})$ is also quite unknown.

However, the functions $O(A)$ and $O_{12}(A_1, A_2. \Theta_{12})$ can be estimated for the zone above $b = 70°$ by using the ~ 5000 E(b-y) values. In fact these distribution functions are not required to be known in details for evaluating the influence of absorption on the clustering of galaxies. If the amplitude of the extinction is small the luminosity function may be expanded in powers of the absorption. For small absorptions only the first and second order moments of the dust distribution are required.

The function O_{12} is the variation of the average of $A_1 A_2$ with separation Θ. For $\Theta = 0$ the function is related to the number of clouds per unit length along a line of sight.

Sorting out the color excess data in preselected separation and color excess intervals consumes much computing time. Before complicating the analysis by binning in distance intervals etc. the autocorrelation was computed for the complete sample of NGP stars. The stars are thus not separated in distance bins before the average absorption products are computed. The effect of this simplification is not quite clear, but it may be of minor importance because a preliminary discussion of a subsample of NGP stars, Knude (1984), indicated that only minor variations of the dust distributions average properties are to be expected within the first 300 pc from the plane. One might think that this problem was easily solved by only including stars beyond a certain distance limit to make sure that the integrated column out of the plane was measured. But with a discrete distribution of the obscuration the most distant stars in magnitude limited samples, as the NGP sample, are only included because they happen to be unreddened. Exclusive use of the most distant stars will thus bias the reddening amplitude towards lower values. In the computation of the mean absorption products, separations from $10'$ to $3°$ have been considered. Rim effects are corrected for by weighting pairs by the fraction of the annulus inside the zone $b > 70°$. The means are computed for all excesses in the range from -0.030 to 0.100 mag. It is tacitly assumed that there is a constant ratio of selective to absolute absorption.

With preselected excess values, E_1 and E_2, excesses in the interval $E_1 \pm 0.005$ mag are combined to excesses in the range $E_2 \pm 0.005$ mag for the 18 separations $10' + n\, 10'$, $n = 0,1,2,\ldots,17$. For a separation Θ the proper E_2's are searched after in an annulus $\Theta \pm 5'$. On Figure 9 the variations of the joint probability to find two excesses with a separation Θ are shown
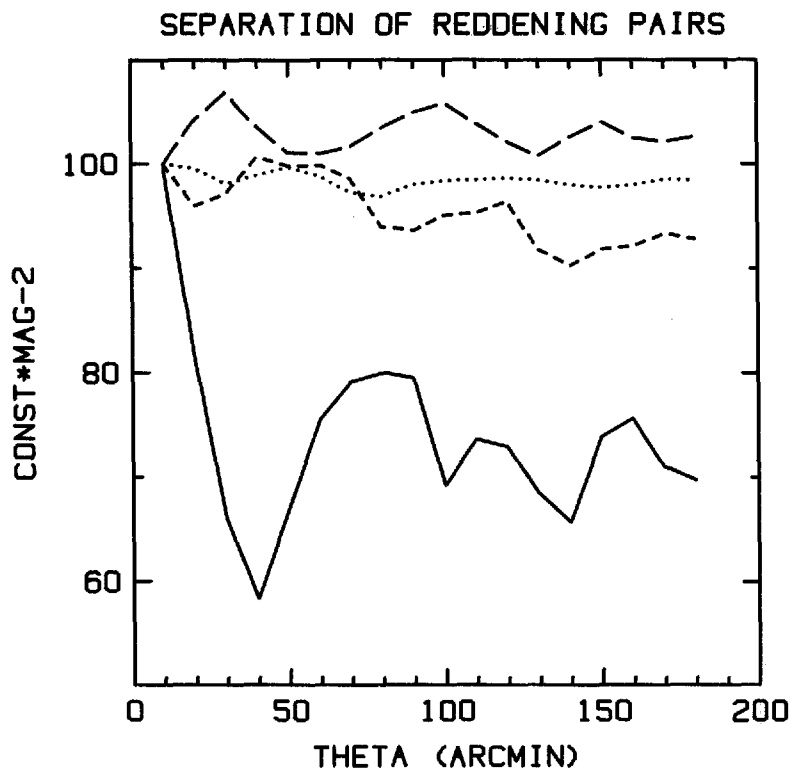
SEPARATION OF REDDENING PAIRS

Fig. 9. Relative frequency of (E_1, E_2) pairs as a function of separation Θ.

(−0.020,−0.010) ....

(0.010, 0.020) — — — —

(0.020. 0.030) – – – – –

(0.030, 0.040) ————

The curves are shifted to a common origin. Note particularly the difference between the ICM curve (.......) and the cloud curve (————).

as a function of Θ. The scale is arbitrary and the curves have been shifted to a common origin. The curves shown are for the (E_1, E_2) pairs (− 20,− 10),(10,20),(20,30),(30,40) in mmag. The two first pairs may be representative for the clear lines of sight and the two last for obscured lines of sight. The probability to have two clear lines of sight is thus constant for the whole range of separations considered. For the pairs (0.020,0.030) the joint probability shows a decreasing tendency with increasing separation. For the excess pairs (0.030,0.040) the decreasing tendency is confirmed. The decrease is however not monotonic but the joint probability indicates that these pairs are distributed on preferred angular scales. Separations below 20′, between 60′ and 100′, and between 150′ and 170′ are the most common.
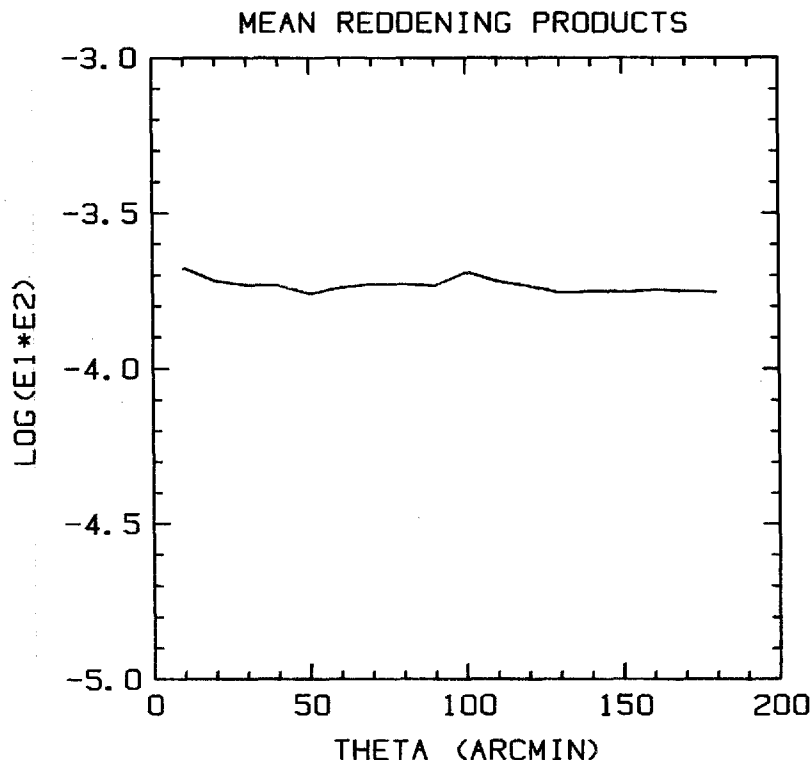
MEAN REDDENING PRODUCTS

Fig. 10. Average excesses $\langle E_1 E_2 \rangle_\Theta$ as a function of separation. The average cross products are constant implying an uncorrelated dust distribution. The dust autocorrelation function, defined in the text, is accordingly ~ 0 unlike the N_H distribution which is a clean exponential.

Finally the products $E_1 E_2 O(E_1, E_2, \Theta_{12})$ are integrated over the observed excesses for constant Θ to obtain $\langle E_1 E_2 \rangle_\Theta$. The integral is computed for the 18 values of Θ considered. In the light of the neat dependence of the N(HI) autocorrelation on Θ the result for the dust is really unexpected, because the mean $\langle E_1 E_2 \rangle_\Theta$ does not show any dependence on separation whereas the HI columns follow an $\exp(-\Theta)$ law. The average products equal the $\sim$mean square for the complete sample. With the definition of the autocorrelation function

$$\omega_E (\Theta) \equiv \langle E_1 E_2 \rangle_\Theta / \langle E \rangle^2 - 1 \simeq 0, \ \Theta \neq 0$$

it its found that ω_E is identical to ~ 0 for the range of separations considered. The values computed for $\langle E_1 E_2 \rangle_\Theta$ are shown on Figure 10. The conclusion seems to be that the dust is uncorrelated in the 'circular sense' at least. This may be understandable from the dust distribution found in

the previous section. When the dust is confined to filaments with density variations, e.g. Figure 2 and 3, 'any' reddening may be found for 'any' small separation. Note that $\omega_E \neq 0$, $\Theta = 0$, which implies that the number of clouds per unit length may be found from the method of moments: $k = 1$ kpc^{-1} compared to $k = 4$-8 kpc^{-1} in the plane.

An uncorrelated dust distribution's influence on the galaxy distribution function is not evident but dust ripples as on Figure 2-8 will certainly have som effect on a homogeneous distribution of galaxies. With a reddening distribution as observed the autocorrelation function does not appear to be the best statistics to describe the spatial dust correlation. As the dust may be confined to strings a statistics sensitive to the orientation of the individual features may be thought of instead. It is emphasized that the conclusion stating that the dust is uncorrelated is preliminary, the reason for this proviso is that when the complete sample is used for calculating the excess products at a given angular separation, excesses from the whole distance range 50-600 pc are included and these excesses may not have any physical relationship. A calculation of the excess products from subsamples limited to excesses from narrow stellar distance intervals may give different results.

Small scale structure in the distribution of matter at high latitudes and the origin of the diffuse soft X-ray background

Since the surveys of the diffuse background at soft röntgen energies were completed an interesting conflict on the spatial location of the emission has come about. As the computed absorption cross section of the ISM gas, assuming a cosmic composition, only requires a few times 10^{20} atoms cm^{-2} to have an optical depth unity, the emission volumes are supposed to be within a few hundred pc. At the galactic poles this may not be the case. Ultraviolet absorption lines indicate the existence of plasmas with temperatures close to 10^5 K, Savage and de Boer (1981). Theoretical considerations on why high latitude clouds do not disperse on short timescales indicate that plasmas with even higher temperatures may be in pressure equilibrium with these clouds.

The consistency of a hot halo and the background emission has been studied within a two component emission model

$$I = I_L + I_R \exp(-\tau) \tag{1}$$

where I_L signifies the intensity from a local unabsorbed emission and I_R the remote emission which will be absorbed by the intervening material with the effective optical depth τ.

τ is computed from atomic cross section, Cruddace et al. (1974), and the observed N_H columns. If the gas/dust ratio is known the optical depth may also be computed from the dust columns E(b-y). Dust column observations may be better to use than 21 cm observations because they relate specifically to the volumes from which the soft emission may be observed. But they introduce of course another parameter which is not well known either.

A plasma code at a given temperature is required to fit the three parameters I_L, I_R and σ_x to the observations I(l,b) and N_H(l,b). $\tau = \sigma_x N_H$, where σ_x is the effective cross section which may differ from the computed atomic cross sections because of a variable distribution of matter inside the beam of the X-ray experiment. The model values of σ_x in fact disagree with the atomic cross sections indicating either that the two component emission is not a proper model or that the matter obscuring the remote emission is not located in nice homogeneous sheets covering the complete X-ray beam.

Two obvious solutions to this problem have been proposed:
(a) There is only an insignificant if any remote soft X-ray emission. The local emission dominates the background.
(b) The absorbing gas has a discrete distribution and is clumped on scales much smaller than the X-ray beam.

The author may be prejudiced from his optical experiences but has a feeling that the (b) suggestion is to be preferred.

Recently a series of papers discussing inter alia the point (b) has appeared, Fried et al. (1980), McCammon et al. (1983), Jahoda et al. (1985). Jahoda et al. have performed new 21 cm observations to address specifically the problem of clumping on scales comparable to the X-ray beams. They have completed detailed mapping of the HI column density distribution in 20 randomly selected areas with a size 4°×5°. The X-ray beams have typically a FWHM of 7°, and are circular with a triangular response function.

The fit of the global observations to equation (1) requires that the effective absorption cross sections are reduced with approximately a factor of two. If the combined X-ray counts and column density data are to be reproduced the diminished absorption efficiency requires an ex-

treme degree of clumping, hence observations of the small scale distribution of matter is important. Twenty regions are mapped by Jahoda et al. with a spacing of only 10' between the observations. The 140 foot telescope observations were corrected for side lobe effects by comparing a synthesized beam to the Crawford Hill beam for identical regions. The Crawford Hill survey, Stark et al. (1984) is supposed to be free from side lobe effects; conversely the telescope has a large beam: 90% of the intensity within 2°. Such a large beam may cause problems. Figure 9 showed that preferred separations of reddening pairs relating to lines of sight penetrating clouds are smaller than 30'. The cross section reduction is due to the difference of the average transmission over the beam, where the amount of matter may vary, from the transmission corresponding to the column density averaged over the beam

$$\alpha \equiv \frac{\sigma_{eff}}{\sigma_{atomic}} = \frac{-\ln\left\{\frac{1}{n}\Sigma\exp(-\sigma_{atomic}\,N_H)\right\}}{\frac{1}{n}\sigma_{atomic}\,\Sigma\,N_H} \tag{2}$$

n is the numbeer of lines of sight observed in one of the 20 regions or in an area of comparable size.

The atomic cross section for the B-band (0.13-0.188 keV) and for the C-band (0.16-0.288 keV) is $1.75\ 10^{-20}$ cm^2/atom and $0.8\ 10^{-20}$ cm^2/atom respectively, McCammon et al. (1983). The effective cross sections resulting from the model fits are $0.65\ 10^{-20}$ and $0.52\ 10^{-20}$ cm^2/atom for the B and the C band respectively, Burrows et al. (1984). McCammon et al. op.cit. quote $0.37\ 10^{-20}$ and $0.40\ 10^{-20}$ cm^2/atom respectively.

Using the numbers by Burrows et al. requires reduction factors $\alpha_B=0.37$ and $\alpha_C=0.65$. The detailed mapping of the 20 regions resulted in reduction factors larger than 0.8 for the B-band as well as for the C-band, Jahoda et al. op.cit., Table 1. Obviously there is no evidence for the extreme gas clumping in the 140 foot observations and consequently little support for soft X-ray emission from a hot halo.

Two of the regions, 5 and 19, mapped by Jahoda et al. fall within the zone b > 70°. When the averages of the excess products were computed for various separations the polar cap was divided in 51 cells. The centers of the regions 5 and 19 are located in cell 42 and cell 15 respectively. The areas of cell 42 and 15 are 23.5 and 27.5 square degrees respectively and contain 95 and 103 lines of sight where the color excess E(b-y) was measured. Both area size and number of observing points are then comparable to the values from the radio survey. The reduction factor α for these two cells may be computed from the dust observations if the relationship between dust and gas was known, which it really is not. A
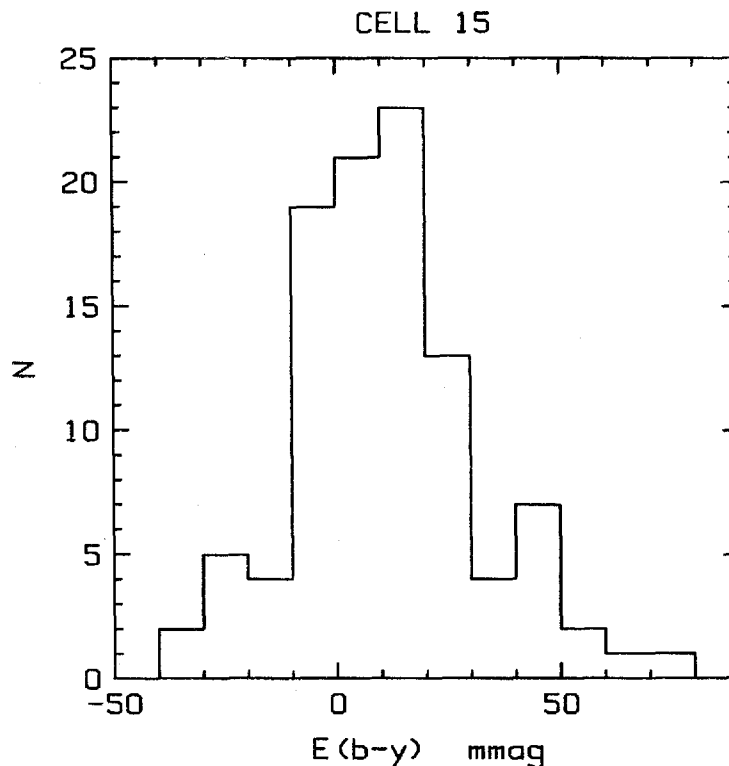
Fig. 11. Dust column distribution in cell 15, see Tabel 1. The histogram is assumed to be made up by observations of two components of the ISM. A truly diffuse part with $\langle E(b-y)\rangle = 0$ and $\sigma_{\langle E(b-y)\rangle} = 0.010$ and a cloud part with $E(b-y) > 0$. See text for details.

constant ratio is anyway assumed: $N_H/E(b-y) = 7.5 \ 10^{21} \ cm^{-2} \ mag^{-1}$, Knude (1978).

Burstein and Heiles (1982) suggest a constant ratio above latitude $+60°$. Figure 11 is a histogram of the dust column distribution in cell 15. There is evidently a preponderance of positive excesses but also a well populated negative tail. For comparison Figure 12 shows a similar histogram for cell 5 which has the same latitude as cell 15 but $l_5 = l_{15} + 180°$. The distribution of dust columns in cell 5 is a beautiful specimen of the distribution of dust within a small area. Cell 5 has a slightly larger average excess than cell 15 but otherwise the two histograms are very similar. When computing the transmissions the negative excesses pose a problem. Negative excesses result from imperfect photometry. They are thought to result from observations of directions with very low dust
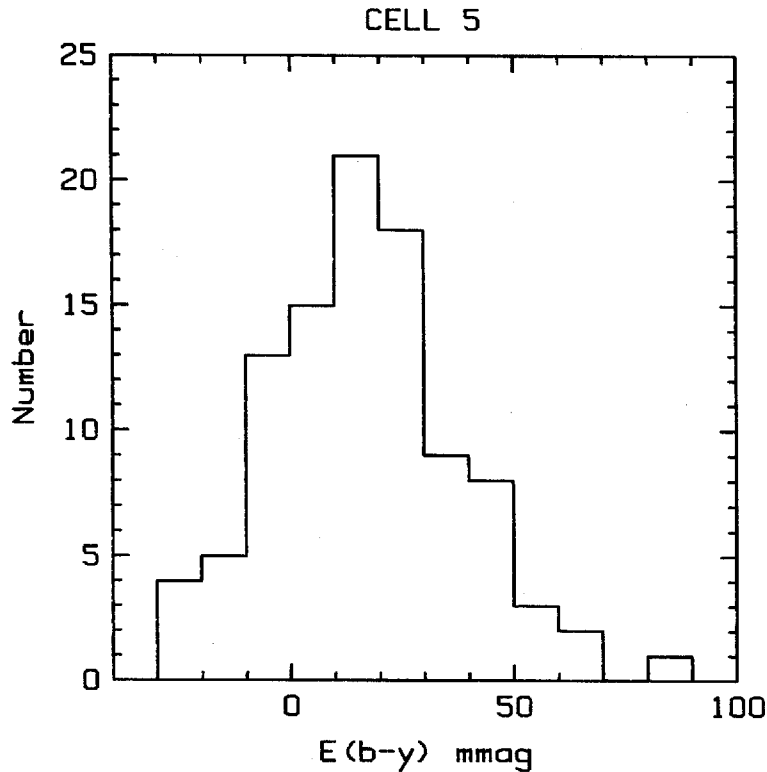
CELL 5

Fig. 12. Caption as to Figure 11, but for cell 5.

columns; the error distribution will then scatter about half of the actually zero reddenings below zero. Following this picture it is suggested that the interstellar dust is distributed on two basic components in the ISM: a truly diffuse part, the inter cloud medium (ICM), and a higher density part, the clouds. The transmission of the ICM is taken to be unity. In order to discriminate between the two components of the ISM in the computation of the reduction factors it is postulated that the ICM red-denings follow a gaussian with average excess ~0 and with a standard deviation 0.010 mag. The number of stars with excesses in the range from -0.01 to -0.020 equals accordingly the number of lines of sight scattered between one and two sigma below zero reddening. The total number of ICM lines of sight is then estimated from the number of stars in this excess interval. For the 99 lines of sight used in cell 5,43 is estimated to run exclusively in the transparent ICM. For the remaining 56 lines of sight individual transmissions are computed. An excess in the range from 0 to 0.030 may either be an ICM or a cloud line of sight. The

ICM lines are selected in sequence following the raster scan of the original observations.

For cell 5 the ratio of average transmission to the transmission for the average column is 0.3343 and 0.5581 for the B- and C-band respectively. The reduction factors computed for four cells are listed in Table 1. The factors depend naturally on the constancy of the gas/dust ratio. As briefly discussed previously this ratio seems to vary inside the pole region. The average N_H column estimated from the average dust column is a factor of two smaller than the average observed for region 5 and 19. The ratio $\langle N_H \rangle / \langle E(b\text{-}y) \rangle$ for these two regions are $1.48\ 10^{22}$ cm^{-2} mag^{-1} and $1.87\ 10^{22}$ cm^{-2} mag^{-1}. If the mean of these ratios replaces the gas/dust ratio used for cell 15 α_B, α_C drops to 0.167 and 0.332 respectively. The difference of the gas/dust ratio may be due to different distribution of gas with different temperatures relative to the dust distribution. The ratio
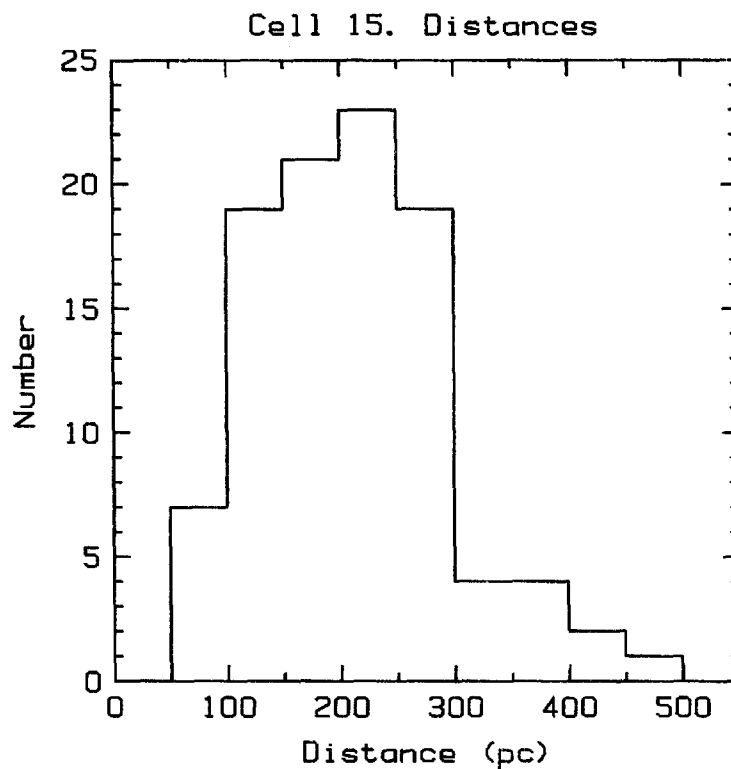
Cell 15. Distances

Fig. 13. Distribution of distances for the stars in cell 15. Note that the major part, ~75%, of the stars are beyond most estimates of the gas scale height.

Table 1. Reduction factors α_B, α_C for the B(0.13-0.188 keV) and C(0.16-0.288 keV) band absorption cross sections computed frem color excesses assuming a constant gas/dust ratio.

Cell	l	b	α_B	α_C	$\langle E(b-y) \rangle$	N
	(°)	(°)			mag	
42	36- 72	80-85	0.3456	0.5985	0.0066	95
5	72- 90	70-75	0.3343	0.5581	0.0166	101
15	252-270	70-75	0.3280	0.5315	0.0106	103
47	216-252	80-85	0.3593	0.5706	0.0117	123

Table 2. Reduction factors of the B and C band absorption cross sections from the observed gas column densities. The last column is the expected neutral hydrogen column density calculated from the observed dust columns assuming the standard gas/dust ratio.

Cell	Region	l	b	α_B	α_C	$\langle N_H \rangle$	$\langle E_H \rangle$
		(°)	(°)			10^{20} cm^{-2}	
42	5	59	84	0.934	0.970	0.98	0.495
15	19	264	71	0.959	0.981	1.98	0.795

7.5 10^{21} cm^{-2} mag^{-1} was estimated from observations in directions where HI was observed in absorption.

Table 1 contains the computed reduction factors for four high latitude cells. The radio results for the factors in region 5 and 19 (cell 42 and 15) are presented in Table 2. The dust data indicate extreme clumping but the radio data do not. For the four regions the average reductions are α_B = 0.34±0.01 and α_C = 0.56±0.03 in reasonable agreement with the requirements α_B = 0.37 and α_C = 0.65 required by the two component models. The dust data thus lend some support to the possibility of a diffuse contribution from a hot halo whereas the radio data do not. The reason for this discrepancy is not obvious. The computed average HI columns for region 5 and 19 in Table 2 are however lower than the average of the observed column densities by the factor of two as mentioned. This deviation is not caused by the limited distance range probed by the optical observations. Figure 13 shows the distribution of stellar

distances or the length of the lines of sight along which the dust is accumulated for cell 15. More than 75% of the stars are beyond 150 pc and then well above one scale height from the plane. If the four cells are compared to the same regions on the Hat Creek maps the E(b-y) predictions of the column densities are low with a factor 3-4 except for cell 5 where the agreement is better. Cell 5 contains the 21 cm maximum of the NGP zone.

As the computation of the E(b-y) values was completed very recently and none of them have been published so far it is thought appropriate to present a table with some of the data. Table 3 contains E(b-y) and distances of the stars in cell 15 where the center of region 19 is located.

As in the previous section it is a difficult matter to state a clear definitive conclusion concerning the small scale structure in the matter at high latitudes. The picture appears more complex than ever. But: part of the ism does clump on the scales required by the two component emission/absorption model for the diffuse soft X-ray background indicating that a significant fraction of the high latitude emission may originate in a hot halo. This conclusion is strongly depending on the assumed gas/dust ratio. To complicate matters further this ratio seems to differ from a previous derivation when formed from gas only seen in emission.

Table 3. Stars in the cell 15 (l: 252°-270°, b: 70°-75°). A star labelled with a DM number followed by a capital letter indicates that it is not in the Bonner Durchmusterung and that the nearest DM star is as indicated.

DM	l^{II}	b^{II}	E(b-y)	D
	DEG	DEG	MAG	PC
10 2380	269.5687	69.7660	0.011	258.8
11 2422	266.7675	70.3590	0.028	174.2
11 2423	267.4446	70.2027	0.044	190.7
11 2424	266.9501	70.5486	0.010	81.0
11 2424 A	267.2786	70.4969	0.028	283.3
11 2426	268.0995	70.2245	0.009	142.8
11 2426 A	267.4739	70.6108	0.016	245.1
11 2427	267.4739	70.6108	0.053	207.9
11 2431	269.1553	70.6877	0.007	133.1
12 2403	262.3851	69.7749	0.006	372.4
12 2408	262.1716	70.5662	−0.024	144.1

DM	l^{II}	b^{II}	E(b-y)	D
	DEG	DEG	MAG	PC
12 2409	262.0745	70.8151	0.048	119.5
12 2410	263.0046	70.4566	−0.022	291.3
12 2411	262.2965	70.7903	−0.001	158.9
12 2413	263.8512	70.2970	−0.020	214.6
12 2417	264.5242	71.0918	−0.024	191.2
12 2418	265.1323	71.0754	0.009	280.4
12 2421	266.0522	70.8070	−0.023	84.8
12 2423	267.0181	71.2336	−0.029	423.3
12 2425	267.4096	71.5542	0.018	261.7
12 2426	267.5265	71.6416	0.014	339.2
12 2427	267.6868	71.6855	0.009	138.1
12 2428	268.8782	71.3211	−0.008	102.5
12 2430	268.1942	71.8948	0.049	139.9
13 2464	254.7128	69.8715	−0.004	357.5
13 2470	257.5502	70.2124	−0.001	279.3
13 2472	257.5490	70.8621	−0.004	242.6
13 2476 A	258.3956	70.8920	0.007	238.7
13 2476	258.4571	70.9756	0.013	185.8
13 2478	259.4741	71.1262	0.053	165.4
13 2481	260.6036	71.6086	0.013	173.6
13 2482	261.9072	71.1325	0.006	128.3
13 2484	261.9296	71.7696	0.035	158.0
13 2485 A	262.1574	71.8126	0.010	263.5
13 2485	262.1237	71.7200	0.019	91.5
13 2487	263.5303	72.4348	0.030	210.5
13 2490	265.1486	71.9236	−0.006	249.5
13 2492	265.3295	72.2481	0.016	161.2
13 2494	265.4537	72.2514	0.012	176.4
13 2495 A	266.5759	72.1208	0.007	456.9
13 2495	265.9141	72.3075	−0.011	273.2
13 2498	266.3042	72.4669	−0.008	193.5
13 2500	267.4013	72.5564	0.001	277.2
13 2502	268.1752	72.5650	−0.003	127.3
13 2503	267.8181	73.1204	−0.004	116.8
13 2504	268.3594	73.0410	0.008	291.3
13 2505	268.6227	73.1537	0.041	170.7

DM	l^{II}	b^{II}	E(b-y)	D
	DEG	DEG	MAG	PC
13 2507 A	268.8483	73.3887	−0.003	267.8
13 2511	269.9527	73.6486	0.067	170.8
14 2438	252.4147	69.8136	0.020	112.6
14 2440	253.5935	70.0971	0.011	265.0
14 2441	253.6926	70.4236	0.023	150.4
14 2442	254.4439	70.1688	0.022	171.2
14 2447	254.3482	71.2410	0.025	106.4
14 2448	254.4727	71.4473	0.020	74.6
14 2448 A	254.1811	71.4062	0.011	297.4
14 2449	255.5264	71.2346	0.009	219.5
14 2451	256.0976	71.1995	0.022	127.1
14 2454	256.9979	71.4241	0.009	151.1
14 2455	257.8257	71.1506	0.001	277.6
14 2457	256.6912	71.9274	0.037	74.9
14 2458	256.9754	72.1582	0.037	142.3
14 2461	258.5009	72.1640	−0.011	694.0
14 2462	259.8231	71.7770	0.015	158.5
14 2465	259.2378	72.1510	0.016	215.5
14 2466	258.7192	72.4401	0.017	195.9
14 2469	261.0262	72.5113	0.009	231.2
14 2470	261.6546	72.2748	−0.011	441.8
14 2472	261.5299	73.0822	−0.002	219.8
14 2473	262.9986	72.9610	−0.001	150.8
14 2476 F	263.2831	73.5220	−0.007	303.7
14 2477	266.2775	73.4953	−0.007	201.7
14 2478	266.6203	73.5812	0.004	133.6
14 2481	267.3817	73.3631	0.001	104.3
14 2482	267.0350	73.6792	−0.003	266.9
15 2386 A	252.7008	70.9734	0.002	242.6
15 2394 A	254.0706	71.9882	−0.033	363.5
15 2394	253.6795	71.9275	0.020	393.1
15 2396	253.1113	72.3000	0.029	287.3
15 2398	254.5440	72.0121	0.049	145.4
15 2399	253.5880	72.6166	0.042	134.5
15 2400 A	255.6022	72.9178	−0.031	556.5
15 2401	256.3252	73.1577	−0.004	337.1

DM	l^{II}	b^{II}	E(b-y)	D
	DEG	DEG	MAG	PC
15 2403	257.0716	73.2121	−0.010	210.1
15 2405	257.9796	73.2490	0.007	155.2
15 2409	261.0343	73.3126	−0.023	201.9
15 2417 Q	261.4269	74.5105	0.018	282.4
15 2418	262.2001	74.2626	0.010	74.2
15 2419	262.5046	74.3499	0.015	195.7
15 2420	263.5779	74.1609	−0.009	217.1
15 2426	263.8356	74.9707	0.004	321.4
15 2427 A	265.8161	74.4124	0,018	262.3
15 2430 A	266.3453	74.8605	0.015	266.0
15 2430	266.6207	74.8690	0.010	215.0
15 2433	267.3352	74.8646	0.005	203.0
16 2325	254.4840	73.8025	0.021	238.7
16 2330	256.9201	73.7845	0.071	169.0
16 2331	257.1060	73.9820	0.024	259.4
16 2335	258.4148	74.0928	0.024	248.5
17 2423	252.6768	73.9673	0.043	247.4
17 2430	255.6209	74.6649	0.007	118.1

Concluding remarks

The incursion into the field of high latitude dust suggests a revision of three major points:

on the existence of high latitude dust: substantial amounts are present. The most reddened lines of sight are organized in a filamentous pattern.

on the autocorrelation of the dust distribution: apparently the dust is uncorrelated with the usual definition of the autocorrelation function. The variable obscuration may have other effects on the galaxy distribution than changing its amplitude and power. One could imagine that the galaxy distribution somehow was complementary to the dust distribution. A statistics sensitive to the orientation of the dust strings is required for such an investigation.

on the small scale dust distribution: the dust distribution in areas comparable in size to the beams applied in the soft X-ray surveys is found to show extreme clumping of a degree required to explain the reduced absorption cross section. If the dust and gas correlates spatially this result indicates that a fraction of the high latitude background may originate in the halo. It is however a serious question whether a general constant gas/dust ratio can be maintained. The NGP data indicates that rather large variations may be anticipated.

The dust investigations make up only part of the studies for which the NGP data were obtained. An immediate application will be the first estimates of density variations perpendicular to the galactic plane for various stellar subgroups.

References

Burstein, D., Heiles, C.: 1978 Astrophys, J. *225,* 40

Burstein, D., Heiles, C.: 1982, Astron, J. *87,* 1165

Burrows, D. N., McCammon, D., Sanders, W. T., Kraushaar, W. L.: 1984, Astrophys. J. December 1 issue

Crawford, D. L., Mander, J.: 1966, Astron. J. *71,* 114

Crawford, D. L.: 1975, Astron. J. *80,* 955

Crawford, D. L.: 1978, Astron. J. *83,* 48

Crawford, D. L.: 1979, Astron. J. *84,* 1858

Cruddace, R., Paresce, F., Bowyer, S., Lampton, M.: 1974, Astrophys. J. *187,* 497

Davis, M., Groth, E. J., Peebles, J. E.: 1977, Astrophys. J. *212,* Letters 107

de Vaucouleurs, G., Buto, R.: 1983, Astron. J. *88,* 939

Fried, P. M., Nousek, J. A., Sanders, W. T., Kraushaar, W. L.: 1980, Astrophys. J. *242,* 987

Heiles, C.: 1975, Astron. Astrophys. Suppl. *20,* 37

Hill, G., Barnes, J. V., Hilditch, R. W.: 1982, Publ. dom. Astrophys. Obs. *XVI,* 111

Hill, G., Hilditch, R. W., Barnes, J. V.: 1983, Mon.Not.R. astr. Soc. *204,* 241

Jahoda, K., McCammon, D.., Dickey, J. M., Lockmann, F. J.: 1985, Astrophys. J., March 1 issue

Knude, J.: 1978, in Reiz, A., Andersen, T. (eds) 'Astronomical Papers Dedicated to Bengt Strömgren', 273

Knude, J.: 1979, Astron. Astrophys. Suppl. *38,* 407

Knude, J.: 1984, IAU Coll. 81, Kondo, Y., Bruhweiler, F. C., NASA Conference Publication *2345,* p. 123

McCammon, D., Burrows, D. N., Sanders, W. T., Kraushaar, W. L.: 1983, Astrophys. J. *269,* 107

Perry, C. L., Johnston, L.: 1982, Astrophys. J. Suppl. *50,* 451

Perry, C. L., Johnston, L., Crawford, D. L.: 1982, Astron. J. *87,* 1751

Sandage, A.: 1973, Astrophys. J. *183,* 711

Savage, B. D., de Boer, K. S.: 1981, Astrophys. J. *243,* 460

Seldner, M., Uson, J. M.: 1983, Astrophys. J. *264,* 1

Spitzer, L.: 1956, Astrophys. J. *124,* 40

Stark, A. A., Bally, J., Linke, R. A., Heiles, C.: 1984, in preparation

Strömgren, B.: 1966, Ann. Rev. Astron. Astrophys. *4,* 437

Thomas Døssing

General Survey of Heavy Ion Reactions and Specific Problems in Damped Nuclear Reactions

ABSTRACT. *A general introduction to heavy ion reactions is given, consisting of a brief survey of the whole bombarding energy spectrum, from damped nuclear reactions to ultrarelativistic collisions, followed by a short review of theories of damped nuclear reactions. A more specialized discussion is made for the angular momentum dynamics in damped nuclear reactions, studied with the nucleon exchange transport theory. The theory is applied to study the polarisation of γ rays emitted in the sequential decay of the reaction products, and to Wilszinsky plots. The results for these quantities compare well to data for energy losses less than half of the maximal energy loss, but the predicted fluctuations in energy loss and scattering angle are too small to account for the data at larger energy losses.*

The Niels Bohr Institute, Blegdamsvej 17,
DK-2100 København Ø, Denmark

1. Introduction

Deep inelastic collisions between atomic nuclei, or, as we shall prefer to call them, damped nuclear reactions, were first observed in 1961. Since the application of more powerful accelerators and more refined detectors around 1975, a more intense study of these reactions has been carried out, both experimentally and theoretically.

A damped nuclear reaction typically proceeds as follows. A heavy projectile nucleus with a kinetic energy of several MeV per nucleon is bombarded onto a heavy target nucleus. The two nuclei engage in a reaction during which a substantial part of the available energy is lost from the relative motion. Still, the emerging nuclei after the reaction resemble the original ones with respect to their mass and charge numbers. This approximate preservation of the size of the original nuclei implies that the system must have maintained its binary character throughout the reaction phase. The energy lost from the relative motion appears as excitation energy in the two reaction products, which after the reaction dispose of this excitation by various processes, typically neutron evaporation followed by emission of γ rays.

On the one side, damped nuclear reactions are distinguished from the gentler quasi-elastic reactions by their large energy loss, while, on the other side, their binary character distinguishes them from reactions in which a mononucleus is formed, such as fast fission or compound nuclear reactions.

Apart from this distinction, the damped nuclear reactions are also distinguished from the more violent reactions which take place when the bombarding energy is increased. To give the reader an impression of the richness of nuclear reactions, a brief overview of the physical phenomena encountered in damped nuclear reactions as well as in the more violent reactions is given in section 2 of the present paper.

Atomic nuclei exhibit a variety of excitations, and different theoretical descriptions of damped nuclear reactions ascribe the energy loss to the excitation of different types of excitations. In section 3 an overview is given of the most important theories, with special emphasis on nucleon exchange transport.

Nucleon exchange transport has recently been applied to the study of the dynamics of angular momentum during damped nuclear reactions, Døssing 1985a, and it was found that the angular momentum carries .characteristic and important information about the reaction process. This development is briefly reviewed in section 4, and section 5 discusses variances in energy loss and scattering angle, which are relevant for differential cross sections. In section 6 theoretical differential cross sections and results for the polarisation of γ rays emitted by the reaction products after the reaction are compared to experiment, thereby widening the confrontation of the theory with data. Section 7 gives a conclusion, and the appendix gives the technical details of the γ ray polarisation calculation and discusses the quality of the information contained in γ ray polarisation observations as compared to the observation of angular distributions of continuum γ rays.

Most of section 2 of the present paper is meant to be accessible for readers without pre-knowledge of nuclear physics. Section 3 is also quite general, but enters into more special topics. The remaining sections as well as the appendix deal with specialized problems. They are centered around the presentation of new results in section 6, and the conclusion drawn from them in section 7.

2. Survey of reactions between heavy ions

Figure 1 illustrates nuclear reactions between heavy nuclei for different bombarding energies, starting with the smallest in the top row and ending with the largest in the bottom row. The left hand column shows the two nuclei approaching each other, and the length of the arrow indicates the velocity in the center of mass frame. The middle column shows schematically the nuclei in a characteristic moment of their interaction. Understanding the physical processes at that moment is the aim of nuclear reaction studies, but in experiments information can only be obtained through careful observation of nuclei, γ rays or other reaction products. The end of the reaction phase is illustrated in the right hand column. The reaction products are still close together, but they move with high speed, about to start their journey out to the detectors, where their type, energy etc. may be determined.

The length scale of the illustration is given by the nuclear radii, which are around 5 to 8 fm (1 fm = 10^{-15} m), and the reaction times are of the order of 10^{-21} to 10^{-23} sec.

For the lowest row, labelled by the name ultrarelativistic collisions, the bombarding energy is so large that the velocities of the nuclei are only slightly smaller than the velocity of light. The nuclei approaching each other in the lower left hand corner are really the same as the ones illustrated in the rows above, but because of their high velocity they are contracted along their direction of motion.

A general reference to reactions between heavy nuclei with emphasis on theoretical questions may be found in the proceedings of a conference held in Paris in May 1984, Martinot 1984.

2.1. Basic properties of stable nuclei

By letting heavy nuclei react with each other, one can study the matter inside nuclei under conditions which are fundamentally different from those present in stable nuclei. Stable nuclei consist of protons and neutrons, or with their common name, *nucleons* (and of virtual particles associated with the mutual interaction of the nucleons). Stable nuclei have an interior of almost constant density of nucleons, and a thin surface region over which the density falls from the value in the interior down to values close to zero. The interior density is practically independent of the size of the nucleus. The thickness of the surface region is approximately 1 fm, which is small compared to the radius of around 6 fm, so for an illustration it is quite realistic to draw the nuclei as having

damped reactions

fragmentation

relativistic collisions
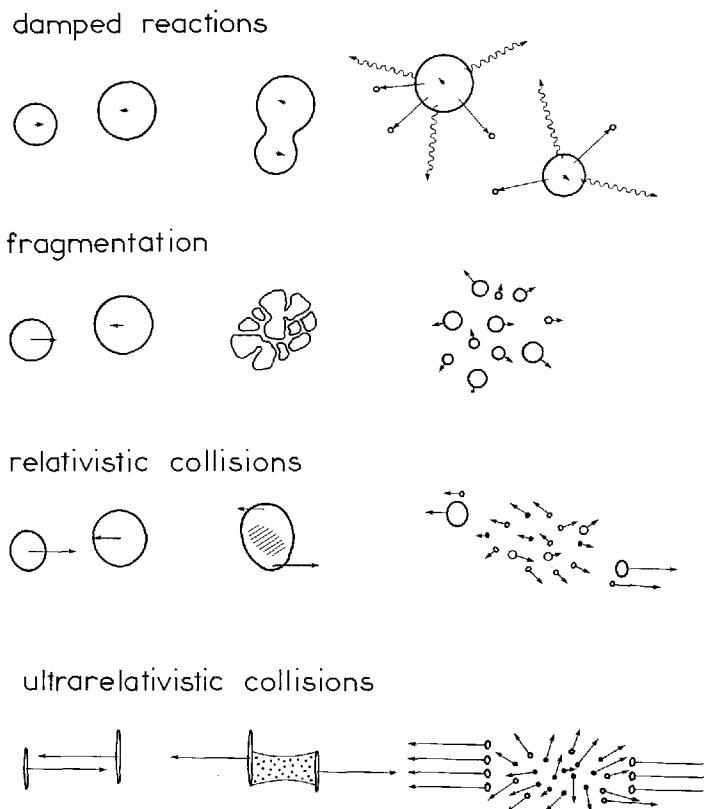
ultrarelativistic collisions

Fig. 1. Schematic illustration of heavy ion reactions. The 4 rows show the time evolution for different sizes of the bombarding energy. The left hand picture shows the nuclei approaching each other, the middle one shows a characteristic moment of the reaction, and finally the right hand picture shows the end of the reaction phase. Open circles or ellipsoids denote nuclei or nucleons, and filled dots denote pions or other particles produced during the reactions.

sharp surfaces. The interaction between nucleons contains both attraction and repulsion, depending on their state of relative motion. The size of stable nuclei balances the attraction and repulsion.

Each nucleon moves in the common attractive potential generated by the interaction with the others. In the simplest picture of nuclei, the lowest nucleon eigenstates in the potential are filled up according to the Pauli principle.

2.2. Energy scales for elastic and inelastic nucleon collisions

The energy unit commonly used in nuclear physics is MeV. (For example the energy released in the fission of one Uranium nucleus is approximately 150 MeV).

Due to the Pauli principle two nucleons in a stable nucleus can not collide and scatter to two new levels. In a reaction between heavy nuclei, all nucleons can move in the common time dependent potential generated by the nucleon distribution. To assess the relative importance of the motion in the potential versus collisions between individual nucleons, the energy per nucleon in the relative motion of the nuclei should be compared to the depth of the potential of approximately 45 MeV, and to the kinetic energy of around 35 MeV of the nucleon occupying the highest level.

For slowly moving nuclei most of the collisions possible for free nucleons will be hindered by the Pauli principle, since there will generally not be energy enough in the relative motion of most pairs of nucleons from the two nuclei to scatter into unoccupied levels. The nucleons will then move with relatively long mean free path between collisions. This applies to the damped reactions where the energy per nucleon is around 4 MeV, and also to some extent to the fragmentation reactions.

For rapidly moving nuclei, the energies of the nucleons are so high that a potential of the order of 45 MeV only will deflect their direction of motion very little, and only few collisions between pairs of nucleons taken from the two different nuclei will be hindered by the Pauli principle. This applies to the relativistic and ultrarelativistic collisions.

Other energy scales are set by the threshold energies for inelastic collisions between nucleons in which other particles are created, or the nucleons themselves are excited or changed. Each nucleon is believed to consist of three smaller particles, quarks. During violent collisions, two quarks can interact and change their nature, and pairs of quarks and antiquarks can be created. For example, a neutron and a proton can collide, forming two protons and a pion, which consists of a quark and an antiquark bound together. The threshold energy for such processes is given by the rest mass energy of the lightest particles which can be created, the pions, 140 MeV.

2.3 Damped reactions

In damped nuclear reactions the nuclei approach each other with a relative energy of the order of 4 MeV per nucleon. During the reaction the nuclear surfaces attract each other and start to overlap, but they do not have energy to penetrate each other because this would lead to a high density and a repulsive potential in the region of overlap. Instead, the density between the two nuclei forms a smooth continuation of their interior densities during most of the reaction. Due to the relative motion

of the nuclei, nucleons can move from an occupied level in one nucleus
to an unoccupied one in the other. Quite many nucleons may be
exchanged this way, and through collisions with nucleons in the nucleus
receiving them, they will heat the nuclei up. Still their energy in the
receiving nucleus will not be very high, so most collisions are hindered
by the Pauli principle, and the nucleons will have an average mean free
path of the order of the nuclear radius before colliding.

The exchange of many nucleons between the two nuclei in motion and
the simultaneous heating pose many intriguing problems, which we
shall touch upon in the next section. Also other excitations than nucleon
exchange will occur, such as substantial deformations of the surfaces of
the nuclei. On the other hand, the heat per nucleon produced is small
compared to the binding energy of the nucleons in the nuclei, and such
quantities as the density inside the nuclei are practically not changed
during the reaction.

Some theories of nuclear reactions yield quite definite results for the
time evolution of charateristic variables. This is for example shown in
section 4 of the present paper, which deals with the application of nu-
cleon exchange transport theory to describe the dynamics of the rotation
of the nuclei during the reaction.

2.4. Fragmentation reactions

Increasing the energy to around 75 MeV per nucleon, a large excitation
energy may be developed, caused by the more frequent collisions pos-
sible between the nucleons. Many collisions will tend to thermalize the
velocity distribution over the volume of the reacting nuclei. Above a
certain temperature, the nuclear matter will not be stable any longer, and
it will expand and crack, leading to a fragmentation of the two colliding
nuclei. These cirumstances are reminiscent of the situation in the hot
matter in supernovae as it expands again after a strong compression. The
important questions are the evaluation of the critical temperature for
fragmentation and of the distribution of the sizes of the smaller nuclei
produced in the fragmentation.

2.5. Relativistic collisions

Increasing the energy per nucleon still further, up to around 500 MeV
per nucleon, the velocities of the nuclei before colliding are of the order
of 60% of the speed of light, hence the name relativistic collisions. As we
have argued, at these energies the reaction will be dominated by colli-
sions between the nucleons. When the nuclei jam into each other, the

nucleons on the sides of the nuclei facing each other will collide first, acquiring sidewards motion at the expense of their velocity along their original direction of motion. Some of the collisions will be inelastic. The nucleons are then not able to leave the interaction zone as quickly as they entered, while nucleons which have not yet collided are still streaming in from the back sides of the nuclei. This results in a substantial buildup of the density, pictured as the hatched area in the center of the nuclei in the reaction phase shown in fig. 1. The density may reach 4 times the normal density inside nuclei. According to most theories of nucleon interactions and nuclear matter, this will result in a strongly repulsive potential in the region of high density, which for the geometry of the collision depicted in fig. 1 will deflect the nucleons moving in from the left downwards, and upwards for the nucleons moving in from the right. The repulsive potential will also tie up a substantial fraction of the kinetic energy of the nucleons into potential energy. Collisions between these nucleons will then be less energetic and result in the production of fewer pions than would be produced if the repulsion was not there.

Towards the end of the reaction, parts of the original nuclei have not suffered collisions, and they move on as smaller heated nuclei. The nucleons which have collided form a gas of nucleons, reminiscent of the situation in the early universe. The gas will expand, and some nucleons may combine to form light nuclei, like ^{2}H, ^{4}He etc. The velocity distribution will still carry memory of the deflection by the repulsion caused by the high density, and the pions will be fewer also beause of this repulsion.

Both the number of pions and the velocity distributions have recently been observed and related to the repulsion associated with the hot dense nuclear matter.

2.6. Ultrarelativistic collisions

Increasing the energy of relative motion considerably further, up to around 20000 MeV per nucleon, the reaction is believed to change its nature completely. At these energies the nuclei are contracted to flat discs. As the two discs pass each other the more violent of the nucleon collisions may first produce an interaction quantum, a gluon string, between the quarks which have interacted. The other two quarks in each of the nucleons do not feel the interaction immediately. The gluon strings later break up, producing showers of particles, and the space between the flat discs will be filled with a highly energetic mixture of quarks and antiquarks and gluons. If the density and temperature in this

region becomes high enough, the quarks and antiquarks will no longer be confined to each other within particles like pions or nucleons, but they will be able to move freely within a »superbag« whose boundaries are indicated in the middle part of the last row of fig. 1.

Having many quarks and antiquarks together in a hot medium within the superbag may be one of the best ways one can learn about these fundamental building blocks of matter and their interaction.

The situation at the boundary of the superbag poses many questions, how will the hot plasma inside the superbag cool off and return to ordinary matter where the quarks are confined within little bags in nucleons or pions etc. No matter how it happens, an enormous shower of particles will be produced in the final phase of the reaction. Until now reactions with these high energies have only been recorded in very few cases on photografic plates where nuclei from cosmic rays have hit nuclei in the emulsion on the plates. Accelerators for the study of these reactions are only proposed at the moment, and it is still not known whether the conditions for producing the superbag will be achieved. Also it is being debated which observation among the many particles formed will give the best diagnostics whether a superbag was formed. The conditions within the superbag and during the return to the final reaction products are reminiscent of the conditions in the very early universe.

3. Theories of damped nuclear reactions

As was argued in section 2, collisions between nucleons are suppressed in damped nuclear reactions, and the dynamics will be dominated by the motion of nucleons in the time dependent mean field.

3.1. Time dependent Hartree-Fock

The time dependent Hartree-Fock theory provides an extreme description of damped nuclear reactions in terms of independent particle motion in the average potential. The wave function for the whole colliding system is at all times a Slater determinant, and the time evolution of the independent particle wave functions occupied by nucleons is given by the Schrödinger equation. Thus collisions between nucleons, leading to more complicated states, are not possible, entropy is not produced, and heating of the nuclei will not take place in the strict sense.

Nevertheless, in applications to damped nuclear reactions, time dependent Hartree-Fock generally gives a good account of the energy loss,

and of the relation between energy loss and average scattering angle. Intuitively, one can say that the energy loss comes about because of the inelastic collisions of the nucleons with the time dependent potential. This time dependence is displayed in pictures. Davies 1981, of the evolution of the calculated density distribution.

More detailed investigations, Köhler 1979, Tang 1981, of the damping mechanism in time dependent Hartree-Fock have applied the Wigner transformation, which transforms the one body density matrix into a phase space distribution. From these investigations it is apparent that transfer of nucleons between the two nuclei play a crucial role for the damping. Since the two nuclei move relative to each other, the momentum distribution of nucleons in the two nuclei are shifted relative to each other, as illustrated in the right hand side of figure 2. This allows phase space points to move from one nucleus to unoccupied parts of the phase space in the other. Also, the boundaries of the potential may move relative to the momentum distribution of phase space points which are close to the boundary, and in this case phase space points may be reflected from the boundary into previously unoccupied points of the phase space distribution.

Both of these kinds of inelastic interactions of nucleons with the time dependent potential give rise to damping. They were first discussed by Swiatecki and coworkers, Blocki 1978, and named *window friction* and *wall friction,* respectively. This was not by using time dependent Hartree-Fock, but by more schematic and general arguments.

Attempts to explain the mass dispersion observed in damped nuclear reactions with the Slater determinant wave function of the system after the reaction phase failed, Davies 1978. This is understood not to be a failure of the mean field description, but specifically due to the restriction to this type of wave function, Dasso 1979. Generally dispersions cannot be addressed by time dependent Hartree-Fock as applied so far, but recent theoretical developments may improve this situation, Balian 1984.

The density distribution calculated with time dependent Hartree-Fock displays quite substantial deformations of the nuclear surfaces, especially when the nuclei are about to separate at the end of the reaction phase. This enables the nuclei to separate with kinetic energies appreciably below the Coloumb barrier for spherical nuclei, in accordance with experiment. Surface vibrations of the nuclear shape are automatically present in time dependent Hartree-Fock calculations.

3.2. Transport theories

Realistic time dependent Hartree–Fock calculations for damped nuclear reactions were long in the making, and were preceded by theories which treated the time dependent field more schematically, but which, on the other hand, also addressed heating of the nuclei. The first such theory was derived by Nörenberg and coworkers, Nörenberg 1975, Ayik 1976. In this work the characteristic time for quantal phase correlations to die out was found to be considerably shorter than the time scale for changes of a set of macroscopic variables. Generally, phase correlations may survive for a while, but those influencing the time evolution of the macroscopic variables are short. This enables the use of a master equation, or transport equation, for the distribution of macroscopic variables, and further, a Fokker–Planck equation for the mean values and covariances of the macroscopic variables. A recent review of these developments with references to the earlier work is contained in reference Nörenberg 1982, which also treats a novel revision of the theory for rather gentle collisions, based upon considerations of the time for specific correlations to die out. A review of the various early formulations of irreversibility and transport theories for damped nuclear reactions has been given by Weidenmüller 1980.

In these theories, the basic excitations giving rise to transport are, in accordance with the overall independent particle picture, taken as inelastic particle–hole excitations within nuclei and nucleon transfers between them. To obtain closed expressions for coefficients, and for the phase correlations to die out fast, the interaction matrix elements for these excitations were taken as Gaussian distributed and with random signs. Microscopic calculations justified this to some extent, Barrett 1978, Shlomo 1979.

Transport theories have been very successful in explaining the width of the mass distribution, Ayik 1976, Wolschin 1981, and later some features of the spin distribution, Wolschin 1978, Wolschin 1981. Also differential cross sections could be reproduced quite well, Agassi 1978, Ko 1979.

3.3. Coherent surface excitation description

A somewhat different description of damped nuclear reactions treats the inelastic particle–hole excitations within the nuclei in a more specific way. When subject to an external field, like the Coulomb and nuclear field from the other nucleus, the particle–hole states will not be excited in a random way, but rather in certain superpositions, collective vibration

states. Within the Coherent surface excitation model, Broglia 1981, specific account is taken of collective surface vibrations. These vibrations correspond to standing waves on the nuclear surface. In actual applications of the coherent surface excitation theory, a low energy and a high energy vibration for each multipolarity from 2 up to around 5 are included. The mean excitation energy and rate of damping of each vibration are taken in accordance with both theoretical estimates and experimental systematics.

It is a big advantage of this description that the deformation of the surfaces are included, being determined by the amplitudes for the vibrations. As in time dependent Hartree-Fock calculations, substantial distortions of the density distribution at the end of the reaction phase lead to final energies below the Coulomb barrier for the exit phase of the reaction, in accordance with experiment. Quantal fluctuations associated with the excitation of the surface modes are found to yield considerable dispersions in quantities such as the energy loss for given impact parameter, Esbensen 1977. This is supported by experiments.

3.4. Nucleon exchange transport

An essentially parameter-free description of nucleon transfers in damped nuclear reactions is given by the nucleon exchange transport theory, Randrup 1979, Randrup 1982.

The theory is based upon transport theory, and in the formal derivation of transport coefficients for one-body operators, the time development of the system is followed during a small time interval. The nucleon transfers are described to take place between eigenstates of the mean fields of the individual nuclei by means of the interaction one body field, which is localized in the region of spatial overlap between the nuclei. A transferred nucleon will occupy an excited state in the new nucleus and leave a hole state behind in the old, and both of these will be damped by collisions with nucleons and with the moving potential boundaries. This damping is assumed to be so fast that the density operator is kept on diagonal form in the eigenstates of the mean fields of the nuclei, given by thermal excitation. This and other approximations applied in the derivation will be valid in the limit of slow reactions between very large nuclei. Especially important is the replacement of matrix elements of the interaction potential by a classical flow of phase space points.

The approximations have clear physical content, but some of them are difficult to justify in a strict sense. Most serious seems to be the argumentation that energy is conserved in the transfers, when referred to a

Fig. 2 Illustration of transfer of a phase space interval between two nuclei. See the text for details.

coordinate space   momentum space
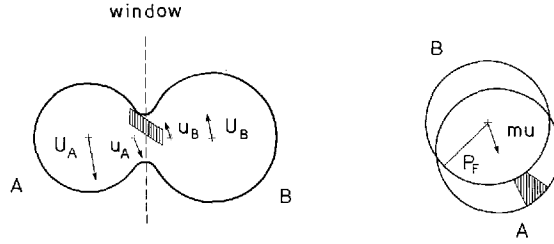
common reference frame. For example, this requires the transferring potential to act undisturbed within a time interval of the order $\Delta t \approx 1.6 \times 10^{-22}$ sec to achieve energy conservation to the accuracy of 2 MeV. This time interval is only slightly smaller than typical time scales for substantial changes in mean values and variances of for example the spin variables of the nuclei.

The transfer of phase space points is illustrated in figure 2, in which the left hand part shows the geometry of the dinuclear system at a certain moment in a reaction. The centers of the nuclei A and B move with velocities $\vec{U}_A$ and $\vec{U}_B$, respectively. Due to the slowing down of the orbital angular momentum during the reaction, the local velocities in the nuclei at the window, $\vec{u}_A$ and $\vec{u}_B$, may be smaller. The hatched area symbolizes the coordinate part of a phase space interval situated around the window plane, which has the possibility of being transferred from B to A or the other way. The right hand part of the figure illustrates the momentum space. The phase space points are filled up according to the Pauli principle, within spheres in momentum space for given coordinate points. The relative motion displaces the spheres relative to each other by the amount $m\vec{u} = m(\vec{u}_A - \vec{u}_B)$, m being the nucleon mass. The hatched area symbolizes the momentum part of the phase space interval, being occupied in nucleus A and not in B. With increasing excitation, the Fermi spheres acquire a diffuse surface, the diffuseness being determined by the temperature τ in the nuclei. Even for the case of no relative motion, nucleon exchanges are then still possible between occupied and unoccupied parts of the phase space in the nuclei, the number of such exchanges being proportional to the temperature. For the general case with both a relative velocity and a temperature, the number of exchanges is given by the *effective temperature* $\tau^\star$, defined as

$$\tau^\star = \left\langle \tfrac{1}{2} |\vec{u} \cdot \overleftarrow{p}| \coth\left(\frac{|\vec{u} \cdot \overleftarrow{p}|}{2\tau}\right) \right\rangle_F \qquad (3.1)$$

where F symbolizes an average over the Fermi sphere of the nuclei and over the window area. In expression (3.1) as well as in the drawing of fig. 2 we have for simplicity neglected differences in the Fermi momenta of the two nuclei.

The transport coefficients contain two types of variables: (i) basic nuclear paramenters, such as the Fermi momentum. (ii) dynamic variables, such as the effective window area, the distance between the centers of the nuclei, the radial momentum of the relative motion etc.

The theory has been successfully applied for studying the mass and charge distributions, Schröder 1981, Britt 1982, and good accordance was also generally found with experiments on the spin distribution, Døssing 1985b. The present application to Wilszinsky plots and γ ray polarisations presents a continuation of these comparisons of the theory with data.

3.5. Statistical models

No matter which excitations are primarily responsible for the main part of the energy loss in damped nuclear reactions, their clean characteristics get lost and cannot be observed because of the thermalisation within the nuclei. For example, in the hot nuclei leaving the reaction, an excited surface vibration will not decay by emission of a γ ray of a specific energy. It will instead get dissolved by coupling to the complicated excitations present in the hot nucleus.

Therefore, in addition to the variables describing the relative motion of the nuclei after the reaction, only variables which are conserved in each nucleus after the reaction due to general principles can be studied experimentally. These are the mass and charge, the angular momentum, (and the parity, which is of little use).

If the reaction time is long enough, the distribution in some of these variables will just be given by statistical excitation, governed by the temperature in the dinuclear system. In this case no information on the primary excitation mechanism survives. Fortunately, it is clear for the mean values of both neutron number, proton number and spins that statistical excitation is not generally achieved. It is only for the second moments of the spin distribution that a statistical model has been formulated and applied for all kinetic energy losses, Moretto 1980, Schmidt 1982. For large energy losses, statistical excitation of the mean spins has also been proposed, Moretto 1984.

The statistical model for the mean spin vector explains well the spin sizes as function of the mass partition in a number af reactions, and also

the model for the variances yields good agreement with quite many experiments, Moretto 1984. However, in our recent analysis, Døssing 1985a,b, the statistical model for the spin distribution is found to predict that the direction of the major in-plane spin variance is a specific function of the scattering angle. The characteristic differences in relaxation times for the various spin modes implied by our dynamical equations, which we shall discuss in the next section, yield a different, but also specific result for this direction. Experiments on the in-plane sequential fission fragment angular distributions, which determine this direction, agree with the dynamical results and disagree with the statistical model.

4. Nucleon exchange transport for spin variables

When applying the Fokker-Planck equation to angular momentum variables, the choice of coordinate system is important. The coordinate system applied here follows the geometry of the dinuclear system, i. e. it is a *body-fixed coordinate system*. The z-axis is along the radius vector of relative motion, and the y-axis is along the orbital angular momentum. Seen by an external observer, this coordinate system turns because of the the orbital rotation and fluctuates because the direction of the orbital rotation may change during the reaction.

General expressions for the transport coefficients of one body operators are given in Randrup 1979, and coefficients for angular momentum transport are presented in Randrup 1982. Finally, the derivation of the transport equations with respect to this coordinate system as well as expressions for transforming the spin moments to the laboratory system are given in Døssing 1985a.

We shall not here repeat the formal development, but rather define the variables and discuss the transport coefficients entering the equations. This will be followed by a discussion of the appearence of the equations and the characteristics of their solutions in terms of relaxation times for the spin variables.

4.1. Spin variables and mobility tensors

We consider the time evolution of the distribution of spins in the two nuclei, $\vec{S}^A$ and $\vec{S}^B$, and the orbital angular momentum $\vec{L}$. With the coordinate system applied, $\vec{L}$ has no x and z components. From the symmetry of the problem, mean values along the x and z axis must be

zero, and also covariances between y components and other components must vanish. Thus, restricting to the first and second moments, the following can be different from zero:

$$\langle S_y^A \rangle, \ \langle S_y^B \rangle, \ \langle L_y \rangle$$
$$\sigma_{yy}^{FG}, \ \ F,G = A,B,L \tag{4.1}$$
$$\sigma_{xx}^{FG}, \ \sigma_{xz}^{FG}, \ \sigma_{zz}^{FG}, \ \ F,G = A,B$$

where, for example, $\sigma_{yy}^{AL} \equiv \langle (S_y^A - \langle S_y^A \rangle)(L_y - \langle L_y \rangle) \rangle$.

As in reference Randrup 1982, a compact notation is achieved by defining the transport coefficients in terms of mobility tensors:

$$\overleftrightarrow{M}^{AA} = mN(a^2 \overleftrightarrow{T} + c_{ave}^2 \overleftrightarrow{T})$$
$$\overleftrightarrow{M}^{AB} = mN(ab \overleftrightarrow{T} - c_{ave}^2 \overleftrightarrow{T}) = \overleftrightarrow{M}^{BA} \tag{4.2}$$
$$\overleftrightarrow{M}^{BB} = mN(b^2 \overleftrightarrow{T} + c_{ave}^2 \overleftrightarrow{T})$$

Here m is the nucleon mass and N is the total flow of nucleons across the window, being proportional to the total flux inside nuclei times the effective window area. The distances from the centers of the nuclei to the window plane are given by a and b respectively, the sum a+b being equal to the dinuclear separation R. c_{ave} is the average off-axis displacement on the window. $\overleftrightarrow{T}$ is the identity tensor, in terms of unit vectors along the coordinate axises $\overleftrightarrow{T} \equiv \hat{x}\hat{x} + \hat{y}\hat{y} + \hat{z}\hat{z}$, and $\overleftrightarrow{T} \equiv \hat{x}\hat{x} + \hat{y}\hat{y}$ projects on the plane perpendicular to the dinuclear axis. Starting with zero variances $\sigma_{ij}^{FG}(t=0)=0$, the time evolution of the spin variances during the first small time interval Δt is given by

$$\overleftrightarrow{\sigma}^{FG}(\Delta t) = 2\tau^\star \overleftrightarrow{M}^{FG} \Delta t \tag{4.3}$$

where $\tau^\star$ is the effective temperature (3.1). It is natural that the increase in variances are proportional to $\tau^\star$, which measures the part of the momentum space available for transfers. The mobility tensors describe how easily the nucleon exchange can build up spin along the various directions in the two nuclei. The transverse directions are clearly preferred for the direction along the dinuclear axis. Figure 2 may illustrate this. Considering the various directions of the momentum and locations on the window, values of $\vec{r} \times \vec{p}$ relative to the center of nucleus A for the nucleons being able to transfer are seen to be generally larger along the transverse directions than along the dinuclear axis.

Since the total angular momentum $\vec{J} = \vec{L} + \vec{S}^A + \vec{S}^B$ has to be conserved, equation (4.2) implies the following expressions for mobility tensors involving the orbital angular momentum $\vec{L}$:

$$\overset{\leftrightarrow}{M}{}^{AL} = -\overset{\leftrightarrow}{M}{}^{AA} - \overset{\leftrightarrow}{M}{}^{AB} = -mN_aR\overset{\leftrightarrow}{T} = \overset{\leftrightarrow}{M}{}^{LA}$$

$$\overset{\leftrightarrow}{M}{}^{BL} = -\overset{\leftrightarrow}{M}{}^{AB} - \overset{\leftrightarrow}{M}{}^{BB} = -mN_bR\overset{\leftrightarrow}{T} = \overset{\leftrightarrow}{M}{}^{LB} \tag{4.4}$$

$$\overset{\leftrightarrow}{M}{}^{LL} = -\overset{\leftrightarrow}{M}{}^{LA} - \overset{\leftrightarrow}{M}{}^{LB} = mNR^2\overset{\leftrightarrow}{T}$$

It is convenient to discuss together with the standard spin variables $\vec{S}{}^A$, $\vec{S}{}^B$ also the absolute and relative spins in the nuclei $\vec{S}{}^+$ and $\vec{S}{}^-$:

$$\vec{S}{}^+ = \vec{S}{}^A + \vec{S}{}^B \ , \ I_+ = I_A + I_B \tag{4.5}$$

$$\vec{S}{}^- = I_- \left(\frac{\vec{S}_A}{I_A} - \frac{\vec{S}_B}{I_B} \right), \ \ I_- = \frac{I_A I_B}{I_A + I_B}$$

where I_A, I_B, I_+, and I_- denote moments of inertia, For I_A and I_B we apply rigid body moments of inertia, which are the relevant ones for heated nuclei. The kinds of rotational motion of the dinuclear system measured by the spins $\vec{S}{}^+$ and $\vec{S}{}^-$ have been given illustrative names. The *wriggling modes* describe rotations of the two nuclei in the same sense perpendicular to the dinuclear axis, which gives non-zero values of S_x^+ or S_y^+. Non-zero values of S_z^+ measure the motion of the *tilting mode,* and S_x^-, S_y^- measure the motion of the *bending modes*, and S_z^- the *twisting mode.* These names were given by Nix and Swiatecki, Nix 1965, in a study of nuclear fission, except for the tilting mode, named by Moretto, Moretto 1980, in the formulation of the statistical model for damped nuclear reactions. The mobility tensors in these variables are easily derived from those in the standard variables

$$\overset{\leftrightarrow}{M}{}^{++} = \overset{\leftrightarrow}{M}{}^{LL} = mNR^2\overset{\leftrightarrow}{T} = -\overset{\leftrightarrow}{M}{}^{+L}$$

$$\overset{\leftrightarrow}{M}{}^{+-} = mNR \left(\frac{I_A b - I_B a}{I_A + I_B} \right) \overset{\leftrightarrow}{T} = -\overset{\leftrightarrow}{M}{}^{-L} \tag{4.6}$$

$$\overset{\leftrightarrow}{M}{}^{--} = mN \left(\frac{I_A b - I_B a}{I_A + I_B} \right)^2 \overset{\leftrightarrow}{T} + mN\, c_{ave}^2\, \overset{\leftrightarrow}{T}$$

Since $\overset{\leftrightarrow}{M}{}^{++}$ only has components along the transversal directions, the tilting mode does not receive excitation directly by nucleon transfer. For symmetric reactions, $a=b$ and $I_A=I_B$, the mobility tensor $\overset{\leftrightarrow}{M}{}^{+-}$ vanishes, and the time evolution in $\vec{S}{}^+$ and $\vec{S}{}^-$ will be decoupled.

4.2. Equations of motion

The following transport equations for the spin distributions are derived in Døssing 1985a:

$$\dot{S}_y^F = -\sum_G (M_t^{FG} S_y^G + \frac{1}{L_y} \sigma_{xx}^{FG} M_t^{GL})/I_G + \frac{\tau^\star}{L_y}(2M_t^{FL} - \frac{S_y^F}{L_y} M_t^{LL})$$

$$\dot{\sigma}_{xx}^{FH} = 2\tau^\star M_t^{FH} - \sum_G (\sigma_{xx}^{FG} M_t^{GH} + M_t^{FG} \sigma_{xx}^{GH})/I_G - \omega_R(\sigma_{xz}^{FH} + \sigma_{zx}^{FH})$$

$$- \frac{S_y^F}{L_y}(2\tau^\star M_t^{LH} - \sum_G M_t^{LG} \sigma_{xx}^{GH}/I_G) - (2\tau^\star M_t^{FL} - \sum_G \sigma_{xx}^{FG} M_t^{GL}/I_G)\frac{S_y^H}{L_y}$$

$$+ 2\tau^\star \frac{S_y^F}{L_y} M_t^{LL} \frac{S_y^H}{L_y}$$

$$\dot{\sigma}_{yy}^{FH} = 2\tau^\star M_t^{FH} - \sum_G (\sigma_{yy}^{FG} M_t^{GH} + M_t^{FG} \sigma_{yy}^{GH})/I_G \tag{4.7}$$

$$\dot{\sigma}_{zz}^{FH} = 2\tau^\star M_n^{FH} - \sum_G (\sigma_{zz}^{FG} M_n^{GH} + M_n^{FG} \sigma_{zz}^{GH})/I_G + \omega_R(\sigma_{xz}^{FH} + \sigma_{zx}^{FH})$$

$$\dot{\sigma}_{xz}^{FH} = -\sum_G (\sigma_{xz}^{FG} M_n^{GH} + M_t^{FG} \sigma_{xz}^{GH})/I_G - \omega_R(\sigma_{xx}^{FH} - \sigma_{zz}^{FH})$$

$$+ \frac{S_y^F}{L_y} \sum_G M_t^{LG} \sigma_{xz}^{GH}/I_G$$

Here the brackets around mean values have been omitted for notational simplicity, ω_R denotes the angular velocity of the orbital rotation. $\omega_R = \frac{L_y}{I_R}$ and M_t^{FG} and M_n^{FG} denote mobility tensors along the transversal and the normal direction, respectively. The sums over the index G run over G = A,B,L, or over G = +, −, L. All terms containing ω_R or $\frac{1}{L_y}$ as factors are due to the special choise af the body fixed coordinate system. The orbital rotation perpendicular to the y axis causes a redefinition of the x and z axises, being taken into account by the terms containing ω_R. The terms containing L_y in the denominator arise from the fluctuation in the direction of $\vec{L}$ caused by the nucleon exchange, and they are derived under the assumption that L_y^2 is large compared to all variances.

4.3. Stationary solution and relaxation times

For given total angular momentum J one can prove that the equations (4.7) have a unique stationary solution given by

$$\langle L_y \rangle = \frac{I_R}{I_0} J \ , \qquad \overleftrightarrow{\sigma}^{LL} = \tau^\star I_+ \frac{I_R}{I_0} \hat{y}\,\hat{y} \tag{4.8}$$

$$\langle S_y^+ \rangle = \frac{I_+}{I_0} J - \tau^\star I_+ \frac{I_0}{I_R} \frac{1}{J}, \qquad \overleftrightarrow{\sigma}^{++} = \tau^\star I_+ \frac{I_0}{I_R} (\hat{x}\hat{x} + \hat{z}\hat{z}) + \tau^\star I_+ \frac{I_R}{I_0} \hat{y}\hat{y}$$

$$\langle S_y^- \rangle = 0 \ , \qquad \overleftrightarrow{\sigma}^{--} = \tau^\star I_- \overleftrightarrow{I}$$

In these expressions $I_0 = I_R + I_A + I_B$ is the total moment of inertia of the dinuclear system. During the reaction the moments of the spin distribu-

tion will at each instant evolve towards these equilibrium values, which in turn vary in time due to the time dependence of the effective temperature $\tau^\star$ and of the moment of inertia for the orbital rotation I_R.

The mean values of the stationary solution correspond to a rigid rotation of the dinuclear complex.

The solutions (4.8) for the variances correspond to statistical excitation of the spin modes, however with the temperature associated with the heat, τ, replaced by the effective temperature $\tau^\star$.

Typical time scales, *relaxation times,* for the approach to the stationary values can be obtained by dividing the stationary solution (4.8) by the corresponding initial time derivative, as for example given in equation (4.3) for the variances.

For a symmetric collision for which the motion in $\vec{S}^+$ and $\vec{S}^-$ are decoupled, this gives the following relaxation time for the wriggling modes

$$t_{++} = \frac{\tau^\star I_+}{2\tau^\star M_\tau^{LL}} = \frac{I_+}{2mNR^2} \tag{4.9}$$

and for the three negative modes

$$t_{--} = \frac{\tau^\star I_-}{2\tau^\star M^{--}} = \frac{I_-}{2mNc_{ave}^2} \tag{4.10}$$

The time evolution of the tilting mode is more complicated, since σ_{zz}^{++} only receives contributions indirectly from σ_{xx}^{++} through the orbital rotation. The relaxation time for the tilting mode is then determined by finding the eigenvalues of the linear system of equations for σ_{xx}^{++}, σ_{xz}^{++} and σ_{zz}^{++}, and the main part of σ_{zz}^{++} is found to approach equilibrium with the relaxation time

$$t_{+z} \simeq \left(4\omega_R^2 \frac{L_y}{J} t_{++} \right)^{-1} \tag{4.11}$$

The relaxation time for the mean values $\langle S_y^+ \rangle$ and $\langle L_y \rangle$ are given by $2t_{++}$

This relation to the statistical model together with the expressions for the relaxation times we consider to be important results of the study in Døssing 1985a, because these results contain some definite predictions of the theory, which can be confronted with data without having to perform detailed calculations.

Inserting typical values of the coefficients appearing in the expressions for the relaxation times, one finds that except for the most peripheral collisions the wriggling modes are expected to reach equilibrium. The relaxation time for the negative modes is substantially longer, and only

for quite central collisions will they come close to equilibrium. The tilting mode receives the strongest excitation for peripheral collisions, due to the occurence of ω_R in the denominator. For more central collisions the tilting mode receives only little excitation. Examples of these relaxation times are shown in Døssing 1985a.

Since the relaxation time for S_y^+ is also quite small and the asymptotic value for this spin is large compared to the equilibrium values of the dispersions, the spin distribution will be dominated by the mean spin for most values of the total angular momentum. For example the average length of the spin vector will for most cases be given by the size of the mean spin vector plus a relatively small correction containing the dispersions.

5. Mean trajectory implementation of nucleon exchange transport

To obtain results for comparing with data, the transport equations (4.7) for the spin distribution are solved together with equivalent equations for the separation R between the two nuclei, the conjugate momentum P and the scattering angle θ. This is done for a grid of values of the total angular momentum J, and subsequently an integration is performed over J to obtain cross sections and spin distributions gated by energy loss and scattering angle.

The degree of contact between the two nuclei during the reaction is related to the geometrical neck connecting them. The neck motion implies a wall friction, and the time evolution of the neck is followed with insertion of the mean values for P and R. Thus, the dynamics with restriction to the mean trajectory determines both the rate of nucleon exchange and thereby the window friction, as well as the wall friction.

Expressions for the Coulomb and nuclear potentials applied can be found in Randrup 1982, and Fokker-Planck equations for the variances are given in Døssing 1985a.

The variances in the variables considered give rise to a variance in the final energy of the relative motion, which must be evaluated at the end of the reaction phase.

After the reaction phase, the two nuclei recede on a Coloumb trajectory, and the average scattering angle can be determined. This angle is inserted into the equations transforming the spin variables from the fixed coordinate system to the external coordinate system. The variance in

scattering angle receives contributions both during the reaction phase and on the Coulomb trajectory, caused by the variances in the orbital angular velocity and in the other dynamical variables determining the angle turned on the trajectory.

For each J, this procedure permits the determination of mean values and covariances for the variables which are of interest experimentally, namely the total kinetic energy loss, the scattering angle, the neutron and proton numbers in one of the nuclei, and the spins in the two nuclei. Denoting these variables by the symbol $\vec{C} \equiv E, \theta, N_A, N_B, Z_A, Z_B,$ $S_X^A, S_Y^A, S_Z^A, S_X^B, S_Y^B, S_Z^B,$ we assume that the distribution is Gaussian, (in accordance with the approximations applied to obtain the Fokker-Planck equations):

$$f_J(\vec{C}) = \pi \lambda^2 \frac{2J + 1}{(2\pi|\overset{\leftrightarrow}{\sigma}|)^6} \exp[-\tfrac{1}{2}(\vec{C} - \langle \vec{C} \rangle) \cdot \overset{\leftrightarrow}{\sigma}^{-1} \cdot (\overset{\leftarrow}{C} - \langle \overset{\leftarrow}{C} \rangle)] \qquad (5.1)$$

where $\overset{\leftrightarrow}{\sigma}$ is the covariance matrix in the variables considered. (Capital letters are used for the axises of the external coordinate system to distinguish from the body fixed system).

In experiments the total angular momentum cannot be determined, so one has to integrate the distribution (5.1) over J, keeping the energy and eventually also the scattering angle fixed, to obtain cross sections and spin distributions gated by E and θ. The technical details of this is given in Døssing 1985a.

5.1. Time evolution of variances in energy loss and scattering angle

For discussing the Wilszinsky plots and γ ray polarisations presented in the next section, it is important to note that the mean trajectory implementation of the theory implies specific results for the variances in energy loss and scattering angle.

The energy of relative motion is given by

$$E = \frac{P^2}{2\mu} + \frac{L^2}{2\mu R^2} + e^2 \frac{Z_A Z_B}{R} \qquad (5.2)$$

The variance in E is determined by the variances and covariances of the variables entering this expression. Keeping the main terms to first order in $\tau^\star$, and neglecting the usually small terms due to the variation in neutron and proton numbers, one obtains:

$$\sigma_{EE} = E_R'^2 \sigma_{RR} + E_P'^2 \sigma_{PP} + 2E_R' E_P' \sigma_{RP} + E_{Ly}'^2 \sigma_{yy}^{LL} \qquad (5.3)$$

where E_R' denotes the derivative of E with respect to R, taken at the mean trajectory, and likewise for the other derivatives. Inserting the stationary solution (4.8) for σ_{yy}^{LL} and the equivalent stationary solutions from the Fokker-Planck equations for the evolution in R and P, one obtains for the stationary variance in E

$$\sigma_{EE} = \tau^\star\left(\frac{1}{2}\frac{(V_C + 2T_{tan})^2}{V_C + 3\,T_{tan}} + 2\,T_{rad} + 2\frac{I_+}{I_0}T_{tan}\right) \tag{5.4}$$

$$\approx \tau^\star\left(\frac{1}{2}V_C + 2\,T_{rad} + \left(\frac{1}{2} + \frac{2\,I_+}{I_0}\right)T_{tan}\right) \approx \frac{1}{2}\tau^\star\langle E\rangle$$

where the three terms in equation (5.2) have been denoted by T_{rad}, T_{tan} and V_C. In the last expression we have used that the Coulomb energy V_C, is appreciably larger than the other contributions to the energy at the end of the reaction phase.

Actually, it takes quite some time for σ_{RR} to relax, so σ_{EE} will usually be smaller than the saturation value (5.4).

Since the scattering angle is a cyclic variable, the equation for the variance in scattering angle has no restoring term. The variance being accumulated during the reaction is determined by the angular momentum evolution according to the equations

$$\dot\sigma_{\theta\theta} = 2\frac{\sigma_{\theta L}}{I_R} \tag{5.5}$$

$$\dot\sigma_{\theta F} = \frac{\sigma_{yy}^{LF}}{I_R} - \sum_G \frac{\sigma_{\theta G}}{I_G}M_t^{GF}$$

which are derived in Døssing 1985a. These relations imply that $\sigma_{\theta L}$ relaxes within a time scale given approximately by $2t_{++}$, i. e. quite fast, the saturation value being given by

$$\sigma_{\theta L} = \tau^\star\,I_R\left(\frac{I_+}{I_0}\right)^2 M_t^{LL^{-1}} \tag{5.6}$$

Thus, after a time of the order of t_{++}, $\sigma_{\theta\theta}$ will grow constantly with the reaction time t:

$$\sigma_{\theta\theta} \approx 2\tau^\star\left(\frac{I_+}{I_0}\right)^2 M_t^{LL^{-1}}\,t \approx 2t\tau^\star\frac{I_+\,I_R}{I_0\,I_0}\cdot\frac{t_{++}}{I_R} \tag{5.7}$$

$$\approx 8\times10^{-5}\,\tau^\star t t_{++}\ \text{radians}^2 \approx 0.25\tau^\star t t_{++}\ \text{deg}^2$$

where the units MeV and 10^{-22} sec are applied for $\tau^\star$ and the times t and t_{++}, respectively. To obtain the numerical value, a reduced mass of 50

mass units has been used together with the values $\frac{2}{7}$ and $\frac{5}{7}$ for the ratios between moments of inertia, and the value 10 fm for the center separation R entering I_R.

The variance accumulated along the outgoing Coulomb trajectory is typically of the same size as the variance estimated so far, so roughly we obtain the following estimate of the total variance of the scattering angle

$$\sigma_{\theta\theta} \approx 0.5\tau^\star t t_{++} \text{ deg}^2 \tag{5.8}$$

The value of $\tau^\star$ to be inserted here should be the average value during the reaction phase.

Both of the above values for the rate of nucleon exchange and the center separation refer to the reaction of ^{86}Kr + ^{139}La, and generally the coefficient in (5.8) will scale with the mass of the dinuclear system to approximately the $-\frac{5}{3}$'th power. The relaxation time t_{++} is of the order of 2×10^{-22} sec. and scales with the mass roughly to the $\frac{1}{3}$'rd power.

The expression (5.4) for the stationary variance in energy loss is a statistical limit, obtained by inserting the thermal values for the variances in the basic variables, except for the occurence of the effective temperature $\tau^\star$ in stead of the heat temperature τ. Apart from this distinction, the result (5.4) will have a general validity for all theories which predict relaxation towards the statistical equilibrium values.

Conversely, the approximate result (5.8) for the accumulated variance in scattering angle is specifically related to the dynamics of the spin evolution, since the relaxation time t_{++} enters.

Feldmeier and Spangenberger, Feldmeier 1984, apply Cartesian coordinates for the relative motion of the two nuclei, but otherwise also the mean trajetory method. Their variances are several times larger than both of the estimates (5.4) and (5.8) for the variances in energy loss and scattering angle, respectively. These estimates provide fair approximations to our calculated variances (to within a factor of 2 for most cases). We do not know what causes this discrepancy between the two different applications of essentially the same theory, but important points may be (i) the slightly different definitions of the effective temperature within the two schemes of calculation, (ii) the apparent lack of relaxation in σ_{yy}^{LL} displayed in figure 6 in Feldmeier 1984.

6. Wilszinsky plots and γ ray polarisations

6.1. Wilszinsky plots

Figure 3 shows contour plots (Wilszinsky plots) of the differential cross section as function of scattering angle and energy loss, together with the experimental result, Vandenbosch 1978, for the reaction 710 MeV ^{86}Kr + ^{139}La. Also, the mean scattering angle and energy loss is shown for every 20 units of total angular momentum on the calculated plots. Plots (b) and (c) are obtained with two different prescriptions for the reduction of the wall friction caused by the motion of the neck connecting the two nuclei. Plot (b) is obtained with the standard reduction in the neck damping, Randrup 1982, which is effective for long thin necks, and in the calculation for plot (c), full neck damping is applied. Below a total angular momentum close to 100 units, the reactions lead to capture according to the calculation.

## 6.2. Comparison of calculated and experimental Wilszinsky plots

The experimental Wilszinsky plot clearly displays two components of the cross section, one at small and one at large energy losses.

The contours for the small energy loss component form a long hill stretching from a scattering angle around 35° at energy loss 0 down towards angle 0° at an energy loss of approximately 250 MeV. In the calculated results, the ridge of the hill is defined by the curve running through the points of mean scattering angle and energy loss for the largest total angular momenta. These correspond to the most peripheral, and thereby the most gentle reactions.

The calculated results agree very well with experiment on both the position of the ridge line and the width of the hill perpendicular to the ridge.

The large energy loss component stretches from scattering angle 0° out to around 80°, and is peaked around 300 MeV of energy loss with a quite large dispersion. In the calculated results, this component is due to the more central and intimate reactions, which for this reaction have turned through 0° and come out at negative scattering angles, as illustrated with one example in figure 4. Experimentally, the information from a Wilszinsky plot alone does not allow for determining the sign of the scattering angle. (The falloff of the cross section for very small angles on the calculated plots is due to the tilting of the outgoing reaction plane

Fig. 3. Experimental, (a) Vandenbosch 1978, and calculated, (b) and (c), Wilszinsky plots for the reaction 710 MeV $^{86}Kr + ^{139}La$. Plot (b) is obtained with the standard prescription for the reduction in the neck damping, while this reduction is removed in the calculation of plot (c). The units for the contours are mb/ (deg×MeV).
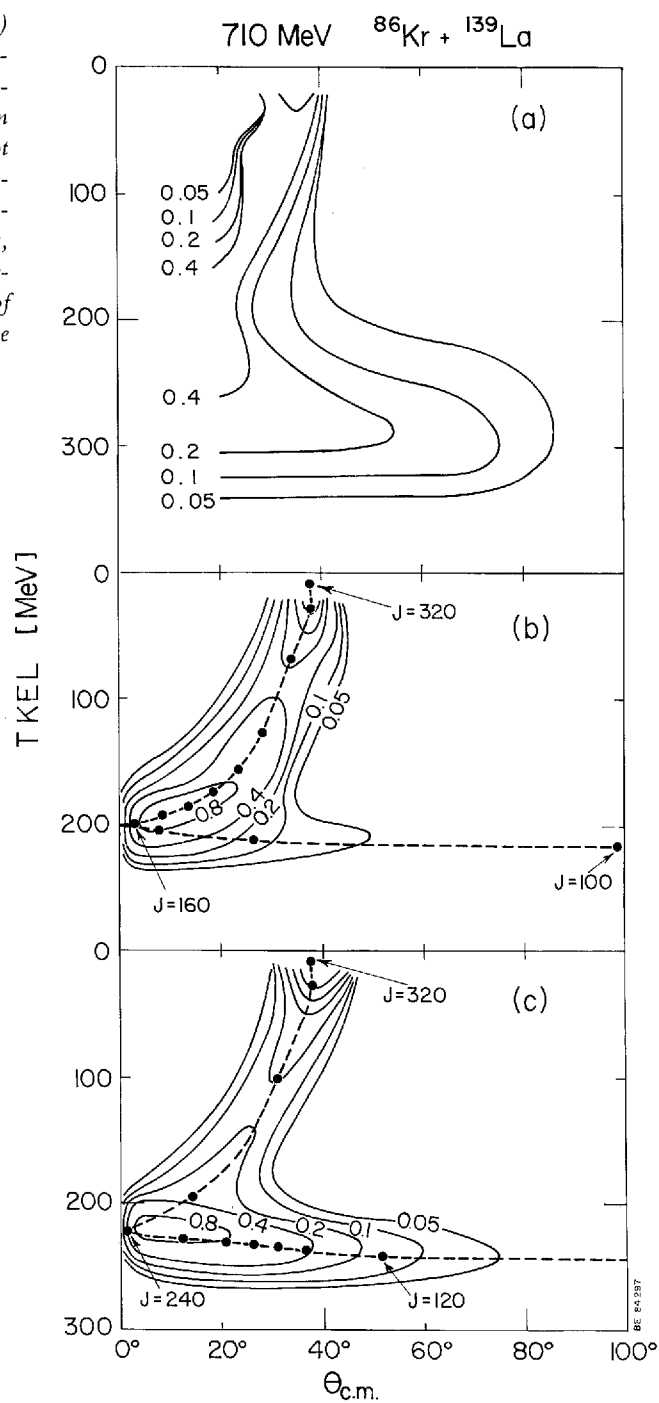
relative to the entry reaction plane. The width of the angular range of this falloff is discussed in Døssing 1985c).

The calculated differential cross sections are too much concentrated around the mean trajectory result for the large energy loss component, the dispersion in energy loss for given scattering angle being a factor of two too small. The calculated dispersions agree to within 12% with the estimate (5.4) for the asymptotic value of the variance. Thus, with the mean trajectory implementation, the nucleon exchange transport theory will not be able to account for this aspect of the data.

The average energy loss for this component is around 80 MeV too small in the calculations. This is probably because the description of the shape of the dinuclear system by means of only two parameters, the neck radius and the center separation, does not allow for the elongation of the dinuclear system at the end of the reaction phase, which is needed to loose the extra amount of energy.

The reduction in the wall damping applied in calculation (b) implies that the small energy loss component receives a higher proportion of the cross section than the large energy loss component, whereas the calculation (c) distributes the cross section more evenly on the two components, in better agreement with the data. An intermediate neck damping between the two prescriptions would yield a better agreement than both (b) and (c). The pronounced difference between the two calculations display a sensitivity of the results upon elements of the application of the theory, which have not been consistently studied yet, and this is somewhat discomforting.
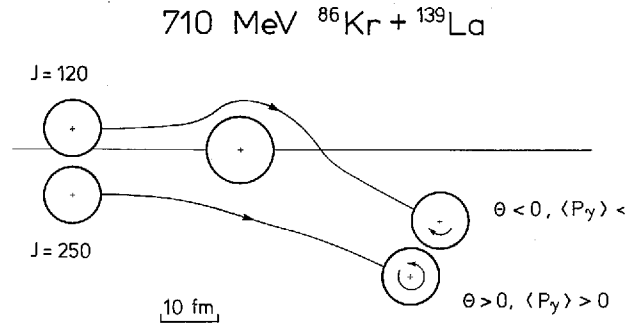
6.3 γ ray polarisations

Information on the spin distribution in the two nuclei and on the sign of the scattering angle can be obtained from the polarisation of γ rays emitted from the nuclei during their sequential decay.

The detailed evaluation of the γ ray polarisation on the basis of calculated spin distributions and its relation to the polarisation of the spin in the nuclei is discussed in appendix A.

Figure 4 illustrates how positive and negative scattering angles lead to different senses of rotation in the nuclei. During the reaction the orbital rotation is slowed down, and the average spins in the nuclei after the reaction will point in the same direction as the total angular momentum vector. With the situation depicted in figure 4, the total angular momentum points upwards from the plane of the figure for positive angle scattering and downwards for negative angle scattering. With the coor-

Fig. 4. Calculated trajectories for two values of the total angular momentum for the reaction ^{86}Kr + ^{139}La. The two trajectories lead to the same size of the final scattering angle, but with opposite sign. The circular arrows on the outgoing light nuclei show the directions and magnitudes of their average rotation.

dinate system applied, the Y axis points upwards, so a positive scattering angle corresponds to positive polarisations of the spin in both nuclei, and vice versa for negative angles. This sign convention for the polarisation, which is easily remembered, is different from that employed conventionally.

In recent experiments, Schandera 1984, the polarisation of the emitted γ rays has been measured for certain intervals in scattering angle and total kinetic energy loss. Figure 5 shows calculated and experimental polarisations as functions of energy loss for the same reaction as considered in figures 3 and 4. For one interval covering small scattering angles (laboratory scattering angle $11°$ $<\theta_{lab}$ $<30°$ corresponding to center of mass scattering angle $20°\lesssim$ θ_{CM} $\lesssim 55°$) three intervals in energy loss were applied, and in addition one interval covered large energy losses and scattering angles ($30°$ $<$ θ_{lab} $<$ $68°$, corresponding to $55°\lesssim$ θ_{CM} $\lesssim$ $120°$).

The thin graphs in fig. 5 include only partial waves above capture. However, the captured nuclei may separate again, and the thick graphs in fig. 5 include the whole captured part of the cross section, from the highest total angular momentum leading to capture all the way down to zero, assuming that it leads to a separation again of the nuclei.

The angular distribution for the captured and re-separated part is assumed to be uniform, implying that the captured system must have turned a couple of times before separation. As the energy loss is concerned, both the average value and the variance are taken as the values obtained for the smallest total angular momentum not being captured, and the average energy loss is then increased due to the smaller centrifugal energy of the relative motion for the partial waves leading to capture.

The centrifugal energies applied in this small correction are determined by the asymptotic value (4.8) for the orbital angular momentum, inserting the relative moment of inertia for the distance where the nuclei loose contact for the smallest partial wave not being captured. The mean spins in the nuclei emerging after capture and re-emission are likewise derived from the asymptotic values (4.8), but with equal probability of pointing up or down, i.e. with spin polarisation zero, leading to γ ray polarisation zero. For the spin variances, the variances calculated with the smallest partial wave not leading to capture are applied for capture and re-separation.

This is, admittedly, a crude way of including capture and re-emission. It can be regarded as leading to maximal dilution of the polarisation, since the maximal possible cross section for capture and re-separation is included. A more consistent account of capture and re-separation would then most probably lead to results for the polarisation which are between the thick and thin curves in fig. 5.

Figure 6 shows the result of a calculation for the same experiment as shown in fig. 5 but now obtained without the reduction in neck damping, as also applied for part (c) of fig. 3. The large peak around 240 MeV for the cross section for the small angle interval comes from the very pronounced hill in the contour plot (c) of fig. 3.

Calculated polarisations and data for the three other reactions studied in Schandera 1984 are shown in figures 7, 8 and 9.

Fig. 5. Calculated and experimental, Schandera 1984, γ ray polarisations for the reaction 710 MeV ^{86}Kr + ^{139}La. The experimental values are denoted by horizontal lines, covering the energy intervals of averaging applied in the experiments, and the shaded regions show the uncertainties reported. The calculations are performed with the standard implementation of nucleon exchange transport. The thin curves include only the calculated direct cross section, whereas the thick curves also includes capture and re-separation as described in the text.
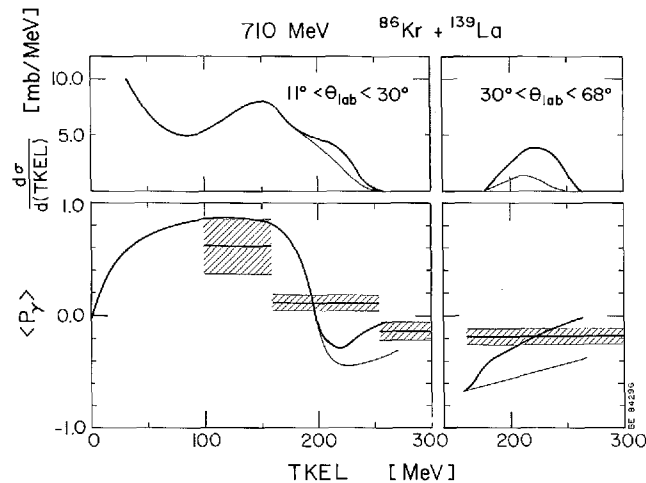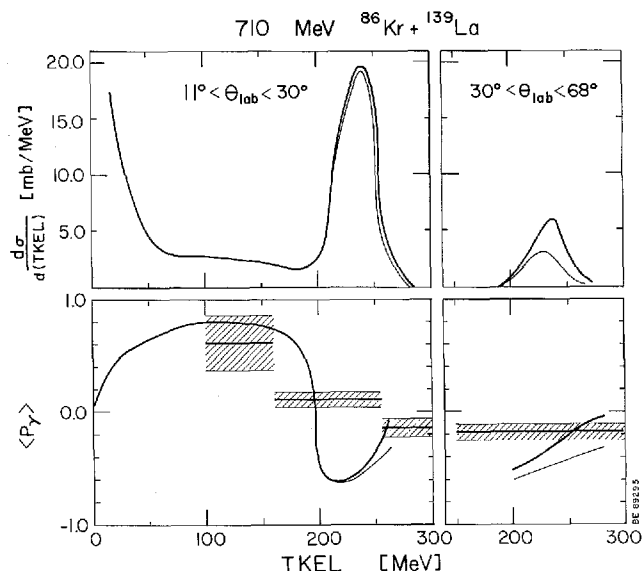
Fig. 6. The same as fig. 5,
but now calculated without
the reduction in the neck
damping, as for part (c) of
fig. 3.

6.4. Comparison between calculated and experimental γ ray polarisations.

For all the reactions the interval of the smallest energy losses covered by the experiment is completely dominated by positive angle scattering, and the interval at small scattering angles covers most of the cross section. Thus, the γ ray polarisation for this interval gives fairly direct information about the spin moments, as calculated by solving the equations (4.7) and subsequently transforming to the external coordinate system. For the reactions with ^{139}La as a target, the calculated polarisations are slightly too large when compared to the data for this interval. For the ^{166}Er data, on the other hand, significant discrepancies with the data are apparent.

The energy loss interval in question is centered around half of the maximally calculated energy loss. For this energy loss a generally good agreement with γ ray multiplicity and fission angular distribution data was found in Døssing 1985b. To the extent one can compare the different reactions, we conclude that, except for the reaction 705 MeV ^{86}Kr + ^{166}Er, the γ ray polarisation data are in reasonably good accordance with the other data and with the calculations for intermediate energy losses.

Going to higher energy losses, still within the interval of small scattering angles, the calculated polarisation first decreases weakly because the mean spin vector starts to decrease and the variances grow. However, this decrease is soon overtaken by a much stronger decrease, caused by

the admixture from negative scattering angles. From a certain energy loss, the negative scattering angles dominate. Thus, the polarisation goes steeply through zero, and reaches negative values which can be quite substantial, except for the reaction of 705 MeV ^{86}Kr + ^{166}Er for which the negative scattering angles receive very little cross section according to the present calculation. The decrease in polarisation is also present in

Fig. 7. Same as fig. 5, but for the reaction 860 MeV ^{86}Kr + ^{139}La.

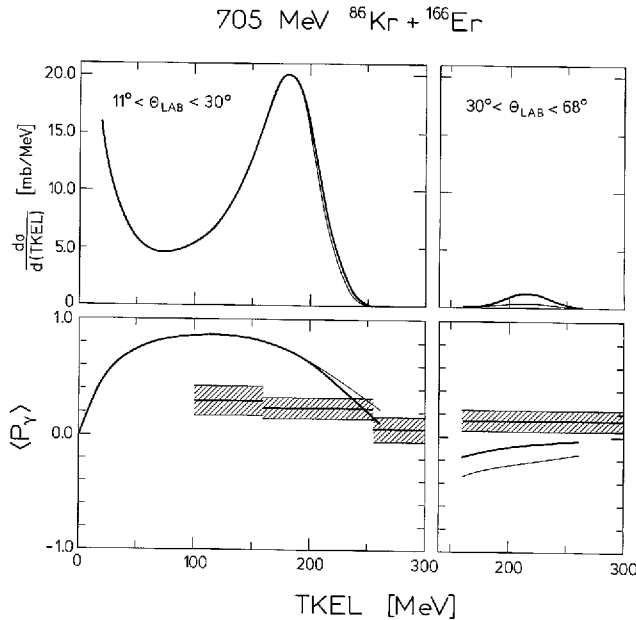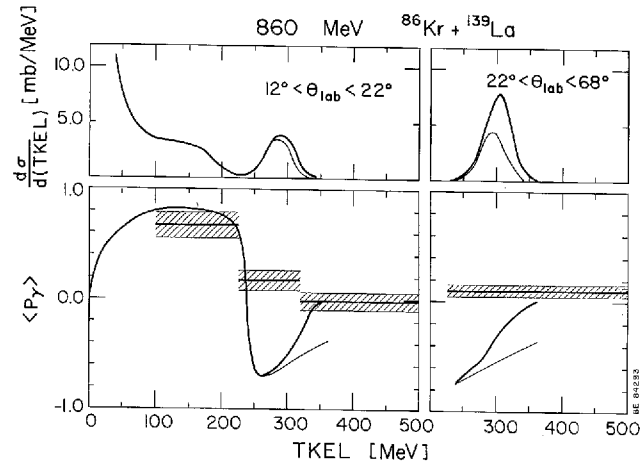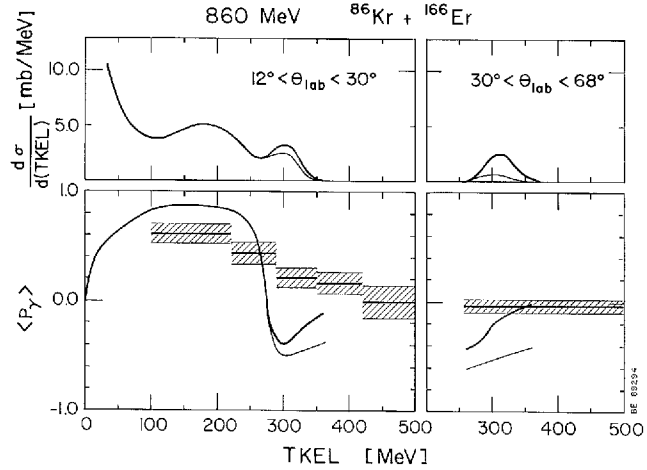Fig. 8. Same as fig. 5, but for the reaction 705 MeV ^{86}Kr + ^{166}Er.

Fig. 9. Same as fig. 5, but for the reaction 860 MeV $^{86}Kr + {}^{166}Er$.

the data, but these display a much smoother behavior than the calculated values. Finally, at the highest energy losses for the small angle interval, the calculated negative values of the γ ray polarsiation are somewhat weakened, because the average spin vector still decreases in size. With inclusion of capture and re-separation, the negative polarisations may be considerably reduced. In the experiments significant negative polarisations are only recorded for one of the reactions at this interval, and the polarisations are generally small.

The comparison to data for the small angle interval for the larger energy losses points in the same direction as the comparison to the Wilszinsky plots, namely that the dispersion in energy loss for given impact parameter is too small. Larger dispersions will mix the positive and negative scattering angles, leading to a smoother behavior of the calculated curves for the polarisation. Also large dispersions in scattering angle for given impact parameter of the order of 40°, which is twice the lower end point of the interval, would explain the data.

The large angle interval only receives contributions from negative angle scattering for the reactions calculated here, and inclusion of capture and re-separation dilutes the polarisation considerably. Without this dilution, the γ ray polarisation is typically calculated to be around –0.5, which tells that the spin dispersions are of approximately the same magnitude as the mean spin vector, cfr. figures A1 and A3. The experimental polarisations are numerically small for this angle interval, and of varying sign. Since both of the two different targets and both of the two bombarding energies display a positive and a neative mean value for the γ ray

polarisation for this angle interval, the only systematic trend seems to be the small values. On the other hand, analysis of fission angular distributions show that the alignment of the spin does not seem to decrease below values of the order of 0.4, Døssing 1985b, even for the largest energy losses. (This is admittedly for other reactions involving heavier targets than the ones discussed here, but the result for the alignment is not expected to be crucially dependent upon whether the target mass is 139 or 208).

The small values of the γ ray polarisation taken together with appreciable spin alignments indicate that in the present reactions both positive and negative scattering angles contribute almost evenly to the cross section for the large energy losses. With the mean trajectory method used here, this will be quite impossible to achieve. For the impact parameters leading to negative scattering angles within this interval, an estimate for the scattering angle dispersion yields 11°, obtained by inserting the values 50×10^{-22} for the reaction time t, 2×10^{-22} for the relaxation time t_{++}, and 2.5 MeV for the effective temperature τ^* into the expression (5.8). Actually a value of twice the lower end point of the interval, around 100°, is needed. Alternatively, a substantial part of the cross section at these energy losses could correspond to reactions like the capture and re-emission discussed here, where the nuclei turn some times before reseparation, thereby averaging the spin polarisation out to small values. Since such a component will have an almost uniform cross section as function of angle, an examination of the Wilszinsky plots will give an upper limit for this component, as discussed in Vandenbosch 1978.

7. Conclusion

The main result of this paper is the application of nucleon exchange transport to calculate Wilszinsky plots and γ ray polarisations. Also, it is demonstrated in the appendix that γ ray polarisations can be quite exactly calculated on the basis of theoretical spin distributions.

Concerning the application of the theory to obtain these results, it is somewhat uncomforting that the results depend so sensitively upon specific details of the implementation, which have not been consistently derived yet. This applies to the prescription for the reduction in the neck damping, and the linear extrapolation of the Coloumb potential for small distances, Randrup 1982.

The comparison of the calculated quantities to data is successful as far

as the small and medium energy losses are concerned. For the larger energy losses, substantial discrepancies between calculated results and data are found. The calculations are not able to account for the large variances in energy loss and scattering angle present in the data for these energy losses. Furthermore, by inspecting the expressions for the variances, it is concluded that variances accumulated during the motion along a mean trajectory will generally be small.

One would expect larger final fluctuations if the fluctuations caused by the nucleon exchange were allowed to couple back on the potentials and form factors for exchange. For example, for motion on the quite flat potential energy surfaces encountered for total angular momenta 100 to $140\hbar$ for the present reactions, fluctuations in the center separation and the radial momentum may cause substantial dispersions in the reaction time, and thereby in scattering angle. Whether improvements in that direction are enough to obtain significantly better agreement with data is still an open question.

Certainly γ ray polarisations, as investigated in the new experiments, give powerful information and the results are challenging to our understanding of damped nuclear reactions.

It would be valuable if the experiments with the new and powerful set up could be extended to cover also the smallest energy losses, where the polarisation is expected to increase with increasing kinetic energy loss. Also the application to reactions with heavier nuclei would be of interest, since the mixing from negative scattering angles will be minimal, and therefore a more pure information about the spin distribution could be obtained.

Appendix A

This appendix presents a procedure for calculating the average γ ray polarisation starting from a theoretically predicted distribution of spins in a hot nucleus produced in a damped nuclear reaction. The last part shows calculated polarisations for a schematic spin distribution and discusses the information contained in γ ray polarisations and angular distributions of continuum γ rays.

After a damped nuclear reaction the nuclei rapidly dispose of their excitation energy and angular momentum by sequential decay. For light nuclei, often protons and α particles are evaporated, and very heavy nuclei may fission. The relatively neutron rich medium mass nuclei of

interest here evaporate neutrons followed by the emission of γ rays. Only through observation of the decay products can one gain information about the angular momentum.

In this appendix we shall describe the decay with the aim of calculating the average polarisation of the γ rays, as being observed in a polarimeter, Trautmann 1981, taking as a starting point the excited nucleus with a Gaussian distribution of spin variables, as specified by the first and second moments of the spin distribution. This program takes four steps, of which the three last follow the time evolution of the decay: (i) One needs to define the moments of the directional distribution of the spin. (ii) The distribution of the spin magnitude as well as the directional distribution is modified due to neutron evaporation. (iii) A γ ray cascade follows, consisting of statistical γ rays, which cool the nucleus, and yrast type γ rays, which take away angular momentum, but which do not lead to cooling. (iv) The γ rays may scatter on magnetized iron in the polarimeter, and then finally be detected, yielding information about the polarisation.

The average polarisation of γ rays determined in step (iv) is quite closely connected to the average polarisation of the nuclear spin, defined as $\langle S_Y/S \rangle$. We shall in the end of this appendix see how this connection between spin -and γ polarisation depends upon the excitation energy in the nuclei, and the types of γ rays emitted.

Proceeding now with step (i), we first define the moments of the directional distribution, which are the statistical tensor components, Fano 1957. For a given spin distribution function $f(\vec{S})$ in the nucleus it is useful to define for each spin magnitude a normalized directional distribution function, such that $f(\vec{S}) = f_o(S) f_s(\hat{S})$. For spins which are large compared to the rank λ, the tensor component of rank λ and magnetic quantum number μ is well approximated by the classical definition as the $\lambda\mu$'th component in an expansion on spherical harmonics:

$$\varrho_{\lambda\mu}(S) \quad = \quad \sqrt{\frac{4\pi}{2\lambda + 1}} \langle Y_{\lambda\mu} \rangle_{f_s} \tag{A.1}$$

$$= \quad \sqrt{\frac{4\pi}{2\lambda + 1}} \int f_s(\hat{S}) \, Y_{\lambda\mu}(\hat{S}) \, d\hat{S}$$

Of special importance for the present discussion are the components with $\mu=0$, which are expansion coefficients on Legendre polynomials:

$$\langle P_{\lambda Y}(S) \rangle \equiv \varrho_{\lambda 0}(S) = \langle P_\lambda \rangle_{f_s} \tag{A.2}$$

Here the Y in $\langle P_{\lambda Y} \rangle$ denotes that we use the Y axis as polar axis. Extending the average to the whole spin distribution, we can write the two lowest in full:

$$\langle P_Y \rangle = \left\langle \frac{S_Y}{S} \right\rangle \tag{A.3}$$

$$\langle P_{YY} \rangle = \langle P_{2Y} \rangle = \left\langle \frac{3S_Y^2 - S^2}{2S^2} \right\rangle$$

$\langle P_Y \rangle$ is called the *polarisation,* and $\langle P_{YY} \rangle$, or $\langle P_{2Y} \rangle$ is called the *alignment* of the spin distribution.

The relations relevant for describing step (ii), the neutron evaporation, are given in Døssing 1985b. Starting at spin S_0 in the original nucleus, the average spin magnitude $\langle S_n \rangle$ after the evaporation of n neutrons is approximately given by

$$\langle S_n \rangle \simeq S_0 \exp\left[-n\left(\tfrac{2}{3} \frac{mR_n^2}{I} + \frac{\hbar^2}{2I\tau_1} - \tfrac{4}{9} \frac{mR_n^2\tau_1}{S_0^2} \right) \right] \tag{A.4}$$

The relation between statistical tensors is given by:

$$\varrho_{\lambda\mu}(S_n) = \varrho_{\lambda\mu}(S_0) \left\langle P_\lambda\!\left(\frac{\overrightarrow{S_0} \cdot \overleftarrow{S_n}}{S_0 S_n} \right) \right\rangle \tag{A.5}$$

$$\approx \varrho_{\lambda\mu}(S_0) \exp\left[-n\cdot P_\lambda'(1)\left(\tfrac{4}{9} \frac{mR_n^2\tau_1}{S_0\langle S_n \rangle} + \tfrac{1}{4} \frac{\hbar^2}{S_0\langle S_n \rangle} \right) \right]$$

with the relevant derivatives of the Legendre polynomials

$$P_1'(1) = 1, \quad P_2'(1) = 3, \quad P_3'(1) = 6, \quad P_4'(1) = 10 \tag{A.6}$$

In these relations I is the moment of inertia of the nucleus and mR_n^2 is the moment of inertia of the neutron at the effective barrier radius R_n. The tempeature τ_1 in the nucleus after the evaporation of the first neutron is given by

$$\tau_1 = \sqrt{ \frac{E_0 - \frac{S_0^2}{2I} - B}{a} } \tag{A.7}$$

Here E_0 denotes the excitation energy in the primary nucleus leaving the reaction, B is the average binding energy of the neutrons, and a denotes the level density constant. The average number of neutrons n emitted is

$$n \approx \left(E_0 - \frac{S_0^2}{2I} - \frac{B}{2} \right)\left(B + \tfrac{1}{3}\tau_1 \right)^{-1} \tag{A.8}$$

All these relations are derived and discussed in Døssing 1985b, and we apply them together with the parameters for a, I, mR_n^2 and B given in that reference.

Proceeding now with step (iii), the γ ray emission, we can readily generalize the procedure, Døssing 1981, for calculating angular distributions of decay products to include also the polarisation. The polarisation is the helicity of the γ ray, and in Døssing 1981 the helicity representation is applied for the state after the emission.

The probability for emission of decay products in a certain direction determined by polar angles θφ (relative to the Y-axis) is obtained by applying the projection operator

$$P_{\theta\varphi} = \sum_{h_1 h_2} |h_1 h_2; \theta\varphi\rangle\langle h_1 h_2; \theta\varphi| \tag{A.9}$$

to the density operator after the decay. Letting h_1 denote the helicity of the nucleus after the γ decay, h_2 denotes the helicity of the γ ray, and can take on values 1 or ÷1. The projection operator for the emission probability times the average polarisation of the γ ray is then simply

$$P_{\theta\varphi}^{(pol)} = \sum_{h_1 h_2} h_2 | h_1 h_2; \theta\varphi\rangle\langle h_1 h_2; \theta\varphi| \tag{A.10}$$

Carrying through the same procedure for $P_{\theta\varphi}^{(pol)}$ as for $P_{\theta\varphi}$, one obtains for the emission probability in the direction θφ

$$\mathcal{W}(\theta\varphi) = \text{tr}\{P_{\theta\varphi} \varrho_S(\text{after decay})\} \tag{A.11}$$

$$= \frac{1}{\sqrt{4\pi}} \sum_{\lambda\mu} A_\lambda(S) \varrho_{\lambda\mu}(S) Y_{\lambda\mu}^*(\theta,\varphi)$$

and for the emission probability times the average polarisation

$$\mathcal{W}^{(pol)}(\theta\varphi) = \text{tr}\{P_{\theta\varphi}^{(pol)} \varrho_S(\text{after decay})\} \tag{A.12}$$

$$= \frac{1}{\sqrt{4\pi}} \sum_{\lambda\mu} A_\lambda^{(pol)}(S) \varrho_{\lambda\mu}(S) Y_{\lambda\mu}^*(\theta,\varphi)$$

In these expressions A_λ (S) is the angular distribution coefficient of rank λ. For γ rays A_λ (S) has the form:

$$A_\lambda(S) = (-)^{S_f - S - \lambda - 1} (2\ell + 1)\sqrt{2S + 1}$$
$$\times \frac{1}{2}(\langle \ell 1 \ell -1|\lambda 0\rangle + \langle \ell -1 \ell 1|\lambda 0\rangle)\mathcal{W}(\ell S \ell S; S_f \lambda) \tag{A.13}$$

where ℓ is the multipolarity of the radiation and S_f is the angular momentum of the final state. The sum over the two Clebs-Gordan coefficients in this expression comes from the summation over $h_2 = 1$ and -1 in $P_{\theta\varphi}$. To obtain $A_\lambda^{(pol)}$ (S), $h_2 = 1$ still enters with the plus sign, but the sign for $h_2 = -1$ is inverted, as in the projection operator $P_{\theta\varphi}^{(pol)}$.

Thus $A_\lambda^{(pol)}(S)$ is obtained from $A_\lambda(S)$ by changing this sign:

$$A_\lambda^{(pol)}(S) = (-)^{S_f - S - \lambda - 1}(2\ell + 1)\sqrt{2S + 1} \tag{A.14}$$
$$\times \tfrac{1}{2}(\langle \ell 1\ell - 1|\lambda 0\rangle - \langle \ell - 1\ell 1|\lambda 0\rangle) \mathscr{W}(\ell S\ell S; S_f\lambda)$$

For all kinds of decay, $A_\lambda(S)$ is zero for odd λ and $A_\lambda^{(pol)}(S)$ is zero for even λ. It is an advantage to change the normalisation of the angular distribution coefficients by defining

$$B_\lambda(S) = \sqrt{2\lambda + 1}\,\langle SS\lambda 0|SS\rangle\, A_\lambda(S) \tag{A.15}$$

and equivalently for $B_\lambda^{(pol)}(S)$.

Actually, quite few of these coefficients are needed, since only multipolarity 1 and 2 are emitted in the γ ray cascades, so only coefficients with $\lambda \leq 4$ will be different from zero. For *stretched transitions*, $S_f = S-\ell$, the coefficients are independent of the size of S, and attain the following values for dipole and quadrupole transitions:

$$\ell = 1: \quad B_0(\ell = 1) = 1, \quad B_1^{(pol)}(\ell = 1) = \tfrac{3}{2}, B_2(\ell = 1) = \tfrac{1}{2} \tag{A.16}$$
$$\ell = 2: \quad B_0(\ell = 2) = 1, \quad B_1^{(pol)}(\ell = 2) = 1, B_2(\ell = 2) = -\tfrac{5}{7},$$
$$B_3^{(pol)}(\ell = 2) = -1, B_4(\ell = 2) = -\tfrac{2}{7}$$

The yrast-type transitions, which make up the bulk of γ transitions are almost exclusively of stretched type. They are preceded by statistical transitions, mainly of multipolarity 1, which are not all stretched. The probability for final spin S_f, $S_f = S-1, S, S+1$ is given by the relative level density at S_f, which is well approximated by the expression:

$$\mathscr{P}(S_f) \quad \alpha \quad \exp\left(-\frac{(S_f-S)S}{\tau_f I}\right) \tag{A.17}$$

where τ_f is a representative temperature for the excitation above the yrast line after emission of a statistical γ ray, and I is the moment of inertia. τ_f is typically around 0.5 MeV. Inserting the B_λ coefficients for $\ell = 1$ and for the different S_f, weighted be the probability factors, one obtains for the average coefficients for statistical transitions:

$$B_0(S) = 1 \tag{A.18}$$

$$B_1^{(pol)}(S)\big|_{stat} = \frac{\tfrac{3}{2}\exp\left(\dfrac{S}{\tau_f I}\right) + 0 - \tfrac{3}{2}\exp\left(-\dfrac{S}{\tau_f I}\right)}{\exp\left(\dfrac{S}{\tau_f I}\right) + 1 + \exp\left(-\dfrac{S}{\tau_f I}\right)}$$

$$= \tfrac{3}{2}\sinh\left(\frac{S}{\tau_f I}\right)\left(\cosh\left(\frac{S}{\tau_f I}\right) + \tfrac{1}{2}\right)^{-1}$$

$$B_2(S)\Big|_{\text{stat}} = \frac{\frac{1}{2}\exp\left(\frac{S}{\tau_f I}\right) - 1 + \frac{1}{2}\exp\left(-\frac{S}{\tau_f I}\right)}{\exp\left(\frac{-S}{\tau_f I}\right) + 1 + \exp\left(\frac{S}{\tau_f I}\right)}$$

$$= \left(\cosh\left(\frac{S}{\tau_f I}\right) - 1\right)\left(2\cosh\left(\frac{S}{\tau_f I}\right) + 1\right)^{-1}$$

Here it is assumed that S and S_f are much larger than 1, otherwise some of the angular distribution coefficients become quite complicated functions of S and S_f. For small S, the coefficients $B_1^{(pol)}$ and B_2 for statistical γ rays are close to zero anyway, so it would be quite superfluous to insert the more exact values. As standard values for the paramenters τ_f and the number, N_{stat} of statistical γ rays, we take the temperature 3 MeV above the yrast line for the nucleus in question, and 3 statistical γ rays per nucleus i.e.

$$\tau_f = \sqrt{\frac{3}{a}} \qquad \mathcal{N}_{\text{stat}} = 3 \qquad a = \frac{A}{10} \tag{A.19}$$

where A is the mass number.

With these definitions, we can now define an effective angular distribution coefficient for the whole γ ray cascade. By p_1 and p_2 we denote the fraction of stretched yrast type γ rays of multipolarity $\ell=1$ and 2, respectively. The average number of $\ell=1$ and 2 transitions and the average number of γ rays as function of the spin S_0 are then given by

$$\mathcal{N}_{\ell=1}(S_0) = p_1\frac{\langle S_n\rangle}{p_1+2p_2}, \quad \mathcal{N}_{\ell=2}(S_0) = p_2\frac{\langle S_n\rangle}{p_1+2p_2},$$

$$\mathcal{N}_\gamma(S_0) = \mathcal{N}_{\ell=1}(S_0) + \mathcal{N}_{\ell=2}(S_0) + \mathcal{N}_{\text{stat}} \tag{A.20}$$

where $\langle S_n\rangle$ is the average spin (A.4) in the nucleus after neutron emission. Including the dilution factors (A.5) for the statistical tensors, the effective angular distribution coefficient as function of S_0 is given by

$$\mathcal{B}_\lambda(S_0) = \left\langle P_\lambda\left(\frac{\vec{S}_0\cdot\overleftarrow{S}_n}{S_0 S_n}\right)\right\rangle \times \Big[\mathcal{N}_{\ell=1}(S_0)\, B_\lambda(\ell=1) \tag{A.21}$$

$$+ \mathcal{N}_{\ell=2}(S_0)\, B_\lambda(\ell=2) + \mathcal{N}_{\text{stat}} B_\lambda(\langle S_n\rangle)\big|_{\text{stat}}\Big]\Big/\mathcal{N}_\gamma(S_0)$$

and equivalently for $\mathcal{B}_\lambda^{(pol)}(S_0)$ for the odd λ.

The angular distribution can be written as

$$4\pi \, \mathscr{W}(\theta,\varphi) = C_0 + C_2 \, P_2(\cos\theta) + C_{22} \sin^2\theta \, \cos 2\varphi$$
$$+ C_4 \, P_4(\cos\theta) + C_{42}(7\cos^2\theta - 1)\sin^2\theta \, \cos 2\varphi \qquad (A.22)$$
$$+ C_{44} \sin^4\theta \, \cos 4\varphi$$

with the coefficients for $\mu=0$ given by

$$C_\lambda = \int f(\vec{S}) \, \mathscr{N}_\gamma(S) \, \mathscr{B}_\lambda(S) P_\lambda\!\left(\frac{S_Y}{S}\right) d\vec{S} \qquad (A.23)$$

Likewise the angular distribution, mulitplied by the average polarisation, can be written as

$$4\pi \, \mathscr{W}^{(\mathrm{pol})}(\theta,\varphi) = C_1^{(\mathrm{pol})} \, P_1(\cos\theta) + C_3^{(\mathrm{pol})} P_3(\cos\theta)$$
$$+ C_{32}^{(\mathrm{pol})} \cos\theta \, \sin^2\theta \, \cos 2\varphi \qquad (A.24)$$

with the coefficients for $\mu=0$ given by

$$C_\lambda^{(\mathrm{pol})} = \int f(\vec{S}) \, \mathscr{N}_\gamma(S) \, \mathscr{B}_\lambda^{(\mathrm{pol})}(S) P_\lambda\!\left(\frac{S_Y}{S}\right) d\vec{S} \qquad (A.25)$$

We now turn to step (iv), to calculate the γ ray polarisation, as it will be determined by the polarimeter. The γ ray polarisation is calculated by integrating the angular distributions (A.22) and (A.24) without and with inclusion of the polarisation over the angular range covered by the polarimeter, weighted by the transmission function $\frac{dT}{d\Omega}$ (θ) and by the sensitivity function A (θ):

$$\langle P_\gamma \rangle \;=\; \frac{\displaystyle\int_{\theta_1}^{\theta_2} \int_0^{2\pi} \mathscr{W}^{(\mathrm{pol})}(\theta,\varphi) \, \frac{A(\theta)}{\langle A \rangle} \frac{dT}{d\Omega}(\theta) \, d\varphi \, \sin\theta \, d\theta}{\displaystyle\int_{\theta_1}^{\theta_2} \int_0^{2\pi} \mathscr{W}(\theta,\varphi) \, \frac{dT}{d\Omega}(\theta) \, d\varphi \, \sin\theta \, d\theta} \qquad (A.26)$$

The functions for the forward scattering polarimeter applied in the experiments under discussion here are evaluated and discussed in Trautmann 1981, and they are quite well approximated by:

$$A(\theta) \quad \alpha \quad \text{constant} \qquad (A.27)$$

$$\frac{dT}{d\Omega}(\theta) \quad \alpha \quad \sin^{-2}\theta$$

Since the polarimeter is symmetric around the reaction normal, the terms containing $\cos 2\varphi$ and $\cos 4\varphi$ in (A.22) and (A.24) integrate out to zero. Applying the functions (A.27) and integrating over the angular

range $20° < \theta < 45°$ covered by the polarimeter, the following result is obtained in terms of the expansion coefficients (A.23) and (A.25):

$$\langle P_\gamma \rangle = \frac{0.850 \ C_1^{(pol)} + 0.290 \ C_3^{(pol)}}{C_0 + 0.591 \ C_2 + 0.016 \ C_4} \tag{A.28}$$

In this procedure, the dependence of the functions $A(\theta)$ and $\frac{dT}{d\Omega}(\theta)$ on the energy of the γ ray energy has been neglected. Below 500 keV of γ ray energy, these functions become very small, and this will hinder the detection of some of the yrast type γ rays, especially those of multipolarity $\ell = 1$.

In the remainder of this appendix we shall discuss results of calculated polarisations, applying a distribution function of the spin with equal variances in all directions:

$$f(\vec{S}) = (2\pi\sigma)^{-3/2} \exp \left(-\frac{(\vec{S} - \langle S_Y \rangle \hat{Y})^2}{2\sigma^2} \right) \tag{A.29}$$

where $\hat{Y}$ is a unit vector along the reaction normal.

It is convenient to plot the results as function of the spin polarisation $\langle P_Y \rangle$ (A.3). The magnitudes of the mean spin vector and the dispersion are shown as function of the polarisation in figure A1. Applying a specific parametrisation like (A.29) the higher order statistical tensors become funtions of the polarisation. These functions are shown in figure A2. For most values of the spin polarisation, the higher order tensors are substantially smaller than the polarisation.
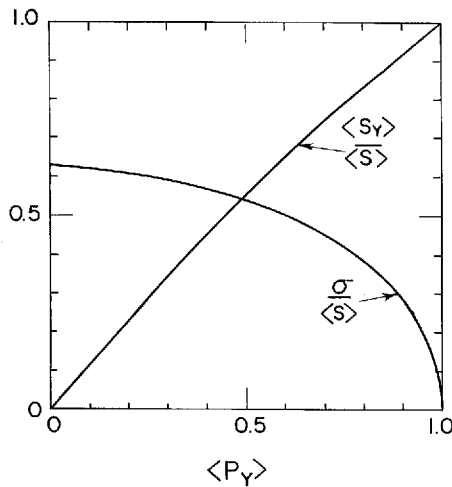

Fig. A1. Sizes of the average spin vector and the standard deviation of the spin distribution along all coordinates for the Gaussian parametrisation applied to illustrate the γ ray polarisation results, shown as function of the average spin polarisation.

Fig. A2. Sizes of higher order tensors as function of the spin polarisation for the Gaussian parametrisation.
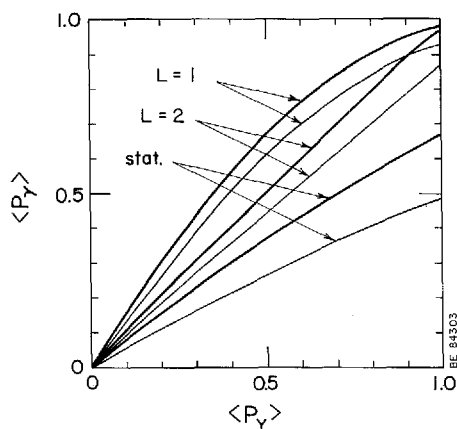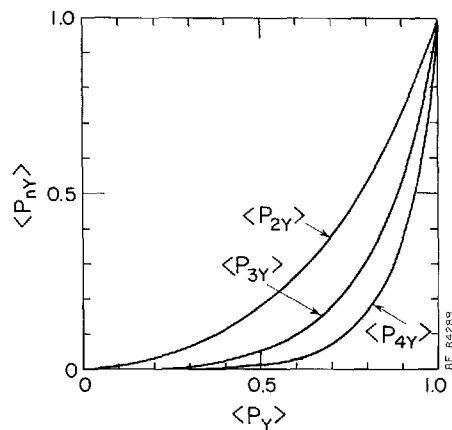

Fig. A3. γ ray polarisation as function of spin polarisation for the three different kinds of γ rays contributing to the cascade. The average spin size is 30 units, and the parameters applied describe the decay of a nucleus with a mass number around 160 and excitation energy of 200 MeV. The effects of neutron evaporation are included in the thin curves and left out for the thick curves.

Figure A3 shows calculated γ ray polarisations as function of the spin polarisation. They are calculated separately for each of the three different kinds of γ rays contibuting to the cascade, stretched dipole, stretched quadrupole, and statistical transitions. The parameters are determined for a nucleus of mass number 160, excitation energy 200 MeV, and average spin magnitude 30ħ. The figure addresses the same question as figure 7 of Trautmann 1981, and the thick curves for the stretched transitions are very similar to the results presented in that figure. They are obtained by completely neglecting the effects of neutron evaporation. Neutron evaporation from the quite high excitation energy of 200 MeV is included in the results shown by the thin lines, and one can see that the decrease in polarisation and higher order tensors caused by the neutrons really changes the γ ray polarisation.

Figure A4 shows the calculated γ ray polarisation for an yrast composition of 90% quadrupole and 10% dipole transitions. This composition we adopt as standard. In figure A4 neutrons are fully included, and the average spin magnitude varies between the different curves. One can see that the spin magnitude has quite some influence upon the results. For the cases we shall deal with in section 6, the average spin magnitude is around $3\bar{0}$, and the excitation energy is around 80 MeV. The γ ray polarisation for these cases will be typically 10% smaller than the spin polarisation, in qualitative agreement with the results shown on fig. A4.

Fig. A4. Same as fig. A3, but for different average spin sizes, and with inclusion of the effects of neutrons. The yrast part of the cascade is assumed to consist of 10% stretched multipolarity 1 transitions and 90% stretched multipolarity 2 transitions, and the number of statistical transitions included is 3 per cascade.
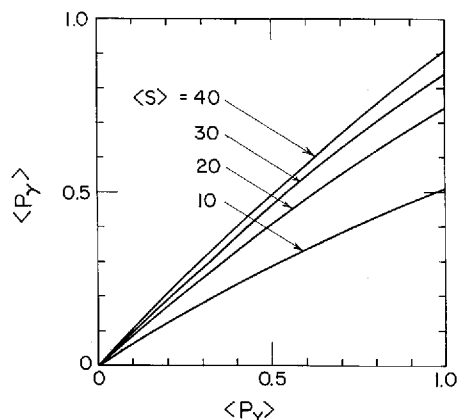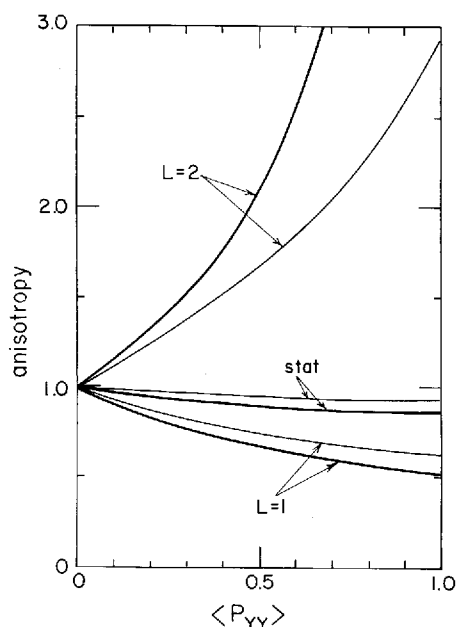
Fig. A5. Anisotropy as function of spin alignment for the three different kinds of γ rays contributing to the cascade. The parameters are the same as for fig. A3.

The results shown in figure A4 do not depend crucially upon the composition of the yrast type γ rays, because the most important polarisation angular distribution coefficient $B_1^{(pol)}$ (A.16) has the same sign and a similar magnitude for stretched dipole and quadrupole transitions. This similarity is also apparent in figure A3.

In contrast to this situation, we show in figure A5 for each of the three kinds of γ rays the anisotropy af the angular distribution, which can be written in terms of the coefficients for the angular distribution (A.22):

$$\text{anisotropy} = \frac{\frac{1}{2\pi} \int \mathscr{W}(\theta=\frac{\pi}{2}, \varphi)d\varphi}{\mathscr{W}(0,\varphi)} = \frac{C_0 - \frac{1}{2}C_2 + \frac{3}{8}C_4}{C_0 + C_2 + C_4} \tag{A.30}$$

In figure A5, the result is plotted as function of the alignment, since the polarisation does not enter, but otherwise the parameters are identical to those used for figure A3. Since the anisotropy has opposite signs for dipole and quadrupole γ rays (due to the opposite signs of the B_2 angular distribution coefficents (A.16)), the angular distribution of continuum γ rays is a problematic tool to study the spin alignment, because the result will depend crucially upon the multipolarity composition of the yrast type γ rays.

References

Agassi 1978: D. Agassi, C. M. Ko and H. A. Weidenmüller, Phys. Rev. **C18** (1978) 223

Ayik 1976: S. Ayik, B. Schürmann and W. Nörenberg, Z. Phys. **A277** (1976) 299, **A279** (1976) 145

Balian 1984: R. Balian, P. Bonche, H. Flocard and M. Veneroni, Nucl. Phys. **A428** (1984), 79 c, and references therein

Barrett 1978: B. R. Barrett, S. Shlomo and H. A. Weidenmüller, Phys. Rev. **C17** (1978) 544

Blocki 1978: J. Blocki, Y. Boneh, J. R. Nix, J. Randrup, M. Robel, A. J. Sierk and W. J. Swiatecki, Ann. Phys. **113** (1978) 330

Britt 1982: H. C. Britt, H. Erkkila, A. Gavron, Y. Patin, R. H. Stokes, M. P. Webb, P. R. Christensen, O. Hansen, S. Pontoppidan, F. Videbaek, R. L. Ferguson, F. Plasil, G. R. Young and J. Randrup, Phys. Rev. **26C** (1982) 1999

Broglia 1981: R. A. Broglia, C. H. Dasso and A. Winther, in Proceedings of The International School of Physics »Enrico Fermi«, held in Varenna, Italy, july 9-21 1979, editors R. A. Broglia, R. A. Ricci and C. H. Dasso. (North Holland 1981)

Dasso 1979: C. H. Dasso, T. Døssing and H. C. Pauli, Z. Phys. **A289** (1979) 395

Davies 1978: K. T. R. Davies, V. Maruhn-Rezwani, S. E. Koonin and J. W. Negele, Phys. Rev. Lett. **41** (1978) 632

Davies 1981: K. T. R. Davies and S. E. Koonin. Phys. Rev. **C23** (1981) 2042

Døssing 1981: T. Døssing, Nucl. Phys. **A357** (1981) 488

Døssing 1985a: T. Døssing and J. Randrup. Nucl. Phys. **A433** (1985) 215

Døssing 1985b: T. Døssing and J. Randrup. Nucl. Phys. **A433** (1985) 280

Døssing 1985c: T. Døssing and J. Randrup. submitted to Physics Letters (1985)

Esbensen 1978: H. Esbensen, A. Winther, R. A. Broglia and C. H. Dasso, Phys. Rev. Lett. **41** (1978) 296

Fano 1957: U. Fano. Rev. Mod. Phys. **29** (1957) 74, and references therein

Feldmeier 1984: H. Feldmeier and H. Spangenberger, preprint. GSI Darmstadt (1984)

Ko 1979: C. M. Ko, Phys. Lett. **81B** (1979) 299

Köhler 1979: H. S. Köhler and H. Flocard, Nucl. Phys. **A323** (1979) 189

Martinot 1984: M. Martinot, C. Ngo and F. Lepage (editors), Proceedings of the International Conference on Theoretical Approaches of Heavy Ion Reaction Mechanisms, Paris may 14-18 1984, published as volume **428** of Nucl. Phys. (1984)

Moretto 1980: L. G. Moretto and R. P. Schmidt. Phys. Rev. **C21** (1980) 204

Moretto 1984: L. G. Moretto, in Proceedings of The International School of Physics »Enrico Fermi«, held in Varenna, Italy, july 9–august 6 1982, editors L. G. Moretto and R. A. Ricci (North Holland 1984)

Nix 1965: J. R. Nix and W. J. Swiatecki, Nucl. Phys. **71** (1965) 1

Nörenberg 1975: W. Nörenberg, Z. Phys. **A274** (1975) 241

Nörenberg 1982: in »Nuclear Physics«, proceedings of the Workshop held at I. C. T. P., Trieste, Italy, 5-30 october 1980, editors C. H. Dasso, R. A. Broglia and A. Winther, (North Holland 1982)

Randrup 1979: J. Randrup, Nucl. Phys **A327** (1979) 490

Randrup 1982: J. Randrup, Nucl. Phys. **A383** (1982) 468

Schandera 1984: C. Schandera, Ch. Lauterbach, J. de Boer, W. Dünnweber and W. Trautmann, preprint, Sektion Physik, Universitat Munchen (1984), to be published in Nukleonika

Schmidt 1982: R. P. Schmidt and A. J. Pacheco, Nucl. Phys. **A379** (1982) 313

Schröder 1981: W. U. Schröder, J. R. Huizenga and J. Randrup, Phys. Lett. **98B** (1981) 355

Shlomo 1979: S. Shlomo, B. R. Barrett and H. A. Weidenmüller, Phys. Rev. **C20** (1979) 1

Tang 1981: H. H. K. Tang, C. H. Dasso, H. Esbensen, R. A. Broglia and A. Winther, Phys. Lett. **101B** (1981) 10

Trautmann 1981: W. Trautmann, C. Lauterbach, J. de Boer, W. Dünnweber, C. Graw, W. Hamann, W. Hering and H. Puchta, Nucl. Inst. Meth. **184** (1981) 449

Vandenbosch 1978: R. Vandenbosch, M. P. Webb. P. Dyer, R. J. Puigh and R. Weisfield, Phys. Rev. **C17** (1978) 1672

Weidenmüller 1980: H. A. Weidenmüller, in Prog. Part. and Nucl. Phys. vol 3. editor D. Wilkinson. (Pergamon Press 1980)

Wolschin 1978: G. Wolschin and W. Nörenberg, Phys. Rev. Lett. **41** (1978) 691

Wolschin 1981: G. Wolschin, in Proceedings of The International School of Physics »Enrico Fermi«, held in Varenna, Italy, july 9-21 1979, editors R. A. Broglia, R. A. Ricci and C. H. Dasso. (North Holland 1981).

Irene Shim

Homonuclear Dimers of First and Second Transition Metal Series

ABSTRACT. *In the present work we have reviewed the experimental and the theoretical knowledge of first and second series transition metal diatomics. In addition, new calculational results have been included for the molecules Ni_2, Fe_2, and Rh_2. Presently, the combined experimental and theoretical knowledge indicates that ab initio calculations provide valuable insight into the nature of the chemical bonds of such molecules, and even reasonable spectroscopic data, if carried far enough. The »d electron rich« transition metal dimers exhibit »bands« of low-lying electronic states. The chemical bonds in the molecules Cu_2, Ni_2, Co_2, and Fe_2, are mainly due to the delocalized $4s\sigma_g$ molecular orbitals. The 3d electrons localize around the nuclei and interact through Heisenberg exchange couplings, giving rise to the small energy splittings between the low-lying electronic states. In the corresponding dimers of the second transition metal series, Ag_2, Pd_2, Rh_2, and Ru_2 the principal bonding orbitals are the delocalized $5s\sigma_g$ molecular orbitals. For Ag_2 and Pd_2 the 4d electrons are essentially localized, while they get increasingly delocalized from Rh_2 to Ru_2. The d electrons in the »d electron deficient« transition metal dimers are appreciably delocalized and their combined contributions to the chemical bonds are comparable to the contributions due to the outermost $s\sigma_g$ molecular orbitals.*

Department of Chemical Physics, Chemical Laboratory B,
The Technical University of Denmark, DTH 301,
DK-2800 Lyngby, Denmark

Introduction

Conceptually, modern chemistry builds on the quantum theory that appeared in the 1920s. The quantum theory was devised to explain a variety of phenomena for which the classical physics did not offer any satisfactory explanations. These phenomena include the black-body radiation, the photoelectric effect, and the line spectra of the atoms. The black-body radiation was explained by Planck in 1901 by introduction of energy quantization and of the Planck constant h. The photoelectric effect led in 1905 Einstein to suggest quantization of light, and in 1913 Bohr proposed quantization of angular momentum in his atomic model,

which accounted for the spectrum of the hydrogen atom in terms of an energy-level diagram.

Based on the prior developments in physics Schrödinger in 1926 suggested a general wave equation for describing the motion of atomic and subatomic particles and soon after, this equation was applied to chemical problems. Thus, already in 1927 Bohr communicated a paper by Burrau, who had utilized the new equation to elucidate the ground state of the H_2^+ molecular ion. However, better known is the work by Heitler and London 1927, in which they discuss the chemical bond in the H_2 molecule. Heitler and London invent a mathematical formulation of the covalent bond, and attribute the energy of the electron pair bond to the resonance energy arising from the exchange of the two electrons. The method introduced by Heitler and London has later become known as the valence bond method.

The molecular orbital method which is widely used in quantum chemistry nowadays was introduced by Hund 1928 and also by Mulliken 1928. This method is an extension of the Bohr theory of electronic configurations from atoms to molecules. Each electron is assigned to a molecular orbital that is the quantum mechanical analogue of the electron orbit in an atom.

It is recognized that the foundation of modern quantum chemistry was laid at an early stage and already in 1929 Dirac made his famous remark: »The underlying physical laws necessary for the mathematical theory of a large part of physics and the whole of chemistry are thus completely known«. However, he did add »the difficulty is only that the exact application of these laws leads to equations much too complicated to be soluble. It therefore becomes desirable that approximate practical methods of applying quantum mechanics should be developed«.

The approximate methods developed since the early days of quantum mechanics have made use of the fact that the Schrödinger equation is equivalent to a variational principle. Hylleraas 1930 carried out very accurate calculations for the He atom using this principle. His methods, however, were not suited for generalization to many electron systems. Thus, the methods applied in quantum chemistry to-day have their origin in the self-consistent-field work by Hartree 1928. After Slater 1929 introduced the determinantal wave functions, Slater 1930 and Fock 1930 independently invented what is now commonly known as the Hartree-Fock method.

Although the development of the quantum theory in principle opened up the possibilities of quantitative studies of atoms and molecules, it was

only with the technological development of the electronic computers that such studies also became practically feasible. Calculations of electronic states of atoms and molecules with more than one or two electrons are strongly dependent on the existence of electronic computers. In 1951 and 1960 Roothaan introduced the formulations of the Hartree-Fock equations which are especially suited for electronic computations, and even though much progress has been achieved since, Roothaan's equations are still the natural starting point for quantum chemistry calculations.

Nowadays, quantum chemical calculations can be performed by routine even on rather large molecules composed of atoms from the first and the second row in the periodic system, such as organic molecules, but compounds containing transition metal atoms still constitute great challenges.

During recent years several research groups have been devoting great efforts to experimental or theoretical investigations striving to understand and elucidate the chemistry and physics of small clusters composed of transition metal atoms. The current interest in the transition metal clusters is influenced by their relevance to surface science and heterogeneous catalysis. Thus, finely dispersed transition metals supported on high surface materials such as porous silica act as catalysts for the hydrogenation of carbon monoxide, and presently it appears likely that this process or similar ones will be of great importance for securing the energy supply in future. Therefore, it is essential to aquire profound insight into the mechanism of such reactions at the atomic and molecular levels.

Both experimental and theoretical investigations of transition metal clusters are very difficult to carry out and strongly dependent on each other for appropriate interpretations.

The present paper has been devoted to the smallest possible units consisting of transition metal atoms, namely the diatomic molecules. In particular, we have concentrated on the theoretical investigations of the molecules where the author has been most actively involved, that is, the homonuclear transition metal dimers composed of atoms with more than half filled d shells belonging to the first and the second transition metal series. These elements also include some of the most commonly used in catalyses.

The paper is structured as follows: The next section contains a brief account of available experimental data concerning first and second row transition metal dimers. Thereafter a few computational details are pre-

sented followed by a detailed discussion of the results for the individual molecules. The conclusions of the work are found in the last section.

Experimental investigations of transition metal dimers

The first experimental data obtained for any transition metal dimers date back to 1954 and 1955, when the electronic spectra of the molecules Cu_2 and Ag_2 were measured by Kleman and Lindkvist and also by Ruamps 1954. A little later Dowart and Honig 1956, 1957 and Schissel 1957 determined the dissociation energies of Cu_2, Ag_2, and Au_2 from measurements of the dimer to monomer ratios in high temperature mass spectrometric studies.

During the 1960s all the homonuclear dimers of the first transition metal series have been studied using the high temperature equilibrium mass spectrometric method. This has been reviewed by Gingerich 1980, and the dissociation energies obtained including later corrections and also results of new measurements are displayed in Table I.

The high temperature mass spectrometric method has also been utilized for studying the homonuclear dimers composed of atoms with non closed d shells of the second transition metal series. The first of these investigations was performed by Verhaegen et al. 1964, and dealt with the Y_2 molecule. The dimers of the most refractory metals have been studied mainly by Gingerich and his collaborators as is seen from Table I.

In the mass spectrometric investigations the dimer to monomer ratios are measured, but in order to derive the dissociation energies from the measured data, it is necessary to evaluate the partition functions for both the monomers and the dimers. This gives rise to inaccuracies in the published dissociation energies, because the spectroscopic constants, such as equilibrium distances, vibrational frequencies, and low–lying electronic states needed for the evaluation of the partition functions are only currently becoming available for the transition metal dimers composed of atoms with partly filled d shells. Recently we have performed new mass spectrometric measurements for the molecules Fe_2, Shim and Gingerich 1982, and Pd_2, Shim and Gingerich 1984. The utilization of the calculated low–lying electronic states in the evaluation of the partition function for Fe_2 resulted in a dissociation energy 0.78 ± 0.17 eV as compared to the value of 1.04 ± 0.22 eV derived by Lin and Kant 1969b.

As reviewed by Huber and Herzberg 1979, well–resolved UV–visible gas phase spectra have been measured many years ago for the molecules

Table I. Experimental spectroscopic constants of the first and second row transition metal dimers.

Molecule	Matrix isolation studies			Gas phase spectroscopic studies				High temperature mass spectrometric studies	Nearest neighbour internuclear distance in bulk metal (a.u.)[1]
	ω_e(cm^{-1})	$\omega_e x_e$(cm^{-1})	r_e(a.u.)	ω_e(cm^{-1})	$\omega_e x_e$(cm^{-1})	r_e(a.u.)	D_0(eV)	D_0^o(eV)	
Sc$_2$	238.91[2]	0.93[2]						1.65±0.22[3]	6.15
Ti$_2$	407.9[4]	1.08[4]						1.41±0.22[5]	5.50
V$_2$	537.5[4]	4.2[4]		535[6]	3.34[6]		1.85[6]	2.47±0.22[5]	4.95
Cr$_2$	427.5[7]	15.75[7]		470[10]	3.17[9,10]			1.56±0.22[11]	4.71
					3.184[8,34]				
				472.7[35]	10.2[35]				
				493.3[35]	20.5[35]				
Mn$_2$	124.7[2]	0.24[2]						0.43±0.30[12]	4.27
Fe$_2$	300.26[2,13]	1.4[13]	3.53±0.25[14]					0.78±0.17[16]	4.69
			3.82±0.04[15]						
Co$_2$	290[7]							0.95±0.26[17,33]	4.72
Ni$_2$	380.9[18]	1.08[18]				4.157±.013[19]	2.068±.01[19]	2.00±0.22[20,21]	4.71
Cu$_2$				264.55[22]	1.025[22]	4.1947[22]		2.04±0.13[12]	4.82
Y$_2$								1.62±0.22[23]	6.72
Zr$_2$									5.97
Nb$_2$								5.21±0.10[24]	5.40
Tc$_2$									5.11
Mo$_2$	475.7[25]			477.1[34]	1.51[34]	3.645[34]	4.12±0.65[34]	4.18±0.22[27]	5.14
						3.666±0.017[26]			
Ru$_2$									5.06
Rh$_2$								2.92±0.22[28]	5.08
								2.80±0.13[29]	
Pd$_2$								1.03±0.17[30]	5.20
Ag$_2$	194[31]			192.4[22]	0.643[22]	4.690[32]		1.65±0.07[12]	5.46

1) From J. Donohue, »The Structure of the Elements«, (Krieger, Malabar, Florida 1982). – 2) Moskovits, DiLella, and Limm 1984 (Ar). – 3) Drowart 1967. – 4) Cossé, Fouassier, Mejean, Tranquille, Dilella, and Moskovits 1980 (Ar). – 5) Kant and Lin 1969. – 6. Langridge-Smith, Morse, Hansen, Smalley, and Merer 1984. – 7) Ford, Huber, Klotzbücher, Kündig, Moskovits, and Ozin 1977 (Ar). – 8) Efremov, Samoilova, and Gurvich 1974. – 9) Michalopoulos, Geusic, Hansen, Powers, and Smalley 1982. – 10) Bondybey and English 1983. – 11) Kant and Strauss 1966. – 12) Kant, Lin, and Strauss 1968. – 13) Moskovits and DiLella 1980 (Ar) – 14) Montano and Shenoy 1980 (EXAFS in Ar) – 15) Purdum, Montano, Shenoy, and Morrison 1982 (EXAFS in Ne). – 16) Shim and Gingerich 1982. – 17) Kant and Strauss 1964. – 18) Ahmed and Nixon 1979. – 19) Morse, Hansen, Langridge-Smith, Zheng, Geusic, Michalopoulos, and Smalley 1984. – 20) Kant 1964. – 21) Noell, Newton, Hay, Martin, and Bobrowicz 1980. – 22) Huber and Herzberg 1979. – 23) Verhaegen, Smoes, and Drowart 1964. – 24) Gupta and Gingerich 1979. – 25) Pellin, Foosnaes, and Gruen 1981. – 26) Hopkins, Langridge-Smith, Morse, and Smalley 1983. – 27) Gupta, Atkins, and Gingerich 1978. – 28) Gingerich and Cocke 1972; Cocke and Gingerich 1974. – 29) Piacente, Balducci, and Bardi 1974. – 30) Shim and Gingerich 1984. – 31) Schulze, Becker, Minkwitz, and Manzel 1978. – 32) Srdanov and Pešić 1981. – 33) Shim and Gingerich 1983b. – 34) Efremov, Samoilova, Kozhukhovsky, and Gurvich 1978. – 35) Riley, Parks, Pobo, and Wexler 1983.

Cu_2 and Ag_2. The spectra of Cu_2 have resulted in accurate determination of both the equilibrium distance and the vibrational frequency of the electronic ground state. Similar spectroscopic data are also known for the Ag_2 molecule, but in this case the equilibrium distance has been derived recently from data of Srdanov and Pešić 1981.

Due to experimental difficulties the knowledge of the spectroscopic data for the open shell transition metal dimers have been scarce until recently. The first spectroscopic investigations of such molecules have been carried out using the matrix isolation technique introduced by Whittle, Dows and Pimentel 1954 and by Becker and Pimentel 1956. In this method, the metal vapor is cocondensed with an inert gas at very low temperatures $\sim 10K$. Of course, use of the matrix isolation technique results in loss of the rotational fine structures, and therefore this method is not suitable for determining the equilibrium distances of the molecules. In addition, it is often difficult or impossible to identify with certainty the carriers of the electronic transitions observed. Compared to gas phase spectra, frequency shifts of the absorptions occur and also possibly splittings due to local site symmetries. Thus, not even the spectra arising from atomic species can unambiguously be assigned to the gas phase spectra.

The first matrix isolation study of the spectroscopic transitions of an open shell transition metal dimer, where an assignment of the spectrum of the diatomic molecule was attempted, has been carried out by Green and Gruen 1972 for the Nb_2 molecule. Klotzbücher and Ozin 1977 and 1980a have also investigated the Nb_2 molecule in inert gas matrices, but they did not observe any absorption in the spectral region where Green and Gruen found the features they attribute to Nb_2.

The difficulties encountered in matrix isolation studies of transition metal atoms and molecules are clearly recognized in the work done on Ni and Ni_2. The first investigation of Ni_2 in an inert gas matrix (Ar) was performed by de Vore et al. 1975. They have reported a single absorption system with an average vibrational spacing of 192 cm^{-1} and with 0-0 band at 21 786 cm^{-1}. Moskovits and Hulse 1977, however, observed two discrete band systems with origins at 18 920 cm^{-1} and 26 500 cm^{-1}, respectively, and also a continuous band peaking at 24 000 cm^{-1}. Furthermore, they pointed out that the matrix shifts of the atomic Ni absorptions are large and not at all uniform ranging from 1270 cm^{-1} to 3450 cm^{-1}. Recently Cellucci and Nixon 1984 have performed laser-induced fluorescence studies of Ni atoms isolated in different inert gas matrices. In their work they find evidence for a $^3F_4(3d)^8(4s)^2$ ground term of Ni in

a Ne matrix while the ground term of Ni isolated in an Ar or Kr matrix probably is $^3D_3(3d)^9(4s)^1$. Furthermore, they only find very small matrix shifts.

Matrix isolation studies are presently known for all first row and a few second row homonuclear transition metal dimers. In Table I we have summarized the ground state spectroscopic data as derived in the matrix isolation investigations.

The matrix isolation technique has also formed the basis for other kinds of experimental investigations of the transition metal dimers such as Mössbauer and ESR studies. Mössbauer studies of the Fe_2 molecule have in particular been carried out by Montano and collaborators as described by Montano et al. 1976 and by Montano 1980. ESR spectra of the Sc_2 molecule obtained by Knight et al. 1983 have established the ground state of Sc_2 as a $^5\Sigma$ state. ESR studies by Van Zee et al. 1981, by Rivoal et al. 1982, and by Baumann et al. 1983 have revealed that the Mn_2 molecule has a $^1\Sigma_g^+$ ground state arising from antiferromagnetic coupling of the atoms. This is in agreement with the early theoretical work by Nesbet 1964.

Gas phase spectroscopic investigations of transition metal dimers are still rather scarce. Due to the refractory nature of the transition metals, special techniques such as laser vaporization or hot ovens are required to produce the metal vapors. Thereafter the clusters can be created in a cold gas bath and finally effused into a vacuum, where the spectra are measured, Powers et al. 1983.

The first gas phase studies of open shell transition metal dimers have been carried out by Efremov et al. They obtained absorption and emission spectra of the molecules Cr_2, 1974 and Mo_2, 1978 in flash photolysis of the molecules $Cr(CO)_6$ and $Mo(CO)_6$, respectively. From the spectra of the Cr_2 molecule they derived an equilibrium distance of only 3.184 a.u. This distance seemed so incredibly short that they suggested other carriers of the observed spectral bands, such as CrO_2 or CrC_2. However, the recent spectroscopic investigations by Michalopoulos et al. 1982, by Bondybey et al. 1983, and by Riley et al. 1983 all confirm the short bond distance in the Cr_2 molecule.

From Table I it is noted that besides the molecules Cr_2 and Mo_2 also V_2 and Ni_2 have been studied in the gas phase. In the work by Morse et al. 1984 of the Ni_2 molecule no spectroscopic transitions were observed over the entire range 570-350 nm, which covers all known matrix absorption systems of Ni_2. They attribute this to predissociation of the excited state. From 600 to 900 nm they found an exceptionally high

density of spectroscopic transitions for a diatomic molecule, and they consider this as a proof of the theoretical predictions by Upton et al. 1978, by Shim et al. 1979, and by Noell et al. 1980 of the many low-lying electronic states.

Computational details

The electronic structures of the molecules Fe_2, Co_2, Ni_2, Cu_2, Ru_2, Rh_2, Pd_2, Ag_2, and Nb_2 have been investigated by the author using all electron ab initio Hartree-Fock (HF) and configuration interaction (CI) calculations. The computations have been carried out in the Hartree-Fock-Roothaan formalism, Roothaan 1951 and 1960, folllowed by configuration interaction treatments. The integrals have been calculated using the program MOLECULE★. For the HF calculations we have utilized the ALCHEMY program system★★, and finally the CI calculations have been performed using ALCHEMY in conjunction with the program ENERGY★★★ for generating the symbolic energy expressions.

The basis sets used consisted of Gaussian type functions. For the first row transition metal atoms we have utilized modified versions of the basis sets optimized for the atomic ground terms by Wachters 1970. Relative to Wachters' our basis sets have been extended by addition of two p functions and also a diffuse d function. The exponents of the two most diffuse s functions have been altered to contract the radial charge densities resulting in improved description of the valence regions in the molecules. For the first row transition metal dimers the primitive bases (14s, 11p, 6d) have been contracted to (8s, 6p, 3d). The coefficients of the contracted functions have been derived in HF calculations on the ground terms of the respective atoms. In the contracted bases the 3d orbitals are represented by triple zeta functions, and all the occupied s and p orbitals

---

★MOLECULE has been written by J. Almlöf, and has been described in »Proceedings of the Second Seminar on Computational Problems in Quantum Chemistry« (Max-Planck Institut, München, 1973), p. 14.

★★The ALCHEMY program system is written at IBM Research Laboratory in San Jose, Ca. by P. S. Bagus, B. Liu, M. Yoshimine, and A. D. McLean.

★★★The program ENERGY has been written by S. Rettrup, and is described in C. R. Sarma and S. Rettrup, Theor. Chim. Acta (Berlin) 46, 63 (1977); S. Rettrup and C. R. Sarma, ibid. 46, 73 (1977).

as well as the empty 4p orbitals are represented by double zeta functions.

For the second row transition metal dimers Ru_2, Rh_2, Ag_2, and Nb_2 the basis sets used are essentially Huzinaga's 1977, but extended by addition of two p functions. The additional p functions are needed to describe the 5p orbitals, and their exponents have been determined using the even tempered method described by Raffenetti 1973. Equivalent to the first row transition metal atoms the exponents of the most diffuse s functions have been altered to contract the radial charge densities. The primitive basis sets (17s, 13p, 8d) were contracted to (10s, 8p, 5d) by using segmented contraction schemes. The coefficients of the contracted functions have been determined in HF calculations on the ground terms of the atoms. In the contracted basis sets all the occupied s and p orbitals and the empty 5p orbitals have been represented by double zeta functions. The 3d orbitals are represented by double zeta functions while the 4d orbitals by triple zeta functions.

The basis set utilized for the Pd atom is similar to Huzinaga's 1977, and it has been described in detail by Shim and Gingerich 1984.

In Table II we compare the relative energies of the lowest lying terms originating from different orbital configurations with the corresponding experimental values, and also with those derived in the numerical HF calculations performed by Martin and Hay 1981. It is observed that we obtain the right ordering of the terms except in the case of the Ni atom for which the $^3F(3d)^8(4s)^2$ term is found 1.28 eV below the $^3D(3d)^9(4s)^1$ term whereas it should be 0.03 eV above. The calculated splittings between terms originating from the different orbital configurations differ to some extent from the experimental values. This is a well-known deficiency of HF calculations and it has been discussed in considerable detail for the first row transition metal atoms by Claydon and Carlson 1968.

It is noted that our calculated splittings are in reasonable agreement with those derived in the numerical HF calculations both for the first and the second row transition metal atoms. This indicates that our basis sets are of good qualities.

In all calculations of electronic structures of molecules containing transition metal atoms, the partly filled inner shells, that is the 3d and the 4d shells for the first and the second row transition metal atoms, respectively, give rise to severe complications. Thus, for the diatomic molecules their presence causes great uncertainties as to electronic ground state assignments, because a considerable number of Slater determinants will have comparable energies. This number increases rapidly as the

Table II. Relative energies (eV) of the low-lying terms for the "d electron rich" transition metal atoms of the first and the second transition metal series.

Atom	Term	Calculated		Experimental [a]
		HF [b]	NHF [c]	
Cu	$^2S(3d)^{10}(4s)^1$	0.00	0.00	0.00
	$^2D(3d)^9(4s)^2$	0.38	0.37	1.49
	$^2P(3d)^{10}(4p)^1$	4.33		3.81
Ni	$^3D(3d)^9(4s)^1$	0.00	0.00	0.00
	$^3F(3d)^8(4s)^2$	-1.28	-1.27	0.03
	$^1S(3d)^{10}$	4.14	4.20	1.74
Co	$^4F(3d)^7(4s)^2$	0.00	0.00	0.00
	$^4F(3d)^8(4s)^1$	1.52	1.53	0.42
	$^2D(3d)^9$	6.98	7.04	3.36
Fe	$^5D(3d)^6(4s)^2$	0.00	0.00	0.00
	$^5F(3d)^7(4s)^1$	1.85	1.80	0.87
	$^3F(3d)^8$	7.59	7.46	4.07
Ag	$^2S(4d)^{10}(5s)^1$	0.00	0.00	0.00
	$^2D(4d)^9(5s)^2$	4.77	4.91	3.97
	$^2P(4d)^{10}(5p)^1$	3.82		3.74
Pd	$^1S(4d)^{10}$	0.00	0.00	0.00
	$^3D(4d)^9(5s)^1$	0.23	0.75	0.95
	$^1D(4d)^9(5s)^1$	0.62		1.45
	$^3F(4d)^8(5s)^2$	3.08	3.76	3.38
Rh	$^4F(4d)^8(5s)^1$	0.00	0.00	0.00
	$^2D(4d)^9$	1.49	0.95	0.34
	$^4F(4d)^7(5s)^2$	2.03	2.19	1.63
Ru	$^5F(4d)^7(5s)^1$	0.00	0.00	0.00
	$^5D(4d)^6(5s)^2$	1.25	1.42	0.87
	$^3F(4d)^8$	2.26	1.69	1.09

number of holes in the d shell increases, and it reaches a maximum value of 184 756, when the d shell is half full.

As has been studied in detail by Shim, Johansen and Dahl 1979 the chemical bond between two Ni atoms is formed when the atoms interact in the $(3d)^9(4s)^1$ configuration. Thus, in the cases of the molecules Ni_2 and Pd_2 the holes in the d shells give rise to $\binom{20}{18} = 190$ Slater determinants. For the molecules Co_2 and Rh_2 this number increases to $\binom{20}{16} = 4845$, and for Fe_2 and Ru_2 to $\binom{20}{14} = 38\ 760$. For the Nb_2 molecule the number is $\binom{20}{8} = 125\ 970$.

It is of course not only practically impossible but also undesirable to perform HF calculations on all the states arising from the large numbers of Slater determinants. Since our goal is determination of all the low-lying electronic states of the molecules investigated, we have chosen to perform HF or hyper-HF (HHF) calculations as introduced by Slater et al. 1969 to derive unique sets of molecular orbitals suitable for utilization in CI calculations to describe all the low-lying states. This procedure, of course, does not provide the optimum description of each state individually, but we believe it results in balanced descriptions of the many low-lying states.

For all the open shell molecules we have performed HF or HHF calculations in search for wave functions that could describe bound molecules, that is, the total energies of the molecules at reasonable internuclear distances should be lower than the sum of the energies of the free atoms in their ground terms. As a starting point we have chosen to doubly occupy the $s\sigma_g$ molecular orbital originating from the combination of the outermost s orbitals of the two atoms. Of the many possible configurations arising because of the d orbital part of the wave functions, there are two fundamentally different types. In one type the bonding molecular orbitals are first fully occupied, and the remaining electrons are then distributed in the antibonding orbitals. In the second type the electrons are distributed evenly in the bonding and in the antibonding orbitals; such an arrangement is required for a correct description of the molecules in the dissociation limit, and it also allows the electrons to localize around the nuclei. For all the open shell transition metal dimers investigated, it turned out that only wave functions with equal numbers

◊ a) Center of gravity of each multiplet has been derived from data of C. E. Moore, Nat. Bur. Stand. Circ. No. 467 (U.S. GPO, Washington, D.C. 1952, 1958) vols. 2 and 3. – b) Preset work. – c) Results of Numerical HF calculations by Martin and Hay 1981.

of electrons in bonding and antibonding molecular orbitals could de-
scribe bound molecules. All the wave functions considered with excess
of electrons in bonding orbitals relative to the antibonding orbitals have
energies far above the dissociation limits of the molecules.

A variety of HF or HHF calculations have been performed for the
transition metal dimers at internuclear distances app. equal to the dis-
tance between nearest neighbours in the bulk metals. The resulting
molecular orbitals have been utilized in CI calculations to describe all the
low-lying electronic states of the molecules. The calculations allowed at
least full reorganization within the valence d shells, ensuring that the d
orbital part of the wave functions is described correctly in the dissocia-
tion limit. The calculations have been performed in the subgroup D_{2h} of
the full symmetry group $D_{\infty h}$ of the transition metal dimers.

Theoretical investigations of transition metal dimers

In the following we present results of ab initio studies of the homonu-
clear dimers consisting of atoms from the first and second transition
metal series. The homonuclear dimers of the first transition metal series
have all been investigated by Harris and Jones 1979 using a local spin
density method, and by Wolf and Schmidtke 1980 using the restricted
HF method. Only occasionally we discuss the results of these investiga-
tions, because both methods are essentially single determinant methods,
and thus unable to describe the physics of the open shell molecules.

»d electron rich« transition metal dimers

Cu₂. The Cu atom has a completely filled 3d shell in its $^1S(3d)^{10}(4s)^1$
ground term, and therefore the Cu_2 molecule represents the simplest
possible transition metal dimer. Unlike other transition metal dimers
there is no ambiguity regarding the electronic ground state which is a $^1\Sigma_g^+$
state. Furthermore, at internuclear distances reasonably close to the
equilibrium distance of the molecule the $^1\Sigma_g^+$ ground state is well de-
scribed in the HF approximation by a single Slater determinant.

As reviewed by Huber and Herzberg 1979, the Cu_2 molecule is the
transition metal dimer for which the equilibrium distance and the vibra-
tional frequency of the electronic ground state have been accurately de-

termined earliest. For this reason and because no low–lying electronic states contribute to the partition function of the Cu_2 molecule the dissociation energy derived from high temperature mass spectrometric data is more reliable for this molecule than for other transition metal dimers.

The Cu_2 molecule has been the subject of many theoretical investigations, and Table III summarizes the spectroscopic data of the molecule as obtained in various calculations with a brief description of the methods used.

The early all-electron ab initio calculations mentioned in Table III employed either minimal basis sets or minimal basis sets with split valence orbitals. The apparent better agreement between the calculated and the experimental spectroscopic data obtained in these investigations relative to those obtained in the more elaborate calculations is fortuitous and stems from basis set superposition errors. However, the calculations by Bachmann et al. 1978, 1980 and by Tatewaki et al. 1980, 1981 were not primarily aimed at studying the Cu_2 molecule, but rather at obtaining basis sets manageable in calculations involving larger clusters.

Some of the difficulties associated with theoretical investigations of transition metal dimers are apparent in Table III, where it is observed that the calculated spectroscopic data vary considerably. Even the most elaborate calculations, which include those of Bauschlicher 1983 involving CI calculations with app. 225 000 functions and also those of Pelissier 1981 involving perturbational CI with contributions from app. 400 000 determinants do not lead to accurate spectroscopic data for the Cu_2 molecule.

The less sophisticated $X\alpha$ type calculations are more successful in deriving spectroscopic constants for the Cu_2 molecule, but these methods are in general only applicable to systems, where the wave functions can be represented by a single Slater determinant as shown by Ziegler 1984. Thus, the $X\alpha$ methods are not suitable for accurate descriptions of the electronic structures of the open shell transition metal dimers that have been the main emphases of our investigations.

The description of the chemical bond in the Cu_2 molecule also differs in the $X\alpha$ and in the HF–CI methods. In the $X\alpha$ methods substantial mixing or hybridization occurs between the 3d and the 4s orbitals. In the HF–CI calculations no such mixing occurs as is illustrated in Table IV, which shows the Mulliken population analyses for the Cu_2 molecule at the experimental internuclear distance. The bond between the two Cu atoms is primarily due to the delocalized doubly occupied $4s\sigma_g$ molecular orbital, and the largest contributions in the CI expansion, apart from the

HF function, arise from angular and left–right correlation of the bonding electrons as discussed in detail by Shim et al. 1983a. The deformation density map in Fig. 1 reveals that the bonding between the two atoms results in a build up of charge in the internuclear region.

Table III.   Experimental and calculated spectroscopic constants for the Cu_2 molecule.

|	Method	Basis set Type; primitive-contracted	Spectroscopic constants		
			r_e(a.u.)	ω_e(cm^{-1})	D_e(eV)
	Experimental		4.1947[1]	264.55[1]	2.04±0.13[2]
	All electron ab initio calculations				
3)	CI(2×2)	STO; minimal + 4d and 4p	4.24		1.75
4)	HF	GTO;(12s,7p,5d)-(5s,3p,2d)	4.43	248	0.84
5)	HF	GTO;(12s,6p,3d)-(4s,2p,1d) optimized	4.48	194	0.42
	HF	GTO;(13s,7p,4d)-(5s,3p,2d)	4.55	220	0.37
6)	MCSCF($4s\sigma_g^2$,$4s\sigma_u^2$)	GTO;(12s,7p,5d)-(5s,3p,2d)	4.61	338	1.16
7)	HF	GTO;(14s,11p,5d)-(8s,6p,2d)	4.54	190	
	HF	GTO;(14s,13p,5d)-(8s,8p,2d)	4.38	210	
8)	HF	GTO;(12s,7p,4d)-(5s,4p,2d)	4.39	252	1.09
	HF	GTO;(14s,10p,7d)-(8s,6p,4d)	4.62	201	0.52
9)	CI	GTO;(12s,9p,4d)-(5s,6p,2d)	4.19	263	1.75
10)	HF	GTO;(14s,11p,6d)-(8s,6p,4d)	4.59		
	HF	GTO;(14s,11p,6d,3f)-(8s,6p,4d.1f)	4.53		
	CI	GTO;(14s,11p,6d)-(8s,6p,4d)	4.42		
	CI	GTO;(14s,11p,6d,3f)-(8s,6p,4d,1f)	4.39		
11)	MCSCF($4s\sigma_g^2$,$4s\sigma_u^2$,$4p\pi_u^2$,$4p\sigma_g^2$)	GTO;(14s,11p,6d,3f)-(8s,6p,4d,1f)	4.62	184	1.25
	CI(SD)	as above	4.42	220	1.51
	CI	as above	4.45	227	1.99
12)	HF	GTO;(14s,11p,6d)-(6s,5p,3d)	4.57	191	0.54
	MCSCF($4s\sigma_g^2$,$4s\sigma_u^2$)	as above	4.68	162	0.83
	HF + rel.perturbations	as above	4.48	206	0.61
	MCSCF + rel. perturbations	as above	4.58	176	0.90
13)	HF	GTO;(14s,11p,6d)-(8s,6p,3d)	4.56	197	0.68
	CI(18×18)	as above	4.62	179	0.83
	CI(378×378)	as above	4.60	186	1.27
	CI(2928×2928)	as above	4.54	200	2.07
14)	HF	GTO;(13s,7p,5d)-(4s,2p,1d)	4.74	155	
	HF	GTO;(13s,7p,5d)-(5s,3p,2d)	4.60	170	
	Pseudopotential calculations				
15)	CI	GTO;(6s,3d)-(2s,2d)	4.20		1.84
16)	MCSCF	GTO;(3s,1p,5d)-(2s,1p,2d)	4.71	282	0.76
	CI	as above	4.40	340	1.30
17)	HF	GTO;(4s,3p,6d)-(3s,2p,3d)	4.54	190	
	CI	as above	4.38	210	
	Xα type calculations				
18)	Xα-SW		4.10	272	2.86
19)	Local spin density		4.30	280	2.30
20)	Xα-LCAO	STO; valence triple zeta	4.23	274	2.30
	Xα-LCAO, relativistic	as above	4.27	268	2.21
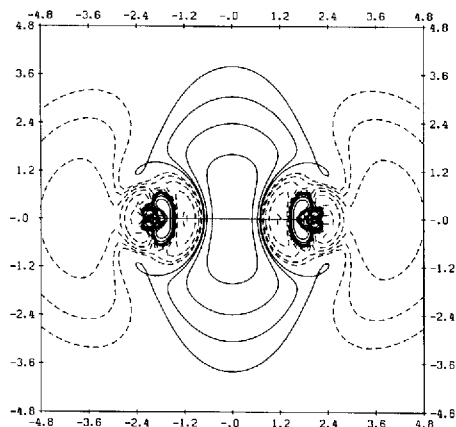
Fig. 1. Deformation density map of the Cu_2 molecule at the internuclear distance 4.1947 a.u. The superpositioned atomic charge densities have been subtracted from the molecular charge density as derived in CI calculations with 18 functions. Solid contours show enhanced electron charge relative to the superpositioned atoms, dashed contours show diminished charge. The smallest contour value is 0.000625 $e/a.u.^3$. Adjacent contours differ by a factor of 2.

The main purpose of our investigation of the Cu_2 molecule was not to derive spectroscopic constants of high accuracy which in any case seem fortuitous, but rather to study the nature of the chemical bond of the molecule. We have carried out CI calculations of various accuracies. The CI calculation with 18 functions allowed full reorganization within the 3d and 4s shells and therefore leads to a correct description of the molecule in the dissociation limit. All other CI calculations performed included additional excitations on top of the full reorganization within the 3d and 4s shells. Thus, the calculation with 378 functions represents complete correlation of the bonding $4s\sigma_g$ electrons within the space spanned by the basis set. Our largest calculation with 2928 functions included selected single and double excitations from the $4s\sigma_g$ and the 3d orbitals.

The calculated spectroscopic constants as derived from the various CI calculations for this simple transition metal dimer have been utilized to estimate the accuracy of the calculated spectroscopic data of the much more complicated open shell transition metal dimers for which experimental data are more scarce.

1) Huber and Herzberg 1979. – 2) D^o_o, Gingerich 1980. – 3) Joyes and Leleyter 1973. – 4) Bachmann, Demuynck, and Veillard 1978. – 5) Tatewaki and Huzinaga 1980; Tatewaki, Sakai, and Huzinaga 1981a. – 6) Basch 1980a – 7) Wolf and Schmidtke 1980. – 8) Tatewaki, Sakai, and Huzinaga 1981b. – 9) Witko and Beckmann 1982. – 10) Bauschlicher, Walch, and Siegbahn 1982. – 11) Bauschlicher 1983. – 12) Martin 1983. – 13) Shim and Gingerich 1983a. – 14) Cingi, Clemente, and Foglia 1984. – 15) Dixon and Robertson 1978. – 16) Basch 1980a. – 17) Pelissier 1981. – 18) Ozin, Huber, McIntosh, Mitchell, Norman Jr., and Noodleman 1979. – 19) Harris and Jones 1979. – 20) Ziegler, Snijders, and Baerends 1981.

Table IV. Mulliken population analyses of the valence orbitals
of the Cu$_2$ molecule as derived in CI calculations with 18
functions at the internuclear distance 4.1947 a.u.

Orbital	Overlap population	Orbital analyses			Occupation number
		s	p	d	
$4s\sigma_g$	0.75	0.94	0.04	0.00	1.97
$3d\sigma_g$	0.09	0.00	0.00	1.00	2.00
$3d\pi_u$	0.14	0.00	0.00	2.00	4.00
$3d\delta_g$	0.03	0.00	0.00	2.00	4.00
$3d\delta_u$	-0.03	0.00	0.00	2.00	4.00
$3d\pi_g$	-0.12	0.00	0.00	2.00	4.00
$3d\sigma_u$	-0.08	0.01	0.00	0.99	2.00
$4s\sigma_u$	-0.04	0.01	0.00	0.00	0.03

Ag$_2$. The Ag atom has a ^{1}S(4d)^{10}(5s)^1 ground term that is well separated
from the higher lying terms. Two Ag atoms interact by forming a stable
Ag$_2$ molecule with a closed shell $^1\Sigma_g^+$ ground state. The ground state is
well described in the HF approximation by a single Slater determinant at
the equilibrium internuclear distance.

Just as for the Cu$_2$ molecule, the ground state of the Ag$_2$ molecule is
well characterized experimentally. In Table V we have listed the spec-
troscopic constants for the Ag$_2$ molecule together with a summary of the
calculated values as derived in the various theoretical investigations. It is
noted that the calculated spectroscopic constants differ considerably
from the experimental values. Thus, all the calculated equilibrium dis-
tances are too long even those derived from the calculations that take
relativistic effects into account. It appears that the spectroscopic con-
stants derived from electronic structure calculations of transition metal
compounds with the presently known computational techniques are
questionable in an absolute sense. It is, however, apparent from Table I
that only very little experimental information is available for the second

row transition metal dimers, and therefore we have utilized our calculated spectroscopic constants for the Ag_2 molecule to judge the spectroscopic constants derived in equivalent calculations for the other transition metal dimers of the second transition metal series.

For the Ag_2 molecule we have carried out two sets of CI calculations, Shim and Gingerich 1983a. One set is completely equivalent to some of the calculations performed for the Cu_2 molecule. In these calculations we have included the 18 functions arising from all rearrangements of the electrons within the 4d and the 5s shells. Such wave functions allow correct description of the molecule in the dissociation limit. In the second set of CI calculations with 684 functions we also included all single and double excitations from the 4d and the 5s shells into the lowest lying virtual σ and π orbitals.

Table V. Experimental and calculated spectroscopic constants for the Ag_2 molecule.

	Method	Basis set Type; primitive-contracted	Spectroscopic constants r_e(a.u.)	ω_e(cm^{-1})	D_e(eV)
	Experimental		4.69[1]	192.4[2]	1.65±0.5[3]
	All electron ab initio calculations				
4)	MCSCF($5s\sigma_g^2,5s\sigma_u^2$)	GTO;(19s,11p,8d)-(6s,4p,3d)	5.37	218	0.76
5)	HF	GTO;(17s,13p,8d)-(10s,8p,5d)	5.24	134	0.89
	CI(18×18)	as above	5.32	120	1.05
	CI(684×684)	as above	5.21	134	
6)	HF	STO;(11s,9p,5d)	5.27	129	0.38
	MCSCF	as above	5.41	108	0.67
	CI(6091×6091)	as above	5.15		1.13
7)	HF	GTO;(14s,8p,7d)-(5s,3p,2d)	5.2	120	
	Pseudopotential calculations				
8)	MCSCF($5s\sigma_g^2,5s\sigma_u^2$)	GTO;(3s,1p,5d)-(2s,1p,2d)	5.46	164	0.51
	CI	as above	5.12	226	0.95
	MCSCF($5s\sigma_g^2,5s\sigma_u^2$), relativistic	as above	5.22	222	0.61
	CI, relativistic	as above	4.95	242	1.12
9)	MCSCF($5s\sigma_g^2,5s\sigma_u^2$)	GTO;(3s,2p,5d)-(2s,2p,1d)	5.07	131	0.94
10)	HF	GTO;(8s,4p,5d)-(4s,4p,3d)	5.29	130	
	HF, relativistic	as above	5.16	145	
	Xα type calculations				
11)	Xα-SW		5.37	187	1.56
12)	Xα-LCAO	STO; valence triple zeta	5.05	184	1.73
	Xα-LCAO, relativistic	as above	4.76	203	2.04

1) Srdanov and Pešić 1981. – 2) Huber and Herzberg 1979. – 3) D_0^o, Gingerich 1980. – 4) Basch 1980a. – 5) Shim and Gingerich 1983. – 6) McLean 1983. – 7) Cingi, Clemente, and Foglia 1984. – 8) Basch 1980a. – 9) Basch 1981. – 10) Klobukowski 1983. – 11) Ozin, Huber, McIntosh, Mitchell, Norman Jr., and Noodleman 1979. – 12) Ziegler, Snijders, and Baerends 1981.

Fig. 2. Deformation density map of the Ag_2 molecule at the internuclear distance 5.20 a.u. The superpositioned atomic charge densities have been subtracted from the molecular charge density as derived in CI calculations with 18 functions. Solid contours show enhanced electron charge relative to the superpositioned atoms, dashed contours show diminished charge. The smallest contour value is 0.000625 $e/a.u.^3$. Adjacent contours differ by a factor of 2.
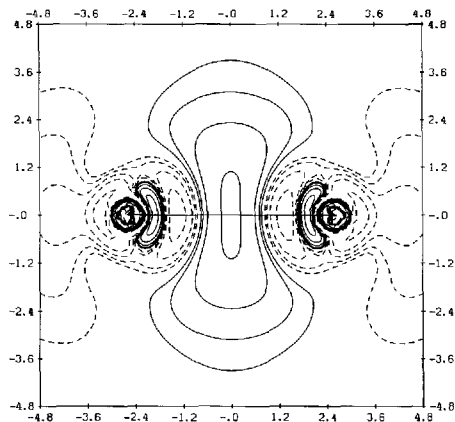
The chemical bond in the Ag_2 molecule resembles that of the Cu_2 molecule considerably. The 4d electrons tend to localize around the individual nuclei and only participate slightly in the formation of the bond. The bond is primarily due to the doubly occupied delocalized $5s\sigma_g$ molecular orbital. This is reflected in the Mulliken population analyses presented in Table VI. It is noted that the overlap population is chiefly due to the $5s\sigma_g$ molecular orbital and, as is the case for the Cu_2 molecule, hardly any hybridization occurs between the s and the d orbitals.

The CI calculations with 684 functions reveal that the major configurations, apart from the HF configuration, originate from double excitations from the $5s\sigma_g$ orbital into the $5p\pi_u$ and $5s\sigma_u$ orbitals. Such configurations are attributed to angular and left-right correlation, respectively, of the bonding $5s\sigma_g$ electrons.

Fig. 2 shows a deformation density map for the Ag_2 molecule at the internuclear distance 5.20 a.u. It is noted that the chemical bond manifests itself through a build up of charge in the region between the two nuclei.

Ni_2. The element just prior to Cu in the periodic system is Ni that has a ground term arising from a non-closed 3d shell. This causes considerable complications in the theoretical investigations of the dimer because it gives rise to many different possibilities for assigning symmetry and configuration of the electronic ground state of Ni_2. As a consequence fewer theoretical investigations have appeared for Ni_2 than for Cu_2 as is evident from Table VII, where we have summarized the spectroscopic constants of the Ni_2 molecule derived in the various calculations.

According to Moore's Tables 1952 the lowest lying level of the Ni atom is $^3F_4(3d)^8(4s)^2$, but after averaging over the spin-orbit components of the lowest lying terms it turns out that the average energy of the $^3D(3d)^9(4s)^1$ term is slightly below that of the $^3F(3d)^8(4s)^2$ term. In our previous work, Shim et al. 1979, we have shown that interaction between two Ni atoms in the $^3F(3d)^8(4s)^2$ term is repulsive, while two Ni atoms interacting in the $^3D(3d)^9(4s)^1$ term results in formation of a stable molecule. The chemical bond in Ni_2 proved to be primarily due to the delocalized doubly occupied $4s\sigma_g$ molecular orbital. The 3d electrons localize around the individual nuclei giving rise to a hole in the 3d shell of each atom. The hole can be in an orbital of either σ, π, or δ symmetry, and the low-lying electronic states of Ni_2 can be characterized by the symmetry of the holes.

The results presented below have been derived in a new investigation of the Ni_2 molecule. The new results confirm our earlier work as to the description of the chemical bond and also regarding the existence of a

Table VI. Mulliken population analyses of the valence orbitals of the Ag_2 molecule as derived in CI calculations with 18 functions at the internuclear distance 5.20 a.u.

Orbital	Overlap population	Orbital analyses			Occupation number
		s	p	d	
$5s\sigma_g$	0.66	0.93	0.04	0.00	1.95
$4d\sigma_g$	0.10	0.00	0.00	1.00	2.00
$4d\pi_u$	0.09	0.00	0.00	2.00	4.00
$4d\delta_g$	0.01	0.00	0.00	2.00	4.00
$4d\delta_u$	-0.01	0.00	0.00	2.00	4.00
$4d\pi_g$	-0.07	0.00	0.01	1.99	4.00
$4d\sigma_u$	-0.08	0.01	0.01	0.98	2.00
$5s\sigma_u$	-0.05	0.02	0.00	0.00	0.05

Table VII. Experimental and calculated spectroscopic constants of the Ni$_2$ molecule

Method	Basis set Type; primitive-contracted	State	Spectroscopic constants		
			r_e(a.u.)	ω_e(cm^{-1})	D_e(eV)
Experimental			4.16[3]	380.9[2]	2.38[1]
All electron ab initio calculations					
[4] CI(252×252)	GTO; (14s,11p,5d)-(8s,6p,3d)	$^1\Sigma_g^+(\delta\delta)$	4.15	289	1.76
[5] CI	GTO;(12s,6p,4d)-(5s,2p,1d)	$^1\Gamma_g(\delta\delta)$	4.46		0.52
[6] Restricted HF	GTO;(14s,11p,5d)-(8s,6p,2d)	$^1\Sigma_g^+$	4.31	240	
[7] CI (252×252)	GTO;(14s,11p,6d)-(8s,6p,3d)	$^1\Sigma_g^+(\delta\delta)$	4.68	185	0.95
CI (3219×3219)	as above	$^1\Sigma_g^+(\delta\delta)$	4.67	186	
Pseudopotential calculations					
[8] CI (GVB)	GTO;(4s,4p,5d)-(3s,2p,2d)	$^1\Gamma_g(\delta\delta)$	3.86	344	2.93
[9] CI	GTO;(4s,2p,5d)-(4s,2p,2d)		4.27		1.88
Xα type calculations					
[10] Local spin density		$^3\Sigma_g^-$	4.12	320	2.70
[11] Xα-LCAO	GTO;(14s,10p,6d,1f)	$^3\Pi_u$	3.84	356	2.91

1) D_0^o from Kant 1964. – 2) Ahmed and Nixon 1979. – 3) Morse, Hansen, Langridge-Smith, Zheng, Geusic, Michalopoulos, and Smalley 1984. – 4) Shim, Dahl, and Johansen 1979. – 5) Wood, Doran, Hillier, and Guest 1980. – 6) Wolf and Smidtke 1980. – 7) Present work. – 8) Upton and Goddard 1978. – 9) Noell, Newton, Hay, Martin, and Bobrowicz 1980. – 10) Harris and Jones 1979. – 11) Dunlap and Yu 1980.

»band« consisting of 30 low-lying electronic states, but some of the states in the middle of the »band« have been reversed. The calculated spectroscopic constants deviate from those of our previous work. This is not surprising since the spectroscopic constants are very sensitive to the calculational details as has been noted for Cu$_2$.

In connection with the present work we have added a diffuse d function to the basis set of the Ni atom, and we have also carried out a counterpoise correction analysis as suggested by Kolos 1979. This has shown that basis set superposition errors are negligible in the present investigation.

HF calculations on Ni$_2$ at the internuclear distance 4.709 a.u. showed that states with holes in localized σ, π, or δ orbitals of each of the two atoms all have energies below the sum of the separated atoms. In the molecular orbital picture these states are arising from holes in the orbital
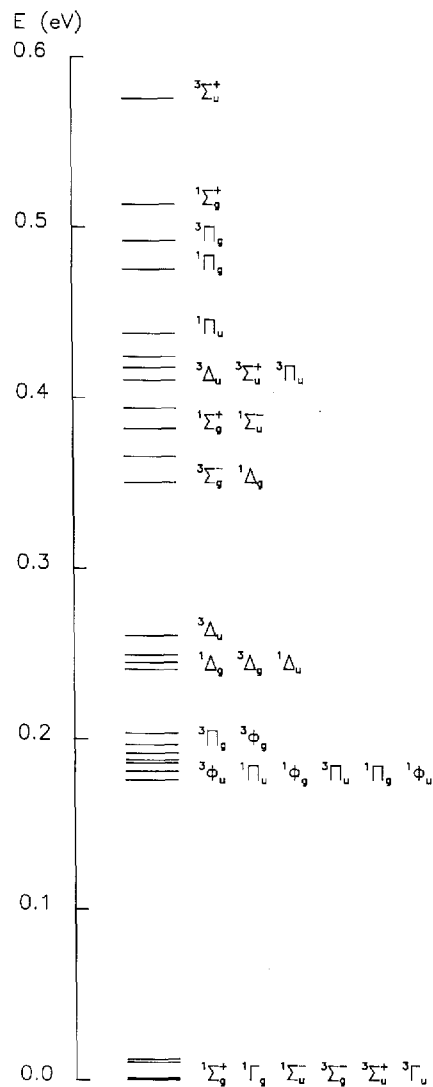
pairs $3d\sigma_g, 3d\sigma_u$ or $3d\pi_u, 3d\pi_g$ or $3d\delta_g, 3d\delta_u$, respectively. We have utilized the molecular orbitals from the three above-mentioned configurations in CI calculations to describe all the low-lying electronic states of the Ni_2 molecule. It turned out that the inclusion of the diffuse d function in the basis set caused the sequence of the low-lying electronic states resulting from the CI calculations to be dependent on the state chosen for optimization of the molecular orbitals. However, the CI calculations based on the molecular orbitals optimized for the $(\delta\delta)$ hole state gave rise to the lowest total energies, and therefore we report only the results of these calculations.

Figs. 3 and 4 show results of CI calculations allowing full reorganization within the 3d and 4s shells. In Fig. 3 the 30 low-lying electronic states of the Ni_2 molecule are depicted at the nearest neighbour internuclear distance in bulk Ni, 4.709 a.u. Table VIII reveals the 3d shell configurations of the low-lying states. It is noted that the 6 lowest lying states all have a hole in the $3d\delta$ subshell of each of the two atoms. After that follows 8 states with a hole in the $3d\delta$ orbital of one atom and in the $3d\pi$ orbital of the other atom. Thereafter 4 states with holes in the $3d\delta$ and in $3d\sigma$ orbitals of the two atoms, respectively. Then 6 $(\pi\pi)$ hole states followed by 4 $(\pi\sigma)$ hole states, and finally at the highest energies the 2 $(\sigma\sigma)$ hole states. From Table VIII it is also seen that mixing of states originating from holes with different symmetries is negligible. Fig. 4 shows the potential energy curves obtained by fitting the calculated points of the

Table VIII. Energy ranges and the d shell configuration for low-lying states of Ni_2 at the internuclear distance 4.709 a.u.

Energy range (eV)	States	d shell population		
		σ	π	δ
0.000 - 0.012	${}^1\Sigma_g^+, {}^1\Gamma_g, {}^1\Sigma_u^-, {}^3\Sigma_g^-, {}^3\Sigma_u^+, {}^3\Gamma_u$	4.00	8.00	6.00
0.176 - 0.203	${}^3\Phi_u, {}^1\Pi_u, {}^1\Phi_g, {}^3\Pi_u, {}^1\Pi_g, {}^1\Phi_u, {}^3\Pi_g, {}^3\Phi_g$	4.00	7.00	7.00
0.241 - 0.261	${}^1\Delta_g, {}^3\Delta_g, {}^1\Delta_u, {}^3\Delta_u$	3.00	8.00	7.00
0.350 - 0.418	${}^3\Sigma_g^-, {}^1\Delta_g, {}^1\Sigma_g^+, {}^1\Sigma_u^-, {}^3\Delta_u, {}^3\Sigma_u^+$	4.00	6.00	8.00
0.424 - 0.492	${}^3\Pi_u, {}^1\Pi_u, {}^1\Pi_g, {}^3\Pi_g$	3.00	7.00	8.00
0.513 - 0.576	${}^1\Sigma_g^+, {}^3\Sigma_u^+$	2.00	8.00	6.00

Fig. 3. Relative energies in eV of the 30 low-lying states of the Ni$_2$ molecule at the internuclear distance 4.709 a.u. States are listed in order of increasing energy.

E (eV)

0.6 — $^3\Sigma_u^+$

0.5 — $^1\Sigma_g^+$
      — $^3\Pi_g$
      — $^1\Pi_g$

      — $^1\Pi_u$

0.4 ≡ $^3\Delta_u$ $^3\Sigma_u^+$ $^3\Pi_u$
    — $^1\Sigma_g^+$ $^1\Sigma_u^-$

    — $^3\Sigma_g^-$ $^1\Delta_g$

0.3

    — $^3\Delta_u$
    ≡ $^1\Delta_g$ $^3\Delta_g$ $^1\Delta_u$

0.2 — $^3\Pi_g$ $^3\Phi_g$
    ≡ $^3\Phi_u$ $^1\Pi_u$ $^1\Phi_g$ $^3\Pi_u$ $^1\Pi_g$ $^1\Phi_u$

0.1

0.0 ≡ $^1\Sigma_g^+$ $^1\Gamma_g$ $^1\Sigma_u^-$ $^3\Sigma_g^-$ $^3\Sigma_u^+$ $^3\Gamma_u$

potential energies to Morse curves. It is noted that the shapes of the potential energy curves are very similar although the equilibrium distances increase slightly and the vibrational frequencies decrease for the higher lying states.

In Table IX we present the Mulliken population analyses of the valence orbitals of Ni$_2$. The total overlap population is almost entirely due to the $4s\sigma_g$ molecular orbital. The 3d electrons are practically non bonding, and analogous with the Cu$_2$ molecule hardly any mixing of the 3d and the 4s orbitals occurs.

Table IX. Mulliken population analyses of the valence orbitals for the $^1\Sigma_g^+$ ground state of the Ni_2 molecule resulting from CI calculations with 252 functions at the internuclear distance 4.709 a.u.

Orbital	Overlap population	Orbital analyses			Occupation number
		s	p	d	
$4s\sigma_g$	0.70	0.93	0.04	0.00	1.94
$3d\sigma_g$	0.06	0.00	0.00	1.00	2.00
$3d\pi_u$	0.12	0.00	0.00	2.00	4.00
$3d\delta_g$	0.02	0.00	0.00	1.51	3.01
$3d\delta_u$	-0.02	0.00	0.00	1.49	2.98
$3d\pi_g$	-0.11	0.00	0.00	2.00	4.00
$3d\sigma_u$	-0.05	0.01	0.00	0.99	2.00
$4s\sigma_u$	-0.04	0.02	0.00	0.00	0.06
Total	0.68	6.96	12.05	8.98	

A picture of the bonding interaction between two Ni atoms emerges from the calculational results: As the two atoms approach each other an axial symmetry is introduced, and this causes the 3d orbitals to split into σ, π, and δ orbitals associated with different energies. One should expect that the holes in the 3d shells of the Ni atoms would reside in the 3dσ subshells, because this should give rise to the formation of a 3dσ bond at closer approach. However, it turns out that the system is more stable when the holes are localized in the 3dδ subshells. This indicates that each atom experiences the other as a positive unit, and therefore the Ni_2 molecule can be regarded as two Ni^+ ions kept together by the delocalized charge cloud originating from the 4s electrons. The 3d electrons localize around the nuclei, and their interaction can be interpreted as a Heisenberg exchange coupling as discussed by Shim 1980a. The interaction between the 3d electrons gives rise to the small energy splittings between the many low lying potential energy curves. The $^1\Sigma_g^+$

Fig. 4. Potential energy curves of the low-lying electronic states of the Ni_2 molecule as derived in CI calculations.

E(a.u.) +3013 a.u.

-.36

-.37

-.38

$^3\Sigma_u^+$

$^1\Sigma_g^+$

$^3\Pi_u\ ^1\Pi_u\ ^1\Pi_g\ ^3\Pi_g$

-.39

$^3\Sigma_g^-\ ^1\Delta_g\ ^1\Sigma_g^+\ ^1\Sigma_u^-\ ^3\Delta_u\ ^3\Sigma_u^+$

$^1\Delta_g\ ^3\Delta_g\ ^1\Delta_u\ ^3\Delta_u$

$^3\Phi_u\ ^1\Phi_g\ ^1\Pi_u\ ^3\Pi_u\ ^1\Pi_g\ ^1\Phi_u\ ^3\Pi_g\ ^3\Phi_g$

-.40

$^1\Sigma_g^+\ ^1\Gamma_g\ ^1\Sigma_u^-\ ^3\Sigma_g^-\ ^3\Sigma_u^+\ ^3\Gamma_u$

-.41

4   5   6   7 R(a.u)
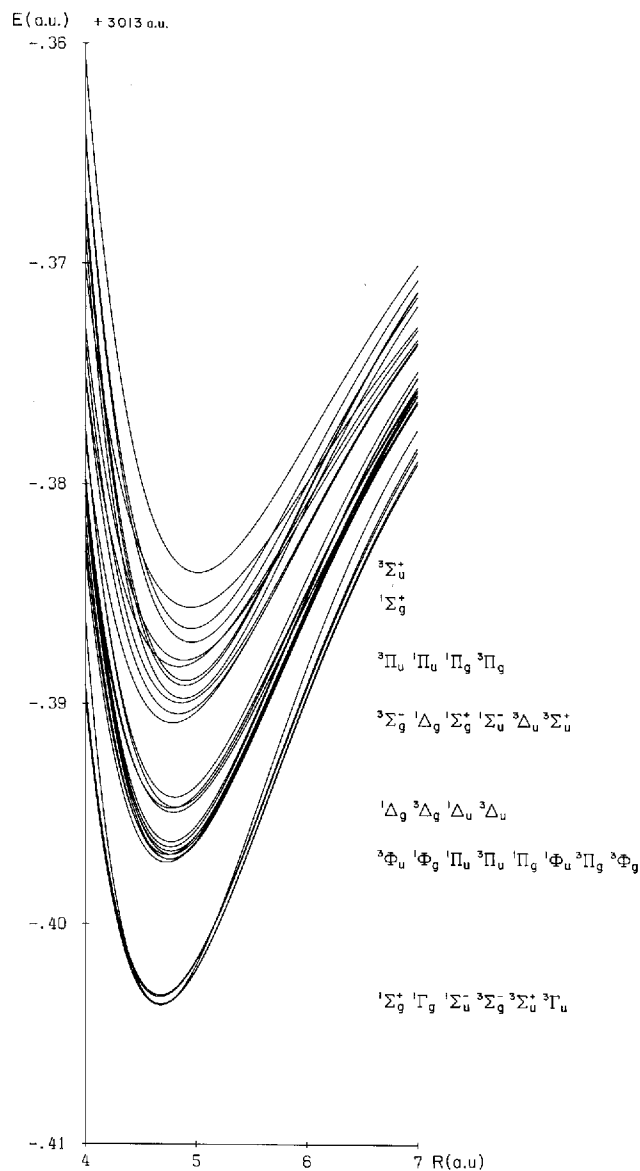
ground state of the Ni_2 molecule has the natural orbital configuration $(3d\sigma_u)^{2.00}(3d\pi_u)^{4.00}(3d\delta_g)^{3.01}(3d\delta_u)^{2.98}(3d\pi_g)^{4.00}(3d\sigma_u)^{2.00}(4s\sigma_g)^{1.94}$ $(4s\sigma_u)^{0.06}$ at the internuclear distance 4.709 a.u.

The $^1\Sigma_g^+$ ground state of the Ni_2 molecule has been investigated further by performing CI calculations which included all single and double excitations into the $4p\sigma_g$, $5s\sigma_g$ and $4p\pi_u$ orbitals from the $4s\sigma_g$ orbital and

Table X. Major configurations of the wave functions describing the $^1\Sigma_g^+$ ground state of the Ni_2 molecule at the internuclear distance 4.709 a.u.

Configuration											Contribution (%) in CI with	
											252	3219
$4s\sigma_g$	$4s\sigma_u$	$3d\sigma_g$	$3d\pi_u$	$3d\delta_g$	$3d\delta_u$	$3d\pi_g$	$3d\sigma_u$	$4p\sigma_g$	$4p\pi_u$	$5s\sigma_g$	configurations	
2	0	2	4	4	2	4	2	0	0	0	49.19	47.92
2	0	2	4	2	4	4	2	0	0	0	47.43	46.07
0	2	2	4	4	2	4	2	0	0	0	1.16	0.72
0	2	2	4	2	4	4	2	0	0	0	1.13	0.70
1	1	2	4	3	3	4	2	0	0	0	0.95	0.59
0	0	2	4	4	2	4	2	0	2	0	-	1.36
0	0	2	4	2	4	4	2	0	2	0	-	1.31

from the 3d shells of the 12 functions having the $4s\sigma_g$ orbital doubly occupied and allowing all rearangements within the 3d shells. This resulted in a CI matrix of dimension 3219.

In Table X we present the major configurations of the wave functions for the $^1\Sigma_g^+$ ground state of Ni_2 as derived in CI calculations at the internuclear distance 4.709 a.u. The two dominating configurations in both calculations account for the localization of the holes in the $3d\delta$ subshells of each atom. This is evident when noting that the two configurations have approximately equal weight and in one configuration the $3d\delta_g$ orbitals are fully occupied while the $3d\delta_u$ orbitals are fully occupied in the other. The two configurations contributing slightly more than 1% in the smaller calculation introduces left-right correlation of the bonding $4s\sigma_g$ electrons. In the larger calculation the angular correlation of the $4s\sigma_g$ electrons is introduced through the configurations derived from double excitations from the $4s\sigma_g$ to the $4p\pi_u$ orbitals. It is noted that the configurations accounting for the angular correlation of the $4s\sigma_g$ electrons contribute more to the wave function than those accounting for the left-right correlation. This is analogous with our findings for the molecules Cu_2 and Ag_2.

Since the electronic states of the Ni_2 molecule are very closely spaced it is evident that spin-orbit coupling might cause considerable mixing of the states. Consequently we have undertaken a study of this effect based on the perturbational Hamiltonian $H^1 = \sum_i \xi(r_i) \, \mathbf{l}_i \cdot \mathbf{s}_i$. The method employed for treating the spin-orbit coupling in the Ni_2 molecule is analogous to that used in our previous work concerning the NiCu molecule, Shim

1980b. We have applied the following approximations: The overlap integrals between 3d orbitals centered at different nuclei have been neglected, since the 3d orbitals are well localized. We have also utilized that hybridization between the 3d, 4s, and 4p orbitals is negligible. Finally, we have assumed that the radial integrals $\xi(r_i)$ arising when evaluating the matrix elements of the spin-orbit coupling operator are all equal, and the value of 603 cm^{-1} for the appropriate radial integral has been taken from work by Laporte and Inglis 1930.

The energies of the LS states have been added to the appropriate diagonal elements of the matrices representing the spin-orbit coupling for each value of Ω, and the spin-orbit coupled states have been derived by diagonalization of the matrices.

As anticipated the spin-orbit coupling causes the low-lying electronic states to mix considerably resulting in a spreading of the »band« of low-lying electronic states. At the internuclear distance 4.709 a.u. all the low-lying states without considering spin-orbit coupling are found in an energy range of app. 0.58 eV. When spin-orbit coupling is taken into account the states cover an energy range of app. 0.84 eV.

Fig. 5 shows the potential energy curves for the spin-orbit coupled states derived by fitting the calculated points of the potential energies to Morse curves. The three lowest lying states in order of increasing energy are 0_g^+, 0_u^- and 5_u. These states are all characterized as having holes in the 3dδ subshells of the two atoms. The higher lying states gradually mix in states originating from different hole symmetries and they can, therefore, not be described by the symmetries of the holes in a simple manner. The spin-orbit coupling does not change the description of the chemical bond in Ni_2. This is not surprising since the effect as treated in the present investigation is basicly atomic.

Table VII reveals that the spectroscopic constants of the Ni_2 molecule derived in our work from 1979 are considerably closer to the experimental values than those derived in our present investigation. This is at least partly due to the basis set superposition errors, which apparently compensate for other deficiencies in our ealier work. The general trends in the calculated spectroscopic constants of the Ni_2 molecule coincide with those of the Cu_2 molecule, that is, the agreement between the calculated and the experimental spectroscopic constants becomes worse as the calculations get more elaborate. The calculated equilibrium distances become too long and the vibrational frequencies too low. Furthermore, only a fraction of the dissociation energy is accounted for.

More important, however, Morse et al. 1984 have recently found the

first experimental evidence in support of the characteristic features of the electronic structures of the transition metal dimers, namely the existence of the many low-lying electronic states. In their spectroscopic studies of the Ni_2 molecule they have found a much higher density of spectroscopic transitions than is usual in a diatomic molecule, and this is considered as confirmation of the large number of low-lying electronic states.

Pd_2. Both experimental and theoretical investigations are very scarce for the Pd_2 molecule. Besides the high temperature mass spectrometric investigations by Gingerich 1967, by Lin et al. 1969a, and by Shim and Gingerich 1984, only matrix isolation study has been reported by Klotzbücher et al. 1980b. These authors claim to have observed the Pd_2 molecule in an Ar matrix, but no spectral assignment whatsoever could be derived from their observations. Previous ab initio studies concerning the Pd_2 molecule are limited to two pseudopotential calculations. Garcia – Prieto et al. 1980 dealt especially with the basis set superposition errors, while Basch et al. 1980b have performed MCSCF calculations for a few of the low-lying states.

The ground term of the Pd atom is the closed shell $^1S(4d)^{10}$ term. In accordance with our expectations the interaction between two Pd atoms in their ground term does not lead to the formation of a stable molecule. However, it has been necessary to carry out a counterpoise correction analysis of our HF results to verify this, Shim and Gingerich 1984.

Formation of a chemical bond between two Pd atoms occurs, when the atoms interact in the $^3D(4d)^9(5s)^1$ term. The interaction between the Pd atoms is very similar to that of the Ni atoms. When the Pd atoms approach each other the 4d orbitals split into σ, π, and δ orbitals with different energies. The split orbitals exchange couple, and this gives rise to the small splittings between the 30 low-lying potential energy curves. At the internuclear distance 5.19788 a.u. which is the nearest neighbour internuclear distance in bulk Pd, the 30 low-lying electronic states cover an energy range of only 0.37 eV as shown in Fig. 6. The 4d electrons localize around the nuclei, and the chemical bond in the Pd_2 molecule is primarily due to the delocalized $5s\sigma_g$ molecular orbital.

Analogous to the electronic structure of Ni_2, the 6 lowest lying states of Pd_2 all have a hole in the $4d\delta$ subshell of each atom. States arising from holes in the $4d\pi$ subshells are found at higher energies, and the highest lying states originate from holes in the $4d\sigma$ subshells. The ground state of the Pd_2 molecule is a $^1\Sigma_g^+$ state, and it has the natural orbital

configuration $(4d\sigma_g)^{2.00}$ $(4d\pi_u)^{4.00}$ $(4d\delta_g)^{3.03}$ $(4d\delta_u)^{2.98}$ $(4d\pi_g)^{3.99}$ $(4d\sigma_u)^{2.00}$ $(5s\sigma_g)^{1.93}$ $(5s\sigma_u)^{0.07}$ at the internuclear distance 5.19788 a.u.

The calculated equilibrium distance and vibrational frequency for the Pd_2 molecule in its $^1\Sigma_g^+$ ground state is 5.30 a.u. and 132 cm^{-1}, respectively. Correction for basis set superposition errors causes the equilibrium distance to increase to 5.49 a.u. and the vibrational frequency to decrease to 104 cm^{-1}.

The calculated equilibrium distance is too long, and on basis of our results for the transition metal dimers Cu_2, Ni_2, and Ag_2 we estimate the true equilibrium distance of Pd_2 to be app. 4.7 a.u. Half of the bond contraction, that is app. 0.3 a.u., will presumably arise from relativistic effects while the other half is attributable to correlation. The magnitude of the relativistic bond contraction is estimated on basis of the relativistic contractions of the 5s orbitals in the second row transition metal series as determined by Desclaux 1973. Ziegler et al. 1981 and Pyykkö et al. 1981 have shown that the relativistic bond contraction is a first order effect and consequently not a result of the orbital contraction. However, the calculational works by Ziegler 1981 on Ag_2 and by McLean 1983 on AgH indicate that the known orbital contractions offer a reasonable measure of the bond contractions.

It is not possible to give a reliable estimate of the true vibrational frequency of the Pd_2 molecule from our calculated value. This is due to the fact that counteracting effects have to be considered. Thus, our calculated vibrational frequency is too low for a Pd_2 molecule dissociating into two Pd atoms in the $^3D(4d)^9(5s)^1$ term, but a real Pd_2 molecule will dissociate into two atoms in the $^1S(4d)^{10}$ ground term, and this will lower the vibrational frequency.

The calculated dissociation energy of Pd_2 is 1.18 eV relative to two Pd atoms in the $^3D(4d)^9(5s)^1$ term, and this value is reduced to 0.93 eV when the basis set superposition errors are taken into account. When the experimental energy splitting between the $^3D(4d)^9(5s)^1$ term and the $^1S(4d)^{10}$ ground term is considered, it turns out that the Pd_2 molecule in our description is unbound by 0.72 eV or 0.97 eV excluding and including corrections for basis set superposition errors, respectively. However, in view of our results for the molecules Cu_2 and Ag_2 we can only expect to account for about half of the dissociation energy of Pd_2 relative to two Pd atoms in the $^3D(4d)^9(5s)^1$ term in our present work. Therefore, it seems likely that more extensive CI calculations based on our sets of molecular orbitals would cause the Pd_2 molecule to be bound relative to two Pd atoms in their $^1S(4d)^{10}$ ground term.
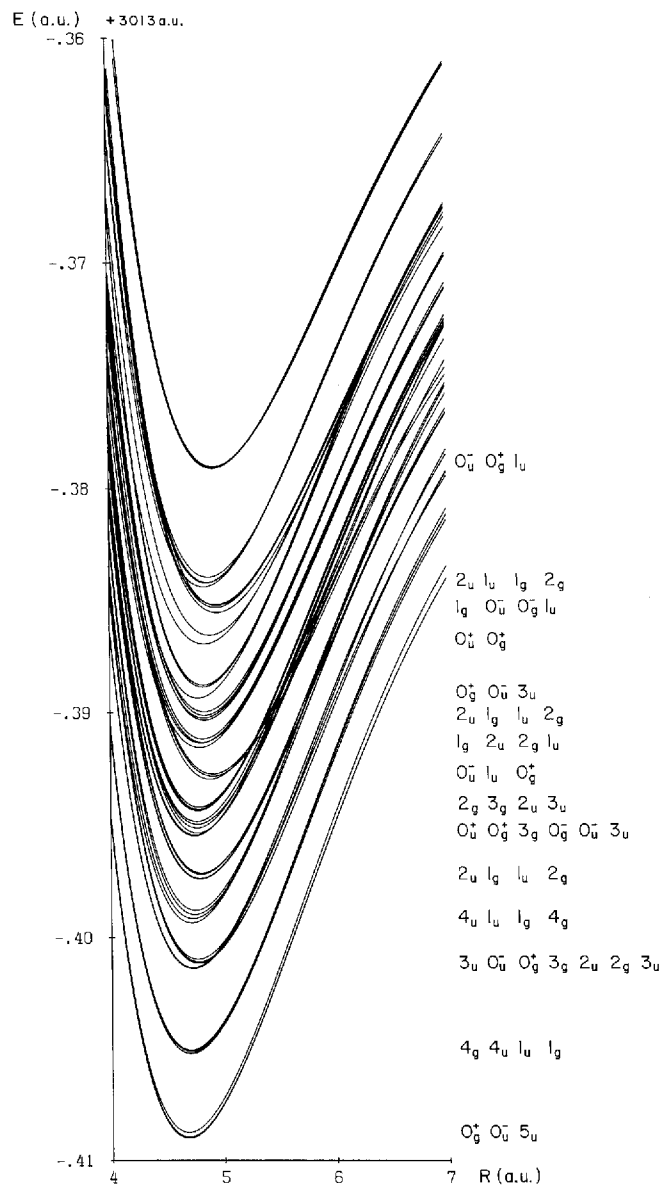
Fig. 5. Potential energy curves of the low-lying electronic states of the Ni_2 molecule taking into account the effect of spin-orbit coupling.
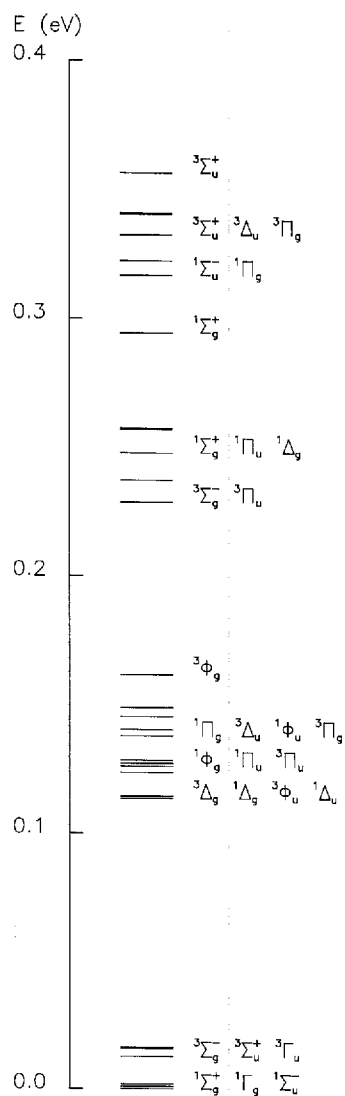

Fig. 6. Relative energies in eV of the 30 low-lying electronic states of the Pd_2 molecule at the internuclear distance 5.19788 a.u. States are listed in order of increasing energy.

In the light of the fact that the more elaborate calculations for the molecules Cu_2 and Ag_2 have not changed the qualitative description of the bonding in these molecules, we believe that our calculations on Pd_2 in general offer an appropriate description of the electronic structure and of the chemical bond in this molecule.

Finally, we have considered the effect of spin-orbit coupling on the low-lying electronic states by applying the same approximations as those described above for the Ni_2 molecule. The »band« of low-lying states is, however, more narrow for Pd_2 than for Ni_2, and the atomic spin-orbit coupling constant is 1412 cm^{-1} for Pd, Laporte and Inglis 1930, relative to 603 cm^{-1} for Ni. Therefore the spin-orbit coupling causes considerable more spreading of the low-lying electronic states for Pd_2 than for Ni_2. At the internuclear distance 5.19788 a.u. the energy range of the »band« of low-lying states changes from app. 0.37 eV to app. 1.17 eV due to spin-orbit coupling. The three lowest lying states in order of increasing energy are 0_g^+, 5_u, 0_u^-, and these states are all characterized by a hole in the $3d\delta$ subshell of each of the Pd atoms. The 0_g^+ and the 0_u^- states consist both of app. equal amounts of the $^1\Sigma_g^+$ and the $^3\Sigma_g^-$ ($\delta\delta$) hole states, while the 5_u state is a pure $^3\Gamma_{u5}$ state. The higher lying states mix considerably and cannot be described by the symmetry of the holes in a simple manner. The spin-orbit coupling as treated in our work is of atomic nature, and it therefore does not change the description of the chemical bond in the Pd_2 molecule.

Co₂. The Co_2 molecule has been observed by Kant and Strauss 1964 in their high temperature mass spectrometric studies. The only experimental data available for Co_2 are the dissociation energy derived by Kant and Strauss 1964 and a vibrational frequency that has been determined in a matrix isolation investigation as quoted by DiLella et al. 1982.

Prior to our theoretical work, Shim and Gingerich 1983b, Harris and Jones 1979 have investigated the Co_2 molecule using a local spin density method. They predicted a $^5\Delta_g$ ground state with the configuration $(3d\sigma_g)^2(3d\pi_u)^4(3d\delta_g)^4(3d\delta_u)^3(3d\pi_g)^2(3d\sigma_u)^1(4s\sigma_g)^2$. They derived the equilibrium distance of the $^5\Delta_g$ state as 3.92 a.u., the vibrational frequency as 360 cm^{-1}, and the dissociation energy as 3.35 eV.

According to Moore's Tables 1952 the ground term of the Co atom is $^4F(3d)^7(4s)^2$. In light of the repulsive interaction between two Ni atoms in the $^3F(3d)^8(4s)^2$ term we presumed that two Co atoms in their ground term also will interact repulsively. However, the Co atom has a

$^4F(3d)^8(4s)^1$ term 0.42 eV above the ground term, and this gives rise to the bonding interaction between the two Co atoms.

Due to the additional hole in the 3d shell of atomic Co relative to Ni it is considerably more difficult to determine the electronic ground state of the Co_2 molecule than of the Ni_2 molecule. As a first attempt we performed HF calculations on the $^5\Delta_g$ state which Harris and Jones have predicted to be the ground state of the Co_2 molecule. Our results have revealed that this state is unbound by app. 0.5 a.u. in the HF approximation.

Of all the configurations we tried out in HF calculations only two had energies below the sum of the energies of the separated atoms. These are $(3d\sigma_g)^1$ $(3d\pi_u)^4$ $(3d\delta_g)^3$ $(3d\delta_u)^3$ $(3d\pi_g)^4$ $(3d\sigma_u)^1$ $(4s\sigma_g)^2$ and $(3d\sigma_g)^2$ $(3d\pi_u)^3$ $(3d\delta_g)^3$ $(3d\delta_u)^3$ $(3d\pi_g)^3$ $(3d\sigma_u)^2$ $(4s\sigma_g)^2$, respectively. Orbitals from both of these configurations have been utilized in CI calculations to describe all low-lying electronic states, but the latter configuration gave rise to the lowest total energies, and only the results based on this configuration are reported.

The molecular orbitals have been utilized in CI calculations that allowed full reorganization within the 3d shells. This insures that the d orbital part of the wave function is described correctly in the dissociation limit. The $4s\sigma_g$ orbital was kept doubly occupied and therefore the total wave functions do not behave correctly in the dissociation limit. This should, however, be of minor importance for the relative energies of the low-lying states at internuclear distances close to the equilibrium distance of the molecule.

Fig. 7 shows all the 84 low-lying electronic states resulting from CI calculations at the internuclear distance 4.72 a.u. The 9 lowest lying states all have holes in orbital pairs 3dδ, 3dπ of each of the two atoms. In the 9 highest lying states the holes are in the 3dδ and in the 3dσ subshells of each of the two atoms, respectively. Most of the remaining states cannot be described by the symmetry of the holes in a simple manner. The interaction between two Co atoms is of a similar nature as the interaction between two Ni atoms. Thus, the chemical bond in Co_2 is mainly due to the delocalized doubly occupied $4s\sigma_g$ molecular orbital. At the internuclear distance 4.72 a.u. the populations in the bonding and in the antibonding 3d orbitals are approximately equal. This indicates that the 3d electrons hardly participate in the bonding, but localize around the nuclei. The interaction between the 3d electrons of the two Co atoms occurs as a Heisenberg exchange coupling resulting in the small energy splittings between the 84 low-lying potential energy curves. Thus, of the 9 lowest lying states all with holes in the orbital pairs 3dδ, 3dπ of each
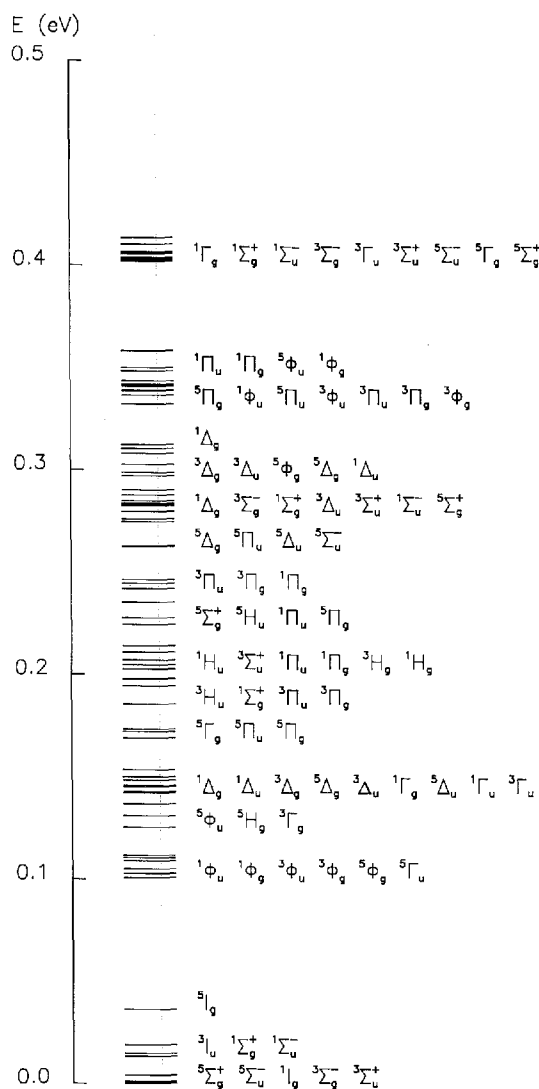
Fig. 7. Relative energies in eV of the 84 low-lying electronic states of the Co_2 molecule at the internuclear distance 4.72 a.u. States are listed in order of increasing energy.
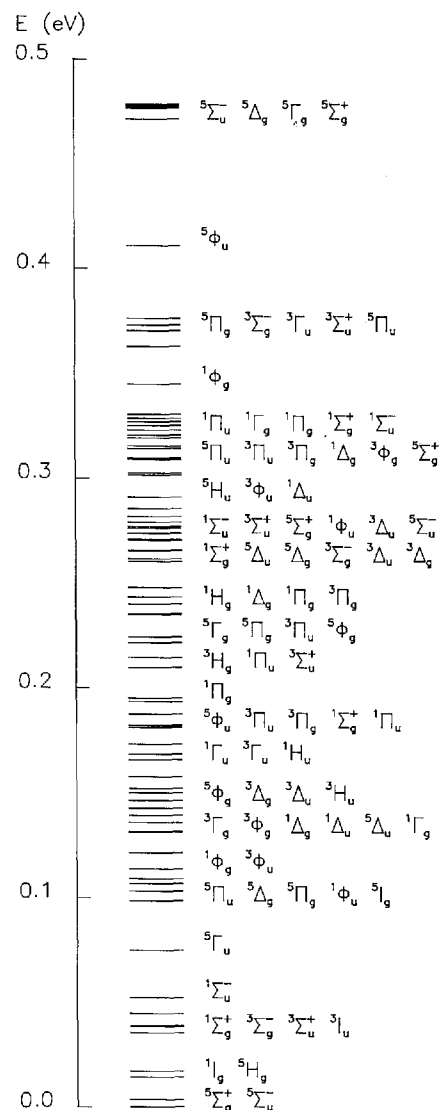
Fig. 8. Relative energies in eV of the 84 low-lying electronic states of the Rh_2 molecule at the internuclear distance 5.082 a.u. States are listed in order of increasing energy.

atom, the Σ states are ferromagnetic coupled while the I states are antiferromagnetic coupled. The exchange coupling constant for the Σ states is 23 cm^{-1} and that for the I states is -43 cm^{-1} at the internuclear distance 4.72 a.u. The 9 highest lying states arising from holes in the orbital pairs $3d\delta$, $3d\sigma$ of each atom are all antiferromagnetic coupled. The exchange coupling constants are -15 cm^{-1} for the Σ^+ states, -8 cm^{-1} for the Σ^- states, and -16 cm^{-1} for the Γ states, respectively.

The spin-orbit coupling which has not been considered for the Co_2 molecule would cause considerable mixing of the low-lying states, but as for Ni_2 and Pd_2 it would not alter the description of the chemical bond.

The $^5\Sigma_g^+$ ground state of Co_2 has been investigated further by performing CI calculations that allowed full reorganization within both the 3d and the 4s shells. The natural orbital configuration of the $^5\Sigma_g^+$ ground state determined in these calculations is $(3d\sigma_g)^{2.00}$ $(3d\pi_u)^{3.09}$ $(3d\delta_g)^{3.02}$ $(3d\delta_u)^{2.98}$ $(3d\pi_g)^{2.91}$ $(3d\sigma_u)^{2.00}$ $(4s\sigma_g)^{1.94}$ $(4s\sigma_u)^{0.06}$ at the internuclear distance 4.72 a.u.

The calculated points of the potential energies for the $^5\Sigma_g^+$ ground state of Co_2 have been fitted to a Morse curve from which we have derived the equilibrium distance as 4.84 a.u. and the vibrational frequency as 162 cm^{-1}. The calculated equilibrium distance is presumably too long by 0.4–0.5 a.u. as is the case for Cu_2 and Ni_2 in equivalent calculations. The calculated vibrational frequency is considerably lower than the experimental value of 290 cm^{-1} quoted by DiLella et al. 1982.

In the present description the dissociation energy relative to two Co atoms in the $^4F(3d)^8(4s)^1$ term is 0.81 eV. but relative to two Co atoms in their $^4F(3d)^7(4s)^2$ ground term the Co_2 molecule is unbound by app. 0.02 eV. However, in the light of our experience with the Cu_2 molecule we are confident that larger CI calculations based on our sets of molecular orbitals would result in a bound Co_2 molecule relative to the atoms in their ground term. Furthermore, it is unlikely that such additional calculations, which would demand considerable resources, would give rise to any significant change in the description of the chemical bond or in the picture of the many low-lying electronic states.

Rh₂. The only experimental investigations of the Rh_2 molecule known are the high temperature mass spectrometric measurements by Gingerich and Cocke 1972, Cocke and Gingerich 1974, and by Piacente et al. 1974. The present work constitutes the first theoretical investigation of the Rh_2 molecule.

According to Moore's Tables 1952 the ground term of the Rh atom is

$^4F(4d)^8(5s)^1$, and therefore no ambiguity arises as to which term gives rise to a bonding interaction. Two Rh atoms interacting in their ground term will lead to the formation of a stable molecule.

In search for a state that would be able to describe a bound molecule, we have performed HF calculations for many different configurations at the internuclear distance 5.082 a.u. which is the nearest neighbour distance in bulk Rh. Only one of the configurations we tried out, namely $(4d\sigma_g)^2(4d\pi_u)^3(4d\delta_g)^3(4d\delta_u)^3(4d\pi_g)^3(4d\sigma_u)^2(5s\sigma_g)^2$ was associated with an energy below the sum of the energies of the separated atoms. It is noted that this configuration is equivalent with the configuration used for optimization of the molecular orbitals for the Co_2 molecule.

The molecular orbitals optimized for the above-mentioned configuration have been utilized in CI calculations to describe all the low-lying states of the Rh_2 molecule. The CI calculations performed are equivalent to those performed for the Co_2 molecule, that is, full reorganization within the 4d shells is allowed, but the $5s\sigma_g$ orbital has been kept fully occupied. In Fig. 8 we show the energies of the 84 low-lying states at the internuclear distance 5.082 a.u.

The 3 lowest lying states $^5\Sigma_g^+$, $^5\Sigma_u^-$, ^1I_g have holes in the orbital pairs $4d\pi$, $4d\delta$ of each of the Rh atoms, and thus they are equivalent to the 3 lowest lying states of the Co_2 molecule. However, contrary to our findings for Co_2 the lowest lying electronic states of the Rh_2 molecule cannot be described as simple Heisenberg exchange couplings. This is clearly recognized from the fact that the energy of the lowest lying $^1\Sigma_g^+$ state is in between those of the lowest lying $^5\Sigma_g^+$ and $^3\Sigma_u^+$ states.

The $^5\Sigma_g^+$ ground state of Rh_2 has been investigated further in CI calculations allowing full reorganization within the 4d as well as the 5s shells. This gave rise to CI matrices of dimension 1084. In an additional set of CI calculations also excitations from the $5s\sigma_g$ into the $5p\pi_u$ orbitals have been included resulting in matrices of dimension 1682.

In Table XI we present the major contributions to the wave functions describing the $^5\Sigma_g^+$ ground state of the Rh_2 molecule. The principal contribution to the chemical bond is due to the delocalized $5s\sigma_g$ molecular orbital. It is noted that the wave function with 1084 configurations introduces left-right correlation of the bonding electrons through double excitations from the $5s\sigma_g$ into the $5s\sigma_u$ orbital. In the largest calculation the left-right correlation of the $5s\sigma_g$ electrons is reduced in favour of the angular correlation. This trend is in agreement with our results for the molecules Cu_2 and Ag_2.

The configurations of the 4d shells have not been specified in detail in

Table XI. Major contributions to the wave functions describing the $^5\Sigma_g^+$ ground state of the Rh_2 molecule at the internuclear distance 5.082 a.u.

Occupations						Contributions in (%) in CI with		
						32	1084	1682
$5s\sigma_g$	$5s\sigma_u$	$5p\pi_u$	$4d\sigma_g+4d\sigma_u$	$4d\pi_u+4d\pi_g$	$4d\delta_g+4d\delta_u$	functions		
2	0	0	4	6	6	97.85	92.77	91.16
2	0	0	3	6	7	1.53	1.52	2.32
1	1	0	4	6	6	-	1.28	0.62
0	2	0	4	6	6	-	1.94	1.29
0	0	2	4	6	6	-	-	3.07

Table XI. If this had been done, it would have revealed that larger contributions stem from configurations with excess of electrons in the bonding 4d orbitals relative to configurations with excess of electrons in the antibonding 4d orbitals. This indicates that the 4d electrons do not localize completely, but to some extent participate in the formation of the chemical bond in the Rh_2 molecule.

The $^5\Sigma_g^+$ ground state of Rh_2 as resulting from the CI calculations with 1084 functions arises from the configuration $(4d\sigma_g)^{1.98} (4d\pi_u)^{3.20} (4d\delta_g)^{3.07} (4d\delta_u)^{2.97} (4d\pi_g)^{2.79} (4d\sigma_u)^{1.98} (5s\sigma_g)^{1.94} (5s\sigma_u)^{0.06}$ at the internuclear distance 5.082 a.u.

The calculated energies for the $^5\Sigma_g^+$ ground state have been fitted to a Morse curve, and the spectroscopic constants have been derived. The equilibrium distance is determined as 5.40 a.u. and the vibrational frequency as 118 cm^{-1}. The calculated dissociation energy is only 0.85 eV as compared to the experimental value of 2.92 eV.

The calculated spectroscopic constants of the Rh_2 molecule are presumably encumbered with similar deficiencies as those of the other transition metal dimers. In analogy with our results for the Ag_2 molecule we estimate the true equilibrium distance of Rh_2 to be in the range 4.7–4.8 a.u.

In the present work we have refrained from treating the spin-orbit

coupling. Due to the participation of the 4d electrons in the bonding the spin-orbit coupling is not solely an atomic effect, and therefore more difficult to treat adequately. It certainly would cause considerable mixing of the low-lying electronic states, but probably not influence the description of the chemical bond significantly.

Fe₂. Of the open shell transition metal dimers the Fe_2 molecule is one of the most widely studied experimentally. Thus, Lin and Kant 1969b, and also Shim and Gingerich 1982 have performed high temperature mass spectrometric measurements to determine the Fe_2^+ / Fe^+ ratios over liquid Fe. Matrix isolation techniques have been utilized in work by de Vore et al. 1975 to obtain a UV-visible spectrum, and by Moskovits and DiLella 1980 to observe resonance Raman spectra. Barrett et al. 1970, McNab et al. 1971, Montano et al. 1976, Montano 1980, and Nagarathna et al. 1983 have investigated the Fe_2 molecule using matrix isolation techniques in conjunction with Mössbauer spectroscopy. Furthermore, Montano and Shenoy 1980, and Purdum et al. 1982 have performed extended X-ray absorption fine structure measurement on Fe and Fe_2 isolated in an Ar and a Kr matrix, respectively.

Nonempirical theoretical calculations have previously been performed by Harris and Jones 1979 using a local spin density approximation. They predicted the ground state of the Fe_2 molecule to be a $^7\Delta_u$ state with the configuration $(3d\sigma_g)^2 (3d\pi_u)^4 (3d\delta_g)^3 (3d\delta_u)^2 (3d\pi_u)^2 (3d\sigma_u)^1 (4s\sigma_g)^2$. From their calculations they derived the equilibrium distance as 3.96 a.u., the vibrational frequency as 390 cm^{-1}, and the dissociation energy as 3.45 eV.

Guenzburger and Saitovitch 1981 have reported results of discrete variational $X\alpha$ type calculations on various electronic configurations of Fe_2 at the internuclear distance 3.53 a.u. These authors compared their calculated hyperfine parameters with the experimental values, and on this basis they concluded that the most likely ground state configuration of Fe_2 is $(3d\sigma_g)^2 (3d\pi_u)^4 (3d\delta_g)^2 (3d\delta_u)^2 (3d\pi_g)^3 (3d\sigma_u)^1 (4s\sigma_g)^2$.

Nagarathna et al. 1983 have performed $X\alpha$-SW calculations on five different configurations of the Fe_2 molecule. The lowest lying state in their calculations is a $^7\Delta_u$ state with the same configuration as found by Harris and Jones, but they find that other configurations give rise to quadrupole splittings in closer agreement with their experimental work.
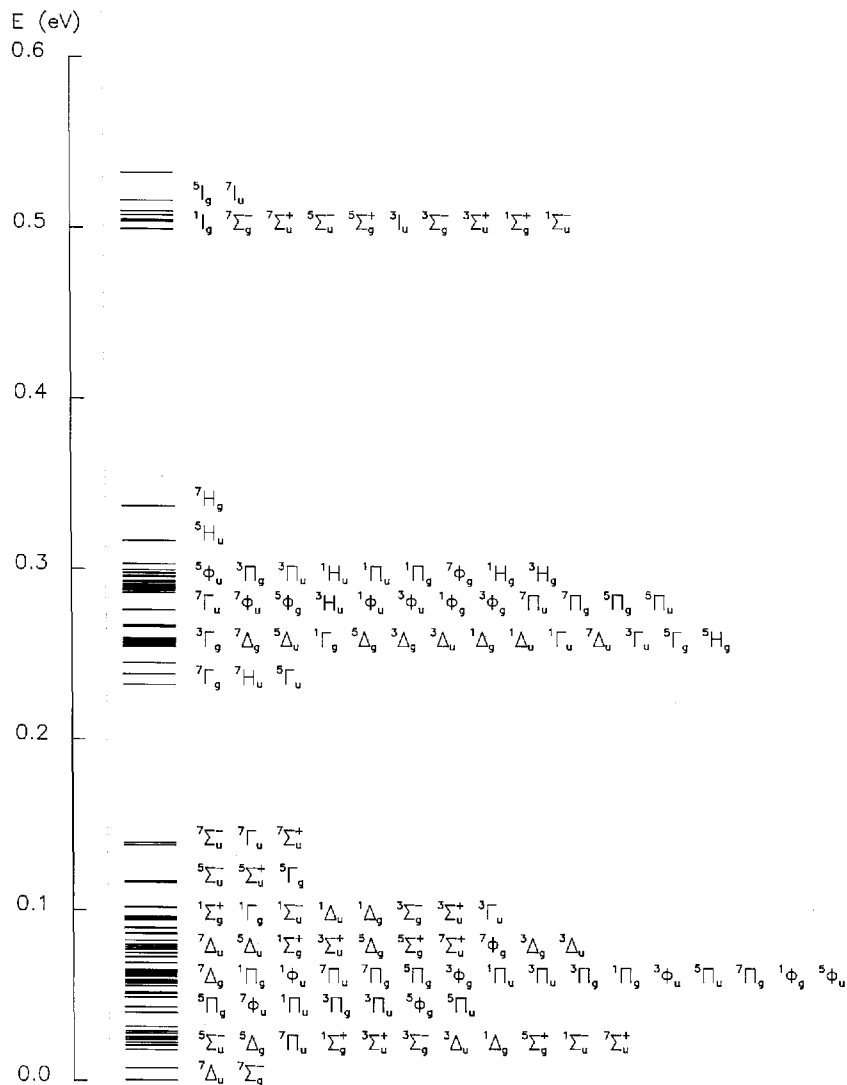
The ground term of the Fe atom is $^5D(3d)^6(4s)^2$. The closed 4s shell of the Fe atom will prevent a bonding interaction between two Fe atoms in their ground term. However, a $^5F(3d)^7(4s)^1$ term is found 0.88 eV above

the ground term, and interaction between two Fe atoms in this term will result in formation of a stable molecule.

In our previous work on Fe_2, Shim and Gingerich 1982, we have employed Wachters' basis set which does not include a diffuse d function for the Fe atom. The molecular orbitals have been optimized for a $^7\Sigma_u^+$ state with the configuration $(3d\sigma_g)^1 (3d\pi_u)^4 (3d\delta_g)^2 (3d\delta_u)^2 (3d\pi_g)^4$ $(3d\sigma_u)^1 (4s\sigma_g)^2$. The resulting orbitals have been utilized in CI calculations that allowed full reorganization within the 3d shells while the $4s\sigma_g$ orbital was kept doubly occupied. The resulting 112 low–lying electronic states are shown in Fig. 9 at the internuclear distance 4.691 a.u. which is the nearest neighbour distance in bulk Fe.

The ground state of the Fe_2 molecule is a $^7\Delta_u$ state with the configuration $(3d\sigma_g)^{1.57} (3d\pi_u)^{3.06} (3d\delta_g)^{2.53} (3d\delta_u)^{2.47} (3d\pi_g)^{2.89} (3d\sigma_u)^{1.49}$ $(4s\sigma_g)^{2.00}$ at the internuclear distance 4.691 a.u. The principal bonding orbital is the delocalized $4s\sigma_g$ molecular orbital. The 3d electrons localize around the nuclei and give rise to the small energy splittings between the potential energy curves. The larger number of holes in the 3d shells of Fe_2 relative to the other transition metal dimers treated give rise to an increasing number of low–lying electronic states, and this of course makes a simple interpretation of the calculational results more difficult. Although the 3d electrons hardly participate in the bonding it is recognized from the configuration of the $^7\Delta_u$ ground state that there is an increased population of the natural orbitals arising from the bonding 3d orbitals relative to those arising from the antibonding 3d orbitals.

Recently we have performed additional calculations on the Fe_2 molecule using a basis set that included a diffuse d function. The molecular orbitals have been optimized for the configuration $(3d\sigma_g)^1 (3d\pi_u)^3$ $(3d\delta_g)^3 (3d\delta_u)^3 (3d\pi_g)^3 (3d\sigma_u)^1 (4s\sigma_g)^2$ and utilized in CI calculations allowing full reorganization within both the 3d and the 4s shells. The new results confirm our previous work as to the description of the chemical bond including the existence of the »band« consisting of 112 low–lying electronic states. The configuration of the $^7\Delta_u$ ground state is $(3d\sigma_g)^{1.50} (3d\pi_u)^{3.08} (3d\delta_g)^{2.72} (3d\delta_u)^{2.59} (3d\pi_g)^{2.78} (3d\sigma_u)^{1.33} (4s\sigma_g)^{1.97}$ $(4s\sigma_u)^{0.03}$ at the internuclear distance 4.691 a.u. It is noted that this configuration is slightly different from that of our earlier work. The net excess of electrons in the bonding 3d orbitals relative to the antibonding 3d orbitals is 0.60 compared to 0.31 in our previous work. This indicates participation of the 3d electrons in the bonding, but the Mulliken population analyses in Table XII reveal that the total overlap population is almost entirely due to the $4s\sigma_g$ orbital.

E (eV)

0.6

0.5 — ^5I_g ^7I_u
^1I_g $^7\Sigma_g^-$ $^7\Sigma_u^+$ $^5\Sigma_u^-$ $^5\Sigma_g^+$ ^3I_u $^3\Sigma_g^-$ $^3\Sigma_u^+$ $^1\Sigma_g^+$ $^1\Sigma_u^-$

0.4

0.3 — ^7H_g
^5H_u
$^5\Phi_u$ $^3\Pi_g$ $^3\Pi_u$ ^1H_u $^1\Pi_u$ $^1\Pi_g$ $^7\Phi_g$ ^1H_g ^3H_g
$^7\Gamma_u$ $^7\Phi_u$ $^5\Phi_g$ ^3H_u $^1\Phi_u$ $^3\Phi_u$ $^1\Phi_g$ $^3\Phi_g$ $^7\Pi_u$ $^7\Pi_g$ $^5\Pi_g$ $^5\Pi_u$
$^3\Gamma_g$ $^7\Delta_g$ $^5\Delta_u$ $^1\Gamma_g$ $^5\Delta_g$ $^3\Delta_g$ $^3\Delta_u$ $^1\Delta_g$ $^1\Delta_u$ $^1\Gamma_u$ $^7\Delta_u$ $^3\Gamma_u$ $^5\Gamma_g$ ^5H_g
$^7\Gamma_g$ ^7H_u $^5\Gamma_u$

0.2

0.1 — $^7\Sigma_u^-$ $^7\Gamma_u$ $^7\Sigma_u^+$
$^5\Sigma_u^-$ $^5\Sigma_u^+$ $^5\Gamma_g$
$^1\Sigma_g^+$ $^1\Gamma_g$ $^1\Sigma_u^-$ $^1\Delta_u$ $^1\Delta_g$ $^3\Sigma_g^-$ $^3\Sigma_u^+$ $^3\Gamma_u$
$^7\Delta_u$ $^5\Delta_u$ $^1\Sigma_g^+$ $^3\Sigma_u^+$ $^5\Delta_g$ $^5\Sigma_g^+$ $^7\Sigma_u^+$ $^7\Phi_g$ $^3\Delta_g$ $^3\Delta_u$
$^7\Delta_g$ $^1\Pi_g$ $^1\Phi_u$ $^7\Pi_u$ $^7\Pi_g$ $^5\Pi_g$ $^5\Phi_g$ $^1\Pi_u$ $^3\Pi_u$ $^3\Pi_g$ $^1\Pi_g$ $^3\Phi_u$ $^5\Pi_u$ $^7\Pi_g$ $^1\Phi_g$ $^5\Phi_u$
$^5\Pi_g$ $^7\Phi_u$ $^1\Pi_u$ $^3\Pi_g$ $^3\Pi_u$ $^5\Phi_g$ $^5\Pi_u$
$^5\Sigma_u^-$ $^5\Delta_g$ $^7\Pi_u$ $^1\Sigma_g^+$ $^3\Sigma_u^+$ $^3\Sigma_g^-$ $^3\Delta_u$ $^1\Delta_g$ $^5\Sigma_g^+$ $^1\Sigma_u^-$ $^7\Sigma_u^+$

0.0 — $^7\Delta_u$ $^7\Sigma_g^-$

Fig. 9. *Relative energies in eV of the 112 low-lying electronic states of the Fe$_2$ molecule at the internuclear distance 4.691 a.u. States are listed in order of increasing energy.*

The potential energies of the $^7\Delta_u$ ground state as obtained in the CI calculations with the different basis sets have been fitted to Morse curves, and the spectroscopic constants of the Fe$_2$ molecule have been derived. The calculations with the smaller basis set resulted in an equilibrium distance of 4.54 a.u. and a vibrational frequency of 204 cm^{-1} while the corresponding values with the larger basis set are 4.99 a.u. and 134

cm^{-1}. The dissociation energy relative to two Fe atoms in the $^5F(3d)^7(4s)^1$ term is 0.69 eV when derived from the calculations with the smaller basis set, but only 0.04 eV based on the calculations with the larger basis set. Relative to two Fe atoms in their ground term the Fe_2 molecule is unbound in both sets of calculations. However, we expect that larger CI calculations would make the molecule bound without changing significantly the description of the chemical bond.

We expect that our calculated equilibrium distance using the smaller basis set, 4.54 a.u., is close to the true equilibrium distance of the Fe_2 molecule, since the experimental equilibrium distance for Ni_2, within the error limits given, has turned out to be identical to our value derived in the equivalent set of calculations. In addition, the deviation of 0.44 a.u. from the calculated value based on the larger basis set is consistent with our findings for the Cu_2 molecule. However, based on extended X-ray absorption fine structure measurements Montano et al. 1980, and Purdum et al. 1982 have derived the equilibrium distance of Fe_2 isolated in

Table XII. Mulliken population analyses of the valence orbitals for the $^7\Delta_u$ ground state of the Fe_2 molecule resulting from a CI calculation with 1152 functions at the internuclear distance 4.691 a.u.

Orbital	Overlap population	Orbital analyses			Occupation number
		s	p	d	
$4s\sigma_g$	0.73	0.93	0.05	0.01	1.97
$3d\sigma_g$	0.06	0.01	0.00	0.74	1.50
$3d\pi_u$	0.14	0.00	0.00	1.54	3.08
$3d\delta_g$	0.03	0.00	0.00	1.36	2.72
$3d\delta_u$	-0.03	0.00	0.00	1.30	2.59
$3d\pi_g$	-0.11	0.00	0.01	1.38	2.78
$3d\sigma_u$	-0.05	0.00	0.00	0.66	1.33
$4s\sigma_u$	0.00	0.01	0.01	0.00	0.03
Total	0.77	6.95	12.07	6.99	

an Ar matrix as only 3.53 a.u. and in a Ne matrix as 3.82 a.u., respectively. These distances appear to be very short perhaps indicating a different structure of Fe_2 in the matrix than in the gas phase.

Montano 1980 has reported the quadrupole splitting of Fe_2 as 4.05 ±0.04 mm/s, and he also found that the electric field gradient at the Fe nucleus is negative. Based on our calculated wavefunctions for the $^7\Delta_u$ ground state of Fe_2 we also estimate that the electric field gradient at the nucleus is negative. The electric field gradient is estimated by assuming that the major contributions are the one-center contributions due to the 3d electrons. It turns out that the one-center contributions from the 3d electrons to the electric field gradient are negative for all the states below 0.09 eV in Fig. 9, whereas they are positive for the highest lying states. Of course, it is necessary to perform accurate calculations to derive numerical values of the electric field gradient and of the quadrupole splitting, since the neglected contribution to the electric field gradient due to core polarization and two-center terms might be sizable as found in the work by Guenzburger and Saitovitch 1981.

To us, however, it appears rather meaningless to argue as to whether the ground state of the Fe_2 molecule is a $^7\Delta_u$ or a $^7\Sigma_g$ state as done by Nagarathna et al. 1983. The spin-orbit coupling that has been neglected in the present work will certainly mix the low-lying electronic states considerably and only leave Ω as a good quantum number.

Ru_2. The ab initio work by Cotton and Shim 1982 is the only known investigation of the Ru_2 molecule.

The ground term of the Ru atom is $^5F(4d)^7(5s)^1$, and two Ru atoms interacting in their ground term will lead to the formation of a stable molecule. HHF calculations revealed two configurations with energies below the sum of the energies of the separated atoms. The molecular orbitals optimized for these configurations: $(4d\sigma_g)^1$ $(4d\pi_u)^3$ $(4d\delta_g)^3$ $(4d\delta_u)^3$ $(4d\pi_g)^3$ $(4d\sigma_u)^1$ $(5s\sigma_g)^2$ and $(4d\sigma_g)^2$ $(4d\pi_u)^2$ $(4d\delta_g)^3$ $(4d\delta_u)^3$ $(4d\pi_g)^2$ $(4d\sigma_u)^2$ $(5s\sigma_g)^2$ have been utilized in CI calculations allowing full reorganization within the 4d shells. Both sets of calculations predict a $^7\Delta_u$ ground state with just slightly different configurations. The lowest energies have been obtained in the calculations based on orbitals optimized for the former configuration, and only these results will be presented.

In Fig. 10 we show the 112 low-lying electronic states resulting from interaction between two ground term Ru atoms at the internuclear distance 5.006 a.u. It is noted that there is a distinct energy gap between the ground state and the low-lying excited states. This has not been found
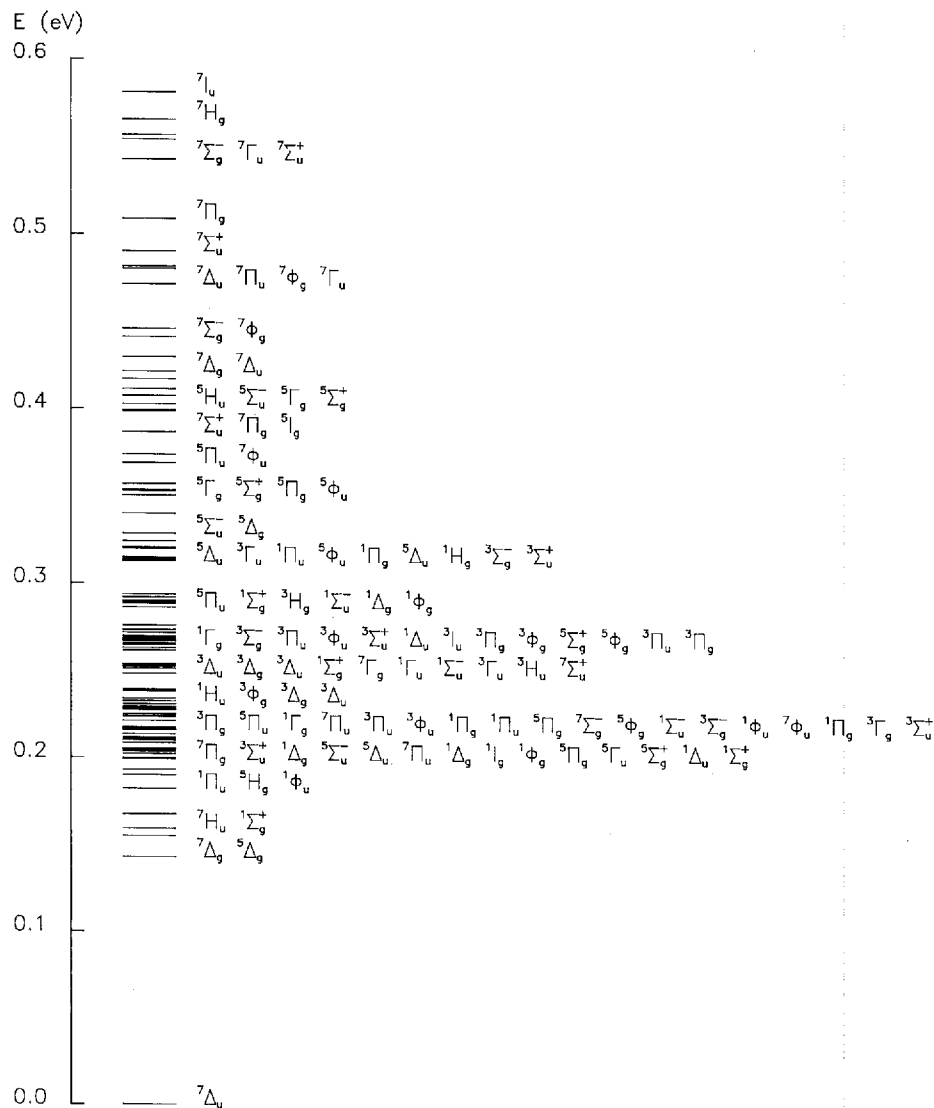
Fig. 10. Relative energies in eV of the 112 low-lying electronic states of the Ru₂ molecule at the internuclear distance 5.006 a.u. States are listed in order of increasing energy.

for any of the other transition metal dimers considered, and it presumably arises from the increased participation of the d electrons in the bond formation.

The $^7\Delta_u$ ground state has been subject to further investigations in CI calculations allowing full reorganization within both 4d and 5s shells.

These CI calculations included 1152 functions, and resulted in a $^7\Delta_u$ ground state with the natural orbital configuration $(4d\sigma_g)^{1.67}$ $(4d\pi_u)^{3.31}$ $(4d\delta_g)^{2.73}$ $(4d\delta_u)^{2.42}$ $(4d\pi_g)^{2.60}$ $(4d\sigma_u)^{1.27}$ $(5s\sigma_g)^{1.94}$ $(5s\sigma_u)^{0.06}$ at the internuclear distance 5.006 a.u.

Analogous with the other transition metal dimers investigated, the chemical bond in the Ru_2 molecule is mainly due to the delocalized $5s\sigma_g$ molecular orbital. However, there is an excess of 1.42 electrons in the natural orbital arising from the 4d bonding relative to the antibonding 4d molecular orbitals. We consider this as a manifestation of the participation of the 4d electrons in the bond formation although it hardly contributes to the overlap population in the Mulliken population analyses.

The calculated points of the potential energies of the $^7\Delta_u$ ground state have been fitted to a Morse curve, and the spectroscopic data have been derived. The equilibrium distance has been determined as 5.13 a.u., the vibrational frequency as 116 cm^{-1}, and the dissociation energy as 0.64 eV.

The calculated spectroscopic constants for the Ru_2 molecule presumably have similar defects as those of the other transition metal dimers. Judging from our results for the Ag_2 molecule we estimate the true equilibrium distance of Ru_2 to be app. 4.5 a.u. This value is quite close to the range 4.25–4.35 a.u. which was found by Bino et al. 1979 to cover the equilibrium distances in various compounds containing the formally Ru_2^{5+} ion. We expect that the calculated vibrational frequency and also the dissociation energy are too low, but we refrain from making any estimates of the true values at this point.

The spin-orbit coupling has not been considered in the present work. This effect, of course, would give rise to mixing of the close lying electronic states. However, contrary to the other open shell transition metal dimers, we expect that the spin-orbit coupling only will have minor effect on the $^7\Delta_u$ ground state of the Ru_2 molecule, since this state is quite well separated from the higher lying states.

The Mn$_2$ molecule

Mn$_2$. Kant et al. 1968 observed of the Mn$_2$ molecule in their high temperature mass spectrometric studies, but already prior to that Nesbet 1964 investigated the molecule theoretically. Nesbet's work represents the very first ab initio investigation performed for any transition metal dimer.

Nesbet utilized a minimal Slater type basis set, but including a 4p function, in his HF calculations on the closed shell $^1\Sigma_g^+$ $(3d\sigma_g)^2$ $(3d\pi_u)^4$ $(3d\delta_g)^4$ $(4s\sigma_g)^2$ $(4s\sigma_u)^2$ state of the Mn_2 molecule. Thereafter, he made use of the optimized molecular orbitals to calculate the energies of other states derived by successive replacement of the bonding 3d orbitals with β spins in the Slater determinant by the corresponding antibonding 3d orbitals with α spins. In this way he achieved localization of some of the 3d electrons around the nuclei, and he identified a $^9\Sigma_g^+(3d\sigma_g)^2$ $(3d\pi_u)^2$ $(3d\delta_g)^2$ $(3d\delta_u)^2$ $(3d\pi_g)^2$ $(4s\sigma_g)^2$ $(4s\sigma_u)^2$ state that was bound by 0.758 eV at the internuclear distance 5.5 a.u.

The configuration of the $^9\Sigma_g^+$ state reveals that the chemical bond in the Mn_2 molecule essentially is due to the delocalized $3d\sigma_g$ molecular orbital. The remaining 3d electrons are localized, and they give rise to a net spin of 2 on each Mn atom. Finally Nesbet determined the molecular ground state by calculating the energies of the states arising when the localized atomic spins were coupled to molecular spin states.

The ground state of the Mn_2 molecule as derived in Nesbet's calculations is a $^1\Sigma_g^+$ state resulting from antiferromagnetic coupling of the localized spins. The equilibrium distance of the molecule was determined as 5.44 a.u., and the dissociation energy as 0.79 eV. Furthermore, he also derived a value for the Heisenberg exchange parameter J in the phenomenological Hamiltonian $-J\mathbf{S}_1\cdot\mathbf{S}_2$ as -8 cm^{-1} at the equilibrium internuclear distance.

Nesbet's predictions of the nature of bonding in the Mn_2 molecule has recently been confirmed by experimental investigations by Van Zee et al. 1981, Rivoal et al. 1982, and by Baumann et al. 1983. In these investigations the exchange coupling constant of Mn_2 has been determined as -8 cm^{-1}, -10.3 cm^{-1}, and -9 cm^{-1}, respectively.

Harris and Jones 1979 have performed calculations on the Mn_2 molecule using a local spin density method. They identified two states with essentially identical energies, namely $^{11}\Pi_u$ $(3d\sigma_g)^1$ $(3d\pi_u)^3$ $(3d\delta_g)^2$ $(3d\delta_u)^2$ $(3d\pi_g)^2$ $(3d\sigma_u)^1$ $(4s\sigma_g)^2$ $(4s\sigma_u)^1$ and $^{11}\Sigma_u^+$ $(3d\sigma_g)^2$ $(3d\pi_u)^2$ $(3d\delta_g)^2$ $(3d\delta_u)^2$ $(3d\pi_g)^2$ $(3d\sigma_u)^1$ $(4s\sigma_g)^2$ $(4s\sigma_u)^1$.
The spectroscopic constants associated with the $^{11}\Pi_u$ state are $r_e=5.03$ a.u., $\omega_e=220$ cm^{-1}, and $D_e=1.25$ eV, and with the $^{11}\Sigma_u^+$ state: $r_e=5.10$ a.u., $\omega_e=210$ cm^{-1}, and $D_e=1.25$ eV. In addition, Wolf and Schmidtke 1980 have performed restricted HF calculations on the closed shell $^1\Sigma_g^+$ state investigated by Nesbet.

None of these later calculations, however, match the physical insight into the bonding of the Mn_2 molecule gained by Nesbet's work.

»d electron deficient« transition metal dimers

Cr_2. The Cr atom has a $^7S(3d)^5(4s)^1$ ground term well separated from the higher lying terms, and therefore, the possible molecular states arising from coupling of the angular momenta of two interacting Cr atoms are limited to $^{13}\Sigma_g^+$, $^{11}\Sigma_u^+$, $^9\Sigma_g^+$, $^7\Sigma_u^+$, $^5\Sigma_g^+$, $^3\Sigma_u^+$, and $^1\Sigma_g^+$. A priori, it is to be expected that the Cr_2 molecule has a $^1\Sigma_g^+$ ground state that is well described by a single Slater determinant with the configuration $(3d\sigma_g)^2$ $(3d\pi_u)^4$ $(3d\delta_g)^4$ $(4s\sigma_g)^2$ corresponding to a »sixtuple« bond between the two atoms.

Such a description would be in accordance with the experimental investigations of the Cr_2 molecule which have revealed, beyond reasonable doubt, that the molecule has an extremely short equilibrium distance, 3.18 a.u. The determination of the equilibrium distance by Efremov et al. 1974, 1978, and especially its confirmation by Michalopoulos et al. 1982, and by Bondybey et al. 1983 have given rise to enhanced activity of the theoretical investigations of the Cr_2 molecule. This is evident from Table XIII, where we have summarized the spectroscopic constants derived in the various calculations together with an abbreviated description of the methods used.

From Table XIII it is noted that two calculations have been reported for the $^1\Sigma_g^+$ $(3d\sigma_g)^2$ $(3d\pi_u)^4$ $(3d\delta_g)^4$ $(4s\sigma_g)^2$ state of Cr_2 in the restricted HF approximation. Wolf and Schmidtke 1980 used a reasonably large basis set consisting of Gaussian type functions, and McLean and Liu 1983 employed an extremely large basis set of Slater type functions. Qualitatively the two calculations are in agreement by resulting in too short bond distances and too high vibrational frequencies. The calculated dissociation energy has not been reported in Wolf and Schmidtke's work, but it would, without doubt, be negative of the same order of magnitude as found by McLean and Liu. In their work the energy associated with the $^1\Sigma_g^+$ $(3d\sigma_g)^2$ $(3d\pi_u)^4$ $(3d\delta_g)^4$ $(4s\sigma_g)^2$ state is app. 19 eV above the dissociation limit of the molecule at the calculated equilibrium distance.

Of the calculations going beyond HF, the one by Goodgame and Goddard 1981 including 1516 functions (GVB without inclusion of van der Waals terms) is almost equivalent with the MCSCF calculations with 3196 functions by Atha and Hillier 1982, and this presumably also holds for the basis sets used. It is noted that the spectroscopic constants derived in the two calculations are in close agreement, but far off the experimental values. As observed by Goodgame and Goddard, the bond in the Cr_2 molecule as resulting from their calculations, is due to an antifer-

le XIII. Experimental and calculated spectroscopic constants of the Cr_2 molecule.

Method	Basis set Type; primitive-contracted	State	r_e (a.u)	ω_e (cm^{-1})	D_e (eV)
Experimental			3.184[3]	~470[2]	1.56[1]
All electron ab initio calculations					
MCSCF(APSG*)	GTO;(13s,7p,5d)-(6s,3p,2d)		3.59		~-4
Restricted HF	GTO;(14s,11p,5d)-(8s,6p,2d)	$^1\Sigma_g^+$	2.95	750	
GVB(1516 functions)	GTO;valence double zeta	$^1\Sigma_g^+$	6.14	70	0.13
GVB(6064 functions)	as above	$^1\Sigma_g^+$	5.78	110	0.35
MCSCF(APSG*)	GTO;(14s,11p,6d)-(8s,6p,3d) + bond centre functions s,p,d	$^1\Sigma_g^+$	3.50	355	-6.76
CI(3196×3196)	as above	$^1\Sigma_g^+$	6.56	58	~0.01
MCSCF(3196 functions)	as above	$^1\Sigma_g^+$	5.93	92	0.14
CI(3520×3520)	GTO;(11s,8p,5d)-(5s,4p,3d) + bond centre functions s,p,d	$^1\Sigma_g^+$	3.27	396	
MCSCF(3088 functions)	GTO;(14s,11p,6d,3f)-(8s,6p,4d,2f)				-1.4
Restricted HF	STO;(9s,6p,4d,3f,2g)		2.784	1181	-19.1
Xα type calculations					
Local spin density		$^{13}\Sigma_g^+$	6.92	55	0.20
Local spin density		$^{11}\Sigma_u^+$	5.37	200	-0.02
Xα-LCAO	GTO;(10s,6p,4d) + bond centre functions s,p,d	$^1\Sigma_g^+$	5.20	110	1.00
Xα-LCAO	as above	$^{13}\Sigma_g^+$	6.92	55	0.20
Local spin density		$^1\Sigma_g^+$	3.21	~450	1.80
Pseudopotential local spin density		$^1\Sigma_g^+$	3.21	470	2.8
Xα-LCAO; $\alpha\rho^{1/3}$-potential	GTO;(14s,11p,7d)-(9s,8p,5d)		4.01	106	1.4
Xα-LCAO;corr. potential	as above		3.72	423	5.0

* Antisymmetric products of strongly orthogonal geminals.

.) D_0^o, Kant and Strauss 1966. – 2) Bondybey and English 1983. – 3) Efremov, Somoilo-
a, and Gurvich 1978. – 4) Wood, Doran, Hillier, and Guest 1980. – 5) Wolf and
chmidtke 1980. – 6) Goodgame and Goddard III 1981. – 7) Atha and Hillier 1982. – 8)
Cok and Hall 1983. – 9) Walch, Bauschlicher Jr., Roos, and Nelin 1983. – 10) McLean
nd Liu 1983. – 11) Harris and Jones 1979. – 12) Dunlap 1983. – 13) Delley, Freeman, and
Illis 1983. – 14) Bernholc and Holzwarth 1983. – 15) Baykara, McMaster, and Salahub
984.

romagnetic coupling of localized spins of 3 on each of the Cr atoms. Thus, not even the 4s orbitals form a bonding molecular orbital at the calculated equilibrium distance. From their calculations, they determined the value of the exchange coupling constant as -93 cm^{-1} at the calculated equilibrium distance.

Kok and Hall 1983 have performed calculations that reproduce quite well the experimentally determined values of the equilibrium distance and the vibrational frequency for Cr_2. However, they do not report any value for the dissociation energy, and without doubt, the Cr_2 molecule is unbound in their description. The nice results obtained in their calculations, most likely, stem from basis set superposition errors combined with an inadequacy of their CI wave function to allow the molecule to dissociate properly into two Cr atoms in the ^7S ground term. The wave function determined by Kok and Hall arises from the natural orbital configuration $(3d\sigma_g)^{1.78}$ $(3d\pi_u)^{3.62}$ $(3d\delta_g)^{3.20}$ $(3d\delta_u)^{0.80}$ $(3d\pi_g)^{0.38}$ $(3d\sigma_u)^{0.22}$ $(4s\sigma_g)^{1.92}$ $(4s\sigma_u)^{0.08}$ at the internuclear distance 3.27 a.u. This configuration is very similar to those derived by Walch et al. 1983 in MCSCF calculations with 3088 functions. Thus, at the internuclear distance 3.0 a.u. their wave function has the natural orbital configuration $(3d\sigma_g)^{1.83}$ $(3d\pi_u)^{3.70}$ $(3d\delta_g)^{3.36}$ $(3d\delta_u)^{0.64}$ $(3d\pi_g)^{0.30}$ $(3d\sigma_u)^{0.16}$ $(4s\sigma_g)^{1.90}$ $(4s\sigma_u)^{0.11}$ and a 3.5 a.u. $(3d\sigma_g)^{1.60}$ $(3d\pi_u)^{3.32}$ $(3d\delta_g)^{2.58}$ $(3d\delta_u)^{1.42}$ $(3d\pi_g)^{0.68}$ $(3d\sigma_u)^{0.39}$ $(4s\sigma_g)^{1.85}$ $(4s\sigma_u)^{0.15}$.

This indicates the similarity of the descriptions of the Cr_2 molecule in Kok and Hall's and in Walch et al.'s calculations, but in Walch et al.'s calculations the Cr_2 molecule is unbound by 1.4 eV.

The $X\alpha$ type calculations also result in diversified values of the spectroscopic constants as is seen from Table XIII.

It is recognized that in spite of the vast amount of theoretical work performed for the Cr_2 molecule no clear picture of the chemical bond in this molecule has emerged. It is possible, however, that internal CI calculations within the 3d and 4s shells, comparable to the calculations done by Goodgame and Goddard 1981 and by Atha and Hillier 1982, will provide a reasonable description of the nature of the chemical bond in the Cr_2 molecule when performed at the experimental internuclear distance.

This would be in agreement with the results obtained for the »d electron rich« transition metal dimers. For the molecules Cu_2 and Ni_2 the calculated spectroscopic constants derived from extensive CI calculations are in reasonable agreement with the experimental values. However, these calculations did not alter the qualitative description of the chemical

XIV. Experimental and calculated spectroscopic constants of the Mo_2 molecule.

Method	Basis set		State	Spectroscopic constants		
	Type; primitive-contracted			r_e(a.u.)	ω_e(cm^{-1})	D_e(eV)
Experimental				3.666[3]	477.1[2]	4.18[1]
All electron ab initio						
MCSCF(APSG*)	GTO;(27s,13p,9d)-(8s,4p,3d)			3.97		~1
CI(3212×3212)	GTO;(27s,13p,9d)-(9s,5p,4d)			3.89	392	
CI(3212×3212)	GTO;(27s,13p,9d)-(9s,5p,4d) + bond centre functions s,p,d			3.72	475	
GVB(6064 functions)	GTO; valence double zeta + 1f		$^1\Sigma_g^+$	3.72	455	1.41
GVB	as above		$^3\Sigma_u^+$	3.91	325	0.60
Restricted HF	GTO;(18s,11p,9d)-(12s,5p,4d)		$^1\Sigma_g^+$	3.48	699	-9.35
	+ bond centre functions 2s,2p,1d					
MCSCF(APSG*)	as above		$^1\Sigma_g^+$	3.82	392	-3.10
CI(3196×3196)	as above		$^1\Sigma_g^+$	3.80	388	0.86
Restricted HF	STO;(11s,8p,6d,3f,2g)		$^1\Sigma_g^+$	3.400	717	-18.1
$X\alpha$ type calculations						
$X\alpha$-SW			$^1\Sigma_g^+$	4.3		
Local spin density			$^1\Sigma_g^+$	3.69	520	4.35
Pseudopotential local spin density			$^1\Sigma_g^+$	3.97	360	4.2
$X\alpha$-LCAO;$\alpha\rho^{1/3}$-potential	GTO;(17s,11p,9d)-(14s,9p,7d)			~5.1	92	0.4
$X\alpha$-LCAO; corr. potential	as above			3.17	441	2.6

★ Antisymmetric products of strongly orthogonal geminals.
1) D_0^0, Gupta, Atkins, and Gingerich 1978. – 2) Efremov, Somoilova, Kozhukhovsky, and Gurvich 1978. – 3) Hopkins, Langridge-Smith, Morse, and Smalley 1983. – 4) Wood, Doran, Hillier, and Guest 1980. – 5) Bursten, Cotton, and Hall 1980. – 6) Goodgame and Goddard III 1982. – 7) Atha, Hillier, and Guest 1980; Atha and Hillier 1982. – 8) McLean and Liu 1983. – 9) Norman, Kolari, Gray, and Trogler 1977. – 10) Delley, Freeman, and Ellis 1983. – 11) Bernholc and Holzwarth 1983. – 12) Baykara, McMaster, and Salahub 1984.

bond derived from internal CI calculations within the 3d and 4s shells. A similar relationship for the »d electron deficient« transition metal dimers still needs to be proven.

Mo_2. Theoretical investigations of the Mo_2 molecule are up against similar difficulties as those encountered in the Cr_2 molecule. Like the Cr

atom, the ground term of the Mo atom is $^7S(4d)^5(5s)^1$ well separated from the higher lying terms. Intuitively, it is to be expected that the ground state of Mo_2 is a $^1\Sigma_g^+$ state, which should be well described in the molecular orbital picture by a one determinant wave function with all valence bonding orbitals fully occupied: $(4d\sigma_g)^2(4d\pi_u)^4(4d\delta_g)^4(5s\sigma_g)^2$. Furthermore, such a description is supported by the experimental findings of the very short bond distance, 3.666 a.u., and the high vibrational frequency, 477.1 cm^{-1}.

However, the data presented in Table XIV reveal that the accurate ab initio calculations based on the above assumptions lead to too short bond distances, too high vibrational frequencies and, more disturbing, the molecule is unbound by 9 eV in the calculations by Atha et al. 1980, 1982, and by 18 eV in McLean and Liu's 1983 calculations, which presumably are very close to the HF limit.

Contrary to the findings for Cr_2, however, reasonable spectroscopic constants have been obtained in the calculations going beyond HF. Basicly, the methods used in these calculations are very much alike, and they also lead to spectroscopic data in quantitative agreement.

Bursten et al. 1980 and Atha et al. 1980, 1982 have optimized their molecular orbitals in MCSCF type calculations, which included selected configurations within the space spanned by the 4d and 5s valence orbitals. Both groups utilized the optimized molecular orbitals in internal CI calculations within the 4d and 5s shells, but including only restricted excitations. Bursten et al. included all single and double excitations from the 64 determinants corresponding to perfect pairing in the GVB method. Atha et al. included all configurations in which the number of electrons in the 4dσ as well as in the 5sσ added up to 2 while those in the 4dπ and in the 4dδ added up to 4. These restrictions reduced the dimension of the CI matrix to 3212 and 3196, respectively, as compared to app. 35 000 for a full internal CI calculation within the 4d and 5s shells.

At the internuclear distance 3.78 a.u. the wavefunction derived by Bursten et al. has the configuration $(4d\sigma_g)^{1.92}(4d\pi_u)^{3.78}(4d\delta_g)^{3.42}$ $(4d\delta_u)^{0.58}(4d\pi_g)^{0.22}(4d\sigma_u)^{0.08}(5s\sigma_g)^{1.88}$ $(5s\sigma_u)^{0.12}$ and that of Atha et al. $(4d\sigma_g)^{1.86}(4d\pi_u)^{3.76}(4d\delta_g)^{3.33}(4d\delta_u)^{0.67}(4d\pi_g)^{0.24}(4d\sigma_u)^{0.14}(5s\sigma_g)^{1.87}$ $(5s\sigma_u)^{0.13}$.

The similarity of the configurations indicates that the wave function determined by Bursten et al. does describe a bound molecule with a dissociation energy similar to that obtained in Atha et al.'s work. The improvement of the spectroscopic data achieved by Bursten et al. by

inclusion of bond centre functions in their basis set probably reflects larger basis set superposition errors.

The calculations by Goodgame and Goddard 1982 are more elaborate than those by Bursten et al. and by Atha et al., but not much different in principle. Their wave functions are constructed by assigning the 4d and 5s electrons pairwise to either doubly occupied bonding orbitals, doubly occupied antibonding orbitals or one in a bonding and the other in the corresponding antibonding orbital. This gives rise to $3^6=729$ spatial configurations, or 1516 spin eigenfunctions for the $^1\Sigma_g^+$ state. On top of this they include excitations from the 5s orbitals into the $5p\sigma$ and the $5p\pi$ orbitals. The resulting wavefunctions consist of 6064 spin eigenfunctions and they are optimized in MCSCF type calculations. The improved spectroscopic constants derived in Goodgame and Goddard's work as compared to those derived by Bursten et al. and by Atha et al. are partly due to the better optimization of the orbitals and partly due to inclusion of correlation of the 5s electrons.

It is gratifying to experience that acceptable spectroscopic constants for the Mo_2 molecule can be derived from conceptually simple wave functions including external correlation only of the 5s electrons. In addition, this certainly implies that the method we have used, that is full internal CI based on molecular orbitals optimized in HHF like calculations, to describe the electronic structure of the »d electron rich« transition metal dimers is appropriate, indeed.

V_2. Recently, Langridge-Smith et al. 1984 have investigated the V_2 molecule spectroscopically in the gas phase. Their results indicate that the molecule has a $^3\Sigma_g^-$ ground state. Furthermore, they determined the equilibrium distance as 3.34 a.u., and the vibrational frequency as 535 cm^{-1}. From evidence of predissociation they derived the dissociation energy as 1.85 eV, and this is considerably less than the value, 2.47 eV, derived from high temperature mass spectrometric measurements.

The first theoretical investigation of the V_2 molecule has been performed by Harris and Jones 1979 using a local spin density method. Their calculations resulted in a $^9\Sigma_u^-$ ground state with the configuration $(3d\sigma_g)^1 (3d\pi_u)^2 (3d\delta_g)^2 (3d\delta_u)^2 (3d\sigma_u)^1 (4s\sigma_g)^2$, but they found numerous other states with similar energies. The calculated spectroscopic constants for the $^9\Sigma_u^-$ state were derived as $r_e=5.01$ a.u., $\omega_e=230$ cm^{-1}, and $D_e=1.00$ eV.

Apparently the experimental results by Langridge-Smith et al. inspired Walch et al. 1983 to perform theoretical investigations of a $^3\Sigma_g^-$

state of V_2. They performed MCSCF type calculations using two different basis sets consisting of Gaussian type functions. Their smaller basis set consisted of (14s, 11p, 6d) primitive functions which they contracted to (8s, 6p, 4d). The larger basis set was derived from the smaller by addition of 3 primitive f functions contracted to 2.

The ground term of the V atom is $^6D(3d)^3(4s)^2$, but the chemical bond in V_2 probably arises from two V atoms interacting in the $^4F(3d)^4(4s)^1$ term that is only 0.25 eV above the ground term. In this case, a simple molecular orbital picture suggests that the V_2 molecule has a $^3\Sigma_g^-$ ground state with the configuration $(3d\sigma_g)^2 (3d\pi_u)^4 (3d\delta_g)^2 (4s\sigma_g)^2$.

In Walch et al.'s MCSCF calculations they constrained the configurations included to those having 4 valence electrons in orbitals of σ symmetry, 2 valence electrons in π_x orbitals, 2 in π_y orbitals, 1 in δ_{xy}, and 1 in $\delta_{x^2-y^2}$. The type of calculations Walch et al. have performed especially takes into account the left-right correlation of the 3d and the 4s electrons.

In the calculations with the smaller basis set the V_2 molecule was found to be bound relative to two V atoms in the $^4F(3d)^4(4s)^1$ term, but not relative to two ground term V atoms. This is, however, achieved in the calculation with the larger basis set. Presumably the two sets of calculations result in very similar descriptions of the chemical bond, but this cannot be judged from the data given.

The spectroscopic constants derived from Walch et al.'s calculations with the larger basis set are in good agreement with the experimental values as to the equilibrium distance and the vibrational frequency. The calculated equilibrium distance is 3.34 a.u., the vibrational frequency is 593.6 cm^{-1}, but the calculated dissociation energy is only 0.33 eV. At the internuclear distance 3.00 a.u. the wave function has the configuration $(3d\sigma_g)^{1.83} (3d\pi_u)^{3.80} (3d\delta_g)^{1.86} (3d\delta_u)^{0.14} (3d\pi_g)^{0.20} (3d\sigma_u)^{0.15} (4s\sigma_g)^{1.93} (4s\sigma_u)^{0.09}$ and at 3.50 a.u. $(3d\sigma_g)^{1.81}(3d\pi_u)^{3.70}(3d\delta_g)^{1.74}(3d\delta_u)^{0.26}(3d\pi_g)^{0.30} (3d\sigma_u)^{0.18} (4s\sigma_g)^{1.93} (4s\sigma_u)^{0.07}$. These configurations indicate considerable participation of the 3d electrons in the bonding.

Thus, as in the case of Mo_2, spectroscopic constants for the V_2 molecule in reasonable agreement with the experimental values have been obtained from conceptually simple wavefunctions.

Nb_2. From high temperature mass spectrometric measurements Gupta and Gingerich 1979 determined the dissociation energy of the Nb_2

molecule to 5.21 eV. Recently Cotton and Shim 1985 have performed a theoretical investigation of the molecule using ab initio methods.

The ground term of the Nb atom is $^6D(4d)^4(5s)^1$, and it is expected that interaction between two Nb atoms in their ground term will result in formation of a stable molecule.

The numerous HF and HHF calculations we have performed at the internuclear distance 5.402 a.u. only revealed two configurations which are associated with energies below the sum of the energies of the separated atoms. These configurations are $(4d\sigma_g)^1$ $(4d\pi_u)^2$ $(4d\delta_g)^1$ $(4d\delta_u)^1$ $(4d\pi_g)^2$ $(4d\sigma_u)^1$ $(5s\sigma_g)^2$ and $(4d\sigma_g)^{1.0}$ $(4d\pi_u)^{1.5}$ $(4d\delta_g)^{1.5}$ $(4d\delta_u)^{1.5}$ $(4d\pi_g)^{1.5}$ $(4d\sigma_u)^{1.0}$ $(5s\sigma_g)^{2.0}$, respectively. The molecular orbitals optimized for the latter configuration have been utilized in CI calculations that allowed full reorganization within the 4d shells.

Fig. 11 shows all 75 low-lying electronic states of the Nb_2 molecule at the internuclear distance 5.402 a.u., which is the nearest neighbour distance in bulk Nb. It is noted that the six lowest lying states are separated from the dense manyfold of higher lying states by an energy gap of app. 0.1 eV. This is of the same order of magnitude as the energy gap separating the ground state from the higher lying states in the Ru_2 molecule. The ground state of the Nb_2 molecule is a $^1\Sigma_g^+$ state with the configuration $(4d\sigma_g)^{1.34}$ $(4d\pi_u)^{2.69}$ $(4d\delta_g)^{1.11}$ $(4d\delta_u)^{0.91}$ $(4d\pi_g)^{1.28}$ $(4d\sigma_u)^{0.67}$ $(5s\sigma_g)^{2.00}$ at the internuclear distance 5.402 a.u. Two other states, $^1\Gamma_g$ and $^1\Sigma_u^-$, lying very close to the ground state arise from almost identical configurations. The lowest lying $^3\Sigma_g^-$ state has the configuration $(4d\sigma_g)^{1.27}$ $(4d\pi_u)^{2.62}$ $(4d\delta_g)^{1.09}$ $(4d\delta_u)^{0.93}$ $(4d\pi_g)^{1.36}$ $(4d\sigma_u)^{0.73}$ $(5s\sigma_g)^{2.00}$, and this is almost identical to the configurations of the lowest lying $^3\Sigma_u^+$ and $^3\Gamma_u$ states. Thus, the six lowest lying states reveal substantial participation of the 4d electrons in the bonding. For the lowest lying singlet states, the excess of electrons in bonding 4d orbitals relative to antibonding 4d orbitals is 2.28, whereas it has decreased to 1.96 electrons for the lowest lying triplet states. Judging from Mulliken population analyses, the principal bonding orbital is the delocalized $5s\sigma_g$ molecular orbital. At 5.402 a.u. this orbital contributes 0.69 out of a total overlap population of 0.81.

The equilibrium distances derived from the calculated potential energy curves for the 75 low-lying states are scattered over app. 1 a.u., ranging from 5.6–6.6 a.u. This is in contrast to the findings for the »d electron rich« transition metal dimers. Thus, for the Pd_2 molecule the corresponding spread of the equilibrium distances is only 0.26 a.u. Due to the

Fig. 11. Relative energies in eV of the 75 low-lying elektronic states of the Nb₂ molecule at the internuclear distance 5.402 a.u. States are listed in order of increasing energy.

E (eV)

1.1

1.0 —————— $^9\Sigma_g^+$

—————— $^9\Pi_u$

0.9 —————— $^9\Sigma_g^+$

—————— $^9\Delta_g$

—————— $^7\Sigma_u^+$

0.8

—————— $^7\Sigma_u^+$ $^7\Pi_g$

—————— $^5\Sigma_g^+$ $^7\Delta_u$

0.7 —————— $^9\Delta_g$

—————— $^3\Sigma_u^+$

—————— $^5\Delta_g$ $^1\Sigma_g^+$ $^5\Pi_u$

0.6 —————— $^1\Pi_g$ $^1\Sigma_u^-$ $^9\Pi_u$ $^5\Sigma_g^+$ $^9\phi_u$

—————— $^3\Pi_g$ $^3\Delta_u$

0.5 —————— $^9\Sigma_g^+$ $^3\Sigma_u^+$ $^9\Gamma_g$ $^1\Delta_g$ $^3\Pi_u$ $^9\Delta_u$

—————— $^9\Sigma_u^-$ $^3\Sigma_g^-$ $^7\Delta_u$ $^7\phi_g$ $^1\Pi_u$

—————— $^5\Pi_g$ $^1\Sigma_g^+$ $^9\Pi_g$ $^7\Pi_g$

0.4 —————— $^5\phi_u$ $^7\Pi_u$

—————— $^5\Sigma_u^-$ $^5\Pi_u$ $^9\phi_g$

—————— $^7\Delta_g$ $^7\Sigma_u^+$ $^7\Gamma_u$ $^3\phi_g$

0.3 —————— $^3\Pi_g$ $^1\phi_u$ $^5\Delta_g$ $^9\Pi_g$ $^7\Sigma_g^-$

—————— $^1\phi_g$ $^1\Pi_u$ $^1\Pi_g$ $^7\phi_u$

—————— $^7\Sigma_g^-$ $^5\Pi_g$ $^3\phi_u$ $^5\phi_g$ $^7\Pi_u$ $^3\Pi_u$

0.2 —————— $^3\Delta_g$ $^1\Delta_u$ $^9\Sigma_u^-$ $^3\Delta_u$ $^5\Delta_u$

—————— $^5\Sigma_u^-$ $^1\Delta_g$ $^5\Sigma_g^+$ $^5\Gamma_g$

0.1

—————— $^3\Sigma_g^-$ $^3\Sigma_u^+$ $^3\Gamma_u$

0.0 —————— $^1\Sigma_g^+$ $^1\Gamma_g$ $^1\Sigma_u^-$
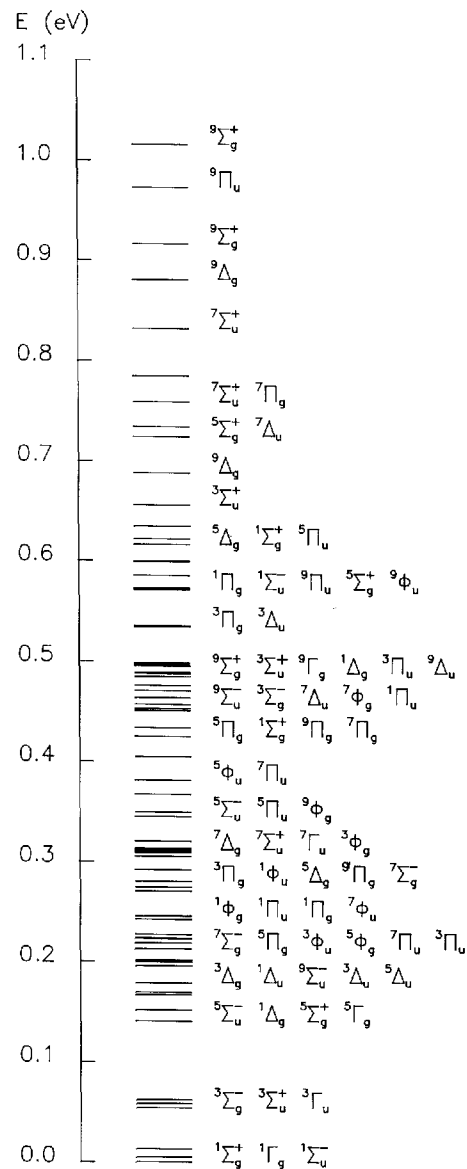
appearence of shoulders in the potential energy curves for the 3 lowest lying states, the calculated potential energies of these states could not with sufficient accuracy be fitted to Morse curves. For the $^1\Sigma_g^+$ and the $^1\Sigma_u^-$ states the shoulders appear at app. 4.8 a.u., and for the $^1\Gamma_g$ state at app. 5.1 a.u. The equilibrium distances for the 3 states are app. 5.6 a.u.

In light of the very short bond distances found experimentally for the

molecules V_2, Cr_2, and Mo_2 we also expect that Nb_2 has a short bond distance. The change in equilibrium distance in going from Cr_2 to Mo_2 is identical with that of going from Cu_2 to Ag_2. If we invoke a similar relationship when going from the V_2 to the Nb_2 molecule we should expect an equilibrium distance of only 3.81 a.u. in Nb_2. This implies, by analogy with our findings for the Ag_2 molecule, that the calculated equilibrium distance for Nb_2 should be app. 4.36 a.u. The calculated equilibrium distance, however, is app. 5.6 a.u.

We expect that the major reason for the shoulders in the potential energy curves as well as for the large discrepancy between the calculated and the expected equilibrium distance is due to the lack of f functions in the basis set. Such functions are required to account properly for the 4d electrons, because they are deeply involved in the bonding.

Based on the simple molecular orbital picture the Nb_2 molecule should have a $^3\Sigma_g^-$ ground state with the configuration $(4d\sigma_g)^2$ $(4d\pi_u)^4$ $(4d\delta_g)^2$ $(5s\sigma_g)^2$. HF calculations reveal that this state does not describe a bound molecule, but it should be noted that the total number of dσ and dδ electrons each add up to app. 2 for the $^1\Sigma_g^+$ ground state, just as the dπ electrons add up to app. 4. Walch et al. 1983 imposed such constraints onto their wavefunctions for the V_2 molecule. In our work no such constraints have been imposed, and therefore the number of electrons associated with each symmetry type is a genuine result of the calculations performed. This implies that the molecular orbital picture offers a useful guidance in determining the ground state of the Nb_2 molecule. A similar result has not been found for the »d electron rich« transition metal dimers, and it still needs to be investigated, if it is valid also for other »d electron deficient« transition metal dimers.

Sc_2. The Sc_2 molecule has been investigated by high temperature mass spectrometry by Verhaegen et al. 1964. However, the dissociation energy derived from the mass spectrometric data appears unreliable, since the original value 1.12 eV derived by Verhaegen et al. later on, without justification, has been changed to 1.65 eV as quoted in Table XV. Lately, the Sc_2 molecule has also been studied by matrix isolation techniques. This has resulted in determination of the ground state vibrational frequency as 238.91 cm^{-1}, and from the ESR studies by Knight et al. 1983 the symmetry of the ground state has been derived as $^5\Sigma$.

The first theoretical investigation of the Sc_2 molecule is a local spin density calculation performed by Harris and Jones 1979. Their calculations resulted in a $^5\Sigma_u^-(3d\sigma_g)^1(3d\pi_u)^2(3d\sigma_u)^1(4s\sigma_g)^2$ ground state with an

equilibrium distance of 5.10 a.u., a vibrational frequency of 200 cm^{-1}, and a dissociation energy of 1.80 eV. Furthermore, they also have reported the spectroscopic constants for a $^3\Sigma_g^-$ $(3d\pi_u)^2$ $(4s\sigma_g)^2$ $(4s\sigma_u)^2$ state as $r_e=6.15$ a.u., $\omega_e=235$ cm^{-1}, and $D_e=1.00$ eV. Harris and Jones 1978 have determined the discrepancies in the local spin density method between the calculated and the experimental energy splittings of atomic states originating from different orbital configurations. Applying this correction to the dissociation energy for the $^5\Sigma_u^-$ state of Sc_2 reduces it to app. 0.4 eV. This is, however, still in disagreement with the results obtained in HF calculations by Wood et al. 1980. They found the $^5\Sigma_u^-$ $(3d\sigma_g)^1$ $(3d\pi_u)^2$ $(3d\sigma_u)^1$ $(4s\sigma_g)^2$ state unbound by app. 2 eV relative to the atomic limit $^2D(3d)^1(4s)^2+{}^4F(3d)^2(4s)^1$. At least for the transition metal dimers, this kind of relationship between dissociation energies derived in HF and Xα type calculations are common, and the reason for the discrepancy is presently not clear.

The most extensive theoretical investigation of the Sc_2 molecule has been carried out by Das 1982 using a pseudopotential method in conjunction with a large valence basis set consisting of Slater type functions. The conclusion of his work is that the Sc_2 molecule is a van der Waals dimer with a binding energy of app. 0.17 eV at the internuclear distance app. 9.4 a.u. His results, of course, are in sharp contrast to the available experimental data for the Sc_2 molecule.

The results by Das were essentially confirmed by Walch and Bauschlicher 1983a. They performed all electron ab initio calculations on a few selected states of the Sc_2 molecule and found that the states dissociating into two $^2D(3d)^1(4s)^2$ ground term Sc atoms were very weakly bound with equilibrium distances of app. 8 a.u. and dissociation energies of app. 0.06 eV. However, they also performed calculations on a $^5\Delta_u$ and a $^5\Sigma_u^-$ state that dissociate into one Sc atom in the $^2D(3d)^1(4s)^2$ ground term and the other in the $^4F(3d)^2(4s)^1$ excited term. Relative to this dissociation limit the $^5\Delta_u$ and the $^5\Sigma_u^-$ states were strongly bound by app. 0.8 eV.

The appearance of the experimental results by Knight et al. 1983 indicating the existence of a bound $^5\Sigma$ state for the Sc_2 molecule influenced Walch and Bauschlicher 1983b to reinvestigate the $^5\Sigma_u^-$ state. In their MCSCF calculations on the $^5\Sigma_u^-$ state they constrained the configurations included to those having a total of 4 valence electrons of σ symmetry and 2 of π symmetry. The optimized molecular orbitals were utilized in CI calculations that allowed single and double excitations from ten selected

.e XV. Experimental and calculated spectroscopic constants of the Sc_2 molecule.

Method	Basis set Type; primitive-contracted	State(atomic limit)	r_e(a.u.)	ω_e(cm^{-1})	D_e(eV)
Experimental				238.91[2]	1.65[1]
All electron ab initio calculations					
MCSCF	GTO;(13s,7p,5d)-(6s,3p,2d)	$^5\Sigma_u^-(^2D(4s^23d^1)+^4F(4s^13d^2))$ 4.86			0.30
CI	as above	$^5\Sigma_u^-(^2D(4s^23d^1)+^4F(4s^13d^2))$ 4.91			1.12
Restricted HF	GTO;(14s,11p,5d)-(8s,6p,2d)	$^1\Sigma_g^+(3d\sigma_g)^2(3d\sigma_u)^2(4s\sigma_g)^2$ 5.76		210	
Restricted HF	as above	$^1\Sigma_g^+(4s\sigma_g)^2(3d\pi_u)^4$ 4.20		360	
CI	GTO;(14s,11p,6d)-(8s,6p,4d)	$^1\Sigma_g^+(^2D(4s^23d^1)+^2D(4s^23d^1))$ ~8			0.045
CI	as above	$^3\Sigma_u^-(^2D(4s^23d^1)+^2D(4s^23d^1))$ ~8			0.045
CI	as above	$^3\Sigma_u^+(^2D(4s^23d^1)+^2D(4s^23d^1))$ ~8			0.029
CI	GTO;(14s,11p,6d,1f)-(6s,6p,3d,1f)	$^3\Sigma_u^+(^2D(4s^23d^1)+^2D(4s^23d^1))$~8			0.046
CI	GTO;(14s,11p,6d)-(8s,6p,4d)	$^5\Delta_u(^2D(4s^23d^1)+^4F(4s^14p^13d^1))$ ~7			0.8
CI	as above	$^5\Sigma_u^-(^2D(4s^23d^1)+^4F(4s^14p^13d^1))$ ~6.5,~7			0.8
CI	GTO;(14s,11p,6d)-(8s,6p,4d)	$^5\Sigma_u^-(^2D(4s^23d^1)+^2D(4s^23d^1))$ 5.27	5.27	184	0.12
CI, corrected	as above	as above	5.27	184	0.44
Pseudopotential calculations					
CI	STO;(3s,3p,4d,1f)	$^1\Sigma_g^+(^2D(4s^23d^1)+^2D(4s^23d^1))$ ~9.4		61	0.17
Xα type calculations					
Local spin density		$^5\Sigma_u^-$	5.10	200	1.80
Local spin density		$^3\Sigma_g^-$	6.15	235	1.00

1) Drowart 1967. – 2) Moskovits, DiLella and Limm 1984. – 3) Wood, Doran, Hillier and Guest 1980. – 4) Wolf and Schmidtke 1980. – 5) Walch and Bauschlicher Jr. 1983a. – 6) Walch and Bauschlicher Jr. 1983b. – 7) Das 1982. – 8) Harris and Jones 1979.

reference configurations. From their calculations they derived an equilibrium distance of 5.27 a.u., a vibrational frequency of 184 cm^{-1}, and a dissociation energy relative to two ground term atoms of 0.12 eV which they corrected to 0.44 eV by taking into account Davidson's correction, correction for errors in the asymptotic limit and also corrections for basis set insufficiencies.

Prior to the appearance of the experimental work by Knight et al. 1983, Wood et al. 1980 suggested a $^5\Sigma_u^-$ ground state of the Sc_2 molecule on basis of their MCSCF and CI calculations. Their calculations, how-

ever, were not convincing by themselves due to errors in the atomic
limit, and substantial superposition errors associated with the basis sets
used.

Conclusion

During the past two decades great efforts have been devoted to experi-
mental and theoretical investigations trying to elucidate the natures of
the chemical bonds in small molecules composed of transition metal
atoms. In the present work we have reviewed the experimental and the
theoretical knowledge of the dimers of the first and second transition
metal series, and in addition, we have presented some new calculational
results for the molecules Ni_2, Fe_2, and Rh_2. At present, it appears that a
unified understanding of the transition metal dimers is emerging from
the combined experimental and theoretical results, which for a long time
have seemed contradictory

By now it must be considered proven that it is extremely difficult,
from ab initio work, to derive spectroscopic constants for the transition
metal dimers, which are in good agreement with the experimental val-
ues. Nevertheless, such good agreements have been achieved for a few
transition metal dimers of the »d electron rich« and recently also of the
»d electron deficient« types. In addition, the theoretical predictions of
the many low-lying electronic states in the Ni_2 molecule have recently
been confirmed by experimental work. Therefore, we are confident that
ab initio methods in general provide physical insight into the complex
chemical bonds of the transition metal dimers. In particular, it appears
that adequate descriptions of the transition metal dimers are obtained in
internal CI calculations involving only the valence d and s shells. Such
calculations do not result in spectroscopic constants of high accuracy,
but for the »d electron rich« transition metal dimers, it appears that the
calculated equilibrium distances deviate systematically from the experi-
mental values. For the »d electron deficient« transition metal dimers the
theoretical data are still too scarce to reach a similar conclusion. In any
case, it is far more difficult to achieve reasonable agreements for these
molecules.

Due to the unfilled d shells of the transition metal atoms, the wave
functions for the dimers usually consist of a large number of Slater
determinants and therefore appear to be very complicated. In spite of

this, however, it has been possible to interpret the wave functions in simple physical pictures.

Thus, the chemical bonds in the »d electron rich« transition metal dimers, Cu_2, Ni_2, Co_2, and Fe_2 are mainly due to the delocalized $4s\sigma_g$ molecular orbitals. The 3d electrons localize around the nuclei and interact through Heisenberg exhange couplings. This gives rise to the small energy splittings between the many low-lying electronic states. The principal bonding orbitals in the corresponding dimers of the second transition metal series are the delocalized $5s\sigma_g$ molecular orbitals. The 4d electrons in Ag_2 and Pd_2 are well localized, but in the sequence Rh_2 to Ru_2 the 4d electrons become increasingly delocalized signifying their participation in the bonding. The d electrons in the »d electron deficient« transition metal dimers are considerably delocalized and strongly involved in the bonding of the molecules. In these molecules the combined contributions to the bonding from the d electrons are comparable to the contributions from the outermost $s\sigma_g$ molecular orbitals.

The chemical bonds in the transition metal dimers cannot be described in a molecular orbital picture, but at least in the case of the Nb_2 molecule, it appears that the simple picture still has a significance.

In summary, accurate spectroscopic constants for the transition metal dimers are not obtained from ab initio calculations, but it appears that the nature of the chemical bonds in such molecules are well described by the conceptually simple wave functions resulting from internal CI calculations within the valence d and s shells.

References

F. Ahmed and E. R. Nixon, J. Chem. Phys. *71*, 3547 (1979).

P. M. Atha, I. H. Hillier, and M. F. Guest, Chem. Phys. Letters *75*, 84 (1980).

P. M. Atha and I. H. Hillier, Mol. Phys. *45*, 285 (1982).

C. Bachmann, J. Demuynck, and A. Veillard, Gazz. Chim. Ital. *108*, 389 (1978).

C. Bachmann, J. Demuynck, and A. Veillard, Faraday Symp. Chem. Soc. *14*, 170 (1980).

P. H. Barrett and T. K. McNab, Phys. Rev. Letters *25*, 1601 (1970).

H. Basch, Faraday Symp. Chem. Soc. *14*, 149 (1980)a.

H. Basch, D. Cohen, and S. Topiol, Isr. J. Chem. *19*, 233 (1980)b.

H. Basch, J. Am. Chem. Soc. *103*, 4657 (1981).

C. A. Baumann, R. J. Van Zee, S. V. Bhat, and W. Weltner, Jr., J. Chem. Phys. *78*, 190 (1983).

C. W. Bauschlicher, Jr., S. P. Walch, and P. E. M. Siegbahn, J. Chem. Phys. *76*, 6015 (1982).

C. W. Bauschlicher, Jr., Chem. Phys. Letters *97*, 204 (1983).

N. A. Baykara, B. N. McMaster, and D. R. Salahub, Mol. Phys. *52*, 891 (1984).

E. D. Becker and G. C. Pimentel, J. Chem. Phys. *25*, 224 (1956).

J. Bernholc and N. A. W. Holzwarth, Phys. Rev. Letters *50*, 1451 (1983).

A. Bino, F. A. Cotton, and T. R. Felthouse, Inorg. Chem. *18*, 2599 (1979).

N. Bohr, Phil. Mag. *26*, 1 (1913); ibid *26*, 476 (1913).

V.. E. Bondybey and J. H. English, Chem. Phys. Letters *94*, 443 (1983).

Ø. Burrau, Kgl. Danske Vid. Selsk. Matt.-Fys. Medd. 7, 14 (1927).

B. E. Bursten and F. A. Cotton, Faraday Symp. Chem. Soc. *14*, 180 (1980).

B. E. Bursten, F. A. Cotton, and M. B. Hall, J. Am. Chem. Soc. *102*, 6348 (1980).

T. A. Cellucci and E. R. Nixon, J. Chem. Phys. *81*, 1174 (1984).

M. B. Cingi, D. A. Clemente, and C. Foglia, Mol. Phys. *53*, 301 (1984).

C. R. Claydon and K. D. Carlson, J. Chem. Phys. *49*, 1331 (1968).

D. L. Cocke and K. A. Gingerich, J. Chem. Phys. *60*, 1958 (1974).

C. Cossé, M. Fouassier, T. Mejean, M. Tranquille, D. P. DiLella, and M. Moskovits, J. Chem. Phys. *73*, 6076 (1980).

F. A. Cotton and I. Shim, J. Am. Chem. Soc. *104*, 7025 (1982).

F. A. Cotton and I. Shim, J. Phys. Chem., *89*, 952 (1985).

G. Das, Chem. Phys. Letters *86*, 482 (1982).

B. Delley, A. J. Freeman, and D. E. Ellis, Phys. Rev. Letters *50*, 488 (1983).

J. P. Desclaux, Atom. Data Nucl. Data Tables *12*, 311 (1973).

D. P. DiLella, W. Limm, R. H. Lipson, M. Moskovits, and K. V. Taylor, J. Chem. Phys. *77*, 5263 (1982).

P. A. M. Dirac, Proc. Roy. Soc. *A123*, 714 (1929).

R. N. Dixon and I. L. Robertson, Mol. Phys. *36*, 1099 (1978).

J. Drowart and R. E. Honig, J. Chem. Phys. *25*, 581 (1956).

J. Drowart and R. E. Honig, J. Phys. Chem. *61*, 980 (1957).

J. Drowart, in »Phase Stability in Metals and Alloys«. Edited by P. S. Rutman, J. Stringer and R. I. Jaffee (McGraw-Hill, New York 1967) pp 305-317.

B. I. Dunlap and H. L. Yu, Chem. Phys. Letters *73*, 525 (1980).

B. I. Dunlap, Phys. Rev. *A27*, 2217 (1983).

Y. M. Efremov, A. N. Samoilova, and L. V. Gurvich, Opt. Spektrosc. *36,* 654 (1974).

Y. M. Efremov, A. N. Samoilova, V. B. Kozhukhovsky, and L. V. Gurvich, J. Mol. Spec. *73,* 430 (1978).

A. Einstein, Ann. Physik *17,* 132 (1905).

V. Fock, Zeit. Physik *61,* 126 (1930).

T. A. Ford, H. Huber, W. Klotzbücher, E. P. Kündig, M. Moskovits, and G. A. Ozin, J. Chim. Phys. *66,* 524 (1977).

J. García-Prieto and O. Novaro, Int. J. Quantum Chem. *18,* 595 (1980).

K. A. Gingerich, Naturwissenschaften *54,* 43 (1967).

K. A. Gingerich and D. L. Cocke, Chem. Commun. 536 (1972).

K. A. Gingerich, Curr. Top. Mat. Sci. *6,* 345 (1980).

M. M. Goodgame and W. A. Goddard III, J. Phys. Chem. *85,* 215 (1981).

M. M. Goodgame and W. A. Goddard III, Phys. Rev. Letters *48.* 135 (1982).

D. W. Green and D. M. Gruen, J. Chem. Phys. *57,* 4462 (1972).

D. Guenzburger and E. M. B. Saitovitch, Phys. Rev. *B24,* 2368 (1981).

S. K. Gupta, R. M. Atkins, and K. A. Gingerich, Inorg. Chem. *17,* 3211 (1978).

S. K. Gupta and K. A. Gingerich, J. Chem. Phys. *70,* 5350 (1979).

J. Harris and R. O. Jones, J. Chem. Phys. *68,* 3316 (1978).

J. Harris and R. O. Jones, J. Chem. Phys. *70,* 830 (1979).

D. R. Hartree, Proc. Cambridge Phil. Soc. *24,* 89 (1928).

W. Heitler and F. London, Zeit. Physik *44,* 455 (1927).

J. B. Hopkins, P. R. R. Langridge-Smith, M. D. Morse, and R. E. Smalley, J. Chem. Phys. *78,* 1627 (1983).

K. P. Huber and G. Herzberg, »Molecular Spectra and Molecular Structure IV, Constants of Diatomic Molecules« (Van Nostrand Reinhold, New York 1979).

F. Hund, Zeit. Physik *51,* 759 (1928).

S. Huzinaga, J. Chem. Phys. *66,* 4245 (1977).

E. A. Hylleraas, Zeit. Physik *65,* 209 (1930).

P. Joyes and M. Leleyter, J. Phys. *B6,* 150 (1973).

A. Kant, J. Chem. Phys. *41,* 1872 (1964).

A. Kant and B. Strauss, J. Chem. Phys. *41,* 3806 (1964).

A. Kant and B. Strauss, J. Chem. Phys. *45,* 3161 (1966).

A. Kant, S.-S. Lin, and B. Strauss, J. Chem. Phys. *49,* 1983 (1968).

A. Kant and S.-S. Lin, J. Chem. Phys. *51,* 1644 (1969).

B. Kleman and S. Lindkvist, Arkiv Fysik *8,* 333 (1954).

B. Kleman and S. Lindkvist, Arkiv Fysik *9,* 385 (1955).

M. Klobukowski, J. Comp. Chem. *4,* 350 (1983).

W. E. Klotzbücher and G. A. Ozin, Inorg. Chem. *16,* 984 (1977).

W. E. Klotzbücher and G. A. Ozin, Inorg. Chem. *19,* 2848 (1980)a.

W. E. Klotzbücher and G. A. Ozin, Inorg. Chem. *19,* 3767 (1980)b.

L. B. Knight Jr., R. J. Van Zee, and W. Weltner, Jr., Chem. Phys. Letters *94,* 296 (1983).

R. A. Kok and M. B. Hall, J. Phys. Chem. *87,* 715 (1983).

W. Kolos, Theoret. Chim. Acta (Berlin) *51,* 219 (1979).

P. R. R. Langridge-Smith, M. D. Morse, G. P. Hansen, R. E. Smalley and A. J. Merer, J. Chem. Phys. *80,* 593 (1984).

O. Laporte and D. R. Inglis, Phys. Rev. *35,* 1337 (1930).

S.-S. Lin, B. Strauss, and A. Kant, J. Chem. Phys. *51,* 2282 (1969)a.

S.-S. Lin and A. Kant, J. Phys. Chem. *73*, 2450 (1969)b.

R. L. Martin and P. J. Hay, J. Chem. Phys. *75*, 4539 (1981).

R. L. Martin, J. Chem. Phys. *78*, 5840 (1983).

A. D. McLean, J. Chem. Phys. *79*, 3392 (1983).

A. D. McLean and B. Liu, Chem. Phys. Letters *101*, 144 (1983).

T. K. McNab, H. Micklitz, and P. H. Barrett, Phys. Rev. *B4*, 3787 (1971).

D. L. Michalopoulos, M. E. Geusic, S. G. Hansen, D. E. Powers, and R. E. Smalley, J. Phys. Chem. *86*, 3914 (1982).

P. A. Montano, P. H. Barrett, and Z. Shanfield, J. Chem. Phys. *64*, 2896 (1976).

P. A. Montano, Faraday Symp. Chem. Soc. *14*, 79 (1980).

P. A. Montano and G. K. Shenoy, Solid State Comm. *35*, 53 (1980).

C. E. Moore, Natl. Bur. Std. Circ. No. 467 (US Government Printing Office, Washington, D. C., 1949, 1952, 1958), vols 1, 2, and 3.

M. D. Morse, G. P. Hansen, P. R. R. Langridge-Smith, L.-S. Zheng, M. E. Geusic, D. L. Michalopoulos, and R. E.. Smalley, J. Chem. Phys. *80*, 5400 (1984).

M. Moskovits and J. E. Hulse, J. Chem. Phys. *66*, 3988 (1977).

M. Moskovits and D. P. DiLella, J. Chem. Phys. *73*, 4917 (1980).

M. Moskovits, D. P. DiLella, and W. Limm, J. Chem. Phys. *80*, 626 (1984).

R. S. Mulliken, Phys. Rev. *32*, 186 (1928); ibid *32*, 761 (1928).

H. M. Nagarathna, P. A. Montano, and V. M. Naik, J. Am. Chem. Soc. *105*, 2938 (1983).

R. K. Nesbet, Phys. Rev. *A135*, 460 (1964).

J. O. Noell, M. D. Newton, P. J. Hay, R. L. Martin, and F. W. Bobrowicz, J. Chem. Phys. *73*, 2360 (1980).

J. G. Norman, Jr., H. J. Kolari, H. B. Gray, and W. C. Trogler, Inorg. Chem. *16*, 987 (1977).

G. A. Ozin, H. Huber, D. McIntosh, S. Mitchell, J. G. Norman, Jr., and L. Noodleman, J. Am. Chem. Soc. *101*, 3504 (1979).

M. J. Pellin, T. Foosnaes, and D. M. Gruen, J. Chem. Phys. *74*, 5547 (1981).

M. J. Pellin and D. M. Gruen, J. Chem. Phys. *79*, 5887 (1983).

M. Pelissier, J. Chem. Phys. *75*, 775 (1981).

V. Piacente, G. Balducci, and G. Bardi, J. Less-Comm. Met. *37*, 123 (1974).

M. Planck, Ann. Physik *4*, 553 (1901).

D. E. Powers, S. G. Hansen, M. E. Geusic, D. L. Michalopoulos, and R. E. Smalley, J. Chem. Phys. *78*, 2866 (1983).

H. Purdum, P. A. Montano, G. K. Shenoy, and T. Morrison, Phys. Rev. *B25*, 4412 (1982).

P. Pyykkö, J. G. Snijders, and E. J. Baerends, Chem. Phys. Letters *83*, 432 (1981).

R. C. Raffenetti, J. Chem. Phys. *58*, 4452 (1973).

S. J. Riley, E. K. Parks, L. G. Pobo, and S. Wexler, J. Chem. Phys. *79*, 2577 (1983).

J.-C. Rivoal, J. S. Emanpour, K. J. Zeringue, and M. Vala, Chem. Phys. Letters *92*, 313 (1982).

C. C. J. Roothaan, Rev. Mod. Phys. *23*, 69 (1951).

C. C. J. Roothaan, Rev. Mod. Phys. *32*, 179 (1960).

J. Ruamps, Compt. rend. *238*, 1489 (1954).

P. Schissel, J. Chem. Phys. *26*, 1276 (1957).

E. Schrödinger, Ann. Physik *79,* 361 (1926); ibid *79,* 489 (1926); ibid *79,* 734 (1926); ibid *81,* 109 (1926).

E. Schrödinger, Phys. Rev. *28,* 1049 (1926).

W. Schulze, H. U. Becker, R. Minkwitz, and K. Manzel, Chem. Phys. Letters *55,* 59 (1978).

I. Shim, J. P. Dahl, and H. Johansen, Int. J. Quantum Chem. *15,* 311 (1979).

I. Shim, Mol. Phys. *39,* 185 (1980).a

I. Shim, Theoret. Chim. Acta (Berlin) *54,* 113 (1980)b.

I. Shim and K. A. Gingerich, J. Chem. Phys. *77,* 2490 (1982).

I. Shim and K. A. Gingerich, J. Chem. Phys. *79,* 2903 (1983)a.

I. Shim and K. A. Gingerich, J. Chem. Phys. *78,* 5693 (1983)b.

I. Shim and K. A. Gingerich, J. Chem. Phys. *80,* 5107 (1984).

J. C. Slater, Phys. Rev. *34,* 1293 (1929).

J. C. Slater, Phys. Rev. *35,* 210 (1930).

J. C. Slater, J. B. Mann, T. M. Wilson, and J. H. Wood, Phys. Rev. *184,* 672 (1969).

V. I. Srdanov and D. S. Pešić, J. Mol. Spectrosc. *90,* 27 (1981).

H. Tatewaki and S. Huzinaga, J. Chem. Phys. *72,* 399 (1980).

H. Tatewaki, Y. Sakai, and S. Huzinaga, J. Comp. Chem. *2,* 96 (1981)a.

H. Tatewaki, Y. Sakai, and S. Huzinaga, J. Comp. Chem. *2,* 278 (1981)b.

T. H. Upton and W. A. Goddard III, J. Am. Chem. Soc. *100,* 5659 (1978).

G. Verhaegen, S. Smoes, and J. Drowart, J. Chem. Phys. *40,* 239 (1964).

T. C. de Vore, A. Ewing, H. F. Franzen, and V. Calder, Chem. Phys. Letters *35,* 78 (1975).

A. J. H. Wachters, J. Chem. Phys. *52,* 1033 (1970).

S. P. Walch and C. W. Bauschlicher, Jr., Chem. Phys. Letters *94,* 290 (1983)a.

S. P. Walch and C. W. Bauschlicher, Jr., J. Chem. Phys. *79,* 3590 (1983)b.

S. P. Walch, C. W. Bauschlicher, Jr., B. O. Roos, and C. J. Nelin, Chem. Phys. Letters *103,* 175 (1983).

E. W. Whittle, D. A. Dows, and G. C. Pimentel, J. Chem. Phys. *22,* 1943 (1954).

M. Witko and H. -O. Beckmann, Mol. Phys. *47,* 945 (1982).

A. Wolf and H. -H. Schmidtke, Int. J. Quantum Chem. *18,* 1187 (1980).

C. Wood, M. Doran, I. H. Hillier, and M. F. Guest, Faraday Symp. Chem. Soc. *14,* 159 (1980).

R. J. Van Zee, C. A. Baumann, and W. Weltner, Jr., J. Chem. Phys. *74,* 6977 (1981).

T. Ziegler, J. G. Snijders, and E. J. Baerends, J. Chem. Phys. *74,* 1271 (1981).

T. Ziegler, in »Local Density Approximations in Quantum Chemistry and Solid State Physics«, edited by J. P. Dahl and J. Avery (Plenum, New York, 1984). p. 273.

Hans L. Skriver

Crystal Structure
from One-Electron Theory

ABSTRACT. *We have studied the crystal structures of all the 3d, 4d, and 5d transition metals at zero pressure and temperature by means of the LMTO method and Andersen's force theorem. We find that, although the structural energy differences seem to be overestimated by the theory, the predicted crystal structures are in accord with experiment in all cases except Au. In addition we have investigated the effect of pressure upon the alkali metals (Li, Na, Rb, Cs) and selected lanthanide metals (La, Ce, Lu) and actinide metals (Th, Pa). In these cases the theory gives accurate predictions of the stability of the close-packed structures but is found to be less accurate for open structures such as α-U.*

Risø National Laboratory, DK-4000 Roskilde, Denmark

1. Introduction

Many of the characteristic properties of the metallic elements are a consequence of their ability at normal temperature and pressure to form crystals in which the metal atoms are arranged in a regular pattern which repeats itself throughout the interior of the crystal. These crystals are the microscopic building blocks of all the pieces of metal which we encounter around us, and it is therefore of great importance to investigate their basic properties both experimentally and theoretically. The hope is of course that by isolating and understanding the factors that govern the stability of the crystal structures found in nature one may eventually be able to design metals with specified properties.

The crystal structures of solid state materials are established by X-ray diffraction experiments, and the results for the elemental metals are compiled in Fig. 1. It turns out that the variety of crystal structures which the metallic elements take on is limited to essentially the five types shown on Fig. 2, and that four of these five structures are so-called close-packed structures. The term close-packed refers to the fact that the fcc, hcp, dhcp, and Sm-type structures can be derived from stacking hexagonal

0.0 - 0.8

Li	Be
hcp	hcp

Na	Mg
hcp	hcp

1	2	3.5	5	6	7	8.5	9.5	10	n_d

K	Ca	Sc	Ti	V	Cr	Mn	Fe	Co	Ni	Cu	Zn
bcc	fcc	hcp	hcp	bcc	bcc	(bcc)	bcc	hcp	fcc	fcc	hcp

Rb	Sr	Y	Zr	Nb	Mo	Tc	Ru	Rh	Pd	Ag	Cd
bcc	fcc	hcp	hcp	bcc	bcc	hcp	hcp	fcc	fcc	fcc	hcp

Cs	Ba	Lu	Hf	Ta	W	Re	Os	Ir	Pt	Au	Hg
bcc	bcc	hcp	hcp	bcc	bcc	hcp	hcp	fcc	fcc	fcc	(fcc)

Fr	Ra
	bcc

La	Ce	Pr	Nd	Pm	Sm	Eu	Gd	Tb	Dy	Ho	Er	Tm	Yb
dhcp	fcc	dhcp	dhcp	dhcp	Sm-t	bcc	hcp	hcp	hcp	hcp	hcp	hcp	hcp
Th	Pa	U	Np	Pu	Am	Cm	Bk	Cf	Es	Fm	Md	No	Lr
fcc	bct	orth.	orth.	mon.	dhcp	dhcp	dhcp	dhcp					

Fig. 1. Crystal structures of the metallic elements at low temperature.

layers of spheres of equal radii in the closest possible fashion. As a result of this close-packing the coordination number in these four structures is 12, each atom being surrounded by 12 nearest neighbours. The bcc structure is a little less close-packed and has a coordination number of 8, although it is sometimes referred to as having a coordination number of 14 on account of the 6 next nearest neighbours, which are only slightly farther away than the nearest neighbours.

It may be seen from Fig. 1 that the crystal structures of the metallic elements tend to occur in sequences when viewed as functions of atomic number or hydrostatic pressure. The most prominent example of this phenomenon occurs with the d transition metals, where all three transition series, excluding the four magnetic 3d metals, exihibit the same hcp→bcc→hcp→fcc sequence as the d states become progressively filled. A similar sequence is found in the lanthanides where the hcp→Sm-type→dhcp→fcc sequence established as a function of decreasing atomic number may also be realized by subjecting each individual lanthanide metal, except Ce, Eu, and Yb, to hydrostatic pressure. Finally, the alkaline earth metals, together with the divalent rare earths Eu and Yb, are part of a short fcc→bcc sequence which is also realized in Ca, Sr, and Yb under high pressure.

In the present contribution we shall establish the extent to which the systematics outlined above can be explained by means of a state-of-the-art theory for the ground state of the bonding electrons. The theory we apply is a one-electron theory in which each electron is treated as an independent particle moving in the effective potential from all the other electrons and the nuclei, and the only input to the calculations is the atomic number of the metal to be treated. In order to be able to reduce the original many-body problem significantly one has to solve the electronic structure problem self-consistently, and to this end we use the Linear Muffin-Tin Orbital (LMTO) method (Andersen 1975) in conjunction with a scaling principle as outlined by Skriver (1984). The structural energy differences which determine the relative stability of the crystal structures to be studied are in turn obtained from the one-electron states by means of Andersen's force theorem (Mackintosh and Andersen 1980). The whole procedure is quite general and allows us to treat all metals on the same footing.

Fig. 2. Close-packed crystal structures of the elemental metals.
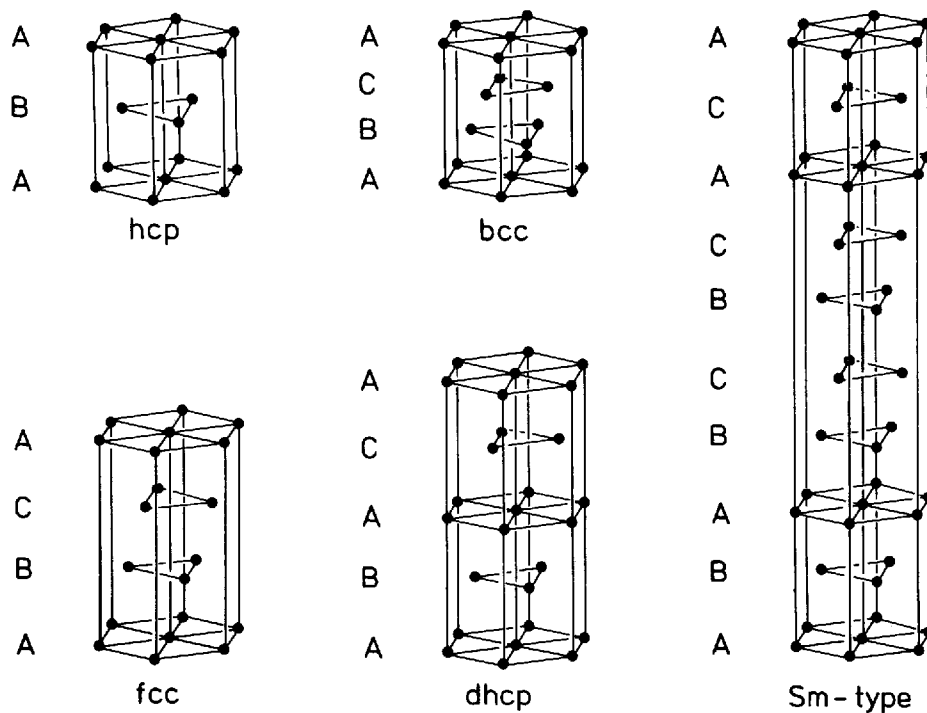
The remainder of the present contribution is organized as follows: In Sect. 1.1 we outline the simplest possible theory of structural stability in terms of the density of electronic states, and in the following section 1.2 we apply this simple theory to state densities obtained by means of canonical band theory. In Sect. 2 we review previous theoretical efforts in the field and compare them with the present approach, the theoretical foundations of which are discussed in Sect. 3. In Sect. 4 we outline an electrostatic correction to the Atomic Sphere Approximation (ASA) which becomes important for structures less close-packed than those shown in Fig. 2. Finally, in Sect. 5 we present the calculated structural energy differences for the alkalis, the alkaline earths, the transition metals, the lanthanides, and the light actinides.

1.1. A simple theory of structural stability

In the main part of the following we shall describe the results of a series of calculations of the relative stability of the crystal structures of some 40 elemental metals. In such a presentation, centred around an account of theoretical results and their relation to experimental observations, it is easy to lose track of the principles upon which the calculations are based. We shall therefore immediately present a simple model which will illustrate these principles and in addition will serve to make more comprehensible the complete calculations to be described later.

According to standard textbooks one may imagine a metal formed in the thought experiment illustrated in Fig. 3 where N initially infinitely separated metal atoms are slowly brought together. Here we shall consider specifically a transition metal in which the important states have d character. As a result of the increasing contact between neighbouring atoms the 5N atomic d states give rise to a band of energies ranging from B which corresponds to bonding between most neighbours to A which corresponds to antibonding between them. The band of energies formed in this way constitutes the energy band of the metal, and it contains all the one-electron states which the conduction electrons may occupy.

The energy gained in the above process is called the cohesive energy, and according to Fig. 3 it is simply the difference between the total atomic energy nE_a and the total band energy $n\bar{E}$, i.e.

$$E_{coh} = n(E_a - \bar{E}) \tag{1}$$

assuming an occupation of n d electrons per atom. In writing down (1) we have furthermore assumed that the d states broaden around the atomic level E_a, that is that the centre C of the d band coincides with E_a.
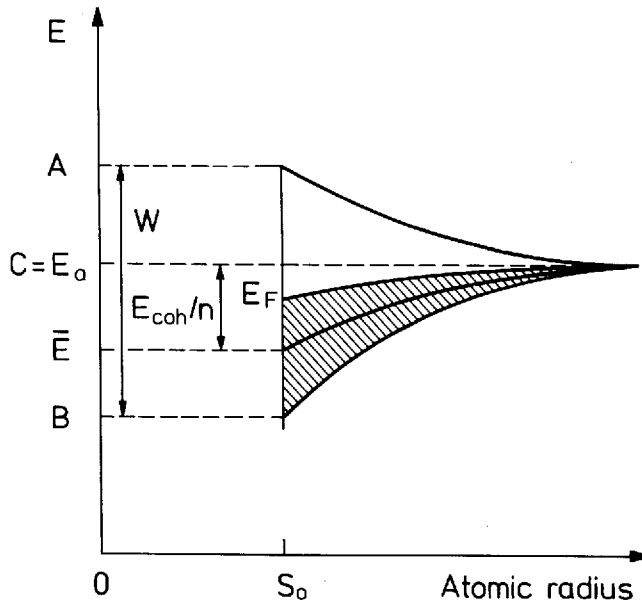
Fig. 3. Formation of the energy band of a metal from an atomic energy E_a. The width is W, the bottom and top B and A, respectively, the Fermi level, i.e. the highest occupied energy E_F, the cohesive energy E_{coh}, and the number of electrons per atom n.

The average energy $\bar{E}$, which corresponds to the centre of gravity of the occupied part of the d band and which enters (1), may be obtained by summing the one-electron energies ε_i between the bottom of the band B and the highest occupied one-electron level E_F, i.e.

$$\bar{E} = n^{-1} \sum_i^{occ} \varepsilon_i$$

$$= n^{-1} \int^{E_F} EN(E)dE \tag{2}$$

where we have introduced the state density function $N(E)$ which describes how the states are distributed in the energy range from B to A.

If we assume that all states within the d band are equally probable the state density will have the rectangular shape shown in Fig. 4a, and the cohesive energy will simply be given by

$$E_{coh}^r = \frac{W}{20} n(10-n) \tag{3}$$

As noted by Friedel (1969) this form clearly exhibits the parabolic variation with the d occupation, cf. Fig. 4, which is also found experimentally (Gschneidner 1969, Friedel and Sayers 1977), especially when proper account is taken of the atomic effects (Brooks and Johansson 1983), and

Fig. 4. Rectangular and skew state densities modelling the dependence of the cohesive energy upon crystal structure. The cohesive energy as a function of d occupation n is shown for the rectangular state density at the bottom.
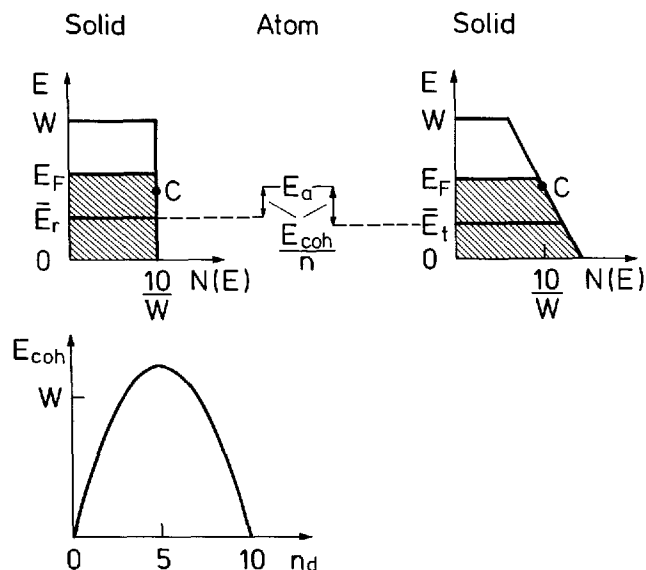
this agreement was taken as confirmation of the assumptions of the model outlined above.

From Eq. (1) and Fig. 4 it is clear that the energy gained in forming a metal from the free atoms depends upon the relative position of the atomic d level E_a and the average band energy $\bar{E}$. The latter depends upon the shape of the state density which in turn depends upon the arrangement of the atoms in the metal crystal, and hence different crystal structures will lead to different cohesive energies.

It follows that the relative stability of all possible crystal structures for a given metal will be determined by the particular shape of the corresponding state densities. We have illustrated this simple result in Fig. 4 from which it is straightforward to see that the crystal structure leading to the skew state density will have a higher cohesive energy and hence be more stable than the structure which leads to the rectangular state density on account of the lowering of $\bar{E}$. Hence, the relative stability of two crystal structures may be estimated simply by comparing the corresponding average band energies $\bar{E}$.

In the complete calculations to be reported later we have applied this simple principle to accurately calculated state densities, and the success with which the results explain the experimental observations may be

taken as a justification of the assumptions underlying the one-electron approach outlined above. As will be explained in Sect. 3 there is however also theoretical justification for such a one-electron approach in the form of the so-called force theorem (Mackintosh and Andersen 1980) which dictates how the band structures and the corresponding state densities of the metals in the different crystal structures should be calculated.

1.2. Structural stability from canonical band theory

The concept of canonical bands (Andersen 1975, Andersen and Jepsen 1977) gives rise to a simple and yet realistic procedure for estimating the relative stability of the close-packed crystal structures which form for instance the transition metal sequence, Fig. 1. According to canonical band theory an unhybridized, pure l band may be obtained from (Andersen and Jepsen 1977, Skriver 1984)

$$E_{li}(\mathbf{k}) = C_l + \frac{1}{\mu_l S^2} \frac{S_{li}^{\mathbf{k}}}{1 - \gamma_1 S_{li}^{\mathbf{k}}} \tag{4}$$

where $S_{li}^{\mathbf{k}}$ are the canonical bands which depend solely upon the crystal structure, S is the atomic Wigner-Seitz radius, C_l the centre of the l band, μ_l the band mass, and γ_l a distortion parameter. The three potential parameters C_l, μ_l and γ_l depend upon potential and volume but not upon crystal structure.

In a transition metal one may to a good approximation neglect all but the d bands. Since furthermore γ_d is small, one has the following potential-, i.e. atomic number-, independent estimate of the band contribution to the cohesive energy E_{coh}

$$\mu_d S^2 E_{coh} = -\mu_d S^2 \int^{E_F} (E - C_d) N_d(E) \, dE$$

$$= -\int^{S_d(n_d)} S_d \tilde{N}_d(S_d) \, dS_d \tag{5}$$

in terms of the first-order moment of the canonical state density $\tilde{N}_d$. Andersen et al. (1977) have evaluated (5) as a function of d occupation number n_d and found the expected parabolic behaviour (Friedel 1969) which may also be obtained directly if $N_d(E)$ is approximated by a rectangular state density as explained in the introduction.

Since the centre C_d and the band mass μ_d are independent of crystal structure, the first-order moment (5) may be used to estimate the structural energy differences according to Eq. (9). The result shown in Fig. 5 is identical to that of Andersen et al. (1977) and similar to the one
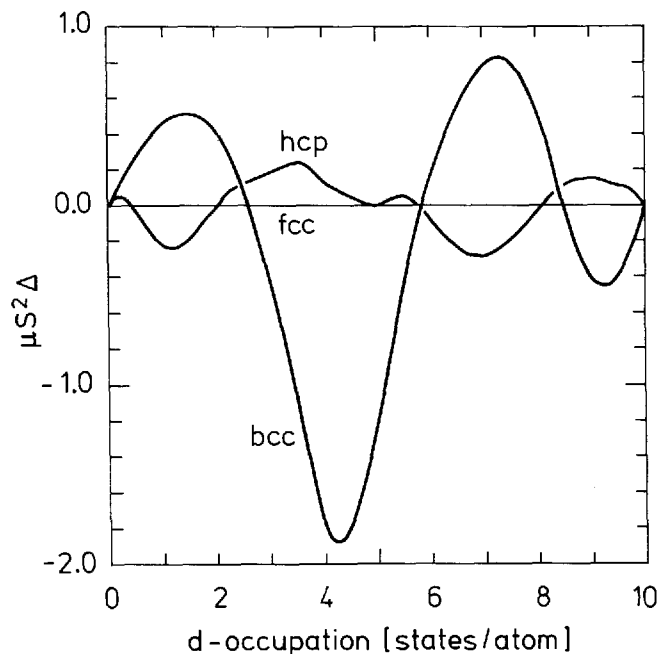
obtained by Pettifor (1970). It accounts qualitatively for the crystal structures of the non-magnetic transition metals, Fig. 1, in the beginning of the series but fails to predict the fcc structure at high d occupations. This failure is attributed either to a failure of the force relation (Mackintosh and Andersen 1980) or to hard-core effects (Pettifor 1970, 1972, 1977) omitted i Eq. (5).

The lanthanide metals are found to have d occupation numbers varying almost linearly with atomic number from 1.99 in La to 1.45 in Lu (Skriver 1983) or from 2.5 to 2.0 if hybridization is neglected (Duthie and Pettifor 1977). Furthermore, their crystal structures are as closely packed as are those of the d transition metals and hence their structural energy differences may be estimated by Eq. (5). The results shown in Fig. 6 are qualitatively similar to but on the average a factor 1.7 smaller than those obtained by Duthie and Pettifor (1977). In this comparison one may take the d-band width to be approximately $25/\mu_d S^2$ in order to bring their Fig. 2 onto the scale of Fig. 6. The results in Fig. 6 account qualitatively for the hcp→Sm-type→dhcp sequence found experimentally in going from Lu to La and more importantly perhaps, since the d occupation for the lanthanides is calculated to increase with pressure and

decrease with atomic number, they also explain that part of the same sequence is realized when a particular lanthanide metal is subjected to pressure. It therefore follows that the d occupation number, which is essentially a measure of the relative position of the s and d bands, may be used to rationalize the structure of the generalized phase diagram for the lanthanides constructed by Johansson and Rosengren (1975).

At the present stage one should realize that the results obtained by canonical band theory and shown in Figs. 5 and 6 are only qualitative. Indeed, if one considers Fig. 7 where the canonical estimates are compared with experimental crystal structures, one finds that the canonical theory in several cases does not predict the correct crystal structure independently of whether one uses the self-consistent d occupation num-
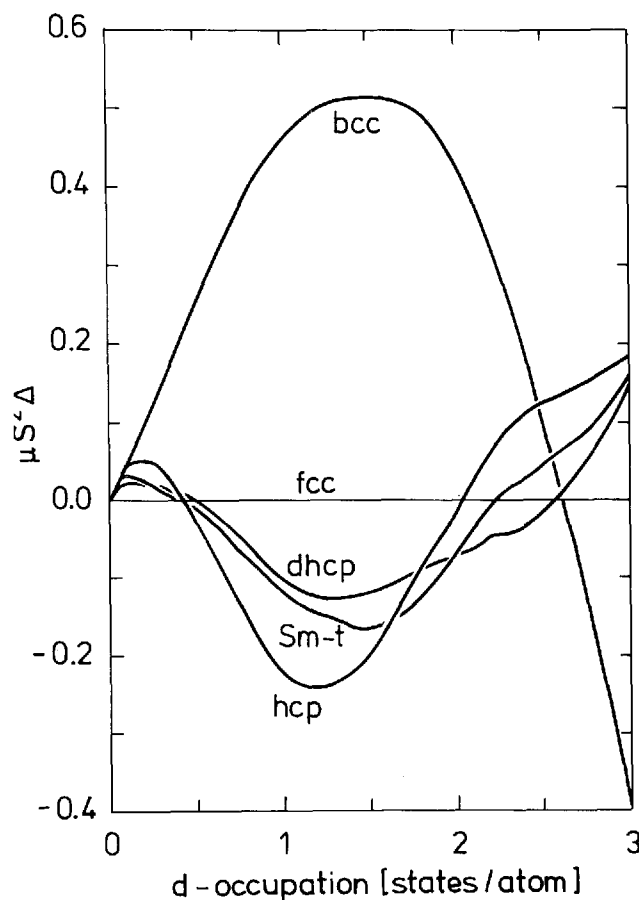
Fig. 6. Structural energy differences obtained from canonical d bands by means of Eq. (5) in the d occupation number range appropriate to the lanthanide crystal structure sequence.
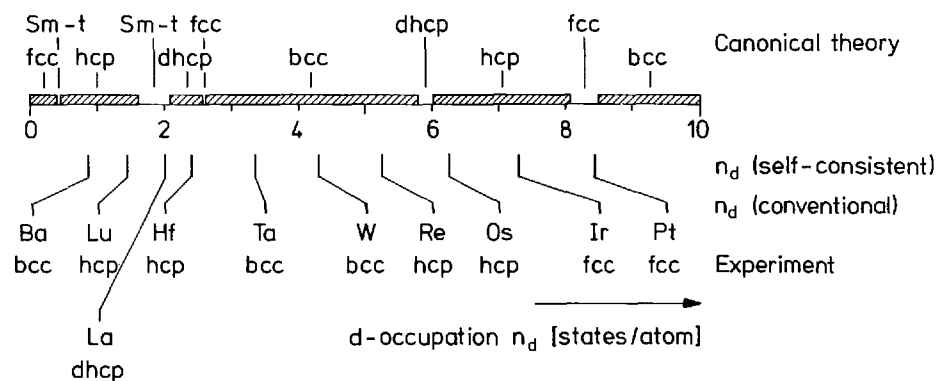
Fig. 7. Canonical estimate of the most stable close-packed crystal structure as a function of the calculated d occupation number compiled from Figs. 2 & 3, horizontal bars. Below are given two estimates of the actual d occupation numbers of the 5d metals together with the experimentally observed crystal structures.

bers or those obtained conventionally by nonlinear interpolation along a row in the periodic table (see Fig. 1). La, Re, and Ir, for instance, are examples of incorrect predictions, but here one may argue that the correct crystal structure is nearby and hence the failure of the theory may be considered less important. Ba is another example and in this case there is no nearby bcc structure. However, in Ba the d occupation number is only a fraction of the total number of electrons and hence a theory based solely upon unhybridized d bands is probably inapplicable. The most important failure is connected with the d occupation range from 1.6 to 2.6 [states/atom]. According to Fig. 7, La, Pr, Nd, and Pm should incorrectly form in the Sm-type structure while Ti, Zr, and Hf are expected to be part of the lanthanide sequence. Instead, the latter three metals form in the hcp structure which is the least stable among those considered in the d occupation range above 2 [states/atom].

It may be concluded that the simple estimate of structural energy differences obtained by means of the first-order moments of the canonical state densities is of limited value as a predictive tool. It is, however, of sufficient physical significance to warrant a study of the crystal structures of metals using a more accurate one-electron theory, and to be used in the interpretation of the results of such a study.

2. Theoretical approaches to structural stability

The most prominent crystal structure sequence in the periodic table is the hcp→bcc→hcp→fcc sequence found among the d transition metals, see Fig. 1. Qualitative explanations of this trend have been given by Brewer (1967) in terms of Engel correlations between the valence sp electrons and by Kaufman and Bernstein (1970) in terms of semi-empirical thermodynamic calculations of phase diagrams, whereas Deegan (1968), Dalton and Deegan (1969), and Ducastelle and Cyrot-Lackmann (1971) have attempted more quantitative approaches based upon one-electron theory.

Deegan (1968) and Dalton and Deegan (1969) showed that the stability of the bcc phase for nearly half-filled d shells might be explained by differences in the sum of one-electron band structure energies, and they pointed to the special double-peak structure of a bcc state density as responsible for this stability. Later, Pettifor (1970, 1972) extended the work of Dalton and Deegan and showed that the entire crystal structure sequence of the transition metals could be accounted for by a one-electron approach. In his calculations Pettifor (1977) found no evidence for the Brewer-Engel correlation (Brewer 1967), which relates crystal structure stability to the sp occupation numbers, and instead he related the hcp→bcc→hcp→fcc sequence to the change in d occupation which takes place across a transition series. This latter viewpoint has proven to be very fruitful in that it may be used as a simple »one-parameter theory« which in many cases provides remarkably good estimates of structural stabilities also for non-transition metals such as the alkaline earths (Skriver 1982).

The crystal structures of the trivalent lanthanides, i.e. Pr through Lu except Eu and Yb, exhibit such regularity, as functions of atomic number, pressure, and temperature, that Johansson and Rosengren (1975) were able to construct a single generalized phase diagram for these metals. In this case the crystal structures observed under ambient conditions, (see e.g., Beaudry and Gschneidner 1978) are found to be part of the sequence hcp→Sm-type→dhcp→fcc→fcc' established by high-pressure experiments (Jayaraman and Sherwood 1964, Piermarini and Weir 1964, Jayaraman 1965, McWhan and Stevens 1965, 1967, Liu et al. 1973, Liu 1975, Nakaue 1978) and alloying (Koch 1970). Here fcc' refers to the recently discovered distorted fcc structure (Grosshans et al. 1981). The lanthanide sequence is also found in Y (Vohra et al. 1981) where there are no occupied f states and in the heavier actinide (Stephens et al. 1968,

Akella et al. 1979, 1980, Roof et al. 1980, Roof 1982, Benedict et al. 1984) at pressures where the 5f states are still localized. Qualitative explanations of the hcp→Sm-type→dhcp→fcc sequence have been attempted in terms of pseudopotential theory by Hodges (1967) and in terms of a 4f contribution to the bonding by Gschneidner and Valletta (1968), while Duthie and Pettifor (1977) gave a quantitative explanation in terms of one-electron theory.

Duthie and Pettifor (1977) showed that the lanthanide crystal structure sequence could be explained by differences in the total one-electron band structure energies, and they found a strong correlation between crystal structure and d-occupation number. Hence it appears that the lanthanide metals, as far as their crystal structures are concerned, behave as ordinary 5d transition metals with a d occupation ranging from approximately 2.0 in La to 1.5 in Lu. This result is very appealing because there is a one-to-one correspondence between the calculated d-occupation number and the single f parameter used by Johansson and Rosengren (1975) and Johansson (1978) to rationalize the lanthanide crystal structure sequence, and because it is immediately possible to understand the behaviour of Y (Vohra et al. 1981) and the heavy actinides (Stephens et al. 1968, Akella et al. 1979, 1980, Roof et al. 1980, Roof 1982, Benedict et al. 1984) within the same framework.

At first sight it may seem surprising that the crystal structures of so many metals can be explained on the basis of differences in the total one-electron band structure energies alone, since the total electronic energy, apart from the one-electron term, has contributions also from double counting and exchange-correlation. However, it has recently been shown (Andersen et al., 1979, Mackintosh and Andersen 1980, see also page 119 of Heine 1980) that, provided the one-electron *potential* is kept frozen upon a displacement of the atoms, the corresponding changes in the double counting and exchange-correlation terms cancel to first order in the appropriate local electron density, and hence the difference in the sum of the one-electron energies, obtained by means of the frozen, i.e. not self-consistently relaxed, potential, will give an accurate estimate of the corresponding self-consistent change in the total electronic energy. It is exactly this cancellation, which also leads to the so-called pressure expression (Nieminen and Hodges 1976, Pettifor 1976) and to the more general force relation derived by Andersen (see Mackintosh and Andersen 1980), that in turn justifies the simple band structure approach taken for instance by Pettifor (1970, 1972, 1977).

In their work Pettifor (1970, 1972, 1977) and Duthie and Pettifor

(1977) focused their attention on the contribution to the total energy from the d bands and either neglected hybridization with the sp bands entirely or included hybridization appropriate to some average element. Hence their picture is essentially a canonical one (cf. Sect. 1.2) in which the energy band structures depend only upon crystal structure and not upon band-filling. It is obvious that such a picture, although adequate for the d transition metals, will fail in cases where states of non d character are as or more important than the d states, as they are for instance in the alkali, the alkaline earth and light actinide metals. Fortunately, the force theorem is not restricted to the canonical approximation and it has recently been used in theoretical investigations of crystal structures in the third row metals (Moriarty and McMahan 1982, McMahan and Moriarty 1983) the alkaline earth metals (Skriver 1982), and in Cs above the s-d transition (McMahan 1984).

In the present work we go beyond the canonical approximation and use the force theorem (Mackintosh and Andersen 1980) to calculate the structural energy differences for all the 3d, 4d, and 5d transition metals at zero pressure and temperature. In addition we investigate the effect of hydrostatic pressure upon the crystal structures of alkali, alkaline earth, lanthanide and actinide metals.

Traditionally the non-transition metals, e.g. alkali and alkaline earth metals, have been treated by means of pseudopotential theory, and the crystal structures predicted from this approach are generally in good agreement with experiment (Animalu 1967, Heine and Weaire 1970, Moriarty 1973, 1982, Hafner and Heine 1983, Young and Ross 1984). It has, however, not been straightforward to generalize the pseudopotential method to treat narrow d band materials, and to do so one has had to add localized orbitals to the plane-wave basis (Zunger and Cohen 1979). Thus the d band in K is described by the d component of plane-waves while that of Cu is described by additional d orbitals, which is somewhat inconsistent with the smooth lowering of the 3d band through the series K, Ca, Sc, ..., Cu. The method has, however, proved to be very accurate.

The present approach, based upon the Linear Muffin-Tin Orbital (LMTO) method (Andersen 1975), has the advantage of employing the same type of basis functions for all the elements thus leading to a conceptually consistent description of trends throughout the periodic table. In addition, the LMTO method is extremely efficient on a computer requiring only the solution of an eigenvalue problem of 9×9 (or 16×16 if f states are included) per atom at each point in reciprocal space. Since we

are mainly interested in trends, we have neglected the nonspherical contributions to the charge density, which may explain what seems to be a systematic overestimate of the calculated structural energy differences. We have furthermore neglected a structure-dependent electrostatic interaction between atomic spheres except in the few cases where it contributes significantly to the energy differences.

3. One-electron theory of structural stability

At low temperatures the crystal structure of a metal is determined by the total electronic energy U in addition to a small contribution from the zero-point motion★, which we shall neglect. Hence, if one wants to determine the stability of some crystal structure, say bcc, against some reference structure, which we shall take to be the close-packed fcc structure, one may calculate the total energy of both phases and form the structural energy difference

$$\Delta_{bcc-fcc} = U_{bcc} - U_{fcc} \tag{6}$$

where the total energy according to the local density approximation (Kohn and Sham 1965) may be written as the sum over occupied states of the one-electron energies ε_i corrected for double counting, plus electrostatic terms (see e.g., sections 13 and 15 of Heine 1980 or sections 7.2 and 7.3 of Skriver 1984), i.e.

$$U = \sum_i^{occ} \varepsilon_i - \text{double counting} + \text{electrostatic} \tag{7}$$

If the difference (6) is negative the bcc structure will be stable against fcc.

The total energy for say a 4d metal is of the order of 10^4 [Ry] mainly because of the contributions from the low-lying core levels while typical structural energy differences are of the order of 10^{-3} [Ry]. Hence, extreme accuracy is needed in order to use (6) directly, and one would like to have a numerically more satisfactory procedure. The force theorem (Mackintosh and Andersen 1980) gives rise to such a procedure, but more importantly perhaps it casts the problem of finding stable crystal

---

★ The zero-point energy is proportional to the Debye temperature i.e. $E_o = (9/8) k_B \Theta_D$. Typically Θ_D varies by 1-10 [K] between different structures of the same metal (see Gschneidner 1964) and hence the ΔE_o to be added to (6) is of the order of 0.01-0.1 [mRy] which in most cases will be too small to affect the structural stabilities.

structures into a form where the significant contribution comes from the one-electron valence energies and not from double counting nor from the deep core-levels.

The force theorem dictates that we adopt the following procedure: For a given metal at a given atomic volume one must solve the energy-band problem self-consistently assuming the reference crystal structure. To this end we use the LMTO method (Andersen 1975) within the Atomic Sphere Approximation (ASA) including the combined correction to the ASA (Andersen 1975). In addition we take account of the relativistic effects, except spin-orbit coupling which we neglect, include exchange-correlation in the form given by von Barth and Hedin (1972), and freeze the appropriate cores. This part of the calculations is described in detail by Skriver (1984). We have now minimized the energy functional $U\{n\}$ with respect to changes in the electron density n and obtained the ground state density n_{fcc}^{sc}. Because of the stationary properties of U one may obtain, for instance, U_{bcc} from a trial charge-density n_{bcc}^{tr} constructed by positioning the self-consistent fcc atomic-sphere *potentials* in a bcc geometry, solving the one-electron Schrödinger equation, and populating the lowest-lying one-electron states. Hence,

$$\Delta_{bcc-fcc} = U_{bcc}\left\{n_{bcc}^{tr}\right\} - U_{fcc}\left\{n_{fcc}^{sc}\right\} \tag{8}$$

where the errors relative to (6) are of second order in $n_{bcc}^{tr} - n_{bcc}^{sc}$. Now, the use of a *frozen*, i.e. not self-consistently relaxed, *potential* to generate n_{bcc}^{tr} ensures that the chemical shifts in the core levels drop out of Eq. (8) and also that the double-counting terms cancel. Hence, the core level energies and the double-counting terms may be neglected entirely in Eq. (7) leaving only the valence one-electron energies and the electrostatic terms to be considered. The fact that the freezing of the potential leads to such a computationally simple and conceptually important result was already noted by Pettifor (1976) in his derivation of the pressure expression.

Within the atomic sphere approximation (Andersen 1975) the atomic Wigner-Seitz sphere of an elemental metal is neutral and there is therefore no electrostatic interaction between the spheres. Hence the electrostatic terms in Eq. (7) vanish and the structural energy difference (8) may be obtained from

$$\Delta_{bcc-fcc} = \int^{E_F} E\, N_{bcc}(E)\, dE - \int^{E_F} E\, N_{fcc}(E)\, dE \tag{9}B$$

where $N(E)$ is the one-electron state density. Furthermore, the ASA allows a separation of the potential- and crystal-structure-dependent

parts of the energy band problem (Andersen 1975, Andersen and Jepsen 1977, Skriver 1984). Hence, all that is required at a given atomic volume, in addition to the self-consistent fcc calculation, is to calculate the energy bands of the relevant crystal structures with the use of the self-consistent fcc potential parameters, evaluate the sums of the one-electron energies, and subtract according to Eq. (9). This procedure is quite general, treats all s, p, d, and f electrons on the same footing, and may be applied to all metals in the periodic table.

4. Madelung correction to the ASA

The errors of neglecting the structure-dependent electrostatic terms in (7) may be estimated by means of what has been called either the Muffin-Tin (Glötzel and Andersen, unpublished) or Ewald (Esposito et al. 1980) correction to the ASA. To derive this correction one observes that the electrostatic energy per ion of a lattice of point ions of charge $q_s|e|$ embedded in a negative neutralizing uniform charge density is given by the well-known Madelung expression

$$U_M = -1/2(q_s|e|)^2 \frac{\alpha_M}{S} \tag{10}$$

where α_M is the lattice Madelung constant and S the atomic Wigner-Seitz radius. In the ASA this expression is approximated by the energy of an ion embedded in a single neutralizing atomic sphere, whereby $\alpha_M(ASA) = 1.8$. The correction is therefore

$$\Delta U_M = 1/2(q_s|e|)^2 \frac{1.8-\alpha_M}{S} \tag{11}$$

In a Muffin-Tin model the effective charge $q_s|e|$ is the charge density in the interstitial region between the Muffin-Tin spheres times the volume of the unit cell. In the ASA this becomes

Tabel 1. Madelung constant to be used in Eq. (11).

	α_M	$1.8-\alpha_M$		$(1.8-\alpha_M)-(\ )_{fcc}$	
fcc	1.79174723	8.253	10^{-3}		
bcc	1.79185851	8.142	10^{-3}	− 0.111	10^{-3}
hcp	1.79167624	8.324	10^{-3}	0.071	10^{-3}
α-U*)	1.78418298	15.817	10^{-3}	7.564	10^{-3}

*) b/a = 1.964, c/a = 1.709, y = 0.1

$$q_s|e| = \frac{4\pi}{3} S^3 \, n(S) \, |e| \tag{12}$$

where $n(S)$ is the electron density at the atomic radius.

For close-packed crystal structures α_M is approximately 1.8, see Table 1, and hence the correction (11) is smallest in these. Typically q_s^2/S lies in the range from 0.5 to 5 [a.u.] so that the Madelung correction for the bcc and hcp structures relative to the fcc structure lies in the range 0.05 to 0.5 [mRy].

5. Structural stability from LMTO band calculations

In the following we shall present structural energy differences for most metallic elements to the left of and including the noble metals as obtained by means of the procedure described in Sect. 3. The results will be valid only at low temperature and at atmospheric pressure, strictly $T = 0[K]$ and $P = 0$ [GPa], except in a few important cases where structural stability has been followed as a function of pressure.

5.1. The alkali metals

The calculated structural energy differences for alkali metals at equilibrium are almost two orders of magnitude smaller than those of, for instance, the alkaline earth metals. To judge the accuracy of our approach we have therefore studied these differences as functions of pressure as shown in Fig. 8 from equilibrium down to a compression of 2.5. The results in Fig. 8 include the Madelung correction (11) which turns out to be crucial in the comparison with recent pseudopotential and LMTO results (Moriarty 1982, Moriarty and McMahan 1982, McMahan and Moriarty 1983).

From Fig. 8 it is expected that the heavy alkalis at low temperature and pressure should form in the bcc structure while Li should be hcp. Experimentally it is known (Donohue 1975, Young 1975) that all five alkali metals at room temperature form in the bcc structure, and that they remain in this structure down to 5 [K] except Na which below 51 [K] transforms into the hcp structure and Li which at low temperature exhibits both an hcp and an fcc phase. Hence, except for Na the low pressure structures are correctly predicted.

Recently, Moriarty (1982) successfully estimated the structural stability for some 20 non-transition metals by means of his Generalized Pseudopotential Theory (GPT). He found incorrectly (see his Table VIII)
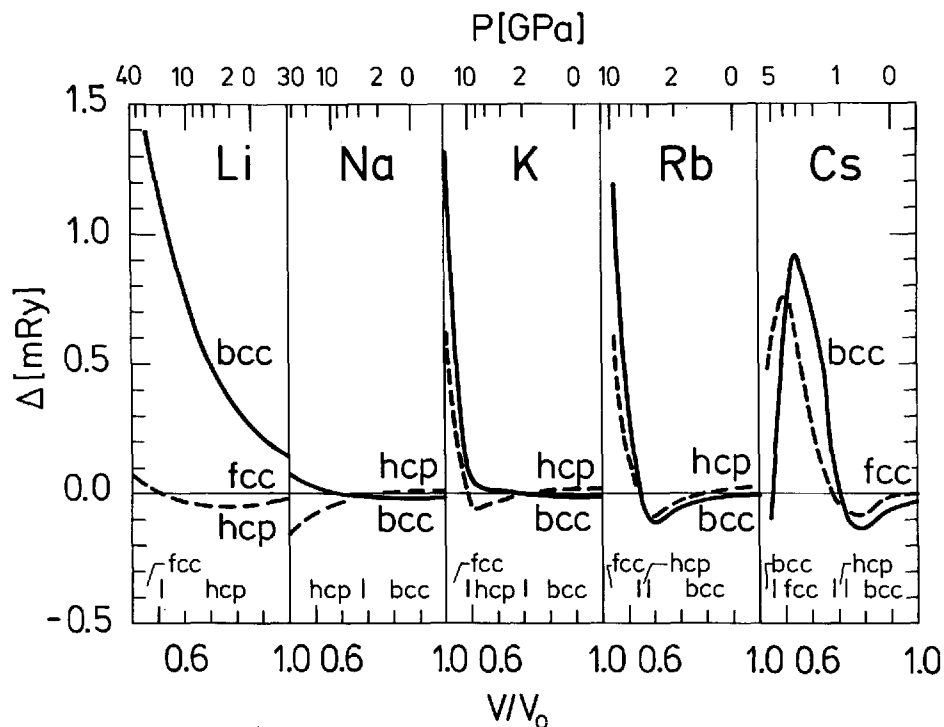
Fig. 8. Structural energy differences for the 5 alkali metals as functions of the relative volume V/V_o. At the top is given the calculated LMTO pressure P. The calculations included s, p, and d orbitals and the Madelung correction Eq. (11).

that all the alkali metals at $P = 0$ and $T = 0$ should form in the hcp structure, but pointed out that at a slight compression the experimentally observed bcc structure would be stable in the heavy alkalies K, Rb, and Cs. A similar problem is encountered in another recent pseudopotential study (Young and Ross 1984) where the structures of Li and K at low temperature and pressure are predicted in agreement with experiment but where Na is expected to be fcc. On the other hand, in view of the extremely small energies involved, see Fig. 8, it is not surprising that the prediction of the low-pressure part of the alkali phase diagrams is a severe test of any calculation.

In their work on the third-row metals McMahan and Moriarty (1983) compared structural energy differences obtained by means of the LMTO and GPT methods and found excellent qualitative agreement except for Na. If we compare our Na results in Fig. 8 with their Fig. 1 we find

somewhat surprisingly that our calculations are in closer agreement with their GPT than with their LMTO results. There are several reasons for the differences between the two LMTO calculations. Firstly, we have included the Madelung correction (11) without which the calculated bcc curve is entirely above and the hcp curve entirely below the fcc, in qualititative agreement with their LMTO results. Secondly, we have sampled the Brillouin zone on a finer mesh, i.e. 916, 819, and 448 points in the irreducible wedge for fcc, bcc, and hcp, respectively, and finally, we have improved the convergence of the reciprocal lattice sums in the expression for the combined correction terms (Andersen 1975) whereby the numerical errors in the structural energy differences for Na are below 0.01 mRy. As a result it appears that in the case of closely packed crystal structures the LMTO method including the Madelung correction (11) has an accuracy comparable to that attained by pseudopotential theory.

Owing to the inclusion of only three crystal structures in Fig. 8, Cs is incorrectly calculated to transform into the bcc structure at a compression of 2.2. However, in a recent study of Cs above the s-d transition, i.e. beyond the pressure range of the present work, McMahan (1984) found that Cs had transformed into the Cs IV structure before the bcc structure became more stable than fcc, in agreement with high pressure experiments (Takemura et al. 1981, 1982).

5.2. The alkali metals at moderate compression

According to Fig. 8 all the alkali metals should at low temperature be part of the same crystal structure sequence bcc→hcp→fcc, and one would anticipate that these transitions are driven by the pressure-induced lowering of initially unoccupied d states through the Fermi level, whereby electrons are gradually transferred from the s into the d band. If one plots the calculated crystal structures as functions of d occupation number as in Fig. 9 it is seen that only in the heavy alkalis K, Rb, and Cs is this mechanism at work while the transitions in Li and Na at least below 35 [GPa] have a different origin.

The experimental situation at room temperature has recently been summarized as follows (Takemura and Syassen 1983, Olijnyk and Holzapfel 1983). Li exhibits a bcc→fcc transition at 6.9 [GPa] (Olinger and Shaner 1983) while Na remains in the bcc structure up to at least 30 [GPa] (Alexandrov et al. 1982) which substantiates the notion that the s-d transition is unimportant in these two metals. The heavy alkalis all exhibit a bcc→fcc transition [K (Takemura and Syassen 1983, Olijnyk and Holzapfel 1983), Rb (Takemura and Syassen 1982), Cs (Hall et al.

Fig. 9. Calculated crystal structures for the alkali metals as functions of the LMTO pressure and d occupation number.
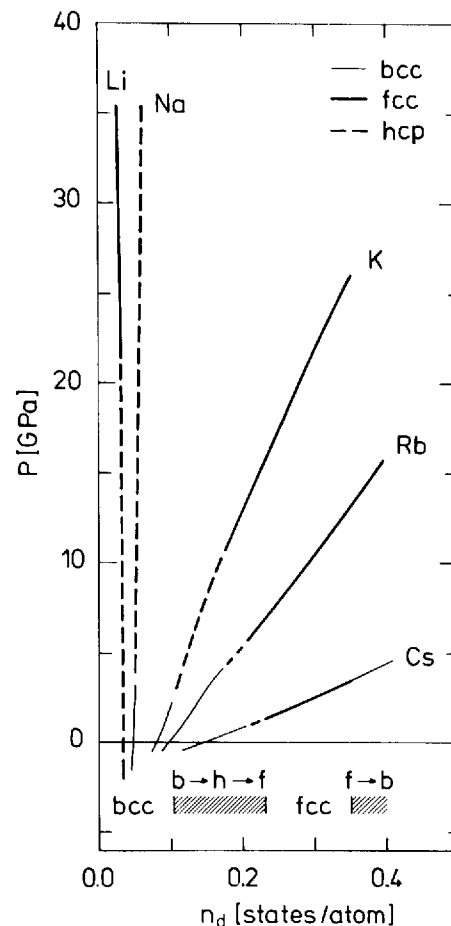
1964)] before they transform into more complex structures of which only the so-called Cs IV has been solved so far (Takemura et al. 1982).

To our knowledge there are no low-temperature high-pressure experiments which could substantiate the existence of the predicted bcc→hcp→fcc sequence, where according to Figs. 8 and 9 the hcp phase at least in K should be stable over an appreciable pressure range. However, in view of the fact that temperature at atmospheric pressure stabilizes the bcc phase to the extent that all the alkali metals are bcc above 100 K it is reasonable to assume that the intermediate hcp phase, which is only marginally stable, is also suppressed at higher temperatures. Thus, in a high-pressure experiment at room temperature one would see a direct bcc→fcc transition, as indeed one has observed (Hall et al. 1964, Take-

mura and Syassen 1982, 1983, Olijnyk and Holzapfel 1983). If the hcp phase is suppressed the best estimate of the room temperature bcc→fcc transition pressure is the critical pressure for the low-temperature hcp→fcc transition (cf. Fig. 8). We find the transition pressures to be 11, 5.5, and 1.4 [GPa] for K, Rb, and Cs, respectively, which should be compared to the experimental values of 11, 7, and 2.2 [GPa] listed in the references cited above.

Independent of whether the intermediate hcp phase exists or not, the high-pressure fcc phase in K, Rb, and Cs is much more stable than the initial bcc phase, see Fig. 8. Bardeen (1938) suggested already in 1938 that the transition observed at 2 [GPa] in Cs was from the normal bcc to an fcc phase and that it resulted from the non-electrostatic interaction energy of the ions, the important term being the Born-Mayer (Born and Mayer 1932) repulsion between the ion cores. Here we shall show that the fcc phase in the heavy alkalies owes its stability directly to the pressure-induced s-d transition which is also shown to be behind, for instance, the isostructural fcc-fcc transition in Cs (Glötzel and McMahan 1979).

In Fig. 10 we compare the important parts of the fcc and bcc band-structures of Cs at the zero-pressure volume, V_o, and at the volume where the fcc phase becomes more stable than the initial bcc phase. The four band structures may be characterized as nearly free-electron and s-like below the Fermi level E_F and d-like above E_F. Typical d states have symmetry labels such as Γ_{12}, $\Gamma_{25'}$, H_{12}, and X_3, and they are seen to approach the Fermi level under compression. At $V = V_o$ the fcc and bcc band-structures are found to be extremely similar in the range below E_F which is important in the sums over occupied states in Eq. (9): They are both parabola shaped and »touch« E_F at a single symmetry point, L_1 for fcc and N_1 for bcc. As a result, the sum of the one-electron band-structure energies are almost equal and the main contribution to the stability of the bcc phase comes from the electrostatic Madelung term (11) which is negative, see Table 1.

At $V = 0.7\ V_o$ hybridization with the descending d band has moved the X_1 and neighbouring levels below E_F thereby lowering the energy in the fcc phase with respect to that in the bcc phase to the extent that the Madelung term is overcome and the structural energy difference is zero. Under further compression the X_1 level continues to descend and the fcc phase becomes increasingly stable, see Fig. 11. This trend is eventually broken because the maximum in the $\Gamma_1\Delta_1X_1$ band moves away from X and because the X_3 level drops below the Fermi level. Both effects de-
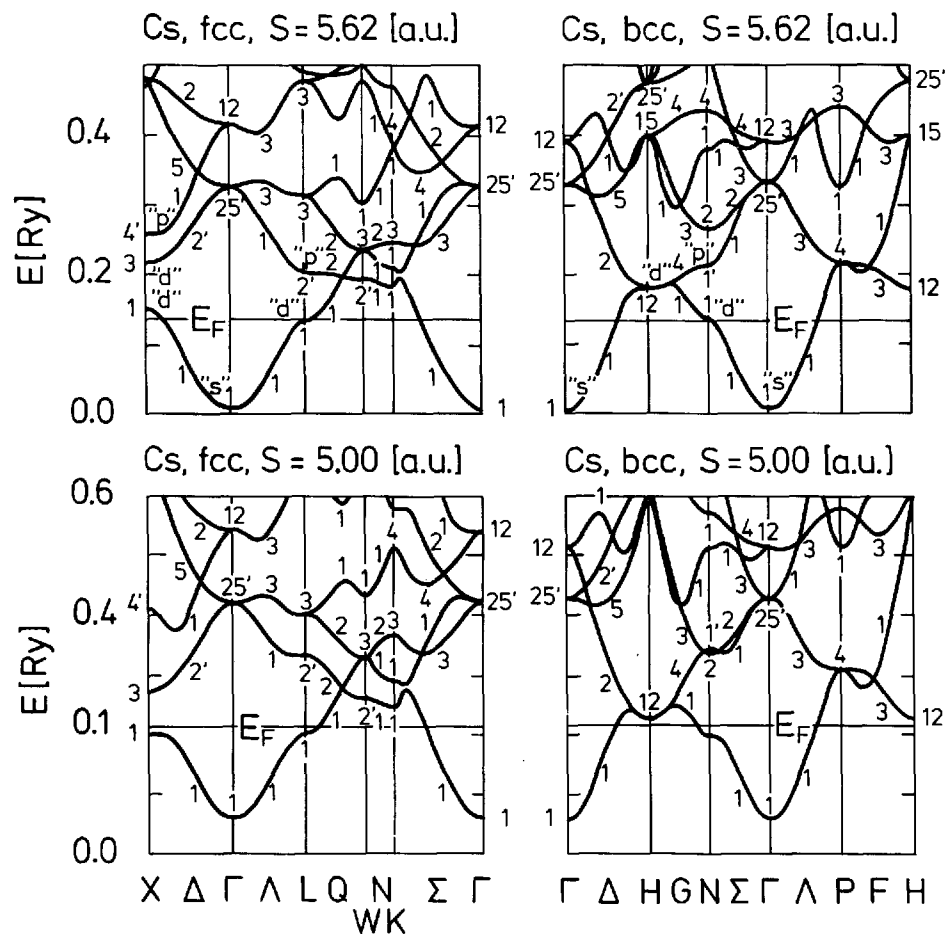
Fig. 10. Energy band structures for Cs at equilibrium, S = 5.62 [a.u.], and at a compressed volume, S = 5.0 [a.u.]. Conventional symmetry labels are given and the dominant s, p or d character is indicated at a few selected energy levels.

stabilize the fcc structure and subsequently Cs transforms into the Cs IV phase. We shall not discuss this development here but refer to the experimental work of Takemura et al. (1982) and the theoretical treatment of McMahan (1984).

The presence of a gap at X (see Fig. 10) near the Fermi level in the compressed fcc phase which has no counterpart in bcc phase (nor in the hcp phase) stabilizes the fcc phase over the bcc in exactly the manner discussed by Jones in his classical work on the phase boundaries in binary

alloys (Mott and Jones 1936, Jones 1937). The electron states below the gap have their one-electron band-energies lowered and are more densely populated than their free-electron or, here, bcc counterparts. The way the fcc phase is stabilized in Cs under pressure is shown in Fig. 11 where one notes that the stabilization occurs gradually from the point where the X_1 level crosses E_F. Hence, although the fcc phase eventually becomes more stable than the bcc phase because of the presence of the band gap at X, there is no direct relation between the volume ($V = 0.70\ V_o$) where the phase transition occurs and the volume ($V = 0.82\ V_o$) where the van Hove singularity connected with the X_1 level moves through the Fermi level. This delayed action is characteristic of many electronically driven transitions.

In the discussion of the stability of the fcc phase we have considered only Cs for simplicity, but examination of the band structures for K and Rb shows that the above picture applies equally well to these two metals although there are quantitative differences between K, Rb, and Cs caused by the fact that the zero-pressure position of the initially unoc-
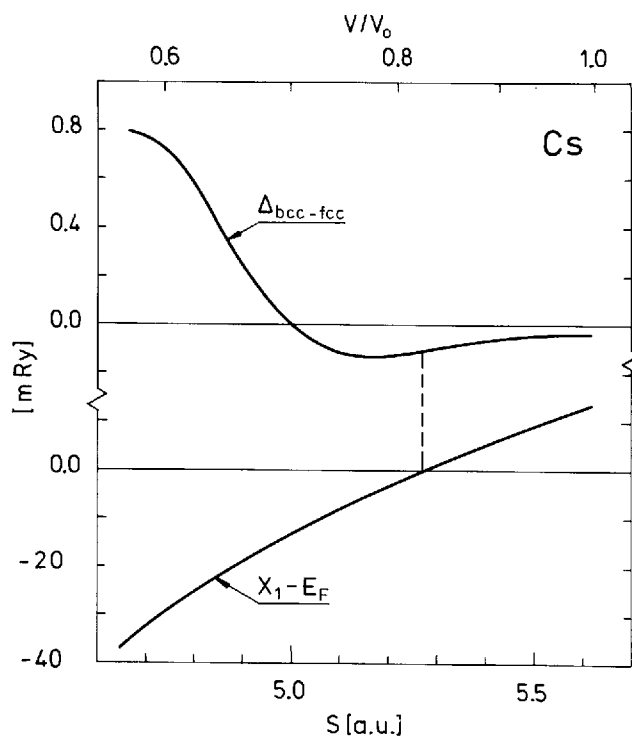
Fig. 11. Structural energy difference $\Delta_{bcc\text{-}fcc}$ for Cs, upper panel, and the position relative to the Fermi level, E_F, of the bottom of the gap at X in the fcc structure, lower panel, as functions of atomic radius, S, or relative volume V/V_o. $V = (4\pi/3)S^3$.
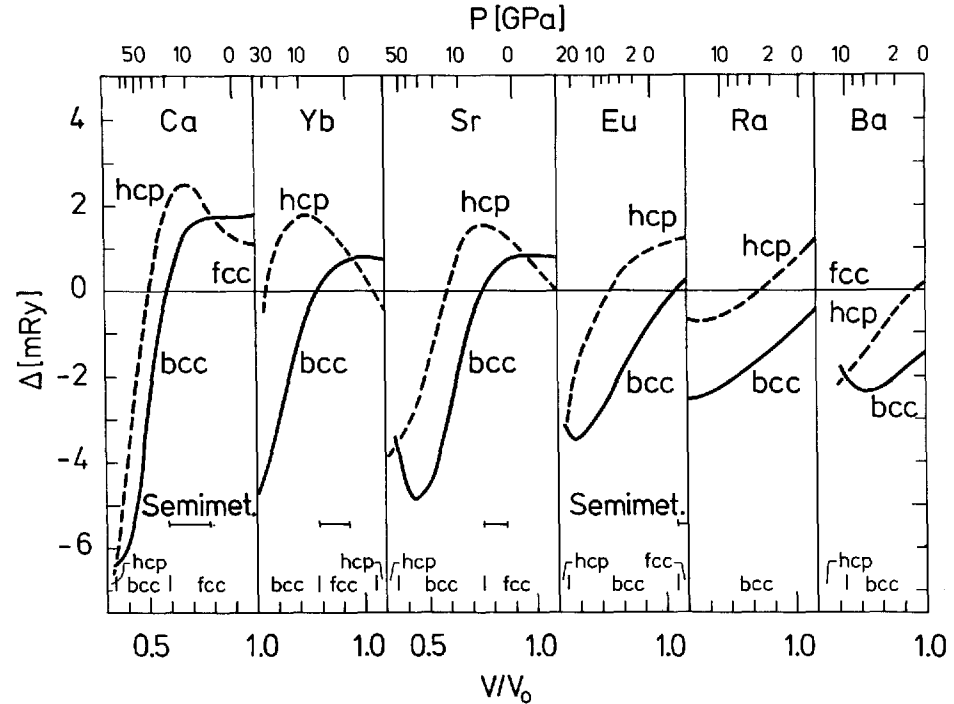
Fig. 12. Structural energy differences for the alkaline earth metals and the two divalent rare earths Eu and Yb as functions of relative volume V/V_o and LMTO pressure P. The volume range over which the elements are calculated to be semimetallic is indicated by horizontal bars. The calculations included s, p, and d orbitals but not the Madelung correction Eq. (11).

cupied d band drops relative to the Fermi level as the atomic number increases.

5.3. The alkaline earth metals

The calculated structural-energy differences for the alkaline earth metals under pressure are shown in Fig. 12. In the figure the metals are ordered according to their calculated d occupation number at equilibrium and we have included the two divalent rare earths Eu and Yb, but excluded the divalent metals Be and Mg since they do not really belong to the crystal structure sequence we shall presently be discussing. The results at zero pressure for Be and Mg may, however, be found in the preliminary account (Skriver 1982) of the present work.

According to Fig. 12, Ca, Yb, and Sr at low temperature and pressure should form in the fcc structure while Eu, Ra, and Ba should be bcc.

These predictions are in agreement with experiments (Donohue 1975, Young 1975) except for Yb which at low temperature takes up the hcp structure (Bucher et al. 1970). However, at a slightly expanded volume the hcp phase is calculated to be the stable phase, and hence one may not have to appeal to zero-point motion to explain the anomalous low-temperature hcp phase in Yb. Previous pseudopotential calculations (Animalu 1967) have explained the bcc structure in Ba and the pressure-(and temperature-) induced fcc→bcc transition in Sr, but gave an incorrect (bcc) zero-pressure crystal structure in Ca. Later pseudopotential results (Moriarty 1973) indicated that the stable structure at ordinary pressure should be the fcc structure for all the alkaline earths. Hence, it is still a challenge to pseudopotential theory to predict the crystal structures of the alkaline earth metals as a function of both atomic number and pressure.

There is a strong correlation between the calculated d occupation number and the calculated crystal structure as may be seen in Fig. 13. According to this the heavy alkaline earth metals should be part of the same hcp→fcc→bcc→hcp sequence. At zero pressure each individual metal
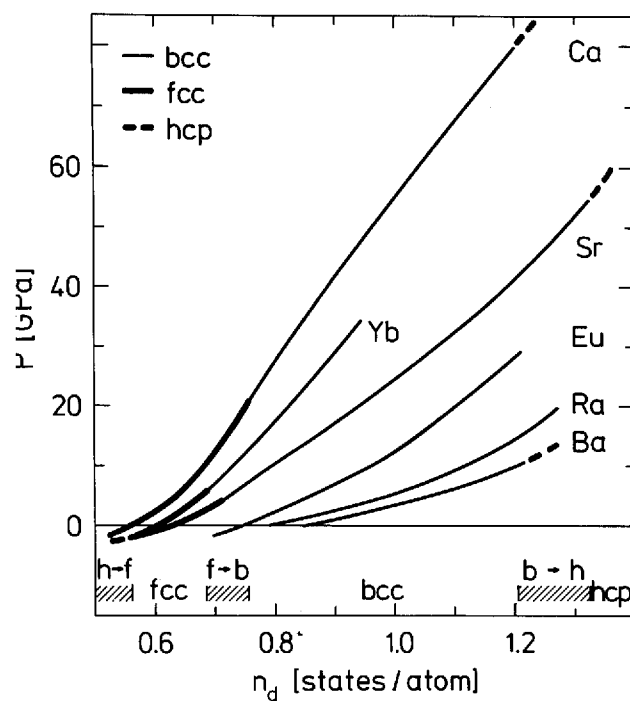
Fig. 13. Calculated crystal structures for the alkaline earth metals as functions of the LMTO pressure and d occupation number.

may be characterized as being at different stages on the continuous s-to-d transition, i.e. by their d occupation number, and the structural phase transitions are then driven by the pressure-induced lowering of the d band with respect to the s band. The correlation is, however, not perfect and the calculated crystal-structure changes occur over a narrow range of d occupation numbers.

Experimentally (Jayaraman et al. 1963a, b, Jayaraman 1964, Olijnyk and Holzapfel 1984) one observes at room temperature the fcc→bcc part of the above sequence but the bcc→hcp transition is found only in Ba whereas the lighter alkaline earth metals transform into more complex high-pressure phases (Olijnyk and Holzapfel 1984) not considered here. The critical pressures for the fcc→bcc transition in Ca, Sr, and Yb plus the bcc→hcp transition in Ba are calculated to be 21, 3.8, 5.5, and 10 [GPa], respectively (cf. Fig. 13). At room temperature Olijnyk and Holzapfel (1984) find experimentally 19.7 [GPa] for the transition in Ca while a low-temperature extrapolation of the high pressure crystallographic measurements by Jayaraman et al. (1983a, b) and Jayaraman (1964) gives 4, 5, and 5 [GPa] for the latter three transitions. In view of the fact that no adjustable parameters have been used to construct Fig. 13, the agreement with the calculated critical pressures may be considered satisfactory.

The band structure calculations show in agreement with the high-pressure resistivity data (Stager and Drickamer 1963a, b, Souers and Jura 1963, McWhan et al. 1963) that Ca, Sr, and Yb in the fcc phase should undergo a metal-semimetal-metal transition under pressure as described in detail for Ca by, for instance, Jan and Skriver (1981). Recently, Dunn and Bundy (1981) re-measured Ca and found the pressure range of the semimetallic phase to be much narrower than that found in earlier measurements (Stager and Drickamer 1963a) or predicted by band theory (McCaffrey et al. 1973, Mickish et al. 1974, Jan and Skriver 1981). Jan and Skriver (1981), for instance, predicted that fcc Ca should be semimetallic from 4 to 29 [GPa]. In the present extension of those calculations it is seen in Fig. 12 that before Ca reaches 29 [GPa] it is expected to transform into the bcc phase whereby the semimetallic behaviou will be terminated already at 21 [GPa]. This termination of the semimetallic phase at approximately 20 [GPa] is in agreement with both resistivity (Dunn and Bundy 1981) and crystallographic (Olijnyk and Holzapfel 1984) measurements. However, the critical pressure of 4 [GPa] for the onset of the semimetallic behaviour is still too low compared to that obtained from the resistivity data of Dunn and Bundy (1981), and this

discrepancy must be due to a failure of local-density theory of the kind mentioned by Jan og Skriver (1981).

In recent high-pressure measurements (Holzapfel et al. 1979, Takemura and Syassen 1985) both Eu and Yb are found to transform from the bcc to the hcp phase in seeming agreement with the systematics exhibited in Fig. 13. However, since Yb (Syassen et al. 1982) and presumably also Eu (Johansson and Rosengren 1975, Rosengren and Johansson 1976) change valence under pressure their high-pressure hcp phase is more appropriately thought of as belonging to the rare earth sequence, see Fig. 1, whereby it follows that Eu and Yb at very high pressures should exhibit the well-known hcp→Sm-type→dhcp→fcc transitions.

5.4. The transition metals

The calculated structural energy differences for the 3d, 4d, and 5d transition metals are shown in Fig. 14 and, as a comparison will show, the predicted crystal structures of all the metals included in this figure, neglecting the three ferromagnetic 3d metals, agree with the experimentally observed crystal structures, Fig. 1, except for the case of Au where the bcc structure is calculated to be marginally more stable than fcc. Hence, it follows that by including complete, i.e. fully hybridized, band structures for each individual metal but still retaining the force theorem one has cured most of the problems connected with the simple canonical picture discussed in Sect. 1.2 and exemplified in Fig. 7. Furthermore, one should note that the correlation between crystal structure and d occupation which the canonical description predicts remains valid also for the complete calculations.

The results in Fig. 14 are very similar to those obtained by Pettifor (1970, 1972, 1977) for the 3d metals and by Williams (quoted by Miedema and Niessen 1983) for the 4d metals. However, in spite of the agreement of the theoretical calculations to within 25% and the correct prediction by the theory of the crystal structures of 27 metals, the calculated structural energy differences are found to be as much as a factor of 3-5 larger than the enthalpy differences obtained from the study of binary phase diagrams (Miedema and Niessen 1983), Fig. 15. At present the cause of this discrepancy is not known. The most likely candidates are either neglect of non-spherical terms in the charge density or a genuine failure of the local density approximation. The force theorem itself does not seem to be the cause of the discrepancy since Williams as quoted by Miedema and Niessen (1983) obtains results similar to ours by subtraction of total energy calculations. Finally, the »experimental« results de-

Fig. 14. Structural energy differences for the 3d, 4d, and 5d transition metals calculated at the experimentally observed equilibrium volume and plotted as functions of the d occupation numbers. The calculations included s, p, and d orbitals but not the Madelung correction Eq. (11).
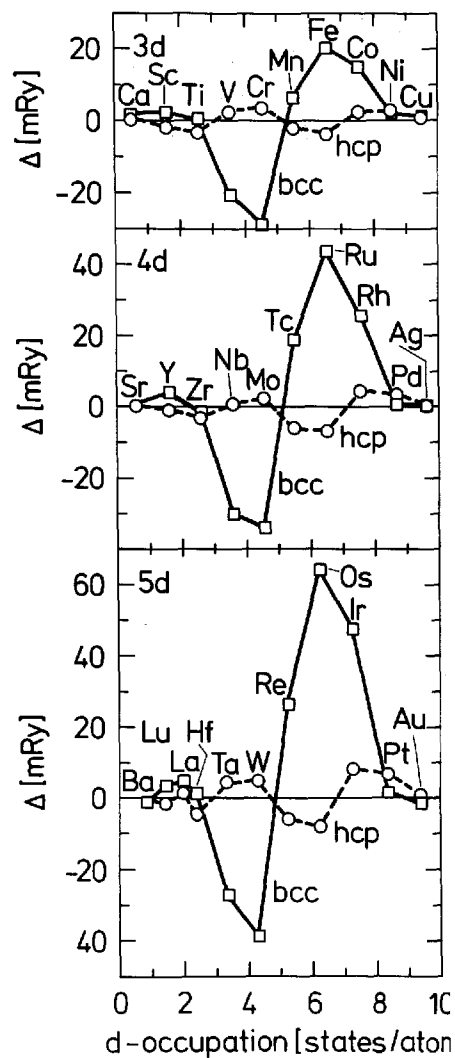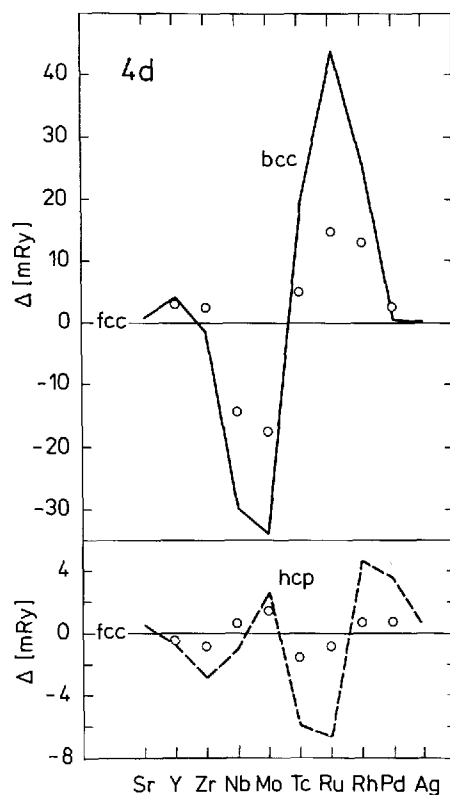
Fig. 15. The calculated bcc-fcc and hcp-fcc structural energy differences (solid and broken lines) for the 4d metals compared with the enthalpy differences derived from phase diagrams (Miedema and Niessen 1983), open circles.

rived by Miedema and Niessen (1983) are certainly model dependent and
may therefore have large error bars.

5.5. The lanthanide metals

The calculated structural-energy differences for the two lanthanide met-
als La and Lu which bracket the lanthanide series are shown in Fig. 16.
To compare directly with the canonical results, Fig. 6, the energy differ-
ences have been brought onto the canonical scale and plotted as functions
of the calculated d occupation number. The results in Fig. 16 are qualita-
tively similar to the canonical results but the energy differences are gen-
erally smaller by approximately a factor of 2, judged by, for instance, the
minimum in the Sm-type curve, than their canonical counterparts.
Furthermore, the lanthanide sequence has been shifted to lower d occu-
pation numbers whereby the problems connected with the canonical
description in the d occupation range above 1.6 have been removed.
Hence, Ti, Zr, and Hf are no longer part of the lanthanide sequence and
are instead correctly predicted to form in the hcp structure, Fig. 14.

In an account of the cohesive properties of the lanthanides Skriver
(1983) found that the d occupation numbers calculated at the experimen-
tally observed equilibrium volume decreased approximately linearly
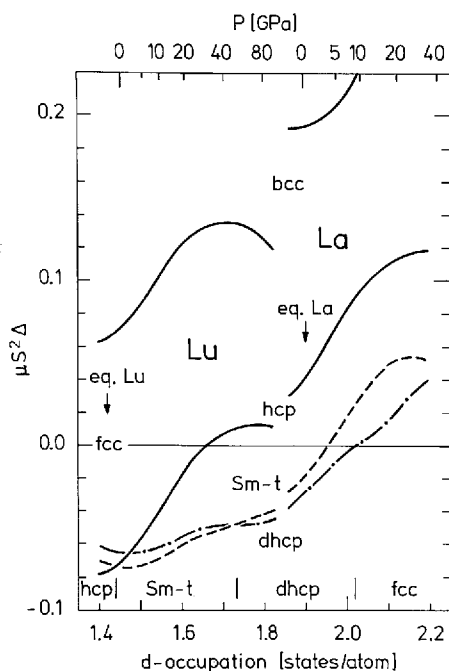
Fig. 16. Structural energy differences for La
and Lu calculated as functions of pressure P and
plotted versus d occupation number n_d. The cal-
culations included s, p, d, and f orbitals, 4f for
La and 5f for Lu, but not the Madelung correc-
tion Eq. (11).
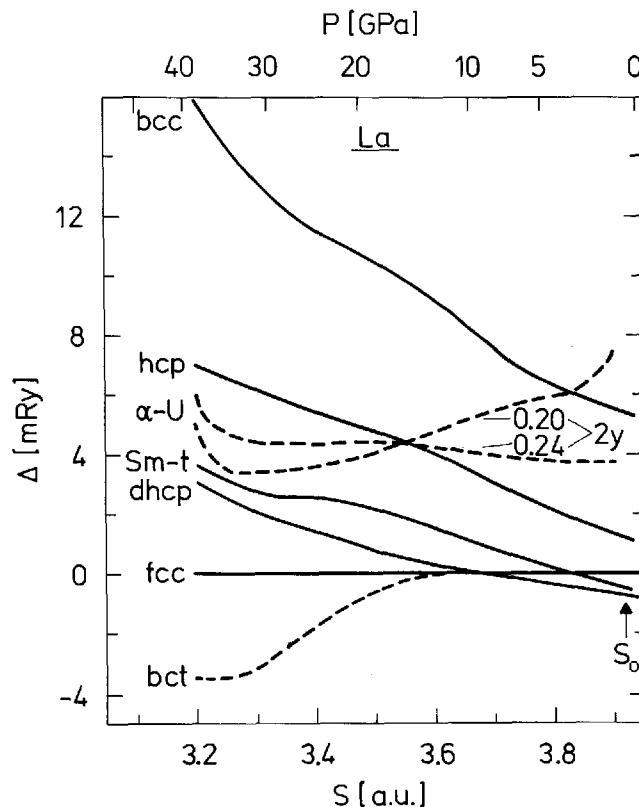
with atomic number between La and Lu. Hence, Fig. 16 may be used to estimate the equilibrium crystal structures of the lanthanide metals, ex-cluding Ce because of its γ-α transition, and the two divalent metals Eu and Yb. In agreement with the generalized phase diagram (Johansson and Rosengren 1975) we find that La, Pr, Nd, and Pm should form in the dhcp structure while Sm should be Sm-type. However, the heavy lan-thanides are incorrectly estimated to form in the Sm-type structure. The immediate reason for this failure seems to be that the stability of the hcp structure at a given d occupation is calculated to be too low compared with dhcp and Sm-type but the deeper cause is not known at present. As a result, the Sm-type structure extends over too wide a d occupation range.

Fig. 16 may also be used to predict the behaviour of La and Lu under pressure. We find that Lu should transform from hcp to the Sm-type structure at − 2 [GPa] and into the dhcp structure at 35 [GPa]. Because of a 2% error in the calculated equilibrium radius and because of the failure

mentioned above, the first estimate is in error by 25 [GPa], the experimental critical pressure being 23 [GPa] (Liu 1975). The second transition has not yet been observed.

Under pressure La is predicted to transform from dhcp to the fcc structure at 8 [GPa], Fig. 17, which compares favourably with the experimental room-temperature transition pressure of 2.5 [GPa] (Piermarini 1964). The distorted fcc phase discovered by Grosshans et al. (1982) has not been considered, but we shall return to the high-pressure properties of La in the following section.

5.6. Cerium metal under pressure

The behaviour of Ce under pressure has been a subject of long-standing and some controversy, primarily because of the unusual isostructural
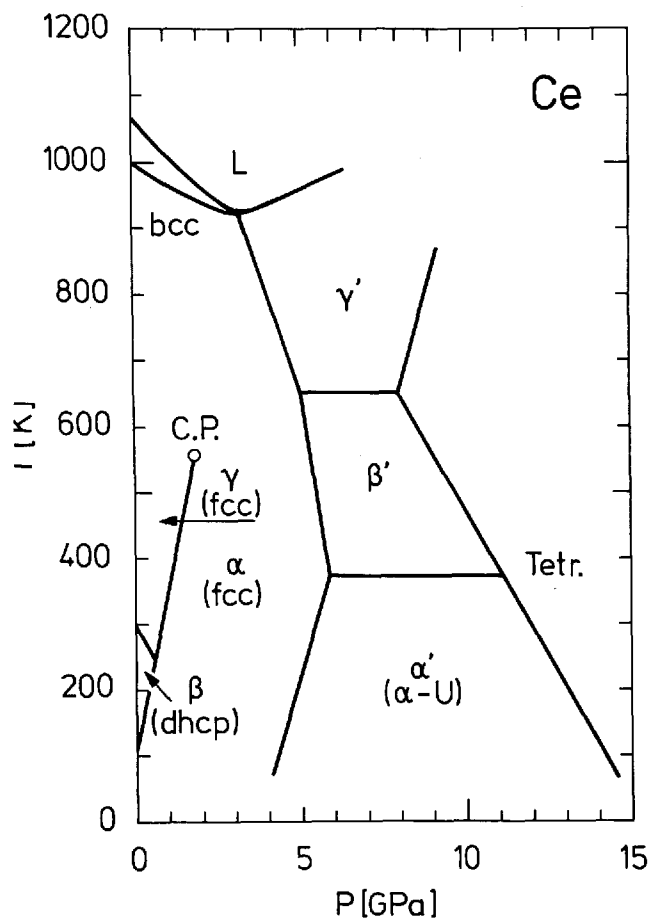
Fig. 18. Phase diagram for Ce compiled from Khvostantsev et al. (1983).

$\gamma \rightarrow \alpha$ transition. Here we shall be concerned with the fcc$\rightarrow \alpha$-U$\rightarrow$tetragonal crystal-structure sequence exhibited by metallic Ce at low temperature in the pressure range up to 20 [GPa] (see Fig. 18). In the calculations we shall treat the s, p, d, and the 4f electrons on the same footing, i.e. as band electrons. Hence, we favour the picture of the $\gamma \rightarrow \alpha$ transition suggested by Gustafson et al. (1969) and elaborated by Johansson (1974) according to which pressure induces a Mott transition within the 4f shell such that the 4f electron goes from a localized state in γ-Ce to a delocalized, i.e. band state, in α-Ce.

According to the Mott-transition picture Ce metal at pressures above the $\gamma \rightarrow \alpha$ transition is different from the other lanthanides (and indeed from all the other metals we have considered so far) in that it has a fourth conduction electron residing in the 4f band. It is this occupation of the 4f band which is expected to be responsible for the stability of the α-U structure found experimentally above 5.6 [GPa] (Ellinger and Zachariasen 1974) and perhaps for the tetragonal phase found above 12.1 [GPa] (Endo et al. 1977). To shed light on this question we shall now present a series of calculations of structural stabilities for Ce under pressure, and compare the results with those obtained for La where the 4f band is essentially empty.

The orthorombic α-U structure may be viewed as distorted fcc, where some of the face-centered atoms have been moved away from their positions as described by the parameter 2y, see Fig. 19. If 2y = 0.5a and a = b = c one has the usual fcc unit cell. In the case of Ce the Madelung contribution to the structural energy favours a 2y of approximately 0.3 (see top panel of Fig. 19) but the one-electron contribution moves the minimum in the energy difference to 2y = 0.21 which is the 2y value found experimentally in U (Donohue 1975). Under pressure the minimum is seen to move to slightly lower 2y values and eventually the α-U structure becomes more stable than the fcc.

From fig. 19 it is expected that Ce will exhibit an fcc$\rightarrow \alpha$-U phase transition at a pressure which is calculated to be 11.7 [GPa]. The experimental transition pressure is 5.6 [GPa] (Ellinger and Zachariasen 1974), and the discrepancy may be attributed to the fact that the atomic sphere approximation is less suited for open crystal structures such as the α-U structure. As may be seen in Fig. 19 the Madelung correction, which we could neglect for the close-packed crystal structures of the alkaline earth and transition metals is now of the same order of magnitude as the one-electron contribution. Hence, inadequacies in the Madelung approximation of the electrostatic contribution to the structural energy are magni-
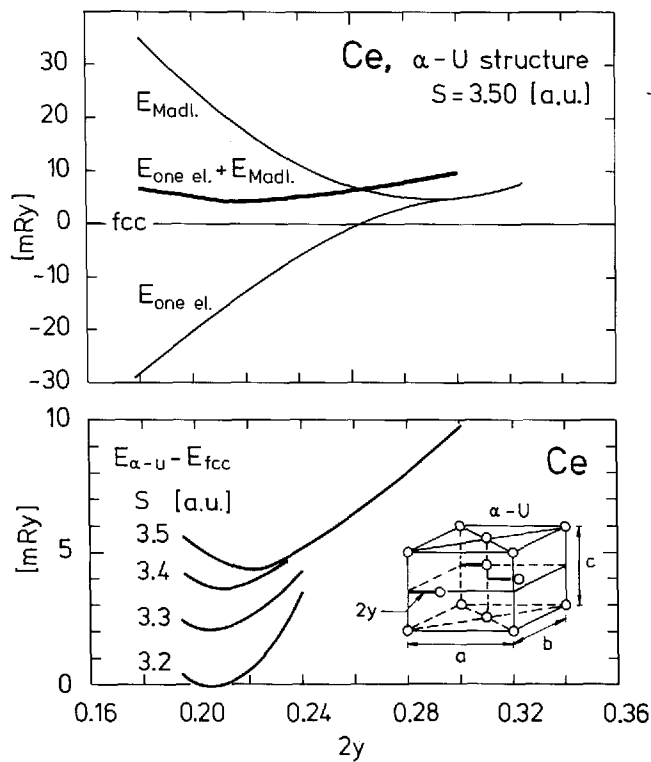
Fig. 19. Energy of Ce in the α-U structure relative to the fcc phase calculated as a function of the positional parameter 2y (see insert) and atomic radius S. The individual Madelung and one-electron contributions for one particular radius are shown in the upper panel.

fied and lead to errors in the estimate of the stability of the α-U structure. A similar problem was recently encountered in the case of the open Cs IV structure in Cs metal (McMahan 1984).

If we compare the structural energy-differences for Ce and La (Figs. 17, 19) under pressure we find that while the α-U structure eventually becomes more stable than fcc in Ce it does not do so in La. Since the 4f band is essentially unoccupied in La, whereas Ce has approximately one 4f band electron, the notion that f-band states are responsible for the stability of distorted crystal structures such as the α-U structure is strongly supported by the present calculations. It follows that the α-U structure would not become stable in Ce under pressure unless the 4f electrons were delocalized, i.e. band like, and therefore any adequate description of the α and α' phases in Ce must treat the 4f states on the same footing as the s, p, and d states. In short, Ce is a 4f band metal.

The high-pressure tetragonal structure (Endo et al. 1977) of Ce may be regarded as a distorted fcc structure in which the unit cell has been elongated along the c axis such that the c/a ratio in a body-centred

Fig. 20. Energy of Ce in the body-centred tetragonal (bct) structure relative to the fcc phase calculated as a function of the c/a ratio and atomic radius (the pressures can be inferred from Fig. 21). The insert shows the bct structure.
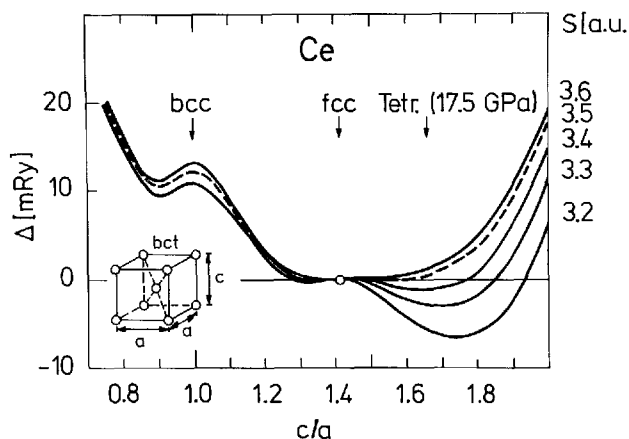
tetragonal (bct) description is approximately 1.7, see Fig. 20. In the same description bcc and fcc correspond to c/a equal to 1 and $\sqrt{2}$, respectively. According to the structural energy differences in Fig. 20 Ce should as a function of pressure start out in the fcc structure and then transform into a bct structure with a c/a ratio which increases with pressure. In this .case the 4f states do not seem to be responsible for the pressure-induced transition, since the same bct structure is also calculated to be the stable high-pressure phase of La, Fig. 17.

In Fig. 21 we have collected the calculated structural energy differences for Ce under pressure. Owing to the less accurate description of open structures discussed above, the α-U structure is seen not to be the stable phase in the pressure range considered, and instead Ce would be expected to go directly from the fcc into the bct phase. However, if we move the α-U curve down by 4.5 [mRy] which is 20% of the Madelung correction (see Fig. 19) we obtain agreement with experiment (Ellinger and Zachariasen 1974, Endo et al. 1977) in the sense that Ce is now expected to exhibit the crystal structure sequence fcc→α-U→tetragonal.

5.7. The light actinides

The calculated structural energy differences for the light actinides Th–Pu are shown in Fig. 22, from which we deduce the most stable close-packed structure to be fcc in Th and Pa and bcc in U, Np, and Pu. This indicates that although these structures are not the stable low-temperature structures in Pa–Pu, they are at least close in energy to the distorted structures observed experimentally and may therefore be realized at elevated temperatures. Experimentally one finds the fcc structure to be

stable in Th up to 1670 [K] (Donohue 1975, Young 1975), and there are indications that Pa has a high temperature fcc phase (Donohue 1975). Furthermore, neither U nor Np has a high temperature fcc phase but instead they become bcc before melting. Pu has a high temperature fcc (δ) phase but since this phase becomes unstable at a pressure of only 0.1 [GPa] it is most probably associated with a localization of the 5f electrons, and the relevant high temperature phase in the present context is then the bcc (ϵ) phase. Thus, experimentally the most stable close-packed structure appears to be fcc in Th and Pa, and bcc in U, Np, and Pu, in agreement with the findings in Fig. 22.

The low–temperature tetragonal structure (α) in Pa may be viewed (Zachariasen 1952) as a distorted bcc structure in which the unit cell has been compressed along the c axis such that the c/a ratio is approximately 0.82, see Fig. 23. According to Fig. 23 the Madelung contribution
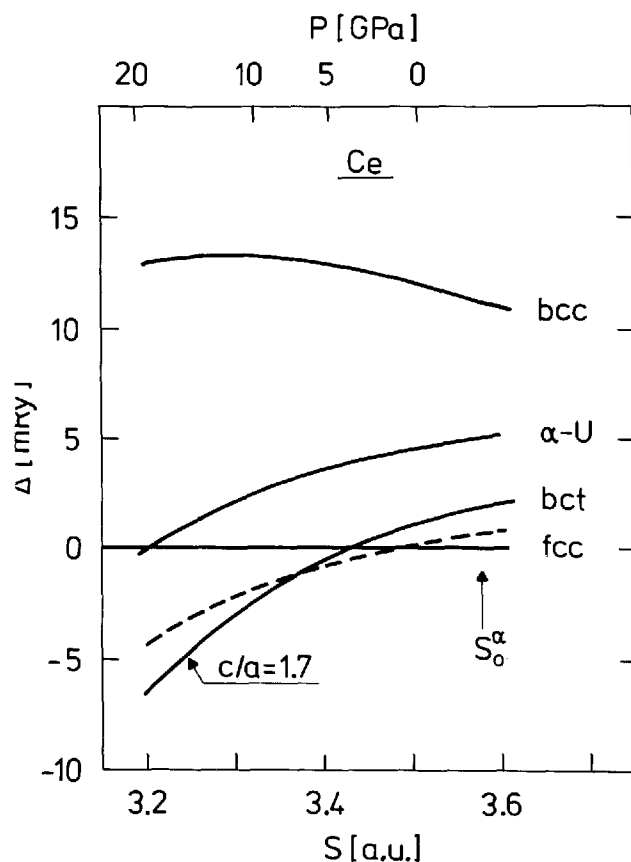
Fig. 21. Structural energy differences for Ce calculated as a function of pressure P and plotted versus atomic radius. S_0^α indicates the experimentally observed equilibrium radius of Ce in the α phase. The calculations included s, p, d, and f orbitals and the Madelung correction Eq. (11).

favours bct structures with c/a in the range from 0.95 to 1.50, whereas structures with c/a outside this range rapidly become extremely unstable. In contrast, the one-electron contribution tends to favour c/a outside the central range, and as a result the energy difference curve for Th has one minimum at c/a $= \sqrt{2}$, corresponding to fcc, in agreement with experiment, while that of Pa exhibits three minima, one of which is close to the c/a observed experimentally in the α phase.

As in the case of the α-U structure in Ce, we are again experiencing problems stemming from the atomic sphere approximation and in particular the Madelung correction, which leads to slightly incorrect estimates of the structural energy differences for open crystal structures. Thus, in the case of Pa the most stable structure is calculated to be bct with c/a $= 1.6$, which incidentally is the high-pressure phase of Ce, whereas the minimum which corresponds to the experimental α structure lies 1.3 mRy above the absolute minimum and is shifted to a c/a of 0.92. However, in view of the rapidly changing Madelung correction in the range below c/a $= 0.95$, it is not unlikely that a better calculation of the electrostatic contribution to the structural energy differences may correct both errors.

Since the 5f band is unoccupied in Th while Pa has approximately one 5f electron it follows from Fig. 23 that the 5f states are responsible for the stability of the tetragonal α phase in Pa. Thus, the situation here is very
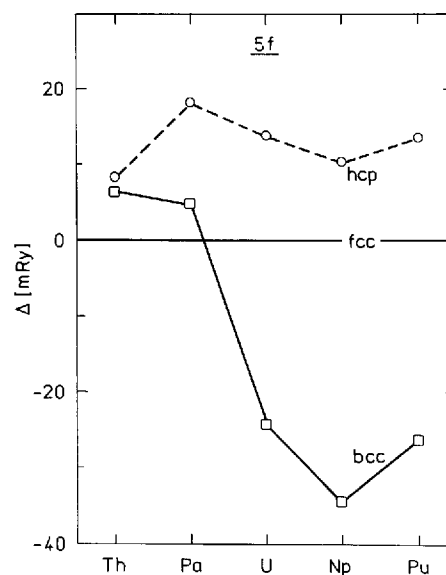
Fig. 22. Calculated structural energy differences for the light actinides plotted versus atomic number. The calculations included s, p, d, and f orbitals but not the Madelung correction Eq. (11).
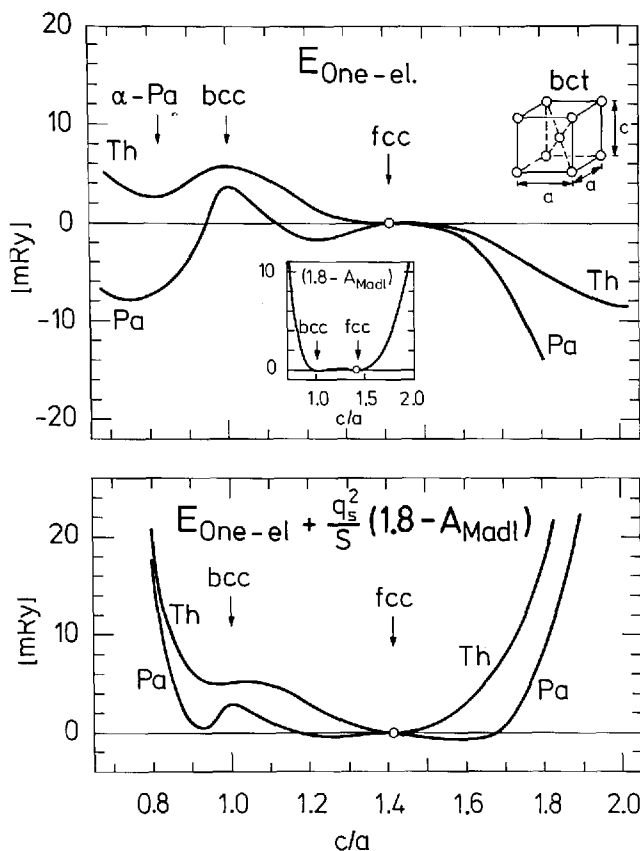
Fig. 23. Energy of Th and Pa in the bct structure relative to the fcc phase calculated as a function of the c/a ratio. The upper panel shows the one-electron contributions, the insert shows the shape of the Madelung correction, and the lower panel shows the total energy differences.

similar to that found earlier in Ce where the presence of one 4f electron stabilized the high pressure α-U structure, and again we take this to mean that the 5f states in the light actinides are itinerant, i.e. band-like, and give rise to distorted crystal structures.

6. Conclusion

We have studied the stability of the crystal structures of some 40 elemental metals within a one-electron approach. The effective one-electron equations have been solved self-consistently by means of the LMTO method and the structural energy differences calculated by means of Andersen's force theorem. This approach has the advantage of treating s, p, d, and f states on the same footing, thus leading to a conceptually

consistent description of trends throughout the periodic table. However, the present implementation of the method is only accurate for close-packed crystal structures, and for that reason we exclude in our study open structures such as CsIV and the more exotic structures found in the actinide series. On the other hand, this shortcoming is not fundamental and will undoubtedly be remedied in the near future.

We find that the theory correctly predicts the crystal structures observed experimentally at low temperature and atmospheric pressure in 35 out of the 42 cases studied. In those few instances where the theory fails we find that the correct crystal structure is only marginally less stable than the calculated structure – this is the case for Na, Au, Yb, and Pa – or the metal is magnetic at low temperature, as in Mn, Fe, and Co. For the light actinides U, Np, and Pu we have not considered the experimentally most stable crystal structures but only the most stable close-packed structures and find the predictions of the theory to be in qualitative agreement with the known phase diagrams.

In a comparison between the calculated structural energy differences for the 4d transition metals and the enthalpy differences derived from studies of phase diagrams we find that, although the crystal structures are correctly predicted by the theory, the theoretical energy differences are up to a factor of 5 larger than their »experimental« counterparts. The reasons for this discrepancy may lie in the local-density approximation or in the neglect of the non-spherical part of the charge distribution. Furthermore, the derived enthalpy differences are certainly model dependent and may change as the model is improved.

In addition to the equilibrium properties we have studied the crystal structures of the alkali, the alkaline earth and some rare earth metals under pressure. We find that the heavy alkalis K, Rb, and Cs should be part of the crystal structure sequence bcc→hcp→fcc where the intermediate hcp phase may be suppressed at room temperature, and explain the experimentally observed bcc→fcc transition in terms of the pressure-induced descent of a zone-boundary energy gap which exists in the fcc band structure but has no counterpart in the bcc case. For the alkaline earth and rare earth metals we find crystal structure sequences which correlate with the calculated d-occupation numbers and which are in agreement with experimental high-pressure observations if we neglect some complex structures found in Ca and Sr.

Finally, we have studied the high-pressure crystal structure sequence fcc→α-U→tet for La and Ce and find that under compression the α-U structure becomes more stable than fcc in Ce, but not in La. This indi-

cates that the presence of itinerant 4f states is responsible for the fcc→α-U transition observed experimentally in Ce. In both La and Ce the calculations predict a tetragonal high-pressure phase. This phase is seen experimentally in Ce but not in La where one instead observes a distorted fcc structure not considered in the present work.

In conclusion, we have studied the stability of crystal structures of metals both at equilibrium and at high pressures by a one-electron approach. We find that we can account for the occurence of most of the close-packed structures observed experimentally. In the few cases where the theory is in disagreement with experiment we find that the correct crystal structure is only marginally less stable than the predicted structure. In order to describe open structures, such as α-U or CsIV, with the same accuracy as the close-packed structures one needs a more accurate approximation for the electrostatic contribution to the total energy.

References

J. Akella, Q. Johnson, W. Thayer, and R. N. Schock, J. Less-Comm. Met. *68*, 95 (1979).

J. Akella, Q. Johnson, and R. N. Schock, Geophysical Res. *85*, 7056 (1980).

I. V. Alexandrov, C. V. Nesper, V. N. Katchinsky and J. Marenko, paper at the 20th meeting of the »European High pressure Research Group«, Stuttgart, 1982 (unpublished).

O. K. Andersen, Phys. Rev. *B12*, 3060 (1975).

O. K. Andersen and O. Jepsen, Physica *91B*, 317 (1977).

O. K. Andersen, J. Madsen, U. K. Poulsen, O. Jepsen, and J. Kollar, Physica *86-88B*, 249 (1977).

O. K. Andersen, H. L. Skriver, H. Nohl, and B. Johansson, Pure Appl. Chem. *52*, 93 (1979).

A. O. E. Animalu, Phys. Rev. *161*, 445 (1967).

J. Bardeen, J. Chem. Phys. *6*, 372 (1938).

U. von Barth and L. Hedin, J. Phys. *C5*, 1629 (1972).

B. J. Beaudry and K. A. Gschneidner, Jr., »Preparation and Basic Properties of the Rare Earth Metals« in »*Handbook on the Physics and Chemistry of Rare Earths*« ed. by K. A. Gschneidner, Jr. and L. R. Eyring (North Holland Publishing Company, Amsterdam 1978).

U. Benedict, J. R. Peterson, R. G. Haire, and C. Dufour, J. Phys. *F14*, L43 (1984).

M. Born and J. E. Mayer, Zeits. f. Physik *75*, 1 (1932).

L. Brewer: »Phase Stability in Metals and Alloys« in »*Batelle Institute Materials Science Colloquia*«, ed. by P. S. Rudman, J. Stringer, and R. I. Jaffee (McGraw-Hill, New York 1967), pp. 39-62.

E. Bucher, P. H. Schmidt, A. Jayaraman, K. Andres, J. P. Maita, K. Nassau, and P. D. Dernier, Phys. Rev. *B2*, 3911 (1970).

M. S. S. Brooks and B. Johansson, J. Phys *F13*, L197 (1983).

N. W. Dalton and R. A. Deegan, J. Phys. *C2*, 2369 (1969).

R. A. Deegan, J. Phys. *C1*, 763 (1968).

J. Donohue, »The Structures of the Elements« (John Wiley & Sons, New York 1975).

F. Ducastelle and F. Cyrot-Lackmann, J. Phys. Chem. Solids *32*, 285 (1971).

K. J. Dunn and F. P. Bundy, Phys. Rev. *B24*, 1643 (1981).

J. C. Duthie and D. G. Pettifor, Phys. Rev. Lett. *38*, 564 (1977).

F. H. Ellinger and W. H. Zachariasen, Phys. Rev. Lett. *32*, 773 (1974).

S. Endo, H. Sasaki, and T. Mitsui, J. Phys. Soc. Japan *42*, 882 (1977).

E. Esposito, A. E. Carlsson, D. D. Ling, H. Ehrenreich, and C. D. Gelatt, Jr., Phil. Mag. *A41*, 251 (1980).

J. Friedel, »Transition Metals. Electronic Structure of the d-band. Its Role in the Crystalline and Magnetic Structures« in »*The Physics of Metals 1. Electrons*« ed. by J. M. Ziman (Cambridge University Press 1969).

J. Friedel and C. M.. Sayers. J. Physique *38*, 697 (1977).

D. Glötzel and A. K. McMahan, Phys. Rev. *B20*, 3210 (1979).

W. A. Grosshans, Y. K. Vohra, and W. B. Holzapfel, Phys. Rev. Lett. *49*, 1572 (1982).

K. A. Gschneidner, »Physical Properties and Interrelations of Metallic and Semimetallic Elements« in »*Solid State Physics*« vol. *16*, ed. by H. Ehrenreich, F. Seitz, and D. Turnbull (Academic Press, New York 1964).

K. A. Gschneidner and R. M. Valletta, Acta Met. *16*, 477 (1968).

D. R. Gustafson, J. D. McNutt and L. O. Roellig, Phys. Rev. *183*, 435 (1969).

J. Hafner and V. Heine, J. Phys. *F13*, 2479 (1983) and references therein.

H. T. Hall, L. Merril, and J. D. Barrett, Science *146*, 1297 (1964).

V. Heine and D. Weaire, »Pseudopotential Theory of Cohesion and Structure« in »*Solid State Physics*« vol. *24* ed. by H. Ehrenreich, F. Seitz, and D. Turnbull (Academic press, New York 1970).

V. Heine, »Electronic Structure from the Point of View of the Local Atomic Environment« in »*Solid State Physics*« vol. *35* ed. by H. Ehrenreich, F. Seitz, and D. Turnbull (Academic Press, New York 1980).

C. H. Hodges, Acta Met. *15*, 1787 (1967).

W. B. Holzapfel, T. G. Ramesh, and K. Syassen, J. de Phys. Coll. *40*, C5-390 (1979).

J.-P. Jan and H. L. Skriver, J. Phys. *F11*, 805 (1981).

A. Jayaraman, W. Klement, Jr., and G. C. Kennedy, Phys. Rev. Lett. *10*, 387 (1963a).

A. Jayaraman, N. Klement, Jr., and G. C. Kennedy, Phys. Rev. *132*, 1620 (1963b).

A. Jayaraman, Phys. Rev. *135*, A1056 (1964).

A. Jayaraman and R. C. Sherwood, Phys. Rev., *134*, A691 (1964).

A. Jayaraman, Phys. Rev. *139*, A690 (1965).

B. Johansson, Phil. Mag. *30*, 469 (1974).

B. Johansson and A. Rosengren, Phys. Rev. *B11*, 2836 (1975).

B. Johansson, »Structural and elastic properties of the f elements« in »*Rare Earths and Actinides, 1977*« ed. by W. D. Corner and B. K. Tanner (IOP, Bristol 1978), p. 39 (Inst. Phys. Conf. Ser. No. *37*).

H. Jones, Prog. Phys. Soc. *49*, 250 (1937).

L. Kaufman and H. Bernstein: »Computer Calculations of Phase Diagrams« (Academic Press, New York 1970).

L. G. Khvostantsev and N. A. Nikolaev, Phys. Stat. Sol. (a) 77, 161 (1983).

C. C. Koch, J. Less-Comm. Met. *22*, 149 (1970).

W. Kohn and L. J. Sham, Phys. Rev. *140A*, 1135 (1965).

L.-G. Liu, W. A. Bassett, and M. S. Liu, Science *180*, 298 (1973).

L.-G. Liu, J. Phys. Chem. Solids *36*, 31 (1975).

J. W. McCaffrey, J. R. Anderson, and D. A. Papaconstantopoulos, Phys. Rev. *B7*, 674 (1973).

A. R. Machintosh and O. K. Andersen, »The electronic structure of transition metals« in »*Electrons at the Fermi surface*« ed. by M. Springford (Cambridge University Press, Cambridge 1980).

A. K. McMahan and J. A. Moriarty, Phys. Rev. *B27*, 3235 (1983).

A. K. McMahan, Phys. Rev. *B29*, 5982 (1984).

D. B. McWhan and A. L. Stevens, Phys. Rev. *139*, A682 (1965).

D. B. McWhan and A. L. Stevens, Phys. Rev. *154*, 438 (1967).

D. B. McWhan, T. M. Rice, and P. H. Schmidt, Phys. Rev. *177*, 1063 (1969).

D. J. Michish, A. B. Kunz, and S. T. Pantalides, Phys. rev. *B10*, 1369 (1974).

A. R. Miedema and A. K. Niessen, CALPHAD 7, 27 (1983).

J. A. Moriarty, Phys. Rev. *B8*, 1338 (1973).

J. A. Moriarty, Phys. Rev. *B26*, 1754 (1982).

J. A. Moriarty and A. K. McMahan, Phys. Rev. Lett. *48*, 809 (1982).

N. F. Mott and H. Jones, »The Theory of the Properties of Metals and Alloys« (Oxford Univ. Press, London 1936).

A. Nakaue, J. Less-Comm. Met. *60*, 47 (1978).

R. M. Nieminen and C. H. Hodges, J. Phys. *F6*, 573 (1976).

H. Olijnyk and W. B. Holzapfel, Phys. Lett. *99A*, 381 (1983).

H. Olijnyk abd W. B. Holzapfel, Phys. Lett. *100A*, 191 (1984).

B. Olinger and J. W. Shaner, Science *219*, 1071 (1983).

D. G. Pettifor, J. Phys. *C3*, 367 (1970).

D. G. Pettifor: »Theory of the Crystal Structures of Transition Metals at Absolute Zero« in »*Metallurgical Chemistry*« ed. by O. Kubashewski (HMSO, London 1972).

D. G. Pettifor, Commun. Phys. *1*, 141 (1976).

D. G. Pettifor, CALPHAD *1*, 305 (1977).

G. J. Piermarini and C. E. Weir, Science *144*, 69 (1964).

R. B. Roof, R. G. Haire, D. Schiferl, L. A. Schwalbe, E. A. Kmetko, and J. L. Smith, Science *207*, 1353 (1980).

R. B. Roof, Z. für Krist. *158*, 307 (1982).

A. Rosengren and B. Johansson, Phys. Rev. *B13*, 1468 (1976).

H. L. Skriver, Phys. Rev. Lett. *49*, 1768 (1982).

H. L. Skriver, »Electronic Structure and Cohesion in The Rare Earth Metals« in »*Systematics and the Properties of the Lanthanides*« ed. S. P. Sinha (D. Reidel Publishing Company, Dordrect 1983).

H. L. Skriver, »The LMTO Method« (Springer-Verlag, Berlin 1984).

P. C. Souers and G. Jura, Science *140*, 481 (1963).

R. A. Stager and H. G. Drickamer, Phys. Rev. *131*, 2524 (1963).

R. A. Stager and H. G. Drickamer, Science *139*, 1284 (1963).

D. R. Stephens, H. D. Stromberg, and E. M. Lilley, J. Phys. Chem. Solids *29*, 815 (1968).

K. Syassen, G. Wortmann, J. Feldhaus, K. H. Frank, and G. Kaindl, Phys. Rev. *B26*, 4745 (1982).

K. Takemura, S. Minomura, and O. Shimomura, »Structure of Cesium and Iodine under Pressure« in *»Physics of Solids under High Pressure«* ed. by J. S. Schilling and R. N. Shelton (North-Holland, Amsterdam 1981).

K. Takemura and K. Syassen, Solid State Commun. *44*, 1161 (1982).

K. Takemura, S. Minomura, and O. Shimomura, phys. Rev. Lett. *49*, 1772 (1982).

K. Takemura and K. Syassen, Phys. Rev. *B28*, 1193 (1983).

K. Takemura and K. Syassen, J. Phys. F (1985, in print).

A. R. Williams, unpublished, and quoted by Miedema and Niessen (1983).

Y. K. Vohra, H. Olijnyk, W. A. Grosshans, and W. B. Holzapfel, Phys. Rev. Lett. *47*, 1065 (1981).

D. A. Young, »Phase Diagrams of the Elements«, Lawrence Livermore Laboratory Report UCRL-51902 (1975, unpublished).

D. A. Young and M. Ross, Phys. Rev. *B29*, 682 (1984).

W. H. Zachariasen, Acta Cryst. *5*, 19 (1952).

A. Zunger and M. L. Cohen, Phys. Rev. *B18*, 5449 (1978); *B20*, 4082 (1979).

Claus S. Jacobsen

Infrared Studies on the Electronic Structure of Organic Conductors

ABSTRACT. *It is experimentally shown that a simple Drude analysis of the reflectance edge in organic conductors yields reliable values for electronic transfer integrals. The integrated infrared oscillator strength is found to be smaller than expected from band theory. The reduction is interpreted as being an effect of the short range electron-electron interaction and is used to compare the strength of this interaction among different materials. It is concluded that highly correlated systems may be semiconductors due to electron-phonon driven instabilities, or, if the interstack coupling is sufficient, may remain good metals to low temperatures. The role of the electron-molecular vibration coupling is stressed, both as contributing to instabilities, and as a microscopic probe.*

Physics Laboratory 3, Technical University of Denmark,
DK-2800 Lyngby, Denmark.

Introduction

An ordinary metal, like copper, is characterized by two basic features: (1) A high concentration of valence electrons, which are in principle free to move through the metal, and (2) a strong overlap of the valence electron orbitals (wavefunctions) on neighbour atoms, which effectively makes the electrons delocalize in the metal. The only force capable of inhibiting the free motion of the electrons is the direct Coulomb repulsion between the negatively charged particles. If strong enough, such a repulsion would localize the electrons, one on each atom (Mott, 1949). Although the arguments are quite complicated, it is now well understood, how the electronic system itself almost completely screens out the Coulomb repulsion. The effectiveness of the screening is due to the same two features listed above: A high carrier density and a good neighbour contact. As a consequence ordinary metals have high electrical conductivities (e.g. copper at room temperature with $\sigma = 6 \times 10^5$ Scm^{-1}).

Furthermore, the conductivity increases when the metal is cooled, since the scattering rate for the electrons decreases as the thermally induced vibrations of the atoms get smaller in amplitude. Some metals

even become superconducting at very low temperatures (a few Kelvin), that is, their electrical resistivity vanishes completely.

Such behaviour is contrasted by semiconductors like silicon, where the charge carriers are thermally excited from a state which is insulating at low temperatures. All electrons take part in the localized crystal binding. Thus typically, the conductivity of semiconductors increases with temperature.

In a recently very active, interdisciplinary field of the materials sciences, chemists and physicists have attempted to mimic metallic, electrical properties in organic compounds. The long term perspective is to make it possible employing the great flexibility of organic chemistry to design, synthesize, and manufacture materials with specific, desirable properties.

Presently, there are two approaches to the synthetic metal problem. A considerable amount of effort goes into attempts of doping to high levels polymeric semiconductors like polyacetylene, $(CH)_x$ (for a review see, for example, Baeriswyl et al. (1982)). Although promising for applications, such materials are not truly metallic, since their carrier concentrations are fairly low.

The other approach has lead to the large class of materials, normally called organic conductors (see, for example, Jerome and Schulz (1982), and references therein). Here the work has been directly aimed at incorporating the two basic features of a metal into crystals of organic molecules. The high concentration of charge carriers is obtained by bringing together at least two species of molecules, one which is willing to accept an extra, unpaired electron (acceptor molecule), and another which readily gives up an electron (donor molecule). Thus in the crystal, charge is transferred from donors to acceptors. The second feature, good contact between neighbour building blocks, i.e. the molecules, is achieved by using near planar, π-bound organic molecules, which tend to form stacks with a fair inside overlap. It follows that the contact between stacks must be rather weak, hence the materials are electrically highly anisotropic. In some contexts, they may even be designated one-dimensional (1D).

Thus to shortly characterize organic conductors, they are synthetic materials, which by elementary solid state physics are expected to be metals in electrical sense. However, they are highly anisotropic, have carrier densities one or two orders of magnitude below those of ordinary metals, and even along the molecular stacks, the neighbour contact is at least ten times weaker than in, for example, copper. The latter features

arise from the use of rather big building blocks, which do not pack as effectively as compact metal atoms.

Therefore, it is not surprising that organic conductors so far have been found to be inferior to the elements with respect to metallic quality. The first organic conductors were in fact semiconducting. These early studies date back to the 1950s and -60s (see Gutmann and Lyons, 1967). In 1973 the first material with genuine metallic properties was synthesized (Ferraris et al., 1973). TTF-TCNQ has a room temperature conductivity of order $600 \, Scm^{-1}$, and a strongly increasing $\sigma(T)$ down to 60K. However, below 60K a metal-insulator transition destroys the conductivity. In the following years many derivatives of TTF-TCNQ were studied, and in 1980 Jerome et al. reported superconductivity in the material $TMTSF_2PF_6$ (below 1K and only under a pressure of ~ 10 kbar). The present state of art involves several ambient pressure superconductors (working up to 2.5K), as well as materials with a wide range of interesting magnetic and non-magnetic ground states. Many of the metal-insulator and magnetic phase transitions may be related to the low-dimensionality of the materials. Thus while applications are still somewhat in the future, the materials constitute extremely interesting model systems for solid state physics.

It is the aim of the present study to use infrared (IR) spectroscopy in characterizing the basic interactions in organic conductors. We shall discuss how the IR properties give direct information on the intra- as well as interstack contacts, on the interplay between electron-electron and electron-vibration interactions, and to some extent on the detailed nature of the phase transitions occuring in these materials. It is a central result of the study, that the short range electron-electron interaction plays a role far more important than in ordinary metals. It indeed appears that the probability for finding two conduction electrons on the same molecule is quite small in several materials. The electrons then more or less behave as spinless fermions in transport and optical properties.

Although essential for a microscopic understanding of the electronic structure, the electron-electron interaction needs not destroy the metallic state. Even the organic superconductors appear to have a sizeable electron-electron Coulomb interaction, but a large interchain overlap reduces its impact on the physical properties.

Materials and methods

All the materials investigated in this study belong to the group of potential metals, which are characterized by partially filled one-electron bands and no strong static disorder. The constituent organic molecules are shown in Fig. 1, and their systematic names are listed in Table I.

We will deal with two groups of compounds. (1) The doublestack conductors, like TTF-TCNQ, have uniform stacks, and donor as well as acceptor chains have unpaired electrons. The crystal structure is sketched in Fig. 2(a). A key parameter for these materials is the degree of charge transfer, ϱ, equal to the average number of carriers per molecule. ϱ is determined by a complicated energy balance (Torrance, 1979), and is best found indirectly by diffuse X-ray scattering, which detects weak superstructures related to the Fermi wavevector. (2) The singlestack conductors, dealt with here, are complex salts, where the stoichiometry is such that there is one closed shell ion for a pair of organic molecules. The counterion may be organic or inorganic, but ϱ for the conducting

Table I. Organic molecules. D = donor. A = acceptor

| Abbr.	Type	Systematic name
TTF	D	$\Delta^{2,2'}$-bi-1,3-dithiolylidene
TMTTF	D	$\Delta^{2,2'}$-bi-4,5-dimethyl-1,3-dithiolylidene
DBTTF	D	$\Delta^{2,2'}$-bibenzo-1,3-dithiolylidene
HMTTF	D	$\Delta^{2,2'}$-bicyclopenteno-1,3-dithiolylidene
TSF	D	$\Delta^{2,2'}$-bi-1,3-diselenolylidene
TMTSF	D	$\Delta^{2,2'}$-bi-4,5-dimethyl-1,3-diselenolylidene
DBTSF	D	$\Delta^{2,2'}$-bibenzo-1,3-diselenolylidene
HMTSF	D	$\Delta^{2,2'}$-bicyclopenteno-1,3-diselenolylidene
BEDT-TTF (ET)	D	$\Delta^{2,2'}$-bi-5,6-dihydro-1,4-dithiino-1,3-dithiolylidene
MEM$^+$	D[a]	N-ethyl-N-methyl-morpholinium
TCNQ	A	7,7,8,8-tetracyano-p-quinodimethane
DMTCNQ	A	2,5-dimethyl-7,7,8,8-tetracyano-p-quinodimethane
TCNQCl$_2$	A	2,5-dichloro-7,7,8,8-tetracyano-p-quinodimethane
TCNQF$_4$	A	2,3,5,6-tetrafluoro-7,7,8,8-tetracyano-quinodimethane
TNAP	A	11,11,12,12-tetracyanonaphto-2,6-quinodimethane

[a] closed shell ion
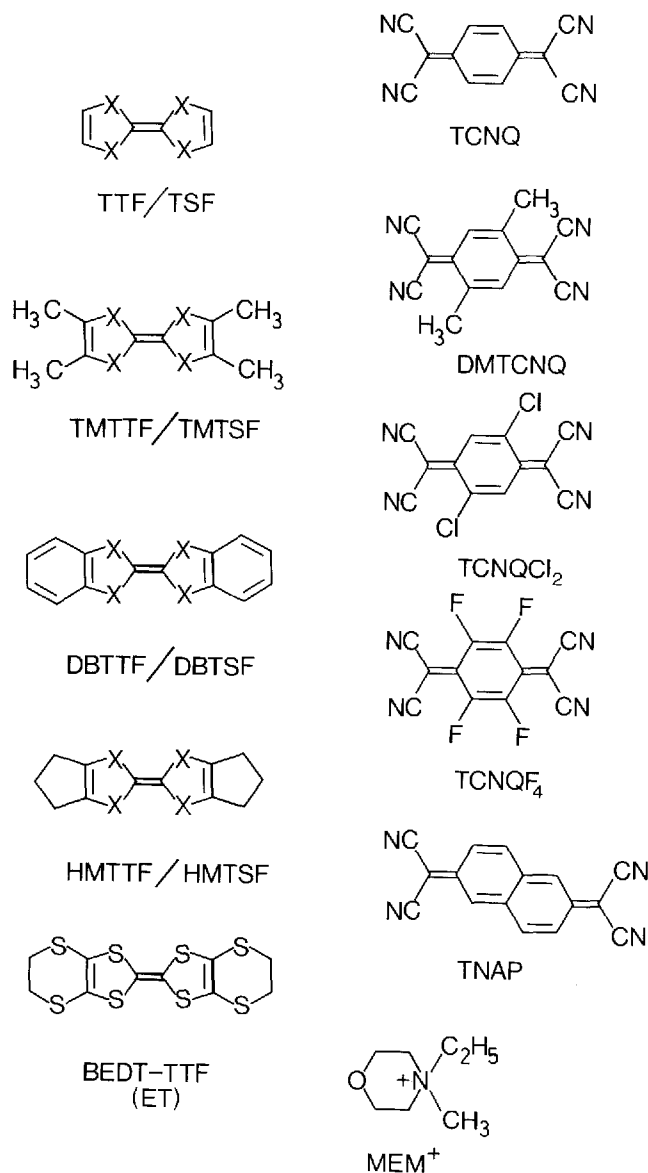
Fig. 1. Donor and acceptor molecules (cfr. Table I).

stack is always 0.5. Due to the stoichiometry alone the stacks show some dimerisation. A typical structure is sketched in Fig. 2(b).

Table II lists the relevant materials with basic physical properties, and gives references to more detailed information.

The organic conductors are usually available as small, 2-4 mm long needles with cross-sectional dimensions of a few tenths of a mm. The
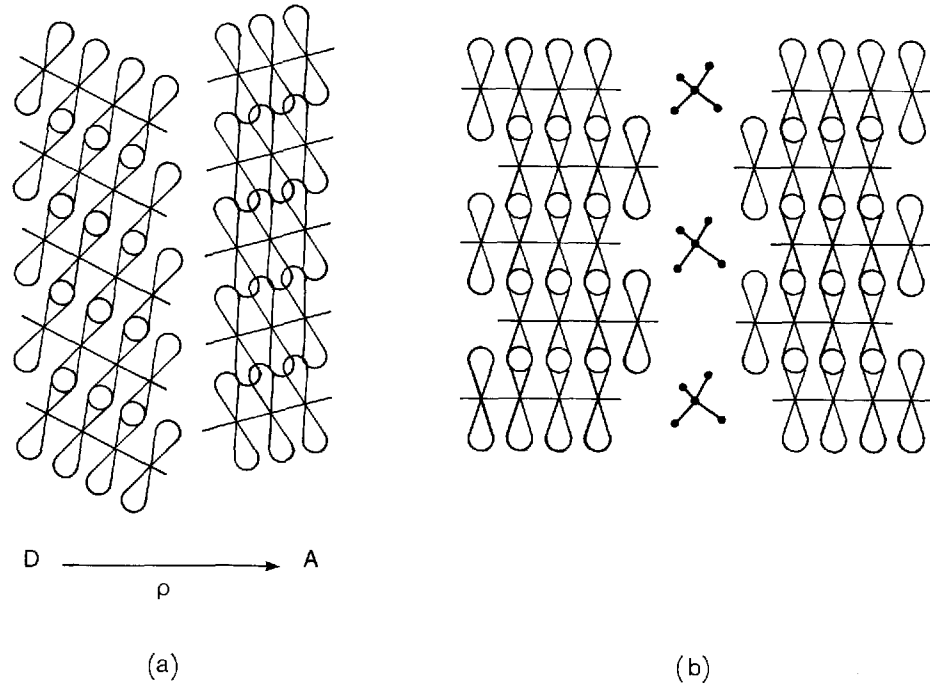
D ————————————▶ A

ρ

(a)   (b)

Fig. 2. Schematic crystal structures. (a) Double-stack conductor. ϱ is the degree of charge transfer. (b) Single-stack conductor with inactive counterions.

faces tend to be of high optical quality, and since the crystals are opaque in the entire range, studies of the IR properties are best conducted as specular, polarized, near-normal incidence reflectance measurements. Details on experimental equipment and procedures are described by Jacobsen et al. (1983).

A frequency range as broad as possible is covered. Then the Kramers-Kronig relations, valid for linear, causal and local response functions may be employed to extract information on the complex dielectric function, $\tilde{\varepsilon}(\omega)$. From the power reflectance, $R(\omega)$, it is possible to calculate the phase shift on reflection, $\theta(\omega)$:

$$\theta(\omega) = \frac{\omega}{\pi} \, P \int_0^\infty \frac{\ln R(\omega')}{\omega^2 - \omega'^2} \; d\omega', \tag{1}$$

and then

$$\tilde{\varepsilon}(\omega) = (\frac{1 + \sqrt{R(\omega)} \; e^{i\theta(\omega)}}{1 - \sqrt{R(\omega)} \; e^{i\theta(\omega)}})^2. \tag{2}$$

Table II. Characteristics of some organic conductors. The third column gives high/low temperature character (M = metal, S = semiconductor, SM = semimetal, SC = superconductor, I = insulator).

Material	σ_{dc}(300K) S cm^{-1}	Character	ϱ	Structure
TTF-TCNQ	600	M/S	0.55	monoclinic
	Cohen et al. (1974)		Kagoshima et al. (1976)	Kistenmacher et al. (1974)
TSF-TCNQ	800	M/S	0.63	monoclinic
	Etemad et al. (1975)		Weyl et al. (1976)	Etemad et al. (1975)
TMTSF-TCNQ	1000	M/S	0.57	triclinic
	Jacobsen et al. (1978)		Pouget (1981)	Bechgaard et al. (1977)
TMTTF -DMTCNQ	120	M/S	–	triclinic
	Jacobsen et al. (1978)			Jacobsen et al. (1978)
TMTSF -DMTCNQ	500	M/S	0.50	triclinic
	Jacobsen et al. (1978)		Pouget (1981)	Andersen et al. (1978)
HMTTF-TCNQ	400	M/S	0.72	orthorhombic
	Greene et al. (1976)		Megtert et al. (1978)	Greene et al. (1976)
HMTSF-TCNQ	2000	M/SM	0.74	orthorhombic
	Bloch et al. (1975)		Weyl et al. (1976)	Phillips et al. (1976)
DBTTF -TCNQCl$_2$	40	S/I	0.56	triclinic
	Jacobsen et al. (1980)		Mortensen et al. (1983)	Soling et al. (1981a)
HMTSF-TNAP	2400	M/SM	0.58	triclinic
	Bechgaard et al. (1978)		Pouget (1984)	Kistenmacher (1978)
DBTSF -TCNQF$_4$	0.0001	S/I	1.0	monoclinic
	Bryden et al. (1984)		Bryden et al. (1984)	Bryden et al. (1984)
MEM-TCNQ$_2$	0.001	S/I	0.5	triclinic
	Huizinga et al. (1979)			Bosch and v.Bodegom (1977)
TMTSF$_2$PF$_6$, -AsF$_6$,-SbF$_6$	500	M/S	0.5	triclinic
	Bechgaard et al. (1980)			Thorup et al. (1981) Soling et al. (1981b)
TMTSF$_2$ClO$_4$	700	M/SC	0.5	triclinic
	Bechgaard et al. (1981a)			Bechgaard et al. (1981b)
TMTTF$_2$Br	260	M/I	0.5	triclinic
	Delhaes et al. (1979)			Liautard et al. (1982)
TMTTF$_2$PF$_6$	20	S/I	0.5	triclinic
	Delhaes et al. (1979)			Liautard et al. (1982)
(BEDT-TTF)$_2$I$_3$	30	M/SC	0.5	triclinic
	Yagubskii et al. (1984)			Kaminskii et al. (1984)

P denotes principal value. Clearly in Eq. (1) suitable extrapolations for the ranges not covered must be adopted (see, for example, Wooten (1972)). However, if the measured range is sufficiently wide, $\bar{\epsilon}(\omega)$ is not very dependent on the particular choice of extrapolations.

For conducting substances, the imaginary part of $\bar{\epsilon}(\omega)$ diverges as $\omega \rightarrow 0+$. Hence it is more convenient to introduce the real dielectric function, $\epsilon(\omega)$, and the frequency dependent conductivity, $\sigma(\omega)$, related to $\bar{\epsilon}(\omega)$ by

$$\bar{\epsilon}(\omega) = \epsilon(\omega) + i\sigma(\omega)/\epsilon_o\omega. \tag{3}$$

It is noted that the area under the $\sigma(\omega)$ curve in a natural way corresponds to the optical oscillator strength. For example, integrating over all frequencies yields the sum rule (Wooten, 1972),

$$\int_0^\infty \sigma(\omega)d\omega = (\pi/2)Ne^2/m, \tag{4}$$

where N is the total electron density and m is the electron mass. As demonstrated later, similar sum rules may with some care be applied to limited frequency ranges and particular groups of electrons.

Basic interactions and instabilities

This section introduces important physical parameters and models, which will be referred to later. Theoretical expectations to the IR properties associated with the models are discussed. Finally, we review shortly the different types of low-dimensional instabilities.

One-electron model

The simplest model for the molecular chain compounds assumes non-interacting electrons, which can move only in the chain direction:

$$H = \sum_{i,\sigma} E_o n_{i,\sigma} - \sum_{i,\sigma} t(c_{i,\sigma}^+ c_{i+1,\sigma} + c_{i+1,\sigma}^+ c_{i,\sigma}). \tag{5}$$

$c_{i,\sigma}^+$ creates an electron of spin projection σ on site i, and $n_{i,\sigma} = c_{i,\sigma}^+ c_{i,\sigma}$ is the occupation number. E_o is the solid state ionization potential, and t is the transfer integral associated with the finite overlap between near neighbour orbitals. More distant overlaps may be safely ignored in molecular crystals. This tight-binding approximation leads to a cosine energy band:

$$\epsilon_k = E_o - 2t\cos kd, \tag{6}$$
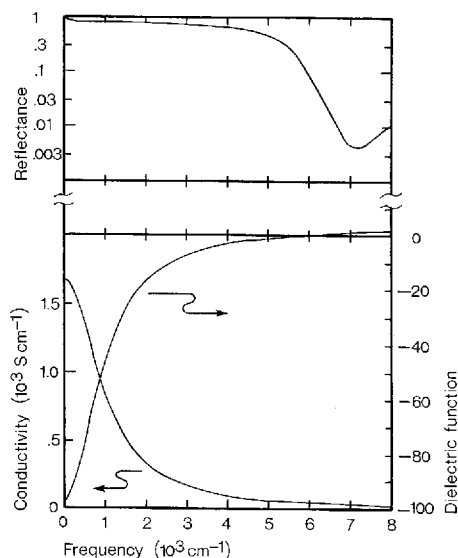
Fig. 3. Optical properties of the Drude model. Notice the logarithmic reflectance scale. Parameters: $\varepsilon_c = 3.0$, $\omega_p = 10000\ cm^{-1}$, $\gamma_{opt} = 1000\ cm^{-1}$.

where d is the molecular repeat distance. With ϱ electrons per site, the band is filled to $\pm k_F = \pm\pi\varrho/2d$ (assuming $t > 0$). Thus the Fermi surface consists of the two parallel planes $k = \pm k_F$. The density of states at the Fermi level is $N(\varepsilon_F) = (\pi t \sin(\pi\varrho/2))^{-1}$.

The IR properties associated with Eq. (5) may be derived in the self-consistent field approximation (see, for example, Wooten (1972)). Assuming a frequency independent relaxation rate, γ_{opt}, and a background dielectric constant arising from virtual high frequency transitions, ε_c, the result is of the Drude form,

$$\tilde{\varepsilon}(\omega) = \varepsilon_c - \omega_p^2/\omega(\omega + i\gamma_{opt}), \tag{7}$$

where the plasma frequency, ω_p, may be calculated from

$$\omega_p^2 = (e^2/\varepsilon_o\hbar^2) \sum_{BZ} f(\varepsilon_k)\partial^2\varepsilon_k/\partial k^2. \tag{8}$$

$f(\varepsilon_k)$ is the Fermi-Dirac occupation number, and the derivative $\partial^2\varepsilon_k/\partial k^2$ is to be taken along the direction of the electric field.

In the present quasi-1D model, Eq. (8) yields

$$\omega_p^2 = 4td^2e^2\sin(\pi\varrho/2)/\pi\varepsilon_o\hbar^2 V_m, \tag{9}$$

where V_m is the crystal volume per molecule. This expression is derived for $T = 0$. The explicit temperature dependence may be ignored when $k_B T \ll \varepsilon_F$, a condition which is normally fulfilled. In Fig. 3 the IR

properties of the Drude model are shown for typical values of the parameters.

Especially noteworthy is the characteristic drop in reflectance in the near IR, which arises from the zero-crossing of $\varepsilon(\omega)$. This is also the frequency of the plasmons, i.e. long wavelength oscillations in the conduction electron charge density. Since the plasmons are longitudinal excitations, they are not optically excitable in a normal incidence experiment, but the sharp drop in reflectance, the plasma edge, is a signature of their existence.

Another point is that the area below the $\sigma(\omega)$ curve is related to ω_p by a partial sum rule

$$\int_{\text{intraband}} \sigma(\omega)d\omega = (\pi/2)\varepsilon_o\omega_p^2. \tag{10}$$

Interchain hopping may easily be incorporated into the model. If, for simplicity, we consider an orthorhombic, 2D model with transfer integrals $t_{\parallel}$ and $t_{\perp}$, the band dispersion is given by:

$$\varepsilon_{\bar{k}} = E_o - 2t_{\parallel}\cos(k_{\parallel}d_{\parallel}) - 2t_{\perp}\cos(k_{\perp}d_{\perp}). \tag{11}$$

Here $d_{\perp}$ is the chain spacing. A small $t_{\perp} \ll t_{\parallel}$ will introduce a warping of the Fermi surface. For considerable interchain coupling, $t_{\perp} \sim t_{\parallel}$, the Fermi surface will be closed, cylindrical.

From Eqs. (8) and (11) a tensorial $\bar{\bar{\varepsilon}}$ may be calculated. By symmetry the principal axes are the chosen directions, along which Drude behaviour is found with plasma frequencies that in the general case must be calculated numerically. As an example to be used later we show in Fig. 4 the normalized plasma frequencies for a quarter-filled band. The crossover from open to closed Fermi surface is indicated.

Electron-phonon coupling

In molecular crystals there are many possible sources to the electron-phonon coupling. Usually, the most important are considered to be: (1) Modulation of t by external modes (acoustic translational and rotational modes), and (2) modulation of E_o by internal modes (molecular vibrations). A good discussion, including estimates for TTF-TCNQ, has been given by Conwell (1980). The second source to the electron-phonon interaction is of central interest to analysis of IR spectra, since the molecular vibration frequencies span the IR range (100-3000 cm^{-1}).

The origin of the electron-molecular vibration (emv) coupling is easily understood. The conduction electron orbital energy is in general a func-
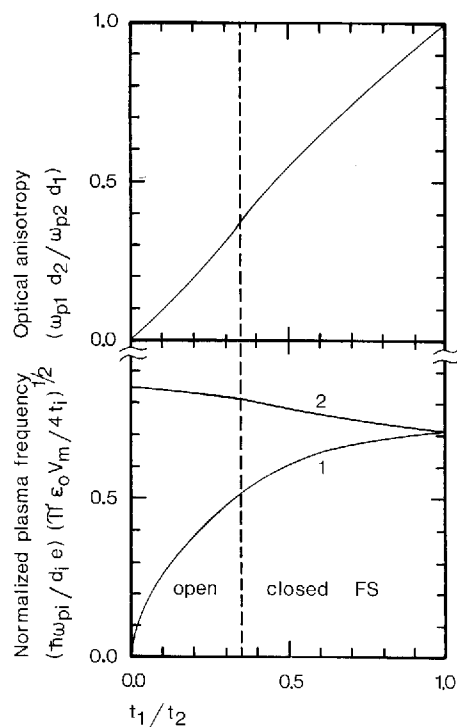
Fig. 4. Anisotropic plasma behaviour in 2D orthorhombic and quarter-filled tight-binding model. The dashed line indicates the cross-over from open (left) to closed (right) Fermi surface. The bottom graphs show normalized plasma frequencies.

tion of the exact atomic configuration in the molecule. Hence the molecular vibrations will modulate the one-electron energies, giving rise to the emv coupling. For a non-degenerate level only the totally symmetric A_g-modes couple linearly to the electrons (Duke et al., 1975). The A_g-modes are Raman active, but IR inactive. However, when charge can move to and from the molecule as in the solid state or in molecular complexes in solution, the modes may, through the emv coupling, borrow oscillator strength from the conduction electrons and give rise to spectacular effects in the IR (see, for example, Bozio and Pecile (1980) and references therein). If the electronic structure is sufficiently simple, information on coupling constants may be extracted from the spectra. One example is the material MEM-$TCNQ_2$ at 300K, where the TCNQ molecules are organized in stacks as quasi-isolated dimers, with one electron per dimer. In Fig. 5 is shown the IR spectra. Note the strong features in the chain axis spectrum, which has been used to obtain the emv coupling constants for TCNQ (Rice et al., 1980). The coupling constants may also be calculated theoretically and reliable values are now known for several molecules.
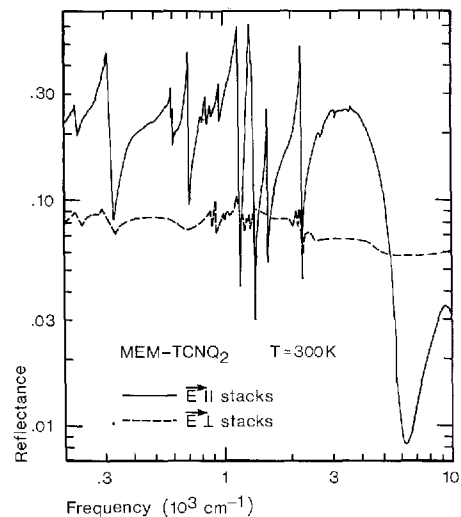
In the organic conductor with uniform stacks, the emv coupling should not have direct resonant effects on the optical spectra. Resonances/antiresonances are only activated if the symmetry is broken, either by structural distortion or by the presence of charge-density waves (CDWs) in the system.

Assuming unbroken symmetry, the question arises how electron-phonon interactions influence the IR behaviour. The main deviations from the Drude spectrum are found in the pure metal at low temperature, where the electron-phonon coupling does not contribute to the dc-resistivity. Then the dc-relaxation rate, γ_{dc}, is determined by residual impurities and defects, and a near δ-function contribution to $\sigma(\omega)$ is obtained. As ω is increased and reaches frequencies of current-degrading phonons, photon absorption assisted by phonon emission becomes possible and a threshold in $\sigma(\omega)$ is anticipated (Holstein (1954, 1964); see also Allen (1971)). At frequencies well above all important phonon frequencies, the relaxation rate $\gamma_{opt} \to \pi\lambda_{tr}<\omega_{ph}>$, where λ_{tr} is an appropriate dimensionless electron-phonon coupling constant and $<\omega_{ph}>$ is an average phonon frequency. In terms of oscillator strength, a fraction $\sim\lambda_{tr}/(1+\lambda_{tr})$ of the low frequency Drude contribution appears as IR absorption with a high frequency Drude tail determined by phonon emission processes. However, the sum rule, Eq. (10), is still expected to be obeyed.

At high temperatures $k_B T >> \hbar<\omega_{ph}>$, and both phonon absorption

and emission contributes to γ so $\gamma_{dc} \simeq \gamma_{opt}$ and a single Drude absorption is found. We note that in the molecular metals the high temperature limit is never reached with respect to the majority of the vibrational modes. Thus Holstein thresholds may be encountered, even at room temperature.

Electron-electron interactions

The electron-electron Coulomb interaction is more difficult to deal with. It is commonly assumed that it can be treated as in ordinary metals. Thus the long range interaction part is frozen in the zero point motion of the plasmons, while the short range part gives rise to quasiparticles with screened interactions (see, for example, Pines (1964)). The screening efficiency was recently discussed by Mazumdar and Bloch (1983). Their conclusions may be described as follows: Only on-site and nearest neighbour interactions need to be considered. Thus the proper model Hamiltonian is of the extended Hubbard type (Hubbard, 1978):

$$H = \sum_{i,\sigma} E_o n_{i,\sigma} - \sum_{i,\sigma} t(c^+_{i,\sigma} c_{i+1,\sigma} + c^+_{i+1,\sigma} c_{i,\sigma})$$
$$+ \sum_i U n_{i\uparrow} n_{i\downarrow} + \sum_{i,\sigma,\sigma'} V n_{i,\sigma} n_{i+1,\sigma'}. \tag{12}$$

U is the extra electrostatic energy associated with two carriers on the same site, and V is the corresponding energy for two carriers on neighbour sites. Both U and V are to be considered effective, screened values, which depend strongly on band filling (ϱ). For $\varrho = 0.5$ and 1.0 the screening is found to be inefficient ($U > 4t$). In the intermediate range, screening may be quite efficient ($U \ll 4t$), mostly so for $\varrho \simeq 0.7$-0.8. $\varrho = 1$ (half-filled band) constitutes a special case, since for any finite U, there is a gap in the excitation spectrum (Lieb and Wu, 1968). Thus the 1D half-filled band is an insulator of the Mott type. For $\varrho < 1$ there is no clear evidence for a gap in the energy spectrum of Eq. (12).

We now turn to the IR properties of a system described by the Hubbard model. First we note the existence of a modified partial sum rule for the intraband absorption (Maldague, 1977):

$$\int_{\text{intraband}} \sigma(\omega) d\omega = -(\pi e^2 d^2/2\varepsilon_o)\langle H_t \rangle \tag{13}$$

$\langle H_t \rangle$ is the ground state expectation value of the transfer terms of H. Since H_t determines the ground state in the absence of correlation effects, it is evident that finite correlation reduces the oscillator strength below that of Eq. (10).

The next issue is the distribution of oscillator strength. Again $\varrho = 1$ is a special case. Even in the weak coupling limit, $U \ll 4t$, optical absorption may occur via Umklapp electron-electron scattering. In the strong coupling limit, $U \gg 4t$ ($V=0$) Lyo and Gallinar (1977) find a symmetric absorption extending from $U-4t$ to $U+4t$. The oscillator strength is proportional to t^2/U. A finite nearest neighbour interaction induces an asymmetry in the absorption (Lyo, 1978). Then there is a strong onset of absorption at $U-4t$ and a tail extending to $U+4t$. Physically the absorption band corresponds to charge transfer transitions into states with doubly occupied sites.

For $\varrho < 1$, the main question is whether the dominant part of the oscillator strength goes into charge transfer bands of the correlation type ($\hbar\omega \sim U,V$) or whether it appears in a low frequency Drude-like absorption. The answer again depends on the band-filling. However, there is strong evidence from various approximative calculations (Maldague, 1977) and finite chain calculations that for $0.5 < \varrho < 0.6$ less than 10% of the oscillator strength appears in correlation bands.

Finally, it is of some interest to describe a specific limit of Eq. (12): $V = 0$ and $U \to \infty$ (double occupancy of sites excluded). In this case the translational and the spin degrees of freedom are decoupled (Sokoloff, 1970). The spin susceptibility is Curie-like and the electrons behave otherwise as a system of non-interacting spinless fermions described by the usual tight-binding model of Eq. (5,6). Because of the spinlessness the density of states is halved and the band is now filled to $k = \pm\pi\varrho/d$. The optical properties are Drude-like, as described above, and the relative reduction of oscillator strength is obtained from Eq. (9):

$$\int_{U\to\infty} \sigma(\omega)d\omega \Big/ \int_{U=0} \sigma(\omega)d\omega = \cos(\pi\varrho/2). \tag{14}$$

It is noted that with respect to oscillator strength, the dense electron system is more sensitive to the high U limit than the less dense system.

Low-dimensional instabilities

The linear chain structure of the molecular conductors has important consequencies for the occurrence and behaviour of instabilities. As discussed below the quasi-one-dimensionality leads to phase transitions not known in isotropic systems. At the same time thermodynamic fluctuations tend to suppress the phase transition temperatures. It is well-known that long range order cannot persist in a 1D system for $T > 0$. Thus usually short range order develops below some scale temperature,
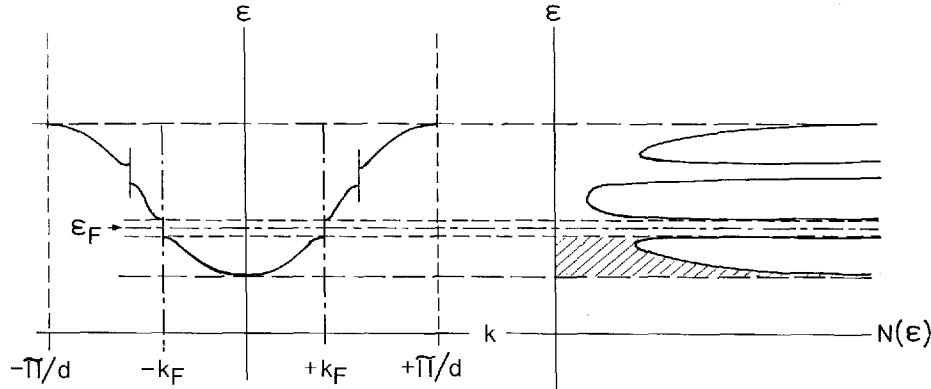
Fig. 6. Effect of $2k_F$-distortion on cosine band and density of states.

T_{MF}. As temperature is lowered, the on-chain correlation length grows and since the real systems consist of arrays of chains any finite interchain coupling will eventually induce long range 3D order at a temperature, T_C, which defines a three-dimensional phase transition. In the range $T_C < T < T_{MF}$, the fluctuations may have important impact on the physical properties.

The most famous of the 1D instabilities is that of the linear chain metal. We shall here repeat the argument by Peierls (1955) with reference to Fig. 6. The figure shows the band structure and density of states of Eq. (6) with the inclusion of a weak $2k_F$-potential which spans the Fermi sea. The crucial point is that this potential opens a gap at the Fermi level, ε_F, and thus lowers the energies of those electrons closest to ε_F. Due to the 1D divergent density of states near a gap this energy gain will always outweigh the cost of creating the $2k_F$-potential. The latter arises from a CDW/periodic lattice distortion mediated by the electron-phonon coupling. For a half-filled band a detailed calculation gives the following zero temperature gap (Rice and Strässler, 1973):

$$E_g = 2\Delta = 2\varepsilon_F/\sinh(1/\lambda\text{-}\ln2) \simeq 8\varepsilon_F\exp(-1/\lambda). \tag{15}$$

The last expression applies for $\lambda \ll 1$. The dimensionless electron-phonon coupling constant, λ, is related to the bare coupling constant, g, the density of states in the metallic state, $N(\varepsilon_F)$, and the unperturbed phonon frequency, ω_{2k_F}, by

$$\lambda = g^2N(\varepsilon_F)/\hbar\omega_{2k_F}. \tag{16}$$

The temperature dependence of the gap is BCS-like (Bardeen et al., 1957). Thus the mean field scale temperature, where the gap vanishes is given by

$$k_B T_{MF} = 2\Delta/3.52. \tag{17}$$

The actual phase transition temperature, T_C, may be fluctuation suppressed below T_{MF}.

There are two kinds of elementary excitations associated with the Peierls state: (1) Electron-hole excitations across the gap and (2) phase and amplitude oscillations of the $2k_F$-CDW. The phase oscillations have a dipole moment and are thus IR active. Fröhlich (1954) noted that in situations where the energy of the CDW is independent of the phase, the CDW is free to move through the crystal and carry current in a way reminiscent of superconductivity. In real systems this may happen in incommensurate cases (where λ_{2k_F} does not match the lattice) for $T \geq T_C$, where, however, a finite correlation length will limit the conductivity. For $T < T_c$ the CDW is pinned and appears as a far IR absorption.

Rice and coworkers (Rice et al. (1975), Rice (1978)) have emphasized the role of simultaneous involvement of many phonons. They find that for the molecular conductors, it is to be expected that much of the Peierls gap is due to the sizeable number of intramolecular modes coupled to the electrons, while the dynamic properties, e.g. effective mass, of the CDW is dominated by the low frequency external modes. The CDW is a complicated superposition of contributions from each mode. In the infrared spectrum phase oscillations may be identified in the vicinity of each unperturbed mode frequency (Rice et al., 1977). This is a good example of IR-activation of the A_g-modes.

A number of other instabilities have close analogies to the Peierls instability. The Overhauser instability (Overhauser, 1960) may occur when the electron-phonon interaction is comparatively weak and a finite short range electron-electron interaction is present. Then a $2k_F$ spin-density wave will act on the electrons as an effective $2k_F$-potential through the modulation of the exchange interaction (Slater, 1951). The energetics are then similar to what is described above, but the effective coupling constant rather is $N(\varepsilon_F)\tilde{U}$, $\tilde{U}$ being an appropriate Coulomb interaction.

Another important modification of the Peierls instability happens in the limit of strong electron-electron interaction, where we may let $U \rightarrow \infty$. As stated above, the translational degrees of freedom are described in terms of non-interacting spinless fermions in a tight-binding band filled

to $\pm 2k_F$. The fermion-phonon interaction is of the same form as that entering the theory for the Peierls instability, thus a $4k_F$-CDW Peierls type of instability may occur (Bernasconi et al., 1975). The behaviour is completely analogous if the differences in wavenumber, in band–filling, and in dimensionless coupling constant are taken into account.

If the electrons are locked into such a $4k_F$-CDW or are localized by direct Coulomb interaction (Mott insulator) the magnetic subsystem is susceptible to yet another $2k_F$–instability, the spin–Peierls instability (Chesnut, 1966), which is a magnetic analogue. In this case the coupling between the antiferromagnetic exchange integral, J, and the phonons induces a $2k_F$ modulation of J, which quenches the magnetic susceptibility.

After this short discussion we stress that for the instabilities to occur, the 1D nature is crucial. The Peierls type instability depends on the ability of a single wavevector to nest the entire Fermi surface. The nesting efficiency will in general deteriorate as interchain coupling increases (see, for example, Horovitz et al. (1975)), but even 3D materials may undergo density wave formation if segments of the Fermi surface allow nesting.

As a last remark it is noted that also superconductivity may occur in 1D systems. However, it is not clear at present how one may distinguish between a quasi-1D superconductor and a highly anisotropic 3D superconductor.

Plasma edges and band structure

Measurements of the polarized reflectance in the vicinity of the plasma edge have frequently been used to obtain estimates for the transfer integrals. The method consists of fitting a reflectance model based on the Drude expression of Eq. (7) to the data in a limited range and then use Eq. (8) in conjunction with information on carrier density and crystallographic data to derive values for t. Such an approach has often been criticized (see, for example, Williams and Bloch (1974)) because the molecular conductors show strong deviations from Drude behaviour at lower frequencies (cfr. next section). The aim of the present section is to use experimental data in arguing for the validity of the Drude analysis. The underlying idea is that the plasma edge is a signature for existence of plasmons. Since these are long wavelength oscillations in the charge density their frequency is intuitively expected to be insensitive to the

Fig. 7. Polarized reflectance of TMTSF-DMTCNQ at 300K. Notice the logarithmic reflectance scale. The solid line is a fit of the Drude model to the chain axis spectrum. An extra oscillator has been added to the model to account for the absorption band near 10000 cm^{-1}.
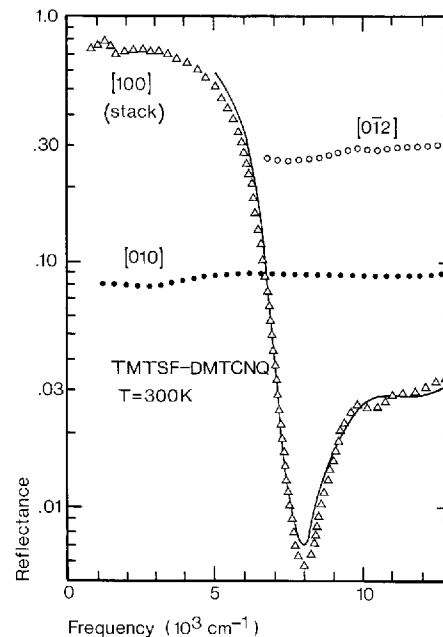
details in the short range interactions, which give rise to the non-Drude features observed in the infrared. Thus the Drude expression should be viewed as a convenient mathematical tool in estimating the plasmon frequency, Ω_p, and the background dielectric constant, ε_c. Then the transfer integral is calculated from the unscreened plasma frequency, $\omega_p \simeq \Omega_p \sqrt{\varepsilon_c}$.

During the argumentation we shall further attempt a decomposition of average transfer integrals in double-stack conductors and show examples of materials with 2D character.

Chain axis

As a typical example we present in Fig. 7 the polarized room temperature reflectance of TMTSF-DMTCNQ with a model fit to the chain axis spectrum. The most striking feature is the well-developed plasma edge observed along the stacks. Virtually no dispersion is seen in the other directions. The infrared spectra are indeed a remarkable manifestation of the linear chain structure.

The plasma edge is quite sharp with a drop in reflectance of more than two orders of magnitude. This hints to the existence of rather well-defined plasmons, i.e. $\varepsilon_1 = 0$ and $\varepsilon_2 \ll 1$ are simultaneously obeyed.

Plasmons have so far been observed directly in TTF-TCNQ only (Ritsko et al., 1975). In that case the plasmon frequency is in complete agreement with the optical properties (Tanner et al., 1976).

The solid line is a fit of a model based on the Drude expression, Eq. (7), with an extra oscillator added. The latter takes into account the absorption band near 10000 cm^{-1}, which is observed in all TCNQ based materials and which is presumably intramolecular in origin (Tanaka et al., 1978).

A close inspection of the quality of the fit reveals a systematic deviation from the Drude model in the edge region. The data points fall below the model both at low frequencies (entering the IR) and near the minimum. The model could be improved by allowing the relaxation rate, γ_{opt}, to decrease slowly with frequency in the near infrared range. This observation, which is made in many of the organic conductors leads us to shortly discuss the origin of optical absorption in the near IR. Usually the absorption is attributed to phonon assisted electron-hole excitations within the one-electron tight-binding band. However, the bandwidth, 4t, is found to be of order 0.7-1.0 eV corresponding to frequencies of 6000-8000 cm^{-1}. But as the frequency exceeds the bandwidth many phonon assisted processes become impossible by energy conservation. For $\hbar\omega > 4t$ only processes involving emission of high energy phonons are conceivable. Thus such absorption mechanisms in a natural way account for the observed frequency dependence of γ_{opt}. This discussion viewed together with the remarks made on the Holstein mechanism previously, strongly suggests that the near IR relaxation rate has little to do with the low frequency scattering, which governs the static conductivity. Indeed, the temperature dependence of γ_{opt} is much weaker than that of the dc-conductivity in most cases (see, for example, Bright et al. (1974)).

In Table III is presented the results of Drude analysis and transfer integral calculation for a number of materials, in all cases for the stacking direction, using Eq. (9). For the double-stack conductors the value given is the average of donor and acceptor bandwidths. For the single-stack conductors the slight dimerisation is neglected.

Since the table contains some results for single- and double-stack conductors with the same molecule, it should be possible to decompose the bandwidth of the double-stack conductors into donor and acceptor contributions adopting certain assumptions. For this purpose interplanar distances (ipd) for the molecules in the stacks have been included. Our principal assumptions are, (1) that the bandwidth depends only on the

Table III. Chain axis Drude parameters and bandwidths.
Also given are cation and anion interplanar distances.

Material	T K	ε_c	γ cm^{-1}	ω_p cm^{-1}	$4\bar{t}$ eV	cation ipd Å	anion ipd Å
TTF-TCNQ	300	3.27	1430	11400	0.61	3.48	3.17
TSF-TCNQ[a]	300	–	–	12200	0.69	3.52	3.21
TMTSF-TCNQ[a]	300	–	–	12000	0.89	3.59	3.26
TMTTF-DMTCNQ[a,b]	300	–	–	10700	0.77	–	–
TMTSF-DMTCNQ	300	2.91	1180	11200	0.88	3.64	3.31
HMTTF-TCNQ	300	3.15	1260	12400	0.78	3.57	3.23
HMTSF-TCNQ	300	3.30	1030	14200	1.03	3.6	3.2
DBTTF-TCNQCl$_2$	300	2.51	2000	7500	0.41	3.51	3.41
HMTSF-TNAP	300	2.95	1100	11300	0.84	3.58	3.28
TMTTF$_2$PF$_6$	300	2.50	1380	8900	0.80	3.58	–
TMTSF$_2$AsF$_6$	300	2.56	1230	9900	1.00	3.63	–
–	30	2.55	1160	10500	1.11	–	–

[a] estimate from edge shift
[b] ϱ is assumed equal to 0.5 (as in the isostructural TMTSF-DMTCNQ)

molecular species and ipd, and (2) that t increases ~5% for a decrease in ipd of 1%. The first assumption is based on the quasi-1D nature of the materials and on the very similar overlap patterns observed for the same molecule in different materials (see references of Table II). The second assumption is based on molecular orbital calculations (Herman, 1977) and on the change in t observed on cooling to low temperatures. This change usually amounts to +10% (Table III), while the stack–contraction is about 2% (Schultz et al., 1976).

The resulting decomposition is given in Table IV. There is a rather large spread in bandwidths from 0.4 to 1.3 eV. Substituting Se for S in TTF-based molecules always results in increases in t as expected from the increased overlap. It is noteworthy that methylation of TTF-based molecules leads to strong increases in bandwidths (Jacobsen et al., 1983). Although we cannot go into a detailed discussion of the results in context of other physical properties the general trends are clearly consistent with independent knowledge. We give four specific examples: (1) The thermoelectric power of TMTSF single stack materials yields a bandwidth slightly larger than 1 eV (Mortensen, 1982). (2) HMTSF-based metals have exceptionally high conductivities (cfr. Table II). (3) The thermoelectric power of TTF-TCNQ is large and negative while it is close to zero for TSF-TCNQ (Chaikin et al., 1976). (4) The conductivity of

TMTSF-TCNQ is significantly higher than that of TSF-TCNQ (Table II).

Another argument for the validity of the present approach is the agreement in values for the DMTCNQ-bandwidths. The number obtained for TMTTF-DMTCNQ is based on analysis of data for the single-stack compound $TMTTF_2PF_6$, which is a semiconductor with strong non-Drude behaviour in the IR (Jacobsen et al., 1983), while the number for the selenium analogue is based on data for an excellent metal, $TMTSF_2AsF_6$, which is close to Drude behaviour in the IR.

A final direct demonstration of the main point i.e. the simple connection between one-electron bandwidth and plasmon frequency will be given next while discussing 2D compounds.

Interchain contact

There are at present two groups of organic conductors, which show considerable interchain coupling. They are both of single-stack type with donor molecules, $\varrho = 0.5$, and inorganic counterions. The basic structural features are also the same: Sheets of molecular stacks interchanging with layers of counterions. The important interchain contact is *in* the sheets so that the materials are effectively two-dimensional. Interestingly these materials among them count the only representatives of organic superconductivity so far.

Table IV. Single-stack bandwidths. T = 300K

Donor		Acceptor	
Stack	4t eV	Stack	4t eV
TTF-(TCNQ)	0.41	(TTF)-TCNQ	0.81
TSF-(TCNQ)	0.62	(TSF)-TCNQ	0.76
TMTSF-(TCNQ)	1.06	(TMTSF)-TCNQ	0.70
TMTTF-(DMTCNQ)	0.80	(TMTTF)-DMTCNQ	0.74
TMTSF-(DMTCNQ)	0.93	(TMTSF)-DMTCNQ	0.70
HMTTF-(TCNQ)	0.80	(HMTTF)-TCNQ	0.76
HMTSF-(TCNQ)	1.3	(HMTSF)-TCNQ	0.76
HMTSF-(TNAP)	1.3	(HMTSF)-TNAP	0.4

Fig. 8. Polarized reflectance of TMTSF$_2$PF$_6$ at 300K, 100K, and 25K. Notice the logarithmic frequency scale. The chain axis is along a. The solid line is a Drude fit to the low temperature spectrum with polarization perpendicular to the chains. One extra oscillator has been added to the model to account for the sharp vibrational line near 800 cm^{-1}. (Jacobsen et al. 1981).
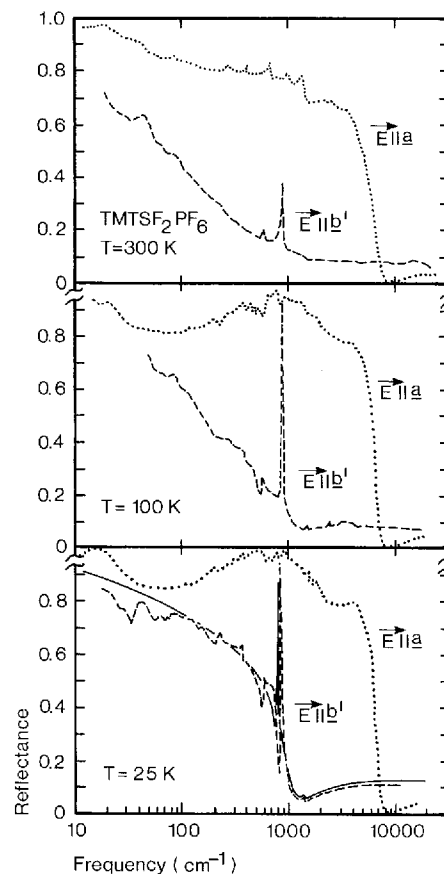
Their actual anisotropy may be deduced from reflectance studies. As an example from the TMTSF$_2$X-family we present in Fig. 8 the polarized reflectance of TMTSF$_2$PF$_6$ at three temperatures: 300K, 100K and 25K (Jacobsen et al., 1981). It is evident that a reasonably well-defined plasma edge appears in the b'-direction at low temperature. The b'-direction is perpendicular to the stacks in the sheets of TMTSF-molecules. Most of the sharp lines superimposed on the edge arise from normal IR active modes in PF$_6^-$. The transverse reflectance edge appears at a frequency about ten times lower than that of the stacking axis edge. A Drude analysis may be performed (solid line) and the ratio $(\omega_{pb}/\omega_{pa'})$ (a'/b') which refers to the model of Fig. 4 is 0.09. Calculation yields $t_{b'}$ $\simeq$ 22 meV, about 10 times smaller than t_a. Although $t_{b'}$ is significant as compared to k_BT for all temperatures of interest the Fermi surface must clearly be open. Table V gives Drude parameters and transfer integrals

Table V. Drude parameters, transfer integrals, and b-axis lattice constants in $(TMTSF)_2X$, $\vec{E}\|b'$

X	ε_c	ω_p cm^{-1}	γ cm^{-1}	$t_{b'}$ meV	b Å
ClO_4^-	3.5	2020	250	24	7.678
SbF_6^-	3.5	1510	300	18	7.728
AsF_6^-	3.5	1670	350	20	7.711
PF_6^-	3.5	1830	500	22	7.711

for several members of the TMTSF$_2$X family (Jacobsen et al., 1983). It should be noted that there is a reasonable correlation between $t_{b'}$ and the b-axis lattice constant. The largest $t_{b'}$ is found in the densely packed TMTSF$_2$ClO$_4$, the only ambient pressure superconductor in the series. This gives some support to the simple band picture of Yamaji (1985) which predicts a critical value of $t_{b'} \simeq 25$ meV. The values are also in good agreement with results of band structure calculations (Grant, 1983).

The other materials group of interest is based on BEDT-TTF (or ET). The first reported ambient pressure superconductor in this family is triclinic (β-phase) ET$_2$I$_3$ (Yagubskii et al., 1984). Fig. 9 shows the polarized reflectance of this material in the a-b plane (Jacobsen et al., 1985). Again this plane corresponds to the sheets of molecular stacks. Interestingly, the highest plasma frequency is associated with the direction perpendicular to the chains, while the chain direction shows much weaker metallic character in the infrared properties. Although unusual, such behaviour is consistent with the molecular arrangement in the crystal (Kaminskii et al., 1984) and has also been seen optically at room temperature in several materials from the family (Tajima et al. (1984) and Koch et al. (1985)).

In Table VI we list Drude parameters and estimated transfer integrals for ET$_2$I$_3$. Again the results of Fig. 4 have been used. Thus the analysis is based on a simplified orthorhombic model and the transfer integrals given are weighted averages of several transfer integrals in the correct triclinic model. The rather small values of t are consistent with a low room temperature conductivity ($\sim$30 Scm^{-1}, isotropic in the a-b-plane) and the near isotropy is confirmed by thermopower measurements of Mortensen et al. (1985). The validity of the plasma edge Drude analysis

Table VI. Drude parameters and transfer integrals in β-ET$_2$I$_3$.
$\parallel$ Denotes the chain axis, $\perp$ the direction perpendicular to the chains in the a-b plane.

axis	T K	ε_c	ω_p cm^{-1}	γ cm^{-1}	$<t>$ eV
$\parallel$	40	4.0	5740	2270	0.10
$\perp$	40	3.8	9600	540	0.13
$\perp$	300	3.8	9100	1360	0.12

is again confirmed. It is particularly interesting to compare the 40K and 300K analysis of the data for the perpendicular direction. It is obvious from Fig. 9 and even more so from the dielectric function reproduced in Fig. 10 that the 300K spectrum is non-Drude in the IR while the 40K spectrum is near-Drude in the entire measured range. Nevertheless, the predicted plasma frequencies are different only by an amount expected
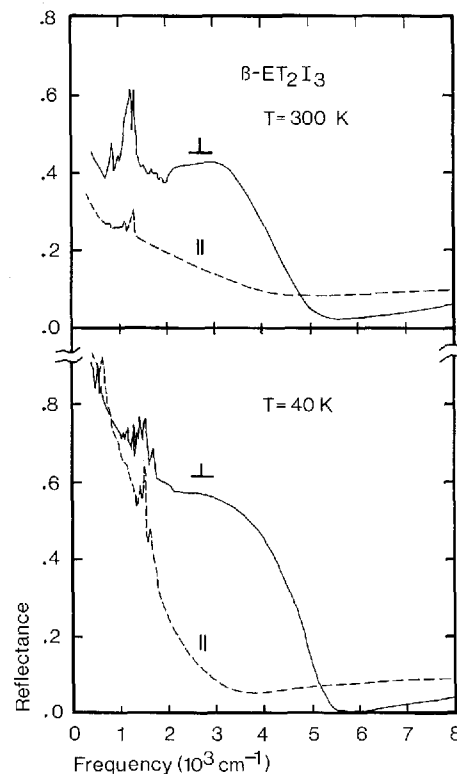
Fig. 9. Polarized reflectance of β-ET$_2$I$_3$ at 300K and 40K. The stacking axis is designated $\parallel$, while $\perp$ refers to a direction perpendicular to the stacks in the a-b plane. (Jacobsen et al., 1985).
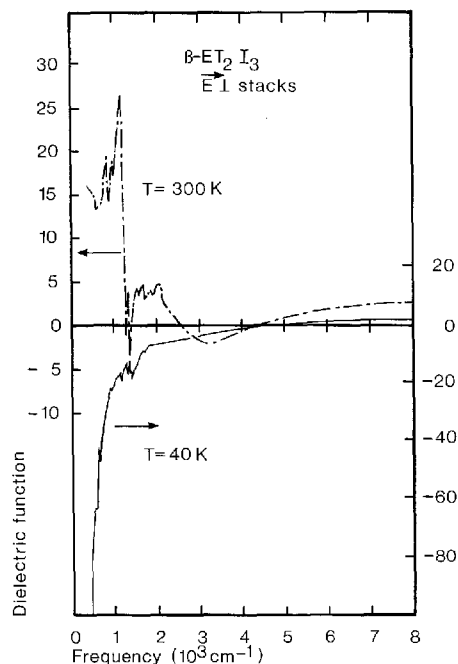
Fig. 10. Real part of $\tilde{\varepsilon}(\omega)$ for β-ET_2I_3 perpendicular to the chains, for $T=300K$ and $40K$. Notice the different scales for the two curves. (Jacobsen et al., 1985).

from a thermal contraction induced change in $t_\perp$ (Table VI). This is also evident from Fig. 10 by noting that the zero-crossing in $\varepsilon(\omega)$ near 5000 cm^{-1} only shifts slightly.

Hence our principal conclusion of this section is that careful analysis of reflectance data in the plasmon region yields reliable estimates for transfer integrals. These estimates will be used subsequently while discussing the IR spectra.

Size and distribution of infrared oscillator strength

After having discussed the plasma edge range we now turn to the actual infrared excitation spectra of organic conductors. The aim is to understand the deviations from Drude behaviour in terms of the short range electron-electron and electron-phonon interactions. In Fig. 11 is shown 300K-spectra of 4 double-stack conductors with widely different physical properties (Jacobsen et al., 1984). HMTSF-TNAP, TTF-TCNQ and DBTTF-TCNQCl$_2$ are incommensurate conductors with slightly more than quarter-filled one-electron bands, while DBTSF-TCNQF$_4$ has half-

Fig. 11. Frequency dependent conductivities of 4 doublestack conductors at T=300K, along the stacks. (Jacobsen et al., 1984).
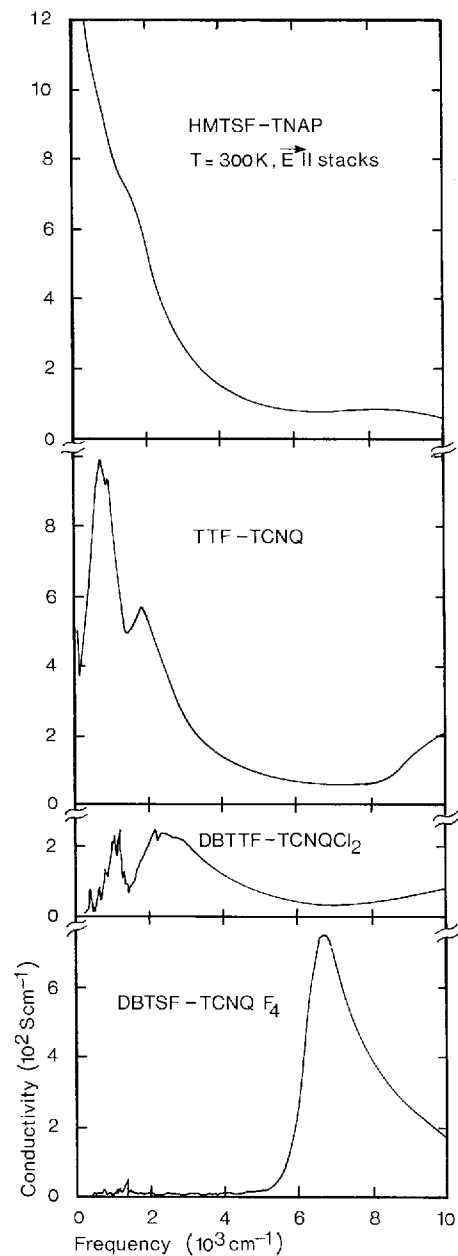
filled bands. All materials are expected to be metals in the absence of Coulomb interactions and at 300K there is no evidence for the $2k_F$-distortion, which might destroy the metallic state by pure structural effects.

DBTSF-TCNQF$_4$ is known to be a Mott insulator (Lerstrup et al., 1983), and as we shall shortly discuss, available theory allows a rather unambiguous interpretation of the spectrum.

HMTSF-TNAP is a high conductivity, wide band metal, and the IR behaviour is indeed rather close to Drude behaviour with a monotonic $\sigma(\omega)$. TTF-TCNQ is also a metal but of intermediate bandwidth and with distinct deviations from the Drude spectrum. The oscillator strength is shifted away from zero frequency and fine structure is seen near molecular vibration frequencies. These features are even more pronounced in the narrow band material DBTTF-TCNQCl$_2$, which is a magnetic semiconductor. It is obvious that these room temperature spectra can not be rationalized within traditional 3D models like the Holstein absorption picture.

In the following we first derive parameters for the Mott insulator case. Next we review the physical properties of DBTTF-TCNQCl$_2$ and argue for using the simple $U \rightarrow \infty$ model for this material. Then the size of the IR oscillator strength for a number of organic conductors is compared with expectations based on bandwidth estimates. It is suggested that Coulomb correlations modify the wavefunctions appreciably in all materials. However, depending on band-filling and dimensionality the effect on other physical properties differs widely. Finally, we discuss the temperature dependent IR properties of TTF-TCNQ with special emphasis on understanding the separate roles of the two chains.

The Mott insulator ($\varrho = 1$)

The frequency dependent conductivity of DBTSF-TCNQF$_4$ resembles surprisingly well the prediction by Lyo (1978) for the extended Hubbard model with half-filled one-electron bands. The absorption is dominated by a charge transfer band corresponding to the creation of a doubly occupied site. A finite near neighbour interaction, V, produces a rather strong onset of absorption at U–4t as observed near 5500 cm$^{-1} \simeq 0.7$ eV in the present case. Additional information may be obtained from the size of the oscillator strength. It is assumed that it follows that of the isolated Hubbard dimer (Rice, 1979):

$$\int \sigma(\omega)d\omega / \int_{(U=0)} \sigma(\omega)d\omega = (1 + (U/4t)^2)^{-\frac{1}{2}}, \tag{18}$$

(correct for $U/4t \ll 1$ and $\gg 1$ (Lyo, 1978)).

Then we find $U \simeq 1.4$ eV and $4t \simeq 0.7$ eV. Such a value for the bandwidth appears reasonable when compared to the results of Table III

Fig. 12. Basic physical properties of DBTTF-TCNQCl$_2$. See the discussion in the text.
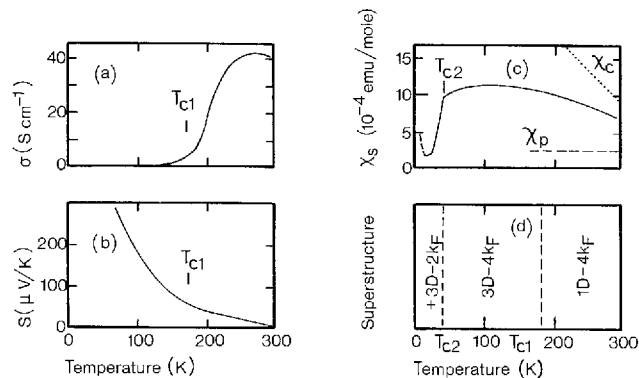
for similarly composed materials (e.g. TSF-TCNQ) but an independent estimate is not available. U/4t $\simeq$ 2 for the half-filled band case is in accord with theoretical expectations (Mazumdar and Bloch, 1983).

As a side-remark it is noted that the A$_g$-vibrational modes are not activated in the Mott insulator. Charge localization does not suffice: symmetry breaking is a necessary prerequisite for IR activation.

The infinite U model (ϱ < 1)

DBTTF-TCNQCl$_2$ is a good example of a non-metallic, but incommensurate (ϱ = 0.56) and near quarter-filled organic conductor. The physical properties are known in rather great detail and are summarized in Fig. 12. The dc conductivity and the thermoelectric power are consistent with the existence of a one-electron gap of order 200-250 meV (1500-2000 cm^{-1}). The activated behaviour is cleanest below T$_{c1}$ = 180K where a slight anomaly is observed. The spin susceptibility, χ_S, is high, about three times the expected non-enhanced Pauli value (χ_P) at 300K, and remains high to T$_{c2}$ = 36K, below which temperature it vanishes rapidly. Note that χ_S (300K) is about $\frac{2}{3}$ of the Curie value (χ_c) for the appropriate carrier density. Finally, diffuse X-ray scattering has shown the existence of rather large amplitude 4k$_F$-CDWs. Down to T$_{c1}$ there are only weak interchain correlations. T$_{c1}$ is found to be a 3D ordering temperature, while T$_{c2}$ involves the onset of 3D-2k$_F$ scattering.

The implications of these observations are obvious: Enhanced magnetic susceptibility and occurrence of 4k$_F$-CDWs may both be taken as evidence for important electron-electron correlations. The two transition temperatures also indicate a substantial decoupling of the spin and translational degrees of freedom. The overall behaviour is common to a

larger group of low conductivity materials and the physical picture is the following: The carriers are fairly localized even at high temperature due to the Coulomb repulsion between them. The spins experience a weak antiferromagnetic exchange coupling and through interaction with the lattice undergo a spin-Peierls transition at low temperature. With this discussion we have established that $DBTTF-TCNQCl_2$ is a strongly correlated, incommensurate organic conductor with a sizeable energy gap in the excitation spectrum.

In Fig. 13(a) $\sigma(\omega)$ is shown at 100K. The main difference from the 300K spectrum is a sharpening of the vibrational structure below 1500 cm^{-1}. In both spectra there is a broad maximum around 2000 cm^{-1}, which may be interpreted as arising from a gap in the electronic spectrum in accordance with the low frequency transport properties. This gap, the intensity of the vibrational structure, the presence of $4k_F$-CDWs, and the apparant decoupling of magnetism and electronic behaviour leads us to suggest that $DBTTF-TCNQCl_2$ is subject to an »infinite«-U Peierls instability partly stabilized by the emv coupling. A zero temperature model for $\sigma(\omega)$ of the ordinary $2k_F$ (U=0) Peierls semiconductor has been given by Rice (1978). Because of the formal analogy with this case the theory can be immediately applied, when proper account for the spinlessness of the fermions is taken. As stated earlier the difference concerns the band-filling and the density of states. Rice gives the following expression for $\bar{\varepsilon}(\omega)$:

$$\bar{\varepsilon}(\omega) = \varepsilon_c + (\omega_f/\omega)^2[f(\omega/2\Delta) - 1 - (\omega/2\Delta)^2 f^2(\omega/2\Delta)\lambda D_\varphi(\omega)]. \tag{19}$$

ω_f is a measure for the oscillator strength so that

$$\int_o^\infty \sigma(\omega)d\omega = (\pi/2)\,\varepsilon_o\omega_f^2. \tag{20}$$

2Δ is the Peierls gap and λ is the total electron-phonon coupling constant given by

$$\lambda = \sum_n \lambda_n = \sum_n g_n^2 N(\varepsilon_F)/\hbar\omega_n, \tag{21}$$
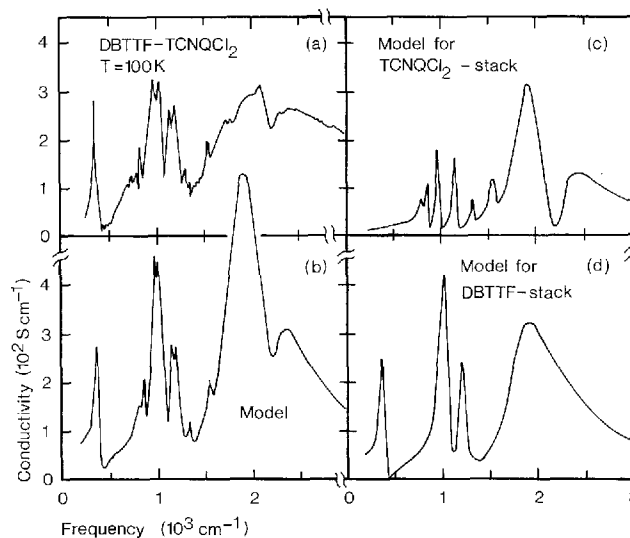
where n is the mode number.

Furthermore, the function, f(x), is defined by

$$f(x) = [\pi i + \ln(1-S)/(1+S)]/2Sx^2,\ S=(1-x^{-2})^{1/2} \tag{22}$$

A small electronic damping may be introduced by the substitution $x^2 \to x(x+i\delta)$ in these expressions. Finally, the phase phonon propagator

$$D_\varphi(\omega) = [D_o^{-1}(\omega) + 1 + \lambda(\omega/2\Delta)^2 f(\omega/2\Delta) + b]^{-1} \tag{23}$$

where

$$D_o(\omega) = -\sum_n (\lambda_n/\lambda)\omega_n^2/(\omega_n^2-\omega^2-i\omega\gamma_n). \tag{24}$$

γ_n is the natural damping rate of mode n. b is a positive constant, which models the pinning of the CDW; if b = 0, the CDW contributes to the dc conductivity.

The physical contents of this model were described previously. The main problem in its application to DBTTF-TCNQCl₂ is the double-stack structure. There are two contributing stacks and we must assume that $\tilde{\varepsilon}(\omega)$ is simply a sum of two individual terms. Clues to the decomposition may be obtained by studying single-stack materials like DBTTF(BF₄)₀.₄₂. It is rather easy to show that DBTTF dominates the full spectrum and we have obtained a model fit to the data of the quality shown in Fig. 13(b). The individual contributions are pictured in Fig. 13 (c+d). The model parameters are given in Table VII, which also contains independent estimates of the emv coupling constants.

The overall quality of the fit is reasonable, especially with respect to distribution of oscillator strength between the vibrational modes and the single particle contribution. We note that it is possible to introduce only a modest electronic damping in the present model hence the gap structure in the fit is sharper than in the data.

From Table VII it follows that the coupling constants (g_n) obtained are of the correct magnitude. This is a crucial point, since in Eq. (21) we have used the U→∞ density of states, which for a quarter-filled band is

Table VII. $4k_F$-CDW parameters for DBTTF-TCNQCl$_2$, T = 100K.

	DBTTF			TCNQCl$_2$		
$\omega_f(cm^{-1})$	4500			3600		
4t(eV)	0.43			0.27		
$2\Delta(cm^{-1})$	1700			1900		
δ	0.2			0.2		
λ	0.46			0.60		
b	0.08			0.08		
$\Delta\varepsilon_c$	1.0			1.0		
n	ω_n cm^{-1}	λ_n	g_n^a cm^{-1}	ω_n cm^{-1}	λ_n	g_n^b cm^{-1}
1	1430	.16	1100 (940)	2253	.04	550(350)
2	1130	.017	320(170)	1573	.01	230(540)
3	473	.11	530(630)	1345	.01	210(500)
4	(40	.17	190)	1200	.04	400(300)
5				1020	.03	340(85)
6				870	.009	160
7				820	.012	180
8				(40	.45	250)

[a] values in parentheses are estimates for TTF for corresponding modes (Lipari et al., 1977).

[b] values in parentheses are estimates for TCNQ for corresponding modes (Rice et al., 1980).

only 35% of the U=0 value. Thus the strength of the vibrational modes constitutes a direct verification of the applicability of the large U model.

A few other points may be emphasized: (1) Assuming mean field behaviour the observed gap position corresponds to a scale temperature $T_{MF} \simeq 600K$. This is consistent with the well-established gap and CDW-structure at 300K and below. (2) In the fitting procedure the estimated gap-values were used to derive the total electron-phonon coupling constant, λ, from the gap equation (Eq.(15)) for each stack. Part of λ is assumed associated with low frequency (external) modes outside the experimental range (given in the last lines of Table VII). However, it is striking that more than 60% of λ for the DBTTF-stack is due to the internal modes. Hence, the CDW is predominantly stabilized by the emv

coupling. On the acceptor chain this is less pronounced. (3) The average bandwidth, $4\bar{t}$, is 0.35 eV from Table VII. This may be compared to $4\bar{t}$ = 0.41 eV from the Drude analysis (Table III). It appears that the oscillator strength is further reduced below what is expected from the large U model. Introduction of a finite nearest neighbour interaction, V, in the theory might account for that.

In conclusion the IR properties of DBTTF-TCNQCl$_2$ are surprisingly well described by the model for the large U, $4k_F$–Peierls system. The infrared properties of several singlestack conductors like TMTTF$_2$PF$_6$, and MEM-TCNQ$_2$ at 350K, may also be analysed satisfactory in terms of the same model (C. S. Jacobsen, to be published). Thus it appears that for a large group of organic conductors the electronic properties are reminiscent of those of a system, where double occupancy of sites is effectively excluded.

Sum rules and correlation effects

To investigate whether the infrared oscillator strength can give information on the strength of Coulomb correlations in general we give in Table VIII a comparison of the observed oscillator strength with the predicted in the U=0 and U→∞ limits for a number of compounds. In particular, the last column gives the ratio, β, between observed reduction of oscillator strength and the reduction associated with the U→∞ model. Thus β=0 corresponds to U=V=0 and β=1 to U→∞, V=0. It is notable that β is in no case smaller than 0.5. HMTSF-TCNQ and -TNAP, and TMTSF$_2$ClO$_4$, which are all excellent metals have β's close to 0.5. The semiconducting materials have β≈0.9-1.3. TTF-TCNQ which will be discussed in more detail below has β = 0.85 decreasing to 0.56 at 60K, the temperature of maximum conductivity. This may indicate a connection between the absolute value of σ and the screening efficiency. A similar trend is observed in ET$_2$I$_3(\perp)$. However, here $\beta > 1$ in spite of the metallic ground state. The large β is attributed to the narrow (Table VI) and quarter-filled band. It appears that the metallic/superconducting ground state must be related to the 2D-nature of this material which precludes, for example, the $4k_F$-CDW instability.

The only material, which appears not to match the pattern is TMTSF-DMTCNQ, which has metallic character, but β = 1.1. We understand such a large β as arising from a Coulomb correlation dominated acceptor stack and a metallic donor stack as previously implied by analysis of the transport properties (Jacobsen et al., 1978).

Thus it largely appears that the β-values of Table VIII are consistent

Table VIII. Infrared oscillator strength and correlation effects. The first column gives the values expected if U=V=0 (based on Tables III and VI). The second column corresponds to U→∞, V=0 (Eq. 14), while the third gives the measured oscillator strength. β is a relative measure for the strength of the correlation effects (see text).

Material (temp.)	ω_p^2 $(10^7 cm^{-2})$	$\omega_p^2 \cos \varrho \pi/2$ $(10^7 cm^{-2})$	ω_f^2 $(10^7 cm^{-2})$	β
TTF-TCNQ (300K)	13.0	8.4	9.1	0.85
TTF-TCNQ (60K)	15.9	9.5	12.3	0.56
TMTSF-DMTCNQ (300K)	12.5	8.8	8.5	1.08
HMTSF-TCNQ (300K)	20.2	8.0	13.0	0.59
DBTTF-TCNQCl$_2$(300K)	5.6	3.6	3.1	1.25
HMTSF-TNAP (300K)	12.8	7.8	10.3	0.50
TMTTF$_2$PF$_6$ (300K)	7.9	5.6	5.8	0.91
TMTSF$_2$ClO$_4$ (300K)	9.8	6.9	8.3	0.52
ET$_2$I$_3$($\perp$) (300K)	8.3	5.9	5.2	1.29
ET$_2$I$_3$($\perp$) (40K)	9.2	6.5	6.2	1.11

with independent information on the importance of correlation effects. The relatively big reduction of oscillator strength found indicates a considerable localization trend in the wavefunctions in full agreement with the enhancement in magnetic susceptibility generally observed (Torrance et al., 1977). The β-values, through Eq. (13), may prove useful in testing specific models for the wavefunctions in the intermediate correlation regime.

TTF-TCNQ: 2k$_F$- and 4k$_F$-instabilities

As the first good organic metal prepared, TTF-TCNQ remains one of the best characterized solids at all. Even so, many details remain controversial, one of them being the roles played by the two stacks. The physical and structural properties may briefly be summarized as follows:

The conductivity increases as T^{-2} or faster down to well below 100K (Cohen et al., 1974). At 60K $\sigma(T)$ is sharply peaked, and from 53K and down a cascade of phase transitions destroys the metallic character. Extensive structural studies (see, for example, Comes and Shirane, 1979) have shown considerable 1D diffuse scattering at 4k$_F$ from 300K and down to the phase transitions. Below 150K appreciable 2k$_F$-scattering

develops. The character is 1D to 53K, where it becomes 3D. Several physical properties indicate that the 53K transition takes place on the TCNQ-stacks and that the TTF-stacks follow at a lower temperature (Schultz and Craven, 1979). It also appears that the TCNQ-stacks carry most of the conductivity in this material. The magnetic susceptibility is enhanced by a factor 2-3 over the Pauli value at room temperature and decomposition into individual stack contributions tends to show that the TTF-stacks have most of the susceptibility. While these results agree with the bandwidth estimates of Table IV they disagree with a recent NMR study (Takahashi et al., 1984).

Here we will discuss the infrared properties in general and in particular try to assign the $2k_F$- and $4k_F$-instabilities to individual stacks. The overall infrared properties have recently been studied by Jacobsen (1979), Tanner et al. (1981), and Tanner and Jacobsen (1982). The temperature dependence of $\sigma(\omega)$ is shown in Fig. 14 in the entire infrared range. Eldridge and Bates (1983) have subsequently studied the low temperature, far infrared spectrum by a different technique. While their results are in general agreement with those shown here, details in especially the sharpness of the features differ.

At 25K, $\sigma(\omega)$ displays a double peak structure with a low frequency band near 40 cm^{-1} and a very intense band near 300 cm^{-1}. The low frequency band contains about 5% of the total oscillator strength. In view of the observed $2k_F$-superstructure and an energy gap estimated

from $\sigma_{dc}(T)$ of order 300 cm^{-1}, the intense band may be ascribed to single particle transitions across the gap in a $2k_F$-Peierls semiconducting state, while the 30 cm^{-1} band is assigned to the Fröhlich (i.e. CDW) pinned mode.

The CDW parameters estimated on basis of such an interpretation agrees with theoretical expectations (Tanner et al. 1981). However, a detailed fit of the spectrum in terms of the multiphonon theory previously employed is not yet possible.

The 60K spectrum shows a broadening of the 300 cm^{-1} structure and apparently the oscillator strength of the low frequency band has moved to zero frequency. Since $\sigma_{dc}(60K) \simeq 10^4$Scm^{-1}, there is a sharp drop in $\sigma(\omega)$ in the millimetre and submillimetre range. Physically, this is consistent with a depinning of the CDWs at the phase transition. They appear to contribute to σ_{dc} and in the IR a pseudo-gap induced absorption, broadened by fluctuations, may be followed to temperatures above 100K. Going to 300K the features are much broadened and the maximum in $\sigma(\omega)$ has moved to about 800 cm^{-1}. The latter change can not be understood in terms of the $2k_F$-instability.

Instead we may focus on the role of the $4k_F$-instability which gives rise to the only detectable superstructure at 300K. It may be associated with only one or with both types of stack. As usual we expect the infrared properties of the $4k_F$-CDW to consist of a maximum in $\sigma(\omega)$ corresponding to a pseudogap plus a number of sharper features near the A_g-vibrational modes. TCNQ has such a mode near 2200 cm^{-1} (C $\equiv$ N stretch), which couples strongly to the electrons. Fig. 15(a) shows a high resolution study of the reflectance near this mode. At 300K and 200K the feature has the strength and shape of an ordinary IR active mode superimposed on the metallic response of the conduction electrons. From 100K and down to 30K the oscillator strength increases and the shape is inverted (the original structure is presumably hidden behind the new band). The low temperature spectrum is exactly what is expected from a Peierls distorted semiconductor. The point is that the temperature dependence follows that of the $2k_F$-scattering. Thus the $4k_F$-instability must (at least largely) take place on the TTF-stacks. This conclusion agrees with recent diffuse X-ray studies on irradiated TTF-TCNQ (Forró et al., 1984).

It is also corroborated by a careful inspection of the far IR reflectance, shown in Fig. 15(b). Being raw data, these curves should be reliable with respect to position and relative strength of fine structure. Also shown is a model calculation for a $2k_F$-CDW system with $2\Delta = 300$ cm^{-1}, using the

Fig. 15. Chain-axis reflectance of TTF-TCNQ. (a) Temperature dependence in the vicinity of the C≡N stretch frequency. (b) Temperature dependence in the far infrared (Tanner et al., 1981). At bottom is shown a $2k_F$-CDW model with identified A_g-mode features. Q refers to TCNQ, F to TTF.
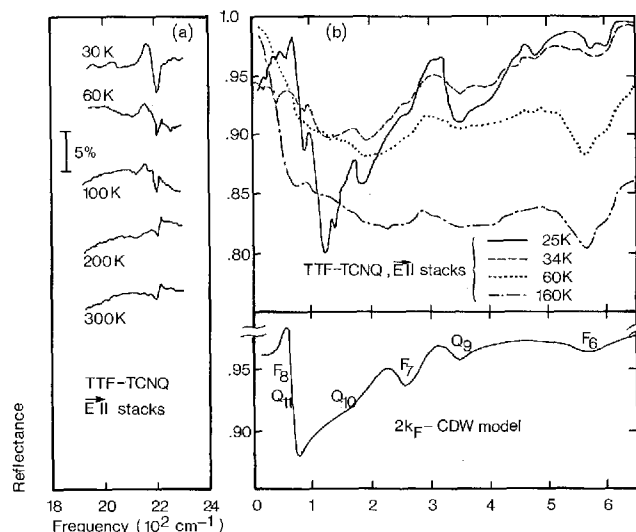
known emv coupling constants of TTF and TCNQ (references from Table VII). The model mainly serves to identify the individual A_g-modes in the far infrared. It is again evident that TCNQ-modes (Q_{10}, Q_9) show a temperature dependence as that of the 2200 cm^{-1} mode, while the TTF-modes (F_6, F_7) are different. F_6 corresponds to a strong, near temperature independent dip in the reflectance from 160K to 60K. Below 60K it moves slightly up in frequency and becomes weaker with a different shape. This behaviour may tentatively be assigned to a cross-over from a $4k_F$- to a $2k_F$-CDW state on the TTF-chains.

The infrared properties are clearly consistent with the idea that the $2k_F$ (ordinary) Peierls instability develops on the TCNQ-chains and perhaps at low temperature induces $2k_F$-order on the TTF-chains as well. The $4k_F$-instability in contrast develops on the TTF-chains. This also agrees with the bandwidth estimates of Table IV. The rather narrow TTF-band is susceptible to a correlation induced $4k_F$-instability. The theory applied to the case of DBTTF-TCNQCl$_2$ is probably inappropriate, but qualitatively we may understand the 300K spectrum of TTF-TCNQ (see Fig. 11) as arising from a near Drude-like contribution from the TCNQ-stack and a contribution from the TTF-stack, which has a maximum near 800 cm^{-1} and emv interference effects in the 1400-1500 cm^{-1} range, where the important carbon skeleton modes are situated (compare Table VII). Interestingly, the rise in $\sigma(\omega)$ at low frequencies may arise from sliding $4k_F$-CDWs, which here (in contrast to the case of DBTTF-

$TCNQCl_2$) experience no Coulomb scattering from oppositely charged density waves.

Conclusions

In the above study we have completed the following line of argumentation: It was shown empirically that the plasma edge Drude analysis of organic conductors yields reliable estimates for bandwidths. This in particular means that the plasmon frequency is largely insensitive to the often strong deviations from Drude behaviour encountered at low frequencies.

By comparing the bandwidth values with the integrated intraband oscillator strength, information on the importance of short range Coulomb correlations was extracted. It appears that all organic conductors have prominent »Coulomb holes«, but clear differences are found between good metals and moderate conductors. For the latter, models where double occupancy of sites is excluded have proven useful in explaining the semiconducting nature. In other materials, where Coulomb correlation effects appear equally strong, interchain interactions preserve the metallic character to low temperature, where even superconductivity may be found (as exemplified by ET_2I_3).

Finally, those molecular vibration modes, which couple to the electrons, were used as »fingerprints« to understand the nature of TTF-TCNQ, where apparently one chain-type shows much stronger correlation effects than the other.

References

Allen, P. B. (1971) Phys.Rev. B *3*, 305.

Andersen, J. R., Bechgaard, K. Jacobsen, C. S., Rindorf, G., Soling, H., and Thorup, N. (1978) Acta Cryst. B *34*, 1901.

Baeriswyl, D., Harbeke, G., Kiess, H., and Meyer, W. (1982) In *Electronic Properties of Polymers,* ed. by Mort, J. and Pfister, G. (Wiley, New York), p. 267.

Bardeen, J., Cooper, L. N., and Schrieffer, J. R. (1957). Phys.Rev. *106,* 162; *108,* 1175.

Bechgaard, K., Kistenmacher, T. J., Bloch, A. N., and Cowan, D. O. (1977). Acta Cryst. B *33,* 417.

Bechgaard, K., Jacobsen, C. S., and Andersen, N. H. (1978). Solid State Commun. *25,* 875.

Bechgaard, K., Jacobsen, C. S., Mortensen, K., Pedersen H. J., and Thorup, N. (1980). Solid State Commun. *33,* 1119.

Bechgaard, K., Carneiro, K., Olsen, M., Rasmussen, F. B., and Jacobsen, C. S. (1981a). Phys.Rev. Lett. *46,* 852.

Bechgaard, K., Carneiro, K., Rasmussen, F. B., Olsen, M., Rindorf, G., Jacobsen, C. S., Pedersen, H. J., and Scott, J. C. (1981b). J.Am.Chem.Soc. *103,* 2440.

Bernasconi, J., Rice, M. J., Schneider, W. R., and Strässler, S. (1975). Phys.Rev. B *12,* 1090.

Bloch, A. N., Cowan, D. O., Bechgaard, K., Pyle, R. E., Banks, R. H., Poehler, T. O. (1975). Phys.Rev.Lett. *34,* 1561.

Bosch, A., and van Bodegom, B. (1977). Acta Cryst. B *33,* 3013.

Bozio, R., and Pecile, C. (1980). In *The Physics and Chemistry of Low Dimensional Solids,* L. Alcácer, ed. (Reidel, Dordrecht), p. 165.

Bright, A. A., Garito, A. F., and Heeger, A. J. (1974). Phys.Rev. B *10,* 1328.

Bryden, W. A., Kistenmacher, T. J., Poehler, T. O., Chappell, J. S., Emge, T. J., Lee, M. M., Lerstrup, K. A., Wiygul, F. M., Cowan, D. O., Stokes, J. P., and Bloch, A. N. (1984). Phys.Rev. B, to be published.

Chaikin, P. M., Greene, R. L., Etemad, S., and Engler, E. (1976). Phys.Rev. B *13,* 1627.

Chesnut, D. B. (1966). J.Chem.Phys. *45,* 4677.

Cohen, M. J., Coleman, L. B., Garito, A. F., and Heeger, A. J. (1974). Phys.Rev. B *10,* 1298.

Comès, R., and Shirane, G. (1979). In *Highly Conducting One-Dimensional Solids,* J. T. Devreese, R. P. Evrard, and V. E. van Doren, eds. (Plenum Press, N.Y.), p. 17.

Conwell, E. M. (1980). Phys.Rev. B *22,* 1761.

Delhaes, P., Coulon, C., Amiell, J., Flandrois, S., Toreilles, E., Fabre, J. M., and Giral, L. (1979). Mol.Cryst. Liq.Cryst. *50,* 43.

Duke, C. B., Lipari, N. O., and Pietronero, L. (1975). Chem.Phys.Lett. *30,*415.

Eldridge, J. E., and Bates, F. E. (1983). Phys.Rev. B *28,* 6972.

Etemad, S., Penney, T., Engler, E. M., Scott. B. A., and Seiden, P. E. (1975). Phys.Rev. Lett. *34,* 741.

Ferraris, J., Cowan, D. O., Walatka, V., and Perlstein, J. H. (1973). J.Am.Chem.Soc. *95,* 948.

Forró, L., Bouffard, S., and Pouget, J. P. (1984). J.Phys. (Paris) Lettr. *45,* L543.

Fröhlich, H., (1954). Proc. Royal Soc. (London) *A223,* 296.

Grant, P. M. (1983). J.Phys. (Paris)-Colloq. *44,* C3-847.

Greene, R. L., Mayerle, J. J., Schumaker, R., Castro, G., Chaikin, P. M., Etemad, S., and LaPlaca, S. J. (1976). Solid State Commun. *20*, 943.

Gutmann, F., and Lyons, L. E. (1967). *Organic Semiconductors* (Wiley, New York).

Herman, F. (1977). Physica Scripta *16*, 303.

Holstein, T. (1954). Phys.Rev. *96*, 535.

Holstein, T. (1964). Ann.Phys. (N.Y.) *29*, 410.

Horovitz, B., Gutfreund, H., and Weger, M. (1975). Phys.Rev. B *12*, 3174.

Hubbard, J. (1978). Phys. Rev. B *17*, 494.

Huizinga, S., Kommandeur, J., Sawatzky, G. A. Kopinga, K., de Jonge, W. J. M. (1979). Lecture Notes in Physics *96*, 45.

Jacobsen, C. S. (1979). Lecture Notes in Physics *95*, 223.

Jacobsen, C. S., Mortensen, K., Andersen, J. R., and Bechgaard, K. (1978). Phys.Rev. B *18*, 905.

Jacobsen, C. S., Pedersen, H. J., Mortensen, K., and Bechgaard, K. (1980). J.Phys.C.: Solid St.Phys. *13*, 3411.

Jacobsen, C. S., Tanner, D. B. and Bechgaard, K. (1981). Phys.Rev.Lett. *46*, 1142.

Jacobsen, C. S., Tanner, D. B., and Bechgaard, K. (1983). Phys.Rev. B *28*, 7019.

Jacobsen, C. S., Johannsen I., and Bechgaard, K. (1984). Phys.Rev.Lett. *53*, 194.

Jacobsen, C. S., Williams, J. M., and Wang, H. H. (1985). Solid State Commun. *54*, 937.

Jerome, D., and Schulz, H. J. (1982). Advances in Physics *31*, 299.

Jerome, D., Mazaud, A., Ribault, M., and Bechgaard, K. (1980). J.Phys. (Paris), Lett. *41*, L95.

Kagoshima, S., Ishiguro, T., and Anzai, H. (1976). J.Phys.Soc.Jpn. *41*, 2061.

Kaminskii, V. F., Prokhorova, T. G., Shibaeva, R. P., and Yagubskii, E. B. (1984). Pis'ma Zh.Eksp.Teor.Fiz. *39*, 15 (JETP Lett. *39*, 17).

Kistenmacher, T. J. (1978). Ann.N.Y.Acad.Sci. *313*, 333.

Kistenmacher, T. J., Phillips, T. E., and Cowan, D. O. (1974). Acta Cryst. B *30*, 763.

Koch, B., Geserich, H. P., Ruppel, W., Schweitzer, D., Dietz, K. H., and Keller, H. J. (1985). Mol.Cryst.Liq.Cryst., *119*, 343.

Lerstrup, K., Lee, M., Wiygul, F. M., Kistenmacher, T. J., and Cowan, D. O. (1983). J.Chem.Soc.Chem.Commun. 294.

Liautard, B., Peytavin, S. Brun, G., and Maurin, M. (1982). J.Phys. (Paris) *43*, 1454.

Lieb, E. H., and Wu, F. Y. (1968). Phys.Rev.Lett. *20*, 1445.

Lipari, N. O., Rice, M. J., Duke, C. B., Bozio, R., Girlando, A., and Pecile, C. (1977). Int.J. Quantum Chem.: Quantum Chem.Symp. *11*, 583.

Lyo, S. K. (1978). Phys.Rev. B *18*, 1854.

Lyo, S. K., and Gallinar, J.-P. (1977). J.Phys.C: Solid St.Phys. *10*, 1696.

Maldague, P. F. (1977). Phys.Rev. B *16*, 2437.

Mazumdar, S., and Bloch, A. N. (1983). Phys.Rev.Lett. *50*, 207.

Megtert, S., Pouget, J. P., Comès, R. Garito, A. F., Bechgaard, K., Fabre, J. M., and Giral, L. (1978). J.Phys. (Paris) *39*, L-118.

Mortensen, K. (1982). Solid State Commun. *44*, 643.

Mortensen, K., Jacobsen, C. S., Lindegaard-Andersen, A., and Bechgaard, K. (1983). J.Phys. (Paris) Colloq. *44*, C3-1349.

Mortensen, K., Jacobsen, C. S., Bechgaard, K., Carneiro, K., and Williams, J. M. (1985). Mol.Cryst.Liq.Cryst., *119*, 401.

Mott, N. F. (1949). Proc.Phys.Soc. (London) *A62,* 416.

Overhauser, A. W. (1960). Phys.Rev.Lett. *9,*462.

Peierls, R. E. (1955). *Quantum Theory of Solids* (Oxford Univ. Press), p. 108.

Phillips, T. E., Kistenmacher, T. J., Bloch, A. N., and Cowan, D. O. (1976). J.Chem. Soc.Chem.Commun. 334.

Pines, D. (1964). *Elementary Excitations in Solids.* (Benjamin, New York).

Pouget, J. P. (1981). Chemica Scripta *17,* 85.

Pouget, J. P. (1984). Unpublished work.

Rice, M. J. (1978). Solid State Commun. *25,* 1083.

Rice, M. J. (1979). Solid State Commun. *31,* 93.

Rice, M. J., and Strässler, S. (1973). Solid State Commun. *13,* 125.

Rice, M. J., Duke, C. B. and Lipari, N. O. (1975). Solid State Commun. *17,* 1089.

Rice, M. J., Pietronero, L., and Brüesch, P. (1977). Solid State Commun. *21,* 757.

Rice, M. J., Yartsev, V. M., and Jacobsen, C. S. (1980). Phys.Rev. B *21,* 3437.

Ritsko, J. J., Sandman, D. J., Epstein, A. J., Gibbons, P. C., Schnatterly, S. E., and Fields, J. (1975). Phys.Rev.Lett. *34,* 1330.

Schultz, A. J., Stucky, G. D., Blessing, R. H., and Coppens, P. (1976). J.Am.Chem.Soc. *98,* 3194.

Schultz, T. D., and Craven, R. A. (1979). In *Highly Conducting One-Dimensional Solids,* J. T. Devreese, R. P. Evrard, and V. E. van Doren, eds. (Plenum Press, N.Y.), p. 147.

Slater, J. C. (1951). Phys.Rev. *82,* 538.

Sokoloff, J. B. (1970). Phys.Rev. B *2,* 779.

Soling, H., Rindorf, G., and Thorup, N. (1981a). Acta Cryst. B *37,* 1716.

Soling, H., Rindorf, G., and Thorup, N. (1981b). Unpublished work.

Tajima, H., Yakushi, K., Kuroda, H., Saito, G., and Inokuchi, H. (1984). Solid State Commun. *49,* 769.

Takahashi, T., Jerome, D., Masin, F., Fabre, J. M., and Giral, L. (1984). J.Phys. C: Solid State Phys. *17,* 3777.

Tanaka, J., Tanaka, M., Tanaka C., Ohno, T., Takabe, T., and Anzai, H. (1978). Ann. N.Y. Acad.Sci. *313,* 256.

Tanner, D. B., and Jacobsen, C. S. (1982). Mol.Cryst.Liq.Cryst. *85,* 137.

Tanner, D. B., Jacobsen, C. S., Garito, A. F., and Heeger, A. J. (1976). Phys.Rev. B *13,* 3381.

Tanner, D. B., Cummings, K. D., and Jacobsen, C. S. (1981). Phys.Rev. Lett. *47,* 597.

Thorup, N., Rindorf, G., Soling, H., and Bechgaard, K. (1981). Acta Cryst. B *37,* 1236.

Torrance, J. B. (1979). Acc.Chem.Res. *12,* 79.

Torrance, J. B., Tomkiewicz, Y., and Silverman, B. D. (1977). Phys.Rev. B *15,* 4738.

Weyl, C., Engler, E. M., Bechgaard, K., Jehanno, G., and Etemad, S. (1976). Solid State Commun. *19,* 925.

Williams, P. F., and Bloch, A. N. (1974). Phys.Rev. B *10,* 1097.

Wooten, F. (1972). *Optical Properties of Solids* (Academic Press, New York).

Yagubskii, E. B., Shchegolev, I. F., Laukhin, V. N., Kononovich, P. A., Karatsovnik, M. V., Zvarykina, A. V., and Buravov, L. I. (1984). Pis'ma Zh.Eksp.Teor.Fiz. *39,* 12 (JETP Lett. *39,* 12).

Yamaji, K. (1985). Mol.Cryst.Liq.Cryst., *119,* 105.

Hans Uffe Petersen

Function of tRNA

in Initiation of Prokaryotic Translation

ABSTRACT. *This paper is a review of studies on structural and functional aspects of the interactions between the methionine accepting tRNAs and other macromolecules (enzymes, protein factors and ribosomes) in the cellular reactions preceding the formation of the first peptide bond during protein biosynthesis. Before discussing the recent research results, the problem will be introduced in a chronological order according to the discovery of the required molecular components and their functions. This introduction also aims at giving the reader an impression of the importance of the chosen subject in the field of molecular biology.*

Division of Biostructural Chemistry,
Department of Chemistry, Aarhus University,
DK-8000 Aarhus C, Denmark

Introduction

All living cells contain a large number of different protein molecules. The exact number is not known, but estimates from the size of the genomes and two-dimensional polyacrylamide gel electrophoretic analysis of crude cell-lysates suggest the order of 2000 to 10000 different natural proteins.

These molecules consist of chains of amino acids linked together by peptide bonds as shown in Figure 1, where R_1 and R_2 are specific side-chains. All known proteins contain up to 20 different amino acids in the polypeptide chain – the primary sequence, which determines the three-dimensional structure and the function of each individual protein. The mechanism by which amino acids are linked together in the sequence specified by the nucleotide sequence of the gene is the biological translation. A four-letter "nucleotide alphabet" in DNA (and in messenger RNA) is translated into a 20-letter "amino acid alphabet" in protein molecules – a sequence of three nucleotides (codon) specifies each amino acid. The biological translation is a complicated process consisting of

Fig. 1. The formation of a
peptide bond.
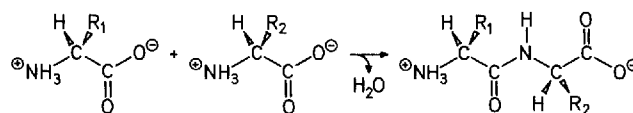
many steps and involving a number of specific macromolecular interactions. One of the most important components of this process is the tRNA molecule, which started its scientific career as a purely intellectual creation.

The suggestion and discovery of transfer RNA

After the elucidation of the DNA structure and the suggestion of the principles in the relation between DNA and protein in the early and mid-1950s, no one could envisage how nucleic acids could programme the synthesis of protein by direct structural interactions with amino acids. The first clue to this problem was the introduction by Francis Crick during the years 1955-57 of the "Adaptor Hypothesis" by which a small adaptor molecule would mediate between amino acids and a piece of nucleic acid which carried the genetic information for specifying the amino acid sequence during polymerisation into proteins. The Adaptor Hypothesis was almost simultaneously confirmed by the discovery of soluble RNA molecules carrying amino acids (Hoagland et al., 1959). The molecules were larger than expected by Crick, and turned out to be nucleic acids containing approximately 80 ribonucleotides and a molecular ratio of 25,000.

The first soluble RNA molecule (called sRNA – and since 1967 transfer RNA or tRNA) was sequenced by Holley et al. (1965) during the years 1958-65. The structure is shown in Figure 2A in the so-called cloverleaf representation. Many other tRNA molecules were soon sequenced, and a similar cloverleaf structure could be drawn for each molecule. The tRNA molecule can form intramolecular Watson–Crick base-pairs in four regions. One of these contains the terminals of the nucleotide chain, and the three others end in singlestranded loops. It is shown in Figure 2B where the amino acid attaches to the molecule and the "anti-codon" nucleotide sequence which "reads" the amino acid-specifying nucleotide sequence on messenger RNA is indicated at the bottom of the molecule.

The first three-dimensional structure of a tRNA molecule was obtained independently by the groups of Aaron Klug in Cambridge and Alexander Rich at M.I.T. in 1975. The folded structure (of phenyl-

alanine specific tRNA from yeast) is shown in Figure 3. Although minor and probably important differences may exist, the overall spatial structure is believed to be general in tRNA molecules.

The knowledge of the three-dimensional structure of the tRNA molecules is one of the prerequisites for the study of structural interactions between tRNA and proteins, which is one of the main subjects of this paper.

Protein biosynthesis starts at the amino terminal

At the time the tRNA molecules were discovered, only very limited knowledge existed about the molecular reactions in which it is involved during its functional cycle. The study of the components and mechanism of protein biosynthesis was just starting. However, it was becoming clear that the process took place on sub-cellular particles – first called microsomes and in 1958 named ribosomes by Richard Roberts.

Then it was a crucial question in which direction the reaction of amino acid polymerisation proceeded. If we look at Figure 1, would R_1 or R_2 be
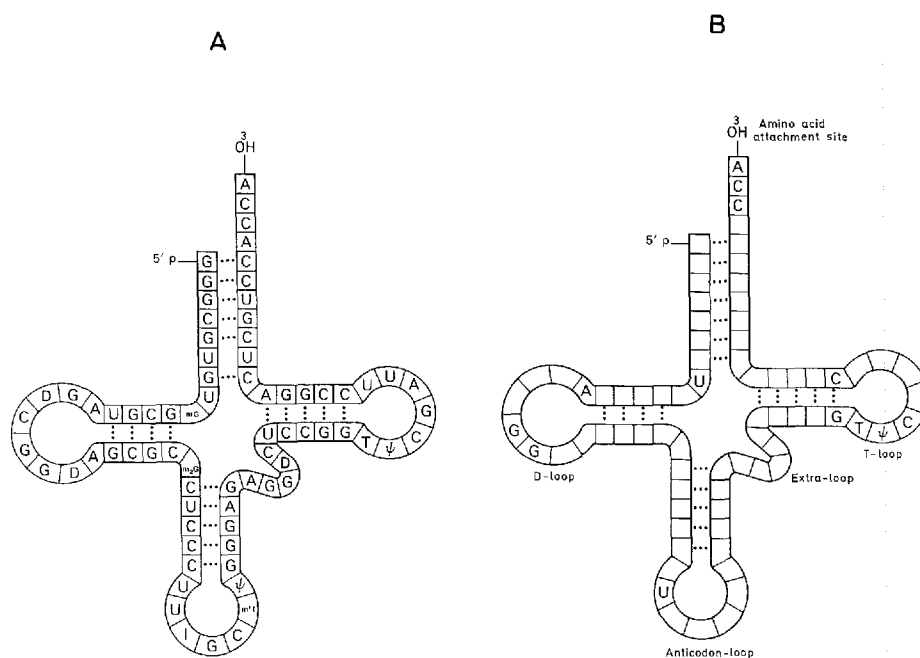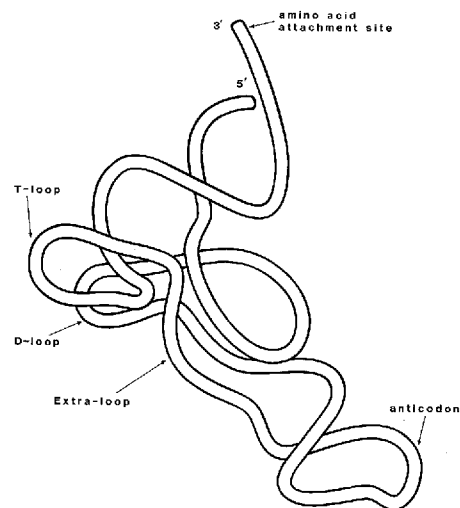

Fig. 2A. *Cloverleaf representation of the nucleotide sequence of tRNA^{Ala} from yeast.*
B: *Common features of tRNA molecules.*

Fig. 3. Schematic diagram of the three-dimensional structure of tRNA^{Phe} from yeast. Based on the X-ray crystallographic data of Ladner et al., 1975.

the first amino acid in the polypeptide – in other words would the initiating amino acid become the N- or C-terminal of the molecule?

The first answer to this question came from a study of the biosynthesis of haemoglobin by Bishop *et al.* (1960), who found that the polypeptide chain growth began with the N-terminal amino acid. This means that R_1 in Figure 1 is the terminal amino acid in a protein starting by this reaction. Shortly after, Goldstein and Brown (1961) showed that *E. coli* proteins are synthesized beginning with the N-terminal amino acid.

N-terminal amino acid = methionine

By that time, other workers were studying sequences of amino acids in proteins. From the work of Moriwitz and Spaulding (1958), it seemed that one particular amino acid appeared more than statistically in the N-terminal position of *E. coli* – namely methionine.

That methionine is found much more than randomly as the N-terminal amino acid of *E. coli* proteins was confirmed by Waller and Harris (1961) – for ribosomal proteins – and finally by Waller (1963) – for total *E. coli* proteins. This led to believe that proteins are synthesized by a mechanism which specifically incorporates methionine as the first and N-terminal amino acid. Twenty years ago, the picture of the molecular mechanism of protein biosynthesis can be presented as shown in Fig. 4 (Watson, 1964).

The genetic information in the chromosomal DNA (in the form of a fourletter nucleotide sequence) is transcribed into messenger RNA by

the enzyme RNA polymerase. The mRNA is then bound to a ribosome and by adaptor molecules – aminoacyl-tRNAs – translated into a 20-letter amino acid sequence in a polypeptide chain.

It was known that special protein factors (transfer enzymes) were needed to stimulate the overall process of translation and that energy was supplied by GTP, but the knowledge specifically concerning the mechanism by which the process started was clearly expressed by Watson: "Almost no hints exist about chain initiation".

The first important discovery of initiation specific molecules came from the Cambridge laboratory of Perutz.

Initiator tRNA

In their work with sulfur containing amino acids (easily labelled with high specific radioactivity) and their interaction with tRNAs from $E.$ $coli$, Marcker and Sanger (1964) found that [^{35}S]-methionyl-tRNA upon mild hydrolysis (which splits off the amino acid as shown in Fig. 16) gave two radioactive spots on electrophoretic analysis – one from methionine and another which was identified as N-formyl-methionine. Shortly after Marcker (1965) showed that two different classes of methionyl-tRNA exist of which one could be N-formylated in the methionine by an in $vitro$ system, whereas the other could not. The two species were named Met-tRNA$_1$ (not formylatable, now called tRNA$_m^{Met}$) and Met-tRNA$_2$ (formylatable, now called tRNA$_f^{Met}$) and the role of formyl-methionyl-tRNA as initiator tRNA in protein synthesis was the authors' immediate suggestion. The cloverleaf structures of the two tRNAs are
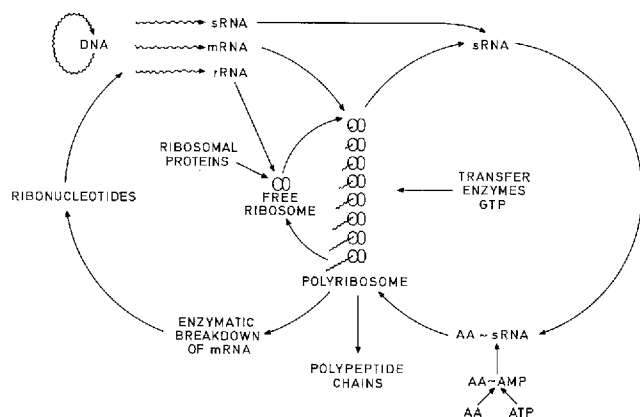

Fig. 4. Schematic view of protein synthesis as of March 1964 (Watson, 1964).
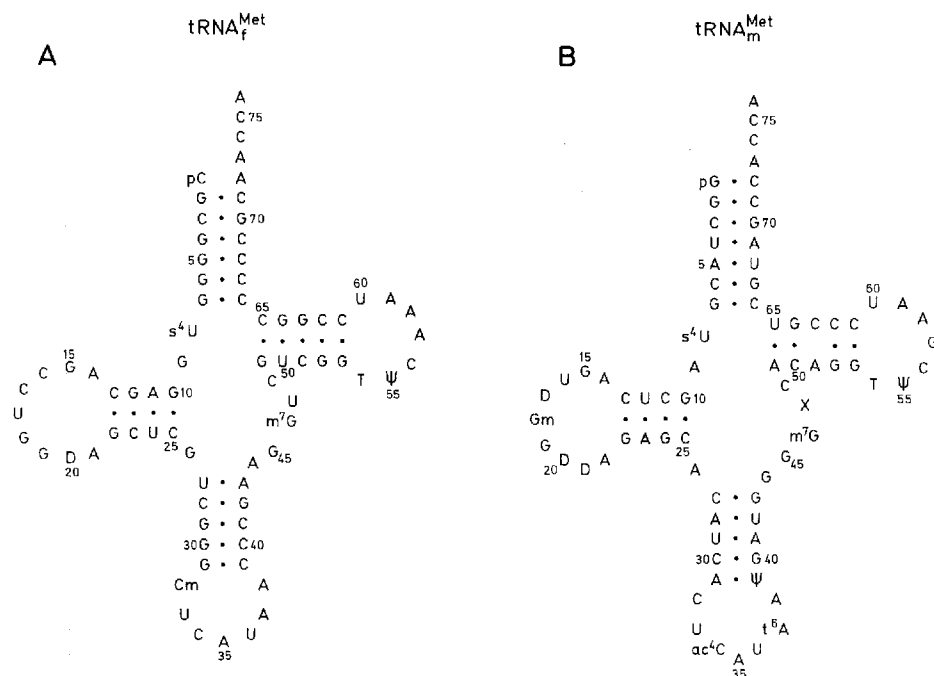
Fig. 5A. Cloverleaf representation of the nucleotide sequence of initiator $tRNA_f^{Met}$ (Dube et al., 1968).

B. Cloverleaf representation of the nucleotide sequence of elongator $tRNA_m^{Met}$ (Cory et al., 1968).

shown in Fig. 5. Similarities and differences in the nucleotide sequences will be discussed further in subsequent paragraphs. In an *in vitro* system similar to the one developed by Nirenberg and Matthaei (1961), Clark and Marcker (1966a) showed that N-formyl-methionyl-tRNA$_f^{Met}$ exclusively incorporated formyl-methionine into the N-terminal of a growing polypeptide chain (in response to poly(U,G)), similarly the same authors showed (1966b) that the non-formylatable Met-tRNA$_m^{Met}$ incorporated methionine into internal positions of polypeptides and not into the N-terminal. This was considered as a proof that tRNA$_f^{Met}$ is the true initiator tRNA in *E. coli*.

Aminoacylation of tRNA$_f^{Met}$

The tRNA molecules carry the amino acids from the cell cytoplasm to the ribosome – the site of protein biosynthesis. Now the question arises: How are the correct amino acids linked to the tRNA molecules? This is

an enzymatic process, which requires catalysis by an aminoacyl-tRNA synthetase specific for each amino acid.

The methionyl-tRNA synthetase aminoacylates both $tRNA_m^{Met}$ and $tRNA_f^{Met}$. The enzyme has been extensively characterized by the group of Sylvain Blanquet at the Ecole Polytechnique in Paris (Blanquet et al., 1973, 1976). The native protein contains two identical polypeptide chains (type α_2) each with an M_r of 76,000.

The monomer can easily be split by trypsin, resulting in a 64 k dalton fragment, which retains the activity of aminoacylation (Dessen et al., 1982). This fragment has been crystallized, and the X-ray crystallography group of Risler in Gif-sur-Yvette has determined the crystal structure at 2.5 Å resolution (Zelwer et al., 1982).

The aminoacylation reaction catalyzed by Met-tRNA synthetase is shown in Fig. 8 (Reactions 1 and 2).

Formylation of initiator tRNA

Marcker (1965) showed that the formylation in the α-amino group of methionine takes place after the aminoacylation of $tRNA_f^{Met}$ and found that N^{10}-formyl-tetra-hydrofolate was a good formyl-donor in the crude *in vitro* system. The formylating enzyme was purified by Dickerman et al. (1967), who confirmed that N^{10}-fTHF was the formyl-donor. Therefore, the enzyme was named: N^{10}-formyl-tetrahydrofolate:L-methionyl-tRNA N-formyltransferase (E.C.2.1.2.9). This means that the formylation of Met-$tRNA_f^{Met}$ is coupled to the C-1 metabolism as shown in Fig. 6.

The transformylase has been extensively purified by Kahn et al. (1980) who showed that at physiological ionic conditions, the enzyme has a significantly higher affinity to charged initiator $tRNA_f^{Met}$ as compared to uncharged $tRNA_f^{Met}$ and to other tRNAs.

From the reactions of aminoacylation and formylation (and as it will be discussed later, also from the interaction with the elongation factor Tu), it seems clear that the tertiary structure of the initiator tRNA must be partially identical to that of $tRNA_m^{Met}$ but also partially different from all other tRNAs, and this specific tertiary structure seems sensitive to aminoacylation.

Not only in *E. coli* but also in cell organelles of eukaryotic organisms (chloroplasts and mitochondria) is the protein synthesis initiated by fMet-tRNA (Galper and Darnell, 1969). This led Marcker (1969) to propose the general rule that prokaryotic cells and eukaryotic cell organelles use N-formyl-methionyl-tRNA as polypeptide chain initiator
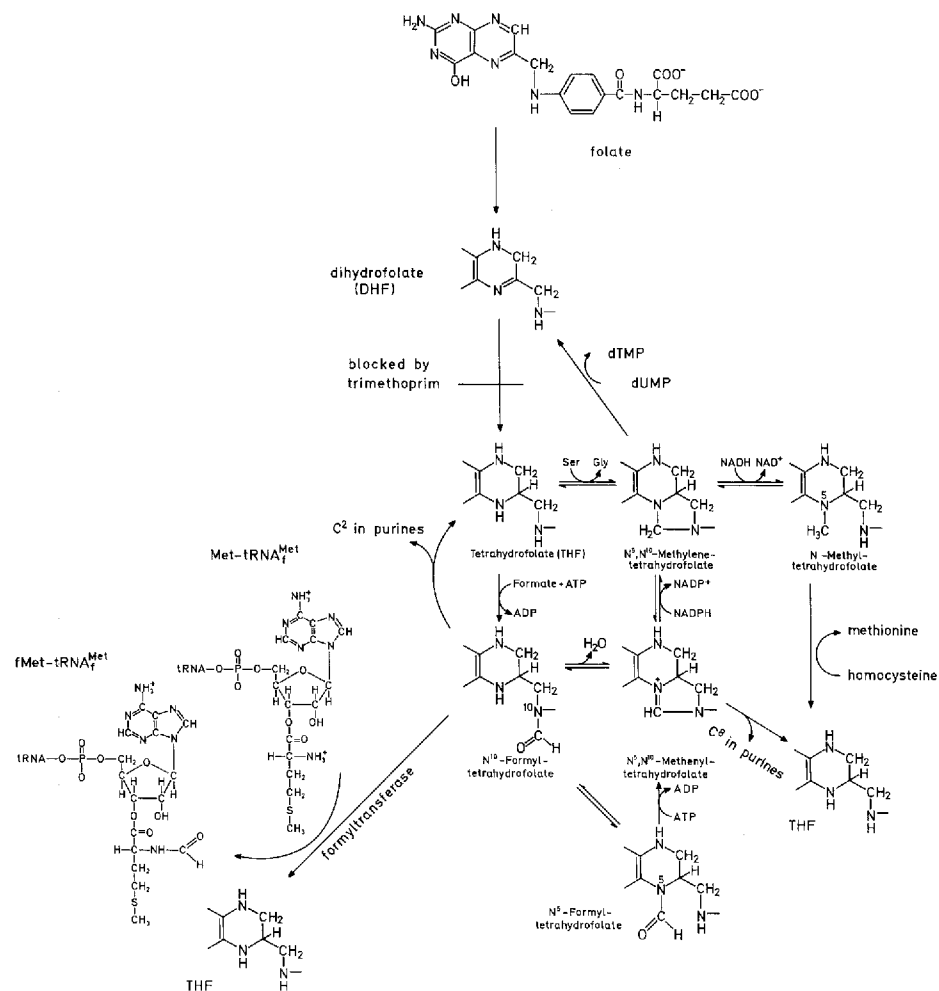
Fig. 6. The folate metabolism including the reaction of formylation of initiator Met-tRNA$_f^{Met}$.

tRNA. The initiator tRNA in eukaryotic cytoplasmic protein synthesis is also methionyl-tRNA. Although it has been shown that this tRNA (tRNA$_i^{Met}$) can be formylated by E. coli transformylase, no formylation takes place in the eukaryotic cytoplasm in vivo (Lodish, 1976).

Formylation of prokaryotic Met-tRNA$_f^{Met}$ is not indispensable.

In vivo evidence against the general rule of formylation

However, formylation of initiator tRNA methionine in prokaryotic organisms is not general – that cells may grow without formylation has been shown in different organisms in four principal classes of cases:

1: organisms which cannot synthesize the formyl-donor *de novo* may grow in the absence of formylation
2: organisms which contain no transformylase enzyme grow without formylation
3: *E. coli* can grow when formylation is inhibited
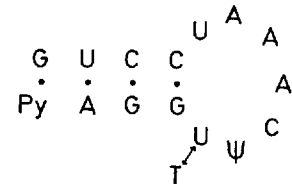4: mutants of *E. coli* have been isolated which grow normally in the presence of an inhibitor of formylation.

An example of each of these cases will be described briefly:

1: The organism *Streptococcus faecalis R* is (in contrast to *E. coli* and other prokaryotes) not able to synthesize folic acid *de novo*, but it was found that the cells could grow in the absence of folic acid when the substrate was supplemented with the folic acid metabolites serine, methionine, thymine and a purine base – see Fig. 6. At such conditions, the formyl-donor N^{10}-formyl-tetrahydrofolate cannot be synthesized, and formylation of the initiator tRNA must (if there is a formylation) follow other metabolic pathways (Samuel *et al.*, 1970). Indeed, no formylation or other blocking of the α-amino group of Met-tRNA methionine took place in the folate-free medium, although in the presence of folic acid, most of the Met-tRNA$_f^{Met}$ was formylated *in vivo* (Samuel *et al.*, 1972). Later, the authors showed that the tRNA$_f^{Met}$ from folate-free cells was altered as compared to the initiator tRNA isolated from cells grown in the presence of folic acid – the ribothymidylic acid normally found in the TψC loop was not found in the "folate-free" tRNA, see Figs 5A and 7. So it seemed that a structural change in the initiator tRNA could compensate for the lack of formylation (Samuel & Rabionwitz, 1974).

However, it was found that the methylase responsible for the formation of rT in the tRNA in *S. faecalis* requires a folate coenzyme as methyldonor. This means that the absence of formylation and of rT in the tRNA of "minus folate" cells are both (and possibly independently) induced by the folate deprivation (Delk & Rabinowitz, 1975).

Rabinowitz and coworkers did not study the *in vitro* binding of fMet-tRNA$_f^{Met}$ from plus and minus folate *S. faecalis* in crossed experi-

Fig. 7. The T-arm of the initiator tRNA$_f^{Met}$ from S. faecalis.
The ribothymidylic acid present in +folate cells is replaced by
uridine in −folate cells (Samuel and Rabinowitz, 1974).

```
                                    U  A
                                       A
        G   U   C   C                      A
        •   •   •   •                       A
        Py  A   G   G
                            U   ψ   C
                           /
                          T
```

ments with ribosomes (and initiation factors) isolated from the two growth conditions. It can therefore not be excluded that the ribosomes (and/or the initiation factors) play an important role for the ribosomal binding of the unformylated (and undermethylated) initiator tRNA from "minus folate" *S. faecalis* stimulated by initiation factors (and thus in the ability of *S. faecalis* cells to grow in the absence of formylation).

2: The strongly halophile *Halobacterium cutirubrum* was studied by White & Bayley (1972) who found that this organism does not synthesize the transformylase enzyme needed for the formylation of Met-tRNA$_f^{Met}$, although the methionine accepting tRNA isolated from *H. cutirubrum* could be separated into two species of which one was formylatable by *E. coli* transformylase.

   As the organism requires extreme high salt concentrations, it is likely that conformational changes of the tRNA (and/or the ribosomes) may occur as compared to a hypothetical low-salt structure. Such salt induced structural changes may explain the ability of *H. cutirubrum* to grow without formylation of the initiator tRNA.

3: The antibiotic trimethoprim is an inhibitor of dihydrofolate reductase, the enzyme which reduces dihydrofolate (DHF) to tetrahydrofolate (THF) − see Fig. 6. Harvey (1973) has studied the effect of trimethoprim on the growth of *E. coli*. He found that *E. coli* wild type (B/r) cells could grow exponentially at a reduced rate in the presence of trimethoprim when the folic acid metabolites were added. Under these conditions, no formylation of Met-tRNA$_f^{Met}$ took place.

   Harvey found that at the growth conditions where the initiator tRNA was unformylated, a two-fold increase in the ratio ribosomal subunits:70S ribosomes arose. As will be discussed further in the following sections, the increased level of ribosomal subunits may be involved in the explanation of the ability of the cells to grow without formylation of Met-tRNA$_f^{Met}$.

4: The isolation of *E. coli* mutants able to grow normally without for-

mylation (Danchin, 1973) is an additional support for the idea that formylation of initiator Met-tRNA is not general and vital for prokaryotic organisms.

Danchin isolated *E. coli* mutants on media containing the C-1 metabolites supplemented with trimethoprim, and found quite surprisingly that among these mutants were strains resistant to streptomycin. Such rpsL mutants are known to be point mutations in the ribosomal protein S12. Therefore, it seems clear that the ability to grow in the absence of formylation in some way is linked to alterations in the structure of the ribosomes.

Another *E. coli* mutant was isolated by Baumstark *et al.* (1977) which was able to grow without formylation of the initiator tRNA. By the same method as previously used by Danchin (1973), a K12 mutant was selected in the presence of sulfathiazole and trimethoprim. The authors showed that the initiator $tRNA_f^{Met}$ of this mutant contained a reduced (but finite) amount of ribothymidine in the $T\psi C$ loop of the tRNA and concluded that this alteration in the initiator tRNA structure was possibly the reason why the mutant could grow without formylation.

However, their *in vitro* f2 directed protein synthesis did not include crossed experiments with mutant ribosomes and unformylated Met-$tRNA_f^{Met}$ isolated from the parental strain cells. This would be required to exclude that the ability to grow in the absence of formylation arises from altered ribosomes. In fact, the mutant of Baumstark is not a single mutation but derived from a parental strain which was streptomycin resistant (altered in the ribosomal protein S12).

E. coli mutants containing unmethylated uridine instead of rT in the tRNA have been isolated by Björk & Isaksson (1970). In order to test the hypothesis of Baumstark and coworkers, trimethoprim was added to the growth medium of the mutants (and the C-1 metabolites). Under such conditions no formylation of Met-$tRNA_f^{Met}$ could take place, and it would show if the lack of rT was sufficient to account for growth in the absence of formylation. The cells were not able to grow under such conditions (Danchin and Isaksson, personal communication). Thus it seems clear that the other mutations in the strain isolated and studied by Baumstark, in addition to the mutation in the methylase, must play a role in the ability of these cells to grow without formylation of the initiator Met-tRNA.

In vitro evidence against the general rule of formylation

Looking back at the first experiments *in vitro* with the initiator tRNA there were indications that formylation might not be indispensable. Clark & Marcker (1966a) did not find any significant difference in the activity of Met-tRNA$_f^{Met}$ whether formylated or not, and just before the discovery of the initiation factors in 1966, Bretscher & Marcker (1966) had shown that at 10-20 mM magnesium, both formylated and unformylated Met-tRNA$_f^{Met}$ could bind to ribosomes and react with puromycin. They concluded that the only role of the formyl group was to increase the rate of initiation.

This led Clark and coworkers to believe that the specificity as initiator tRNA lay in the tRNA structure and not in the presence of the formyl group on the methionine. Therefore, the two methionine accepting tRNAs were sequenced in the hope that the nucleotide primary structure could reveal some characteristic differences between the two tRNAs (on the one hand and between tRNA$_f^{Met}$ and all other tRNAs on the other).

In the two cloverleaf structures shown in Fig. 5, one observes a number of differences in nucleotides at the individual positions. However, an intensive comparison of the tRNA$_f^{Met}$ sequence with other tRNAs shows that all individual nucleotides and local sequences of tRNA$_f^{Met}$ can be found in other tRNAs. Only one difference in the primary structure seems to be characteristic for tRNA$_f^{Met}$ – namely the fact that the 5'-terminal nucleotide (cytidine) is not involved in a Watson-Crick base-pair which is the case for the 5'-terminal nucleotide of all other tRNAs.

Although this may be very important, it is unlikely that it accounts for all the specificities which are found for the initiator tRNA as compared to tRNA$_m^{Met}$ and all other tRNAs, especially as this difference is not found in eukaryotic cells which also use a formylatable (by *E. coli* tranformylase) Met-tRNA species as initiator tRNA.

Other workers then found that formylation was required for the translation *in vitro* of natural mRNA (from phage f2) at 5 mM magnesium (Eisenstadt & Lengyel, 1966), and after the discovery of the initiation factors and the establishment of their optimal salt conditions (5-10 mM magnesium), many *in vitro* experiments suggested that fMet-tRNA$_f^{Met}$ was the correct initiator tRNA as only the formylated tRNA species could bind to 70S ribosomes strongly stimulated by initiation factors (the concept of "enzymatic binding") (Grunberg-Manago *et al.*, 1969; Drews *et al.*, 1973).

In most of these experiments, 70S ribosomes were used for studying

the initiation factor stimulated binding. As the initiation mechanism was supposed to involve the formation of a 30S initiation complex with mRNA and initiator tRNA (see Fig. 8), one could ask whether 30S subunits would behave differently from the 70S ribosomes in such *in vitro* binding experiments. A first indication of such a difference can be seen from the work of Grunberg-Manago *et al.* (1969). In one experiment, 30S subunits were used, and indeed, a small stimulation (in absolute scale, but 50% relative) by the initiation factors of the binding of unformylated Met-tRNA$_f^{Met}$ at 5mM magnesium is observed.

In the work of Samuel & Rabinowitz (1974) previously described, the initiator tRNA from "minus-folate" *S. faecalis* cells was extracted and purified. In the *in vitro* ribosomal binding assay, the authors showed that initiation factors stimulated the unformylated and the formylated form of this Met-tRNA$_f^{Met}$ to the same degree. (This IF-stimulated binding was seen at Mg^{++} concentrations up to 30 mM.)

Together these results indicate that although the formylation may increase the rate of interaction of the initiator tRNA with ribosomes, the enzymatic binding of Met-tRNA$_f^{Met}$ to ribosomes or ribosomal subunits does not absolutely require formylation.

More recently, Rich and collaborators have used the single-strand specific endonuclease S1 to study structural characteristics of initiator tRNAs compared to elongator tRNAs (Wrede *et al.*, 1979). They found that S1 cleaved at two distinct sites in the anticodon loop of three different initiator tRNAs (from *E. coli,* yeast and mammalian), whereas elongator tRNAs were cut at four sites. The authors suggest that the specificity is caused by the three G-C base-pairs of the anticodon arm (see Fig. 5), which are common in the initiator tRNAs and different from the elongator tRNAs included in the experiments by Rich & Wrede. However the initiator tRNAs in Bean chloroplasts and in yeast mitochondria contain only two G-C base pairs in these positions. The nucleotide at position 29 is here A in stad of the G in *E. coli* tRNA$_f^{Met}$ (Fig. 5A). Furthermore, at least two examples are known of elongator tRNAs which contain three G-C base pairs at position 29-41, 30-40 and 31-39, namely tRNA^{Met} from Bovine liver mitochondria and tRNA^{Ser} from *Halobacterium vol.* (Sprinzl & Gauss, 1984). Therefor it seems clear that no single local nucleotide sequence in the anticodon stem of the initiator tRNA$_f^{Met}$ is determining its specific function. Indeed as it will be discussed in later paragraphs, there are indications that unformylated Met-tRNA$_f^{Met}$ can function as an elongator tRNA.

As it seems unlikely that formylation should cause a drastic change in

the structure of the anticodon stem, the results of Rich *et al.* are in agreement with our results presented in the following sections, that formylation is not the determining factor but that the tertiary structure of the initiator tRNA most probably is one of the most important features in the functional specificity of fMet-tRNA$_f^{Met}$. We have studied the accessibility of different regions of tRNA$_f^{Met}$ and tRNA$_m^{Met}$ to a number of ribonucleases and compared the results in the presence and absence of proteins. These results will be discussed in detail in subsequent paragraphs. Other important elements which will be discussed in the following is the presence *in vivo* of translation factors. The fact that unformylated Met-tRNA$_f^{Met}$ binds to the elongation factor EF-Tu (see later) indicates that at extreme growth conditions, some of the initiator tRNAs might in fact function in the elongation step of translation.

Buckingham and collaborators have found that initiation factors stimulate the binding of formylated or acetylated Trp-tRNA^{Trp} to 30S or 70S ribosomes in the presence of poly(U,G). A number of other tRNAs have been tested for similar initiator activity with negative results (Leon *et al.*, 1979). These results indicate some structural similarity between tRNA$_f^{Met}$ and tRNA^{Trp}, although such similarity does not appear from a comparison of the nucleotide sequences of the two tRNAs. One point which may seem rather odd is that these two tRNAs, alone among the 21 different amino acid acceptors, do not show degeneracy in their corresponding codons, namely AUG and UGG respectively, are codons for tRNA$_f^{Met}$ and tRNA^{Trp} (with the exception that the valine codon GUG and the normal codon for isoleucine AUU in a few cases have been found as initiator codons).

Finally, the amino acid part of fMet-tRNA$_f^{Met}$ seems to be of minor importance for the functional specificity as initiator tRNA. Giegé *et al.* (1973) showed that the methionine of fMet-tRNA$_f^{Met}$ could be replaced by valine or phenylalanine without any change in the initiation factor-stimulated binding to ribosomes. The puromycin reactivity too was unchanged by the mischarged f-aa-tRNA$_f^{Met}$s.

As a conclusion, it seems that the ribosome-mRNA interaction with the initiator tRNA must be considered when determining the specificity of a tRNA as initiator. The proper selection of the initiator tRNA may at least in a final step be controlled by the initiator codon of the mRNA, and although formyl-Trp-tRNA^{Trp} can bind to the P-site of the 30S or 70S ribosome *(in vitro)*, the use as initiator tRNA *in vivo* is prevented by the lack of formylation and by the mis-matching of the tRNA^{Trp} anticodon and the initiator codon of the mRNA.

So the total recognition between the components in the initiation complex is most probably a combination of the mRNA-aa-tRNA, the mRNA-30S, the aa-tRNA-IF2 and the 30S-aa-tRNA interactions, and although one or more of these interactions might proceed by species other than (f)Met-tRNA$_f^{Met}$, the final complex will not be stable in such cases.

A summary of the reactions involving the initiator tRNA$_f^{Met}$ during the initiation of translation

A short summary of the present view of the mechanism of polypeptide chain initiation follows. Fig. 8 is a schematic representation of the steps involved in the initiation process (Petersen et al., 1984b).

After the aminoacylation (reaction 1+2) and formylation (reaction 3) of tRNA$_f^{Met}$, a pre-initiation complex between fMet-tRNA$_f^{Met}$ and initiation factor IF2 is formed (reaction 4). GTP may be involved in the formation of a ternary complex fMet-tRNA$_f^{Met}$:IF2:GTP, but no direct evidence for such a complex has yet appeared; a later section discusses this subject in more detail.

The next step involves the ribosome and in particular the 30S ribosomal subunit. The 70S particle exists in equilibrium with the 30S and 50S subunits (reaction 11). In vitro experiments have shown that temperature, pH and especially ionic conditions are parameters of importance for this equilibrium. Thus increased concentration of potassium or decreased concentration of magnesium promotes dissociation (see also Fig. 10). However, in the cell, the equilibrium is supposed to be controlled by special proteins, the initiation factors IF1 and IF3. IF1 increases the rates of dissociation and association, and IF3 prevents reassociation by binding to the 30S subunit. IF3 is thus acting as an anti-association factor, and in the presence of IF3, IF1 acts as a dissociation factor, thus in collaboration, the two factors shift the equilibrium towards the 30S + 50S state (Grunberg-Manago, 1980).

The sequence in the following steps, the binding of mRNA and fMet-tRNA$_f^{Met}$ to the 30S subunit, is not known. There exist indications for both molecules being bound prior to the other. Therefore, in Fig. 8, the binding of both components is shown simultaneously.

In the review previously mentioned, Watson (1964) introduced the concepts of two distinct ribosomal sites for interaction with mRNA and aminoacyl-tRNA – now called the P- and A-sites. The initiator region

$$\text{tRNA}_m^{\text{Met}} + MetRS \rightleftharpoons \text{tRNA}_m^{\overset{I}{\text{Met}}}{:}MetRS$$

$$1 \quad \left\{ \begin{array}{l} \text{ATP + Methionine} \\ \text{PP}_i \end{array} \right.$$

$$\text{tRNA}_m^{\text{Met}} + MetRS{:}\text{AMP}{:}\text{Met} \overset{\text{AMP}}{\underset{2}{\rightleftharpoons}} \text{Met-tRNA}_m^{\text{Met}}{:}\ MetRS$$

$$3 \quad \left\{ \begin{array}{l} EF\text{-}Tu{:}\text{GTP} \\ MetRS \end{array} \right.$$

$$\begin{array}{r}\text{R-site?}\\ \text{Met-tRNA}_m^{\text{Met}}{:}EF\text{-}Tu{:}\text{GTP} \underset{4}{\overset{70S}{\longrightarrow}}\ \text{A-site}\\ \text{II} \qquad \text{E-site?}\end{array}$$

Fig. 8. Principal steps in the initiation of prokaryotic translation. Reactions involving the initiator tRNA$_f^{Met}$.

(the nucleotide sequence preceding and including the initiator AUG codon) of the mRNA is supposed to form a varying number of base-pairs with the 3'-OH terminal region of the 16S ribosomal RNA (Shine & Dalgarno, 1975), similarly a part of the fMet-tRNA$_f^{\text{Met}}$ molecule, including in particular the anticodon region, binds to the 30S ribosome. Both these interactions take place at the P-site. The P-site is thus a functional as well as a structural definition.

The implication of the P-site and the role of formylation of Met-tRNA$_f^{\text{Met}}$ in the formation of the 30S initiation complex will be discussed in more detail in the subsequent sections.

The last step in the formation of the functional initiation complex is the association of the 50S subunit with the 30S initiation complex (reaction 6). During this step, GTP is hydrolyzed, and the three initiation factors are released. The role of the GTP hydrolysis is not clear, but it seems reasonable that a final correct positioning of the four macromolecular components in the initiation complex requires a conformational adjustment which could be energy-requiring. Other molecules may play an important role in the regulation of the initiation-complex formation as for instance the ribosomal protein S1; this is currently under investigation in a number of laboratories, and is therefore not included in this short review of the initiation mechanisms.

In addition to the described classical mechanism of initiation, Fig. 8 shows reactions involving Met-tRNA$_f^{\text{Met}}$ or fMet-tRNA$_f^{\text{Met}}$, which have

Table 1: Functional differences between $tRNA_f^{Met}$ and other tRNAs

	Codon specificity	Interaction with proteins and ribosomes					
		Met-tRNA synthetase (E.C.6.1.1.10)	Transformylase* (E.C.2.1.2.9)	Initiation factor IF2	Elongation factor EF-Tu	70S ribosomal A-site	P-site
$tRNA_f^{Met}$	AUG (GUG)#, (AUU)#, (UUG)	⊕	+	⊕	⊕	±	⊕
$tRNA_m^{Met}$	AUG	⊕	–	–	⊕	+	–
other tRNAs	not AUG	–	–	–	+	+	–

* after charging with the cognate amino acid

·· shown to stimulate Met-tRNA$_f^{Met}$ binding to ribosomes *in vitro* (Clark & Marcker, 1966b)

\# found as initiator codon in mRNA (Steitz, 1980; Sacerdot *et al.*, 1982).

⊕ complexes discussed in this paper.

only recently been investigated. Such studies are partly the subject of the following sections. The functional differences between $tRNA_f^{Met}$ and other tRNAs are shown in Table 1. The proteins and ribosomal interactions involving the different tRNAs are indicated with encircled symbols at complexes which are discussed in the subsequent sections.

In vitro studies of the 30S and 70S ribosomal Met-tRNA complex

The initiation of translation is believed to proceed via the formation of a complex between mRNA, 30S ribosomal subunit and formylmethionyl-tRNA$_f^{Met}$ as shown in Fig. 8. Because of the several exceptions to the general rule that the initiator tRNA methionine must be formylated, we wanted to study the *in vitro* formation of the 30S initiation complex. We have measured the binding of initiator Met-tRNA$_f^{Met}$, formylated and unformylated, to 30S ribosomal subunits, and we have studied the effects of different molecular components on this binding (Petersen *et al.*, 1976a).

Table 2 shows that crude initiation factor extracts stimulate the binding of both tRNA species in the presence of the synthetic messenger poly(A,G,U). In addition, it was shown that purified initiation factors

Table 2: Effect of different messengers on the binding of fMet-tRNA$_f^{Met}$, Met-tRNA$_f^{Met}$, and Met-tRNA$_m^{Met}$ to 30S ribosomal subunits in the absence and in the presence of initiation factors and GTP

Messenger	GTP	Crude IF	[Mg^{++}], mM	Relative molar binding to 30S ribosomal subunits		
				fMet-tRNA$_f^{Met}$	Met-tRNA$_f^{Met}$	Met-tRNA$_m^{Met}$
No	+	−	5	1	3	2
	+	+	5	4	2	1
ApUpG	+	−	5	3	2	2
	+	+	5	27	7	3
R17RNA	+	−	5	1	6	1
	+	+	5	74	13	1
Poly(A,G,U)	+	−	5	21	17	3
	+	+	5	183	35	8
	−	−	5	12	18	
	−	+	5	112	68	
	−	−	15	46	45	
	−	+	15	127	107	
	−	−	35	49	52	
	−	+	35	117	95	

(Petersen *et al.* 1976a).

had the same effect. This stimulation also exists in the presence of the trinucleotide codon for methionine ApUpG and in the presence of the natural messenger RNA from phage R17. No significant binding of the elongator Met-tRNA$_m^{Met}$ is found under any of these conditions.

Subsequently, preassociated 70S (tight couples) ribosomes were used in similar binding experiments, and as seen in Table 3, unformylated initiator Met-tRNA$_f^{Met}$ binds to 70S ribosomes in the absence of initiation factors. At low magnesium concentration, this binding is almost completely inhibited when initation factors are present during the incubation.

Contrastingly, formyl-Met-tRNA$_f^{Met}$ does not bind significantly to 70S ribosomes at low magnesium concentration. The addition of initiation factors shows the well-known stimulation of the binding of fMet-tRNA$_f^{Met}$.

Furthermore, Tables 2 and 3 show that GTP inhibits the binding of the unformylated initiator tRNA to both 30S and 70S ribosomes, both in the

Table 3: Effect of GTP on the binding of Met-tRNA$_f^{Met}$ and fMet-tRNA$_f^{Met}$ to 70S ribosomes in the absence and in the presence of initiation factors

Addition	Crude IF	pmol	
		Met-tRNA$_f^{Met}$	fMet-tRNA$_f^{Met}$
none	−	1.89	0.15
GTP	−	1.64	0.50
none	+	0.07	0.24
GTP	+	0.04	1.85

Incubation mixtures contained: 3.8 pmol of Met-tRNA$_f^{Met}$ or 2.8 pmol of fMet-tRNA$_f^{Met}$; 15 pmol of 70S ribosomes and, where indicated, 1 mM GTP and 49 μg of crude IF. Magnesium acetate, Tris-HCl buffer, ammonium chloride, and poly(A,G,U) were in the amounts described in the legend to figure 9 (Petersen et al., 1976b).

absence and in the presence of initiation factors, whereas this highenergy nucleoside triphosphate, as is well-established, stimulates the binding of fMet-tRNA$_f^{Met}$ in all cases. This may indicate that GTP binds directly to the 30S subunit and not through a complex with IF2.

To test whether the Met-tRNA$_f^{Met}$ bound to 30S ribosomal subunits is bound at the ribosomal P-site, 50S subunits were added after the binding to 30S, and subsequently puromycin was added. This antibiotic resembles the 3'-end of aminoacyl-tRNA and reacts with aminoacyl or peptidyl groups of P-site bound aa-tRNA or peptidyl-tRNA.

The results are seen in Figure 9 which shows that at least a part of the Met-tRNA$_f^{Met}$ which is bound to 30S ribosomal subunits is bound at a site which after addition of the 50S ribosomal subunit corresponds to the ribosomal P-site. About 50% of the totally bound Met-tRNA$_f^{Met}$ transfer methionine to puromycin.

The results show that formylation does not seem to be needed for the formation of a 30S initiation complex. Unformylated Met-tRNA$_f^{Met}$ is recognized by initiation factors in the presence of 30S ribosomal subunits and bound like fMet-tRNA$_f^{Met}$ at a puromycin reactive site (measured after addition of 50S ribosomal subunits).

As it will be discussed in a later section, this recognition may be caused by ribosome-bound initiation factors as free IF2 does not seem to have any significant affinity to Met-tRNA$_f^{Met}$.

This indicates that it is the structure of the initator tRNA$_f^{Met}$ – and not the formyl group – which is recognized by the 30S ribosomal subunit in the presence of initiation factors.

Fig. 9A. Binding of fMet-tRNA$_f^{Met}$ to 30S ribosomal subunits, effect of 50S subunits, and puromycin sensitivity in the absence (○) and presence (●) of initiation factors. Incubation mixtures (50 μl) contained, at time 0, 15 pmol of 30S subunits, 50 mM Tris-HCl (pH 7.4), 0.11 A$_{260}$ unit of poly(A,G,U), 5 mM magnesium acetate, 50 mM ammonium chloride, 1 mM GTP and 2.1 pmol fMet-tRNA$_f^{Met}$, and where indicated, 26 μg of crude initiation factor extract. After 10 min incubation at 37°C, 15 pmol of 50S ribosomal subunits were added. After an additional 10 min incubation, 5 μl of puromycin (5 μg/μl) were added. The amount of fMet-tRNA$_f^{Met}$ bound to ribosomes was measured by nitrocellulose filtration, and the amount of formylmethionine reacted with puromycin was measured by ethyl acetate extraction.

B. Binding of Met-tRNA$_f^{Met}$ to 30S ribosomal subunits, effect of 50S subunits, and puromycin sensitivity in the absence (○) and presence (●) of initiation factors. Same incubation mixtures as in A, except 3.0 pmol of Met-tRNA$_f^{Met}$ were used instead of fMet-tRNA$_f^{Met}$, and no GTP was added. Incubation periods are indicated with arrows corresponding to the time of the various additions (Petersen et al., 1976a).
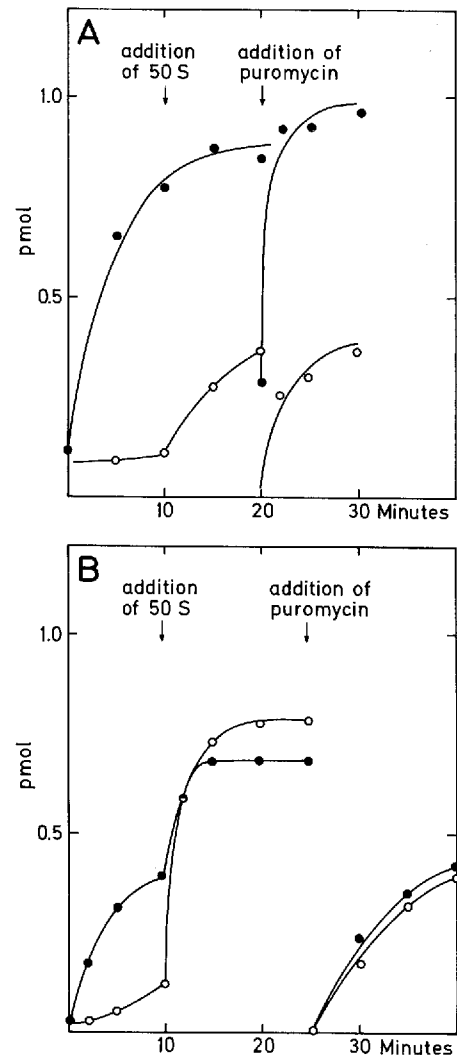
The finding that formylation is not essential for the formation of the 30S initiation complex may explain why some *E. coli* mutants can grow in the presence of trimethoprim (which inhibits the enzyme dihydrofolate reductase and thus the formation of the formyl donor [10]N-formyltetrahydrofolate (see previous section)).

Nevertheless, the initiator Met-tRNA$_f^{Met}$ has been found to be entirely formylated in almost all *E. coli* cells. What then is the role of the formylation? One explanation is that the N-blocking of the initiator tRNA methionine speeds up the rate of formation of the initiation complex as

suggested by Bretscher & Marcker (1966). A second or additional possible explanation arises from our finding that only the formylated Met-tRNA$_f^{Met}$ binds to 70S ribosomes in the presence of the initiation factors which were discovered after Bretscher's and Marcker's experiments.

Thus, the formyl group is necessary in cases where initiation of translation proceeds via the (untraditional) formation of a 70S initiation complex without a previous involvement of 30S ribosomal subunits. This possibility is investigated in the following section.

A two-state model for the 70S ribosome

In the preceding section it was shown that the 30S ribosomal subunit is apparently not able to distinguish between formylated and unformylated initiator Met-tRNA$_f^{Met}$, whereas the 70S ribosome discriminates strongly in favour of the formylated species in the presence of initiation factors (which is relevant to the situation *in vivo*) but – also in the absence of initiation factors – it was found that the 70S ribosome can distinguish between the two initiator tRNA species.

The behaviour of the 70S ribosome in this binding reaction has been studied in more detail, as it seems to possess the property to select the N-formylated initiator Met-tRNA$_f^{Met}$ (Petersen *et al.*, 1976b).

The ability of the 70S ribosome to discriminate between Met-tRNA$_f^{Met}$ and fMet-tRNA$_f^{Met}$ is found to be particularly strong at low

Table 4: Effect of potassium and magnesium ion concentration on the binding of fMet-tRNA$_f^{Met}$ and Met-tRNA$_f^{Met}$ to 70S ribosomes.

Potassium conc. (mM)	Magnesium conc. (mM)	fMet-tRNA$_f^{Met}$ (pmol)	Met-tRNA$_f^{Met}$ (pmol)
0	5	0.22	1.29
0	20	1.16	1.33
0	35	1.29	1.11
100	20	0.99	1.20
200	20	0.81	1.23
400	5	0.06	0.18
400	20	0.69	1.21
400	35	1.06	1.02

Incubation for 20 min at 37°C of the following mixture (50 µl): 15 pmoles of 70S ribosomes; 0.11 A$_{260}$ unit of poly(A,G,U); 1 mM GTP; 50 mM Tris-HCl (pH 7.4); 50 mM ammonium chloride; magnesium acetate and potassium chloride as indicated; and 3.0 pmol of fMet-tRNA$_f^{Met}$ or 3.8 pmol of Met-tRNA$_f^{Met}$. The amount of tRNA bound was analyzed by the Millipore filter assay (Petersen et al., 1976b).

Fig. 10. The equilibrium between 70S ribosomes and 30S + 50S subunits measured by light-scattering at 24°C as a function of magnesium concentration in the absence of potassium (○) and at 400 mM (●) (Petersen et al., 1976b).
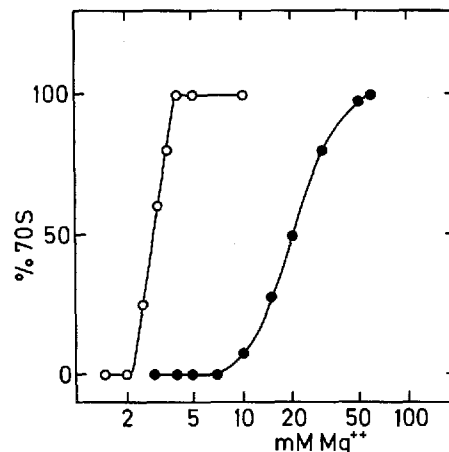
magnesium concentration (around 5 mM), whereas it disappears when the Mg^{++} concentration is increased to 20-35 mM (Table 4). It was also found (especially at low Mg^{++} concentrations) that high concentration of potassium (400 mM) strongly inhibits the binding of both initiator tRNA species to the ribosomes. The dissociation curve of ribosomes as a function of magnesium concentration (Fig. 10) shows that the ribosomes are 100% associated at 5 mM Mg^{++} in the absence of potassium (but in the presence of 50 mM ammonium chloride), whereas the ribosomes at 400 mM K^+ and 5 mM Mg^{++} are 100% dissociated. Thus the effect of potassium is in agreement with the results shown in the previous paragraph, neither of the two initiator tRNAs binds to ribosomal subunits in the absence of initiation factors.

Met-tRNA$_f^{Met}$ first bound to 30S subunits can react with puromycin after addition of 50S subunits (Fig. 9). A similar puromycin reaction is not possible for the Met-tRNA$_f^{Met}$ bound directly to the 70S ribosomes in the absence of initiation factors and at low concentrations of K^+ and Mg^{++} (50 mM and 5 mM, respectively). However, when the concentrations of these ions are increased to 400 mM and 35 mM, respectively (almost completely associated ribosomes), the Met-tRNA$_f^{Met}$ binds to a puromycin reactive site on the ribosome (Fig. 11).

The assay for the binding reaction requires filtration on nitrocellulose filters and therefore a reasonably high affinity between the compounds we want to isolate in complexed form, whereas the puromycin reaction takes place on the ribosome and liberates into solution the puromycin covalently bound to the radioactive amino acid, and the reaction product is easily extracted by ethylacetate. Thus, a much weaker binding to the

Table 5: Effect of messenger RNA (poly(A,G,U)) on the binding and puromycin reaction of fMet-tRNA$_f^{Met}$ and Met-tRNA$_f^{Met}$

	(pmol)	
	− poly(A,G,U)	+ poly(A,G,U)
fMet-tRNA$_f^{Met}$ binding	0.30	1.05
fMet-puromycin	2.01	1.68
Met-tRNA$_f^{Met}$ binding	0.11	0.95
Met-puromycin	1.75	1.41

Same incubation mixture as in Table 4 except that GTP was omitted; the amounts of magnesium acetate and of potassium chloride were 35 and 400 mM, respectively. Binding was measured after 20 min at 37°C. For the puromycin reaction, 25 µg of puromycin was added after 20 min at 37°C, and the reaction was continued for 5 min. The reacted amounts were analyzed by the ethyl acetate extraction technique (Petersen et al., 1976b).

ribosome of the Met-tRNA$_f^{Met}$ can be detected by the puromycin reaction compared to the "binding assay". It was therefore interesting to compare the effect of mRNA (synthetic poly(A,G,U)) in the two assays. As shown in Table 2, the binding of Met- and fMet-tRNA$_f^{Met}$ to 30S subunits in the presence of initiation factors depends completely on the presence of a messenger RNA. Table 5 shows that the binding to 70S ribosomes also is messenger-dependent, whereas the puromycin reactivity is found in the total absence of messenger.

It is also shown that the binding of Met-tRNA$_f^{Met}$ as well as fMet-tRNA$_f^{Met}$ is uninfluenced by tetracyclin, an antibiotic which at low con-

Fig. 11. Puromycin reaction of prebound initiator tRNA as a function of potassium concentration. The incubation mixture contained: 16 pmol of 70S ribosomes, 50 mM Tris-HCl (pH 7.4), 1 mM GTP, 35 mM magnesium acetate and 4.2 pmol of fMet-tRNA$_f^{Met}$ (○), 3.8 pmol of Met-tRNA$_f^{Met}$ (□) or 4.6 pmol of Met-tRNA$_m^{Met}$ (△). The reaction products were analyzed as described in the legend to Figure 9 (Petersen et al., 1976b).
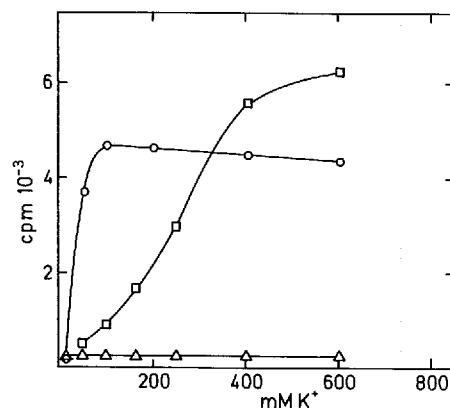
Table 6: Effect of tetracyclin on the binding of fMet-tRNA$_f^{Met}$, Met-tRNA$_f^{Met}$ and Met-tRNA$_m^{Met}$ to 70S ribosomes

	Translation Factors	tetracyclin	tRNA bound (pmol)
fMet-tRNA$_f^{Met}$	none	−	0.55
"	"	+	0.61
"	crude IF	−	1.44
"	"	+	1.47
Met-tRNA$_f^{Met}$	none	−	1.96
"	"	+	2.20
"	crude IF	−	0.39
"	"	+	0.52
Met-tRNA$_m^{Met}$	none	−	0.42
"	"	+	0.42
"	EF-Tu	−	0.84
"	"	+	0.40

Incubation mixtures were as in Table 4, except for the amount of magnesium acetate which was 5.5 mM and, where indicated: 50 µg of crude initiation factors (IF); 50 µg of elongation factor EF-Tu; 0.1 mM tetracyclin; 2.3 pmol of fMet-tRNA$_f^{Met}$; 5.2 pmol of Met-tRNA$_f^{Met}$; or 4.6 pmol of Met-tRNA$_m^{Met}$ (Petersen et al., 1976b).

centrations inhibits the binding of aminoacyl-tRNA to the ribosomal A-site (Table 6).

Parallel experiments were made with the elongator Met-tRNA$_m^{Met}$. In no case was this tRNA bound in response to initiation factors or showed any reaction with puromycin.

Thus, the 70S ribosome is able to distinguish between the initiator Met-tRNA$_f^{Met}$ and the elongator Met-tRNA$_m^{Met}$. In the absence of initiation factors, the initiator Met-tRNA$_f^{Met}$ binds very well to 70S ribosomes and can be triggered to react with puromycin. Under these conditions the elongator tRNA$_m^{Met}$ does not bind to the ribosome and reacts under no conditions with puromycin. Furthermore, the results show that 70S ribosomes discriminate strongly between formylated and unformylated initiator Met-tRNA$_f^{Met}$ both in the absence and in the presence of initiation factors. Contrary to the unformylated initiator tRNA, fMet-tRNA$_f^{Met}$ does not bind to 70S ribosomes in the absence of initiation factors. The amount of Met-tRNA$_f^{Met}$ bound in the absence of initiation factors is unaffected by tetracyclin.

This raises the following question:

1: Do two different 70S ribosomal sites exist for binding of fMet-tRNA$_f^{Met}$ and Met-tRNA$_f^{Met}$, respectively, or

2: Do two different conformations exist of the ribosomal P-site – the initiator tRNA binding site?

The latter is most likely because: The Met-tRNA$_f^{Met}$ does not bind to the A-site (no effect of tetracyclin) but can be triggered to react with puromycin (the definition of P-site bound aa-tRNA).

Therefore, we propose the existence of the equilibrium:

$$70S \rightleftharpoons 70S\star$$

between a 70S ribosome containing a P-site with inactive peptidyl transferase and a 70S$\star$ ribosome with an active peptidyl transferase (or a P$\star$-site).

This also suggests a function of the formylation of the initiator tRNA as fMet-tRNA$_f^{Met}$ only binds to the active P$\star$-site and thus pulls the equilibrium towards the active conformation, whereas Met-tRNA$_f^{Met}$ binds equally well to both conformations and thus does not change the equilibrium. Fig. 12 shows how Met-tRNA$_f^{Met}$ (M) and fMet-tRNA$_f^{Met}$ (FM) are supposed to bind to the two conformations at different conditions.
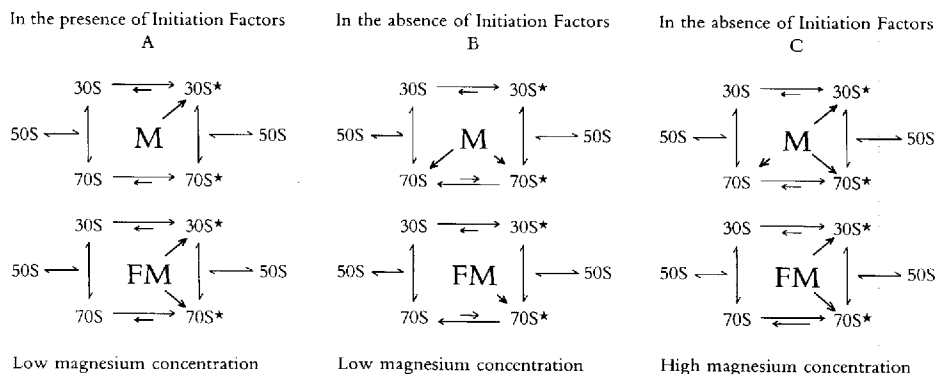
Fig. 12. A schematical presentation of how the position of the 30S and 70S ribosomal initiator tRNA binding site conformational equilibrium is supposed to be at low magnesium concentration (5 mM) (A and B), and high magnesium concentration (35 mM) (C) in the presence (A) and absence (B and C) of initiation factors. The length of the arrows from each initiator tRNA species indicates the relative affinity for the different ribosomal conformations, and the sum of arrows from one tRNA indicates the total binding at the respective conditions. M: Met-tRNA$_f^{Met}$, FM: fMet-tRNA$_f^{Met}$ (Petersen, 1980).

TP9 – a puromycin resistant E. coli *mutant*

As a consequence of the proposed hypothesis that the ribosomal P-site exists in two conformations, one would expect the equilibrium between these two conformations to be sensitive to mutations in the ribosomal components involved in the tRNA binding area. We know that puromycin binds to the ribosome in the region between the A-site and the P-site (Cooperman, 1980), and it would therefore be expected that bacterial strains permeable for but resistant to puromycin would be affected in the 70S $\rightleftharpoons$ 70S* equilibrium.

From the parental strain DL1 (a puromycin sensitive strain of *E. coli* K12), Dr. Antoine Danchin, Institut Pasteur, Paris, isolated a mutant (TP9) which was able to grow in broth medium supplied with the C-1 metabolites plus puromycin and trimethoprim.

In collaboration with Dr. Leif Isaksson at the Wallenberg laboratory, Uppsala, ribosomes isolated from TP9 were analyzed by two-dimensional polyacrylamide gel electrophoresis, and we found displaced positions of the ribosomal proteins S7, S20 (= L26) and L27. S7 is located at the tetracyclin binding site (A-site), and L27 is part of the peptidyl transferase centre and thus both the ribosomal A- and P-sites (Ofengand *et al.*, 1984). S20 is situated at the "head" of the 30S subunit and most probably at the interface between the two subunits (Stöffler *et al.*, 1979).

Ribosomes isolated from TP9 and DL1 were used in *in vitro* experiments where the kinetics of binding and puromycin reaction of Met-

Fig. 13. Kinetics of the puromycin reaction of Met-tRNA$_f^{Met}$ bound to 70S ribosomes from wild type (DL1) and puromycin resistent (TP9) E. coli cells. The curves show the amount of Met-puromycin formed as a function of time after 20 min binding incubation at 37°C in 50 mM Tris-HCl (pH 7.5), 35 mM magnesium chloride, 150 mM potassium chloride and 64 pmol of Met-tRNA$_f^{Met}$. The radioactivity corresponding to the amount of Met-tRNA$_f^{Met}$ bound to the ribosomes after 20 min is indicated (100%). Dotted lines indicate the time required for a puromycin reaction of twice the amount of Met-tRNA bound after 20 min (15.0 min for wild type and 21.8 min for TP9 ribosomes) (Petersen, 1980).
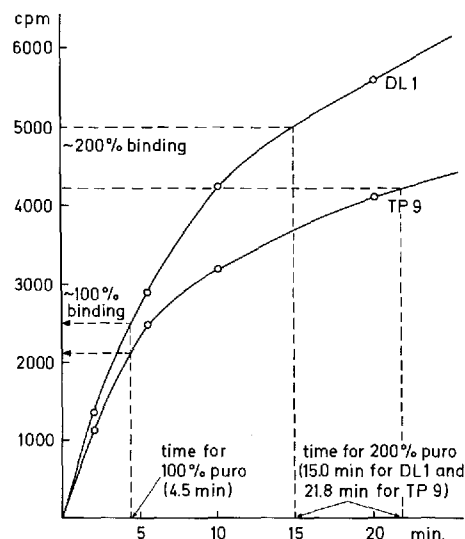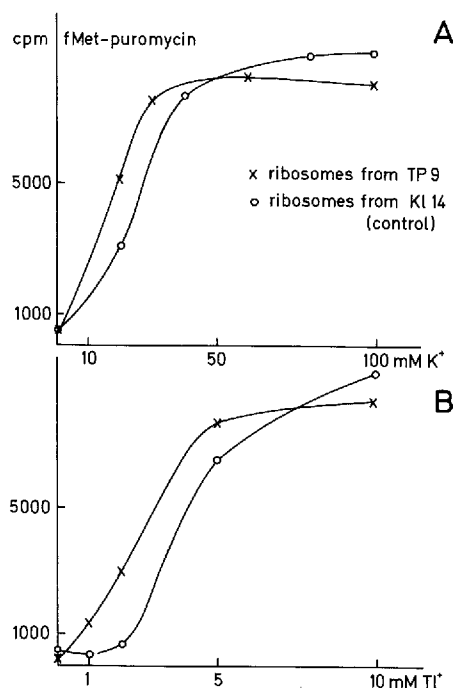
Fig. 14. Puromycin reaction of fMet-tRNA$_f^{Met}$ bound to wild type (Kl14) and TP9 ribosomes as a function of (A) potassium and (B) thallium concentration. Incubation conditions as described in the legend to Figure 13. Ethyl acetate extraction after 5 min puromycin reaction (Petersen, 1980).

tRNA$_f^{Met}$ were measured. No difference was found in the kinetics of the binding reaction, whereas a difference was observed in the puromycin reaction at prolonged time of incubation. As shown in Figure 13, the time needed to obtain a puromycin reaction corresponding to the amount of Met-tRNA$_f^{Met}$ bound is the same for the two types of ribosomes. A higher amount of puromycin reaction can be obtained if the incubation is continued, but in that case, the reaction proceeds much more slowly with the mutant ribosomes as compared to the control ribosomes.

This result may indicate that the mutation leading to puromycin resistance affects the ribosomal site of translocation in some so far unknown way.

The binding of fMet-tRNA$_f^{Met}$ to the wild type and mutant ribosomes was studied as a function of K$^+$ concentration (Figure 14.A). One sees the previously found sigmoidal shaped curve for the control ribosomes – indicating the double function of potassium ions in the 70S $\rightleftharpoons$ 70S$\star$ equilibrium and in the puromycin reaction, whereas the corresponding experiment with TP9 ribosomes gives a hyperbolic shaped binding curve. This indicates that with TP9 ribosomes, one of the two functions

of K^+ is suppressed – possibly the effect on the 70S $\rightleftharpoons$ 70S$\star$ equilibrium – as this may be strongly displaced toward the active form in the mutant.

As potassium ions may have a specific catalytic site at the peptidyl transferase center and not merely be required to obtain a certain ionic environment for the protein biosynthesis, we did similar experiments of binding and puromycin reaction replacing the potassium with varying concentrations of thallium, which is similar to K^+ with respect to stereochemical properties. Fig. 14B shows the results. To obtain similar amounts of fMet-puromycin, 10 times lower concentrations of Tl^+ as compared to K^+ is needed. This is a further indication of a specific ribosomal site for K^+ (Petersen, 1980).

Hypothesis on the role of the formyl group of fMet-tRNA$_f^{Met}$ in the translation of polycistronic messenger RNAs

Based on the *in vitro* experiments, a general function of the formyl group of fMet-tRNA$_f^{Met}$ in initiation of translation has been proposed (Petersen *el al.*, 1976b). In prokaryotes, the traditional view of the mechanism of initiation involved the formation of a 30S initiation complex. As shown in Table 2, the 30S ribosomal subunit (even in the presence of initiation factors) cannot discriminate between formylated and unformylated initiator tRNA, whereas in the presence of initiation factors, only the formylated species binds to 70S ribosomes (Table 3). Now, recall the situation in eukaryotic cells: 1) no formylation of the initiator Met-tRNA exists, and 2) no polycistronic mRNAs are known. Therefore, no initiation is possible at internal initiation sites in eukaryotic mRNAs.

In prokaryotes, the mRNAs commonly are polycistronic and one can imagine that the 5'-end proximal initation site always (as in eukaryotes) forms an initiation complex with 30S ribosomal subunits. This would not require formylation of initiator tRNA (although the rate of initiation is increased by the formylation which is in agreement with the fact that prokaryotic translation is 9-12 times faster than eukaryotic translation).

If the ribosome translating a polycistronic messenger does not dissociate into subunits after terminating the translation of the first cistron but as a 70S particle migrates through the intercistronic region of the mRNA (which varies considerably in length in different mRNAs), this 70S ribosome will be directly involved in the initiation complex formation at the next initiator codon. As only the formylated initiator tRNA binds to the

Table 7: Effect of trimethoprim, chloramphenicol and kasugamycin on the coordinate synthesis of β-galactosidase (Gz) and thiogalactoside acetyltransferase (Ac)

Strain	Addition (μg/ml)		Ratio (Gz/Ac)
CP78	None		1
	Trimethoprim	0.75	1.5
	Trimethoprim	1.5	2.4
	Chloramphenicol	1.5	1.06
	Chloramphenicol	2	1.14
	Kasugamycin	40	0.92
CP781a	None		1
	Trimethoprim	0.75	1.15
	Trimethoprim	1.5	1.2
	Chloramphenicol	1.5	1.1
	Chloramphenicol	2	1.2
	Kasugamycin	20	0.96

(Petersen *et al.*, 1978).

70S ribosome in the presence of initiation factors, the formylation is an absolute requirement in this situation.

From this hypothesis, one can predict that formylation of initiator tRNA methionine can be related to the polarity in the translation of polycistronic mRNAs in such a way that a decrease in the level of formylation under otherwise normal conditions will result in an increased polarity, 5'-end proximal cistrons being translated relatively more efficiently compared to 5'-end distal cistrons.

In vivo *polarity in lactose operon expression, role of formylation of initiator tRNA methionine*

It has been observed that *E. coli* mutants which were able to grow in the presence of low levels of trimethioprim – an inhibitor of formylation, see Figure 6 – contained an increased proportion of ribosomal subunits to 70S ribosomes as compared to wild type cells (Harvey, 1973). This is an indication that the cell can overcome the lack of formylation by increasing the proportion of 30S to 70S ribosomes, which is in agreement with the results that 30S and not 70S ribosomes are able to use unformylated Met-tRNA$_f^{Met}$ as initiator tRNA.

It is also expected from our hypothesis that depression of formylation

Fig. 15. Light-scattering measurement of the association of ribosomal subunits as a function of magnesium concentration at 150 mM potassium chloride and at 37°C. Ribosomes from strain CP78 (rpsL⁺) (○) and from strain CP781a (rpsL) (●) of E. coli (Petersen et al., 1978).
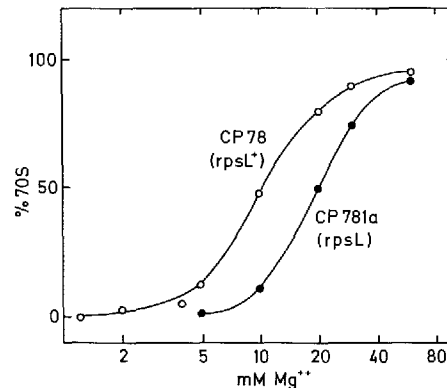
in normal growing cells will affect the ratio between the efficiency of translation of the 5'-end proximal and distal cistrons of polycistronic mRNAs in such a way that lack of formylation would favour the synthesis of the first protein rather than later proteins from the operon.

This is tested by measuring the *in vivo* translation of the first and the last cistron of the lactose operon in *E. coli* – β-galactosidase and thiogalactoside acetyltransferase, respectively (Petersen *et al.*, 1978). We have studied the effect of inhibition of formylation of initiator tRNA methionine on the relative synthesis of these two proteins in wild type cells and in *E. coli* mutants resistant to streptomycin and trimetroprim.

The presence of trimethoprim in the growth medium has a significant effect on the differential translation of the first and last cistrons of the lactose operon in *E. coli* wild type cells. This inhibitor of formylation results in a two-fold increase in the ratio: β-galactosidase/thiogalactoside acetyltransferase synthesized in wild type cells, whereas no significant effect was found in streptomycin resistant strains (Table 7). Control experiments with other antibiotic inhibitors (kasugamycin and chloramphenicol – which are inhibitors of initiation of translation without affecting the formylation of initiator tRNA methionine) showed that these compounds had no effect on the relative expression of the different cistrons in any of the tested strains.

Ribosomes were extracted from all tested strains and dissociation curves were measured. This showed that at conditions of pH, temperature and concentrations of mono- and divalent cations comparable to those found *in vivo*, the ribosomes from the mutant cells were significantly more dissociated than those from wild type cells (Fig. 15).

These results are consistent with the hypothesis that a significant part

of the ribosomes may pass through the intercistronic region from the previous termination step to the following initiation step without dissociating off the messenger. This could be the case when an unlimited amount of fMet-tRNA$_f^{Met}$ is available for the initiation, whereas the ribosome must dissociate and use a 30S subunit for the following initiation at low levels of formylation.

Our suggested mechanism also explains why, in eukaryotic cytoplasm, no formylation of initiator tRNA methionine is needed – as no cellular polycistronic mRNAs apparently exist.

Structural elements in initiator tRNA involved in specific interactions with proteins

As a consequence of the results discussed above, we have been interested in further investigation of the question: What are the specific structural elements in tRNA$_f^{Met}$ which are involved in and thus responsible for the different specific interactions with other macromolecules during the initiation process as shown schematically in Fig. 8? Recent developments in the methodology of nucleic acids research has made such investigations of molecular details possible.

In the following paragraphs, we will look a little more closely at the regions within the initiator tRNA$_f^{Met}$ which are implicated in these interactions. The effect of formylation is studied, and the results are compared to experiments with the elongator tRNA$_m^{Met}$ in the cases where the two tRNAs are involved in similar macromolecular interactions.

Two methods have been employed in these investigations: The footprinting method, in which ribonucleases are used for cutting the tRNA molecule at specific sites. The resulting RNA fragments are analyzed by polyacrylamide gel electrophoresis, which makes it possible to determine the exact cutting positions in the nucleotide sequence. Results from the treatment of free tRNA are compared to those from tRNA complexed to a protein molecule. In the case where different ribonucleases cut a particular position less efficiently in complexed tRNA as compared to free tRNA, it is concluded that this position is protected by the protein. The technical details of this method has been described recently (Petersen et al., 1984c).

The second method is based on the lability of the aminoacyl-ester bond in aminoacyl-tRNAs. The reaction of hydrolysis of this linkage is
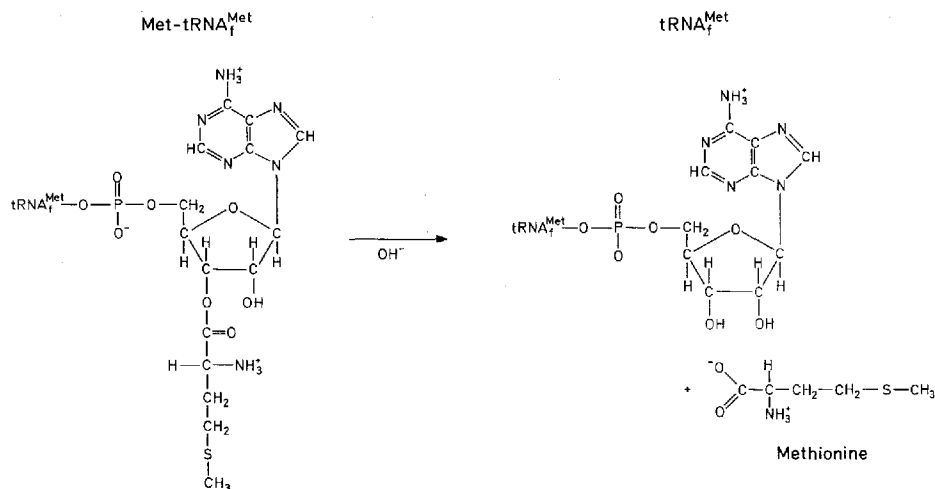
Fig. 16. Reaction of spontaneous hydrolysis of the aminoacyl ester bond in Met-tRNA$_f^{Met}$.

shown in Fig. 16. At neutral pH, the ester bond is hydrolyzed spontaneously at a rate which among other factors depends on the temperature. This method has been applied successfully in the study of interactions between elongation factor EF-Tu, GTP and different aminoacyl-tRNAs (Pingoud et al., 1977). The rate of hydrolysis of fMet-tRNA$_f^{Met}$ or Met-tRNA$_f^{Met}$ is measured in the absence or presence of proteins. In the case where the halflife of the ester bond is increased by the addition of a protein, it is concluded that an interaction takes place between the two macromolecules and in particular that a closer contact must take place at the amino acid attachment site.

In the following, results are described from such studies on interactions with methionyl-tRNA synthetase, initiation factor IF2, elongation factor EF-Tu and the 70S ribosome.

Interaction with methionyl-tRNA synthetase (MetRS)

Some characteristic features of the structure of the initiator tRNA$_f^{Met}$ as compared to that of the elongator tRNA$_m^{Met}$ can be studied by comparing the footprinting results from complexes between methionyl-tRNA synthetase and the two tRNAs. As described in an earlier paragraph, the enzyme aminoacylates both tRNAs with methionine in the reactions 1 and 2 shown in Figs. 8 and 23. Although, as shown, the tRNA enzyme interaction *in vivo* takes place after the binding of a methionyl-adenylate

to the enzyme (which may change the conformation of the enzyme), a stable complex between $tRNA_f^{Met}$ or $tRNA_m^{Met}$ and MetRS can be formed and isolated *in vitro* in the absence of other ligands (complex I in Fig. 8 and complex I in Fig. 23).

Results from experiments using T1, T2 and cobra venom RNases on the binary complex enzyme:tRNA with each of the two tRNAs are shown in Figs. 17 and 18 (Petersen *et al.*, 1984a). Regions which are protected by MetRS are shown in black, whereas locations which seem more accessible for nucleases in the complexed tRNAs are shown hatched.

The 3'-side of the anticodon loop is markedly protected by MetRS in both tRNAs. Differences are seen in the 5'-side of the anticodon stem, which is protected in $tRNA_f^{Met}$, but cut more intensely in $tRNA_m^{Met}$ when complexed to MetRS. Alternatively, the D-loop and the extra-loop are
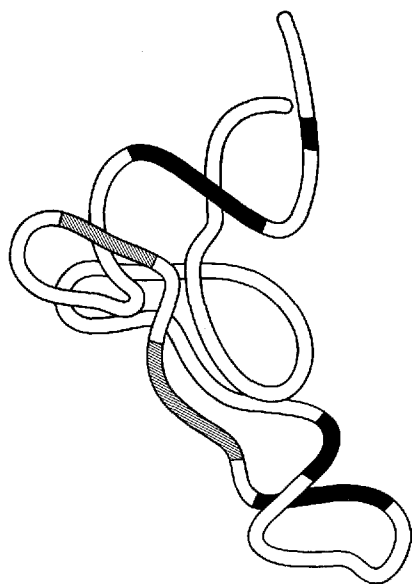
Fig. 17. Footprinting results from $tRNA_f^{Met}$ complexed to dimeric methionyl-tRNA synthetase are transferred to a tertiary structure model of $tRNA^{Phe}$ (see Fig. 3). Regions within $tRNA_f^{Met}$ which are protected (■) or cut more intensely by ribonucleases (▨) when complexed to MetRS are indicated (Petersen et al., 1984a).
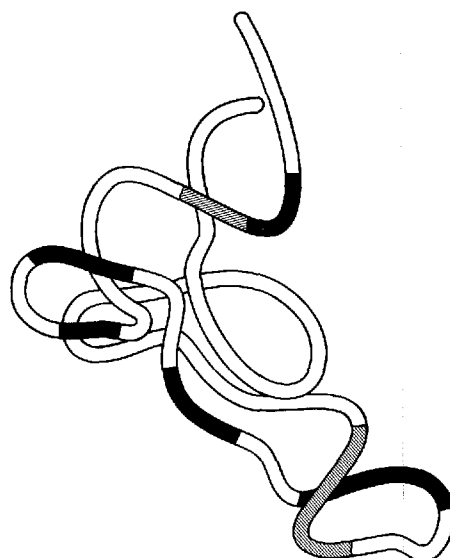
Fig. 18. Footprinting results from $tRNA_m^{Met}$ complexed to dimeric methionyl-tRNA synthetase are transferred to a tertiary structure model of $tRNA^{Phe}$ as described in the legend to Fig. 17 (Petersen et al., 1984a).

protected in complexed $tRNA_m^{Met}$, whereas both these regions are cut more intensely by RNases in $tRNA_f^{Met}$ as a result of complex formation.

It is known that cobra venom ribonuclease cuts tRNA at many positions in the acceptor region (Boutorin et al., 1981). MetRS shows only weak protection in the amino acid region. This supports the idea that (at least in the absence of the other substrates of the aminoacylation reaction), the acceptor region of tRNA is not strongly bound at the surface of the enzyme (Jacques & Blanquet, 1977).

Recent data indicate that also in the presence of methionine and ATP, no strong protection against cobra venom RNase digestion in the acceptor region takes place (H. U. Petersen, G. E. Siboska & S. Blanquet, unpublished). This result is in good agreement with the effect of MetRS on the spontaneous hydrolysis of the aminoacyl ester bond in fMet-$tRNA_f^{Met}$ in the presence of the initiation factor IF2, which is discussed in the next paragraph.

The interactions with the synthetase seem to be similar in the extreme parts (amino acid attachment site and anticodon region) of the tRNAs, whereas only $tRNA_m^{Met}$ seems to bind to the protein in the central part of the molecule. Thus, it can be concluded that the three-dimensional structures of the two molecules have differences in the region around the extra loop. In later paragraphs, it will be seen that the extra loop probably plays an important role for the specificity of the initiator tRNA.

Interaction with the initiation factor IF2

The initiation factor IF2 exists in 2 forms: IF2α (M_r 97300) and IF2β (M_r 79700), which are coded for by the same gene (Plumbridge et al., 1985). The DNA sequence of this gene has recently been determined in the laboratory of Dr. M. Grunberg-Manago (Sacerdot et al., 1984). As the available amounts of pure initiation factor protein has been used for functional studies and no attempt to crystallize the protein has been done, no information has been obtained on the higher order structure of these proteins. However, using small angle neutron scattering (at the equipment D11 of the Institut Laue-Langevin in Grenoble, France) we have determined the radius of gyration, R_g, of IF2 to be 45–48Å in solution, which indicates that the protein has a rather elongated shape (H. U. Petersen, M. Grunberg-Manago and B. Jacrot, unpublished).

Whilst it is well established that the protein chain elongation factor EF-Tu functions as an aminoacyl-tRNA carrier protein in a tertiary complex: EF-Tu:GTP:aa-tRNA during the elongation step of the prokaryotic translation, the question whether a similar complex is formed be-
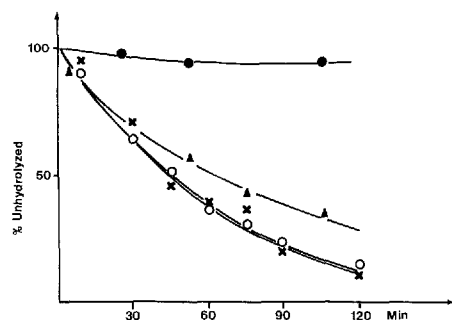
Fig. 19. Kinetics of the non-enzymatic hydrolysis of the aminoacyl ester bond of fMet-tRNA$_f^{Met}$ at 37°C in the absence (○) and presence (●) of initiation factor IF2 at 8 times molar excess, MetRS at 16 times molar excess (x) or both IF2 and MetRS at 8 and 16 times molar excess, respectively, (▲) (Petersen et al., 1984c).

tween the initiation factor IF2, GTP and fMet-tRNA$_f^{Met}$ during chain initiation (complex II in Fig. 8) has been the subject of intense debate for more than a decade. Although many different chemical and physical methods have been applied in such investigations, a complex of native IF2, fMet-tRNA$_f^{Met}$ and GTP has never been isolated (Petersen et al., 1979).

Previous studies have shown that IF2 invariably interacts with fMet-tRNA$_f^{Met}$. However, the extent of interaction with unformylated Met-tRNA$_f^{Met}$ varied from no detectable interaction to almost the same level as for the formylated species. Although it is clear that GTP hydrolysis is necessary for the formation of the functional 70S ribosomal initiation complex, no experiments have shown that GTP is required for IF2 to interact with the initiator tRNA. In addition, the ionic requirements for the formation of a binary complex IF2:fMet-tRNA$_f^{Met}$ has varied considerably. A general feature of all earlier experiments is the attempt to isolate a macromolecular complex, and such a complex may dissociate during the preparation, whereas the methods employed here do not require the isolation of a complex.

Fig. 19 shows the rate of hydrolysis of the aminoacyl-esterbond of fMet-tRNA$_f^{Met}$, free and in the presence of MetRS, IF2 or both proteins (Petersen et al., 1984c). This shows that MetRS has no effect itself on the rate of hydrolysis. The lack of protective effect is an indication that MetRS does not bind strongly at the aminoacyl-linkage. It also shows that MetRS (in the absence of AMP) does not catalyze the de-aminoacylation. In the presence of IF2, complete protection is observed. When increasing amounts of MetRS are added in the presence of sufficient amount of IF2 to obtain such complete protection, the effect of IF2 disappears. This is taken as an indication that MetRS and IF2 have overlapping binding sites on the tRNA molecule and, thus, in this experi-

Fig. 20. Footprinting results from fMet-tRNA$_f^{Met}$ in the presence of initiation factor IF2 are transferred to a tertiary structure model of tRNA^{Phe} as described in the legend to Fig. 17 (Petersen et al., 1984c).
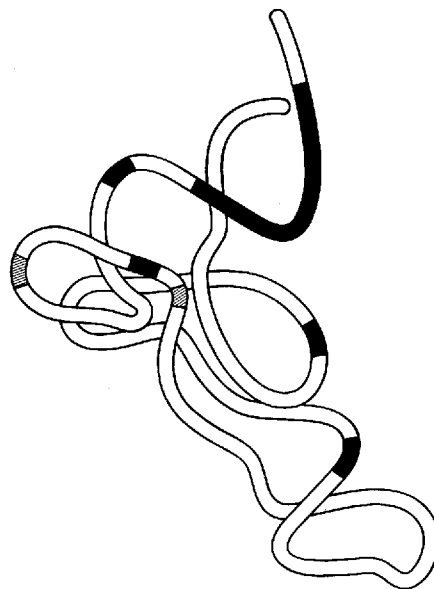
ment, compete for the binding to this site. However, it is also clear that the binding site of MetRS is not the 3'-terminal part of fMet-tRNA$_f^{Met}$, which, on the other hand, seems to be one of the important binding sites for IF2.

Similar experiments were done using unformylated initiator Met-tRNA$_f^{Met}$ or elongator Met-tRNA$_m^{Met}$ (Petersen *et al.*, 1979). In both cases, no effect was observed on the rate of hydrolysis when increasing amounts of IF2 were added. Although this method does not exclude the possibility that the protein binds to the tRNA, it is clear that an interaction similar to the one found with fMet-tRNA$_f^{Met}$ does not take place.

The binding site of IF2 on fMet-tRNA$_f^{Met}$ has been further investigated by footprinting experiments (Petersen *et al.*, 1981). Fig. 20 shows the regions which are protected or cut more intensely in fMet-tRNA$_f^{Met}$ complexed to IF2. In this case, only the double strand specific ribonuclease isolated from the venom of *Naja oxiana* has been used to digest the tRNA.

The protected regions include the 3'-end, both sides of the T-stem, the anticodon stem (in particular the 5'-side) and the D-stem. It seems that the protected regions are mainly located at the extreme parts of the L-shaped tRNA molecule, and no protection is found in the extra loop. This result is very similar to the one found with MetRS except that IF2 seems to be in closer contact with the 3'-end of the tRNA.

Footprinting experiments were also done with unformylated initiator tRNA. However, IF2 had no effect on the results obtained with free Met-tRNA$_f^{Met}$. This is a further indication that no binding takes place between IF2 and Met-tRNA$_f^{Met}$ and supports the idea that formylation adds a signal to the initiator tRNA for the specific interaction with IF2 in the absence of ribosomes.

Interaction with the 70S ribosome

As shown in reaction 7 of Fig. 8 and as discussed in detail in previous paragraphs, fMet-tRNA$_f^{Met}$ can bind non-enzymatically to the ribosomal P-site at 15-20 mM magnesium ion concentration. The complex described here was formed in this way in the absence of initiation factors, using a poly(A,G,U) RNA chain as a messenger (Petersen *et al.*, 1984c). In order to ensure that no unbound tRNA is present in the footprinting study, the complex was isolated on a Sepharose 6B column prior to enzymic digestion. Fig. 21 shows the regions in the tRNA$_f^{Met}$, which are protected against ribonuclease (RNases T1 and T2) digestion in the initiation complex in the absence of initiation factors. These are seen to be located in the aminoacyl-stem, the variable loop and in the part of the anticodon stem close to the extra loop. When compared to the footprinting results with MetRS and IF2, this is the first time we observe a strong protection of tRNA$_f^{Met}$ in the extra loop. The involvement of the extra
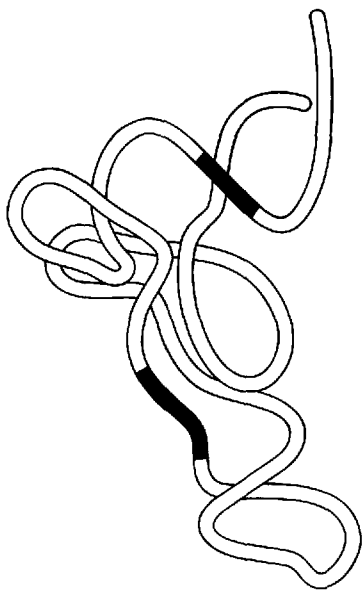
Fig. 21. Footprinting results from fMet-tRNA$_f^{Met}$ bound non-enzymatically to 70S ribosomes are transferred to a tertiary structure model of tRNA^{Phe} as described in the legend to Fig. 17 (Petersen et al., 1984c).

loop in tRNA interaction with the 70S ribosome has also been observed for the A-site binding of tRNA^{Phe} (Petersen *et al.*, 1984a), whereas other regions within the two tRNA molecules seem to have different degrees of involvement in A-site and P-site interactions (T. Jørgensen, personal communication). It must be noted that all the protected regions are found located at one side of the tRNA$_f^{Met}$ molecule, the side exposing the extra loop. Although it is too early to make a firm conclusion, this indicates the contact-face of the initiator tRNA when bound at the 70S ribosomal P-site.

Interaction with elongation factor EF-Tu

During the elongation steps of protein biosynthesis, aminoacyl-tRNAs form a ternary complex with the elongation factor EF-Tu and GTP. Elongation factor EF-Tu is an acidic protein consisting of 393 amino acids. The amino acid sequence has been determined in Aarhus (Jones *et al.*, 1980), where also a three-dimensional structure model of the molecule at 2.9 Å resolution has been obtained by X-ray crystallography (Morikawa *et al.*, 1978; Rubin *et al.*, 1981). Using the footprinting method, we have been investigating the interaction between this protein and different aminoacyl-tRNAs – in particular the elongator tRNA$_m^{Met}$ (Boutorin *et al.*, 1981; Wikman *et al.*, 1982). A summary of these results is seen in Fig. 22. In this case as well, all protected sites are found at one side of the tRNA$_m^{Met}$ molecule. Again, the extra loop seems involved in the interaction together with parts of the T-arm and the region near the amino acid attachment site.

As a comparison with tRNA$_f^{Met}$ (Fig. 8), the interactions involving tRNA$_m^{Met}$ prior to the binding at the ribosomal A-site in protein biosynthesis are shown schematically in Fig. 23. The aminoacylation is cataly-zed by MetRS (Reactions 1 and 2), and the synthetase is probably dis-placed by EF-Tu:GTP during the formation of the ternary complex (Reaction 3). Subsequently, the Met-tRNA$_m^{Met}$ is bound at the 70S ribosomal A-site carried by EF-Tu (Reaction 4).

Until recently, it was believed that only tRNA$_m^{Met}$ and not tRNA$_f^{Met}$ could take part in these two last reactions (reactions 3 and 4 in Fig. 23) (Ofengand, 1977). However, new experiments based on the protection by EF-Tu against pancreatic RNase digestion of the (unformylated) in-itiator Met-tRNA$_f^{Met}$ revealed that a ternary complex Met-tRNA$_f^{Met}$:EF-Tu:GTP can actually be formed (Tanada *et al.*, 1982). This is shown as reaction 8 in Fig. 8. We have confirmed this observation by isolating a ternary complex Met-tRNA$_f^{Met}$: EF-Tu:GTP. In experiments similar to
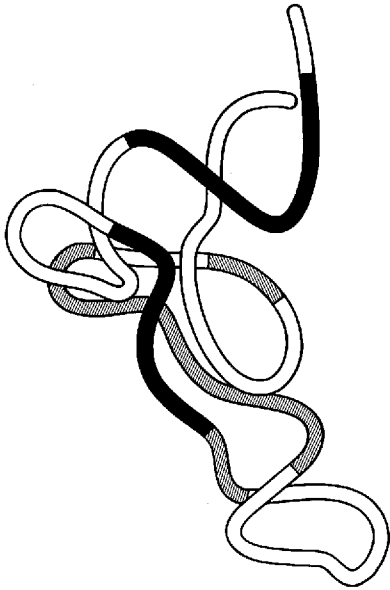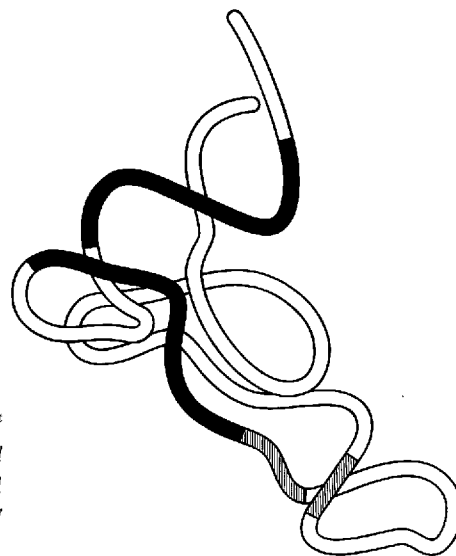
Fig. 22. Footprinting results from Met-tRNA$_m^{Met}$ complexed to the elongation factor EF-Tu and GTP are transferred to a tertiary structure model of tRNA^{Phe} as described in the legend to Fig. 17 (Wikman et al., 1982).

those shown in Fig. 19, we obtained a strong protection against hydrolysis of Met-tRNA$_f^{Met}$ by addition of EF-Tu:GTP, whereas no effect is found on the rate of hydrolysis of fMet-tRNA$_f^{Met}$ (P. Kamp Hansen, H. U. Petersen, J. W. B. Hershey & B. F. C. Clark, unpublished).

Thus, EF-Tu:GTP in bacteria may well discriminate against only the species fMet-tRNA$_f^{Met}$. The formylation could help play a role as security against the Met-tRNA$_f^{Met}$ acting as an elongator and translating incor-
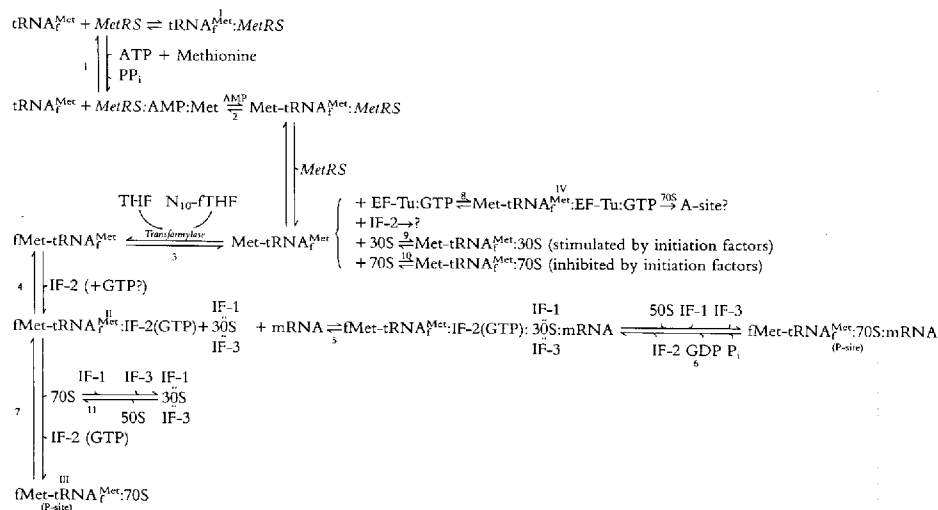
Fig. 23. Reactions involving the elongator tRNA$_m^{Met}$ prior to the binding at the 70S ribosomal A-site.

rectly at GUG and UUG, which the initiator species theoretically can do during initiation (Clark & Marcker, 1966b). What happens during eukaryotic protein biosynthesis in this connection is rather unclear, because the initiator species itself is not formylated and exists as Met-tRNA$_i^{Met}$. However, the whole selection of the initiator tRNA is more restricted in eukaryotes in the sense that more protein components are involved (Hershey et al., 1984). Of course, during bacterial protein initiation, as discussed in previous sections, initiation factors play a significant role in placing the initiator tRNA in the correct P-site for initiation. More detailed information about this interaction of the initiator tRNA were obtained by footprinting studies on the complex similar to those described above for elongator tRNA. Our results (Clark et al., 1984) are shown in Fig. 24. Although the studies have not been so extensive, we observed a similar general pattern of protection by EF-Tu:GTP against nuclease cutting of the initiator tRNA as for the elongator tRNA$_m^{Met}$ (Fig. 22) but with some small differences.

Again, we see protection in the aa-stem, T-stem and extra loop. In addition, the protection runs into the T-loop on both sides where we saw no changes for the elongator tRNA.

We are not able to decide at this time whether this should be interpreted in terms of extra covering by EF-Tu:GTP of the tRNA or steric hindrance due to local conformational changes.

What appears to be a reasonable conclusion is that bacterial Met-

Fig. 24. Footprinting results from Met-tRNA$_f^{Met}$ complexed to the elongation factor EF-Tu and GTP are transferred to a tertiary structure model of tRNA^{Phe} as described in the legend to Fig. 17 (Clark et al., 1984).

tRNA$_f^{Met}$, the initiator tRNA in the unformylated state, can indeed form a ternary complex with EF-Tu:GTP. This ternary complex also appears almost normal in the disposition of the aa-tRNA on the EF-Tu:GTP, so it should be able to bind to the ribosomal A-site if its formation is possible *in vivo*. We are presently investigating whether the small differences in the T-loop binding are sufficient for making a fit poor enough in the A-site to be selected against.

Conclusion

In summary this paper has described work on the function of initiator tRNA during the steps of protein biosynthesis initiation. We have suggested a role for the specific formylation of prokaryotic initiator tRNA methionine in the translation of polycistronic messenger RNAs. The
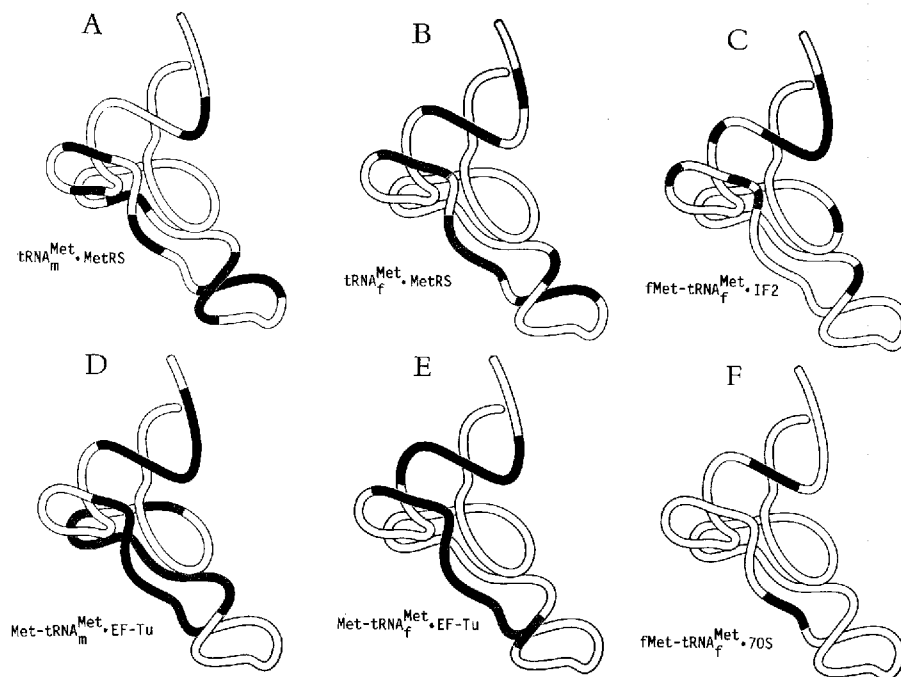
Fig. 25. A summary of the footprinting results shown in Figures 17, 18, 20-22, and 24. Regions protected in complexed tRNA are shown in red and regions cut more intesely are green. (A): tRNA$_m^{Met}$: Met-RS; (B): tRNA$_f^{Met}$: Met-RS; (C): fMet-tRNA$_f^{Met}$: IF2 (D): Met-tRNA$_f^{Met}$: EF-Tu; (E): Met-tRNA$_f^{Met}$: EF-Tu; (F): fMet-tRNA$_f^{Met}$: 70S.

regions within this tRNA which are involved in the interactions with proteins during the initiation process have been studied and the results are compared in figure 25. Although a firm conclusion about the exact sites of interactions with proteins requires further investigations – and ultimately the crystallization and X-ray diffraction structural determination of the tRNA within the complex – our results indicate some similarities and differences between the $tRNA_f^{Met}$ interactions with MetRS, IF2, EF-Tu and 70S ribosomes and also between the interactions with MetRS or EF-Tu of $tRNA_f^{Met}$ and the elongator $tRNA_m^{Met}$. The regions within the two tRNAs which are protected by proteins are shown in red and the regions which are cut more intensely in complexed tRNA are green.